frontiers | Research Topics

Application of remote sensing in coastal oceanic processes

Edited by
Lei Ren, Michael Hartnett, Xiaoteng Shen and Qing Xu

Published in
Frontiers in Marine Science



FRONTIERS EBOOK COPYRIGHT STATEMENT

The copyright in the text of individual articles in this ebook is the property of their respective authors or their respective institutions or funders. The copyright in graphics and images within each article may be subject to copyright of other parties. In both cases this is subject to a license granted to Frontiers.

The compilation of articles constituting this ebook is the property of Frontiers.

Each article within this ebook, and the ebook itself, are published under the most recent version of the Creative Commons CC-BY licence. The version current at the date of publication of this ebook is CC-BY 4.0. If the CC-BY licence is updated, the licence granted by Frontiers is automatically updated to the new version.

When exercising any right under the CC-BY licence, Frontiers must be attributed as the original publisher of the article or ebook, as applicable.

Authors have the responsibility of ensuring that any graphics or other materials which are the property of others may be included in the CC-BY licence, but this should be checked before relying on the CC-BY licence to reproduce those materials. Any copyright notices relating to those materials must be complied with.

Copyright and source acknowledgement notices may not be removed and must be displayed in any copy, derivative work or partial copy which includes the elements in question.

All copyright, and all rights therein, are protected by national and international copyright laws. The above represents a summary only. For further information please read Frontiers' Conditions for Website Use and Copyright Statement, and the applicable CC-BY licence.

ISSN 1664-8714
ISBN 978-2-8325-4750-2
DOI 10.3389/978-2-8325-4750-2

About Frontiers

Frontiers is more than just an open access publisher of scholarly articles: it is a pioneering approach to the world of academia, radically improving the way scholarly research is managed. The grand vision of Frontiers is a world where all people have an equal opportunity to seek, share and generate knowledge. Frontiers provides immediate and permanent online open access to all its publications, but this alone is not enough to realize our grand goals.

Frontiers journal series

The Frontiers journal series is a multi-tier and interdisciplinary set of open-access, online journals, promising a paradigm shift from the current review, selection and dissemination processes in academic publishing. All Frontiers journals are driven by researchers for researchers; therefore, they constitute a service to the scholarly community. At the same time, the *Frontiers journal series* operates on a revolutionary invention, the tiered publishing system, initially addressing specific communities of scholars, and gradually climbing up to broader public understanding, thus serving the interests of the lay society, too.

Dedication to quality

Each Frontiers article is a landmark of the highest quality, thanks to genuinely collaborative interactions between authors and review editors, who include some of the world's best academicians. Research must be certified by peers before entering a stream of knowledge that may eventually reach the public - and shape society; therefore, Frontiers only applies the most rigorous and unbiased reviews. Frontiers revolutionizes research publishing by freely delivering the most outstanding research, evaluated with no bias from both the academic and social point of view. By applying the most advanced information technologies, Frontiers is catapulting scholarly publishing into a new generation.

What are Frontiers Research Topics?

Frontiers Research Topics are very popular trademarks of the *Frontiers journals series*: they are collections of at least ten articles, all centered on a particular subject. With their unique mix of varied contributions from Original Research to Review Articles, Frontiers Research Topics unify the most influential researchers, the latest key findings and historical advances in a hot research area.

Find out more on how to host your own Frontiers Research Topic or contribute to one as an author by contacting the Frontiers editorial office: frontiersin.org/about/contact

Application of remote sensing in coastal oceanic processes

Topic editors

Lei Ren — Sun Yat-sen University, China
Michael Hartnett — University of Galway, Ireland
Xiaoteng Shen — Hohai University, China
Qing Xu — Ocean University of China, China

Citation

Ren, L., Hartnett, M., Shen, X., Xu, Q., eds. (2024). *Application of remote sensing in coastal oceanic processes*. Lausanne: Frontiers Media SA.
doi: 10.3389/978-2-8325-4750-2

Table of contents

04 Mapping the Changjiang Diluted Water in the East China Sea during summer over a 10-year period using GOCI satellite sensor data
Young Baek Son and Jong-Kuk Choi

22 Remote sensing and buoy based monitoring of chlorophyll *a* in the Yangtze Estuary reveals nutrient-limited status dynamics: A case study of typhoon
Yuying Xu and Jianyu Chen

40 Exploring CYGNSS mission for surface heat flux estimates and analysis over tropical oceans
Xiaohui Li, Jingsong Yang, Yunwei Yan and Weiqiang Li

54 Satellite-detected phytoplankton blooms in the Japan/East Sea during the past two decades: Magnitude and timing
Dingqi Wang, Guohong Fang, Shumin Jiang, Qinzeng Xu, Guanlin Wang, Zexun Wei, Yonggang Wang and Tengfei Xu

74 Analysis and prediction of marine heatwaves in the Western North Pacific and Chinese coastal region
Yifei Yang, Wenjin Sun, Jingsong Yang, Kenny T. C. Lim Kam Sian, Jinlin Ji and Changming Dong

94 Impact of ashes from the 2022 Tonga volcanic eruption on satellite ocean color signatures
Andra Whiteside, Cécile Dupouy, Awnesh Singh, Philipson Bani, Jing Tan and Robert Frouin

109 Intensification of "river in the sea" along the western Bay of Bengal Coast during two consecutive La Niña events of 2020 and 2021 based on SMAP satellite observations
Zhiyuan Li, Yu Long, Xiao-Hua Zhu and Fabrice Papa

125 Seasonal variability in spatial patterns of sea surface cold- and warm fronts over the continental shelf of the northern South China Sea
Jiayuan Chen and Zifeng Hu

136 Reconstructing three-dimensional salinity field of the South China Sea from satellite observations
Huarong Xie, Qing Xu, Yongcun Cheng, Xiaobin Yin and Kaiguo Fan

153 Sea level variation in the Arctic Ocean since 1979 based on ORAS5 data
Ying Jin, Meixiang Chen, Han Yan, Tao Wang and Jie Yang

165 Waves from compact SeaSonde® High Frequency radars in the southeastern Bay of Biscay: measurement performance under different noise and wind conditions
Lohitzune Solabarrieta, Maria Fernandes, Irene Ruiz, Macu Ferrer, Pedro Liria, Iñaki de Santiago, Jorge Sánchez, Jose Antonio Aranda and Anna Rubio

frontiers | Frontiers in Marine Science

TYPE Original Research
PUBLISHED 17 November 2022
DOI 10.3389/fmars.2022.1024306

Check for updates

OPEN ACCESS

EDITED BY
Michael Hartnett,
University of Galway, Ireland

REVIEWED BY
Shengqiang Wang,
Nanjing University of Information Science and Technology, China
Kui Wang,
Zhejiang University, China

*CORRESPONDENCE
Jong-Kuk Choi
jkchoi@kiost.ac.kr

SPECIALTY SECTION
This article was submitted to Ocean Observation, a section of the journal Frontiers in Marine Science

RECEIVED 21 August 2022
ACCEPTED 28 October 2022
PUBLISHED 17 November 2022

CITATION
Son YB and Choi J-K (2022) Mapping the Changjiang Diluted Water in the East China Sea during summer over a 10-year period using GOCI satellite sensor data.
Front. Mar. Sci. 9:1024306.
doi: 10.3389/fmars.2022.1024306

COPYRIGHT
© 2022 Son and Choi. This is an open-access article distributed under the terms of the Creative Commons Attribution License (CC BY). The use, distribution or reproduction in other forums is permitted, provided the original author(s) and the copyright owner(s) are credited and that the original publication in this journal is cited, in accordance with accepted academic practice. No use, distribution or reproduction is permitted which does not comply with these terms.

Mapping the Changjiang Diluted Water in the East China Sea during summer over a 10-year period using GOCI satellite sensor data

Young Baek Son[1] and Jong-Kuk Choi[2]*

[1]Jeju Marine Research Center, Korea Institute of Ocean Science and Technology, Jeju, South Korea, [2]Korea Ocean Satellite Center, Korea Institute of Ocean Science and Technology, Busan, South Korea

The Changjiang River loads freshwater into the East China Sea (ECS) and the Yellow Sea (YS). A low-salinity plume known as Changjiang Diluted Water (CDW) is formed by mixing with saline ambient waters; it disperses toward Jeju Island and the East/Japan Sea due to the dominant southerly wind and tide during summer. To map the offshore surface CDW in the ECS, a proxy was developed using surface water beam attenuation (*c*) and salinity from 18 annual summer cruises matched with synchronous Geostationary Ocean Color Imager (GOCI) satellite data. We followed a two-step empirical approach. First, a relationship between *in situ* salinity and *c* was obtained from hydrographic cruises (1998, 2003–2018, and 2021). Second, *in situ c* was matched with GOCI remote-sensing reflectance (Rrs) band ratios of all available blue-to-green wavelengths (2011–2018). Finally, satellite-derived surface salinity was determined directly by combining the two empirical relationships, providing a robust estimate over a range of salinities (22–34 psu). Our algorithm was then compared and validated with five previous satellite-derived salinity algorithms based on colored dissolved organic matter and particle concentrations. In the first step, surface salinity was matched and well correlated with *c* using an 18-year full conductivity–temperature–depth (CTD) dataset (N = 1,345, R^2 = 0.93). In the second step, *c* was synchronously matched and well correlated with GOCI Rrs band ratios using an 8-year summer CTD dataset (N = 391, R^2 = 0.93). The satellite-derived surface salinity based on the GOCI was compared with five other approaches and validated using an 8-year summer CTD dataset (2011–2018, N = 707, RMSE = 0.43, bias = 0.053, mean ratio = 1.002). We mapped satellite-derived surface salinity using monthly GOCI images during the summer from 2011 to 2020. The spatial patterns of the CDW were connected to the Changjiang River

mouth and extended to the east–northeast during summer. Saline water was confined to the warm current and the upper slope in the eastern part of the study area. Anomalous dispersion of the CDW occurred in August 2016, 2017, and 2020, and limited dispersion occurred in August 2014 and 2019.

KEYWORDS

Changjiang Diluted Water (CDW)1, East China Sea2, GOCI3, satellite-derived surface salinity4, Changjiang river discharge5

Introduction

The East China Sea (ECS) is a continental marginal sea in the Western Pacific that interacts with various surface water systems, including freshwater from the Changjiang River, Kuroshio, and Taiwan Warm Current. The Changjiang River (also called the Yangtze River) is the third largest river in the world based on length (6,300 km) and the fifth largest based on discharge (Beardslev et al., 1985). The Changjiang River Discharge (CRD) shows large seasonal and interannual changes. It discharges into the ECS and Yellow Sea (YS) as a major freshwater source and forms the Changjiang Diluted Water (CDW) by mixing with saline ambient waters. In winter, the CDW flows south or southeastward due to the dominant northeasterly wind. In summer, the CDW extends eastward from western Jeju Island to the Korea/Tsushima Strait due to the prevailing southerly wind and the increasing CRD (Chang and Isobe, 2003; Lie et al., 2003; Senjyu et al., 2006), which takes 1–2 months to travel from the Changjiang River mouth to the Korea/Tsushima Strait (Kim et al., 2009b; Yamaguchi et al., 2012). In August 1996, the CDW (< 20 psu) passed about 50 km west of Jeju Island, causing widespread death of coastal wildlife (economic damage: US$600 million). In August 2016, abnormally low-salinity and high sea surface temperature waters were observed along the coast of Jeju Island (Moh et al., 2018; Moon et al., 2019). Anomalous sea surface warming during the summer in the ECS is associated with the dispersion of the CDW, forming a boundary layer that enhances vertical stratification and reduces vertical mixing (Park et al., 2011; Park et al., 2015; Moh et al., 2018; Moon et al., 2019). However, the CDW plays an important role in sea surface warming (Park et al., 2011; Park et al., 2015; Moon et al., 2019) and exerts a considerable effect on the oceanographic and ecological environment in the ECS, including the coast of Jeju Island, Korea. Previous studies have found that the extensive CDW corresponds with higher particle concentrations during summer, suggesting the possibility of determining the relationship between the CDW and the particle load from field measurements and satellite data (Kim et al., 2009b; Moh et al., 2018).

The ability to determine surface salinity from satellite data may significantly aid physical, chemical, and biological oceanography research. Salinity generates no optical signal and is therefore difficult to measure using ocean color satellite images. The Aquarius satellite is designed to measure salinity from space using microwave sensing (Wentz and LeVine, 2012). After the launch of the Aquarius, many satellite sensors, including the Soil Moisture and Ocean Salinity (SMOS) and Soil Moisture Active Passive (SMAP) sensors, were developed to improve salinity estimates from space. Although this was a major step forward, the spatial and temporal resolutions (25–100 km, 5–7 days) were too coarse to observe small mesoscale features, the sensors could not be used close to land, and the data had to be calibrated using *in situ* measurements. The spatial and temporal coarseness of measurements has limited our ability to monitor the rapidly changing ocean environment in the ECS.

In many previous studies, colored dissolved organic matter (CDOM) signals provided a reliable indicator of river plumes and low-salinity water conditions in coastal areas (Binding and Bowers, 2003; Ahn et al., 2008; Sasaki et al., 2008; Bai et al., 2013). The optical parameters derived from satellite-based remote-sensing reflectances (Rrs), such as CDOM and detritus, are difficult to quantify individually but provide a c response term when combined (absorption coefficient of detritus/gelbstoff (a_{dg})) (Roesler and Boss, 2005; Siegel et al., 2005b). Particles and CDOM may be useful proxies for detecting low-salinity water. However, particulate matter (PM) and CDOM in the water column cause light attenuation due to absorption and scattering and can be used to detect and monitor river plumes or water quality based on *in situ* observations and ocean color satellite studies (Binding and Bowers, 2003; Ahn et al., 2008; Sasaki et al., 2008; Choi et al., 2012; Son et al., 2012; Bai et al., 2013; Moh et al., 2018; Choi et al., 2021). Several previous studies have shown a correlation between salinity and CDOM (Binding and Bowers, 2003; Ahn et al., 2008; Sasaki et al., 2008; Bai et al., 2013) and between salinity and particles or chlorophyll-*a* (Kim et al., 2009b; Son et al., 2012; Choi et al., 2021), thus allowing the estimation of satellite-derived salinity. Moh et al. (2018)

observed a loaded sediment plume extending eastward along the shelf from the Changjiang River to Jeju Island *via in situ* and satellite data obtained within the CDW. Beam attenuation due to particles has been studied using in-water transmissometer measurements (Gardner et al., 1993; Chung et al., 1998); it is well correlated with PM and particulate organic carbon (POC), and thus with satellite observations (Mishonov et al., 2003; Gardner et al., 2006; Son et al., 2009a; Son et al., 2009b; Son et al., 2012). Detecting salinity using PM (including organic and inorganic matter and perhaps CDOM) is more useful for tracing the CDW in the offshore ECS than focusing solely on the relationship between CDOM and low-salinity water.

In the present study, we identified the limitations of previous approaches for detecting the CDW, including their use of different satellite sensors, regions, and/or salinity ranges. We aimed to develop an effective salinity detection algorithm in the ECS based on satellite data (e.g., Geostationary Ocean Color Imager (GOCI) data) by comparing salinity estimates with *in situ* measurements and compared our approach with five existing salinity algorithms.

Material and methods

Shipboard data

Surface salinity and temperature data obtained from conductivity–temperature–depth (CTD) casting were collected from the National Institute of Fisheries Science (NIFS, http://www.nifs.go.kr/kodc.eng/eng_soo_list.kodc). Data were collected during the serial hydrographic cruises carried out around the ECS four to six times per year and during the hydrographic cruises by the Korea Institute of Ocean Science and Technology (KIOST) in the ECS (Table 1). Both full hydrographic datasets were collected by a SeaBird CTD sensor at each station (Figure 1). During each CTD cast of the KIOST research survey, the optical beam attenuation (c) was observed synchronously. The c due to particles was measured in the red spectral band (660 ± 10 nm) with a SeaTech 25-cm path length transmissometer using standard protocols (Gardner et al., 2006). The percent transmission (T) was determined and converted to the total beam attenuation coefficient (c) by $c = (\ln(T))/r$, where r is the path length of the transmissometer.

Both surface salinity datasets used the climatological mean value to understand the spatial distribution of summer salinity in the study area. The surface salinity and c data of KIOST cruises were collected in September 1998, July–September in the period 2003–2018, and June 2021. The surface datasets collected from KIOST research cruises were used to develop a satellite-derived salinity algorithm. The surface salinity data obtained from NIFS cruises in the summer season from 2011 to 2018 were used to validate each method. Another surface salinity validation dataset was collected using a Liquid Robotics Wave Glider SV3 (Moh et al., 2018; Son et al., 2020). A SeaBird Electronics CTD was mounted on a submersible glider at depths of 0 and 8 m. Temperature and salinity were recorded at 30-min intervals and transferred to the Wave Glider management system *via* the Wave Glider's Iridium satellite link. The Wave Glider was directed from the west region (low-salinity and high-turbidity water) to the east region of Jeju Island, Korea (high-salinity and low-turbidity water). The Wave Glider was launched from the south of Jeju Island from 19 August to 22 September 2016 and from 24 August to 14 September 2017 (Figure 1). The surface salinity data from NIFS cruises and both Wave Glider deployments were used to validate the satellite-derived salinity algorithm.

Changjiang river discharge

The daily flow rate of the Changjiang River measured at Datong Station (1998–2021) was collected (www.cjh.com.cn) and converted to monthly discharge to understand its variations during summer (Figure 2). The climatological mean values in

TABLE 1 *In-situ* measurement data collected from KIOST and NIFS research cruise.

Match-up data between *in-situ* salinity vs. c_p	Sep. 1998	CTD	KIOST
	Jul.-Sep. 2003-2018	CTD	KIOST
	Jun. 2021	CTD	KIOST
Validation data between *in-situ* salinity and estimated salinity	Jul.- Aug. 2011-2018	CTD	NIFS
	19 Aug.-22. Sep. 2016	Wave Glider (CPCTD)	KIOST
	24 Aug.-14 Sep. 2017	Wave Glider (CPCTD)	KIOST

* KIOST, Korea Institute of Ocean Science Technology; NIFS, National Institute of Fishery Science.

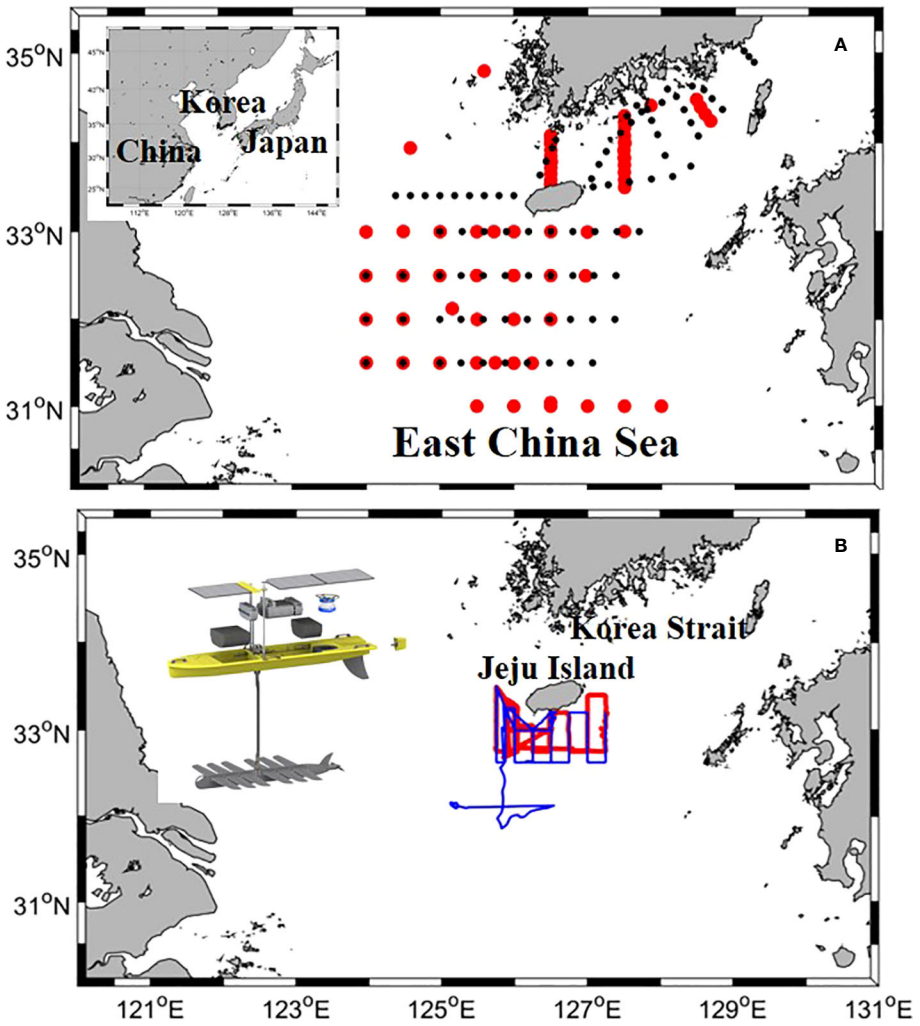


FIGURE 1
Study area and sampling stations of summer cruises conducted in 1998, 2003–2018, and 2021. **(A)** Red dots indicate matched *in situ* and satellite data sampling points; black dots indicate sampling points for validating the model and *in situ* data. **(B)** Red and blue lines indicate the sampling lines used for algorithm validation, as observed by wave gliders during the summer of 2016 and 2017.

summer were 40,849 (June), 50,752 (July), and 43,867 (August) m^3/s.

Satellite data

The Moderate Resolution Imaging Spectroradiometer (MODIS) climatological monthly means (2003–2021, level 3) of the chlorophyll-*a* and PM covering the ECS were obtained from the NASA Ocean Biology Processing Group (http://oceancolor.gsfc.nasa.gov/) and remapped with a 9-km resolution.

The daily Quick SCATterometer (QuickSCAT) and Advanced SCATterometer (ASCAT) sea surface wind (SSW) data were downloaded from PO.DAAC (http://podaac.jpl.nasa.gov/), and monthly mean values were calculated.

The GOCI, the world's first geostationary ocean color satellite, was developed to monitor the marine environment and provide prompt and timely warnings of marine hazards. It has six visible bands (412, 443, 490, 555, 660, and 680 nm) and two near-infrared (NIR) bands (745 and 865 nm), and provides images with a 500-m spatial resolution at hourly intervals up to eight times per day in the Northeast Asian region (Ryu and Ishizaka, 2012). Daily GOCI data (level 1b) were collected from the Korea Ocean Satellite Center (KOSC, http://kosc.kiost.ac.kr/) on 1 June and 31 September from 2011 to 2020 (eight images from 09:00 to 16:00 local time each day). GOCI Rrs(λ) data were derived from level 1b data using the standard atmospheric

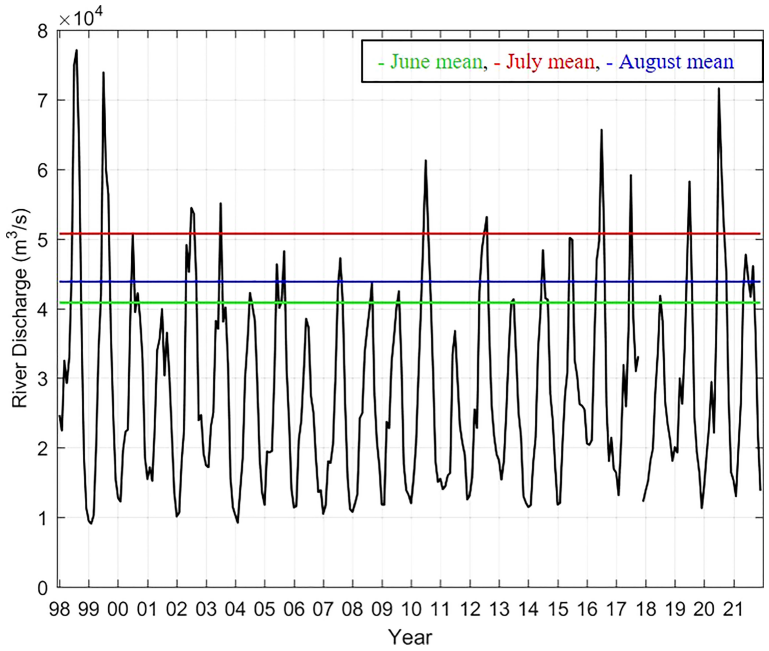


FIGURE 2
Monthly Changjiang River Discharge (CRD) from 1998 to 2021 (obtained by averaged daily observations).

correction algorithm embedded in the GOCI data processing software (GDPS) (Ryu et al., 2012).

A dataset matching *in situ c* and synchronously obtained GOCI Rrs(λ) was generated. To ensure reasonable matches, Bailey and Werdell (2006) and Son et al. (2009a; 2009b; 2012) suggested that SeaWiFS data be extracted for the locations of ship stations when *in situ* and satellite measurements are made within a ± 3-h window of local noon (09:00–15:00 local time). However, GOCI provided eight images during the daytime (09:00 to 16:00 local time). In this study, we matched the synchronous time without using a ± 3-h window. Additional conditions for the satellite data were that the matrix size did not significantly degrade the geophysical homogeneity among the pixels used and that >50% of the pixels were free of clouds and other sources of error. A 5 × 5 pixel grid provided sufficient pixels for confidence in the average value, without being so large as to cross parameter gradients. Using these criteria, 391 subsamples (~29.1% of the 1,345 total samples) were matched with GOCI spectral data. GOCI Rrs(λ) was used to determine *c* and was then correlated with surface salinity using empirical approaches. For error assessment of the present and previous approaches, we used 707 subsamples (391 matched subsamples and 316 surface-salinity subsamples from NIFS and Wave Glider surface salinity).

To develop our satellite-derived salinity estimates in the ECS, we used ocean color data derived from apparent optical properties (remote-sensing reflectance), and then we computed the forward or inverse correlation of the data with in-water constituents. We used a two-step approach to estimate the surface salinity from ocean color satellite data (Binding and Bowers, 2003; Ahn et al., 2008; Sasaki et al., 2008; Son et al., 2012; Bai et al., 2013). The first step was to correlate *in situ* salinity with *in situ* parameters (*c*). The second step was to correlate Rrs band ratios with *c*, which had a much stronger correlation than PM, POC, and chlorophyll-*a* (Son et al., 2012). Satellite-derived salinity was then determined by combining these two relationships. A multiple-wavelength approach was used to determine *c*. Son et al. (2009b) demonstrated that when the surface particle concentration increased, the radiance peak shifted toward longer wave bands. They proposed the maximum normalized difference carbon index (MNDCI), which uses the maximum band ratio among 412, 443, or 490 over 555 nm for SeaWiFS data and regresses the results with the surface concentrations of POC. We used the maximum band ratio among 412, 443, or 490 over 555 nm for GOCI data. Salinity was also calculated from previous studies to provide an error assessment with 707 subsamples (NIFS and Wave Glider CTD data). Five previous approaches for estimating salinity relied on Rrs data to estimate CDOM absorption and particles and then estimated empirical relationships with salinity. Two studies were performed in different parts of the ocean [the

Clyde Sea, Scotland (Binding and Bowers, 2003) and the Gulf of Mexico (Son et al., 2012)], and three were conducted in the ECS (Ahn et al., 2008; Sasaki et al., 2008; Bai et al., 2013). The Sasaki et al. (2008) approach used CDOM absorption and total chlorophyll-*a* (under high and low chlorophyll-*a* concentration conditions; chl-*a* > 1.3 and< 1.3 mg m^{-3}) to estimate salinity. Binding and Bowers (2003); Ahn et al. (2008), and Bai et al. (2013) used CDOM absorption, and Son et al. (2012) used particle concentration. However, all previous and new algorithms used two-step approaches for deriving satellites from satellite images. The measurement error of all salinity algorithms was given by the root mean square error (RMSE), the bias, and the mean ratio.

$$RMSE = \sqrt{\frac{\sum((estimated_Salinity) - (in\quad situ_Salinity))^2}{N}}$$

$$bias = \frac{1}{N}\sum((estimated_Salinity) - (in\quad situ_Salinity))$$

$$mean\quad ratio = \frac{1}{N}\sum\left(\frac{(estimated_Salinity)}{(in\quad situ_Salinity)}\right)$$

Finally, to determine the offshore CDW in the ECS during the summer season, maps of satellite-derived surface salinity were created and compared in terms of *in situ* surface salinity and GOCI-derived salinity. Monthly climatological satellite images of salinity were used to understand the annual and interannual variation of the CDW in the ECS over the summer season.

Results and discussion

The spatiotemporal oceanic environment in the ECS

We focused on the summer season (June–August) to examine the temporal and spatial development of the CDW. The MODIS climatological monthly means (2003–2021) of surface chlorophyll-*a* and PM estimates were used to create distribution maps of the summer seasons for the ECS (Figure 3). The highest chlorophyll-*a* and PM values were consistently seen on the inner shelf and diminished offshore. During August, moderate chlorophyll-*a* and PM patches extended into Jeju Island with east- or northeastward plumes. A CDW patch with elevated surface chlorophyll-*a* and PM values stretched over the shelf from the Changjiang River mouth in the northeast direction. This was related to the increasing river discharge (Figure 2) and change in wind direction (from northerly in winter to southerly and/or southeasterly in summer). The CDW is dispersed in the eastward direction, and salinity gradually increases through mixing with saline ambient waters (Lie et al., 2003; Chang and Isobe, 2005; Senjyu et al., 2006; Kim et al., 2009b; Moon et al., 2019).

The CRD showed distinct seasonal variations that peaked in July and reached a minimum in January (Figure 2). The CRD was at its highest during summer in 1998–1999, which is related to flooding events (Delcroix and Murtugudde, 2002). The CRD was at its lowest during the summers of 2006 and

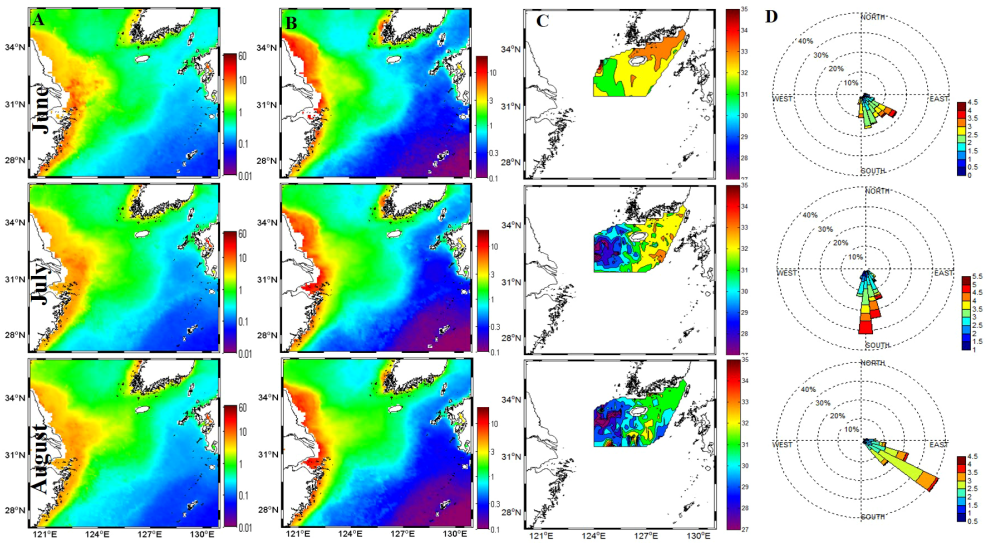


FIGURE 3
Distributions of **(A)** chlorophyll-*a* (mg/m^3), **(B)** particulate matter (g/m^3), **(C)** *in situ* surface salinity (psu), and **(D)** sea surface wind (m/s) in the East China Sea in summer.

2011, with decreased seasonal variation; these events may have been related to extreme drought conditions and the second impounding of the Three Gorges Dam (TGD) (Dai et al., 2008). The CRD continuously decreased until 2009, following the completion of the TGD, and then slightly increased during July 2010. However, the CRD was at its highest during the summer of 2016 since 1999, although the freshwater was controlled by the TGD. Extreme flooding occurred in mainland China, which increased suddenly in early July and reached >70,000 m^3/s. During August 2016, the CRD was also larger than the mean value. Delcroix and Murtugudde (2002) suggested that the anomalous riverine input is linked to anomalous precipitation over large areas of China, resulting in a change in sea surface salinity of about 6 psu and transportation of freshwater over 500 km in the ECS. To determine the influence of the CDW in the ECS, especially the middle ECS and Jeju Island (Figure 1), we used summertime-series data to develop the satellite-derived salinity results.

Validation of a two-step approach based on *in situ* data

The CRD showed distinct annual cycles, with the highest flow occurring in the summer and the lowest in the winter (Figure 2). The wide range of the CRD led to seasonal variation in the transport of particles to shelf and coastal regions (Figure 3). The fate of surface PM released to the shelf area in the ECS is controlled by wind and physical forcing (Kim et al., 2009b; Moh et al., 2018; Moon et al., 2019). We followed a two-step approach to develop a reliable method for detecting the offshore CDW, focusing especially on the summer seasons and the middle ECS.

Figure 4A shows the relationship between surface salinity and c obtained *via* 18 yearly summer cruises (in 1998, 2003–2018, and 2021). There were 1,345 data points from >100 sampling stations in the ECS. The surface salinity ranged from 22 to 34 psu, and c from 0.01 to 1.5 m^{-1}, during all summer cruises. The mean, maximum, and minimum salinity values were 30, 34.4, and 22 psu, respectively; those of c were 0.7, 1.5, and 0.01 m^{-1}, respectively. Gong et al. (1996) and Kim et al. (2009a) suggested a definition of the CDW based on water-type classification below 31 psu. We followed this definition in the present study, and qualifying data points comprised ~48% of the total dataset.

From the 18-year dataset of ECS summer cruises, we were able to assess the relationship between surface c and salinity over a wide range of summer water conditions (22–34 psu). To determine the spatial coverage of this correlation, c and salinity data were used from the middle of the ECS to the south coast of Korea. The resulting regression (Figure 4A) using a logarithmic fit is

$$Salinity(psu) = 10^{[-0.135\times C+1.53]} \quad (1)$$

Surface salinity was proportional to beam attenuation (Figure 4A, F = 53.9, p< 0.01, R^2 = 0.93, N = 1,345). Saline water was accompanied by a lower c, and the CDW was inversely correlated with c during these cruises. The correlations between a proxy of particle concentration (c) and salinity suggested that the concentration of particle-laden water could provide a useful estimate of salinity from space (Kim et al., 2009b; Son et al., 2012). Particle components (PM, POC, and chlorophyll-*a*) are determined by applying empirical, semianalytical, and/or modeling approaches to ocean color products (Mishonov et al., 2003; Gardner et al., 2006; Son et al., 2009a; Son et al., 2009b). It is reasonable to expect c and salinity to vary widely in the area of the ECS (Figures 3, 4) because the Changjiang River delivers a large mass of particles to the shelf environment, and particulate plumes are widely dispersed along and across the shelf (Moh et al., 2018). Although c varies as a function of the particle size and shape and the index of refraction, as long as the average bulk particle properties remain similar, c is linearly correlated with total PM and/or POC concentrations (Baker and Lavelle, 1984; Chung et al., 1998; Gardner et al., 2006). PM and/or POC sink in the water column individually or through aggregation/feeding. The results of the present study do not distinguish between the salinity of the water with which the plume mixes and the particle concentration of the mixing water. However, the correlation between c and PM showed that the CDW has a higher particle concentration than saline waters (Figure 4A). This suggested that the CDW continued to deliver a fairly homogeneous mix of particles even though their concentrations may vary with the annual- and interannual differences in the CRD (Sasaki et al., 2008; Moh et al., 2018). The sea surface temperature of the CDW in the offshore ECS is increased by sunlight, resulting in a highly stable water column due to the enhanced buoyancy of the low-density surface water and the enhanced stratification of the water column (Moh et al., 2018; Moon et al., 2019). The relationship between the surface *in situ* c and salinity reflects a linear decrease in particle concentration and a logarithmic decrease in salinity (Figure 4A).

Figure 4B shows the results of a regression between Rrs band ratios versus c, which used a multiple-wavelength approach to produce the MNDCI (Son et al., 2009b; Son et al., 2012, Eq. 2).

$$MNDCI = \left[\frac{Rrs(555) - max\,.\,(Rrs(412), Rrs(443), Rrs(490))}{Rrs(555) + max\,.\,(Rrs(412), Rrs(443), Rrs(490))}\right] \quad (2)$$

The MNDCI uses the band with the highest radiance among 412, 443, and 490 nm to calculate the band ratio, similar to the normalized difference vegetation index (NDVI) for land plants. The use of multiple wavelengths improves the likelihood of distinguishing multiple or shifting radiance peaks resulting from diverse particle types in the water column, thereby strengthening the correlation between the radiance ratio and c. Son et al.

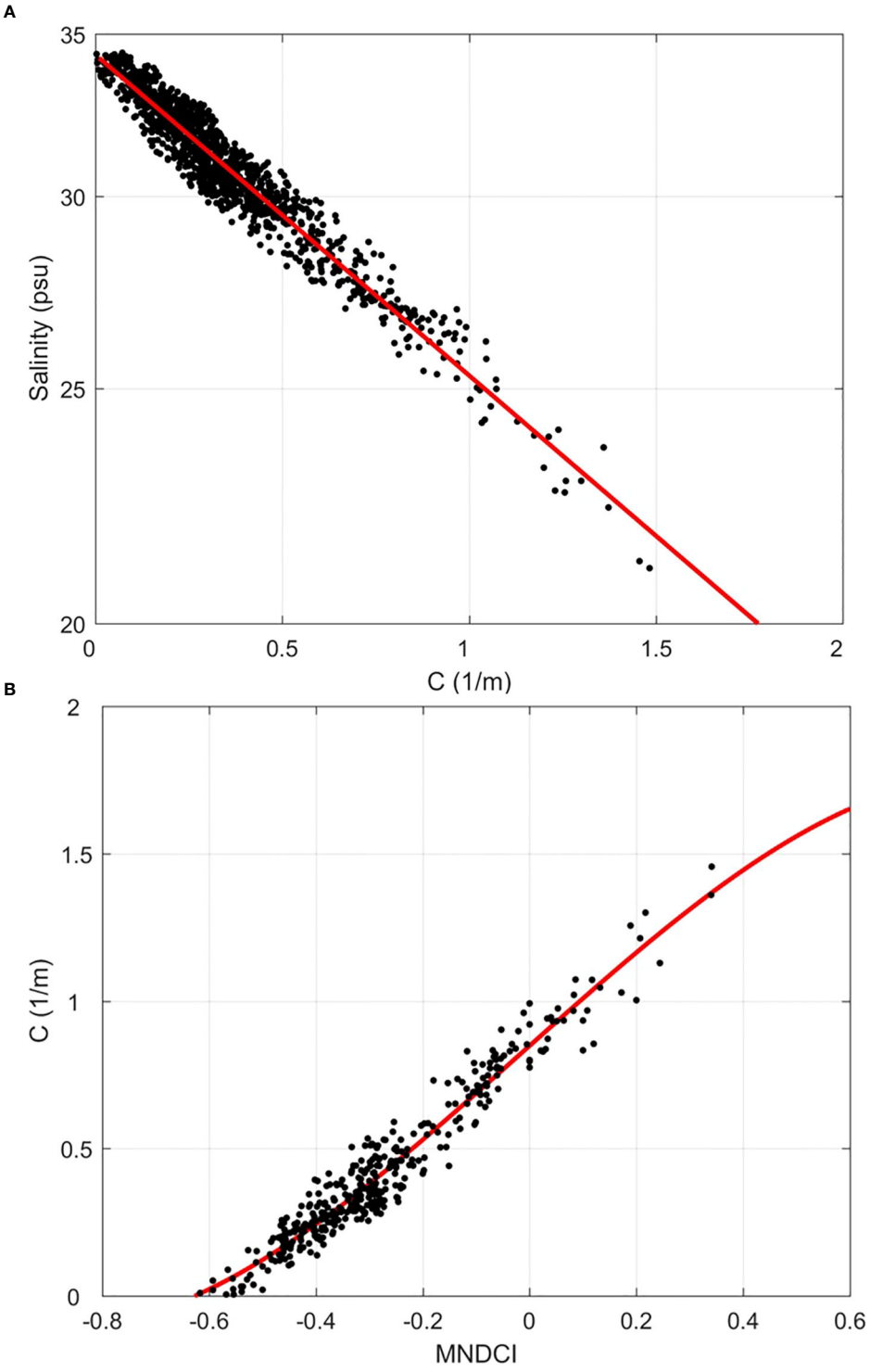


FIGURE 4
(A) Surface salinity as a linear function of beam attenuation, obtained by analyzing data from 1,345 sampling points during KIOST summer cruises. **(B)** Least-squares regression between beam attenuation coefficient and the maximum normalized difference carbon index (MNDCI). The MNDCI was calculated from the GOCI Rrs(λ) band ratio within the matched dataset *in situ* beam attenuation and synchronously obtained GOCI satellite data.

(2009b; 2012) compared the MNDCI values to the data from sampling stations where profiles were collected within a ±3-h window of local noon. In the present study, we matched the GOCI Rrs and *c* data obtained during the daytime without using a time-averaged window. Figure 4B plots the relationship between *c* and the MNDCI. The CDW covered 60% of the matched dataset, and the regression equation is given as follows:

$$C(m^{-1}) = [-0.72 \times MNDCI^3 - 0.03 \times MNDCI^2 + 1.61 \times MNDCI + 0.87] \quad (3)$$

The multiple band ratio provides a robust means for distinguishing bio-optical regimes according to the concentration range over which each band is dominant (Son et al., 2009b; Son et al., 2012). In this study, the values were directly (but not linearly) proportional to beam attenuation and were fitted with a cubic polynomial (Figure 4B, $F = 61.4$, $p < 0.01$, $R^2 = 0.93$, $N = 391$).

Finally, *c* was derived for each pixel by using the MNDCI in Eq. 3 and inserting the data into Eq. 1 to estimate salinity. Equation 4 is the combined equation for GOCI-derived surface salinity:

$$GOCI \quad Salinity(psu) = 10^{[-0.135\times[-0.72\times MNDCI^3-0.03\times MNDCI^2+1.61\times MNDCI+0.87]+1.53]} \quad (4)$$

Comparison of the two-step approach with previous salinity remote-sensing algorithms

We calculated the correlations and errors between the measured *in situ* salinity and the salinity estimated from our analysis and five previous methods using data from stations in the ECS where well-matched *c* and satellite data were available (Figure 5; Table 2). The RMSE, bias, and mean ratio between the *in situ* and the estimated salinity were calculated for a quantitative evaluation (Table 2).

Using *c*, the result of Eq. 4 was in strong agreement with *in situ* data over the various ranges of measured salinity (Figure 5A). The approaches of Binding and Bowers (2003); Ahn et al. (2008); Son et al. (2012), and Bai et al. (2013) overestimated salinity, especially that of Binding and Bowers (2003) at lower salinities in the ECS (Figures 5B, C, E, F). The approach used by Sasaki et al. (2008) underestimated salinity at higher levels and overestimated it at lower levels (Figure 5D). Binding and Bowers (2003) and Son et al. (2012) carried out studies under different regional salinity conditions (in the Clyde Sea, Scotland, and the Gulf of Mexico) and with different satellite sensors. Although Ahn et al. (2008) and Bai et al. (2013) carried out their studies in the ECS, they used different satellite sensors (SeaWiFS and MODIS satellites) and developed their algorithms using coastal data. Sasaki et al. (2008) covered similar regions to the present study but used different satellite sensors (MODIS). Our proposed two-step approach shows that the correlation between salinity and *c* was much stronger than that between salinity and CDOM or the chlorophyll-*a* concentration.

The difference between the *in situ* and estimated salinity is greater in low-salinity waters, which occur in optically complex ocean environments under particle-laden conditions and/or under the influence of CDOM (Baker and Lavelle, 1984; Siegel et al., 2005a; Ahn et al., 2008; Son et al., 2009b; Son et al., 2012). Although CDOM was inversely calculated from ocean color parameters, the correlation with CDOM was not relevant to the present study owing to the lack of *in situ* CDOM data. An increase in particles leads to increased scatter at visible and NIR bands, whereas an increase in CDOM, chlorophyll-*a*, or nonliving carbon particles results in decreased radiance at blue wavelengths with little change in scattering, thereby altering the spectral reflectance ratio (Carder et al., 1999; Siegel et al., 2005a). The satellite-derived salinity estimates in the complex ECS were obtained with Eq. 4. GOCI-derived surface salinity estimated by the simple two-step approach exhibits no discontinuities in complex surface salinity conditions (Figure 5; Table 2). The results obtained using *c* suggest that the use of multiple band ratios was effective in optically complex waters and met the criteria of the proposed two-step algorithm.

The empirical salinity algorithms of the previous and present studies were applied to average GOCI Rrs values during summer cruise periods (16–19 August 2016) to map surface salinity (Figure 6) and a longitudinal line at 33° N (Figure 7). The surface water in the summer of 2016 was loaded with freshwater due to the increased CRD (Figure 2) (Moh et al., 2018; Moon et al., 2019). Cross- and along-shelf export of the CDW from the Changjiang River mouth manifested as patches/plumes, with salinity increasing to the northeast from 26 to 31 psu. Salinities< 25 psu were seen along the Changjiang River estuary, and persistent patches of the CDW extended over Jeju Island, South Korea.

All approaches showed similar spatial patterns, but the surface salinity ranges were quite different. Most approaches captured the offshore CDW and clearly showed distinct variations over wide ranges of salinities. The results generated using the approaches of Binding and Bowers (2003) and Son et al. (2012) showed an overestimation of salinity (Figures 6C, F). Surface salinity ranges in the ECS studies (Ahn et al., 2008; Sasaki et al., 2008; Bai et al., 2013) were well correlated with *in situ* data but slightly overestimated salinity (Figures 6, 7). The present study showed similar spatial patterns to previous methods, but the results were closely correlated with *in situ* salinity (Figures 6B, 7). From comparison images and crosslines created by the previous and present methods, this study demonstrated that the CDW can be identified using GOCI

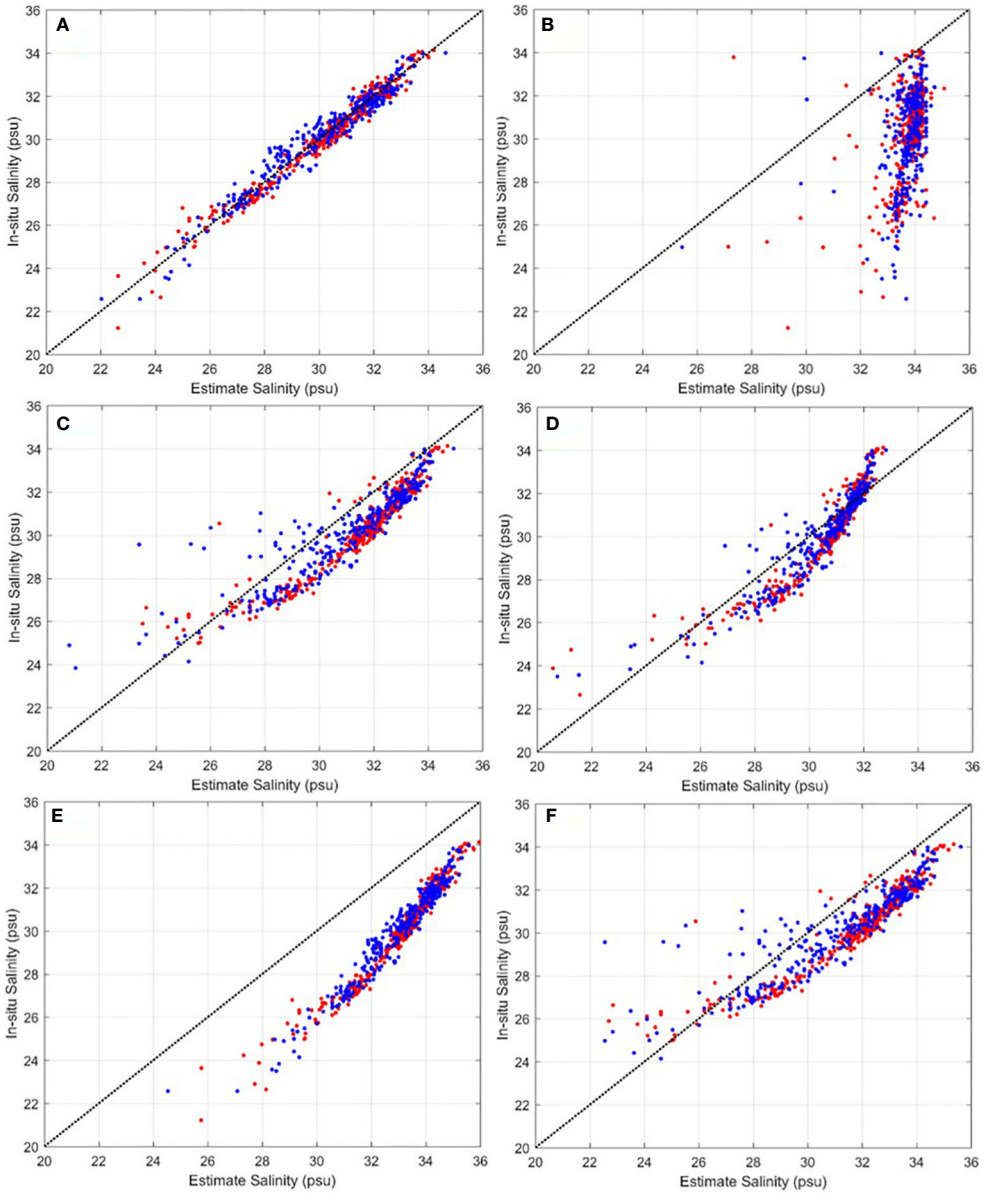


FIGURE 5
Comparison between *in situ* salinity and satellite-derived salinity estimated using **(A)** Eq. 4 and the methods of **(B)** Binding and Bowers (2003), **(C)** Ahn et al. (2008), **(D)** Sasaki et al. (2008), **(E)** Son et al. (2012), and **(F)** Bai et al. (2013). Red dots indicate the matched dataset (Figure 4); blue dots indicate the validation dataset, comprising data collected during NIFS and KIOST cruises (Figure 1).

ocean color data in a two-step approach based on *in situ* observation data (Figures 6B, 7).

The proposed two-step approach assumed that the particle-loaded plume consisted of low-salinity water, and that clear water had high salinity. The loaded sediment plume determined by satellite and *in situ* observations was persistent around the Korean and Chinese coasts. Both coastal areas were characterized by variations between low- and high-salinity conditions. Moreover, the settling particles in coastal water and/or offshore water below the mixed layer were not reflected in the surface water column. This influenced the results because satellites observed only the ocean surface and therefore did not provide information on the water below the mixed surface layer. It is difficult to distinguish well-mixed surface water from a low-salinity plume. Therefore, the proposed two-step approach may be less accurate for estimating salinity conditions in coastal

TABLE 2 Error of *in situ* and satellite-derived estimated salinity: comparison between the proposed two-step approach and five other approaches.

	RMSE	Bias	Mean ratio	*N*
Eq. 4	0.435	0.053	1.002	707
Binding and Bowers (2003)	4.268	3.541	1.123	707
Ahn et al. (2008)	1.801	0.915	1.026	707
Sasaki et al. (2008)	1.996	0.170	1.006	707
Son et al. (2012)	3.069	2.974	1.101	707
Bai et al. (2013)	2.148	1.084	1.034	707

RMSE, bias, and mean ratio values are calculated using matched and validation datasets.

regions and well-mixed water. We assumed that there was no particle input from bottom sediment or biogenic production. During summer in our study area, the thermocline was shallow, and biogenic production was low due to a strong stratification. Although satellite-derived data can estimate salinity in coastal areas beyond shipboard stations, we used salinity conditions in the middle of the ECS to obtain matched data to develop the algorithm.

The CDW variability in the period 2011–2020

To elucidate the spatial and temporal variation in the CDW in the ECS, monthly satellite-derived surface salinity maps for the summer season from 2011 to 2020 were derived using Eq. 4. Figure 8 shows the climatological mean value of the satellite-derived surface salinity, which was used to map salinity in the ECS over the summer season. Low-salinity values were found on the inner shelf and near the Changjiang River estuary. When southerly winds prevailed during the summer, the CDW tended to move northeast in the Chinese coastal area and then separated from the coastal zone to travel eastward across the western shelf, reaching the vicinity of Jeju Island. Numerical simulation results also indicated that, during the southerly monsoon in summer, the CDW extends offshore and moves northeastward near Jeju Island to the Korea/Tsushima Strait, whereas about 70% of the CRD flows through the Korea/Tsushima Strait (Chang and Isobe, 2003; Lie et al., 2003; Chang and Isobe, 2005; Senjyu et al., 2006; Moon et al., 2019). The depth of the mixed layer increased from 5 to 15 m with the enhanced water column stratification (Chang et al., 2003; Lie et al., 2003). Park et al. (2011; 2015) noted that the CDW moves into the upper layer of the thermocline during the summer and is enhanced by the formation of a strong barrier layer. In this process, the increase in sea surface temperature was greater as the stratification was enhanced by surrounding waters. Moh et al. (2018) reported that the CDW maintains the particle-loaded water within the mixed layer and those sinking particles are related to the depth of the mixed layer. The spatial distributions of the CDW were similar to those of chlorophyll-*a* and PM (Figures 3, 8).

Figure 9 shows maps of the monthly satellite-derived surface salinity during the summer in the period 2011–2020. The CDW was present in the middle of the ECS in all years and was mainly transported eastward and northeastward (Figure 9). The dispersion patterns of the CDW might be related to changing wind systems. Chang et al. (2005) and Yamaguchi et al. (2012) noted that the east and northeast movement was driven by the dominant southerly wind and that the south and southeast dispersion was caused by the prevailing northerly wind. The dispersion patterns of the CDW varied from eastward to southeastward in the summers of 2015, 2016, 2018, and 2020, which might be related to changing wind systems.

Figure 10 shows the satellite-derived salinity values and anomalies relative to the August mean along 125° E and 127° E from 29° N to 33.5° N. The eastward extension of the CDW appeared in June with increasing CRD and reached Jeju Island and the south coast of Korea after 1–2 months. The CDW dispersed along 125° E in all years (Figure 10A, B), but its dispersal varied along 127° E (Figures 10C, D). Figures 10B, D show that the anomalous CDW in the summers of 2016, 2017, and 2020 loaded freshwater into the offshore ECS, especially in July (Figure 2) (Moh et al., 2018; Moon et al., 2019). These abnormal periods may have been affected by climatological variables (e.g., the El Niño Southern Oscillation (ENSO), East Asia Monsoon, Pacific Decadal Oscillation (PDO), etc.). The ENSO and PDO can increase the summer precipitation and modulate the CRD in the ECS (Park et al., 2011; Park et al., 2015; Wang et al., 2022). Park et al. (2015) supported this premise by establishing a link between summer SST variation and sea surface salinity variation in the ECS, which is known as ENSO-related precipitation. The increased sea surface temperature in August 2016 and 2017 was associated with an absence of typhoons (Moh et al., 2018; Moon et al., 2019; Park et al., 2020; Son et al., 2020). Sea surface temperatures in August 2016 and 2017 were 1.5°C and 1°C higher than normal August temperatures in the ECS, respectively (Park et al., 2020). The CRD had its highest discharge in 2020 within the past 10 years,

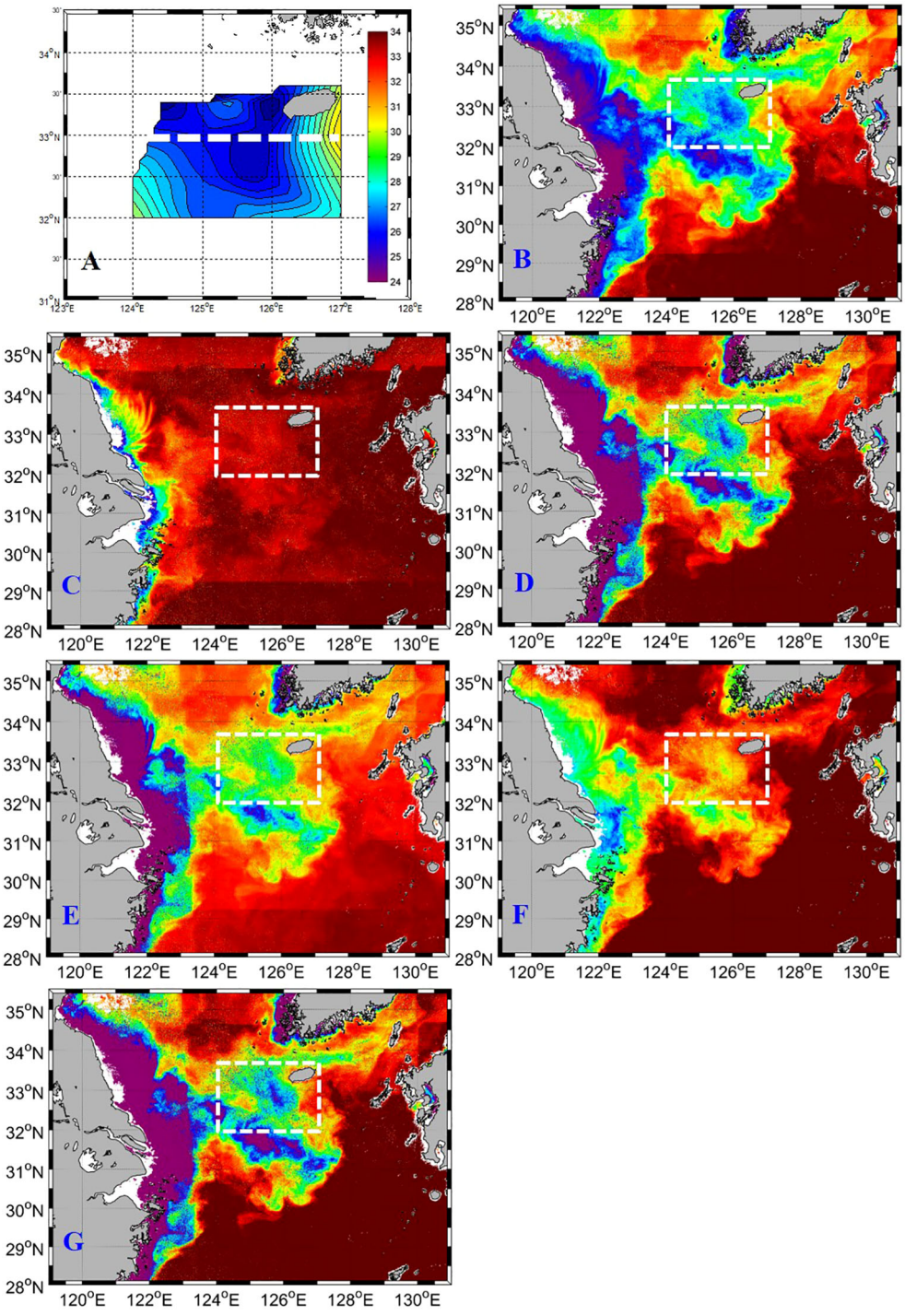


FIGURE 6
(A) Sea surface salinity (psu) calculated from CTD data obtained during the period 16–19 August 2016. **(B–G)** Satellite images from which salinity (psu) was calculated using the **(B)** proposed two-step approach (Eq. 4), as well as the methods of **(C)** Binding and Bowers (2003), **(D)** Ahn et al. (2008), **(E)** Sasaki et al. (2008), **(F)** Son et al. (2012), and **(G)** Bai et al. (2013). Data obtained during a 4-day cruise were averaged.

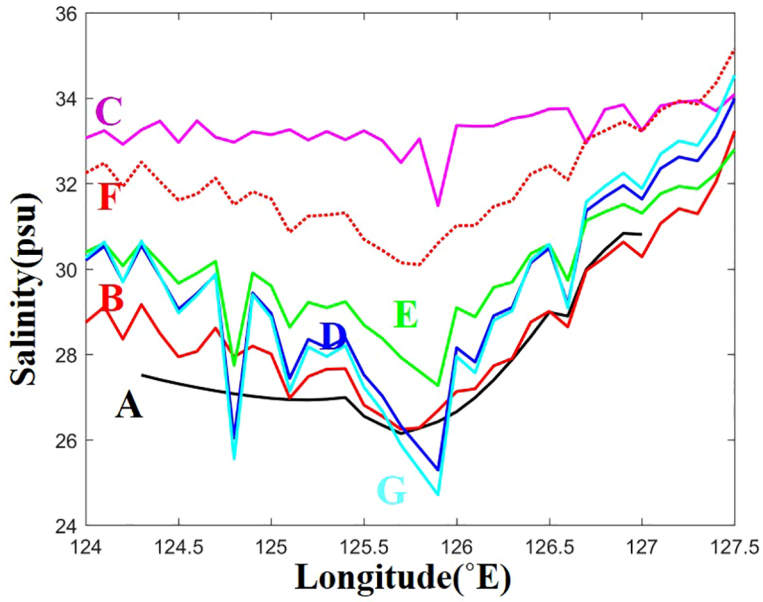


FIGURE 7
Longitudinal transects of *in situ* **(A)** and satellite-derived salinities obtained along 33° N during the 2016 summer cruise (longitudinal lines are shown in **(A)**. **(A)** *In situ* salinity and **(B)** results of the proposed two-step approach (Eq. 4) and methods of **(C)** Binding and Bowers (2003), **(D)** Ahn et al. (2008), **(E)** Sasaki et al. (2008), **(F)** Son et al. (2012), and **(G)** Bai et al. (2013). Data were averaged over a 4-day cruise (16–19 August 2016).

followed by 2016 and 2017 (Figure 2). Park et al. (2011) suggested that an increased CRD may increase the SST around the Changjiang River mouth. During the summer of 2016, Moh et al. (2018) and Moon et al. (2019) found that the low-salinity plume was linked to increasing sea surface temperature. The increasing CRD might be influenced by the ENSO and PDO and contributed to the extension of the CDW.

The positive anomaly periods in August 2014 and 2019 might be associated with climatological effects and atmospheric forcing (e.g., ENSO, typhoons, and/or the presence of cold air masses). The increase in sea surface salinity during summer in the ECS may be influenced by decreased CRD and/or increasing vertical mixing. Park et al. (2015) showed that the CRD in summer is relatively low in La Niña years compared to the following El Niño year. Park et al. (2020) noted that abnormal surface cooling in August 2014 leads not only to the expansion of the Okhotsk High (low East Asia Monsoon index) but also to passing typhoons. The expansion of the Okhotsk High is caused by a weakening of the northeasterly wind field (Yu et al., 2004). Passing typhoons also cause strong vertical/horizontal advection and cold-water upwelling along the trajectory of the typhoon (Moon and Kwon, 2012; Son et al., 2020). Strong winds increase mixing in saline ambient water and temporally suppress the expansion of the CDW. The combination of climatological and atmospheric effects may limit the dispersion of the CDW in the offshore ECS. In the present study, we ignore interannual variations in the CDW. Recent climatological studies have found that significantly increased precipitation in Chinese territory is related to an interaction between ENSO and the East Asia Summer Monsoon (Gong and Ho, 2003; Yu et al., 2004; Park et al., 2015; Birkinshaw et al., 2017; Wang et al., 2022). The increasing riverine input is linked to abnormal precipitation over large areas of China, which might change the surface salinity over the offshore ECS (Delcroix and Murtugudde, 2002). Further studies are required to understand the relationship between the presence of the CDW and physical factors and the climatological effects of the CRD.

Conclusions

Ocean color remote-sensing studies can provide useful temporal and spatial information on PM, as well as surface salinity in the surface ocean. The GOCI satellite was developed to measure changes in the marine environment eight times per day (with a 500-m spatial resolution) in our study area (Ryu and Ishizaka, 2012). To detect a recurrent low-salinity plume in the ECS, a simple two-step empirical algorithm using GOCI Rrs(λ) was developed based on a large 18-year *in situ* dataset of satellite-derived surface salinity (*in situ* salinity and *c* values). The algorithm showed continuity across salinities of 24–34 psu in the middle of the ECS. The proposed two-step approach was then compared with five

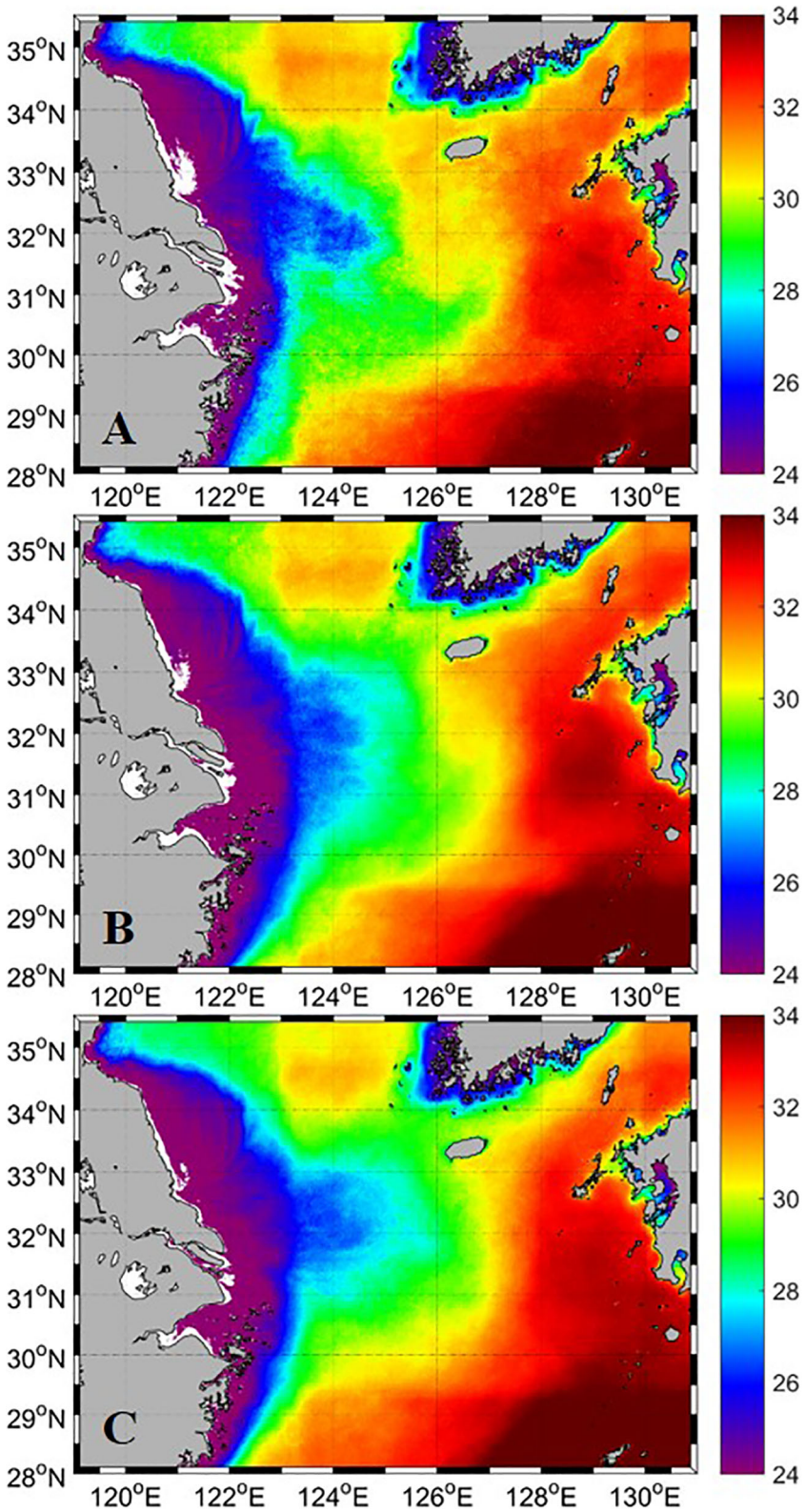


FIGURE 8
Satellite-derived salinities (psu) in **(A)** June, **(B)** July, and **(C)** August calculated using Eq. 4.

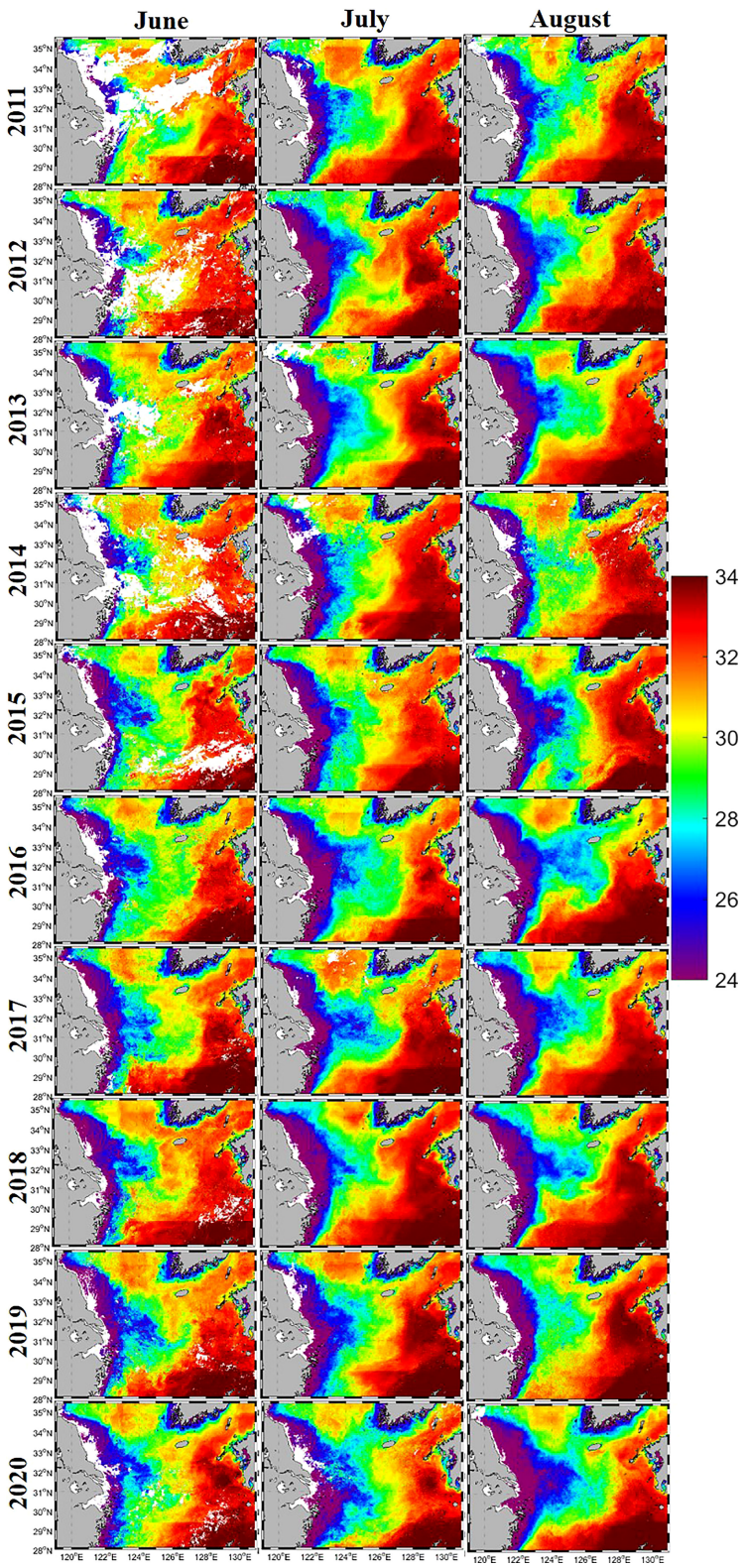


FIGURE 9
Salinity (psu) calculated from monthly GOCI images using Eq. 4 during summer in the period 2011–2020.

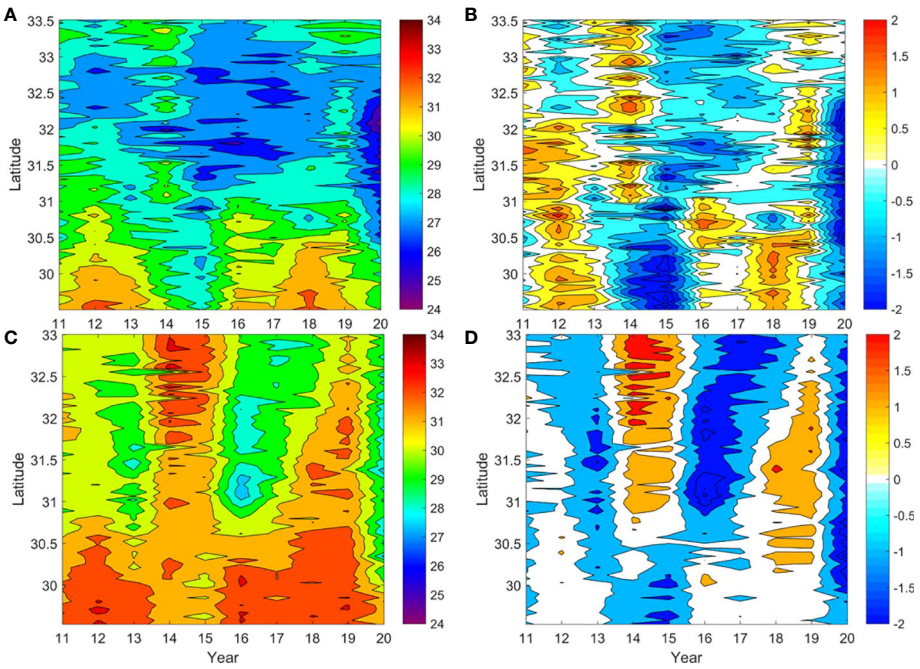


FIGURE 10
Time series of satellite-derived salinity (pus) **(A, C)** and anomalous salinity **(B, D)**. Mean values for August in the period 2011–2020 are shown along 125° E **(A, B)** and 127° E, **(C, D)** and from 29° N to 33.5° N, as a function of year and longitude. Mean and anomalous values are shown across years to emphasize the annual variation.

other salinity methods based on CDOM and particle concentrations. The errors of previous and present methods were estimated and compared using a matched dataset of *in situ* salinity and GOCI Rrs values. Previous approaches captured the CDW in the middle of the ECS, but salinity was over- or underestimated. These differences might be due to the different study areas and/or satellite sensors used. Our method was more reliable and sensitive for deriving the correlation between *c* and multiple spectra of Rrs in the ECS environment than previous methods.

We mapped salinity based on ocean color remote-sensing data, clearly reproducing the distribution of the regional low-salinity plume. Although the satellite-based approach with a regionally tuned algorithm estimated the offshore surface salinity conditions only during the summer, this approach aids the interpretation of salinity patterns in dynamic waters. Our approach enables surface salinity in the middle of the ECS to be monitored hourly. Monthly maps of satellite-derived surface salinity from 2011 to 2020 outlined the interannual motion of the CDW, extending from the coast of China to the shelf in the ECS. Although the presence and dispersion of the CDW were affected by various complex physical factors, regional mapping of summer salinity based on remote-sensing data was useful for understanding and monitoring the dynamics of salinity in the ECS.

Data availability statement

The original contributions presented in the study are included in the article/supplementary material. Further inquiries can be directed to the corresponding author.

Author contributions

Conceptualization: YS and J-KC. Methodology: YS. Data analysis: YS and J-KC. Writing—original draft preparation: YS. Supervision: J-KC. Funding acquisition: YS. and J-KC. All authors contributed to the article and approved the submitted version.

Funding

This research was supported by the Korea Institute of Marine Science and Technology Promotion (KIMIST) funded by the Ministry of Oceans and Fisheries of Korea (Grant Number: PM63010, 2022, and 20220546 (PM63170)) and the "Biogeochemical cycling and marine environmental change

studies" funded by the Korea Institute of Ocean Science and Technology (KIOST Grant Number: PEA0012).

Conflict of interest

The authors declare that the research was conducted in the absence of any commercial or financial relationships that could be construed as a potential conflict of interest.

Publisher's note

All claims expressed in this article are solely those of the authors and do not necessarily represent those of their affiliated organizations, or those of the publisher, the editors and the reviewers. Any product that may be evaluated in this article, or claim that may be made by its manufacturer, is not guaranteed or endorsed by the publisher.

References

Ahn, Y. H., Shanmugam, P., Moon, J. E., and Ryu, J. H. (2008). Satellite remote sensing of a low-salinity plume in the East China Sea. *Ann. Geophys.* 26, 2019–2035. doi: 10.5194/angeo-26-2019-2008

Bailey, S. W., and Werdell, P. J. (2006). A multi-sensor approach for the on-orbit validation of ocean color satellite data products. *Remote Sens. Environ.* 102, 12–23. doi: 10.1016/j.rse.2006.01.015

Bai, Y., Pan, D. L., Cai, W. J., He, X. Q., Wang, D. F., Tao, B. Y., et al. (2013). Remote sensing of salinity from satellite-derived CDOM in the changjiang river dominated East China Sea. *J. Geophys. Res. Oceans.* 118, 227–243. doi: 10.1029/2012JC008467

Baker, E. T., and Lavelle, J. W. (1984). The effect of particle size on the light attenuation coefficient of natural suspensions. *J. Geophys. Res.* 89, 8197–8203. doi: 10.1029/JC089iC05p08197

Beardslev, R. C., Limeburner, R., Yu, H., and Cannon, G. A. (1985). Discharge of the changjiang (Yangtze river) into the East China Sea. *Cont. Shelf. Res.* 4 (1-2), 57–76. doi: 10.1016/0278-4343(85)90022-6

Binding, C. E., and Bowers, D. G. (2003). Measuring the salinity of the Clyde Sea from remotely sensed ocean color. *Est. Coast. Shelf. Sci.* 57, 605–611. doi: 10.1016/S0272-7714(02)00399-2

Birkinshaw, S. J., Guerreiro, S. B., Nicholson, A., Liang, Q., Quinn, P., Zhang, L., et al. (2017). Climate change impacts on Yangtze river discharge at the three gorges dam. *Hydrol. Earth Syst. Sci.* 21, 1911–1927. doi: 10.5194/hess-21-1911-2017

Carder, K. L., Chen, F. R., Lee, Z. P., Hawes, S. K., and Kamykowski, D. (1999). Semianalytic moderate-resolution imaging spectrometer algorithms for chlorophyll-a and absorption with bio-optical domains based on nitrate-depletion temperatures. *J. Geophys. Res.* 104, 5403–5421. doi: 10.1029/1998JC900082

Chang, P. H., and Isobe, A. (2003). A numerical study on the changjiang diluted water in the yellow and East China seas. *J. Geophys. Res.* 108 (C9), 3299. doi: 10.1029/2002JC001749

Chang, P.-H., and Isobe, A. (2005). Interannual variation of freshwater in the yellow and East China Sea: roles of the changjiang discharge and wind forcing. *J. Oceanogr.* 61, 817–834. doi: 10.1007/s10872-006-0002-5

Choi, J.-K., Park, Y. J., Ahn, J. H., Lim, H.-S., Eom, J., and Ryu, J.-H. (2012). GOCI, the world's first geostationary ocean color observation satellite, for the monitoring of temporal variability in coastal water turbidity. *J. Geophys. Res. Oceans.* 117. doi: 10.1029/2012JC008046

Choi, J.-K., Son, Y. B., Park, M. S., Hwang, D. J., Ahn, J. H., and Park, Y. G. (2021). The application of the geostationary ocean color imager to the mapping of sea surface salinity in the East China Sea. *Remote Sens.* 13 (4), 2676. doi: 10.3390/rs13142676

Chung, S. P., Gardner, W. D., Landry, M. R., Richardson, M. J., and Walsh, I. D. (1998). Beam attenuation by microorganism and detrital particles in the equatorial pacific. *J. Geophys. Res.* 103, 12669–12681. doi: 10.1029/98JC00608

Dai, Z., Du, J., Li, J., Li, W., and Chen, J. (2008). Runoff characteristics of the changjiang river during 2006: Effect of extreme drought and the impounding of the three gorges dam. *Geophys. Res. Lett.* 35, L07406. doi: 10.1029/2008GL033456

Delcroix, T., and Murtugudde, R. (2002). Sea Surface salinity changes in the East China Sea during 1997–2001: Influence of the Yangtze river. *J. Geophys. Res. Oceans.* 2002, 107(C12). doi: 10.1029/2001JC000893

Gardner, W. D., Mishonov, A. V., and Richardson, M. J. (2006). Global POC concentrations from in-situ and satellite data. *Deep. Sea. Res. II.* 53, 718–740. doi: 10.1016/j.dsr2.2006.01.029

Gardner, W. D., Walsh, I. D., and Richardson, M. J. (1993). Biophysical forcing of particle production and distribution during a spring bloom in the north Atlantic. *Deep. Sea. Res. II.* 40, 171–195. doi: 10.1016/0967-0645(93)90012-C

Gong, G.-C., Chen, Y.-L., and Liu, K.-K. (1996). Chemical hydrography and chlorophyll-a distribution in the East China Sea in summer: implications in nutrient dynamics. *Cont. Shelf. Res.* 16, 1561–1515. doi: 10.1016/0278-4343(96)00005-2

Gong, D.-A., and Ho, C.-H. (2003). Artic oscillation signals in the East Asian summer monsoon. *J. Geophy. Res.* 108 (D2), 4066. doi: 10.1029/2002JD002193

Kim, D., Choi, S. H., Kim, K. H., Shim, J. H., Yoo, S., and Kim, C. H. (2009a). Spatial and temporal variations in nutrient and chlorophyll-a concentration in the northern East China Sea surrounding cheju island. *Cont. Shelf. Res.* 29 (11-12), 1426–1436. doi: 10.1016/j.csr.2009.03.012

Kim, H.-C., Yamaguchi, H., Yoo, S. J., Zhu, J., Okamura, K., Kiyomoto, Y., et al. (2009b). Distribution of changjiang diluted water detected by satellite chlorophyll-a and its interannual variation during 1998-2007. *J. Oceanogr.* 65, 129–135. doi: 10.1007/s10872-009-0013-0

Lie, H.-J., Cho, C.-H., Lee, J.-H., and Lee, S. (2003). Structure and eastward extension of the changjiang river plume in the East China Sea. *J. Geophys. Res.* 108 (C3). doi: 10.1029/2001JC001194

Mishonov, A. V., Gardner, W. D., and Richardson, M. J. (2003). Remote sensing and surface POC concentration in the south Atlantic. *Deep. Sea. Res. II.* 50, 2997–3015. doi: 10.1016/j.dsr2.2003.07.007

Moh, T., Cho, J. H., Jung, S.-K., Kim, S.-H., and Son, Y. B. (2018). Monitoring of the changjiang river plume in the East China Sea using a wave glider. *J. Coast. Res.* 85, 26–30. doi: 10.2112/SI85-006.1

Moon, J. H., Kim, T., Son, Y. B., Hong, J. S., Lee, J. H., Lee, J. H., et al. (2019). Contribution of low-salinity water to sea surface warming of the East China Sea in the summer of 2016. *Prog. Oceanogr.* 175, 68–80. doi: 10.1016/j.pocean.2019.03.012

Moon, J. H., and Kwon, S. J. (2012). Impact of upper-ocean thermal structure on the intensity of Korean peninsular landfall typhoons. *Prog. Oceanogr.* 105, 61–66. doi: 10.1016/j.pocean.2012.04.008

Park, T., Jang, C. J., Jungclaus, J. H., Haak, H., Park, W., and Oh, I. S. (2011). Effects of the changjiang river discharge on sea surface warming in the yellow and East China seas in summer. *Cont. Shelf. Res.* 31, 15–22. doi: 10.1016/j.csr.2010.10.012

Park, T., Jang, C. J., Kwon, M., Na, H., and Kim, K. Y. (2015). An effect of ENSO on summer surface salinity in the yellow and East China seas. *J. Mar. Sys.* 141, 122–127. doi: 10.1016/j.jmarsys.2014.03.017

Park, G. S., Lee, T., Min, S.-H., Jung, S.-K., and Son, Y. B. (2020). Abnormal sea surface warming and cooling in the East China Sea during summer. *J. Coast. Res.* 95, 1505–1509. doi: 10.2112/SI95-290.1

Roesler, C. S., and Boss, E. (2005). Spectral beam attenuation coefficient retrieved from ocean color inversion. *Geophys. Res. Lett.* 30, 1468. doi: 10.1029/2002GL016185

Ryu, J. H., Han, H. J., Cho, S., Park, Y. J., and Ahn, Y. H. (2012). Overview of geostationary ocean color imager (GOCI) and GOCI data processing system (GDPS). *Ocean. Sci. J.* 47 (3), 223–233. doi: 10.1007/s12601-012-0024-4

Ryu, J. H., and Ishizaka, J. (2012). GOCI data processing and ocean applications. *Ocean. Sci. J.* 47 (3), 221. doi: 10.1007/s12601-012-0023-5

Sasaki, H., Siswanto, E., Nishiuchi, K., Tanaka, K., Hasegawa, T., and Ishizaka, J. (2008). Mapping the low salinity changjiang diluted water using satellite retrieved colored dissolved organic matter (CDOM) in the East China Sea during high river flow season. *Geophys. Res. Lett.* 35, L04604. doi: 10.1029/2007GL032637

Senjyu, T., Enomoto, H., Matsuno, T., and Matsui, S. (2006). Interannual salinity variations in the tsushima strait and its relation to the changjiang discharge. *J. Oceanogr.* 62 (5), 81–692. doi: 10.1007/s10872-006-0086-y

Siegel, D. A., Maritorena, S., Nel, N. B., and Behrenfeld, M. J. (2005a). Independence and interdependencies among global ocean color properties: Reassessing the bio-optical assumption. *J. Geophys. Res.* 110, C07011. doi: 10.1029/2004JC002527

Siegel, D. A., Maritorena, S., Nelson, N., Behrenfedl, M. J., and McCalin, C. R. (2005b). Colored dissolved organic matter and its influence on the satellite-based characterization of the ocean biosphere. *Geophys. Res. Lett.* 32, L20605. doi: 10.1029/2005GL024310

Son, Y. B., Gardner, W. D., Mishonov, A. V., and Richardson, M. J. (2009a). Model-based remote sensing algorithms for particulate organic carbon (POC) in the northeastern gulf of Mexico. *J. Earth Sys. Sci.* 1, 1–10. doi: 10.1007/s12040-009-0001-1

Son, Y. B., Gardner, W. D., Mishonov, A. V., and Richardson, M. J. (2009b). Multispectral remote-sensing algorithms for particulate organic carbon (POC): The gulf of Mexico. *Remote Sens. Environ.* 113, 50–61. doi: 10.1016/j.rse.2008.08.011

Son, Y. B., Gardner, W. D., Richardson, M. J., Ishizaka, J., Ryu, J. H., Kim, S. H., et al. (2012). Tracing offshore low-salinity plumes in the northeastern gulf of Mexico during the summer season by use of multispectral remote-sensing data. *J. Oceanogr.* 68 (5), 743–760. doi: 10.1007/s10872-012-0131-y

Son, Y. B., Jung, S.-K., Cho, J. H., and Moh, T. (2020). Monitoring of the surface ocean environment under a passing typhoon using a wave glider. *J. Coast. Res.* 95, 168–172. doi: 10.2112/SI95-033.1

Wang, Y., Liu, S., Chen, J., Zhou, Z., and Shi, H. (2022). Investigating the spatiotemporal variations of extreme rainfall and its potential driving factors with improved partial wavelet coherence. *Front. Environ. Sci.* 10. doi: 10.3389/fenvs.2022.951468

Wentz, F. J., and LeVine, D. (2012). *Algorithm theoretical basis document (version 2). Aquarius RSS Technical Report 082912, Aquarius Ground Segment, Goddard Space Flight Center, August 2012.* Available at: https://podaac-tools.jpl.nasa.gov/drive/files/allData/aquarius/docs/v2/AQ-014-PS-0017_AquariusATBD_Level2.pdf

Yamaguchi, H., Kim, H. C., Son, Y. B., Kim, S. W., Okamura, K., Kiyomoto, Y., et al. (2012). Seasonal and summer interannual variations of SeaWiFS chlorophyll a in the yellow Sea and East China Sea. *Pro. Oceanogr.* 105, 22–29. doi: 10.1016/j.pocean.2012.04.004

Yu, R., Wang, B., and Zhou, T. (2004). Tropospheric cooling and summer monsoon weakening trend over East Asia. *Geophys. Res. Lett.* 31, L22212. doi: 10.1029/2004GL021270

frontiers | Frontiers in Marine Science

TYPE Original Research
PUBLISHED 18 November 2022
DOI 10.3389/fmars.2022.1017936

Check for updates

OPEN ACCESS

EDITED BY
Lei Ren,
Sun Yat-sen University, China

REVIEWED BY
Yang Ding,
Ocean University of China, China
Yunhai Li,
Third Institute of Oceanography,
Ministry of Natural Resources, China

*CORRESPONDENCE
Jianyu Chen,
chenjianyu@sio.org.cn

SPECIALTY SECTION
This article was submitted to Ocean Observation, a section of the journal Frontiers in Marine Science

RECEIVED 12 August 2022
ACCEPTED 01 November 2022
PUBLISHED 18 November 2022

CITATION
Xu Y and Chen J (2022) Remote sensing and buoy based monitoring of chlorophyll *a* in the Yangtze Estuary reveals nutrient-limited status dynamics: A case study of typhoon. *Front. Mar. Sci.* 9:1017936. doi: 10.3389/fmars.2022.1017936

COPYRIGHT
© 2022 Xu and Chen. This is an open-access article distributed under the terms of the Creative Commons Attribution License (CC BY). The use, distribution or reproduction in other forums is permitted, provided the original author(s) and the copyright owner(s) are credited and that the original publication in this journal is cited, in accordance with accepted academic practice. No use, distribution or reproduction is permitted which does not comply with these terms.

Remote sensing and buoy based monitoring of chlorophyll *a* in the Yangtze Estuary reveals nutrient-limited status dynamics: A case study of typhoon

Yuying Xu[1,2] and Jianyu Chen[1]*

[1]State Key Laboratory of Satellite Ocean Environment Dynamics, Second Institute of Oceanography, Ministry of Natural Resources, Hangzhou, China, [2]Ocean College, Zhejiang University, Zhoushan, China

Nutrient concentrations and its limited statuses can affect phytoplankton community structure and marine primary productivity. Identifying limiting nutrients under different ocean conditions, the causes, and the nature of such limitations, has important implications for understanding ecosystem changes and interpretation of *in situ* data. However, there is still a lack of retrieval methods for nutrients in seawater, especially in coastal waters. We propose to characterize the spatiotemporal variability of phytoplankton and nutrient-limited status in the surface ocean with diurnal valuevs of chlorophyll concentration. In this paper, the sediment fronts and plume fronts are used as a reference to select the relative and absolute nutrient-limited status regions. The variance of the six times per day (9:30-14:30) is calculated to represent the diurnal variation of chlorophyll, and the diurnal variation and concentration of chlorophyll combined are used to analyze nutrient-limited status. The results indicate that the diurnal variation of chlorophyll is greater after the typhoon, and the nutrient-limited status is different following each typhoon passing by. The *in situ* data shows that the highest chlorophyll *a* concentration reached 20.7 mg/m^3 after the typhoon in August 2011.

KEYWORDS

remote sensing, buoy, chlorophyll *a*, Yangtze estuary, nutrient-limited status, typhoon

1 Introduction

The Yangtze River is one of the largest rivers in the world and has a total length of 6,397 kilometers. It delivers approximately 9.1×10^{11} m^3 of freshwater and more than 8×10^7 tons of sediments into the East China Sea (ECS) every year from Yangtze Estuary (Dai et al., 2014, Luan et al., 2016). The current system in the area is complex with two major currents, the Changjiang diluted water (CDW) and Taiwan warm current (TWC). The abundant nitrogen and phosphorous loads from the rivers and TWC make ECS one of the most productive areas in the North Pacific (Chen et al., 1999). Nutrients can affect the phytoplankton community structure of the Yangtze Estuary, together with the suspended sediment. Further, nutrient-limited status can constrain the extent to which oceanic primary production influences global nutrient and carbon cycles (Moore et al., 2008). Establishing the limiting nutrient under different oceanographic conditions, and identifying the causes and nature of such limitation, has important consequences for understanding ecosystem changes and the interpretation of *in situ* data (Moore et al., 2008).

As non-optically sensitive substances, the retrieval of nutrients is gradually developing (Xu et al., 2010; Du et al., 2021). However, most of the current statistical models are applied to freshwater water bodies such as lakes, rivers, and reservoirs, and there are no effective approaches to large-area, long-term Case II water studies (Xu et al., 2011; Sun et al., 2014). Monitoring the nutrient-limited status on a large scale, and the high frequency of spatiotemporal distribution characteristics is a key way to understand the feedback relationship between marine biota and the ocean environment (Arrigo, 2005). A major challenge to observing the complex dynamic nutrient-limited status of the sea in time and space is the lack of tools to monitor the nutrient limitation variation, although some progress has been made to explore a temporal shift in nutrients concentrations using local *in situ* data (Martiny et al., 2016; Talarmin et al., 2016).

Remote sensing has emerged as an efficient approach for observing surface Chl *a* concentration on a regional or a global scale. GOCI-derived Chl *a* observations have been widely used to monitor near-coastal water quality with high spatial and temporal resolution (Matthews et al., 2010; Siswanto et al., 2013). Quite a several studies have shown that nutrient concentration has a good correlation with the concentration of Chl *a* (Song et al., 2012; Chen et al., 2015). Overall phytoplankton community biomass appears to be co-limited by nitrogen (*N*) and phosphorus (*P*). In the classical Redfield paradigm, where 16 mol *N*: 1 mol *P* is assumed to be optimal for phytoplankton growth (Falkowski, 1997; Tyrrell, 1999), the high *N*: *P* ratios (nutrient ratio) suggest *P* limitation (Moore et al., 2008). The consequences of variable biological *N*: *P* stoichiometry, caused by environmental changes, for phytoplankton growth remain to be elucidated.

At present, the research on the influencing factors of nutrient transport in the Yangtze Estuary mostly involves atmospheric wet deposition, the Yangtze River runoff, and upwelling. Water in the Yangtze Estuary is generally stratified most of the time in summer, and previous studies have demonstrated that storms and typhoons can break down the strong stratification and thus break the original balance of nutrient ratios (Chen et al., 2014; Chen et al., 2017). Coupled with the influence of the cold water mass in the north, the warm current in the southeast, and the effect of upwelling, the nutrient ratios in surface water response to typhoons have been a subject of both great scientific and practical significance (Wu and Chen, 2012; Guan et al., 2017; Li et al., 2021).

Previous papers have focused on observing changes in chlorophyll and suspended sediment concentration in the study region during typhoons, thus exploring physicochemical changes that occur in this area. The mature operation of the GOCI sensor allows us to simplify the observation of nutrient status. Instead of just applying the average value of chlorophyll at the intermediate time, in this paper, we designed a remote sensing based workflow to observe the changes in nutrients. Taking typhoon as a case study, we observed the changes of nutrient-limited status by judging the diurnal variations in chlorophyll *a* (Chl *a*). The information on the typhoons that affected the Yangtze Estuary was collected from 2011 to 2020. We combined the observation from remote sensing and mooring buoy to analyze the growth mechanism of chlorophyll before and after the typhoon in 2011. Sediment fronts and plume fronts can significantly affect the spatial distribution of materials in the Yangtze Estuary, which in turn affects the growth of phytoplankton. Bounded by nutrient-limited statuses, we analyzed the spatial distribution characteristics of chlorophyll a before and after the typhoon and explored the changes in the nutrient-limited status in different regions.

The paper is structured as follows. We introduce the background in Section 1 and describe the scientific hypothesis and whole procedure in Section2. Data resources and study areas are described in Section 3. Section 4 shows the main results and our viewpoints with figures and tables. Conclusions are provided in Section 5.

2 Research methods

2.1 Scientific hypothesis

Nutrient-limited statuses can be divided into two categories. One is absolute nutrient-limited (ANL) status, which always happens in the open sea with low nutrient concentration. The other is named relative nutrient-limited (RNL) status. It restricts the growth of phytoplankton in the eutrophication areas because the ratio of nutrients does not match that of phytoplankton uptake. However, influenced by runoff flow and currents field, as

well as the extreme weather environment such as typhoon, the physicochemical environment of the Yangtze Estuary changes dynamically, and nutrient-limited status also changes.

As shown in (Figure 1A), the Yangtze Estuary enriched with nutrients tends to be in RNL status, while farther offshore areas tend to be in ANL status. In winter, the CDW forms a narrow freshwater band along China's southeast coast; in spring, the intrusion of the nearshore Kuroshio branch current triggers stratification (Jiang et al., 2015). Thereafter, stratification is enhanced in summer and gradually expanded northward. At this time, the nutrients in the surface water mainly come from the CDW, without the supplementation of the bottom water. However, the movement of water masses and the change of stratification induced by typhoons or strong winds both influence the development of nutrient-limited statuses in waters (Figure 1B). The vertical mixing and upwelling can uplift the deeper Chl *a* to the surface and bring nutrients from intermediate depths into the euphotic zone (Wang and Zhang, 2021). The bottom waters of the open ocean contain higher nutrients than surface waters, thus altering the nutrient-limited status and stimulating phytoplankton communities and primary production; the opposite is true for nearshore (Figure 1C, D). When the water body reverts to a stratified state, the regions return to their original nutrient-limited statuses (Figure 1E).

At the same time as the nutrient-limited status changes, we guess that the concentration and diurnal variation of chlorophyll will vary as Figure 2 shows. Strong near-surface wind creates internal friction. The physical driving forces associated with typhoons or strong winds that modulate phytoplankton dynamics, such as the nutrient and phytoplankton transportation, result in greater diurnal variation of chlorophyll in both nearshore regions and open sea surface waters. However, the chlorophyll concentrations in the above two areas will vary differently.

In coastal water, the phytoplankton will decline attributed to the increase of water turbidity, accompanied by the vertical

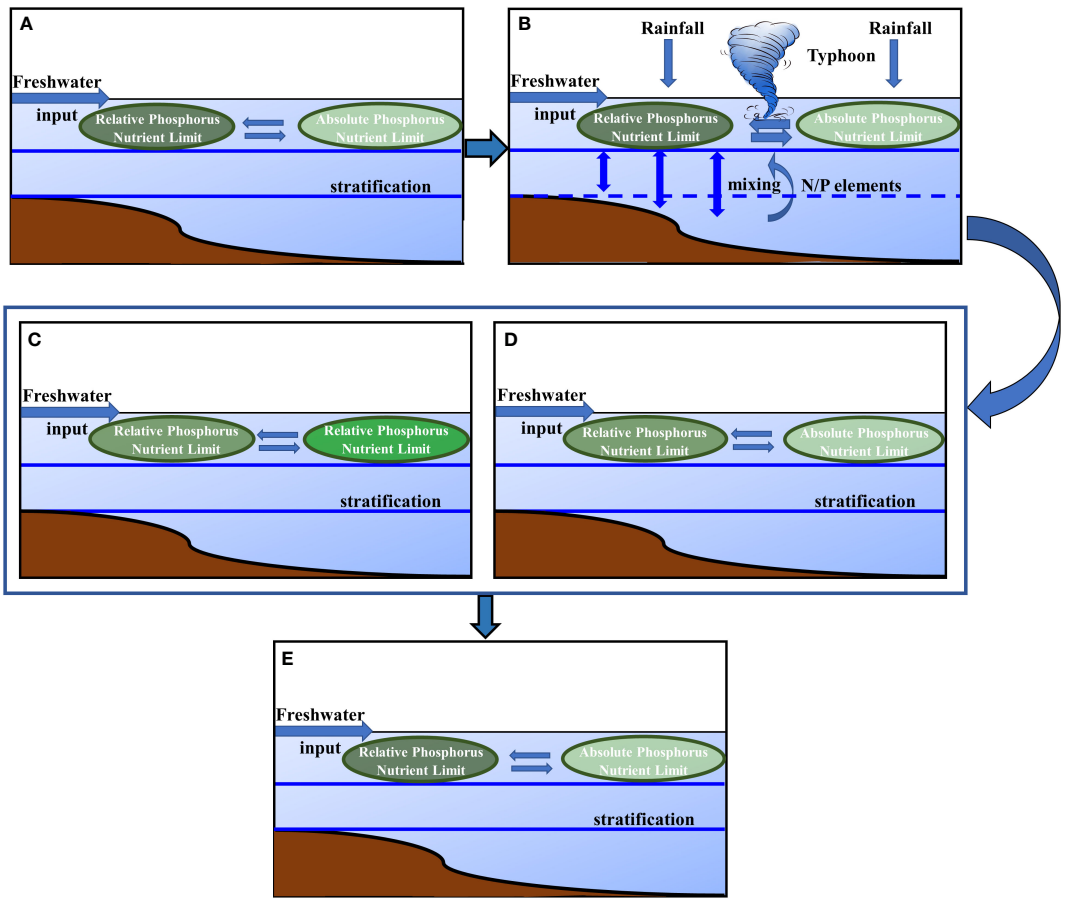


FIGURE 1
Schematic diagram of changes in nutrient status before the typhoon **(A)**, during the typhoon **(B)**, and after the typhoon **(C–E)**. Among them, **(C, D)** show two kinds of statuses may occur within a short time after the typhoon passes by, and **(E)** shows the status after a period of time after the typhoon passes by.

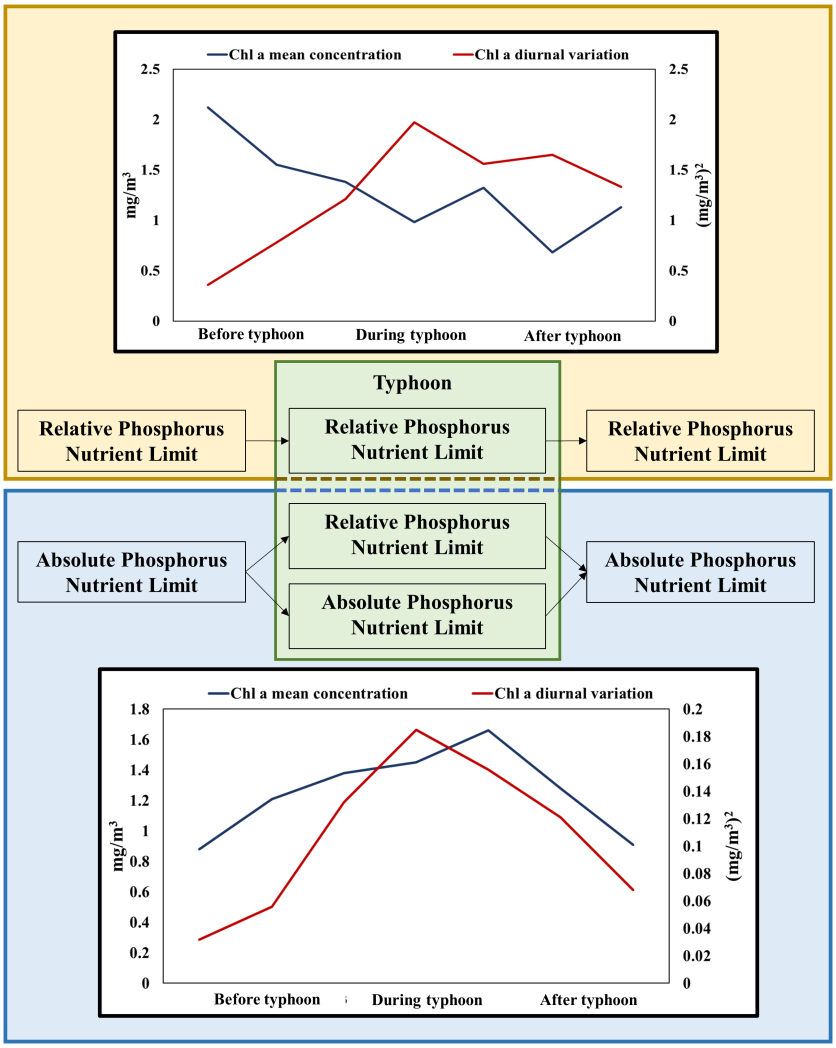


FIGURE 2
Scientific hypothesis of chlorophyll concentration and diurnal changes before and after typhoon. The large background boxes in yellow and blue represent the hypotheses of changes in two different nutrient-limited status regions.

redistribution of phytoplankton with reduced nutrients. The Kuroshio intrusion water, with high salinity and few nutrients, may also play role in the phytoplankton decline. It can inhibit nutrient uplift driven by typhoon-induced vertical mixing and upwelling (Wang and Zhang, 2021).

In the open sea, nutrient-rich upwelling near the surface will provide an ideal environment for the growth of phytoplankton. So, the diurnal variation will reach its maximum while the nutrient limitation is the weakest, and the chlorophyll concentration maximum occurs after the diurnal variation maximum. The increase in chlorophyll concentration during the typhoon may be caused by the upwelling bringing the high concentration of chlorophyll *a* from the bottom to the upper water body. The increase of chlorophyll concentration in the post-typhoon stage may be due to the change in the nutrient-limited status, and it is precisely because of the change in the limited status that the chlorophyll concentration further increases and the diurnal variation is larger than it was before the typhoon. Therefore, conversely, if the concentration of chlorophyll *a* in the post-typhoon stage is larger than that before the typhoon, and the diurnal variation is large, we believe that the nutrient-limited status at this location has changed.

2.2 Processing approach

In situ observations were performed in the Yangtze Estuary during typhoons in 2011, including the collection of Chl *a* concentrations and physicochemical characteristics. Satellite remote sensing data covering the typhoon periods were also

acquired, and the remotely sensed data were used to describe the key factors associated with typhoons that controlled phytoplankton dynamics, thereafter analyzing the effects of changes in nutrient ratios on short-term phytoplankton dynamics in and near the Yangtze Estuary. The whole procedure in the paper consists of three steps: determination of the study area, selection of typhoons, and analysis of nutrient-limited status.

Due to the characteristics of low salinity, a huge plume area is formed after the freshwater enters the sea from the Yangtze Estuary (Chen et al., 1999; Sun et al., 2014; Wu and Wu, 2018). Meanwhile, under the impact of the low-salinity plume and tidal mixing, a large number of suspended sediments brought by the flushing water settle in the estuary and form a sediment front because of the dynamics of vertical resuspension (Ge et al., 2020). Moreover, the transitional region between the sediment and plume fronts is wide, ranging from 122.5°E to 123.5°E eastward. Sediment and nutrients from freshwater input have a direct impact on underwater light field distribution and nutrient supply in the Yangtze Estuary, and further influence the spatial pattern of phytoplankton productivity (Zhao et al., 2004; Chai et al., 2006; Li et al., 2015). According to the peculiarities of the environment, we chose two regions to represent the relative and absolute nutrient-limited regions, the former region is located west of 123°E, and the latter is located outside the above two fronts. They were both described in Section 3.1.

As one of the major disastrous meteorological events, the typhoon is one of the top ten natural disasters in the world (Guan et al., 2018). From 2010 to 2020, about 25 typhoons were generated every year in the western Pacific, which is the region with the most active typhoon activities (Elsner and Liu, 2003). China is one of the countries most affected by typhoons, and typhoons pass through the Yangtze Estuary almost every year (Oey and Chou, 2016). We screened the typhoons with a seventh-level wind circle covering the Yangtze Estuary for analysis.

In addition to the diurnal variations in parameters, we divided all data into three time periods for mean analysis: before the typhoon, during the typhoon, and after the typhoon. The variance of 6-time (9:30-14:30) values per day is used to show the diurnal variation of Chl *a*. The diurnal variation and concentration of chlorophyll can be used to analyze the nutrient-limited status.

3 Research data

3.1 Study area

The Yangtze Estuary is the gateway for the river to go to sea and marine transportation. The interaction between the East Asian monsoon and various flows constitutes the unique hydrodynamic mechanism of the Yangtze Estuary (Figure 3).

In recent years, eutrophication in the ECS, which can lead to frequent red tides outbreaks, has become a growing concern. The Yangtze Estuary can be divided into three parts to study the relationship between nutrients and primary productivity: the light-limited area near the estuary, the RNL area in the transition zone, and the ANL area far from the estuary. Taking two fronts as the boundary, the location (122.85°E, 30.75°N) where placed the mooring buoy is named Nearshore Area, where high turbidity will cause light limitation (Xu et al., 2021), and it can be referred to as the RNL area. This area is shown by the blue dot in Figure 3. It is close to the coast and is greatly affected by the CDW. The area marked by the blue box in Figure 3 is away from the two fronts, named Offshore Area, the water at this area is relatively deep without light limitation. It is mainly limited by nutrient concentration, so it can be referred to as the ANL area. The range of the Offshore Area is 123.5-124°E, 30-30.5°N.

3.2 Typhoon

The information on typhoons that affected the Yangtze Estuary from 2011 to 2020 collected was listed in Table 1, the track and period of the typhoon in 2011 were supported by data from the mooring buoy. The selected 11 typhoons include tropical storms (TS), severe tropical storms (STS), severe typhoons (STY), and super typhoons (Super TY). Information on typhoons was obtained from Japan Meteorological Agency (http://www.jma.go.jp/jma/jma-eng/jma-center/rsmc-hp-pub-eg/trackarchives.html). The tracking dataset includes the typhoon location, intensity, and atmospheric pressure every 6 h.

The historic tracks of typhoons collected were illustrated in Figure 4. Among them, "Meari" was formed in the ocean east of the Philippines on the afternoon of 22 June 2011. It intensified into an STS after two days and moved northward along the eastern coast of China. "Meari" had successively combined with the tropical monsoon cloud cluster and the northern westerly belt cloud system. Its fastest moving speed was 40-60 km/h. Super Typhoon "Muifa" (2011) was formed on 28 July 2011. As a Category 5 storm with winds once up to 140 knots, it landed on the eastern coast of China on 6 August. The storm's sustained winds reached 40 m/s when it approached the study area.

3.3 *In situ* and GOCI data

A mooring buoy was established off the Yangtze Estuary in 2011 and collected data for about three months at a 30-min interval (Chen et al., 2012). The bio-optical dataset includes *in situ* dissolved oxygen (DO), salinity, temperature, Chl *a*, photosynthetically active radiation (PAR), pressure, conductance, and turbidity.

As the first geostationary orbit ocean color satellite sensor launched by the Korea Ocean Satellite Center (KOSC), the Geostationary Ocean Color Imager (GOCI) performs eight

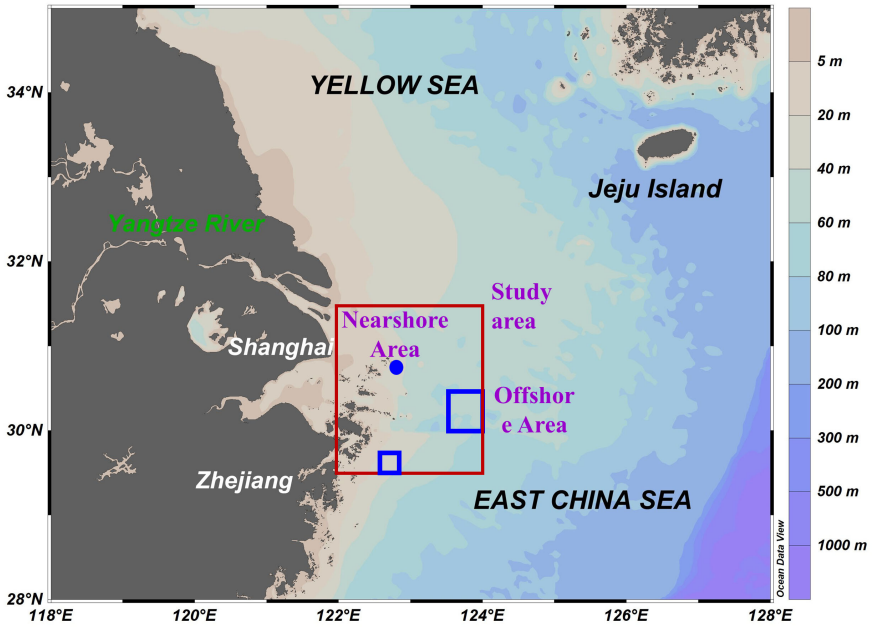


FIGURE 3
A map showing study sites. The red box indicates the entire research area in the paper. The blue dot marks the location of the mooring buoy, and the blue box represents the Offshore Area that is not affected by the plume and high turbidity. Bathymetry is shown from light to dark blue for the range of 5 to 2500 m.

measurements in a day. In the paper, we used GOCI Level-2A data obtained from the KOSC (URL: http://kosc.kiost.ac/) for comparison. The dataset covers all the data before and after the typhoon passed the Yangtze Estuary from 2011 to 2020. There are many literatures on GOCI data, and retrieval algorithms have been shown to be useful in retrieving water-column constituents in the Yellow Sea (YS) and East China Sea (ECS) (Min et al., 2014; Kim et al., 2016).

In this paper, we also analyze the temperature, salinity, mixed layer depth, and the flow field changes. The analysis results help to determine the changes in the nutrient ratios. The information on sea surface temperature (SST) data was obtained from Operational Sea Surface Temperature and Sea Ice Analysis (OSTIA) system (Good et al., 2020), which was developed at the Met Office (the UK's national meteorological service; https://www.metoffice.gov.uk/). The *in situ* SST data used are those distributed in near real time through the WMO GTS, and are from a mixture of sources including *in situ* data (drifting and moored buoy platforms and ships), and satellite SST data. Information on salinity, mixed layer thickness, and ocean current velocity were all obtained from GLORYS12V1 product (https://resources.marine.copernicus.eu/product-detail/

TABLE 1 Information on typhoons that affected the Yangtze Estuary from 2011 to 2020.

Year	Name	Start date	End date	Date passing through the mouth of the Yangtze River	Type	Impact area (kilometer)
2011	Meari	Jun. 21th	Jun. 27th	Jun. 25th	STS	200
2011	Muifa	Jul. 27th	Aug. 9th	Aug. 7th	super TY	400
2012	Bolaven	Aug. 19th	Aug. 30th	Aug. 27th	super TY	350
2014	Neoguri	Jul. 2nd	Jul. 11th	Jul. 9th	super TY	420
2014	Nakri	Jul. 29th	Aug. 4th	Aug. 2nd	STS	350-450
2017	Talim	Sept. 9th	Sept. 18th	Sept. 16th	super TY	300-380
2018	Kong-rey	Sept. 29th	Oct. 7th	Oct. 15th	super TY	400-530
2019	Danas	Jul. 15th	Jul. 21th	Jul.19th	TS	200-350
2019	LingLing	Sept. 1st	Sept. 8th	Sept. 6th	super TY	260-300
2020	Bavi	Aug. 21th	Aug. 27th	Aug. 26th	STY	150-250
2021	Chanthu	Sept. 7th	Sept. 18th	Sept. 14th	super TY	220-280

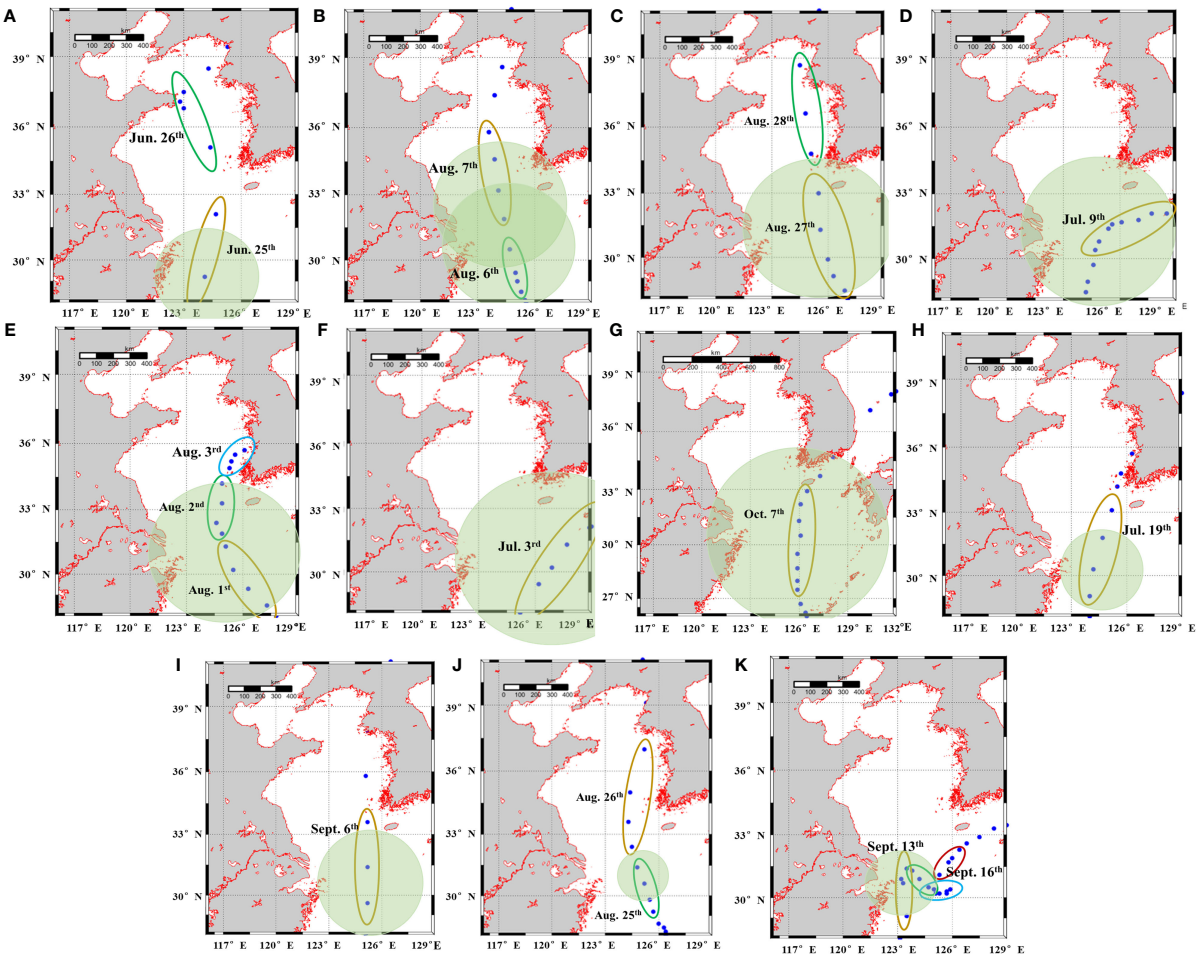


FIGURE 4
The historic track of typhoons. The green circles indicate the influence area of Category 7 wind circle of typhoon **(A)** 2011 Meari; **(B)** 2011 Muifa; **(C)** 2012 Bolaven; **(D)** 2014 Neoguri; **(E)** 2014 Nakri; **(F)** 2017 Talim; **(G)** 2018 Kong-rey; **(H)** 2019 Danas; **(I)** 2019 LingLing; **(J)** 2020 Bavi; **(K)** 2021 Chanthu. The trajectory points in colored different ellipses are all within the same day, and the date is indicated next to the ellipse.

GLOBAL_MULTIYEAR_PHY_001_030/DATA-ACCESS), which is the CMEMS global ocean eddy-resolving reanalysis products with 1/12° horizontal resolution and 50 vertical levels. It covers from 1st of January 1993 until 30 May 2020 (Le Traon et al., 2019), and the products available for users are daily averages and monthly mean averages. The sea surface salinity (SSS hereafter) is generally fresher than both the climatology with regional biases of less than 0.2 psu.

4 Results and discussion

4.1 Measured data results of buoys before and after the typhoons in 2011

Buoy observations revealed the impact of the typhoon on the Chl *a* concentration in 2011. During the typhoons, Chl *a*, oxygen content, turbidity, temperature, and salinity all changed to varying degrees.

4.1.1 Typhoon "Meari"

According to Figure 5, In early summer, the sea surface temperature is about 20 °C, and the salinity of the surface water where the buoy was located was about 27-28. Typhoon "Meari" passed the Yangtze River Estuary on 25 June 2011, and the concentration of Chl a was high at this time, reaching 7.5 mg/m^3. Then, the temperature and Chl *a* concentration decreased obviously on 26 June, and the temperature dropped by about 2°C, while Chl *a* decreased about 3mg/m^3 with a small diurnal variation (Figures 5B, C). (Figure 5A) shows that the increase of the river's freshwater discharge and strong winds that caused surface salinity and temperature generally decreased suddenly on June 27, and the highest Chl *a* concentration reached 20.7

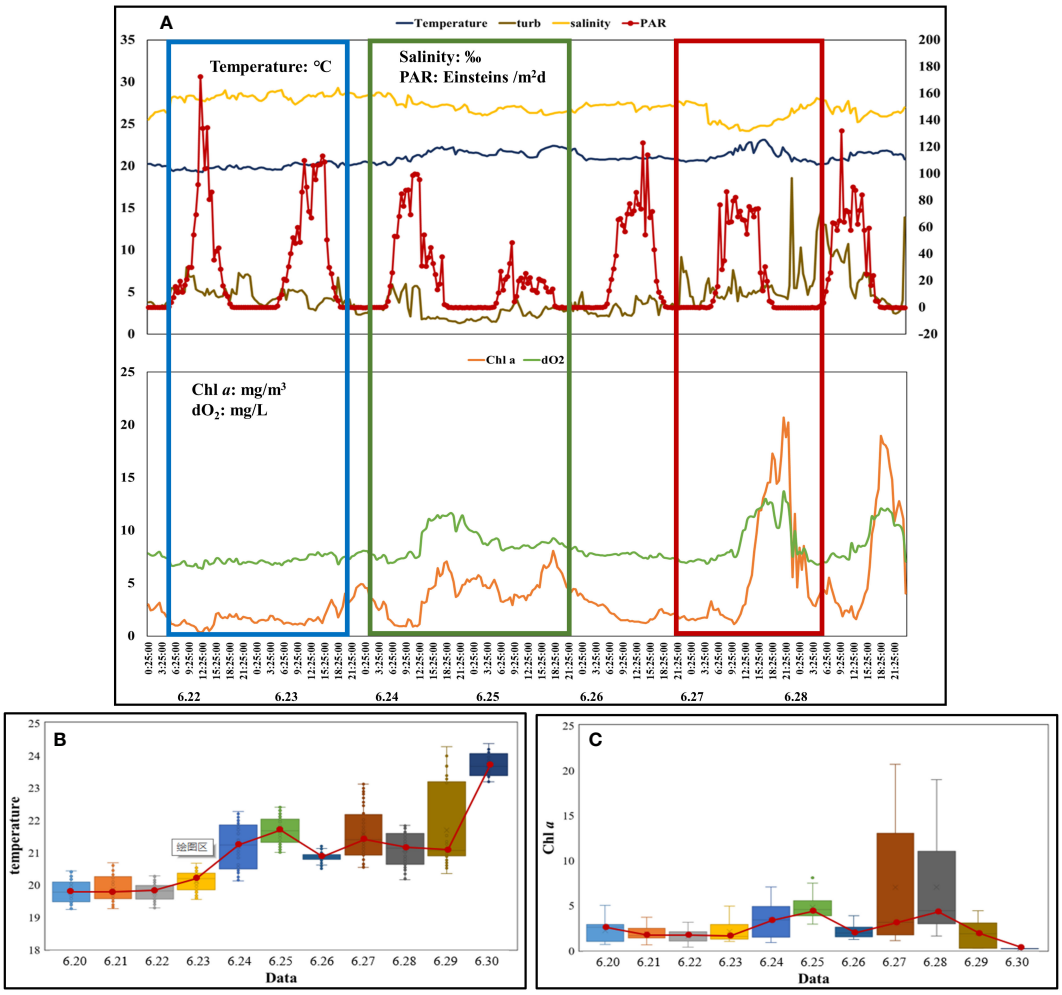


FIGURE 5
The variations of parameters measured by buoy during typhoon "Meari". The variations when the typhoon passes are marked with red box. The typhoon passed through the Yangtze Estuary on June 25. The red, green and blue boxes represent several typical situations analyzed in the paper. **(A)** show the daily changes before, during, and after the typhoon, **(B, C)** show the Chl *a* and temperature changes with box plots, respectively.

mg/m^3. It was reported that the study area was sunny to cloudy on June 27 and cloudy on June 28, but the Chl *a* concentration varied greatly on these two days. This also shows that PAR has less effect on chlorophyll, and the change of chlorophyll was mostly affected by nutrients and CDW input.

Three sets of data are intercepted from (Figure 5A), which are framed by blue, green, and red boxes respectively. The content of the blue box indicates that there was water intrusion with high salt and low temperature at that time, or the phenomenon that low salt and high temperature water dominated the previous day disappeared. Changes in temperature and salinity were smaller on the days in the green box, while there was a small peak in Chl *a*, which we consider being because of rainfall. The previous report stated that the heavy rains occurred on 24 and 25 June. The red box mainly shows the parameter changes on June 27. As mentioned above, the intrusion of CDW brought rich nutrients and a large number of suspended solids. Moreover, phytoplankton consumed a large amount of carbon dioxide and released oxygen in the process of life activities, which increased the dissolved oxygen in the surface seawater.

4.1.2 Typhoon " Muifa"

Typhoon "Muifa" passed the Yangtze Estuary on 7 August 2011. The parameter changes before and after the typhoon in August, as Figure6 shows, were different from those in June. Before the typhoon "Muifa" came, the sea surface temperature was relatively high, and due to the strong wind and rainfall, the sea surface temperature dropped largely on 7 August, with the temperature dropping by nearly 5.0°C. After that, the temperature slowly rose. At the same time, the salinity

increased slowly from 5 August and decreased after the typhoon passed. Chl *a* changed greatly on 5 August with the difference between the maximum and minimum values reaching 2.56 mg/m^3. The overall value of Chl *a* on 7 August was lower, with the lowest value being 0.61 mg/m^3 and the highest being only 1.02 mg/m^3 (Figures 6B, C). Surveys have shown that the area was cloudy and rainy during this time, with the temperature remaining at around 25 °C. Dilution effects of heavy rainfall and increased freshwater flow in rivers, and unsuitable temperature caused an overall decrease in Chl *a* concentration.

Judging from the content displayed in the red box, on August 2, CDW with high temperature and low salinity brought a large amount of suspended matter and phytoplankton, and as a result, the dissolved oxygen in the surface seawater increased significantly. The content displayed in the blue box shows that there was a high saltwater intrusion in the area, and the temperature changed relatively large. Water bodies of different thermohaline states mixed up and down. In addition, there may be reasons for heavy rainfall (5-8 August).

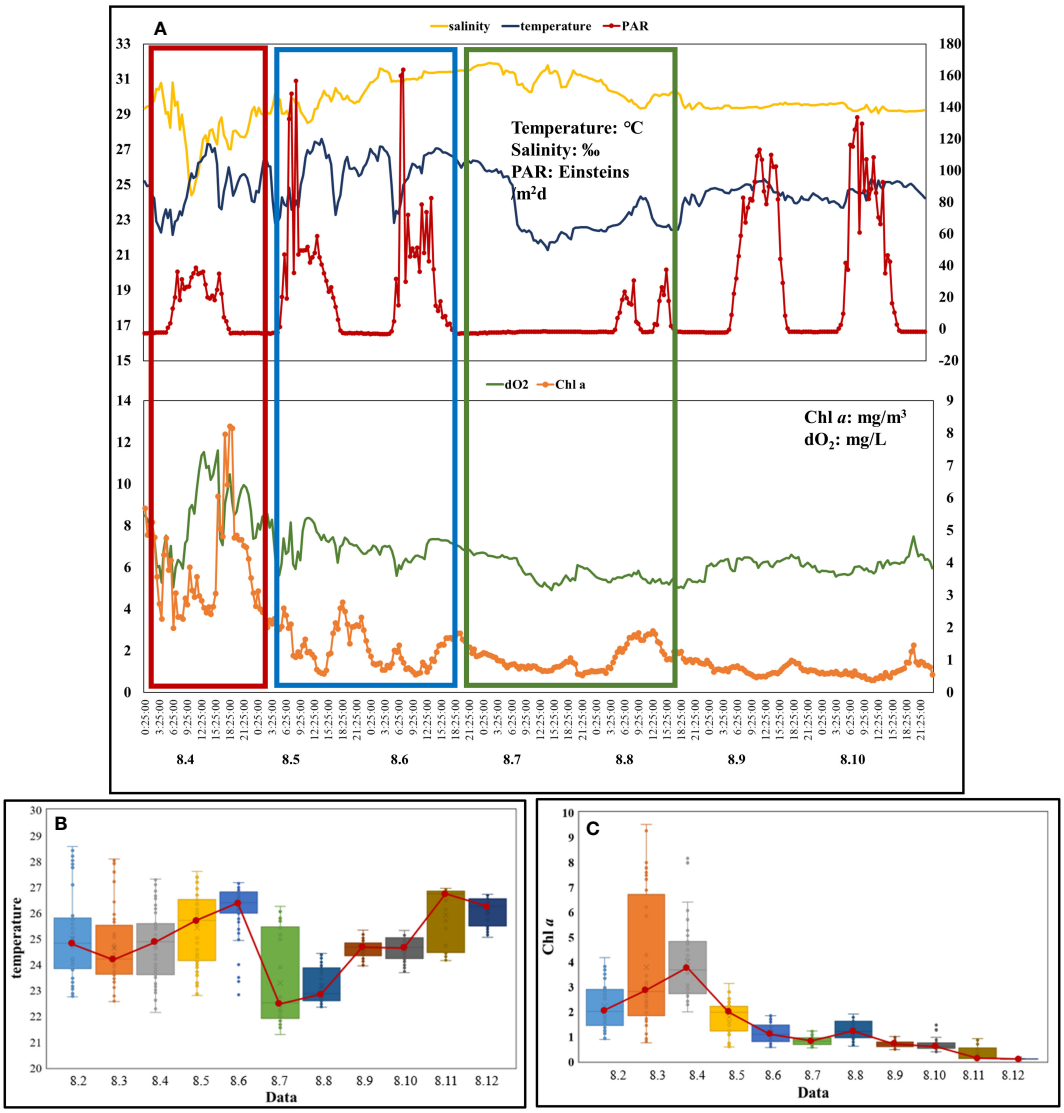


FIGURE 6
The variations of parameters measured by buoy during typhoon "Muifa". The variations when the typhoon passes are marked with red box. The typhoon passed through the Yangtze Estuary on August 7. The red, green and blue boxes represent several typical situations analyzed in the paper. **(A)** show the daily changes before, during, and after the typhoon, **(B, C)** show the Chl *a* and temperature changes with box plots, respectively.

4.2 The variations of GOCI-derived parameters during typhoons

4.2.1 Diurnal variation of GOCI-retrieved parameters during typhoon–Muifa (2011)

Figure 7 shows satellite-observed variations in Chl *a*, SST, salinity, and mixing layer depth from 1 August to 13 August during the typhoon "Muifa" in 2011. The images available for analysis are limited by the no-data pixels in GOCI imagery, which is mainly due to the contaminating effects of cloud, sea fog, and aerosols.

Before the typhoon, the northeast of the Yangtze Estuary was influenced by the coastal current that represented a cold tongue with a surface temperature of approximately 25°C. Overall, temperatures remained low near the shore and the high-temperature water area was cut off at 123°E. The minimum surface salinity in the study area was below 25‰ and the temperature was above 24°C. The depth of the mixed layer at 29.5°N, 123-124°E was 10 m at first and increased to nearly 16 m on 5 and 6 August. From 2 August to 5 August, the mean Chl *a* in the southern part of Yangtze Estuary changed little, but the diurnal variation increased largely. In the northern part, both the mean and the diurnal variation were larger. The mean Chl *a* could reach about 2.5mg/m^3, and the maximum diurnal variation could be above 0.2 $(mg/m^3)^2$. Moreover, the diurnal variations of Chl *a* in the near shore were all large, increasing from 0.06 $(mg/m^3)^2$ to 0.2 $(mg/m^3)^2$ as the typhoon approached, while the diurnal variations of Chl *a* in the oligotrophic ocean region were low, less than 0.04 $(mg/m^3)^2$ in most locations.

After the typhoon, the overall mean Chl *a* concentration in the water body was higher than that before the typhoon, and the diurnal variation showed differences. On 9 and 10 August, the area with Chl *a* concentration exceeding 1.0 mg/m^3 was further expanded, and it in the oligotrophic ocean region could even exceed 1.5 mg/m^3. Chl *a* over 3 mg/m^3 appeared at the intersection of the Yangtze Estuary and Hangzhou Bay. On 9 and 10 August, the diurnal variation in the eutrophic coastal water was close to that on 4 and 5 August, while it was significantly larger in the low-productivity region, which could even be greater than 0.3 $(mg/m^3)^2$. The temperature in the study area decreased significantly, with an overall drop of about 2°C. Satellite images revealed a wide patch of cold water in the Nearshore Area. The upwelling held temperature below 23°C in the patch center, and then gradually weakened. Then, a surface warm water (about 27°C) with salinity above 34 moved northward offshore Zhejiang from 9 August, and there was an increasing depth of mixed layer in the southeast corner. The intrusion of the CDW was stronger due to the strong precipitation, and its southward front had reached 29.5°N southward and 123°E eastwards. From 9 to 11 August, the low-salt area expanded eastward to 123.5°E and southward to 29.5°N. Combined with the results in Figure 6, the bottom material came to the surface for mixing due to the influence of upwelling, so there was a small peak of chlorophyll in Nearshore Area on 8 August.

The direction of flow field in the early stage was mainly from south to north. On August 5th, due to the influence of typhoon, the flow field in the southeast direction impacted the study area. Due to the heavy rainfall caused by the typhoon on 9th and 10th, the diluted water of the Yangtze River flowed into the study area obviously, which is also consistent with the content of our previous analysis.

4.2.2 The variations of GOCI-derived parameters during typhoons

The 13-day data were divided into three categories: before typhoon (5 days), during the typhoon (3 days), and after typhoon (5 days). Calculate average values of each category, Fig. 8 shows five typical results in 2012, 2018, 2019, and 2020.

Before the typhoon, most areas west of 123°E were all in high RNL statuses, whereas most areas to the east were in ANL statuses. The results showed that typhoon events have different effects on plankton biomass, even within the same area. Many typhoons have little contribution to, or even have negative effects on, phytoplankton in the nearshore region. During the typhoon, Chl *a* peaks were observed in the transitional region between the sediment and plume fronts, and the highest diurnal variation appeared in the transitional waters beyond the sediment front. After the typhoon, the chlorophyll concentration in the western part of the 123°E meridian had two situations: the overall decrease (Figures 8A-C), or the increase (Figures 8D, E).

4.3 GOCI data results in different areas during the typhoons

Phytoplankton in the Yangtze Estuary and adjacent shelves exhibit complex spatial-temporal heterogeneity. As shown in Figure 8, with 123.5° as the dividing line, there were obvious differences in the changes of results in the Nearshore Area and Offshore Area before and after the typhoon passes.

In the transitional area, the strong vertical mixing and upwelling induced by the typhoon rolled up sedimentation, which is caused by physical-chemical effects near the sediment front. Therefore, the nutrients deposited in the bottom layer are also swept up into the upper water body, resulting in the increase of Chl *a* concentration and the increase of diurnal variation. Thus, we believe that the original ANL area turned into low ANL status or RNL status. Among them, the southeast corner of the study area is mostly in low ANL status, and the northeast may turn to RNL status.

4.3.1 GOCI data results in Nearshore Area

We compared the GOCI data with the buoy data. Taking the mooring buoy position as the center, we averaged the 3*3

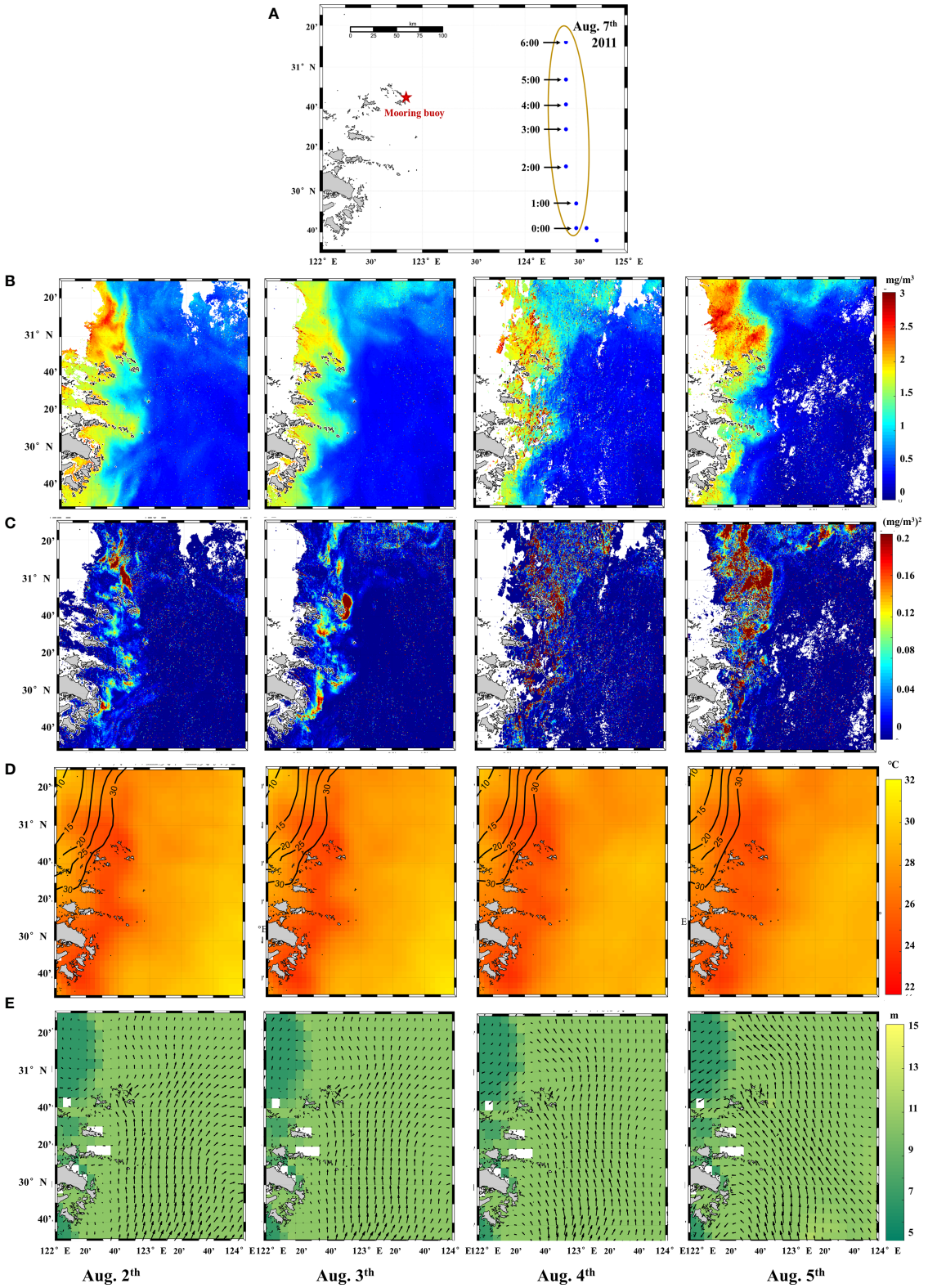


FIGURE 7 (Continued)

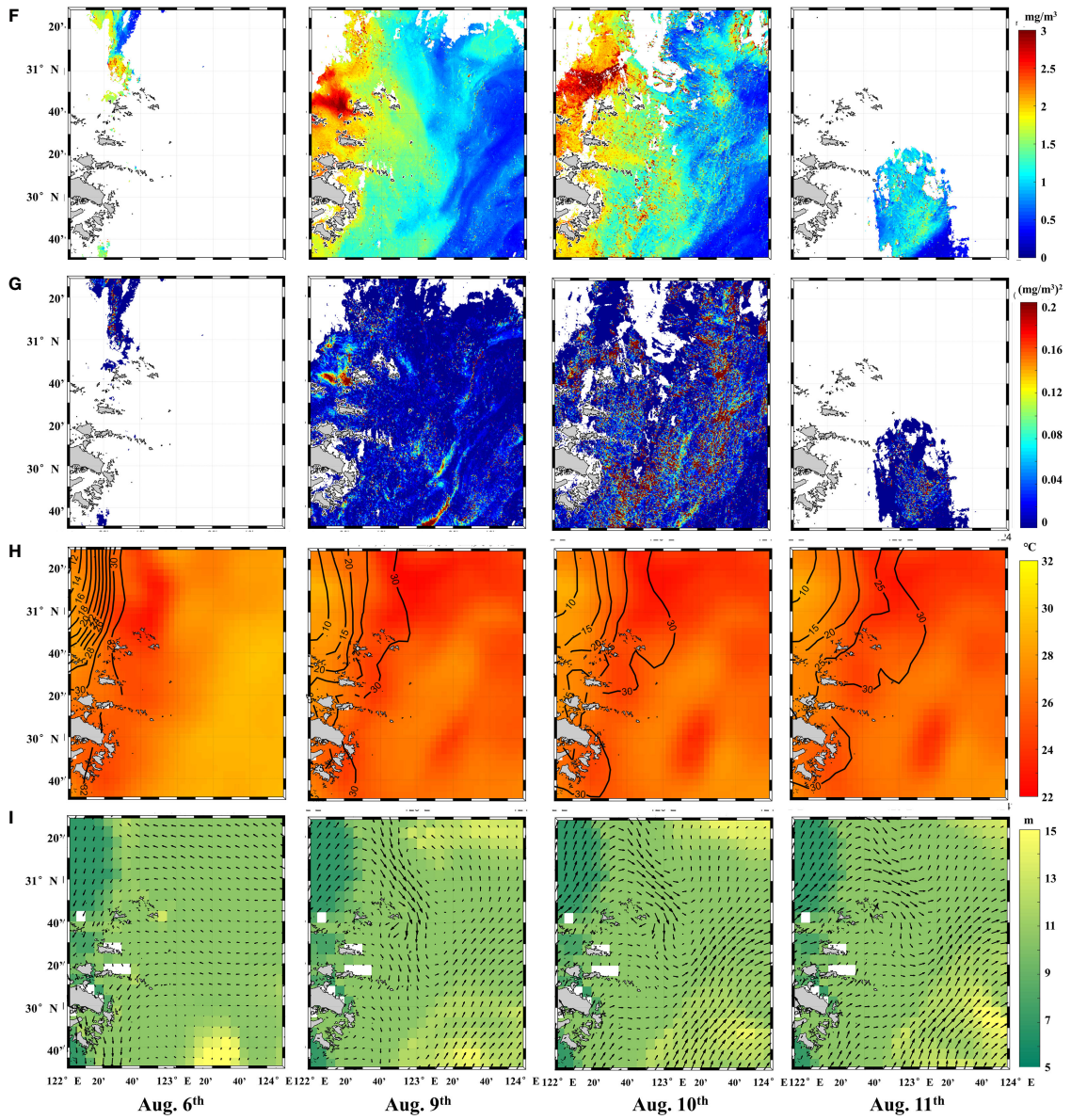


FIGURE 7 (Continued)
Spatial and temporal distribution of parameters in study area in 2011. The parameter **(A, F)** Chl *a* (mg/m3), and **(B, G)** diurnal variation changes from blue to red. Water temperature **(C)** is shown in subfigures **(D, H)**, and salinity (unit: spu) is represented by contour lines. Depth of the mixed layer and the flow rate state are shown in subfigure **(E, I)**. White represents cloud coverage.

window and used the result as the parameter value of the buoy position. Each pixel in the GOCI image represents an area of 500*500, so there were some differences from the point data measured by the buoy. Table 2 shows the results of valid values from 2011 to 2020. The segmentation rules for the three time periods are consistent with those described in Section 4.2.2.

Appropriate nutrient ratios are required for phytoplankton production, and most of the Yangtze Estuary region is relatively nutrient-limited, despite high nutrient levels. When the CDW enters the sea, it provides high levels of nutrients to areas affected by plumes and high suspended matter further stimulates phytoplankton productivity. During and after the typhoon, the intense rainfall and floodwaters introduce high quantities of nutrients to the area from atmospheric sources and the adjacent land respectively, strongly enhancing the surface nutrient concentrations. Therefore, changes in the nutrient-limited status led to an increase in the diurnal variation of Chl *a* in the Nearshore Area after typhoon.

However, heavy rainfall and increased river freshwater flow diluted Chl *a* concentration. Moreover, massive sediment

TABLE 2 Results at Nearshore Area in GOCI from 2011 to 2020.

Year	Name	Time	Mean	Diurnal variation	Year	Name	Time	Mean	Diurnal variation
2011	Meari	Before	1.501	0.406	2018	Kong-rey	Before	1.675	0.043
		During	1.492	0.906			During	1.675	0.208
		After	1.488	0.005			After	1.481	0.063
2012	Bolaven	Before	1.434	0.086	2019	Danas	Before	0.942	0.027
		During	1.479	0.223			During	1.437	0.001
		After	1.375	0.134			After	1.612	0.036
2014	Nakri	Before	1.441	0.115	2019	Ling-Ling	Before	NaN	NaN
		During	1.277	0.052			During	1.510	0.298
		After	1.431	0.129			After	1.704	0.026
2017	Talim	Before	3.108	0.055	2020	Bavi	Before	1.675	0.043
		During	2.189	0.637			During	1.675	0.208
		After	2.162	0.440			After	1.481	0.063

inflows as well as intense tidal forcing and wind induce bottom resuspension that results in increased turbidity (Cho et al., 2020), which further contributes to changes in the underwater light field, and makes phytoplankton in this area light-limited (Smith and Demaster, 1996; Lohrenz et al., 1999). Therefore, the Chl *a* concentration decreased after the typhoon passed. The analysis and comparison of Chl *a* concentration and diurnal variation were consistent with our assumptions described in Section 2.1.

4.3.2 GOCI data results in Offshore Area

The parameter changes in the areas outside the plume front and the sediment front are different from those on the nearshore. The Offshore Area is less affected by turbidity and other factors, and productivity levels are mainly limited by the ratio of nutrients. Taking the average value of the three time periods, the data can be obtained as shown in Table 3.

The offshore oligotrophic open sea is characterized by limited nutrients and low turbidities. The upwelling caused by the typhoon rolled the nutrients deposited at the bottom to the surface layer, replenishing the missing phosphorus element, and increasing the productivity of phytoplankton in the area. Therefore, the change in the sea area east of 123° after the typhoon passes is mainly due to the change in the nutrient-limited status. After typhoon Muifa in 2011, typhoon Bolaven in 2012, and typhoon Kong-rey in 2018, the chlorophyll concentration increased significantly, but it was lower than the average value after typhoon Talim in 2017 (more than 1mg/m^3). The diurnal variation also increased, and we believe that the nutrient-limited statuses in these time periods all turned to weak RNL statuses.

5 Conclusions

In this paper, we combined remote sensing and mooring buoy based dataset to analyze the growth mechanism of chlorophyll in the Yangtze Estuary before and after the typhoon in 2011. The sediment fronts and plume fronts are

TABLE 3 Results at Offshore Area in GOCI from 2011 to 2020.

Year	Name	Time	Mean	Diurnal variation	Year	Name	Time	Mean	Diurnal variation
2011	Meari	Before	0.349	0.001	2018	Kong-rey	Before	0.576	0.074
		During	0.349	0.009			During	0.888	0.150
		After	0.347	0.060			After	0.859	0.137
2011	Muifa	Before	0.363	0.669	2019	Danas	Before	0.499	0.556
		During	0.390	4.089			During	0.424	0.099
		After	0.743	0.362			After	0.527	0.119
2012	Bolaven	Before	0.272	0.292	2019	Ling-Ling	Before	0.527	0.119
		During	0.351	0.611			During	0.497	0.422
		After	0.352	0.601			After	0.510	0.015
2017	Talim	Before	1.108	0.679	2020	Bavi	Before	0.882	0.200
		During	1.056	0.552			During	0.333	1.643
		After	0.874	0.697			After	0.492	0.441

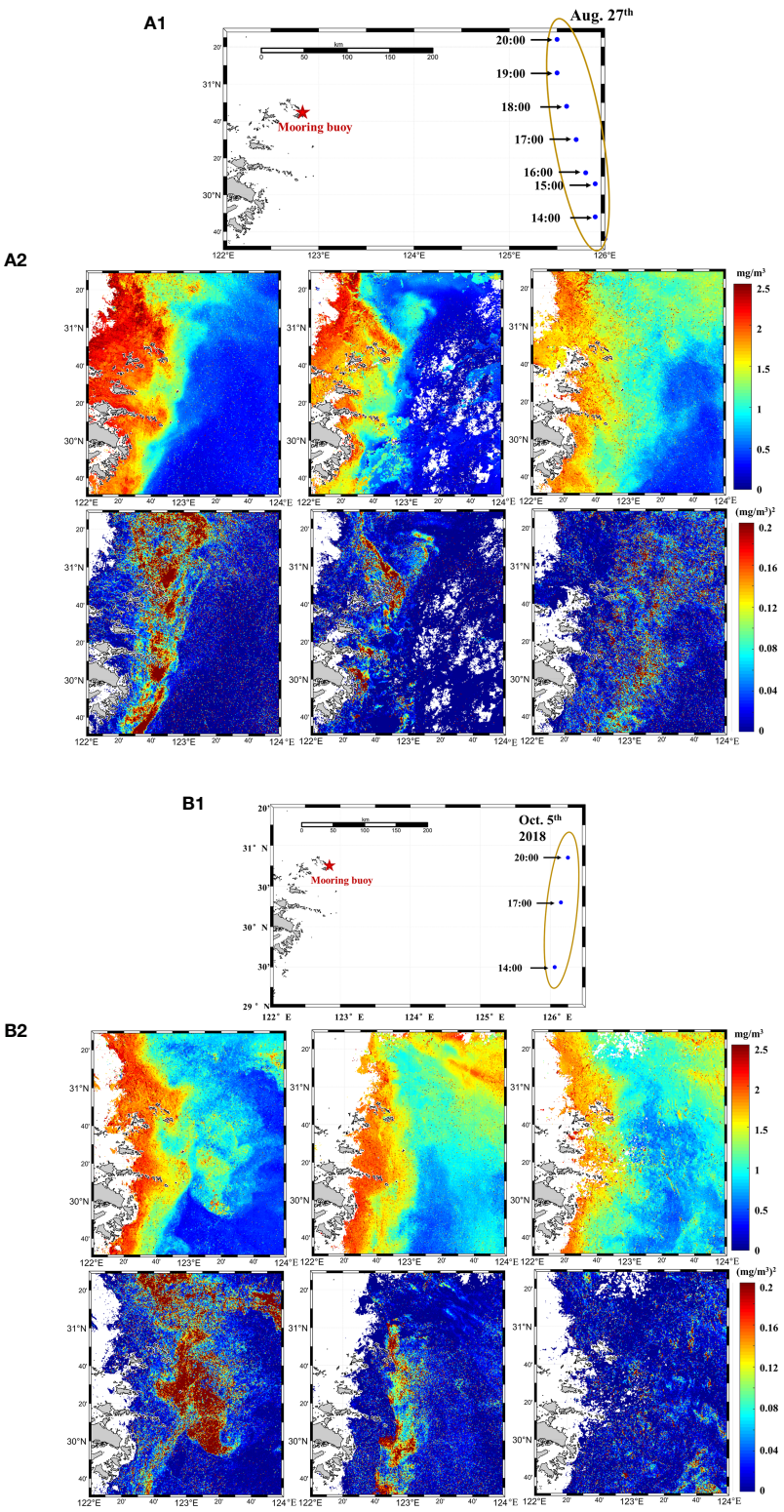


FIGURE 8 (Continued)

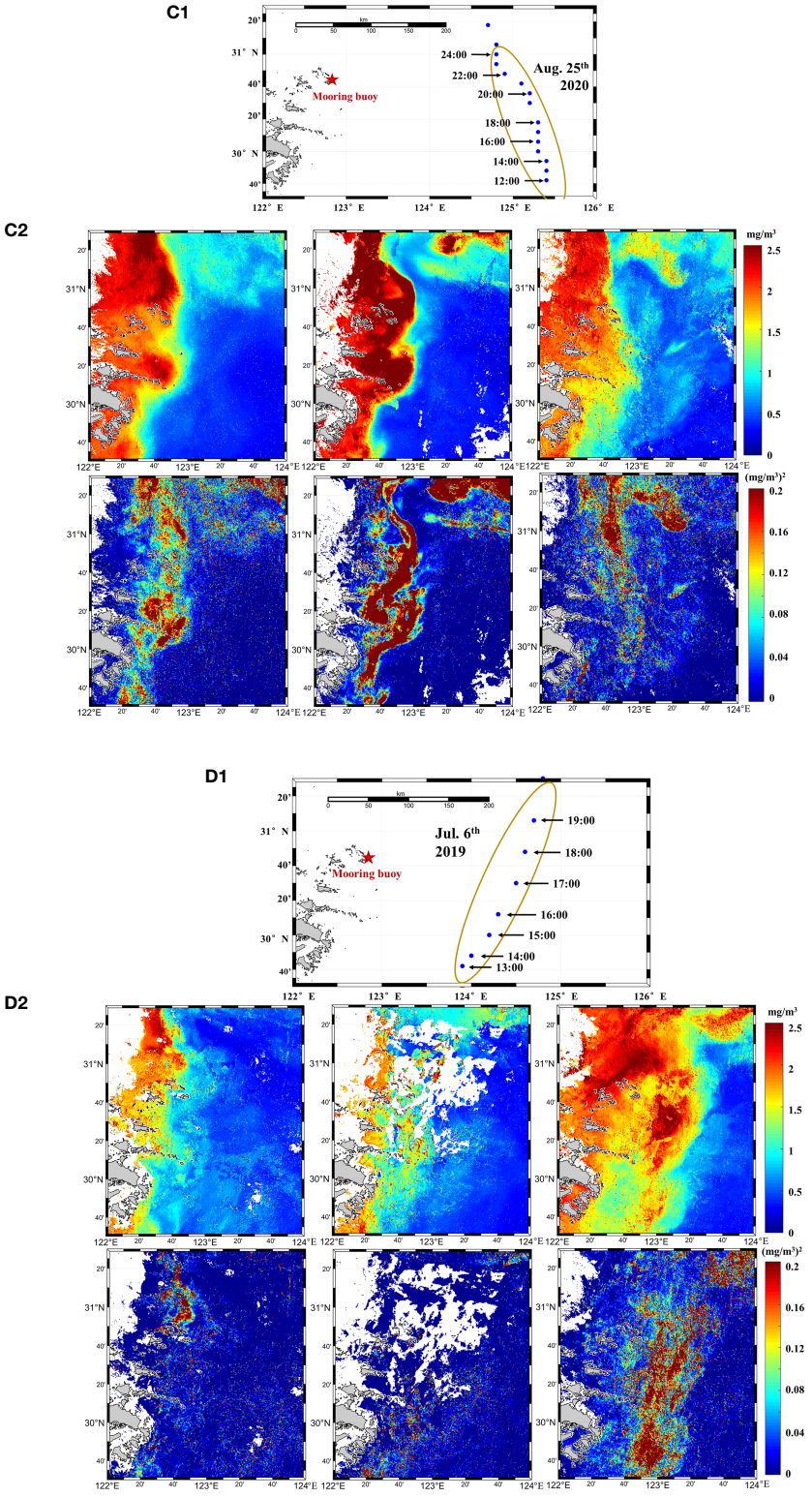


FIGURE 8 (Continued)

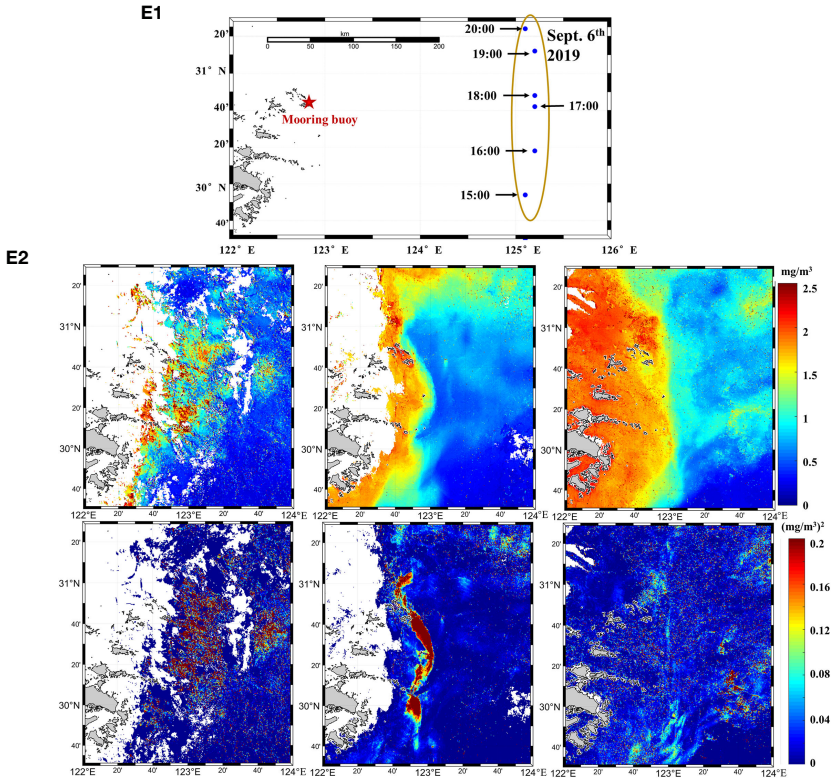


FIGURE 8 (Continued)
Spatial distribution of parameters measured by GOCI in three periods. The subgraph with suffix 1 shows the time and track of typhoons passing near the study area. Different colors in the subgraph with suffix 2 indicate the concentrations (top row) and variations (bottom row) before (left row), during (left row) and after (left row) **(A)** Bolaven (2012), **(B)** Kong-rey (2018), **(C)** Bavi (2020), **(D)** LingLing (2019), and **(E)** Danas (2019) in study area.

used as a reference to select the relative and absolute nutrient-limited status regions to analyze the spatial distribution characteristics of Chl *a* and to explore the effect of different nutrient statuses on Chl *a* under typhoon from 2011-2020. During the analysis, the variance was used to display diurnal variation in addition to observing the change of mean Chl *a* concentrations.

Case studies have shown that the passage of typhoons would cause changes in Chl *a* concentration. When the typhoon passes by, winds caused by typhoons destroy the stratification of the water and cause strong vertical mixing and upwelling. The GOCI images from 2011 to 2020 show that the Chl *a* peak appeared in the transition area between the sediment and the plume front, and the highest diurnal variation appeared in the transition water area beyond the sediment front. In addition, the parameter changes in the areas outside the plume front and the sediment front are different from those in the nearshore in RNL status. In the Offshore Area, the mean Chl *a* after the typhoon is significantly higher than that before the typhoon because of the nutrient status change, while the mean of Chl *a* within 122-123° decreased, which is affected by the turbidity and the dilution effect of heavy rainfall. The nutrient-limited statuses in the Offshore Area can turned to weak RNL statuses after the typhoon. Chl *a* diurnal variation calculated from satellite data is larger after the typhoon compared to that before the typhoon throughout the study area, and the nutrient-limited status had different changes.

Data availability statement

The original contributions presented in the study are included in the article/supplementary material. Further inquiries can be directed to the corresponding author.

Author contributions

YX and JC contributed to conception and design of the study. JC organized the database. YX performed the statistical analysis. YX wrote the first draft of the manuscript. YX and JC wrote sections of the manuscript. Both authors contributed to the article and approved the submitted version.

Funding

This research was funded by the Project of State Key Laboratory of Satellite Ocean Environment Dynamics, Second Institute of Oceanography (No. SOEDZZ2203), NSFC-Zhejiang Joint Fund for the Integration of Industrialization and Informatization (Grant U1609202), the National Key Research and Development Program of China (Grant 2016YFC1400903), and National Natural Science Foundation of China (Grants 42076216, 41376184 and 40976109).

Acknowledgments

The authors thank the Korea Institute of Ocean Science & Technology (KIOST) for providing the freely available GOCI data (http://kosc.kiost.ac.kr/, accessed on Jul.13, 2021), European Space Agency for the information on mixed layer thickness and salinity (ftp://anon-ftp.ceda.ac.uk/neodc/esacci/sea_surface_salinity/data/v03.21/), and Met Office for temperatures data (ftp://nrt.cmems-du.eu/Core/SST_GLO_SST_L4_NRT_OBSERVATIONS_010_001/METOFFICE-GLO-SST-L4-NRT-OBS-SST-V2).

Conflict of interest

The authors declare that the research was conducted in the absence of any commercial or financial relationships that could be construed as a potential conflict of interest.

Publisher's note

All claims expressed in this article are solely those of the authors and do not necessarily represent those of their affiliated organizations, or those of the publisher, the editors and the reviewers. Any product that may be evaluated in this article, or claim that may be made by its manufacturer, is not guaranteed or endorsed by the publisher.

References

Arrigo, K. R. (2005). Marine microorganisms and global nutrient cycles. *Nature* 438, 122–122. doi: 10.1038/nature04265

Chai, C., Yu, Z. M., Song, X. X., and Cao, X. H. (2006). The status and characteristics of eutrophication in the Yangtze river (Changjiang) estuary and the adjacent East China Sea, China. *Hydrobiologia* 563, 313–328. doi: 10.1007/s10750-006-0021-7

Chen, S. S., Han, L. S., Chen, X. Z., Li, D., Sun, L., and Li, Y. (2015). Estimating wide range total suspended solids concentrations from MODIS 250-m imageries: An improved method. *Isprs J. Photogram. Remote Sens.* 99, 58–69. doi: 10.1016/j.isprsjprs.2014.10.006

Chen, J. Y., Li, D. J., Chen, B. L., Hu, F. X., Zhu, H. F., and Liu, C. Z. (1999). The processes of dynamic sedimentation in the changjiang estuary. *J. Sea Res.* 41, 129–140. doi: 10.1016/S1385-1101(98)00047-1

Chen, C., Mao, Z. H., Tang, F. P., Han, G. Q., and Jiang, Y. Z. (2017). Declining riverine sediment input impact on spring phytoplankton bloom off the Yangtze river estuary from 17-year satellite observation. *Continental Shelf Res.* 135, 86–91. doi: 10.1016/j.csr.2017.01.012

Chen, J. Y., Ni, X. B., Liu, M. L., Chen, J. F., Mao, Z. H., Jin, H. Y., et al. (2014). Monitoring the occurrence of seasonal low-oxygen events off the changjiang estuary through integration of remote sensing, buoy observations, and modeling. *J. Geophys. Res. Oceans* 119, 5311–5322. doi: 10.1002/2014JC010333

Chen, J. Y., Ni, X. B., Mao, Z. H., Wang, Y. F., Liang, L. J., and Gong, F. (2012). Remote sensing and buoy based effect analysis of typhoon on hypoxia off the Changjiang (Yangtze) Estuary. *Conference on Remote Sensing of the Ocean, Sea Ice, Coastal Waters and Large Water Regions*, Sep 26-27 2012 Edinburgh, Scotand.

Cho, J. H., Son, Y. B., Shin, D.-H., Moh, T., Jang, S., Lee, S. Y., et al. (2020). Changes in underwater visibility due to turbidity associated with typhoon soulik. *J. Coast. Res.* 95, 417–421. doi: 10.2112/SI95-081.1

Dai, Z. J., Liu, J. T., Wei, W., and Chen, J. Y. (2014). Detection of the three gorges dam influence on the changjiang (Yangtze river) submerged delta. *Sci. Rep.* 4, 6600. doi: 10.1038/srep06600

Du, Z. H., Qi, J., Wu, S. S., Zhang, F., and Liu, R. Y. (2021). A spatially weighted neural network based water quality assessment method for Large-scale coastal areas. *Environ. Sci. Technol.* 55, 2553–2563. doi: 10.1021/acs.est.0c05928

Elsner, J. B., and Liu, K. B. (2003). Examining the ENSO-typhoon hypothesis. *Climate Res.* 25, 43–54. doi: 10.3354/cr025043

Falkowski, P. G. (1997). Evolution of the nitrogen cycle and its influence on the biological sequestration of CO2 in the ocean. *Nature* 387, 272–275. doi: 10.1038/387272a0

Ge, J. Z., Torres, R., Chen, C. S., Liu, J., Xu, Y., Bellerby, R., et al. (2020). Influence of suspended sediment front on nutrients and phytoplankton dynamics off the changjiang estuary: A FVCOM-ERSEM coupled model experiment. *J. Mar. Syst.* 204, 103292. doi: 10.1016/j.jmarsys.2019.103292

Good, S., Fiedler, E., Mao, C., Martin, M. J., Maycock, A., Reid, R., et al. (2020). The current configuration of the OSTIA system for operational production of foundation Sea surface temperature and ice concentration analyses. *Remote Sens* 12, 720. doi: 10.3390/rs12040720

Guan, S. D., Li, S. Q., Hou, Y. J., Hu, P., Liu, Z., and Feng, J. Q. (2018). Increasing threat of landfalling typhoons in the western north pacific between 1974 and 2013. *Int. J. Appl. Earth Observation Geoinformation* 68, 279–286. doi: 10.1016/j.jag.2017.12.017

Guan, S. D., Liu, Z., Song, J. B., Hou, Y. J., and Feng, L. Q. (2017). Upper ocean response to super typhoon tembi) explored using multiplatform satellites and argo float observations. *Int. J. Remote Sens.* 38, 5150–5167. doi: 10.1080/01431161.2017.1335911

Jiang, Z. B., Chen, J. F., Zhou, F., Shou, L., Chen, Q. Z., Tao, B. Y., et al. (2015). Controlling factors of summer phytoplankton community in the changjiang (Yangtze river) estuary and adjacent East China Sea shelf. *Continental Shelf Res.* 101, 71–84. doi: 10.1016/j.csr.2015.04.009

Kim, W., Moon, J. E., Park, Y. J., and Ishizaka, J. (2016). Evaluation of chlorophyll retrievals from geostationary ocean color imager (GOCI) for the north-East Asian region. *Remote Sens Environ.* 184, 482–495. doi: 10.1016/j.rse.2016.07.031

Le Traon, P. Y., Reppucci, A., Alvarez Fanjul, E., Aouf, L., Behrens, A., Belmonte, M., et al. (2019). From observation to information and users: The Copernicus marine service perspective. *Front. Mar. Sci.* 6, 234. doi: 10.3389/fmars.2019.00234

Li, W. Q., Ge, J. Z., Ding, P. X., Ma, J. F., Glibert, P. M., and Liu, D. Y. (2021). Effects of dual fronts on the spatial pattern of chlorophyll-a concentrations in and off the changjiang river estuary. *Estuaries Coasts* 44, 1408–1418. doi: 10.1007/s12237-020-00893-z

Li, Y. L., Shen, Z. L., Xian, W. W., and Liu, S. M. (2015). Structure characteristics of nutrients and their restrictive effect on phytoplankton in the Yangtze river estuary. *Mar. Sci.* 39 (4), 125–134. doi: 10.11759/hykx20140714001

Lohrenz, S. E., Fahnenstiel, G. L., Redalje, D. G., Lang, G. A., Dagg, M. J., Whitledge, T. E., et al. (1999). Nutrients, irradiance, and mixing as factors regulating primary production in coastal waters impacted by the Mississippi river plume. *Continental Shelf Res.* 19, 1113–1141. doi: 10.1016/S0278-4343(99)00012-6

Luan, H. L., Ding, P. X., Wang, Z. B., Ge, J. Z., and Yang, S. L. (2016). Decadal morphological evolution of the Yangtze estuary in response to river input changes and estuarine engineering projects. *Geomorphology* 265, 12–23. doi: 10.1016/j.geomorph.2016.04.022

Martiny, A. C., Talarmin, A., Mouginot, C., Lee, J. A., Huang, J. S., Gellene, A. G., et al. (2016). Biogeochemical interactions control a temporal succession in the elemental composition of marine communities. *Limnology Oceanography* 61, 531–542. doi: 10.1002/lno.10233

Matthews, M. W., Bernard, S., and Winter, K. (2010). Remote sensing of cyanobacteria-dominant algal blooms and water quality parameters in zeekoevlei, a small hypertrophic lake, using MERIS. *Remote Sens. Environ.* 114, 2070–2087. doi: 10.1016/j.rse.2010.04.013

Min, J. E., Choi, J. K., Yang, H., Lee, S., and Ryu, J. H. (2014). Monitoring changes in suspended sediment concentration on the southwestern coast of Korea. *J. Coast. Res.* 70, 133–138. doi: 10.2112/SI70-023.1

Moore, C. M., Mills, M. M., Langlois, R., Milne, A., Achterberg, E. P., La Roche, J., et al. (2008). Relative influence of nitrogen and phosphorus availability on phytoplankton physiology and productivity in the oligotrophic sub-tropical north Atlantic ocean. *Limnology Oceanography* 53, 291–305. doi: 10.4319/lo.2008.53.1.0291

Oey, L. Y., and Chou, S. (2016). Evidence of rising and poleward shift of storm surge in western north pacific in recent decades. *J. Geophys. Res. Oceans* 121, 5181–5192. doi: 10.1002/2016JC011777

Siswanto, E., Ishizaka, J., Tripathy, S. C., and Miyamura, K. (2013). Detection of harmful algal blooms of karenia mikimotoi using MODIS measurements: A case study of seto-inland Sea, Japan. *Remote Sens. Environ.* 129, 185–196. doi: 10.1016/j.rse.2012.11.003

Smith, W. O., and Demaster, D. J. (1996). Phytoplankton biomass and productivity in the Amazon river plume: Correlation with seasonal river discharge. *Continental Shelf Res.* 16, 291–319. doi: 10.1016/0278-4343(95)00007-N

Song, K. S., Li, L., Wang, Z. M., Liu, D. W., Zhang, B., Xu, J. P., et al. (2012). Retrieval of total suspended matter (TSM) and chlorophyll-a (Chl-a) concentration from remote-sensing data for drinking water resources. *Environ. Monit. Assess.* 184, 1449–1470. doi: 10.1007/s10661-011-2053-3

Sun, L., Li, Y. X., Yang, Y. J., Wu, Q., Chen, X. T., Li, Q. Y., et al. (2014). Effects of super typhoons on cyclonic ocean eddies in the western north pacific: A satellite data-based evaluation between 2000 and 2008. *J. Geophysical Research-Oceans* 119, 5585–5598. doi: 10.1002/2013JC009575

Talarmin, A., Lomas, M. W., Bozec, Y., Savoye, N., Frigstad, H., Karl, D. M., et al. (2016). Seasonal and long-term changes in elemental concentrations and ratios of marine particulate organic matter. *Global Biogeochemical Cycles* 30, 1699–1711. doi: 10.1002/2016GB005409

Tyrrell, T. (1999). The relative influences of nitrogen and phosphorus on oceanic primary production. *Nature* 400, 525–531. doi: 10.1038/22941

Wang, T. Y., and Zhang, S. W. (2021). Effect of summer typhoon linfa on the chlorophyll-a concentration in the continental shelf region of northern south China Sea. *J. Mar. Sci. Eng.* 9 (8), 794. doi: 10.3390/jmse9080794

Wu, Q. Y., and Chen, D. K. (2012). Typhoon-induced variability of the oceanic surface mixed layer observed by argo floats in the Western north pacific ocean. *Atmosphere-Ocean* 50, 4–14. doi: 10.1080/07055900.2012.712913

Wu, T. N., and Wu, H. (2018). Tidal mixing sustains a bottom-trapped river plume and buoyant coastal current on an energetic continental shelf. *J. Geophysical Research-Oceans* 123, 8026–8051. doi: 10.1029/2018JC014105

Xu, J. J., Zhou, P., Lian, E. G., Wu, H., and Liu, D. Y. (2021). Spatial distribution of chlorophyll a and its relationships with environmental factors influenced by front in the changjiang river estuary and its adjacent waters in summer 2019. *Mar. Sci. Bull.* 40 (5), 541–549. doi: 10.11840/j.issn.1001-6392.2021.05.006

Xu, S. S., Song, J. M., Li, X. G., Yuan, H. M., Li, N., Duan, L. Q., et al. (2010). Changes in nitrogen and phosphorus and their effects on phytoplankton in the bohai Sea. *Chin. J. Oceanology Limnology* 28, 945–952. doi: 10.1007/s00343-010-0005-3

Xu, Y., Zhang, Y., Chen, H. Q., and Zhang, D. (2011). Stndy on Dissolved Inorganic Nitrogen Monitoring Based on MODIS Imaging for Haizhou Bay. *Adv. In Mar. Sci.* 29 (1), 73–80. doi: 10.3724/SP.J.1011.2011.00403

Zhao, W., Li, J., and Wang, J. (2004). Study on nutrient limitation of phytoplankton in field experiment of changjiang estuary in summer. *Mar. Environ. Sci.* 23 (4), 1–5. doi: 10.3969/j.issn.1007-6336.2004.04.001

frontiers | Frontiers in Marine Science

TYPE Original Research
PUBLISHED 18 November 2022
DOI 10.3389/fmars.2022.1001491

Check for updates

OPEN ACCESS

EDITED BY
Lei Ren,
Sun Yat-sen University, China

REVIEWED BY
Patrizia Savi,
Politecnico di Torino, Italy
Haokui Xu,
University of Michigan, United States

*CORRESPONDENCE
Jingsong Yang
jsyang@sio.org.cn
Weiqiang Li
weiqiang@ice.csic.es

SPECIALTY SECTION
This article was submitted to Ocean Observation, a section of the journal Frontiers in Marine Science

RECEIVED 23 July 2022
ACCEPTED 24 October 2022
PUBLISHED 18 November 2022

CITATION
Li X, Yang J, Yan Y and Li W (2022) Exploring CYGNSS mission for surface heat flux estimates and analysis over tropical oceans.
Front. Mar. Sci. 9:1001491.
doi: 10.3389/fmars.2022.1001491

COPYRIGHT
© 2022 Li, Yang, Yan and Li. This is an open-access article distributed under the terms of the Creative Commons Attribution License (CC BY). The use, distribution or reproduction in other forums is permitted, provided the original author(s) and the copyright owner(s) are credited and that the original publication in this journal is cited, in accordance with accepted academic practice. No use, distribution or reproduction is permitted which does not comply with these terms.

Exploring CYGNSS mission for surface heat flux estimates and analysis over tropical oceans

Xiaohui Li[1], Jingsong Yang[1,2]*, Yunwei Yan[3,4] and Weiqiang Li[5,6]*

[1]State Key Laboratory of Satellite Ocean Environment Dynamics, Second Institute of Oceanography, Ministry of Natural Resources, Hangzhou, China, [2]Southern Marine Science and Engineering Guangdong Laboratory (Zhuhai), Zhuhai, China, [3]Key Laboratory of Marine Hazards Forecasting, Ministry of Natural Resources, Hohai University, Nanjing, China, [4]College of Oceanography, Hohai University, Nanjing, China, [5]Institute of Space Sciences (ICE, CSIC), Barcelona, Spain, [6]Institut d'Estudis Espacials de Catalunya (IEEC), Barcelona, Spain

The Cyclone Global Navigation Satellite System (CYGNSS) mission can measure sea surface wind over tropical oceans with unprecedented temporal resolution and spatial coverage, so as to estimate surface latent and sensible heat fluxes (LHF and SHF). In this paper, the satellite-derived LHF/SHF estimates from CYGNSS are quantitatively evaluated and analyzed by those from the Global Tropical Moored Buoy. Comparisons of the LHF and SHF estimates demonstrate the good performance and reliability of CYGNSS heat flux products during the period of 2017–2022, including CYGNSS Level 2 Ocean Surface Heat Flux Climate Data Record (CDR) Version 1.0 and Version 1.1. Different latent heat characteristics in the tropical oceans are evaluated separately based on each buoy array, suggesting better agreement in the Atlantic for LHF/SHF products. Based on the Coupled Ocean-Atmosphere Response Experiment 3.5 algorithm, the impact of wind speed on the LHF/SHF estimates is analyzed by using the the Science Data Record V3.1 and NOAA V1.2 science wind products. The results show that the performance of satellite-derived wind speed directly affects the accuracy of LHF products, with an improvement of 17% in root-mean-square error over that of LHF CDR V1.0. Especially, in the Indian Ocean, accuracy can be improved by 26.8%. This paper demonstrates that the heat flux estimates along the orbit of the CYGNSS are an important supplement to *in situ* observational data and will benefit the study of global climate change.

KEYWORDS

global navigation satellite system reflectometry (GNSS-R), cyclone GNSS (CYGNSS), surface heat fluxes, latent heat flux, sensible heat flux, tropical ocean

1 Introduction

Surface latent and sensible heat fluxes (hereafter referred to as LHF and SHF) are associated with the exchange of mass and energy between the ocean, land, and atmosphere and thereby have a significant effect on ocean surface energy balance, global weather, and climate change (Businger, 1982; Large and Pond, 1982; Zeng et al., 2009; Zhou et al., 2015; Bentamy et al., 2017; Crespo et al., 2019; Tauro et al., 2022). Sea surface winds, sea surface temperature, and the specific humidity at the ocean surface are closely related to heat flux and are often used to estimate LHF and SHF *via* a bulk algorithm (Hartmann, 1994; Bentamy et al., 2003). Fortunately, remote sensing satellites can measure and provide these parameters, which have become a valuable tool for the large-scale and rapid estimation of these flux measurements (Grodsky et al., 2009; Shie and Hilburn, 2011). In tropical oceans, high sea surface temperatures and saturated humidity will accelerate the interactions between the ocean and the atmosphere (Back and Bretherton, 2005), which directly affect the global climate, (e.g., El Niño-Southern Oscillation). Therefore, it is especially important to use remote sensing satellites to quickly monitor the changes of heat fluxes in tropical oceans.

Accurate LHF and SHF information is essential to understand the changes in the global energy cycle, and great efforts have been made to estimate these based on remote sensing satellite observations (Pinker et al., 2014; Cronin et al., 2019). Among the parameters required by a bulk algorithm, sea surface temperature can be monitored by passive satellite microwave radiometers, such as the SSM/I (Special Sensor Microwave/Imager) and the TMI (Tropical Rainfall Measuring Mission Microwave Imager). Sea surface winds can be observed by active scatterometers [e.g., ASCAT (Advanced Scatterometer), HY-2 (Haiyang-2), and CFOSAT (China-France Oceanography SATellite)] and passive microwave radiometers [e.g., SMAP (Soil Moisture Active and Passive), WindSat, and AMSR-E (Advanced Microwave Scanning Radiometer for the Earth Observing System)]. Water vapor (specific humidity) measurements can be obtained from can be obtained from radiometers, including SSM/I, AMSR-E, WindSat, and AMSR2. These remote sensing satellites have provided us with useful information about ocean surface behavior, as well as input parameters for estimating heat fluxes. Currently, several satellite-derived heat flux products have been developed and released to the public, such as the Objectively Analyzed Air-Sea Heat Fluxes (OAFlux, Yu et al. 2004), the Goddard Satellite-based Surface Turbulent Fluxes (GSSTF, Chou et al., 2002), and the Japanese Ocean Flux Data Sets with use of Remote Sensing Observations (J-OFURO, Masahisa et al., 2002), which are widely used for various climate studies (KonDa et al., 1996; Masahisa et al., 2002; Gao et al., 2013; Wang et al., 2013; Bharti et al., 2019; Tomita et al., 2021).

In addition to the above mentioned remote sensing means, as of the 1990s, the Earth-reflected Global Navigation Satellite System (GNSS) signal has also been used as a new type of remote sensing signal source, resulting in the GNSS Reflectometry (GNSS-R) technique (Li et al., 2022). Different space-borne missions have been successfully launched, such as the UK Disaster Monitoring Constellation satellite (UK-DMC, Gleason et al., 2005), the UK TechDemoSat-1 (TDS-1, Unwin et al., 2017), the NASA CYclone GNSS (CYGNSS) mission (Ruf et al., 2016), the Chinese BuFeng-1 A/B satellites (Jing et al., 2019), and the FengYun-3E mission (Yang et al., 2022). It has been proved that this technology can provide a valid option for remote sensing Earth observations.

CYGNSS is a constellation of 8 micro-satellites that can receive 32 specular points (the reflected GNSS signals) per second in parallel, so that it has the capability of exceptional spatio-temporal sampling and rapid revisit time. In addition, CYGNSS can provide sea surface wind speed under all precipitation conditions because the GNSS signal (L-band) is hardly affected. The design purpose of the CYGNSS mission is to detect the sea surface wind in and near the inner-core of tropical cyclones of all tropical oceans (± 35°) with unprecedented temporal resolution and spatial coverage, so as to monitor the wind field evolution process in the life cycle of tropical cyclones (Ruf et al., 2016). Several sea surface wind products have been developed and released to the public, including Science Data Record (SDR) Versions, Climate Data Record (CDR) Versions, and NOAA Science Versions, as shown in Table 1. This provides a good prerequisite to quickly estimate and monitor sea surface heat flux in tropical oceans. A recent study estimated the surface net heat flux from the CYGNSS winds CDR Version 1.0 and 1.1 products, as shown in Table 1 (Crespo et al., 2019).

Crespo et al., 2019 and Crespo and Posselt, 2019 developed and evaluated the early results of the surface heat flux products from the CYGNSS mission. Comparisons indicated that the satellite-derived estimates were in good agreement with those from the Kuroshio Extension Observatory (KEO) buoy and National Data Buoy Center (NDBC) at lower flux values (Crespo et al., 2019). Considering the importance of heat flux, it is necessary to observe sea surface winds, sea surface temperature, and specific humidity and estimate heat fluxes by satellite over a long time. However, how reliable are satellite-derived estimations of surface net heat flux in tropical oceans (e.g., the Pacific, Atlantic, and Indian oceans) remains an open question that is not self-evident. But with the continuous updating of the inversion model based on CYGNSS observables, the accuracy is gradually improved. In particular, NOAA V1.2 and SDR V3.1 wind speed products have considered the impact of waves, leading to significant improvements to wind speed accuracy. However, there are few studies related to surface heat flux based on CYGNSS SDR and NOAA wind versions. In order to make better use of the

TABLE 1 Statistics of CYGNSS Level 2 sea surface wind speed and heat flux products.

CYGNSS Wind products	CYGNSS Heat flux products	Temporal extent
Level 2 wind SDR[1] V2.1	–	2017.03.18 ongoing
Level 2 wind SDR V3.0	–	2018.08.01 ongoing
Level 2 wind SDR V3.1	–	2018.08.01 ongoing
Level 2 wind CDR[2] V1.0	Level 2 Heat Flux CDR V1.0	2017.03.18–2021.01.31
Level 2 wind CDR V1.1	Level 2 Heat Flux CDR V1.1	2018.08.01 ongoing
NOAA wind V1.0	–	2017.05.01–2019.12.31
NOAA wind V1.1	–	2017.05.01 ongoing
NOAA wind V1.2	–	2017.05.01 ongoing

[1]Science Data Record is abbreviated as SDR.
[2]Climate Data Record is abbreviated as CDR.

advantages of GNSS-R technology to estimate and analyze the heat flux characteristics of tropical oceans, the accuracy of the satellite-derived estimates from the CYGNSS SDR and NOAA wind versions should be evaluated.

The sections of this paper are arranged as follows: The satellite-derived surface net heat flux products, CYGNSS wind speed products, the bulk algorithm of the surface heat fluxes, and *in situ* measurements are briefly described in Section 2. Section 3 evaluates the accuracy of the surface net heat flux between CYGNSS heat flux CDR V1.0 and V1.1, and the impact of the SDR and NOAA sea surface wind products from the CYGNSS mission on the accuracy of LHF and SHF is analyzed, respectively. Conclusions are drawn in Section 4.

2 Materials and methods

2.1 Satellite-derived surface heat flux datasets from CYGNSS

Two versions of the satellite-derived surface heat flux products are adopted and evaluated in this paper: the CYGNSS Level 2 Ocean Surface Heat Flux CDR V1.0 (https://doi.org/10.5067/CYGNS-C2H10) and CDR V1.1 (https://doi.org/10.5067/CYGNS-L2C11) products. CYGNSS Level 2 Ocean Surface Heat Flux CDR V1.0 is the first release version, which is derived from CYGNSS Level 2 Ocean Surface Windspeed CDR V1.0 with the thermodynamic variables of temperature and humidity provided by the NASA Modern-Era Retrospective Analysis for Research and Applications Version 2 (MERRA-2) (CYGNSS, 2020). The CYGNSS L2 Ocean Surface Heat Flux CDR datasets are available here: https://podaac.jpl.nasa.gov/dataset/.

Table 2 provides information on the CYGNSS heat flux products used for analysis, including product version and time span. These versions of heat flux products can cover a latitude range of −40∼ 40° and a longitude range of 0∼ 360° , and the spatial resolution is 25 km (along) × 25 km (across) for each data product. The time span of each CYGNSS heat flux product is different, and the CDR V1.0 product has stopped updating. CYGNSS Level 2 Ocean Surface Heat Flux CDR Version 1.1 supersedes the previous version, and it is also based on Windspeed CDR V1.1 to estimate the heat flux of global tropical oceans. In this study, the time span of CYGNSS Surface Heat Flux CDR V1.0 is 18 March 2017 to 31 January 2021, and that of CYGNSS CDR V1.1 is 1 August 2018 to 28 February 2022.

2.2 CYGNSS level 2 ocean surface windspeed datasets

CYGNSS Level 2 Ocean Surface Windspeed is estimated by the Level 1 Bistatic Radar Cross Section of Earth Surface product based on the Minimum Variance (MV) estimator (Clarizia et al., 2014). The normalized bistatic radar cross section (NBRCS) and the leading edge slope of the Doppler-integrated delay waveform (LES) from the CYGNSS Level 1 product are commonly used to retrieve sea surface wind speed in the CYGNSS Level 2 product (Ruf and Balasubramaniam, 2018). Table 1 gives the basic information of the currently published wind speed datasets. Each SDR ocean surface wind speed product is implemented from the corresponding version of Level 1 data. Therefore, the time span of each product is different. More information on how the ocean surface wind speed data are produced and validated can be found in Michigan Engineering CYGNSS (https://cygnss.engin.umich.edu/data-products/).

Considering the influence of waves on CYGNSS observables, NOAA/NESDIS (National Environmental Satellite, Data and Information Service) attempted to improve the accuracy of

TABLE 2 Summary of CYGNSS Level 2 CDR heat flux products information used for analysis.

Heat flux products	Time span
CYGNSS Level 2 Heat Flux CDR V1.0	2017.03.18–2021.01.31
CYGNSS Level 2 Heat Flux CDR V1.1	2018.08.01–2022.02.28

CYGNSS wind speed by using wave height information. NOAA's Along Track Retrieval Algorithm (ATRA) is expressed as $\sigma_0=F(U_{10},\mathrm{SWH},\theta)$, where σ_0 is a CYGNSS observable, U_{10} is wind speed, SWH is significant wave height, and θ is the angle of incidence at the specular point. This track-wise algorithm is used to reduce the systematic errors due to the uncertainties of the transmitted power and receiver instrumental effects (Said et al., 2019). NOAA CYGNSS Level 2 Science Wind Speed Product Version 1.1 (https://doi.org/10.5067/CYGNN-22511) is the first science-quality release using a wind–wave GMF (Geophysical Model Function); the latest version is NOAA CYGNSS Level 2 Science Wind Speed Product Version 1.2 (https://doi.org/10.5067/CYGNN-22512). The following is a summary of the processing changes reflected in this version: 1) CYGNSS observables associated with a spacecraft roll angle exceeding ± 5 degrees are also used to retrieve wind speed. 2) The performance of high wind speeds is improved. 3) A full revision of quality flags is implemented. 4) A wind speed retrieval error variable is added.

In addition, CYGNSS provides the latest version of wind speed product (CYGNSS Level 2 SDR Version 3.1, https://doi.org/10.5067/CYGNS-L2X31. The following is a summary of processing changes reflected in the Level 2 SDR V3.1 product: 1) GMFs (the same as for SDR V3.0) are used to retrieve ocean surface wind speed based on Level 1 SDR V3.1 observables. 2) Both the Fully Developed Seas (FDS) and Young Seas Limited Fetch (YSLF) winds in the SDR V3.1 product are corrected by a function of the SWH from the ERA5 reanalysis product. In this study, SDR V3.1 and NOAA V1.2 sea surface wind products from the CYGNSS mission are used to evaluate the impact on the accuracy of LHF and SHF, respectively.

2.3 The bulk flux algorithm description

In general, sea surface heat fluxes are primarily driven by ocean wind fields and air-sea differences in temperature and humidity (Liu et al., 1979; Hartmann, 1994). Therefore, a bulk flux algorithm requires input parameters, including sea and air thermodynamic variables. Currently, the Coupled Ocean-Atmosphere Response Experiment (COARE) algorithm is widely applied for estimating LHF/SHF according to the Monin-Obukhov similarity theory (MOST), which was initially developed for understanding the processes that occur in the western Pacific warm pool with the support of the Tropical Ocean—Global Atmosphere (TOGA) program (Webster and Lukas, 1992; Fairall et al., 1996; Edson et al., 2013). The COARE algorithm has good performance under the condition of low to medium wind speed, but the latest version (COARE 3.5) has been verified by *in situ* flux measurements with wind speeds as high as 25 m/s. The CYGNSS Level 2 Ocean Surface Heat Flux datasets are produced using the COARE 3.5 algorithm (as shown in Equation 1). In this paper, to investigate the effect of wind speed on the accuracy of heat flux, COARE 3.5 is used to estimate LHF and SHF according to two versions of CYGNSS Level 2 Ocean Surface Wind speed:

$$\begin{aligned} LHF &= \rho_a L_v C_{DE} U(q_s - q_a) \\ SHF &= \rho_a C_p C_{DH} U(T_s - T_a) \end{aligned} \tag{1}$$

where ρ_a is the density of air at sea level, L_v is the latent heat of vaporization, and C_p is the specific heat capacity. C_{DE} and C_{DH} are the turbulent transfer coefficients of latent heat and sensible heat, respectively, U is the sea surface wind speed, q_s and T_s are the sea surface specific humidity and temperature, respectively, and q_a and T_a are the specific humidity and temperature at 10-m above the surface, respectively.

2.4 *In situ* measurements from Global Tropical Moored Buoy Array

It has always been considered that *in situ* measurements create the most reliable datasets, and they are widely used to verify and evaluate the performance of satellite-driven products. Measurements from moored surface buoys are used to estimate the sea surface heat flux. This requires the buoys to simultaneously observe the input variables required in a bulk flux algorithm to estimate the surface heat flux. Due to the need for radiation sensors, few buoys can estimate heat flux.

In this study, 52 buoys from the Global Tropical Moored Buoy Array in the global oceans that captured all input variables required by the COARE 3.5 algorithm, as shown in Figure 1. These buoys are mainly distributed in the tropical oceans, including 21 buoys from the Research Moored Array for African-Asian-Australian Monsoon Analysis and Prediction (RAMA) in the Indian Ocean, 18 buoys from the Prediction and Research Moored Array in the Tropical Atlantic (PIRAA) in the Atlantic Ocean, and 13 buoys from the Tropical Atmosphere Ocean (TAO)/Triangle Trans-Ocean Buoy Network (TRITON) array in the Pacific Ocean. Heat flux estimates from the 52 buoys provide valuable measured data for estimating the accuracy of satellite-derived heat flux from the CYGNSS Mission in each tropical ocean basin.

2.5 Statistical metrics

Two statistical metrics, bias and the root-mean-square error (RMSE), are used to evaluate the performance of the CYGNSS Ocean Surface Heat Flux products, which are calculated for both LHF and SHF.

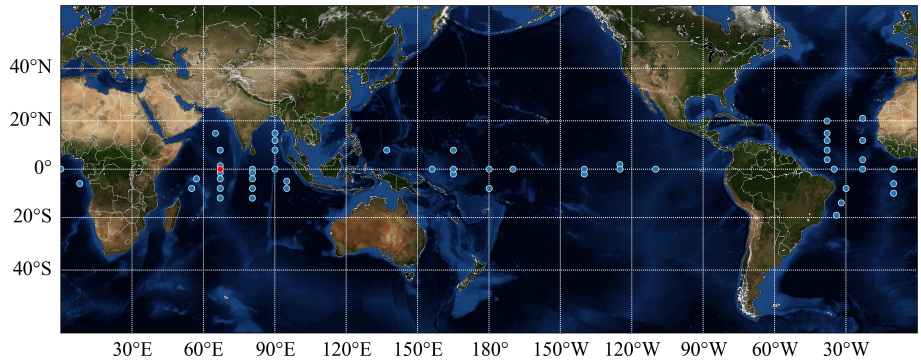


FIGURE 1
Locations of buoys from the Global Tropical Moored Buoy Array used for comparison indicated as circles.

$$\text{bias} = \frac{1}{n}\sum_{i=1}^{n}(X_i - Y_i) \quad (2)$$

$$\text{RMSE} = \sqrt{\frac{1}{n}\sum_{i=1}^{n}(X_i - Y_i)^2}$$

where X is the CYGNSS latent or sensible heat flux, Y is the buoy latent or sensible heat flux, n is the number of total matchups, $\bar{X}$ is the mean of the CYGNSS latent or sensible heat flux, and $\bar{Y}$ is the mean of the buoy latent or sensible heat flux.

2.6 Methodology

To evaluate the performance of the CYGNSS CDR V1.0 and V1.1 heat flux products in the global tropical oceans, collocations between CYGNSS and *in situ* measurements are processed at each CYGNSS specular point, as shown in the top sub-figures in Figure 2. A spatio-temporal collocating criterion is used to ensure that the acquisition time of the CYGNSS measurement is close to that of *in situ* measurements from the buoys. To ensure the consistency of heat flux from different sources, the CYGNSS specular points have been produced by in in a temporal window within ±30 min relative to the time of the *in situ* measurements. Then, the nearest buoy within 25 km is selected according to the distance between the CYGNSS specular point and each buoy location. Finally, the collocations can be obtained from *in situ* measurements, and the statistical metrics are used to evaluate the performance of the CYGNSS CDR V1.0 and V1.1 heat flux products relative to those estimated by Global Tropical Moored Buoy Array *in situ* measurements.

In addition, as seen in the bottom of Figure 2, matchups between CYGNSS (SDR and NOAA) wind speed products are collocated by the same criteria of spatio-temporal matching, including the density of air at sea level and the specific humidity and temperature at the surface and 10-m above the surface from MERRA-2, respectively. Surface latent and sensible heat fluxes can be calculated by the COARE 3.5 bulk flux algorithm. Thus, the impact of different sea surface wind products from the CYGNSS mission on the accuracy of LHF and SHF is evaluated and analyzed.

3 Results

3.1 Comparison with *in situ* measurements

In this paper, we use heat flux estimates from the Global Tropical Moored Buoy Array to evaluate the accuracy of the CYGNSS heat flux products in the global tropical oceans. The collocated data from 52 buoys (as shown in Figure 1) are matched with CYGNSS specular points within the above-mentioned spatial and temporal windows. Considering the time range of buoys is different, and the number of buoys used for validating the CYGNSS CDR V1.0 and V1.1 products is also different, Figure 3 shows the spatial distribution of the buoys used for verification: 52 buoys for CYGNSS CDR V1.0 and 45 buoys for CYGNSS CDR V1.1.

Figure 4 compares LHF/SHF estimates from *in situ* measurements and from CYGNSS CDR V1.0 and V1.1. The statistical metrics are calculated using Equation 2, which are also shown in Figure 4. From 18 March 2017 to 31 January 2021, LHF/SHF estimates from CYGNSS CDR V1.0 are validated using the *in situ* heat flux estimates, where the sample size is 147,165, and the RMSEs of CYGNSS LHF/SHF CDR V1.0 are 35.77 W/m^2 and 6.75 W/m^2 , respectively. For CYGNSS CDR V1.1, the time span is from 1 August 2018 to 28 February 2022, and the RMSEs of CYGNSS LHF/SHF CDR V1.1 are 33.60 W/m^2 and 6.67 W/m^2 . Note that the sample size

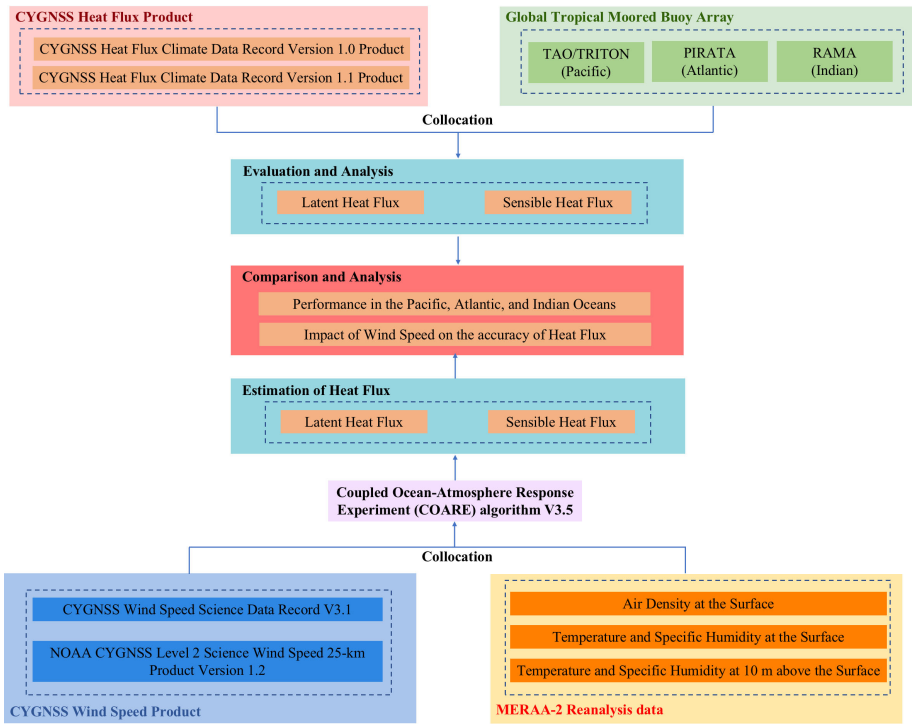


FIGURE 2
Technical structure and data processing flow of this study of this study.

is 67,882 after applying CYGNSS flux quality flags (flag!=1), which is less than that of CYGNSS CDR V1.0. This is because some buoys do not provide data for the year of 2022, and the number of buoys for CYGNSS CDR V1.1 is less than that for CYGNSS CDR V1.0.

The highest scatterplot density of LHF occurs between 100 and 200 W/m^2 , and that of SHF is between 0 and 15 W/m^2. Figure 4A demonstrates that some LHF estimates are overestimated in CYGNSS CDR V1.0 compared with the *in situ* measurements, whereas overall the CYGNSS CDR V1.1 fluxes agree with the LHF estimates from *in situ* measurements, as shown in Figure 4B. Figures 4C, D show that there is a discrepancy at high values. In general, both CDR V1.0 and V1.1 fluxes seem to be in agreement with SHF estimates from the *in situ* measurements, with RMSEs of 6.75 and 6.67 W/m^2 , respectively. Overall, it can be seen that the performance of heat flux heat flux estimates from CYGNSS CDR V1.1 is slightly better than that of CYGNSS CDR V1.0.

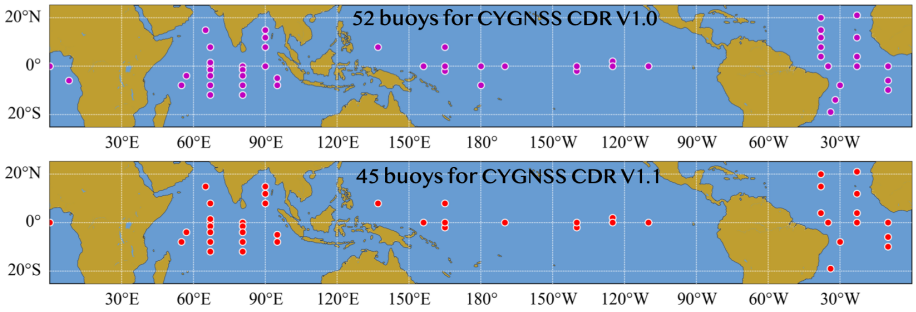


FIGURE 3
Maps of buoys from the Global Tropical Moored Buoy Array used for comparing the CYGNSS CDR V1.0 and V1.1 heat flux products.

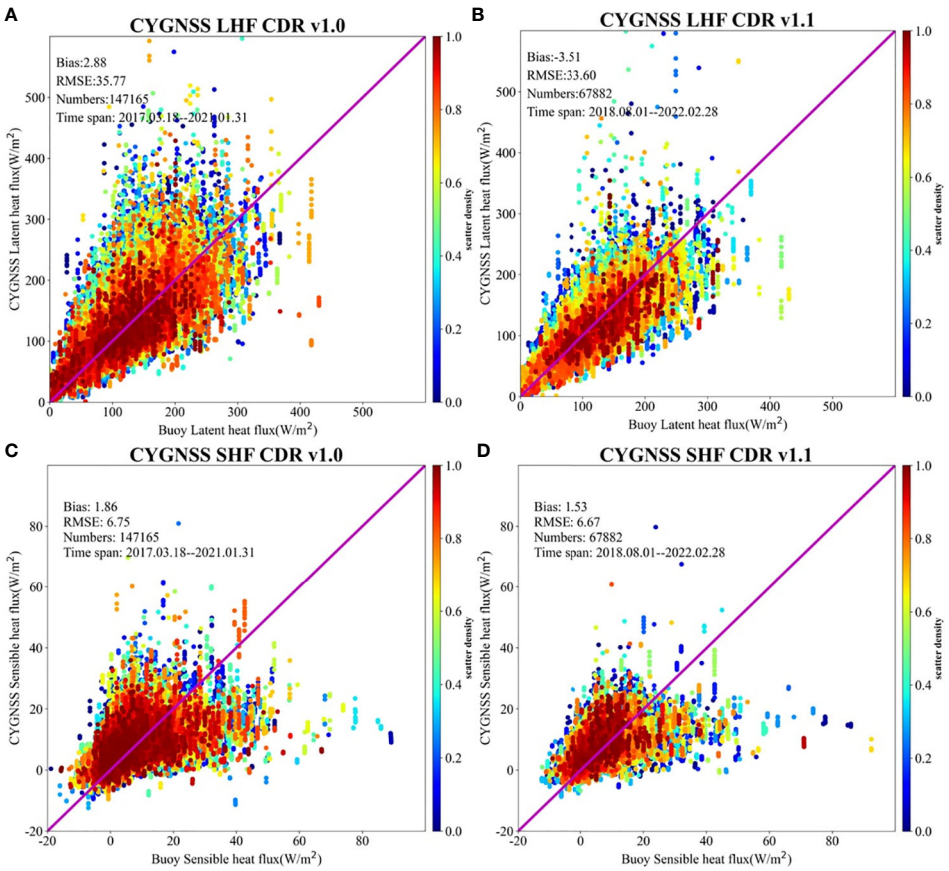


FIGURE 4
Comparisons between LHF **(A, B)**/SHF **(C, D)** estimates from *in situ* measurements and from CYGNSS CDR V1.0 during 2017-2021 and V1.1 during 2018-2022, respectively. The bias, RMSE, number of matchups, and time span are given in each subfigure. The colorbar is the number density of points, and the purple line shows the 1:1 diagonal.

3.1.2 Accuracy in each tropical ocean basin

CYGNSS can observe the sea surface over the global tropical ocean, providing the chance to estimate the sea surface heat fluxes in each basin. According to Equation 2, we calculate the statistical metrics of latent and sensible heat fluxes for the Pacific, Atlantic, and Indian oceans, respectively. The accuracy assessment in each tropical ocean basin depends on the location of the TAO/TRITON array in the Pacific, PIRATA in the Atlantic, and RAMA in the Indian Ocean, Then, matchups from buoys in each tropical ocean basin are used to estimate the sea surface heat fluxes from CYGNSS CDR V1.0 and V1.1.

Compared to the LHF estimates from the buoys, the CYGNSS mission still shows different latent heat characteristics in the tropical oceans of the Pacific, Atlantic, and Indian oceans as shown in Figure 5. There are some things worth noting. First, LHF is overestimated by CYGNSS CDR V1.0 with a large bias of 10.4 W/m^2 , and a positive deviation (bias) is shown for each buoy in the Pacific ocean, especially for the buoy with a latitude of 0°N and a longitude of 180° W, where the bias exceeds 30 W/m^2. Second, in the Atlantic and Indian oceans, negative deviations appear for some buoys, especially the buoy with a latitude of 10°S and a longitudeof 10°W in the Atlantic ocean, whose bias exceeds −20 W/m^2. In addition, we also noticed that the bias of the buoy with a latitude of 19°S and a longitude of 34°W exceeds 40 W/m^2. The amount of matchups from this buoy exceeds 2,700, which basically rules out that the bias is not because of insufficient data. There are 21 buoys in the tropical ocean of the Indian ocean, which exhibit a bias of 3.59 W/m^2 and an RMSE of 38.14 with respect to the sea surface heat flux. Compared to the accuracy of CYGNSS latent heat in the tropical oceans of the Pacific and the Atlantic oceans, the RMSE of the Indian Ocean is high and the amount of matchups is large, suggesting that the accuracy of CYGNSS heat flux products is low in the tropical regions of the Indian Ocean.

For CYGNSS LHF CDR V1.1, Table 3 shows the statistical metrics of matchups in the tropical oceans of the Pacific, Atlantic, and Indian oceans. More details are shown in Figure A1 in Appendix. In the Pacific Ocean, the accuracy of CDR V1.1

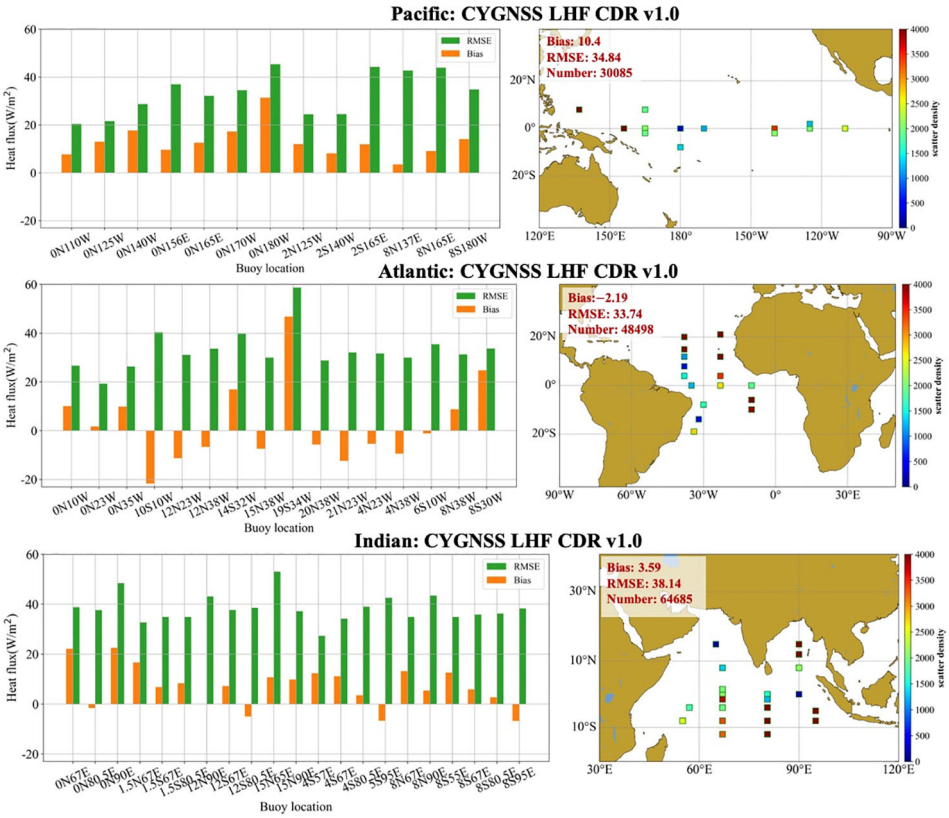


FIGURE 5
Left column: Biases (yellow bars) and RMSEs (green bars) between CYGNSSLHF CDR V1.0 product and *in situ* measurements from the tropical oceans of the Pacific, Atlantic, and Indian oceans. Right column: Spatial distribution of buoys from the Global Tropical Moored Buoy Array in each tropical ocean basin. The color density represents the number of matchups for each buoy. The average accuracy (bias and RMSE) and the number of matchups in each tropical ocean are marked in red font.

is slightly better than that of CDR V1.0, with a bias of 7.58 W/m^2 and an RMSE of 32.60 W/m^2 . In addition, we also noticed that the number of matchups is 13,028, which is less than that of CYGNSS LHF CDR V1.0. From Figure A1 in Appendix, the RMSE of the buoy (marked in rectangle with red border) with a latitude of 8°N and a longitude of 165°E exceeds 40 W/m^2. This difference between CYGNSS and the the buoy is inconsistent due to insufficient data (less than 300). It can be seen from Table 3 that the biases are negative in the Atlantic and Indian oceans, which are similar to those of CYGNSS CDR V1.0; especially, the

TABLE 3 Statistical metrics (bias and RMSE) calculated from the matchups between CYGNSS and *in situ* measurements in the Pacific, Atlantic, and Indian oceans.

Version	Tropical ocean	Latent heat flux		Sensible heat flux	
		Bias (m/s)	RMSE (m/s)	Bias (m/s)	RMSE (m/s)
CYGNSS V1.0	Pacific Ocean	10.4	34.84	1.73	6.88
	Atlantic Ocean	-2.19	33.74	1.75	5.71
	Indian Ocean	3.59	38.14	2.09	7.47
CYGNSS V1.1	Pacific Ocean	7.58	32.60	1.27	6.82
	Atlantic Ocean	-10.27	31.76	1.34	5.61
	Indian Ocean	-2.95	35.73	1.87	7.44

deviation at a latitude of 10°S and a longitude of 10°W in the Atlantic Ocean exceeds –20 W/m^2 (Figure A1 in Appendix). However, the accuracy (RMSE) of CDR V1.1 is slightly better than that of CDR V1.0 in the Atlantic and Indian Oceans.

In terms of sensible heat, Table 3 and Figure A2 (in Appendix) give the statistical metrics and and a histogram of CYGNSS SHF CDR V1.0 and V1.1 for bias (yellow bars) and RMSE (green bars), which demonstrate a good agreement between CYGNSS and *in situ* measurements from buoys. For the deviation in the tropical oceans of the Pacific, Atlantic, and Indian oceans, it can be seen that CYGNSS SHF CDR V1.0 and V1.1 overestimate the sensible heat relative to buoys, especially in the Indian Ocean (a large bias of 2.09 W/m^2). In the Pacific, we also noticed that the deviation of CYGNSS SHF CDR V1.1 exceeds in –3 W/m^2 and RMSE exceeds 20 W/m^2 at a latitude of 8°N and a longitude of 165°E (Figure A2 in Appendix). However, the deviation of CYGNSS SHF CDR V1.0 is close to 0 W/m^2 at this buoy (Figure A2 in Appendix). Except for this unusual buoy, the two versions of CYGNSS can give similar accuracies for SHF on the whole, which is consistent with *in situ* measurements from the buoy.

3.2 Annual variation characteristics of LHF/SHF in CYGNSS CDR products

To analyze the heat flux characteristics of LHF/SHF estimated by CYGNSS during this mission, the annual variation trends are investigated and analyzed according to several typical buoys. Figure 6 shows the ability of the CYGNSS mission to estimate heat flux at a specific location, which is consistent with those estimated from buoys. It can be seen that the buoys had missing data in the Pacific and Atlantic at various times: 2018.03~2018.08 for buoy (8°N, 137°E) in the Pacific (Figure 6A), and 2018.11~2019.01, 2020.08~2022.01 and 2021.07~2021.11 for buoy (20°N,38°W) in the Atlantic (Figure 6D). For buoy (8°S, 95°E) in the Indian Ocean, the heat flux data are normal and continuous. The blue dotted-line represents the CYGNSS LHF CDR V1.0 product, and the orange dotted-line represents the heat flux estimated by buoy data, as shown in Figure 6E. From the three heat flux products, it can see that there is a peak in August of each year, especially in 2017, 2018, and 2019. There is an obvious growth trend between July and August, as well as an obvious downward trend between September and November. However, these phenomena do not occur in the other two buoys in the Pacific and the Atlantic oceans. Thus, the CYGNSS mission produce heat flux estimates over the tropical ocean, providing an important reference for analyzing global tropical ocean heat flux changes.

3.3 Impact of wind speed on the accuracy of LHF/SHF

3.3.1. LHF/SHF estimated by CYGNSS SDR and NOAA wind speed

In this study, the latest versions of wind speed products are used to analyze the impact of wind speed on the accuracy of LHF/SHF, including the NOAA CYGNSS Level 2 V1.2 and SDR V3.1 wind speed products. Table 4 gives a summary of CYGNSS Level 2 wind speed product information, including product version and time span.

According to Equation 1, both wind speed products from the CYGNSS satellite constellation are used to derive the surface heat fluxes (LHF/SHF) using the sea and air thermodynamic variables of temperature and humidity. To ensure the consistency of the sea and air thermodynamic variables of the CYGNSS CDR heat flux products, according to the time and position at each specular point, the Level 2 wind speed is first spatio-temporally collocated with LHF/SHF estimated by the buoys, and then collocated with the Level 2 heat flux product to obtain the thermodynamic parameters provided by NASA MERRA-2 for calculating the heat flux.

3.3.2. Comparisons of CYGNSS heat fluxes

For LHF, CYGNSS NOAA V1.2 can provide stable wind speeds to estimate heat flux with a bias of 5.83 W/m^2 and an RMSE of 29.68 W/m^2 . An improvement (RMSE) of 17% for the CYGNSS LHF product is obtained using the CYGNSS NOAA V1.2 wind speed product. However, the number of data pairs matched with the buoy decreased significantly from 147,165 to 54,219. During NOAA V1.2 wind speed inversion, a large number of outliers were identified and eliminated through quality control. From Figure 7A, it can be seen that the LHF estimated from CYGNSS NOAA V1.2 winds is consistent with that estimated from buoy data compared to the CYGNSS CDR V1.0 heat flux product (Figure 4A). In terms of deviation (CYGNSS – Buoy), LHF is overestimated by CYGNSS NOAA V1.2. It can be seen from Figure 7C that the bias and RMSE of the LHF estimated from CYGNSS SDR V3.1 are –1.39 W/m^2 and 33.03 W/m^2, respectively, which are slight better than those of the CYGNSS LHF CDR V1.1 product during the same period of 2018.08.01–2022.02.28.

Figures 7B, D also illustrate the performance of the CYGNSS NOAA V1.2 and CYGNSS SDR V3.1 wind products in estimating SHF. It is noted that CYGNSS SDR V3.1 gives a large RMSE of 6.97 W/m^2 , whereas the RMSE of the other SHF product is ~ 6.7 W/m^2 . By using different wind speed products to estimate SHF, it is found that the impact on the accuracy of SHF is minor, and there is no obvious improvement in accuracy.

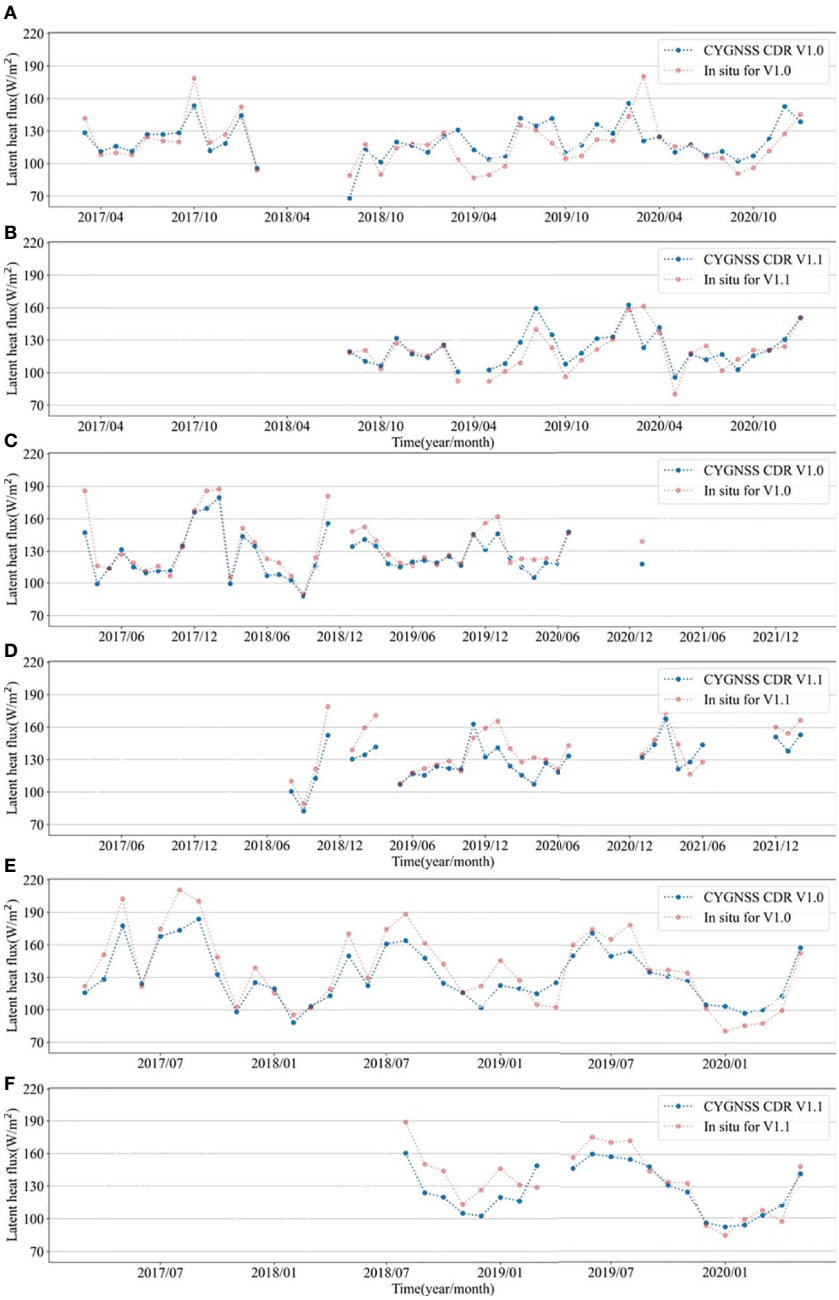


FIGURE 6
Comparisons of CYGNSS LHF CDR products and *in situ in situ* buoys heat flux in the tropical oceans of the Pacific (**A, B**:8°N, 137°E), Atlantic **C, D**:20°N, 38°W), and Indian (**E, F**:8 °S, 95°E) oceans, respectively.

TABLE 4 CYGNSS Level 2 wind speed products and time spans for estimating heat flux.

Wind speed products	Time span
NOAA CYGNSS Level 2 V1.2	2017.05.01–2022.02.28
CYGNSS Level 2 SDR V3.1	2018.08.01–2022.02.28

3.3.3. Performance in the Pacific, Atlantic, and Indian Oceans

According to the RAMA, PIRATA, and TRITON, the performance of CYGNSS LHF/SHF NOAA V1.2 is analyzed, as shown in Figure 8. The characteristics of the NOAA V1.2 LHF/SHF product are the same as that of CYGNSS CDR V1.0, which has a positive deviation for every buoy in the Pacific

Ocean, and RMSE decreases from 34.84 W/m^2 to 29.59 W/m^2 (15% improvement). In addition, improvements of the Indian Ocean and the Atlantic, it has improved to varying degrees, 11.6% and 26.8%, respectively. It is noted that the buoy with a latitude of 19°S and a longitude of 34°W also gives a large deviation (> 50 W/m^2) and RMSE (> 60 W/m^2). For the LHF product, there is no improvement in accuracy in any tropical ocean basin.

4 Conclusions

A preliminary evaluation of the heat flux (LHF/SHF) estimates from the remotely sensed wind speed measurements of the CYGNSS mission during the period of 2017–2022 is performed. We systematically compare temporally and spatially coincident CYGNSS heat fluxes and those estimated from various tropical moored buoy systems (i.e., TAO, TRITON, PIRATA, and RAMA). The comparisons show that the CYGNSS CDR V1.1 heat flux is in good agreement with estimates from the buoys, with overall average RMSEs of 33.60 W/m^2 and 6.77 W/m^2 for LHF/SHF, respectively. The overall average bias is –3.51 W/m^2 , demonstrating that CYGNSS LHF CDR V1.1 underestimates compared to the *in situ* measurements for global tropical oceans, whereas SHF CDR V1.1 slightly overestimates, with a bias of 1.53 W/m^2 . Furthermore, the differences in each tropical ocean basin are investigated according to the heat flux estimates from the TAO/TRITON, PIRATA, and RAMA buoys. It is found the CYGNSS heat flux in the Atlantic Ocean has better performance than that in the Pacific and Indian oceans. For CYGNSS CDR V1.0 and V1.1, it is shown that the SHF product is slightly overestimated, with a a positive bias in the Pacific, Atlantic, and Indian oceans. Additionally, it should be noted that the amount of matchups between CYGNSS and the the buoys is limited, which may have resulted in some uncertainty in the evaluation accuracy of CYGNSS heat flux products in each tropical ocean basin. In addition, the impact on the accuracy of LHF/SHF estimates is investigated by the CYGNSS NOAA V1.2 and CYGNSS SDR V3.1 wind products. The results illustrate that CYGNSS NOAA

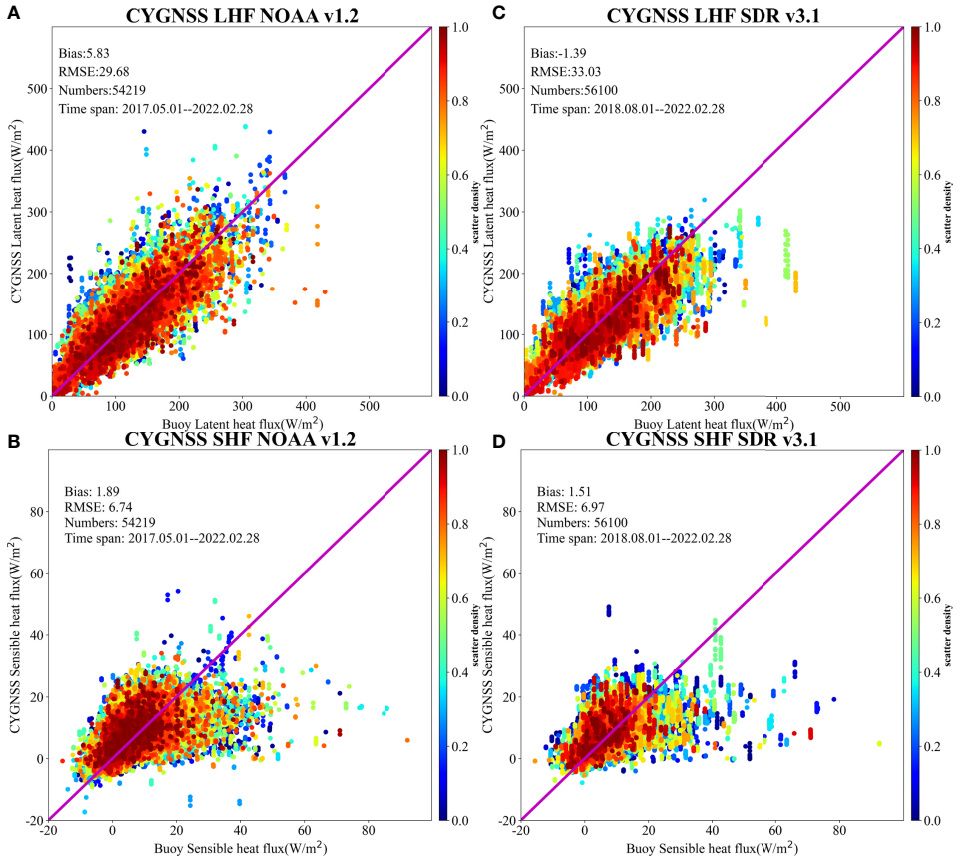


FIGURE 7
Comparisons between LHF **(A, B)**/SHF **(C, D)** estimates from *in situ* measurements and from CYGNSS NOAA V1.2 during 2017-2021 and SDR V3.1 during 2018-2022, respectively. The bias, RMSE, number of matchups, and time span are given in each subfigure. The colorbar is the number density of points, and the purple line shows the 1:1 diagonal.



FIGURE 8
Left column: Performance of the CYGNSS LHF NOAA V1.2 product compared to the TAO/TRITON array in the Pacific, PIRATA in the Atlantic, and RAMA in the Indian Ocean. Right column: The same for the CYGNSS SHF NOAA V1.2 product.

V1.2 winds can significantly improve the accuracy of LHF estimates by 17%, and both wind products have almost no impact on SHF estimates. Overall, the heat flux products acquired from the CYGNSS mission in 2017–2022 are valuable for practical use.

Data availability statement

The original contributions presented in the study are included in the article/supplementary material. Further inquiries can be directed to the corresponding authors.

Author contributions

XL and JY designed the study and managed the project. XL and WL led the research, interpreted the data, drew figures, and wrote the manuscript. YY collected *in situ* buoy observation data calculated surface heat fluxes, and analyzed the satellite-based surface heat flux datasets from the CYGNSS mission. XL and WL compared satellite estimates with buoy observations. YY and WL contributed some useful scripts for this study. JY and YY were involved with reviewing and editing the manuscript. All authors contributed to improving the manuscript. All authors contributed to the article and approved the submitted version.

Funding

This work was supported by the Scientific Research Fund of the Second Institute of Oceanography, MNR, grand no. JB2205, as well as the Innovation Group Project of Southern Marine Science and Engineering Guangdong Laboratory (Zhuhai) (No. 311021004), by the European Space Agency and Ministry of Science and Technology Dragon 5 Cooperation Programme under Grant 58009. We also thank the staff of the satellite ground station, satellite data processing and sharing center, and marine satellite data online analysis platform of the State Key Laboratory of Satellite Ocean Environment Dynamics, Second Institute of Oceanography, Ministry of Natural Resources (SOED/SIO/MNR), for their help with data collection and processing.

Conflict of interest

The authors declare that the research was conducted in the absence of any commercial or financial relationships that could be construed as a potential conflict of interest.

Publisher's note

All claims expressed in this article are solely those of the authors and do not necessarily represent those of their affiliated organizations, or those of the publisher, the editors and the reviewers. Any product that may be evaluated in this article, or claim that may be made by its manufacturer, is not guaranteed or endorsed by the publisher.

References

Back, L. E., and Bretherton, C. S. (2005). The relationship between wind speed and precipitation in the Pacific ITCZ. *J. Climate* 18, 4317–4328. doi: 10.1175/JCLI3519.1

Bentamy, A., Katsaros, K. B., Mestas-NunEz, A. M., Drennan, W. M., Forde, E. B., and Roquet, H. (2003). Satellite estimates of wind speed and latent heat flux over the global oceans. *J. Climate* 16, 637–656. doi: 10.1175/1520-0442(2003)016<0637:SEOWSA>2.0.CO;2

Bentamy, A., Piollé, J., Grouazel, A., Danielson, R., Gulev, S., Paul, F., et al. (2017). Review and assessment of latent and sensible heat flux accuracy over the global oceans. *Remote Sens. Environ.* 201, 196–218. doi: 10.1016/j.rse.2017.08.016

Bharti, V., Schulz, E., Fairall, C. W., Blomquist, B. W., and Manton, M. J. (2019). Assessing surface heat flux products with *in situ* observations over the Australian sector of the southern ocean. *J. Atmos. Ocean Tech.* 36, 1849–1861. doi: 10.1175/JTECH-D-19-0009.1

Businger, J. A. (1982). The fluxes of specific enthalpy, sensible heat and latent heat near the earth's surface. *J. Atmos.* 39, 1889–1894. doi: 10.1175/1520-0469(1982)039<1889:TFOSES>2.0.CO;2

Chou, S. H., Nelkin, E., Ardizzone, J., Atlas, R. M., and Shie, C. L. (2002). Surface turbulent heat and momentum fluxes over global oceans based on the goddard satellite retrievals, version 2 (GSSTF2). *J. Climate* 16, 3256–3273. doi: 10.1175/1520-0442(2003)016<3256:STHAMF>2.0.CO;2

Clarizia, M. P., Ruf, C. S., Jales, P., and Gommenginger, C. (2014). Spaceborne GNSS-R minimum variance wind speed estimator. *IEEE Trans. Geosci. Remote Sens.* 52, 6829–6843. doi: 10.1109/TGRS.2014.2303831

Crespo, J. A., and Posselt, D. J. (2019). *Development and early results of the surface heat flux product for the CYGNSS mission* (Jet Propulsion Laboratory, California Institute of Technology). Tallahassee techreport.

Crespo, J. A., Posselt, D. J., and Asharaf, S. (2019). CYGNSS surface heat flux product development. *Remote Sens.* 11, 2294. doi: 10.3390/rs11192294

Cronin, M. F., Gentemann, C. L., Edson, J., Ueki, I., and Zhang, D. (2019). Air-sea fluxes with a focus on heat and momentum. *Front. Mar. Sci.* 6, 430. doi: 10.3389/fmars.2019.00430

CYGNSS (2020) *CYGNSS level 2 ocean surface heat flux climate data record version 1.0. ver. 1.0* (Accessed 2022-04-10).

Edson, J., Jampana, V., Weller, R., Bigorre, S., Plueddemann, A., Fairall, C., et al. (2013). On the exchange of momentum over the open ocean. *J. Phys. Oceanogr.* 43, 1589–1610. doi: 10.1175/JPO-D-12-0173.1

Fairall, C., Bradley, E., Rogers, D., Edson, J., and Young, G. (1996). Bulk parameterization of air-sea fluxes for tropical ocean-global atmosphere coupled ocean-atmosphere response experiment. *J. Geophys. Res.* 101, 3747–3764. doi: 10.1029/95JC03205

Gao, S., Chiu, L. S., and Shie, C. L. (2013). Trends and variations of ocean surface latent heat flux: Results from GSSTF2c data set. *Geophys. Res. Lett.* 40, 380–385. doi: 10.1029/2012GL054620

Gleason, S. T., Hodgart, S., Sun, Y., Gommenginger, C., and Unwin, M. (2005). Detection and processing of bistatically reflected GPS signals from low earth orbit for the purpose of ocean remote sensing. *IEEE Trans. Geosci. Remote Sens.* 43, 1229–1241. doi: 10.1109/TGRS.2005.845643

Grodsky, S. A., Bentamy, A., Carton, J. A., and Pinker, R. T. (2009). Intraseasonal latent heat flux based on satellite observations. *J. Climate* 22, 4539–4556. doi: 10.1175/2009JCLI2901.1

Hartmann, D. L. (1994). "Chapter 4 the energy balance of the surface," in *Global physical climatology*, vol. 56. (Amsterdam, Academic Press), 81–114. doi: 10.1016/S0074-6142(08)60561-6

Jing, C., Niu, X., Duan, C., Lu, F., and Yang, X. (2019). Sea Surface wind speed retrieval from the first Chinese GNSS-R mission: Technique and preliminary results. *Remote Sens.* 11, 3013. doi: 10.3390/rs11243013

KonDa, M., Imasato, N., and Shibata, A. (1996). Analysis of the global relationship of biennial variation of sea surface temperature and air-sea heat flux using satellite data. *J. Oceanogr.* 52, 717–746. doi: 10.1007/BF02239462

Large, W. G., and Pond, S. (1982). Sensible and latent heat flux measurements over the ocean. *J.phy.oceanogr.* 12, 464–482. doi: 10.1175/1520-0485(1982)012<0464:SALHFM>2.0.CO;2

Li, W., Cardellach, E., Ribó, S., Oliveras, S., and Rius, A. (2022). Exploration of multi-mission spaceborne GNSS-R raw if data sets: Processing, data products and potential applications. *Remote Sens.* 14, 1344. doi: 10.3390/rs14061344

Liu, W., Katsaros, K., and Businger, J. (1979). Bulk parameterization of the air-sea exchange of heat and water vapor including the molecular constraints at the interface. *J. Atmos. Sci.* 36, 2052–2062. doi: 10.1175/1520-0469(1979)036<1722:BPOASE>2.0.CO;2

Kubota, M., Iwasaka, N., Kizu, S., Konda, M., and Kutsuwada, K.. (2002). Japanese Ocean flux data sets with use of remote sensing observations (J-OFURO). *J. Oceanogr.* 58, 213–215. doi: 10.1023/A:1015845321836

Pinker, R. T., Bentamy, A., Katsaros, K. B., Ma, Y., and Li, C. (2014). Estimates of net heat fluxes over the Atlantic ocean. *J. Geophys. Res. Oceans* 119, 410–427. doi: 10.1002/2013JC009386

Ruf, C., Atlas, R., Chang, P., Clarizia, M. P., and Zavorotny, V. (2016). New ocean winds satellite mission to probe hurricanes and tropical convection. *Bull. Am. Meteorol. Soc* 97, 385–395. doi: 10.1175/BAMS-D-14-00218.1

Ruf, C., and Balasubramaniam, R. (2018). Development of the CYGNSS geophysical model function for wind speed. *IEEE J. Sel. Topics Appl. Earth Obs. Remote Sens.* 12, 66–77. doi: 10.1109/JSTARS.2018.2833075

Said, F., Jelenak, Z., Park, J., Soisuvarn, S., and Chang, P. S. (2019). A 'track-wise' wind retrieval algorithm for the CYGNSS mission. *IEEE Int. Geosci. Remote Sens. Symp.*, 8711–8714. doi: 10.1109/IGARSS.2019.8898099

Shie, C., and Hilburn, K. A. (2011). The Goddard satellite-based surface turbulent fluxes (GSSTF) datasets and the Uncertainties/Impact due to the SSM/I brightness temperature. *In AGU Fall Meeting Abstracts* vol. 2011, IN21A–I1417.

Tauro, F., Maltese, A., Giannini, R., and Harfouche, A. (2022). Latent heat flux variability and response to drought stress of black poplar: A multi-platform multi-sensor remote and proximal sensing approach to relieve the data scarcity bottleneck. *Remote Sens. Environ.* 268, 112771. doi: 10.1016/j.rse.2021.112771

Tomita, H., Kutsuwada, K., Kubota, M., and Hihara, T. (2021). Advances in the estimation of global surface net heat flux based on satellite observation: J-OFURO3 v1.1. *Front. Mar. Sci.* 8, 612361. doi: 10.3389/fmars.2021.612361

Unwin, M., Jales, P., Tye, J., Gommenginger, C., Foti, G., and Rosello, J. (2017). Spaceborne GNSS-reflectometry on TechDemoSat-1: Early mission operations and exploitation. *IEEE J. Sel. Top. Appl. Earth Obs. Remote Sens.* 9, 4525–4539. doi: 10.1109/JSTARS.2016.2603846

Wang, D., Zeng, L., Li, X., and Shi, P. (2013). Validation of satellite-derived daily latent heat flux over the South China Sea, compared with observations and five products. *J. Atmos. Ocean. Tech.* 30, 1820–1832. doi: 10.1175/JTECH-D-12-00153.1

Webster, P., and Lukas, R. (1992). Toga coare: The coupled ocean-atmosphere response experiment. *Bull. Amer. Meteor. Soc* 73, 1376–1416. doi: 10.1175/1520-0477(1992)073<1377:TCTCOR>2.0.CO;2

Yang, G., Bai, W., Wang, J., Hu, X., Zhang, P., Sun, Y., et al. (2022). FY-3E GNOS II GNSS reflectometry: Mission review and first results. *Remote Sens.* 14, 988. doi: 10.3390/rs14040988

Yu, L., Weller, R. A., and Sun, B. (2004). Improving latent and sensible heat flux estimates for the Atlantic ocean, (1988 99) by a synthesis approach. *J.Climate* 17, 373–393. doi: 10.1175/1520-0442(2004)017<0373:ILASHF>2.0.CO;2

Zeng, L., Shi, P., Liu, W. T., and Wang, D. (2009). Evaluation of a satellite-derived latent heat flux product in the South China Sea: A comparison with moored buoy data and various products. *Atmos. Res.* 94, 91–105. doi: 10.1016/j.atmosres.2008.12.007

Zhou, L. T., Chen, G., and Wu, R. (2015). Change in surface latent heat flux and its association with tropical cyclone genesis in the Western North Pacific. *Theor. Appl. Climatol.* 119, 221–227. doi: 10.1007/s00704-014-1096-0

Appendix

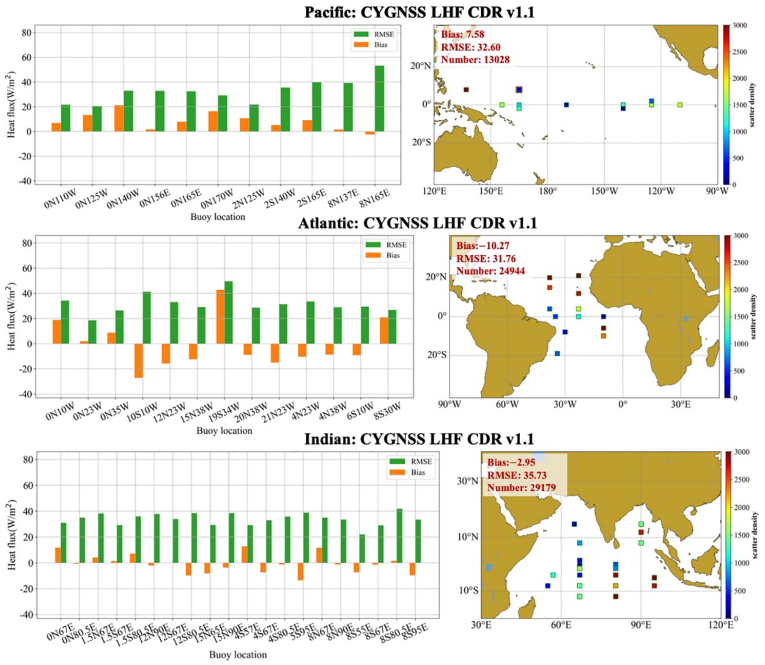


FIGURE A1
Left column: Biases (yellow bars) and RMSEs (green bars) between the CYGNSS LHF CDR V1.1 product and in situ measurements from the tropical oceans of the Pacific, Atlantic, and Indian oceans. Right column: Spatial distribution of buoys from the Global Tropical Moored Buoy Array in each tropical ocean basin. Color density represents the number of matchups for each buoy. The average accuracy (bias and RMSE) and the number of matchups in each tropical ocean are marked in red font.

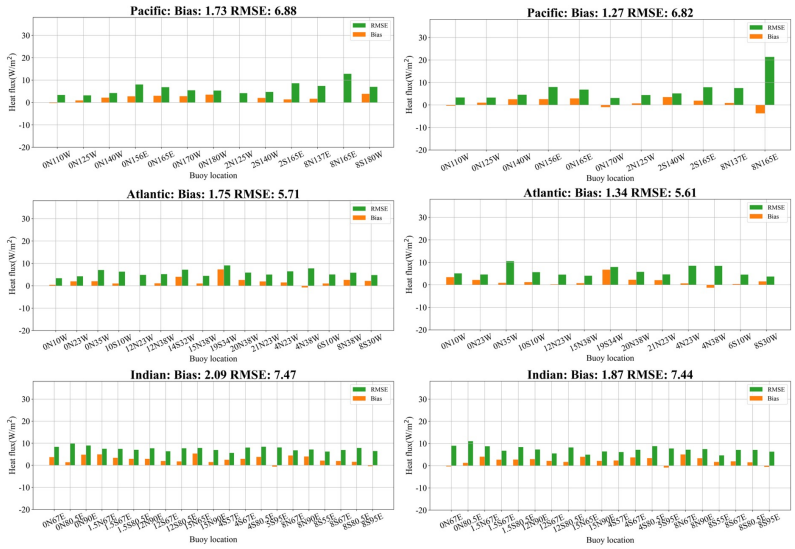


FIGURE A2
Left column: Biases (yellow bars) and RMSEs (green bars) between the CYGNSS SHF CDR V1.0 product and in situ measurements from the tropical oceans of the Pacific, Atlantic, and Indian oceans. Right column: The same for the CYGNSS SHF CDR V1.1 product. The same for the CYGNSS SHF CDR V1.1 product.

frontiers | Frontiers in Marine Science

TYPE Original Research
PUBLISHED 01 December 2022
DOI 10.3389/fmars.2022.1065066

Check for updates

OPEN ACCESS

EDITED BY
Michael Hartnett,
University of Galway, Ireland

REVIEWED BY
Xingru Feng,
Institute of Oceanology (CAS), China
Shengqiang Wang,
Nanjing University of Information Science and Technology, China

*CORRESPONDENCE
Tengfei Xu
xutengfei@fio.org.cn

SPECIALTY SECTION
This article was submitted to Ocean Observation, a section of the journal Frontiers in Marine Science

RECEIVED 09 October 2022
ACCEPTED 17 November 2022
PUBLISHED 01 December 2022

CITATION
Wang D, Fang G, Jiang S, Xu Q, Wang G, Wei Z, Wang Y and Xu T (2022) Satellite-detected phytoplankton blooms in the Japan/East Sea during the past two decades: Magnitude and timing.
Front. Mar. Sci. 9:1065066.
doi: 10.3389/fmars.2022.1065066

COPYRIGHT
© 2022 Wang, Fang, Jiang, Xu, Wang, Wei, Wang and Xu. This is an open-access article distributed under the terms of the Creative Commons Attribution License (CC BY). The use, distribution or reproduction in other forums is permitted, provided the original author(s) and the copyright owner(s) are credited and that the original publication in this journal is cited, in accordance with accepted academic practice. No use, distribution or reproduction is permitted which does not comply with these terms.

Satellite-detected phytoplankton blooms in the Japan/East Sea during the past two decades: Magnitude and timing

Dingqi Wang[1,2], Guohong Fang[2,3,4], Shumin Jiang[1,2], Qinzeng Xu[2], Guanlin Wang[2,3,4], Zexun Wei[2,3,4], Yonggang Wang[2,3,4] and Tengfei Xu[2,3,4]*

[1]College of Oceanic and Atmospheric Sciences, Ocean University of China, Qingdao, China, [2]Key Laboratory of Marine Science and Numerical Modeling, First Institute of Oceanography, Ministry of Natural Resources, Qingdao, China, [3]Laboratory for Regional Oceanography and Numerical Modeling, Pilot National Laboratory for Marine Science and Technology, Qingdao, China, [4]Shandong Key Laboratory of Marine Science and Numerical Modeling, Qingdao, China

The Japan/East Sea (JES) is known as a mid-latitude "Miniature Ocean" that features multiscale oceanic dynamical processes. Using principal component analysis (PCA), we investigate the variability of the sea surface chlorophyll-a concentration (SSC) and its bloom timing in the JES based on satellite remote sensing products spanning 1998–2019. The JES SSC exhibits strong seasonal variability and blooms twice annually. The spring bloom is induced under combined factors of increased photosynthetically active radiation (PAR), weakened wind speeds and sea ice melting, and terminated by the enhanced stratification. The fall bloom is induced by destratification and active dynamic processes (such as upwelling and front), and terminated by decreased PAR. The interannual variability of spring and fall bloom occur along the northwestern coast of the JES and in the deep Japan Basin, respectively. The positive SSC anomalies along the northwestern coast of the JES in spring is associated with more sea ice in the previous winter, weaker wind speed, and stronger stratification induced by the El Niño events. No significant relationship has been found between the fall bloom and the El Niño events. The bloom timing is controlled by the critical depth hypothesis. The initiation/termination timing of spring blooms has shifted earlier by 0.37/0.45 days, and the counterpart of fall blooms has shifted 0.49/1.28 days earlier per year. The duration and magnitude are independent with each other for spring bloom at interannual time scale. In contrast, they are positively correlated for fall bloom, because of both bloom timing and magnitude are dominated by active oceanic dynamical processes in fall.

KEYWORDS

sea surface chlorophyll-a concentration (SSC), Japan/East Sea (JES), spring bloom, fall bloom, interannual variability

Introduction

As the most common primary producer in the marine food chain, phytoplankton respond quickly to changes in their physical environment and are thus sensitive to climate change (Hays et al., 2005). To date, only satellite-based ocean color observations can provide globally covered sea surface chlorophyll-a concentrations (SSCs), which are commonly used for estimating phytoplankton concentrations (Banse, 1977; Taboada et al., 2019; Liu and Wang, 2022). The Japan/East Sea (JES) involves multi-scale oceanic dynamical processes (e.g., Ichiye, 1984; Minobe et al., 2004; Park et al., 2014), thereby resulting in complicate SSC variations by changing nutrient supply (Park et al., 2020). For instance, the warm Tsushima Warm Current and cold Liman Cold Current forms a thermal boundary in Sea Surface Temperature (SST), namely, a subpolar front (Yamada et al., 2004). The subpolar front induces nutrients accumulation and further favor SSC increases (Lee et al., 2009; Wang et al., 2021). Featured with strong offshore monsoons, the JES is abundant with wind-driven Ekman upwelling. This upwelling can carry nutrient-rich water from deeper layers and thus nourish phytoplankton, resulting in heightened SSC (Price, 1981; Liu et al., 2019; Park et al., 2020). Sea ice-melted water carries high nutrients, promoting the increase of SSCs along the coast of Russia (Martin and Kawase, 1998; Park et al., 2006; Ivanova and Ivanov, 2012; Park et al., 2014; Nihashi et al., 2017). Mesoscale eddies would induce large heat exchange and mass transportation variabilities, which also play important roles in SSC variations (Lee and Niiler, 2010; Maúre et al., 2017). In addition, previous investigations show that SSC tends to increase following the passage of typhoons (Son et al., 2006; Liu et al., 2019; Ji et al., 2021). Overall, the upper dynamics in the JES are quite complex, leading to the complexities of SSC variations that require scrupulous research.

The phytoplankton concentrations in the JES blooms twice each year, i.e., the spring bloom (March–May) and the fall bloom (October–November), both of which can be detected from satellite observed SSCs (Kim et al., 2000; Jo et al., 2014; Ishizaka and Yamada, 2019). Spring blooms, occurring in almost the entire JES, are initiated earlier in the southern region and later in the northern region (Yamada et al., 2004; Maúre et al., 2017). Basically, spring blooms can be explained by the critical depth hypothesis (Sverdrup, 1953). In winter, phytoplankton growth is light-limited (due to deep mixing) rather than being nutrient limited. In spring, the mixed layer becomes shallower than the critical depth, resulting in unlimited light availability to initiate spring bloom (Kim et al., 2000). The critical depth hypothesis is extended by considering the relaxation of turbulent mixing conditions associated with surface warming (Taylor & Ferrari, 2011) and weakened wind stress (Kim et al., 2007; Chiswell et al., 2013; Lee et al., 2015). Brody and Lozier (2014) further predicted that spring blooms tend to occur when the mixing mechanism shifts from convection to wind driven. These extended hypotheses were employed over the JES, where the spring bloom is usually initiated after the local wind stress is weakened over several days (Kim et al., 2007). Additionally, eddy-driven stratification could regulate the initiation timing of the spring bloom (Mahadevan et al., 2012), with anticyclonic/cyclonic eddy playing different mechanisms, since the mixed layer depth (MLD) is deepened/shallowed in an anticyclonic/cyclonic eddy, respectively (Maúre et al., 2017). In comparison, fall blooms are much weaker and occur only in the western JES (Yamada et al., 2004; Kim et al., 2007). In contrast to the winter-spring seasons, the upper layer of the JES is oligotrophic in the summer-fall seasons. Consequently, fall blooms rely on the vertical transport of nutrient-rich water from deeper layers and are expected to start when the MLD deepens and becomes equal to the critical depth (Kim et al., 2000; Yamada et al., 2004). In terms of MLD deepening, previous studies have suggested that this process is caused by enhanced wind and surface cooling favoring the destratification of the water column (Yamada et al., 2004; Kim et al., 2007).

Park et al. (2022) proposed that the interannual variability of SSC is significant in the JES, because the contribution of seasonal cycles to the total variance in SSC variability is less than 30%. Park et al. (2020) suggested that interannual SSC anomalies have only one dominant annual peak that occurs in March or April. The interannual SSC anomaly along the JES's northwestern coast in spring is highly related to the sea ice concentration (SIC) in the Tartar Strait in the previous winter from 1999 to 2007, as more winter SIC would provide more nutrients when melting (Park et al., 2014). For the initial timing, the spring blooms tend to start early/late in El Niño/La Niña years in response to weak/strong wind speed-induced turbulent mixing (Yamada et al., 2004). Meanwhile, the El Niño-Southern Oscillation (ENSO) events could influence the strength and direction of the Tsushima Warm Current to modify the location and maintenance of the subpolar front, which in turn influences the initiation region and timing of the spring bloom (Yoo and Kim, 2004). In comparison, the interannual variability of fall blooms is much weaker, and their initiation timing is less correlated to ENSO-induced wind speed anomalies over the JES (Yamada et al., 2004). During positive Arctic Oscillation (AO), the SSC anomaly in spring might slightly increase due to the weakening of wind speed and the weak increase of SST in previous winter (Park et al., 2022).

The temporal variation in bloom magnitude and timing, including initiation timing, termination timing and duration, has significant ecological and biogeochemical influences (Behrenfeld and Boss, 2017). The strong phytoplankton blooms will lead to the imbalance of marine ecosystem, resulting in huge economic losses, especially harmful algal blooms (Ok et al., 2021). Based on observation data from 1972 to 2002, Yamada and Ishizaka (2006) proposed that spring bloom in the southern JES started relatively earlier in mid-

1980s, resulting in a regime shift of the community structure of spring diatom from cold water species to warm water species, which are small and adapted to oligotrophic condition. Additionally, in the southern JES, the recruitment of Japanese sardine was positively affected by delays in the start and end timing of the spring bloom, because the overlap of bloom duration and sardine larval periods prolonged (Kodama et al., 2018).

In summary, JES SSC is characterized by bimodal blooms in spring and fall each calendar year. Although the dominant mechanism of these blooms can be attributed to the critical depth hypothesis for both spring and fall blooms, the detailed processes differ between the blooms and involve different physical environmental factors. Therefore, these different theories are still a matter of debate and lack a coherent explanation (Maúre et al., 2017). Moreover, the dominant factors that favor and/or restrict SSC during its bloom and decay stages have not yet been clearly discussed. Due to the different candidate initiation mechanisms of spring blooms and fall blooms, their interannual variation mechanisms are also supposed to differ. Furthermore, there is a lack of a study synthesizing variability of bloom magnitude and timing in the seasonal and interannual cycle. In this study, we attempt to reveal the favorable/restricting factors during the SSC raise and decline stages, and to investigate the interannual variations of SSC in terms of bloom magnitude and timing in spring and fall, respectively.

Data and methods

Study region

The Japan/East Sea (JES) is a semi-enclosed marginal sea located in the middle latitudes of the Northwest Pacific Ocean (Figure 1). JES includes three basins, Tsushima Basin, Ymato Basin and Japan Basin. The maximum depth is over 3500 m in Japan Basin. JES connect to the other outer seas with four straits,

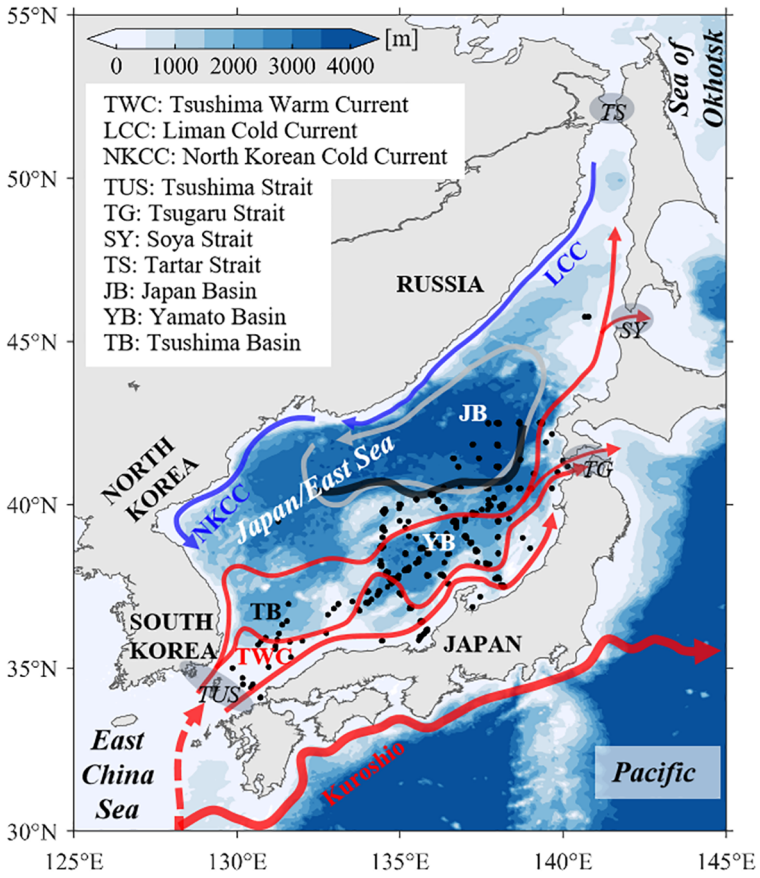


FIGURE 1
Topography of the JES. Red/blue arrows represent warm/cold currents (Yabe et al., 2021). Black dots indicate the *in-situ* observation stations of chlorophyll-a concentration, as derived from the WOD18. The dark black line indicates the position of the subpolar front (Zhao et al., 2016; Xi et al., 2022).

that is, with Tsushima Strait to East China Sea, with Tsugaru Strait and Soya Strait to Pacific, with Tartar Strait to Sea of Okhotsk (Yabe et al., 2021). There are two main cold currents along the western coast, Liman Cold Current and North Korean Cold Current, and are Tsushima Warm Current and its branches over the south and southeast JES (Yoon and Kim, 2009). The subpolar front in the 38~40°N region divides the JES into a subpolar zone in the north and a subtropical zone in the south (Zhao et al., 2016; Xi et al., 2022). In the southern JES, there is the Tsushima Warm Water with high salinity above the permanent thermocline. JES has its own thermohaline conveyor belt system, thus forming the Japan Sea Proper Water with the potential temperature less than 1°C, which is the most homogeneous water masses in the marginal sea of the world ocean. The Japan Sea Intermediate Water is located between the Tsushima Warm Water and the Japan Sea Proper Water (Kim et al., 2008). Seasonal variations in sea surface temperature (SST) and sea surface wind fields were significant over JES. The eddy kinetic energy (EKE) in the southern sea is multiple times more than that in the southern JES (Trusenkova, 2014).

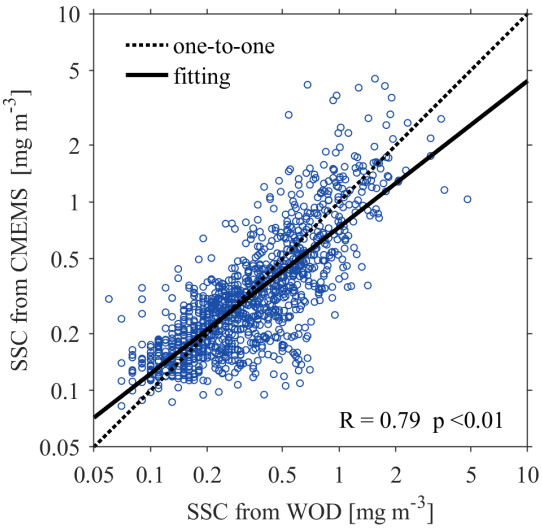


FIGURE 2
Regression between the *in-situ* observed chlorophyll-a concentrations from WOD18 (x-axis) and satellite-derived (y-axis) sea surface chlorophyll-a concentrations (SSCs). The dashed line indicates the one-to-one relation.

Data

The daily SSC data is a Level-4 product providing globally cloud-free estimations during 1998–2019 at a 4-km resolution. The product is published by the Copernicus Marine Environment Monitoring Service (CMEMS), and has merged ocean color observations from multiple sourced satellites (Garnesson et al., 2019). The Level-4 product preserves the information of Level-3 product, and can resolve the SSC variations with time scales longer than intraseasonal (Garnesson et al., 2019; Xu et al., 2021). The *in-situ* chlorophyll-a concentration measurements at 10 m depth obtained from the World Ocean Database 2018 (WOD18), as shown by the black dots in Figure 1, are used to validate the satellite-derived SSC data in the JES (Boyer et al., 2018). A total of 1172 chlorophyll-a profiles during 1998–2019 was obtained. The satellite-derived SSC data are generally consistent with the *in-situ* observations, with a high correlation coefficient of 0.79 ($p<0.01$) (Figure 2). Thus, the satellite-detected SSC data used in this study is reliable for the following research.

The photosynthetically active radiation (PAR) and its attenuation coefficient (k) are provided by the European Service for Ocean Colour with a 4-km horizontal resolution and daily interval (Maritorena et al., 2010). Satellite-based SIC data in the Tatar Strait (47°–52°N, 139°–142°E) are obtained from the National Snow and Ice Data Center of the National Oceanic and Atmospheric Administration (Comiso, 2017). The sea surface height (SSH) and sea surface geostrophic current anomalies, with a horizontal resolution of 0.25°×0.25°, are derived from the daily gridded absolute dynamic topography products version 5 and are distributed by the Archiving, Validation, and Interpretation of Satellite Oceanography (Ducet et al., 2000). Daily SST are derived from the CMEMS with a 0.05°×0.05° horizontal resolution (Good et al., 2020). The surface wind vector data are provided by the European Centre for Medium-Range Weather Forecasts ERA5 high-resolution reanalysis project, with a horizontal resolution of 0.25°×0.25° (Hersbach and Dee, 2016). The monthly Niño3.4 and Arctic Oscillation (AO) indices data are collected from the Koninklijk Nederlands Meteorologisch Instituut (KNMI) climate explorer (Trouet and Van Oldenborgh, 2013). In this study, all data described above cover the period from 1 January 1998 to 31 December 2019. Climatological monthly mean temperature, salinity and nutrient profiles are obtained from the World Ocean Atlas 2018 (WOA18) (Garcia et al., 2019). Details for the datasets used in this study are presented in Table 1.

Methods

A phytoplankton bloom is defined as a period while the SSC exceeds a certain percentage (20%) of its annual median value over a duration longer than three weeks (spring bloom) or one week (fall bloom), consistent with that used in Maúre et al. (2017). As shown in Figure 3, each grid point has its own threshold SSC value for a bloom. To depict the overall SSC variation characteristics in the JES, we average the SSC over the entire JES. As the definition of blooms on each grid, we identify the blooms for the entire JES with a threshold SSC value

TABLE 1 Parameters of the datasets used in this study.

Source	Variables	Temporal Coverage	Temporal resolution	Spatial resolution	URL
CMEMS	SSC	1998–2019	daily	4-km	https://resources.marine.copernicus.eu
WOD18	SSC	1998–2019	-	-	https://www.ncei.noaa.gov/products/world-ocean-database
GlobColour	PAR and k	1998–2019	daily	4-km	http://www.globcolour.info/
NSIDC	SIC	1998–2019	daily	-	http://nsidc.org/
AVISO	SSH, and sea surface geostrophic current anomalies	1998–2019	daily	0.25°×0.25°	http://www.aviso.altimetry.fr/duacs/
CMEMS	SST	1998–2019	daily	0.05°×0.05°	https://resources.marine.copernicus.eu
ERA5	surface wind	1998–2019	6-hourly	0.25°×0.25°	https://cds.climate.copernicus.eu/cdsapp#!/dataset/reanalysis-era5-single-levels?tab=form
KNMI	Niño3.4, and AO indices	1998–2019	monthly	-	http://climexp.knmi.nl/selectindex.cgi?id=someone@somewhere
WOA18	temperature, salinity and nutrient profiles	climatology	monthly	0.25°×0.25°	https://www.ncei.noaa.gov/access/world-ocean-atlas-2018

calculated from the area-averaged SSC (~0.55 mg m^{-3}). The averaged SSC could also be used to test the EOF results.

The Ekman pumping velocity is calculated as follows:

$$w_E = -\nabla \times \left(\frac{\tau}{\rho_0 f}\right) \quad (1)$$

where $\rho_0 = 1.025 \times 10^3$ kg/m^3, is the mean sea water density, f is the Coriolis parameter, and τ is the wind stress derived from ERA5 wind field product.

The EKE is calculated as follows:

$$EKE = \frac{1}{2}\left(u'^2 + v'^2\right) \quad (2)$$

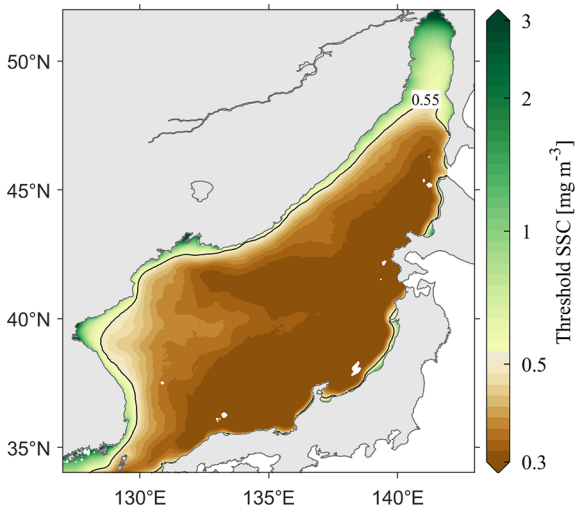


FIGURE 3
Distribution of threshold SSC for a bloom at each grid in the JES over 1998–2019.

where u' and v' are the sea surface geostrophic current anomalies.

The wind-induced near-inertial energy flux (WNEF) is estimated by a simple slab mixed layer model as follows (Pollard & Millard, 1970):

$$\Pi(H) = Re(\boldsymbol{Z} \cdot \boldsymbol{\tau}^*) \quad (3)$$

where $\boldsymbol{Z}=u+iv$ represents the mixed-layer current, H is the area-averaged climatological monthly mean MLD, and $\boldsymbol{\tau}^*$ is the conjugate of $\boldsymbol{\tau}$. A spectral solution through a two-sided Fourier transform is used here, expressed as the following equation:

$$\hat{\boldsymbol{Z}}(\sigma) = \frac{\hat{\tau}(\sigma)}{H}\frac{r - i(f+\sigma)}{r^2 - i(f+\sigma)^2} \quad (4)$$

Where $r(\sigma) = r_0(1 - e^{-\sigma^2/2\sigma_c^2})$ is the frequency-dependent damping parameter, σ represents the angular frequency, $r_0 = 0.15f$ and $\sigma_c = f/2$ (Alford, 2003).

The Brunt Väisälä frequency, N, is used to estimate the vertical stability in the upper 200 m of the ocean as follows:

$$N = \sqrt{-\frac{g}{\rho}\left(\frac{d\rho}{dz}\right)} \quad (5)$$

where g is the gravitational acceleration, ρ is the potential density of sea water, and z is the depth.

The MLD is calculated by defining a temperature threshold of 0.3°C from 10 m, as suggested by Jo et al. (2014). Both N and MLD are calculated from the WOA18 data.

The gradient-based edge detection algorithm is employed to detect SST fronts (Castelao & Wang, 2014; Wang et al., 2021). The monthly frontal probability (FP), which represents the occurrence frequency of SST fronts, is defined as the ratio between the occurrence days of frontal conditions and the total days in the corresponding month.

The critical depth (CRD) is computed as follows:

$$CRD = \frac{I_0}{kI_c} \quad (6)$$

where I_0 is the PAR (E m^{-2} d^{-1}) and k denotes the attenuation coefficient of PAR. The compensation light intensity I_c is taken as 3.8 E m^{-2} d^{-1} (Kim et al., 2000).

Principal component analysis (PCA) is an adaptive data analysis technique to reduce confusing datasets to a lower dimension to increase interpretability, but simultaneously preserves as much 'variability' (i.e. statistical information) as possible (Shlens, 2014; Jolliffe and Cadima, 2016; Trombetta et al., 2019). This technique is popular for analysis of atmospheric and oceanic data, and is often referred to as Empirical orthogonal function (EOF) called by Lorenz (1956). Both names are commonly used, and the essence of the two is the same. However, EOF often examines the variability in data through space, which is widely used to extract patterns, while PCA is often used to highlight the relationships between different variables over time (Hannachi et al., 2007; Trombetta et al., 2019). In this study, PCA is used to identify the relevant factors that might influence the seasonal SSC cycle following Trombetta et al. (2019), while EOF is employed to explain the spatiotemporal distribution of SSC in the JES on seasonal and interannual time scales (Legaard and Thomas, 2006; Greene et al., 2019). Prior to the PCA and EOF analysis, the monthly mean SSC data is logarithmically transformed due to its lognormal distribution (Campbell, 1995), as suggested in previous studies (Dandonneau, 1992; Xu et al., 2021).

Results

Seasonal bloom magnitude

The seasonal cycle of the SSC in the JES shows double peaks associated with the bimodal blooms of phytoplankton concentrations in spring and fall, respectively (Figure 4). The JES SSC is at a low level in boreal winter, with values generally smaller than 0.5 mg m^{-3} (Figures 4A, B). In spring, a bloom occurs around the subpolar front region in March and then extends southward and northward to cover most areas of the JES in April, with SSC values up to 10 mg m^{-3} (Figures 4C, D). In May, SSC begins to decrease from the southeastern JES (Figure 4E). From June to September, the SSC values are smaller than 0.2 mg m^{-3} in most regions of the JES except for the Tartar Strait (Figures 4F–I). Fall bloom begins in October, when the SSCs increase slightly over the entire JES, with smaller magnitudes than spring bloom (Figure 4J). The SSCs are higher along the Russian and Korean coasts until December (Figures 4K, L).

The seasonal evolution of SSC can be derived by applying EOF analysis on the logarithmic monthly mean SSC (Figure 5). The first three leading EOF modes explain 64.2%, 8.8% and 3.6% of the total variance. The first EOF mode (EOF1) essentially represents the basin-scale seasonal variability in the JES SSC (Figure 5A). The EOF1 is reminiscent of the SSC distribution in April, showing positive values in the entire JES with relatively small magnitudes in the Japan Basin (Figures 5B, C). The seasonal time coefficient of EOF1 coincides with the area-averaged SSC in the JES, showing double peaks of 1.36 ± 0.28 mg m^{-3} and 0.74 ± 0.07 mg m^{-3} in April and November, respectively (Figure 5B). During the December–February and June–September periods, the area-averaged SSC is smaller than the threshold criterion, suggesting poor primary production during these stages.

Figure 6 shows the seasonal evolutions of the potential factors accounting for the seasonal variability of SSC in the JES, which have been qualitatively discussed in previous investigations (e.g., Lee et al., 2009; Park et al., 2014; Maúre et al., 2017; Liu et al., 2019; Park et al., 2020). Here, we summarize these factors as four aspects:

(1) PAR and nutrient supply (Figure 6A). In boreal winter, a lower solar altitude angle results in less PAR with an average value of 30.55 E m^{-2} d^{-1}. In spring or summer, PAR increases due to the raise of solar altitude angle. The upper layers of the JES are rich in nutrients during the boreal winter. Part of these nutrients are stored in sea ice, which serve as an important nutrient supply source when melting in boreal spring (Park et al., 2014). Both nitrogen and phosphate are rapidly consumed during spring blooms, with the nitrogen concentration decreasing from a peak value of 7.68 μmol kg^{-1} in March to 1.06 μmol kg^{-1} in May and the phosphate concentration decreasing from a peak value of 0.58 μmol kg^{-1} in March to 0.25 μmol kg^{-1} in May. The nutrients supplementation is poor from June to September when SSC is at a low level, and enhance following October.

(2) MLD and CRD (Figure 6B). Due to the annual cycle of PAR, the CRD is deepening from January and becomes equal to the shoaling MLD around February, when SSC becomes to increase rapidly. In autumn, SSC reaches the second peak around November when the deepening MLD the shoaling CRD coincides. However, the initiation timing of spring bloom and fall bloom are later than February and earlier than November, respectively. This time bias might be caused by the value of the I_c, as the temporal variations of I_c, of 6.3 E m^{-2} d^{-1} during spring and 1.4 E m^{-2} d^{-1} during fall, is not considered in the calculation of CRD (Kim et al., 2000). Thus, the Sverdrup hypothesis (Sverdrup, 1953) is basically applicable to explain the bloom initiation in the JES, indicating that the variations in the JES SSC are mainly governed by the physical environmental conditions.

(3) Stratification (Figure 6C). The JES shows enhanced stratification from March to August due to weakened wind speeds (Figure 6E) and strengthened buoyancy fluxes contributed by both surface warming (Figure 6C) and sea ice melting (Figure 6D). In contrast, destratification occurs from

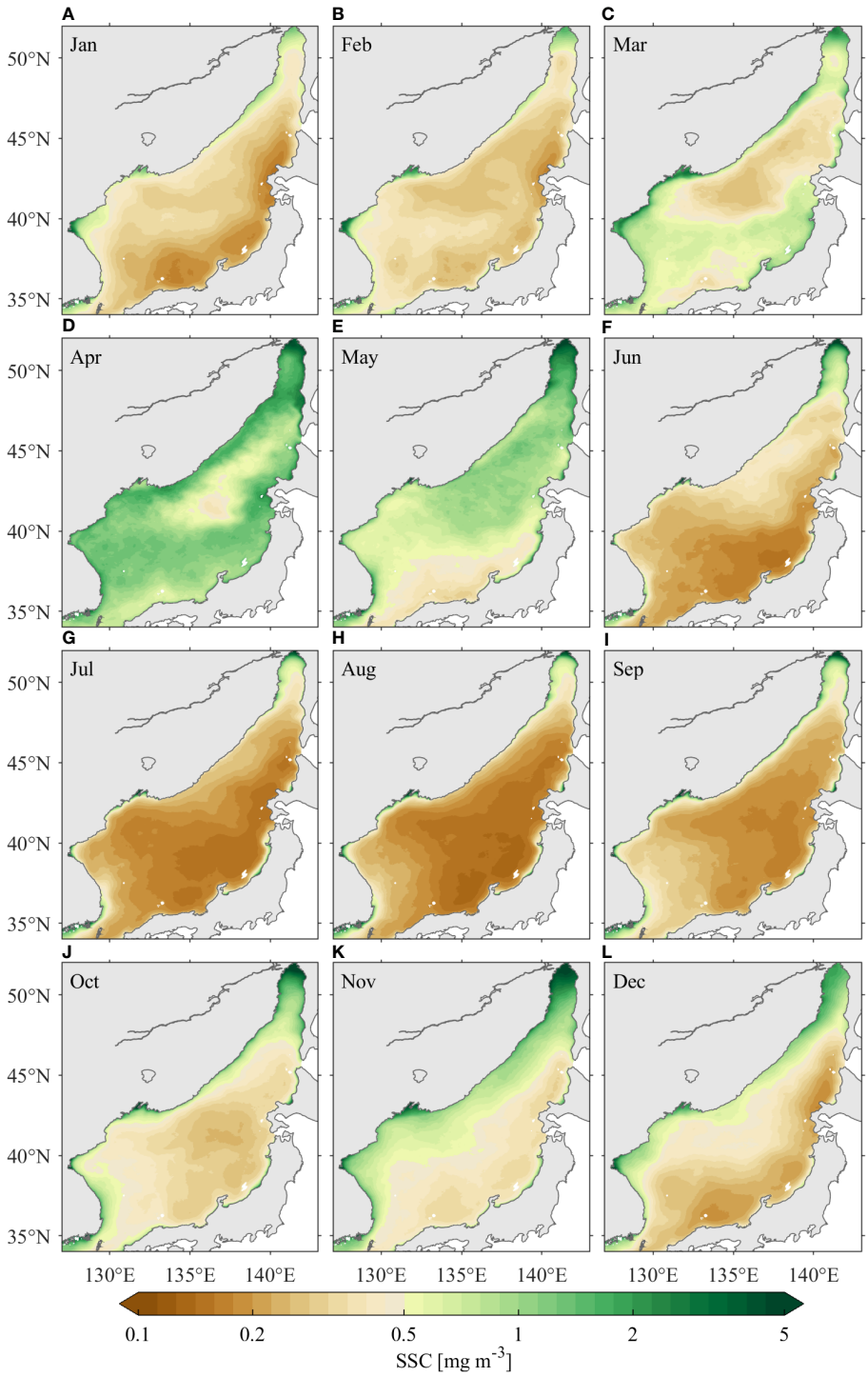


FIGURE 4
Distribution of climatological monthly mean SSC in the JES over 1998–2019. The subfigures **(A–L)** are from January to December, respectively.

September until the following February. Stratification is basically out of phase with the MLD; this process can be explained by the fact that strong/weak stratification corresponds MLD shoaling/deepening. Since the temporal variations of BV frequency and SST are almost identical, SST is used as the index to quantify stratification in the following analysis.

(4) Ocean dynamics contribute to vertical nutrient-water transport (Figures 6D–F). Ocean dynamics dominate the upper

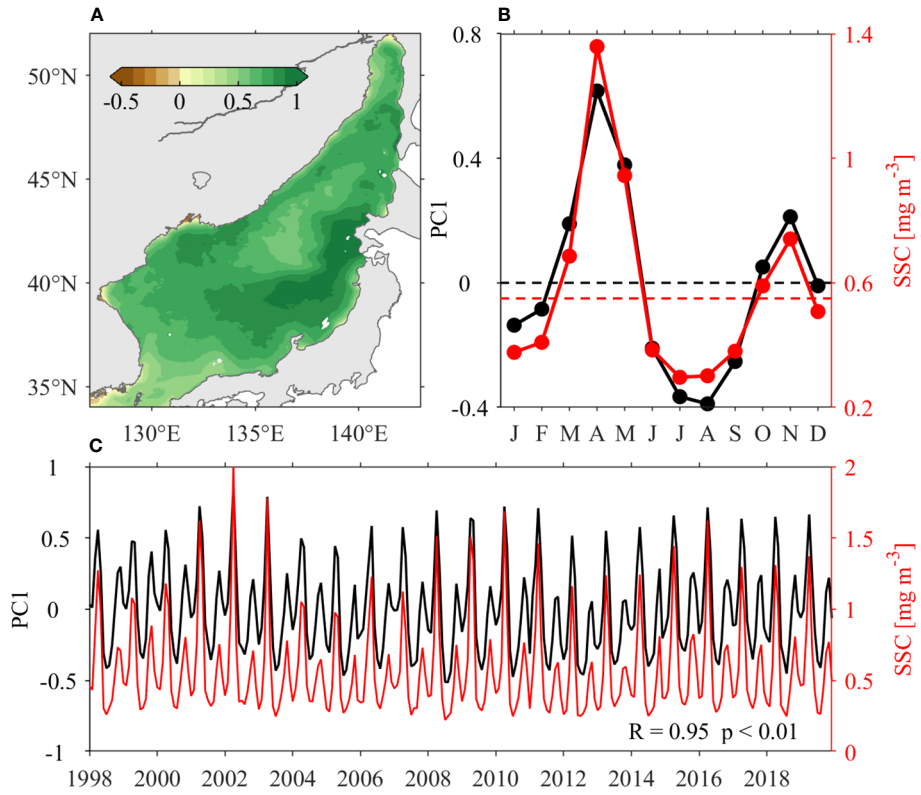


FIGURE 5
EOF analysis of the logarithmic monthly mean SSC in the JES: **(A)** spatial pattern of the first EOF mode, **(B)** climatological and **(C)** time series (black lines). The red lines in **(B)** and **(C)** represent climatological and monthly mean area-averaged SSC values in the JES, respectively. In **(B)**, the black dash line indicates the zero, while the red dashed line indicates the threshold criteria (0.55 mg m^{-3}) of SSC blooms for the entire JES, respectively.

layer nutrients only in boreal summer and fall, when the upper JES is oligotrophic. After October, nutrients increase in accordance with the enhanced upwelling and frontal probability, and under these processes, deeper nutrient-rich waters are entrained to the upper layer. The EKE is larger in the southern JES from August through December, consistent with previous investigation results (Trusenkova, 2014). The WNEF shows larger energy in response to the more frequent typhoons in boreal summer and fall. However, since mesoscale eddies and typhoon-induced near-inertial oscillations generally occur in the southeastern JES, an area that also has strong stratification, it is suggested that only a few typhoons appreciably increase the nutrient supplies in this area (Iwasaki, 2020). Moreover, the high nutrients induced by WNEF are locally distributed along typhoon tracks and thus do not significantly contribute to the area-averaged nutrients over the entire JES. As a result, the monthly averaged nutrients are not efficiently entrained from the deeper layer to the upper layer to nourish the phytoplankton during the June-September period. Nevertheless, the EKE and WNEF remain at relatively high levels until November; therefore, these factors may still contribute to vertical nutrient transport, albeit they are not critical factors.

To identify the dominant and limiting factors affecting the seasonal variability of SSC in the JES, we classify the JES SSC evolution into four stages: the raise stage (January–April) and decline stage (April–July) of spring blooms, and the raise stage (July–November) and decline stage (November–next January) of fall blooms. The relationships between SSC and environmental factors during different stages are examined by PCA analysis (Figure 7). During the raise stage of spring bloom, the SSC is positively correlated with PAR and negatively correlated with wind speed and SIC, suggesting dominant factors inducing spring blooms include increased PAR, weakened winds and sea ice melting. In comparison, oceanic dynamics are not correlated with SSC, as revealed by that they are approximately orthogonal to each other. During the decline stage of spring bloom, the stratification shows a symmetrically opposite relationship with SSC, suggesting that SSC decline is related to enhanced stratification. The PAR is saturated and is thereby orthogonal to SSC, and oceanic dynamics are depressed at this time and thus rarely impact SSC. The coincident

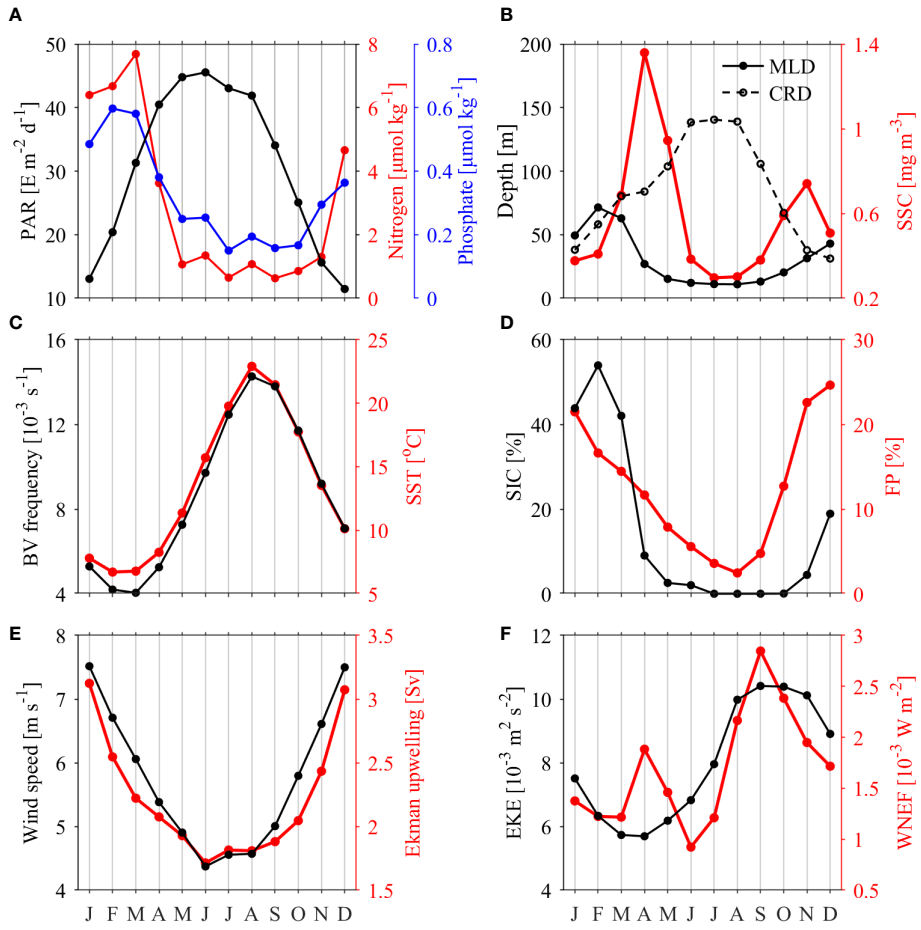


FIGURE 6
Climatological monthly mean series of area-averaged physical environmental factors and area-averaged SSC: **(A)** photosynthetically active radiation (PAR, black line), nitrogen (red line) and phosphate (blue line); **(B)** mixed layer depth (MLD, solid line), critical depth (CRD; dashed line) and SSC (red line); **(C)** Brunt Väisälä (BV) frequency (black line) and sea surface temperature (SST, red line); **(D)** sea ice concentration (SIC, black line) and frontal probability (FP, red line); **(E)** wind speed (black line) and Ekman upwelling transport (red line); **(F)** eddy kinetic energy (EKE, black line) and wind-induced near-inertial energy flux (WNEF, red line).

directions of SSC and FP occur because subpolar fronts are also undergoing a weakening phase at this time (Park et al., 2007). During the raise stage of fall blooms, SSC is positively correlated with the wind speed, upwelling and oceanic fronts; and negatively correlated with PAR and stratification. These results suggest that destratification, strengthening winds and associated upwelling, and enhanced oceanic fronts, favors an increase in SSC by entraining more nutrient-rich waters to the upper layer. The declining PAR tends to act as a limiting factor for phytoplankton growth when it is reduced to a certain extent. During the decline stage of fall blooms, the winds and associated upwelling tend to enhance the upward transport of nutrient-rich waters to the upper JES. However, limited by decreased PAR and increased sea ice, SSC is still suppressed, resulting in the decay of fall blooms. It is worth noting that the nutrients accumulated during the decline stage of a fall bloom essentially contribute to the following spring bloom.

Interannual bloom magnitude

The spring and fall blooms are attributed to different mechanisms. Therefore, we conduct EOF analyses for the interannual anomalies (remove climatological monthly mean) of logarithmic monthly SSC during spring (March–May) and fall (October–November), respectively. EOF1 accounts for 21.2% and 27.0% of the total variances for the spring and fall blooms, respectively. The large interannual variability of SSC in spring and fall occurs along the JES's northwestern coast (Figure 8A), and in the deep Japan Basin (Figure 8B), respectively. The

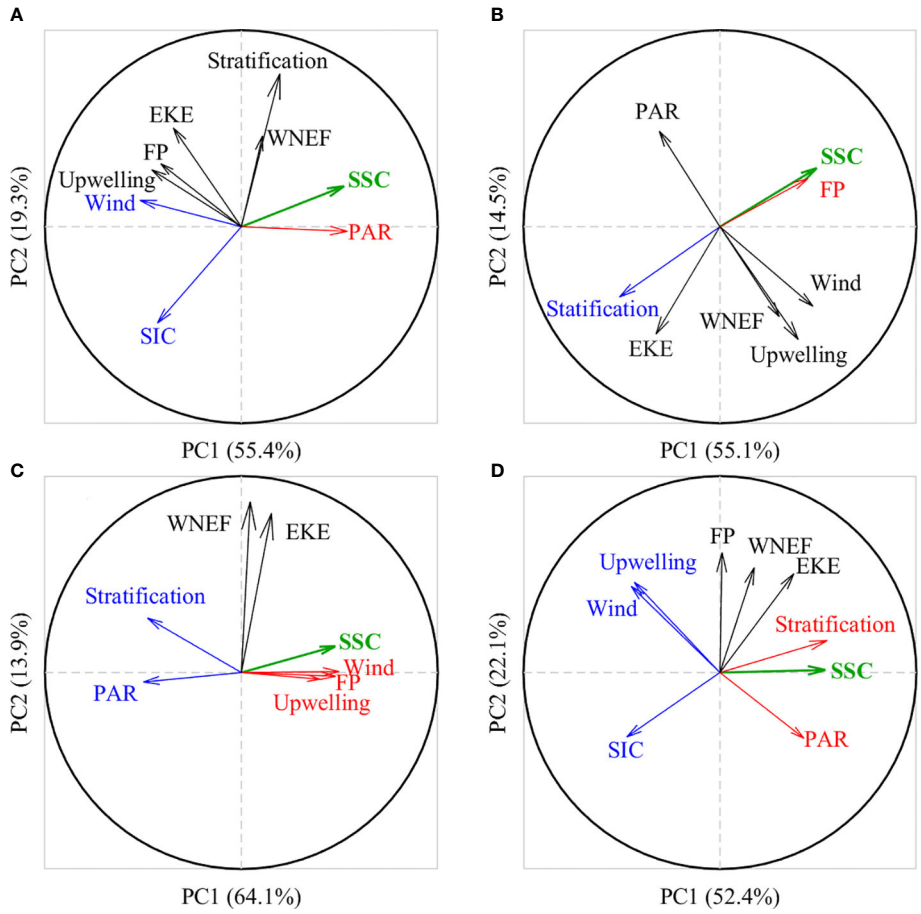


FIGURE 7
PCA analysis of physical environmental factors (arrows) during different SSC evolution stages: **(A)** raise (January–April) and **(B)** decline (April–July) stages of spring blooms; **(C)** raise (July–November) and **(D)** decline (November–January) stages of fall blooms. The x- and y-axes represent the first and second principal components (PC1 and PC2), with their variance contributions marked as percentages in brackets of the x- and y-labels respectively. Arrows close to each other denote that the corresponding factors are positively correlated, whereas those are symmetrically opposed to each other suggest they are negatively correlated. Orthogonal arrows mean they are not correlated with each other. The projections of the arrows on the x- and y-axes indicate the extent to which the factors are explained by PC1 and PC2, respectively. The factors positively (negatively) correlated with SSC (green thick arrows) are highlighted with red (blue) arrows.

positive spring SSC events occur in 2001, 2002, 2009 and 2016, while negative spring SSC events occur in 2005, 2006, 2012 and 2013 (Figure 8C). Positive fall SSC events occur in 1999 and 2015, while negative ones occur in 2008 and 2012 (Figure 8D). Additionally, there is decadal variability in fall blooms, with positive phases during 1998–2002, and 2014–2019, whereas negative phase during 2003–2013.

The interannual variability of JES SSC is positively correlated with PAR, with correlation coefficient (R) of 0.37 at a confidence level of $p< 0.1$ in spring and of $R = 0.12$, $p > 0.1$ in fall (Figures 9A, C). For stratification anomalies, the correlations are $R = 0.55$, $p< 0.01$ in spring and $R = -0.44$, $p< 0.05$ in fall (Figures 9B, D). These correlations suggest that PAR positively contributes to the interannual SSC variability in the JES in spring. Meanwhile, strong stratification favors positive SSC anomalies in spring, as explained by the critical depth hypothesis. In contrast, PAR anomalies are not significantly correlated with SSC anomalies in fall, whereas stratification shows a significant negative correlation, suggesting that stronger stratification leads to smaller SSCs by inhibiting the upward transport of nutrient-rich waters to the mixed layer. For spring bloom, the interannual variability of JES SSC shows weak positive correlation with AO ($R = 0.38$, $p<0.1$) and ENSO ($R = 0.26$, $p > 0.1$). These correlations suggest that the spring bloom magnitude would increase during positive AO and El Niño events, corroborating with the previous study (Park et al., 2022). On the contrary, both the ENSO and AO are not significantly correlated with the interannual variability of fall

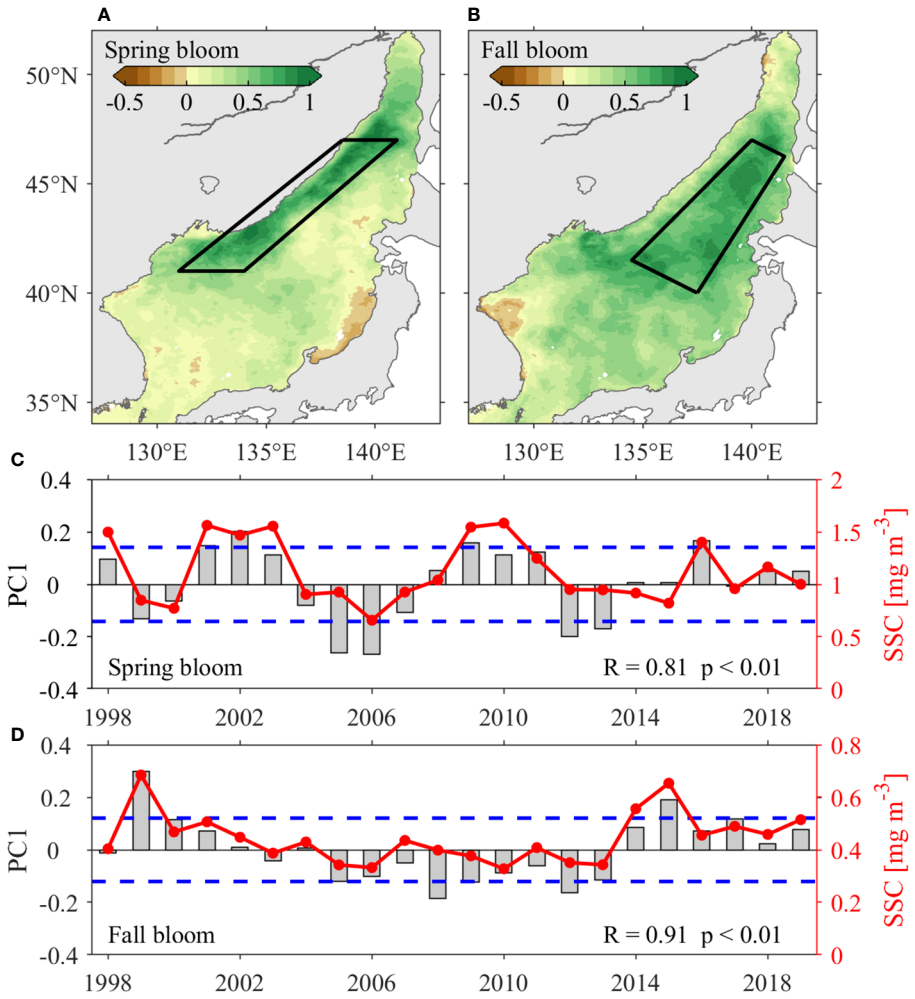


FIGURE 8
EOF analysis of SSC anomalies in the JES. Spatial patterns of the first EOF mode (EOF1) during **(A)** spring (March–May) and **(B)** fall (October–November). The annual time series of EOF1 (PC1, grey bars) with standard deviation (blue dash lines), and area-averaged SSC anomalies (red lines) during **(C)** spring and **(D)** fall. The areas averaged SSC anomalies for **(C)** and **(D)** are marked with black boxes in **(A)** and **(B)**, respectively.

bloom magnitude, with correlation coefficients of 0.05 and –0.04, respectively, below the 90% confidence level.

Bloom timing

Spring bloom initiates in the southern and southeastern JES in February–March and in the northwestern JES in April (Figure 10A), in agreement with previous investigations (e.g., Kim et al., 2000; Yamada et al., 2004; Park et al., 2020). Fall blooms initiates in the Tsushima Basin and along the JES coasts from September to early October and in the central basin of the JES from late October to early November (Figure 10B). Spring blooms are terminated generally in the southwestern JES on 11 April ± 9 days and subsequently in the northeastern JES on 29 May ± 9 days (Figure 10C). Fall blooms generally terminate on 29 November ± 12 as a result of the rapidly decreasing PAR beginning in late November (Figure 10D).

Figure 11 shows the initiation and termination timing of spring blooms along the JES's northwestern coast during 1998–2019. Spring blooms were initiated earlier in 2002, 2010, 2011 and 2014 and later in 1999, 2005, 2006, and 2013; and were terminated earlier in 2002, 2003, 2010 and 2011 and later in 1999, 2000, 2003, and 2006, identified by a threshold value of one standard deviation beyond the climatological mean initiation/termination timing (Figure 11A). The interannual variability in initiation timing is jointly correlated by PAR, stratification, and sea ice melting, i.e., higher PAR, stronger stratification, and earlier sea ice melting are favorable for earlier spring blooms (Figures 11B–D). The termination and initiation

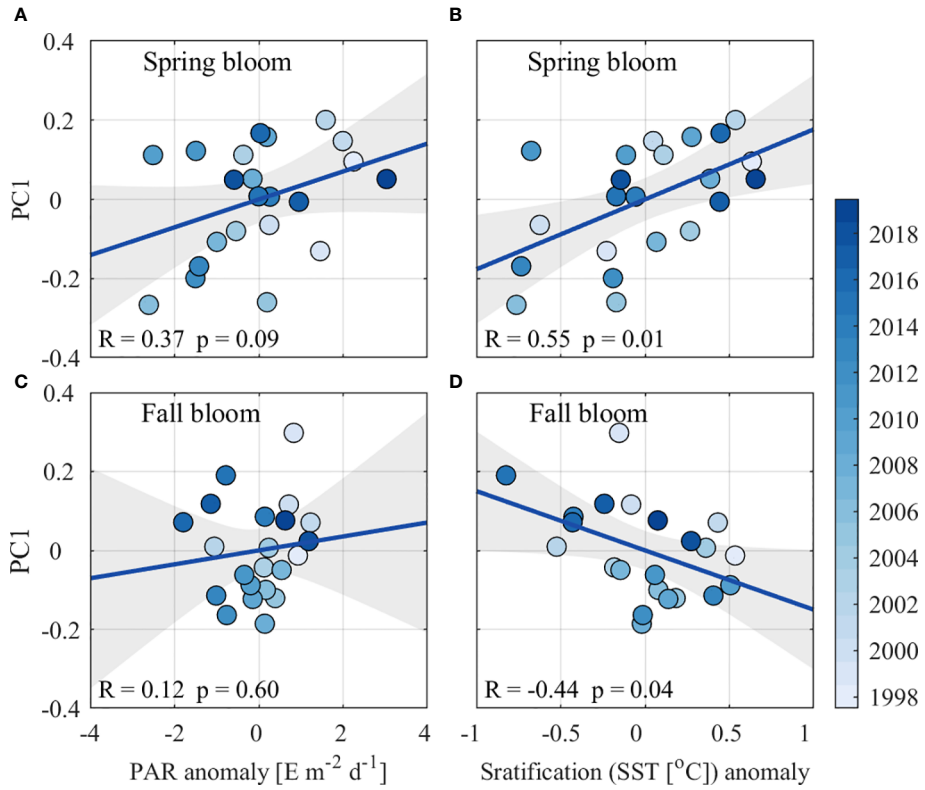


FIGURE 9
Scatterplots (colored dots) and linear fitting (blue lines) between PAR anomalies and PC1 in **(A)** spring and **(C)** fall and between stratification anomalies and PC1 in **(B)** spring and **(D)** fall. The gray shading indicates the 95% two-sided confidence bounds.

timing of spring blooms are significantly correlated, with a correlation coefficient of 0.74 (p<0.01). Additionally, the initiation/termination timings show trends of occurring earlier by 0.37/0.45 days per year during 1998–2019, coinciding with the increasing trends in PAR and stratification identified in March and April.

In the deep Japan Basin, fall blooms were initiated earlier in 1999, 2015, and 2019, in accordance with strong winds and weak stratification; and were initiated later in 2003, 2006, 2008 and 2010, when weak winds and strong stratification occurred. The fall blooms were terminated early in 2011, 2012, 2017 and 2018 and late in 1998, 1999, 2000, and 2015 (Figure 12A). In comparison to the significant positive correlation observed between the termination and initiation timing of spring blooms, the corresponding correlation coefficient of fall blooms is only 0.21 (p>0.1). In addition, the initiation/termination timing show trends of occurring earlier by 0.49/1.28 days per year during 1998–2019, which may be related to the weakened stratification (caused by the intensified wind speeds)/weakened wind speeds during the fall bloom development/decay periods, respectively (Figures 12B, C).

As shown in Figure 13A, for spring bloom along the JES's northwestern coast, in case the bloom occurs earlier, its duration tends to be longer (R = -0.72, p< 0.01). The SSC anomalies from March to May are negatively correlate with initiation (R = -0.50, p< 0.05) and termination (R = -0.55, p< 0.01) timing anomalies, but not statistically correlated with duration anomalies (R = 0.16, p > 0.1). In addition, the spring blooms along the JES's northwestern coast would occur earlier (R = -0.47, p< 0.05) and be more prolonged (R = 0.37, p< 0.1) during positive AO, and would terminate earlier during El Niño events (R = -0.42, p< 0.1). For fall bloom in the deep Japan Basin, duration anomalies are mainly affected by the initiation timing anomalies with a negative correlation coefficient of -0.57 above 99% confidence level (Figure 13B). In addition, on interannual time scale, the bloom magnitude is negatively correlated with the initiation timing with a value of -0.73 (p<0.01), and positively correlated with bloom duration with a value of 0.78 (p<0.01). Furthermore, neither the ENSO nor the AO show significant correlations with the interannual variability of fall bloom timing.

Discussion

The JES is known as a mid-latitude "Miniature Ocean" in which multiscale oceanic dynamical processes (e.g., cross-basin

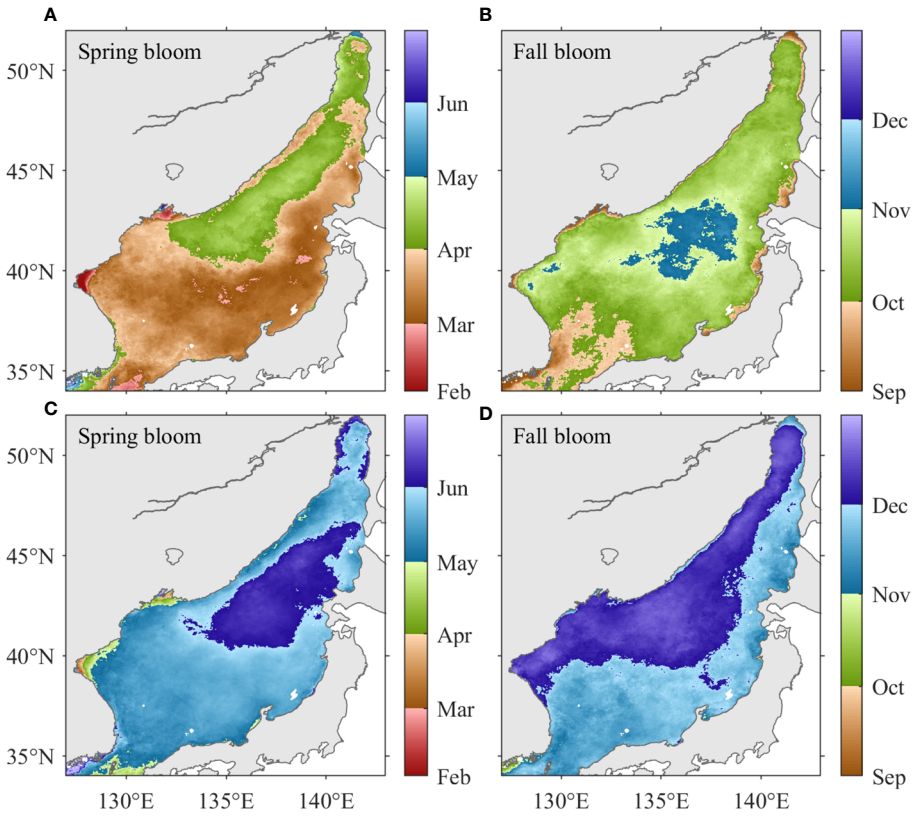


FIGURE 10
The climatological distributions of the initiation timing of **(A)** spring and **(B)** fall blooms; and the termination timing of **(C)** spring and **(D)** fall blooms.

warm and cold currents, upwelling, oceanic fronts, mesoscale eddies, and near-inertial oscillations) and sea ice occur. The marine ecosystems of the JES are influenced by these complicated processes. The phytoplankton concentrations can be evidenced by the SSC variability. Previous investigations have revealed bimodal phytoplankton concentrations blooms occurring in spring and fall. In this study, based on a newly released high-resolution satellite-derived SSC product, we revisit the spring and fall phytoplankton blooms and their driven factors during the raise and decline stages. In addition to the previously MLD-CRD theory, here we emphasize that different factors tend to play dominant role during the raise and decline stages of the spring and fall blooms. The increased PAR, weakened winds and sea ice melting are dominant for the spring bloom until the nutrients are exhausted and with no supplementary because of enhanced stratification, and thus terminates the spring bloom. The intensified wind and oceanic dynamical processes lead to destratification, which then triggers the fall bloom by entraining nutrient-rich water to the upper layer. The fall bloom is terminated by the rapidly declining of PAR, which acts as a limiting factor for phytoplankton growth when it is reduced to a certain extent.

It is interesting that the interannual JES SSC are not statistically significant correlated with the ENSO. However, existing studies have suggested that the JES is indeed influenced by ENSO on interannual time scales (e.g., Wang et al., 2000; Wang and Chan, 2002; Son et al., 2016; He et al., 2017; Cheon, 2020). Furthermore, case studies suggest the El Niño events could induce JES SSC anomaly in terms of bloom timing (Yamada et al., 2004; Yoo and Kim, 2004). Hence, we conducted composite analyses by comparing the JES SSC anomaly and initiation timing anomaly in El Niño and La Niña years, respectively (Figure 14). A total of three El Niño events (2002–2003, 2009–2010 and 2015–2016) and six La Niña events (1998–1999, 1999–2000, 2007–2008, 2010–2011, 2011–2012 and 2017–2018) are considered for the composite analyses, with the weak events (the absolute Niño 3.4 index below 1.0°C) being excluded. As shown in Figures 14A–C, there are high/low SSC anomaly in El Niño/La Niña years, with differences above the 95% confidence level along the northwestern coast of the JES, coincide with the EOF pattern (see Figure 8A). The coincidence patterns between the composite and EOF analyses suggest the interannual variability of the JES SSC in spring should closely associate with the ENSO events. Meanwhile, earlier spring

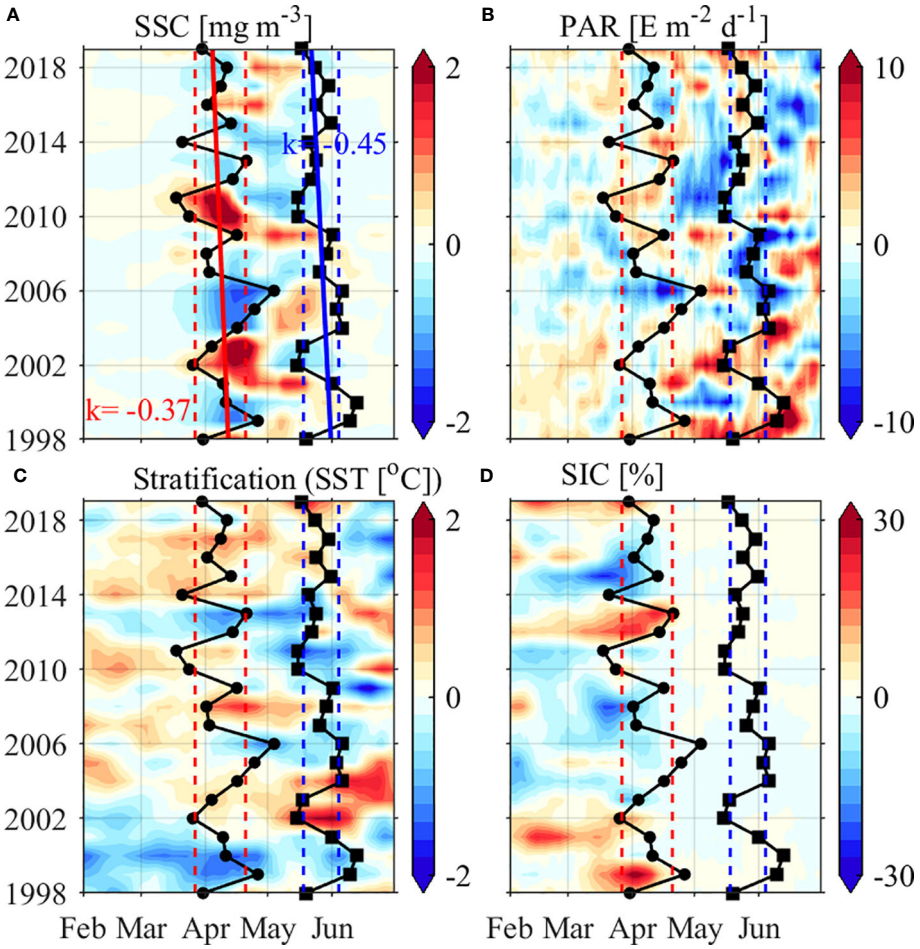


FIGURE 11
(A) SSC, **(B)** PAR, **(C)** stratification, and **(D)** SIC anomalies (shadings) averaged along the JES's northwestern coast (marked by the black box in Figure 8A) from 1998 to 2019. The spring bloom initiation and termination timing are represented by solid dots and square lines, with the solid red/blue lines indicating the linear trends, and the dashed red/blue lines indicating the one standard deviation beyond the climatological mean initiation/termination timing, respectively.

blooms are found in El Niño years, which is in agreement with Yamada et al. (2004). In comparison, the composite analyses of JES SSC in fall show different pattern from the EOF analysis, albeit there are significant differences of SSC anomalies in the northwestern of the JES (Figures 14G–I).

Figure 15 shows the time series of composed SSC and physical environmental factors anomalies along the northwestern coast of the JES in El Niño/La Niña years. There are high SSC anomalies in the following spring of El Niño peak (Figure 15A). The positive SSC anomalies of spring blooms in El Niño years can be explained by more sea ice in the previous winter, weaker wind speed during the raise stage and stronger stratification throughout the spring bloom period (Figures 15C, D, F), which lead to the spring blooms start slightly earlier. Similar composite analysis has been done for fall blooms, which does not show out of phase relationship for JES SSC anomalies between El Niño and La Niña years (Figures omitted). This can be explained by the fact that ENSO event-induced anomalies somehow result in contradictory SSC responses in the JES. For instance, higher SSCs and longer bloom durations are expected, as active typhoons benefit the vertical transport of nutrient-rich waters during El Niño years (Goh and Chan, 2010). However, at the same time, the warmer background states that occur during the summer-fall seasons in the JES act to inhibit SSC increases and thus cancel out the role of typhoons (Cheon, 2020). The insensitive response of JES SSC in fall is in agreement with previously investigation (Park et al., 2020).

The bloom magnitude anomaly is not statistically correlated with bloom duration anomaly in spring at interannual time scale. This lack of correlation can be attributed to different control factors affecting the durations and magnitudes of spring blooms. There is adequate light in the entire JES during the spring bloom

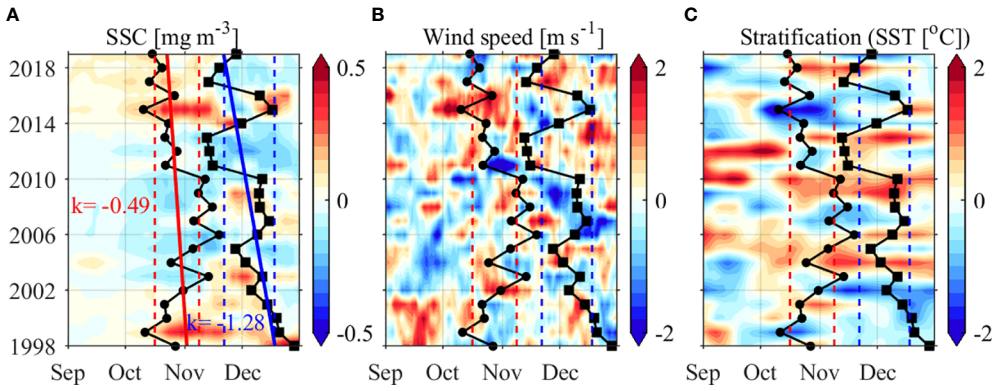


FIGURE 12
(A) SSC, **(B)** PAR, and **(C)** stratification anomalies (shadings) averaged in the deep Japan Basin (marked by the black box in Figure 8B) from 1998 to 2019. The fall bloom initiation/termination timing are represented by solid dots/square lines, with the solid red/blue lines indicating the linear trends, and the dashed red/blue lines indicating the one standard deviation beyond the climatological mean initiation/termination timing, respectively.

period, while strong stratification prevents the upward transport of deep, nutrient-rich waters to supply the upper layer. Therefore, the bloom duration is mainly controlled by the consumption rate of the accumulated nutrients in the upper layer (e.g., Bouman et al., 2011; Jo et al., 2014; Park et al., 2020). SSC is a phytoplankton biomass indicator that is related to the amount of accumulated nutrients (Maúre et al., 2017). Both the phytoplankton biomass and the bloom duration are positively correlated with the accumulated nutrients. However, more phytoplankton biomass leads to faster nutrient consumption. Thus, this relation tends to result in a negative correlation between the durations of and SSC anomalies associated with

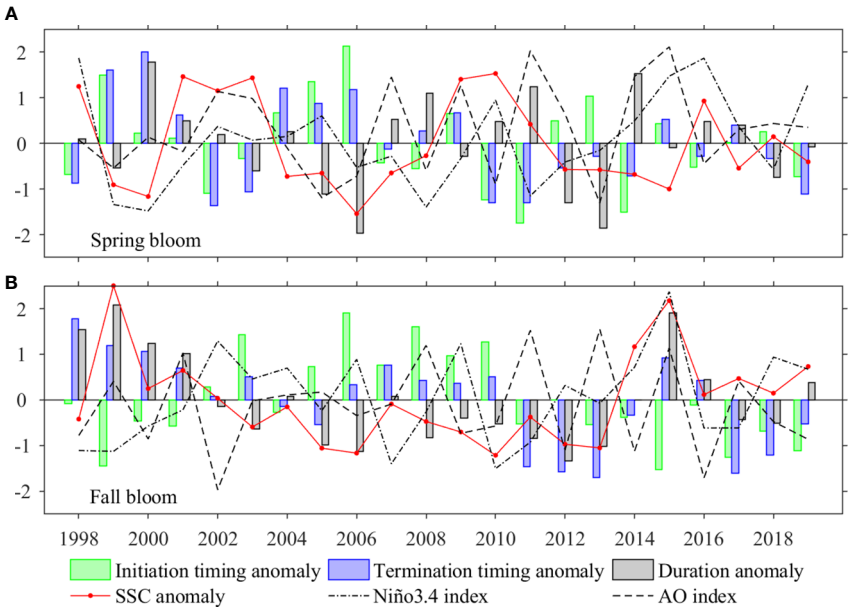


FIGURE 13
Time series of initiation timing anomalies (green bars), termination timing anomalies (blue bars), duration anomalies (gray bars), area averaged SSC anomalies (red lines), Niño 3.4 index (black dot-dash lines) and AO index (black dashed lines) for **(A)** spring, and **(B)** fall blooms. The averaged areas are marked by black box in Figures 8A, B for spring and fall blooms, respectively. The time series of all variables are normalized, i.e., divided by their corresponding standard deviations (STD).

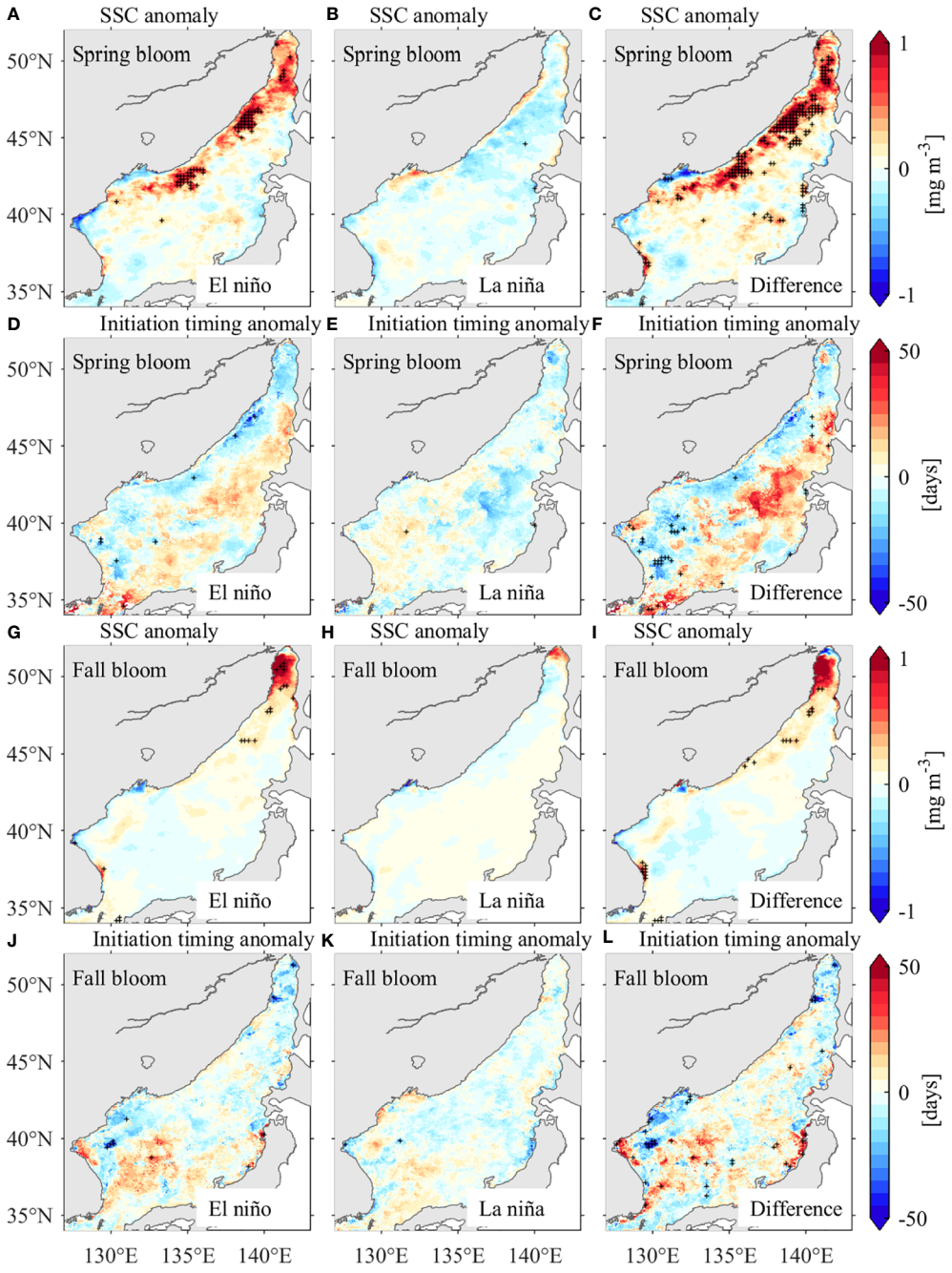


FIGURE 14
Spring bloom magnitude anomalies during El Niño events **(A)** and La Niña events **(B)**, and their difference **(C)**. **(D–F)** are same as **(A–C)**, but for the spring bloom initiation timing anomalies. **(G–L)** are same as **(A–F)**,but for fall blooms. Areas with plus sighs indicate that the difference is statistically significant at the 95% confidence level. El Niño events: 2002–2003, 2009–2010 and 2015–2016. La Niña events: 1998–1999, 1999–2000, 2007–2008, 2010–2011, 2011–2012 and 2017–2018.

spring blooms. As a result, no significant correlation is found between the spring bloom durations and SSC anomalies.

In comparison, the interannual variability of fall bloom magnitude is significantly correlated with the interannual variability its duration. Nutrients are limited during the fall bloom period. Therefore, the growth of phytoplankton biomass depends on the nutrients supplied by the vertical transport of deep waters through dynamic oceanic processes (e.g., Yamada et al., 2004; Andreev, 2014; Jo et al., 2014). Moreover, these nutrients are consumed immediately after being transported to

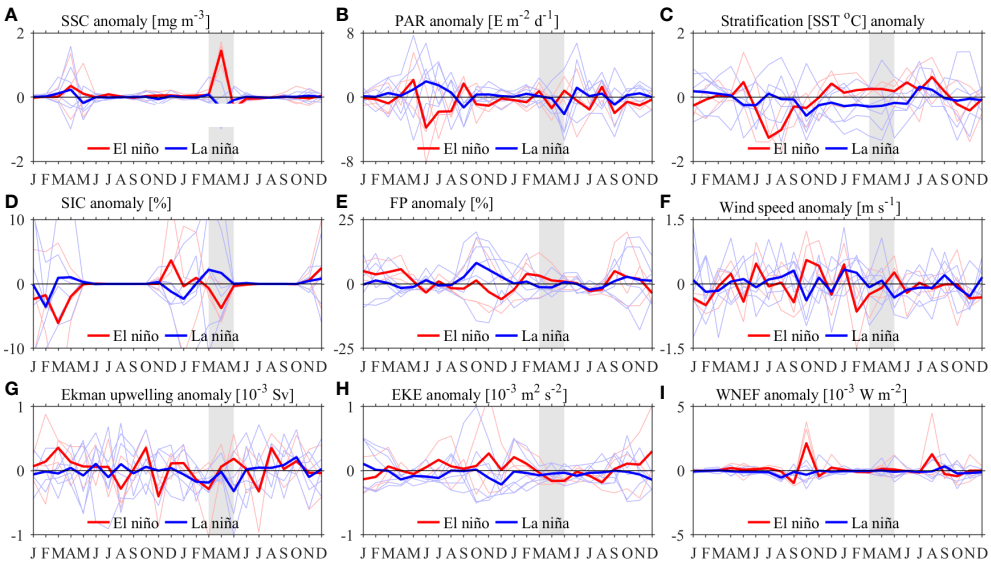


FIGURE 15
Time series of SSC anomalies and physical environmental factors anomalies averaged along the JES's northwestern coast (marked by the black box in Figure 8A) during El Niño events (red lines) and La Niña events (blue lines), while the thick lines represent the average of the corresponding time series: **(A)** SSC; **(B)** PAR; **(C)** Stratification; **(D)** SIC; **(E)** FP; **(F)** wind speed; **(G)** Ekman upwelling transport; **(H)** EKE and **(I)** WNEF. Gray shaded areas indicate spring bloom period following El Niño peak. El Niño events: 2002–2003, 2009–2010 and 2015–2016. La Niña events: 1998–1999, 1999–2000, 2007–2008, 2010–2011, 2011–2012 and 2017–2018.

the upper layer, and thus, the consumption rate of the nutrients can be ignored. Persistent and active oceanic dynamic processes tend to transport more nutrient-rich waters to the upper layer, favoring both increased SSCs and prolonged fall bloom durations.

Beyond of above discussion, some issues remain unclear, including but not limited to (1) obtaining a quantitative assessment of the driving factors that account for JES SSC variabilities; (2) the relation between JES SSCs and climate change; and (3) the JES SSC variabilities induced by changes in the phytoplankton community structure and the interactions between grazers and phytoplankton. Especially, the complex predator-prey interactions are crucial to the temporal changes in phytoplankton concentrations (Behrenfeld, 2010; Behrenfeld and Boss, 2017). Thus, these pending issues must be further investigated through interdisciplinary collaboration.

Summary

In this study, we investigate the spring and fall phytoplankton blooms and their interannual variability by employing high-resolution satellite remote sensing products. The new findings are summarized as follows.

(1) JES SSC is characterized by bimodal blooms in spring and fall. Different physical environmental factors are responsible for the JES SSC evolution during the raise and decline stages of the spring and fall blooms. Increased PAR, weakened winds and melting sea ice are the favorable factors for the initiation of spring blooms. Enhanced stratification, which inhibits the upward transport of nutrient-rich waters to the upper layer to compensate for the rapid consumption of nutrients, is the controlling factor inducing the termination of spring blooms. Destratification and active oceanic dynamic processes are favorable factors for fall blooms because they transport nutrient-rich waters to the upper layer. Declining PAR tends to serve as a limiting factor for phytoplankton growth when it is reduced to a certain extent, thereby resulting in the termination of fall blooms.

(2) The interannual variability in the JES SSC consists of spring and fall components, which occur along the JES's northwestern coast and in the deep JES basin, respectively. Stronger PAR and stratification favor positive SSC anomalies of spring bloom, whereas weaker stratification favors positive SSC anomalies of fall bloom. It is found that positive SSC anomalies along the northwestern coast of the JES tend to occur in the following spring of El Niño peak, as a result of more sea ice in the previous winter, weaker wind speed during the raise stage and stronger stratification throughout the spring bloom period. No significant relationship has been found between the fall bloom and ENSO.

(3) Spring blooms are initiated in the southern and southeastern JES in February–March and in the northwestern JES in April, with climatological mean initiation dates of 13 March ± 9 and 8 April ± 10 days, respectively. Fall blooms are

initiated in the Tsushima Basin and along the JES coasts from September to early October and in the central basin of the JES from late October to early November, with climatological mean initiation dates of 6 October ± 12 and 27 October ± 6 days, respectively. Spring blooms are terminated in the southwestern JES on 11 April ± 9 days and, subsequently, in the northeastern JES on 29 May ± 9 days. Fall blooms are generally terminated on 29 November ± 12. For spring blooms, the interannual variability in the bloom duration are not statistically correlated with the that in bloom magnitude because these characteristics are dominated by different factors, i.e., PAR and wind speed affect the initiation timing, while accumulated nutrients affect the bloom magnitude. For fall blooms, the interannual variabilities in the bloom duration and that in bloom magnitude are significantly correlated with each other with a correlation coefficient of 0.78, which are both dominated by oceanic dynamical processes. The initiation/termination timing of spring blooms has shifted earlier by 0.37/0.45 days annually along the JES's northwestern coast; the counterpart of fall blooms has shifted 0.49/1.28 days earlier annually in the deep Japan Basin.

Data availability statement

The original contributions presented in the study are included in the article/supplementary material. Further inquiries can be directed to the corresponding author.

Author contributions

DW: Data curation, Methodology, Visualization, Writing – original draft. GHF: Writing – review & editing, Supervision. SJ: Methodology, Writing – original draft. QX, GW, and YW: Writing – review & editing. ZW: Writing – review & editing, Funding acquisition. TX: Writing – review & editing, Resources, Funding acquisition. All authors contributed to the article and approved the submitted version.

Funding

This study is jointly supported by the National Key Research and Development Program of China (Grant No. 2020YFA0608800), and the National Natural Science Foundation of China (Grant No. 41821004). This work got the data service support from the Marine Environment Data Service System which supported by the National Key Research and Development Program of China (2019YFC1408405).

Conflict of interest

The authors declare that the research was conducted in the absence of any commercial or financial relationships that could be construed as a potential conflict of interest.

Publisher's note

All claims expressed in this article are solely those of the authors and do not necessarily represent those of their affiliated organizations, or those of the publisher, the editors and the reviewers. Any product that may be evaluated in this article, or claim that may be made by its manufacturer, is not guaranteed or endorsed by the publisher.

References

Alford, M. H. (2003). Improved global maps and 54-year history of wind-work on ocean inertial motions. *Geophys. Res. Lett.* 30 (8), 1424. doi: 10.1029/2002GL016614

Andreev, A. G. (2014). Interannual variations of sea water parameters and chlorophyll a concentration in the Japan Sea in autumn. *Russian Meteorol. Hydrol.* 39 (8), 542–549. doi: 10.3103/S1068373914080068

Banse, K. (1977). Determining the carbon-to-chlorophyll ratio of natural phytoplankton. *Mar. Biol.* 41, 199–212. doi: 10.1007/BF00394907

Behrenfeld, M. J. (2010). Abandoning sverdrup's critical depth hypothesis on phytoplankton blooms. *Ecology* 91 (4), 977–989. doi: 10.1890/09-1207.1

Behrenfeld, M. J., and Boss, E. S. (2017). Student's tutorial on bloom hypotheses in the context of phytoplankton annual cycles. *Global Change Biol.* 24 (1), 55–77. doi: 10.1111/gcb.13858

Bouman, H. A., Ulloa, O., Barlow, R., Li, W. K., Platt, T., Zwirglmaier, K., et al. (2011). Water-column stratification governs the community structure of subtropical marine picophytoplankton. *Environ. Microbiol. Rep.* 3 (4), 473–482. doi: 10.1111/j.1758-2229.2011.00241.x

Boyer, T. P., Baranova, O. K., Coleman, C., Garcia, H. E., Grodsky, A., Locarnini, R. A., et al. (2018). *World ocean database 2018*. Ed. A. V. Mishonov, 87, NOAA Atlas NESDIS. Available at: https://www.ncei.noaa.gov/sites/default/files/2020-04/wod_intro_0.pdf.

Brody, S. R., and Lozier, M. S. (2014). Changes in dominant mixing length scales as a driver of subpolar phytoplankton bloom initiation in the North Atlantic. *Geophysical Research Letters* 41, 3197–3203. doi: 10.1002/2014GL059707

Campbell, J. W. (1995). The lognormal distribution as a model for bio-optical variability in the sea. *J. Geophys. Res.* 100 (C7), 13237–13254. doi: 10.1029/95JC00458

Castelao, R. M., and Wang, Y. (2014). Wind-driven variability in sea surface temperature front distribution in the California current system. *J. Geophys. Res. Oceans* 119 (3), 1861–1875. doi: 10.1002/2013JC009531

Cheon, W. G. (2020). The Summer/Fall variability of the southern East/Japan Sea in the ENSO period. *Ocean Sci. J.* 55, 341–352. doi: 10.1007/s12601-020-0027-5

Chiswell, S. M., Bradford-Grieve, J., Hadfield, M. G., and Kennan, S. C. (2013). Climatology of surface chlorophyll a, autumn-winter and spring blooms in the southwest pacific ocean. *J. Geophys. Res. Oceans* 118, 1003–1018. doi: 10.1002/jgrc.20088

Comiso, J. C. (2017). *Bootstrap Sea Ice Concentrations from Nimbus-7 SMMR and DMSP SSM/ISSMIS, Version 3 Boulder*. Colorado USA: NASA National Snow and Ice Data Center Distributed Active Archive Center. doi: 10.5067/7Q8HCCWS4I0R

Dandonneau, Y. (1992). Surface chlorophyll concentration in the tropical pacific ocean: an analysis of data collected by merchant ships from 1978 to 1989. *J. Geophys. Res.* 97 (C3), 3581–3591. doi: 10.1029/91JC02848

Ducet, N., Le, Traon, P. Y., and Reverdin, G. (2000). Global high-resolution mapping of ocean circulation from TOPEX/Poseidon and ERS-1 and-2. *J. Geophys. Res. Oceans* 105 (C8), 19477–19498. doi: 10.1029/2000JC900063

Garcia, H. E., Boyer, T. P., Baranova, O. K., Locarnini, R. A., Mishonov, A. V., Grodsky, A., et al. (2019) *World ocean atlas 2018: Product documentation*. Ed. A. Mishonov. Available at: https://www.ncei.noaa.gov/sites/default/files/2022-06/woa18documentation.pdf.

Garnesson, P., Mangin, A., D'Andon, O. F., Demaria, J., and Bretagnon, M. (2019). The CMEMS GlobColour chlorophyll a product based on satellite observation: multi-sensor merging and flagging strategies. *Ocean Sci.* 15, 819–830. doi: 10.5194/os-15-819-2019

Goh, A. Z., and Chan, J. C. L. (2010). Variations and prediction of the annual number of tropical cyclones affecting Korea and Japan. *International Journal of Climatology* 32 (2), 178–189. doi: 10.1002/joc.2258

Good, S., Fiedler, E., Mao, C., Martin, M. J., Maycock, A., Reid, R., et al. (2020). The current configuration of the OSTIA system for operational production of foundation Sea surface temperature and ice concentration analyses. *Remote Sens.* 12, 720. doi: 10.3390/rs12040720

Greene, C. A., Thirumalai, K., Kearney, K. A., Delgado, J. M., Schwanghart, W., Wolfenbarger, N. S., et al. (2019). The climate data toolbox for MATLAB. *Geochemistry, Geophysics, Geosystems* 20, 3774–3781. doi: 10.1029/2019GC008392

Hannachi, A., Jolliffe, I. T., and Stephenson, D. B. (2007). Empirical orthogonal functions and related techniques in atmospheric science: A review. *Int. J. Climatol.* 27 (9), 1119–1152. doi: 10.1002/joc.1499

Hays, G., Richardson, A., and Robinson, C. (2005). Climate change and marine plankton. *Trends Ecol. Evol.* 20 (6), 337–344. doi: 10.1016/j.tree.2005.03.004

He, S., Gao, Y., Li, F., Wang, H., and He, Y. (2017). Impact of Arctic oscillation on the East Asian climate: A review. *Earth-Sci. Rev.* 164, 48–62. doi: 10.1016/j.earscirev.2016.10.014

Hersbach, H., and Dee, D. (2016). ERA5 reanalysis is in production. *ECMWF Newslett.* 147, 7.

Ichiye, T. (1984). Some problems of circulation and hydrography of the Japan Sea and the tsushima current. *Elsevier Oceanogr. Ser.* 39, 15–54. doi: 10.1016/S0422-9894(08)70289-7

Ishizaka, J., and Yamada, K. (2019). "Phytoplankton and primary production in the Japan Sea," in *Remote sensing of the Asian seas*. Eds. V. Barale and M. Gade (Cham: Springer), 177–189. doi: 10.1007/978-3-319-94067-0_9

Ivanova, E. V., and Ivanov, V. V. (2012). The amur river runoff formation in the amur liman. *Russian Meteorol. Hydrol.* 37, 631–639. doi: 10.3103/S1068373912090075

Iwasaki, S. (2020). Daily variation of chlorophyll-A concentration increased by typhoon activity. *Remote Sensing* 12 (8), 1259. doi: 10.3390/rs12081259

Ji, C., Zhang, Y., Cheng, Q., and Tsou, J. Y. (2021). Investigating ocean surface responses to typhoons using reconstructed satellite data. *Int. J. Appl. Earth Obs. Geoinfo.* 103, 102474. doi: 10.1016/j.jag.2021.102474

Jolliffe, I. T., and Cadima, J. (2016). Principal component analysis: a review and recent developments. *Philos. Trans. R. Soc. A* 374, 20150202. doi: 10.1098/rsta.2015.0202

Jo, C. O., Park, S., Kim, Y. H., Park, K., Park, J. J., Park, M., et al. (2014). Spatial distribution of seasonality of SeaWiFS chlorophyll-a concentrations in the East/Japan Sea. *J. Mar. Syst.* 139, 288–298. doi: 10.1016/j.jmarsys.2014.07.004

Kim, K., Chang, K., Kang, D., Kim, Y. H., and Lee, J. (2008). Review of recent findings on the water masses and circulation in the East Sea(Sea of Japan). *J. Oceanogr.* 64, 721–735. doi: 10.1007/s10872-008-0061-x

Kim, S., Saitoh, S., Ishizaka, J., Isoda, Y., and Kishino, M. (2000). Temporal and spatial variability of phytoplankton pigment concentrations in the Japan Sea derived from CZCS images. *J. Oceanogr.* 56, 527–538. doi: 10.1023/A:1011148910779

Kim, H., Yoo, S., and Oh, I. S. (2007). Relationship between phytoplankton bloom and wind stress in the sub-polar frontal area of the Japan/East Sea. *J. Mar. Syst.* 67, 205–216. doi: 10.1016/j.jmarsys.2006.05.016

Kodama, T., Wagawa, T., Ohshimo, S., Morimoto, H., Iguchi, N., Fukudome, K., et al. (2018). Improvement in recruitment of Japanese sardine with delays of the spring phytoplankton bloom in the Sea of Japan. *Fish. Oceanogr.* 27, 289–301. doi: 10.1111/fog.12252

Lee, J., Kang, D., Kim, I., Rho, T., Lee, T., Kang, C., et al. (2009). Spatial and temporal variability in the pelagic ecosystem of the East Sea (Sea of japan): A review. *J. Mar. Syst.* 78 (2), 288–300. doi: 10.1016/j.jmarsys.2009.02.013

Lee, D. K., and Niiler, P. (2010). Eddies in the southwestern East/Japan Sea. *Deep-Sea Res. I* 57 (10), 1233–1242. doi: 10.1016/j.dsr.2010.06.002

Lee, S., Yoo, S., and Son, Y. B. (2015). Variability of chlorophyll-a bloom timing associated with physical forcing in the East Sea/Sea of Japan, (1998–2014). 167.

Legaard, K. R., and Thomas, A. C. (2006). Spatial patterns in seasonal and interannual variability of chlorophyll and sea surface temperature in the California current. *J. Geophys. Res.* 111, C06032. doi: 10.1029/2005JC003282

Liu, Y., Tang, D., and Evgeny, M. (2019). Chlorophyll concentration response to the typhoon wind-pump induced upper ocean processes considering air-Sea heat exchange. *Remote Sens.* 11, 1825. doi: 10.3390/rs11151825

Liu, X., and Wang, M. (2022). Global daily gap-free ocean color products from multi-satellite measurements. *Int. J. Appl. Earth Obs. Geoinfo.* 108, 102714. doi: 10.1016/j.jag.2022.102714

Lorenz, E. N. (1956). *Empirical orthogonal functions and statistical weather prediction, scientific report, 1, statistical forecasting project* (MIT, Cambridge: Department of Meteorology).

Mahadevan, A., D'Asaro, E., Lee, C., and Perry, M. (2012). Eddy-driven stratification initiates north Atlantic spring phytoplankton blooms. *Science* 337, 54–58. doi: 10.1126/science.1218740

Maritorena, S. ,. O., D'Andon, H. F., Mangin, A., and Siegel, D. A. (2010). Merged satellite ocean color data products using a bio-optical model: characteristics, benefits and issues. *Remote Sens. Environ.* 114, 1791–1804. doi: 10.1016/j.rse.2010.04.002

Martin, S., and Kawase, M. (1998). The southern flux of sea ice in the tatarskiy strait, Japan Sea and the generation of the liman current. *J. Mar. Res.* 56, 141–155. doi: 10.1357/002224098321836145

Maúre, E. R., Ishizka, J., Sukigara, C., Mino, Y., Aiki, H., Matsuno, T., et al. (2017). Mesoscale eddies control the timing of spring phytoplankton blooms: A case study in the Japan Sea. *Geophys. Res. Lett.* 44, 11,115–11,124. doi: 10.1002/2017GL074359

Minobe, S., Sako, A., and Nakamura, M. (2004). Interannual to interdecadal variability in the Japan Sea based on a new gridded upper water temperature dataset. *J. Phys. Oceanogr.* 34, 2382–2397. doi: 10.1175/JPO2627.1

Nihashi, S., Ohshima, K. I., and Saitoh, S. (2017). Sea-Ice production in the northern Japan Sea. *Deep-Sea Res. Part I* 127, 65–76. doi: 10.1016/j.dsr.2017.08.003

Ok, J. H., Jeong, H. J., You, J. H., Kang, H. C., Park, S. A., Lim, A. S., et al. (2021). Phytoplankton bloom dynamics in incubated natural seawater: Predicting bloom magnitude and timing. *Front. Mar. Sci.* 8. doi: 10.3389/fmars.2021.681252

Park, K., Kang, C., Kim, K., and Park, J. (2014). Role of sea ice on satellite-observed chlorophyll-a concentration variations during spring bloom in the East/Japan sea. *Deep-Sea Res. I* 83, 34–44. doi: 10.1016/j.dsr.2013.09.002

Park, K., Kim, K., Comillon, P. C., and Chung, J. Y. (2006). Relationship between satellite-observed cold water along the primorye coast and sea ice in the East Sea (the Sea of Japan). *Geophys. Res. Lett.* 33, L10602. doi: 10.1029/2005GL025611

Park, K., Park, J., and Kang, C. (2022). Satellite-observed chlorophyll-a concentration variability in the East Sea (Japan sea): Seasonal cycle, long-term trend, and response to climate index. *Front. Mar. Sci.* 9. doi: 10.3389/fmars.2022.807570

Park, J., Park, K., Kang, C., and Kim, G. (2020). Satellite-observed chlorophyll-a concentration variability and its relation to physical environmental changes in the East Sea (Japan Sea) from 2003 to 2015. *Estuaries Coasts* 43, 630–645. doi: 10.1007/s12237-019-00671-6

Park, K., Ullman, D. S., Kim, K., Chung, J. Y., and Kim, K. (2007). Spatial and temporal variability of satellite-observed subpolar front in the East/Japan Sea. *Deep Sea Res. Part I: Oceanogr. Res. Pap.* 54 (4), 453–470. doi: 10.1016/j.dsr.2006.12.010

Pollard, R. T., and Millard, R. C. (1970). Comparison between observed and simulated wind-generated inertial oscillations. *Deep Sea Res. Oceanogr. Abstr.* 17 (4), 813–821. doi: 10.1016/0011-7471(70)90043-4

Price, J. F. (1981). Upper ocean response to a hurricane. *J. Phys. Oceanogr.* 11, 153–175. doi: 10.1175/1520-0485(1981)011<0153:UORTAH>2.0.CO;2

Shlens, J. (2014). A tutorial on principal component analysis. doi: 10.48550/arXiv.1404.1100

Son, H., Park, J., and Kug, J. (2016). Precipitation variability in September over the Korean peninsula during ENSO developing phase. *Climate Dyn.* 46, 3419–3430. doi: 10.1007/s00382-015-2776-x

Son, S., Platt, T., Bouman, H., Lee, D., and Sathyendranath, S. (2006). Satellite observation of chlorophyll and nutrients increase induced by typhoon megi in the Japan/East Sea. *Geophys. Res. Lett.* 33, L05607. doi: 10.1029/2005GL025065

Sverdrup, H. U. (1953). On conditions for the vernal blooming of phytoplankton. *ICES J. Mar. Sci.* 18 (3), 287–295. doi: 10.1093/icesjms/18.3.287

Taboada, F. G., Barton, A. D., Stock, C. A., Dunne, J., and John, J. G. (2019). Seasonal to interannual predictability of oceanic net primary production inferred from satellite observations. *Prog. Oceanogr.* 170, 28–39. doi: 10.1016/j.pocean.2018.10.010

Taylor, J., and Ferrari, R. (2011). Shutdown of turbulent convection as a new criterion for the onset of spring phytoplankton blooms. *Limnol. Oceanogr.* 56 (6), 2293–2307. doi: 10.4319/lo.2011.56.6.2293

Trombetta, T., Vidussl, F., Mas, S., Parin, D., Simier, M., and Mostajir, B. (2019). Water temperature drives phytoplankton blooms in coastal waters. *PloS One* 14 (4), e0214933. doi: 10.1371/journal.pone.0214933

Trouet, V., and Van Oldenborgh, G. J. (2013). KNMI climate explorer: A web-based research tool for high-resolution paleoclimatology. *Tree-Ring Res.* 69, 3–13. doi: 10.3959/1536-1098-69.1.3

Trusenkova, O. O. (2014). Variability of eddy kinetic energy in the Sea of Japan from satellite altimetry data. *Oceanology* 54 (1), 8–16. doi: 10.1134/S0001437014010111

Wang, B., and Chan, J. C. L. (2002). How strong ENSO events affect tropical storm activity over the Western north pacific. *J. Climate* 15, 1643–1658. doi: 10.1175/1520-0442(2002)015<1643:HSEEAT>2.0.CO;2

Wang, Y., Ma, W., Zhou, F., and Chai, F. (2021). Frontal variability and its impact on chlorophyll in the Arabian Sea. *J. Mar. Syst.* 218, 103545. doi: 10.1016/j.jmarsys.2021.103545

Wang, B., Wu, R., and Fu, X. (2000). Pacific-east Asian teleconnection: How does ENSO affect east Asian climate? *J. Climate* 13 (9), 1517–1536. doi: 10.1175/1520-0442(2000)013<1517:PEATHD>2.0.CO;2

Xi, J., Wang, Y., Feng, Z., Liu, Y., and Guo, X. (2022). Variability and intensity of the Sea surface temperature front associated with the kuroshio extension. *Front. Mar. Sci.* 9. doi: 10.3389/fmars.2022.836469

Xu, T., Wei, Z., Li, S., Susanto, R. D., Radiarta, N., Yuan, C., et al. (2021). Satellite-observed multi-scale variability of Sea surface chlorophyll-a concentration along the south coast of the Sumatra-Java islands. *Remote Sens.* 13, 2817. doi: 10.3390/rs13142817

Yabe, I., Kawaguchi, Y., Wagawa, T., and Fujio, S. (2021). Anatomical study of tsushima warm current system: Determination of principal pathways and its variation. *Prog. Oceanogr.* 194, 102590. doi: 10.1016/j.pocean.2021.102590

Yamada, K., Ishizaka, J., Yoo, S., Kim, H., and Chiba, S. (2004). Seasonal and interannual variability of sea surface chlorophyll a concentration in the Japan/East Sea (JES). *Prog. Oceanogr.* 61, 193–211. doi: 10.1016/j.pocean.2004.06.001

Yoo, S., and Kim, H. (2004). Suppression and enhancement of the spring bloom in the southwestern East Sea/Japan Sea. *Deep-Sea Res. II* 51, 1093–1111. doi: 10.1016/j.dsr2.2003.10.008

Yoon, J., and Kim, Y. (2009). Review on the seasonal variation of the surface circulation in the Japan/East Sea. *J. Mar. Syst.* 78, 226–236. doi: 10.1016/j.jmarsys.2009.03.003

Zhao, N., Iwasaki, S., Isobe, A., Lien, R. C., and Wang, B. (2016). Intensification of the subpolar front in the Sea of Japan during winter cyclones. *J. Geophys. Res. Oceans* 121, 2253–2267. doi: 10.1002/2015JC011565

frontiers | Frontiers in Marine Science

TYPE Original Research
PUBLISHED 05 December 2022
DOI 10.3389/fmars.2022.1048557

Check for updates

OPEN ACCESS

EDITED BY
Lei Ren,
Sun Yat-sen University, China

REVIEWED BY
Mohammed Magdy Hamed,
Arab Academy for Science, Technology and Maritime Transport (AASTMT), Egypt
Yunwei Yan,
Hohai University, China
Zifeng Hu,
Sun Yat-sen University, China

*CORRESPONDENCE
Wenjin Sun
sunwenjin@nuist.edu.cn

SPECIALTY SECTION
This article was submitted to Ocean Observation, a section of the journal Frontiers in Marine Science

RECEIVED 19 September 2022
ACCEPTED 15 November 2022
PUBLISHED 05 December 2022

CITATION
Yang Y, Sun W, Yang J, Lim Kam Sian KTC, Ji J and Dong C (2022) Analysis and prediction of marine heatwaves in the Western North Pacific and Chinese coastal region. *Front. Mar. Sci.* 9:1048557. doi: 10.3389/fmars.2022.1048557

COPYRIGHT
© 2022 Yang, Sun, Yang, Lim Kam Sian, Ji and Dong. This is an open-access article distributed under the terms of the Creative Commons Attribution License (CC BY). The use, distribution or reproduction in other forums is permitted, provided the original author(s) and the copyright owner(s) are credited and that the original publication in this journal is cited, in accordance with accepted academic practice. No use, distribution or reproduction is permitted which does not comply with these terms.

Analysis and prediction of marine heatwaves in the Western North Pacific and Chinese coastal region

Yifei Yang[1], Wenjin Sun[1,2,3]*, Jingsong Yang[2,3], Kenny T. C. Lim Kam Sian[4], Jinlin Ji[1,3] and Changming Dong[1,3]

[1]School of Marine Sciences, Nanjing University of Information Science and Technology, Nanjing, China, [2]State Key Laboratory of Satellite Ocean Environment Dynamics, Second Institute of Oceanography, Ministry of Natural Resources, Hangzhou, China, [3]Southern Marine Science and Engineering Guangdong Laboratory (Zhuhai), Zhuhai, China, [4]College of Atmospheric Science and Remote Sensing, Wuxi University, Wuxi, China

Over the past decade, marine heatwaves (MHWs) research has been conducted in almost all of the world's oceans, and their catastrophic effects on the marine environment have gradually been recognized. Using the second version of the Optimal Interpolated Sea Surface Temperature analysis data (OISSTV2) from 1982 to 2014, this study analyzes six MHWs characteristics in the Western North Pacific and Chinese Coastal region (WNPCC, 100°E ~ 180°E, 0° ~ 65°N). MHWs occur in most WNPCC areas, with an average frequency, duration, days, cumulative intensity, maximum intensity, and mean intensity of 1.95 ± 0.21 times/year, 11.38 ± 1.97 days, 22.06 ± 3.84 days, 18.06 ± 7.67 °Cdays, 1.84 ± 0.50°C, and 1.49 ± 0.42 °C, respectively, in the historical period (1982 ~ 2014). Comparing the historical simulation results of 19 models of the Coupled Model Intercomparison Project Phase 6 (CMIP6) with the OISSTV2 observations, five best-performing models (GFDL-CM4, GFDL-ESM4, AWI-CM-1-1-MR, EC-Earth3-Veg, and EC-Earth3) are selected for MHWs projection (2015 ~ 2100). The MHWs characteristics projections from these five models are analyzed in detail under the Shared Socio-economic Pathway (SSP) 1-2.6, 2-4.5 and 5-8.5 scenarios. The projected MHWs characteristics under SSP5-8.5 are more considerable than those under SSP1-2.6 and 2-4.5, except for the MHWs frequency. The MHWs cumulative intensity is 96.36 ± 56.30, 175.44 ± 92.62, and 385.22 ± 168.00 °Cdays under SSP1-2.6, 2-4.5 and 5-8.5 scenarios, respectively. This suggests that different emission scenarios have a crucial impact on MHW variations. Each MHWs characteristic has an obvious increasing trend except for the annual occurrences. The increase rate of MHWs cumulative intensity for these three scenarios is 1.02 ± 0.83, 3.83 ± 1.43, and 6.70 ± 2.61 °Cdays/year, respectively. The MHWs occurrence area in summer is slightly smaller than in winter, but the MHWs average intensity is stronger in summer than in winter.

KEYWORDS

marine heatwaves, characteristic analysis, model evaluation, future estimates, CMIP6

1 Introduction

The global ocean has significantly warmed in the past century, profoundly impacting marine ecosystems. More than 90% of heat increase due to global warming is absorbed by the ocean's upper layer (Pörtner et al., 2019). The long-term continuous warming of the ocean resulted in an increase in the frequency of discrete extreme regional oceanic warming events (i.e., marine heatwaves, MHWs). MHWs occur in almost every area of the world's oceans (Scannell et al., 2016; Han et al., 2022; Yao et al., 2022), such as in the Pacific Ocean (Capotondi et al., 2022; Holbrook et al., 2022), the tropical Indian Ocean (Zhang et al., 2021), the Arctic (Huang et al., 2021), the Mediterranean Sea (Black et al., 2004; Olita et al., 2007), the South China Sea (Yao and Wang, 2021; Liu et al., 2022; Wang et al., 2022a; Wang et al., 2022b), the Japan/East Sea (Wang et al., 2022c), the Mozambique Channel (Mawren et al., 2021), the Oyashio Region (Miyama et al., 2021), and China's adjacent offshore waters (Gao et al., 2020; Yao et al., 2020).

Based on the OISSTV2 data, the frequency and duration of global MHWs have increased by 34 and 17%, respectively, in the past century (Oliver et al., 2018). From 1982 to 2016, the average MHW days increased by 30 days/year. It is important to note that the changing trend correlates well with the rise in the average sea surface temperature (SST). This correction indicates that MHWs will occur more frequently under continuous global warming. The multi-model ensemble average results based on the Coupled Model Intercomparison Project Phase 5/6 (CMIP5/6) show that most of the world's oceans will reach the annual sustainable MHW state by the end of this century (Oliver et al., 2019).

MHW events are expected to increase in frequency and intensity, pushing marine organisms and ecosystems to the limit of their resilience or even higher, which may lead to irreversible damage (Frölicher et al., 2018; Garrabou et al., 2022). MHWs can damage marine biodiversity (Bond et al., 2015; Hughes et al., 2017; Jones et al., 2018; Straub et al., 2019; Thomsen et al., 2019; Morrison et al., 2020; Yao and Wang, 2022), the world fisheries, and aquaculture industries (Mills et al., 2013; Cavole et al., 2016; Chandrapavan et al., 2019) by leading to large-scale coral bleaching and reduced kelp forests and seagrass meadows (Holbrook et al., 2020; Feng et al., 2022). According to field surveys and satellite images, MHWs in 2010/11 damaged 36% of the seagrass meadow in Shark Bay (Arias-Ortiz et al., 2018). Wernberg et al. (2013) pointed out that extreme MHWs have forced coastal forests to shrink by 100 km, and temperate species have been replaced by seaweeds, invertebrates, corals, and fishes unique to subtropical and tropical waters. This propagation of the whole community has fundamentally changed the critical ecological processes, resulting in irreversible changes in coastal forests. When seawater temperature during MHWs exceeds the thermal tolerance limit of marine species, it results in the large-scale death of fish and invertebrates, especially those species distributed in shallow water or low-tide areas.

MHWs also promote the development of harmful algal blooms (HABs), negatively impacting food security, tourism, the local economy and human health. Large-scale HABs cause environmental problems such as fish death and environmental degradation due to high biomass. Consumption of HAB-contaminated fish by humans can lead to various diseases. The adverse effects of MHWs on marine ecosystems are long-lasting. Caputi et al. (2019) found that after seven years, only some ecosystems in Western Australia showed promising recovery due to the impact of the extreme MHW in 2011. During this MHW event that affected 2,000 km of the Australian Midwest coast, the SST was 2 ~ 5°C higher than the climatological average temperature (Caputi et al., 2016).

The generation mechanism of MHWs is very complex, not only with local dependence but also related to large-scale atmospheric and oceanic background fields (e.g., Misra et al., 2021; Hu et al., 2021). Specific generation mechanisms include the followings.

1.1 Local oceanic current anomalies

An MHW with the longest duration (251 days) and highest intensity (2.9°C) on record occurred in the Tasman Sea in 2015/16. The anomalous heat concentration associated with the southward-flowing East Australian Current was the main reason for this MHW event (Oliver et al., 2017). Similarly, the weakening of cold advection in the South China Sea is considered the inducing factor of MHW in 2021 (Yao and Wang, 2021).

1.2 Compound effect of extreme La Niña events, oceanic current anomalies and air-sea heat flux anomalies

Pearce and Feng (2013) pointed out that the MHW along the western coast of Australia during the austral summer of 2010/11 was a combination of a near-record more significant La Niña event, a record strength Leeuwin Current, and an anomalously high air-sea heat flux into the ocean. This MHW event in February 2011 led to an anomalous SST peak in the coastal and offshore areas (more than 200 km) from Ningaloo (22°S) to Cape Leeuwin (34°S), which was 3°C higher than the long-term monthly average.

1.3 El Niño teleconnections

Combining observation results with climate model simulations, it is reported that the teleconnections between the

North Pacific and the weak 2014/15 El Niño induced the MHW event in the Northeast Pacific during the winters of 2013/14 and 2014/15 (Di Lorenzo and Mantua, 2016). The El Niño event also drives the MHWs in tropical Australia during 1997/98 and 2015/16 (Zhang et al., 2017; Benthuysen et al., 2018).

Besides, the weakening of the wind field (Garrabou et al., 2009), air-sea heat flux and heat advection anomaly (Xu et al., 2018), and ENSO events (Holbrook et al., 2019) could also induce MHWs. In conclusion, the MHWs generation mechanism is very complex, and its impact area and occurrence frequency are getting broader and higher.

Previous studies based on CMIP5 models indicate that the increase in MHWs intensity and days is expected to accelerate. However, the inadequacy of the CMIP5 and the regional dependence of MHWs require further study with improved numerical models. Hamed et al. (2022) pointed out that most climate variables simulated in CMIP6 are less biased than in CMIP5. Preliminary studies show that the WNPCC region is one of the regions most affected by MHWs (Li et al., 2019). Since 1970, the SST rise in this region has been higher than the global average in the same period. Under different projection scenarios, the WNPCC area may become one of the areas with the highest global ocean temperature rise. During the stagnation period of global warming, the frequency and intensity of MHW in the WNPCC area did not decrease, but it was more frequent and lasted longer than in other regions. Oliver et al. (2018) pointed out that the frequency and average intensity of MHW in the Northwest Pacific from 2000 to 2016 increased by 1 ~ 4 times/year and 1 ~ 2.5°C, respectively, compared with 1982 ~ 1998.

In summary, MHWs impact is getting increasingly severe, and the resulting loss is getting larger. For proactive marine management, it is essential to understand how MHWs will change (Yao et al., 2022). Operators in the coastal and marine sectors can use MHW events projections for better planning. These sectors include subsistence and commercial fishing, diving, aquaculture, fisheries management, tourism, conservation management, and policy development. It is urgent to discuss and analyze MHWs in the WNPCC area.

The rest of this study is organized as follows. Section 2 introduces the data employed in this study, the definition of MHW, MHWs characteristics, and seven parameters used in model evaluation. Section 3 presents the basic characteristics of MHWs in the WNPCC area during the historical period (1982 ~ 2014). The projection characteristics (2015 ~ 2100) under SSP1-2.6, 2-4.5 and 5-8.5 are illustrated in Section 4. In Section 5, we discuss the seasonal variation of MHWs characteristics, the impact of different climate thresholds and the subsurface MHWs. The conclusions are given in Section 6.

2 Data and methods

2.1 OISSTV2

This study employs the Optimal Interpolated Sea Surface Temperature version 2 (OISSTV2) data to evaluate the ability of CMIP6 global climate models (GCMs) to capture MHWs in the historical period (1982 ~ 2014). It is the product of data synthesis and interpolation of multiple observation platforms (satellites, ships, buoys, and Argo profiles) into a regular global grid, with a spatial resolution of 0.25° by 0.25° and a daily time resolution. Many researchers have used this data to study MHWs or SST variation (Yan et al., 2020; Jacox et al., 2022; Noh et al., 2022; Zhang et al., 2022). For more details about this dataset, please refer to Reynolds et al. (2007).

2.2 CMIP6

CMIP6 is the latest global climate simulation that provides information for the sixth assessment report of the Intergovernmental Panel on Climate Change (O'Neill et al., 2016). This dataset has the most significant number of participation GCMs, a well-designed array of scientific experiments, and an enormous amount of simulation data during the 20 years of implementation of the plan (Eyring et al., 2016; Wei et al., 2021; Kajtar et al., 2022; Scafetta, 2022). The CMIP6 historical simulation experiment was completed at the end of 2014, and future scenarios were gradually added later. A new set of emission scenarios driven by different socio-economic models, the Shared Socioeconomic Pathways (SSP), developed in CMIP6, replaces the four Representative Concentration Pathways (RCP) in CMIP5 and dramatically improves the inadequacy of RCP scenarios. Climate prediction under different SSP scenarios reflects different carbon emission policies' climate impacts and socio-economic risks.

This study extracts MHW characteristics from CMIP6 data during the historical period in the WNPCC area and compares them with the results obtained from OISSTV2 data to evaluate the ability of 19 CMIP6 models (Table 1) to simulate MHWs. Top-performing models are then selected to analyze the projected changes in MHWs characteristics and trends. This study considers three emission scenarios for projection studies: SSP1-2.6, 2-4.5, and 5-8.5. They represent a low, medium, and high emission scenario, where solar radiation will increase by 2.6, 4.5, and 5.8 W/m^2 by the end of 21 century. To compare the difference in MHWs characteristics between the OISSTV2 and CMIP6 model data, all the data are interpolated to a 1° by 1° resolution grid. All analyses are conducted using the interpolated data.

TABLE 1 Basic information of 19 models from CMIP6.

	Model	Institution (Country or Region)	Spatial Resolution (km)	Oceanic Grid (lon×lat)
1	AWI-CM-1-1-MR	AWI(Germany)	25	unstructured grid
2	GFDL-CM4	NOAA-GFDL (America)	25	1440 x 1080
3	GFDL-ESM4	NOAA-GFDL (America)	50	720 x 576
4	MPI-ESM1-2-HR	MPI-M (Germany)	50	802 x 404
5	BCC-CSM2-MR	BCC (China)	100	360 x 232
6	CanESM5	CCCma (Canada)	100	360 x 291
7	CESM2-WACCM	NCAR (America)	100	384 x 320
8	CMCC-CM2-SR5	CCMC (Italy)	100	362 x 292
9	CMCC-ESM2	CCMC (Italy)	100	362 x 292
10	EC-Earth3	EC (Europe)	100	362 x 292
11	EC-Earth3-CC	EC (Europe)	100	362 x 292
12	EC-Earth3-Veg	EC (Europe)	100	362 x 292
13	EC-Earth3-Veg-LR	EC (Europe)	100	362 x 292
14	IPSL-CM6A-LR	IPSL (France)	100	362 x 332
15	MIROC6	MIROC (Japan)	100	360 x 256
16	MRI-ESM2-0	MRI (Japan)	100	360 x 180
17	NESM3	NUIST (China)	100	362 x 292
18	NorESM2-LM	NCC (Norway)	100	360 x 385
19	NorESM2-MM	NCC (Norway)	100	360 x 385

2.3 Definition of MHWs

This study follows the MHW identification method proposed by Hobday et al. (2016). An MHW event requires an SST above a certain threshold (green curve in Figure 1) for at least five consecutive days. This work adopts the 90th percentile of SST recorded in 33 years (1982 ~ 2014) as the threshold. It is calculated at each point of each day within an 11-day window centered on the calculation days of all years and then using a 31-day moving average on each Julian day. This method ensures that enough samples are used in the calculation. Thus, the obtained climate state and threshold can reflect the multi-year average and upper limit characteristics of the SST in the area and its seasonal change. If the maximum interval between consecutive events is less than or equal to two days, it is regarded as the same event (such as MHW 2 in Figure 1).

Figure 1 shows three MHW cases identified at an arbitrary point (159.125°E, 49.125°N) in the WNPCC area. The reddish shading indicates three MHWs, occurring on August 08, 2012 ~ August 14, 2012 (MHW 1), August 27, 2012 ~ October 20, 2012 (MHW 2), and October 26, 2012 ~ November 20, 2012 (MHW 3). The average intensities of these three MHWs are 2.95, 1.98, and 2.01°C, respectively (Please refer to subsection 2.4 for specific definitions). For more detailed information about these three MHWs, please refer to Table S1 in the supporting information. The climate state and threshold from the OISSTV2 data (1982 ~ 2014) are also selected as the benchmark to detect MHWs in the projection period (2015 ~ 2100).

2.4 Characteristics of MHWs

The following six MHWs characteristics are selected for analysis. 1) Number: the total annual number of MHWs occurring at an arbitrary point in the WNPCC area. 2) Duration: the period from the beginning to the end of an MHW event. 3) Days: the total duration of all MHWs occurring at an arbitrary point within a year. 4) Cumulative-Intensity (CumInt): the cumulative sum of the difference between the daily SST and the corresponding climatic temperature during one MHW event. 5) Max-Intensity (MaxInt): the maximum difference between the daily SST and the corresponding climatic temperature during one MHW event. 6) Mean-Intensity (MeanInt): the average difference between the daily SST and the corresponding climatic temperature during one MHW event.

2.5 Optimal selection method for CMIP6 models

To evaluate the simulation ability of the 19 CMIP6 models, we compare the MHWs characteristics simulated by these models from 1982 to 2014 with the OISSTV2 data. The algorithm flowchart used in this study is shown in Figure 2. Seven evaluation indexes are selected to rank the simulation performance of the GCMs, assuming the proportion of each evaluation index is the same. Each index is assigned a value between 60 and 100 points, considering the difference between

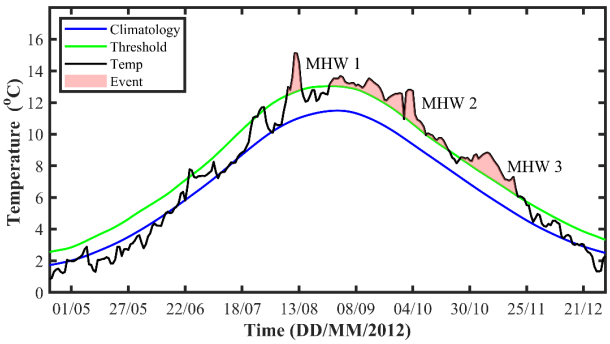


FIGURE 1
Identification of marine heatwaves at an arbitrary point (159.125°E, 49.125°N) in the WNPCC area between August 1 and December 21, 2012. The blue, green, and black curves represent the average climate temperature (1982 ~ 2014), the 90th percentile threshold value, and the point's daily sea surface temperature curves, respectively. The reddish shading indicates three marine heatwave events.

the GCMs and OISSTV2 data. The absolute deviation between the simulation parameters of each index (such as MHWs MeanInt) and the results from OISSTV2 is first calculated. The 19 models are then scored according to the calculated absolute deviation value using the following formula:

$$S_i = \frac{f_{\max} - f_i}{f_{\max} - f_{\min}} \times 40 + 60, \quad (1)$$

where S_i is the index score for the characteristic parameter simulation. f_i represents the absolute deviation value between model i and OISSTV2. f_{min} and f_{max} are the minimum and maximum values of the absolute deviation, respectively, representing the deviation of the best and worst simulation results. After conversion, the simulation effect of each index on each MHWs characteristic is given a score between 60 and 100. Finally, the scores are ranked after equal weight averaging,

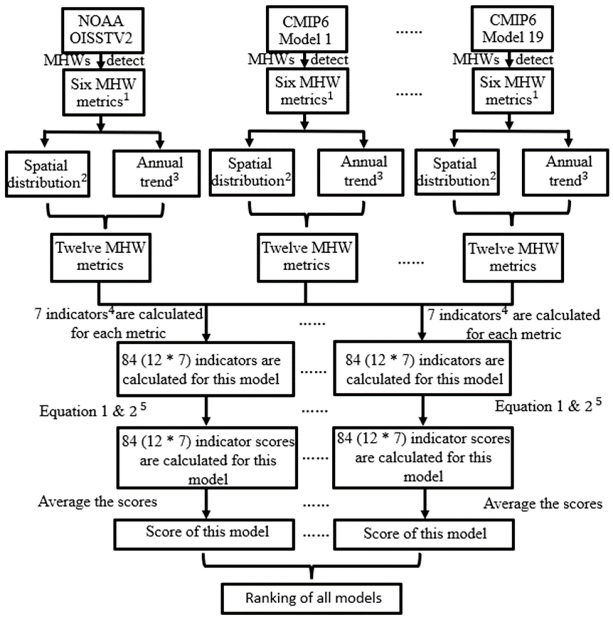


FIGURE 2
Flowchart summarizing the evaluation methods used in this study. [1]Six MHW metrics: Number, Duration, Days, CumInt, MaxInt and MeanInt. [2]Spatial distribution: spatial distribution of multi-year average. [3]Annual trend: spatially weighted average of annual average. [4]Seven indicators: Root Mean Square Error, Mean Absolute Percentage Error, Correct-Recognition Rate, Under-Recognition Rate, Over-Recognition Rate, Regression Coefficient and Taylor Scores. [5]Equation 1 & 2: Equation 1 for Taylor Scores and Correct-Recognition Rate, Equation 2 for the other five indicators. Equation 1: $Grade = \frac{x_i - x_{min}}{x_{max} - x_{min}} \times 40 + 60$, Equation 2: $Grade = \frac{x_{max} - x_i}{x_{max} - x_{min}} \times 40 + 60$.

and the top five models are selected for projection analysis of MHWs.

The seven correlation indicators are:

2.5.1 Root mean square error

$$RMSE = \sqrt{\frac{\sum_{k=1}^{N}(x_k - y_k)^2}{N}} \quad (2)$$

where x_k and y_k represent the MHWs characteristics (e.g., MeanInt) from OISSTV2 and CMIP6 model, respectively, at an arbitrary point, and N represents the total grid points in the WNPCC area. *RMSE* represents the degree of dispersion between the results from the model and OISSTV2.

2.5.2 Mean absolute percentage error

$$MAPE = \frac{1}{N}\sum_{k=1}^{N}\left|\frac{x_k - y_k}{x_k}\right| \times 100\,\% \quad (3)$$

The meaning of each symbol is the same as that in equation (2). *MAPE* represents the percentage of deviation between the model and OISSTV2.

2.5.3 Correct-recognition rate

$$CRR = \frac{m_a}{N} \times 100\,\% \quad (4)$$

CRR represents the ratio of grid points (m_a) in which both the CMIP6 models and OISSTV2 data detect MHWs to the total grid points (N) in the WNPCC area.

2.5.4 Under-recognition rate

$$URR = \frac{m_b}{N} \times 100\,\% \quad (5)$$

URR is the ratio of the grid points (m_b) where the OISSTV2 data recognize MHWs but not the CMIP6 model data to the total grid points (N) in the WNPCC area.

2.5.5 Over-recognition rate

$$ORR = \frac{m_c}{N} \times 100\,\% \quad (6)$$

ORR indicates the ratio of the grid points (m_c) where OISSTV2 data do not identify MHWs, but the CMIP6 model data incorrectly recognizes them as MHWs, to the total grid points (N) in the WNPCC area.

2.5.6 Regression coefficient (k)

$$y_k = kx_k + b, \quad (7)$$

where x_k and y_k represent MHWs characteristics identified by the CIMP6 and OISSTV2 data, respectively. The symbol b represents the intercept of the fitting line. Regression coefficient represents the slope of the regression curve obtained by performing linear regression on the MHWs parameters identified by the OISSTV2 and the CMIP6 data. The closer the coefficient to 1.0, the closer the simulated MHWs characteristic is to OISSTV2.

2.5.7 Taylor score

$$TS = \frac{4(1+R)^4}{\left(\frac{\sigma_m}{\sigma_0} + \frac{\sigma_0}{\sigma_m}\right)^2 (1+R_0)^4} \quad (8)$$

where R represents the correlation coefficient of MHW detection results between the CMIP6 and OISSTV2 data. R_0 is the maximum value of the correlation coefficient (taken as 1.0 in this study). σ_m and σ_0 represent the standard deviation of the MHWs characteristics' spatial distribution from CMIP6 and OISSTV2, respectively. The Taylor score varies from 0.0 to 1.0 (Taylor, 2001). The larger the value, the closer the spatial distribution of the CMIP6 results is to OISSTV2.

Each MHW characteristic has two quantities: the spatial distribution of the average intensity in the WNPCC region and the annual trend of the regional average. Therefore, the above seven evaluation indicators correspond to fourteen evaluation scores (annual-RMSE, annual-MAPE, annual-CRR, annual-URR, annual-ORR, annual-k, annual-TS, mean-RMSE, mean-MAPE, mean-CRR, mean-URR, mean-ORR, mean-k, and mean-TS). However, since the mean-ORR scores in the 19 models are all 100 points (that is, there is no over-recognition phenomenon), only thirteen indicators are valid. Figure 3 presents the evaluation index scores and ranking of each model. The five top-performing CMIP6 models are GFDL-CM4, GFDL-ESM4, AWI-CM-1-1-MR, EC-Earth3-Veg and EC-Earth3. These models are used for the MHWs projection in Section 4.

3 Historical characteristics of MHWs

3.1 Spatial distribution of MHWs characteristics

Figure 4 gives the spatial distribution of MHWs characteristics in the historical period (1982 ~ 2014) obtained from the OISSTV2 data. MHWs occur in most WNPCC areas, with an average number of 1.95 ± 0.21 times/year from 1982 to 2014 (Figure 4A). The number of MHWs is relatively low in the open ocean, especially in the southeast area of the WNPCC, while it is relatively high in the continental region. The region with the largest MHWs number is located at (122.125°E, 24.125° N), with 2.73 times/year.

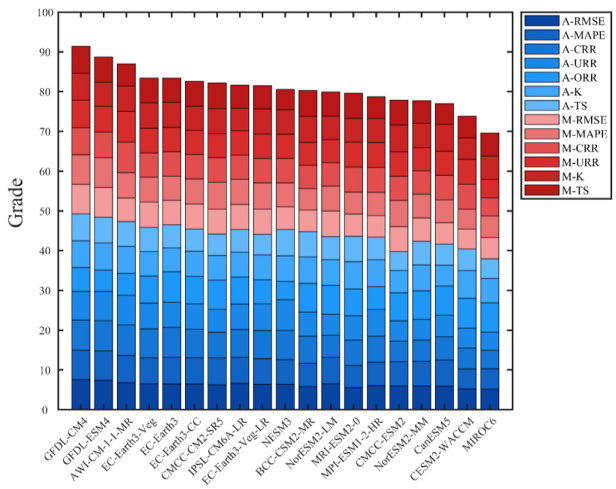


FIGURE 3
Evaluation scores for the 19 CMIP6 models. The thirteen color blocks from bottom to top correspond to thirteen weighted scoring indicators: annual-RMSE, annual-MAPE, annual-CRR, annual-URR, annual-ORR, annual-k, annual-TS, mean-RMSE, mean-MAPE, mean-CRR, mean-URR, mean-k, and mean-TS.

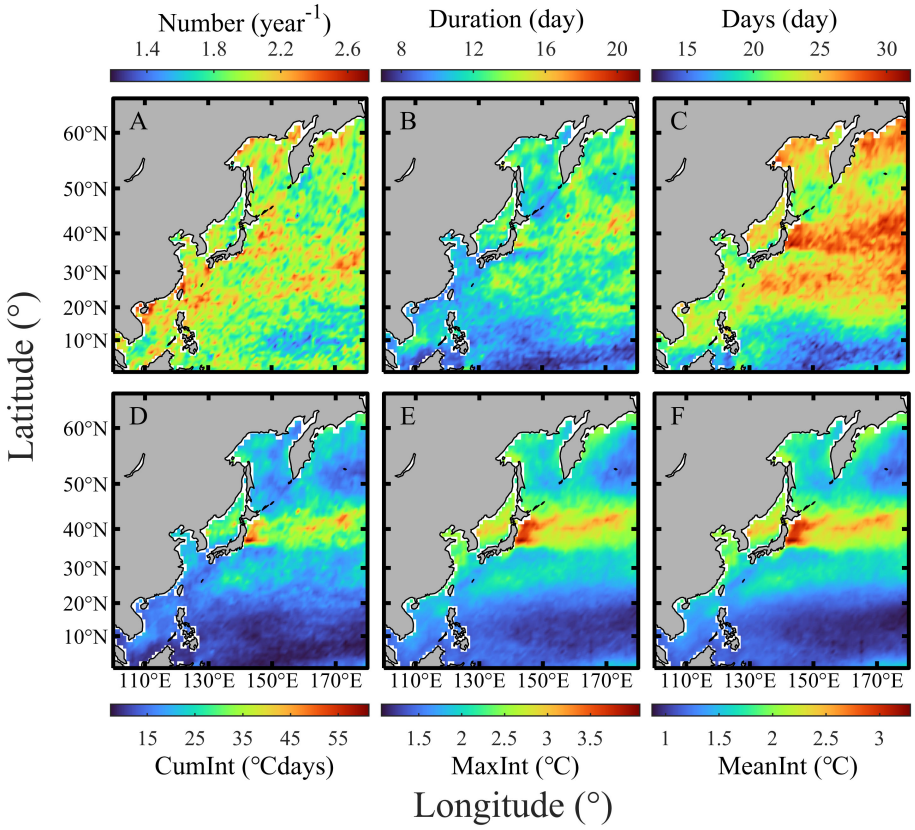


FIGURE 4
Spatial distribution of multi-year averages historical MHWs characteristics in the WNPCC area based on OISSTV2 data. Multi-year averages MHWs **(A)** Number (units: year^{-1}), **(B)** Duration (units: day), **(C)** Days (units: day), **(D)** CumInt (units: °C days), **(E)** MaxInt (units: °C), and **(F)** MeanInt (units: °C).

Figure 4B shows the multi-year average of MHWs duration from 1982 to 2014, with an average value of 11.38 ± 1.97 days. The maximum value is 21.26 days, which occurs at (158.125°E, 44.125°N). It should be noted that this maximum duration is the average annual result rather than the maximum value of each MHWs. The longest duration is 128 days (from November 8, 2010 to May 12, 2011), occurring at (172.125°E, 43.125°N). Unlike the distribution in Figure 4A, the multi-year average duration shows a more significant value in the open ocean than in the coastal area. That is, MHWs frequently occur in coastal areas but with relatively short duration.

Figure 4C gives the spatial distribution of the multi-year average MHWs days. It means the total durations of multiple MHWs in a year. The average value is 22.06 ± 3.84 days/year, and the maximum value is 31.79 days/year, which appears at (143.125°E, 37.125°N). Compared with Figure 4B, there is a more apparent meridional difference than in the MHWs duration. This difference is mainly because MHWs can occur several times in one year (Figure 4A). That is, Figure 4C is equivalent to the cumulative result of Figures 4A, B.

Figures 4D–F illustrate the multi-year average MHWs cumulative intensity, maximum intensity, and mean intensity in the historical period, with average values of 18.06 ± 7.67 °C days, 1.84 ± 0.50 °C and 1.49 ± 0.42 °C, respectively, and all appears at point (143.125°E, 37.125°N). The high intensity of MHWs in the WNPCC area is located in the Oyashio extension region. This distribution may be caused by the intersection of a cold current (Oyashio) and a warm current (Kuroshio) in this area. The intersection of cold and warm currents leads to significant changes in water temperature, which can induce strong MHWs. For more detailed information about the extreme value of MHWs characteristics, please refer to Table S2 in the supporting information. The discussion of specific physical mechanisms is beyond the scope of this study and will be addressed in future research.

3.2 Spatial distribution of the trend for MHWs characteristics

Figure 5A illustrates the trend of MHWs number from 1982 to 2014. The average value is 0.08 ± 0.04 times/year, and the maximum value is 0.20 times/year, located at (168.125°E, 57.125°N). It indicates an increase by about two more MHW events each decade. A negative value indicates the MHWs decreases, and the extreme value is -0.05 times/year, appearing at (148.125°E, 41.125°N). In the southeast WNPCC area, the trend of MHW number increases (Figure 5A) but with a low annual average frequency (Figure 4A).

The trend of the MHW duration is given in Figure 5B. Its average value is 0.15 ± 0.16 days/year, and the maximum value is 0.90 days/year, appearing at (178.125°E, 18.125°N). This indicates that the average duration of each MHW gradually increases during the historical period. Figure 5C shows the trend of MHW days, with an average value of 1.17 ± 0.50 days/year. Its maximum value is 3.68 days/year, appearing at (164.125°E, 62.125°N).

Figures 5D–F show the annual trend of MHWs cumulative intensity, maximum intensity, and average intensity in the historical period. The average values are 0.26 ± 0.32 °Cdays/year, 0.003 ± 0.01 °C/year, and 0.001 ± 0.01 °C/year, respectively. The increasing trend of these three MHW characteristics is very homogenous in the WNPCC area. The maximum values are 2.24°Cdays/year, 0.10°C/year, and 0.08°C/year, which appear at (160.125°E, 40.125°N), (162.125°E, 58.125°N), and (162.125°E, 58.125°N), respectively. There are apparent high-value areas in Figures 4D–F, while the distribution in Figures 5D–F is relatively uniform. Please refer to Table S3 in the supporting information for more details about the extreme value for MHWs characteristics trends.

3.3 Annual average trend of MHWs characteristics

Figure 6 gives the annual trend of spatially-averaged historical MHWs characteristics in the WNPCC region. The MHWs number, duration, days, and CumInt have a significant increasing trend, with rates of 0.04 ± 0.01 times/year (Figure 6A), 0.11 ± 0.02 days/year (Figure 6B), 0.71 ± 0.18 days/year (Figure 6C), and 0.21 ± 0.06°C days/year (Figure 6D), respectively. However, the annual trend of the MaxInt (Figure 6E) and MeanInt (Figure 6F) are almost zero.

4 Projection of MHWs characteristics

4.1 Spatial distribution of MHWs characteristics

Projection scenarios help us understand MHWs trends to formulate early corresponding countermeasures. In this study, the future scenarios SSP1-2.6, 2-4.5, and 5-8.5 of the five best-performing numerical models are analyzed. Only four models are used for evaluation under the SSP1-2.6 scenario since GFDL-CM4 does not simulate this scenario. Figures 7–9 show the spatial distribution of the multi-year average MHWs characteristics and their differences under the SSP2-4.5 and 5-8.5 scenarios (SSP5-8.5 minus SSP2-4.5). For the SSP1-2.6 scenario, please refer to the supporting information (Figures S1–S6). The MHWs number in the south of the WNPCC area is significantly higher than that in the north area (Figure 7A). The average value in the whole WNPCC region is 3.33 ± 0.87 times/year. For more detailed information about the extreme value of the MHWs characteristics under

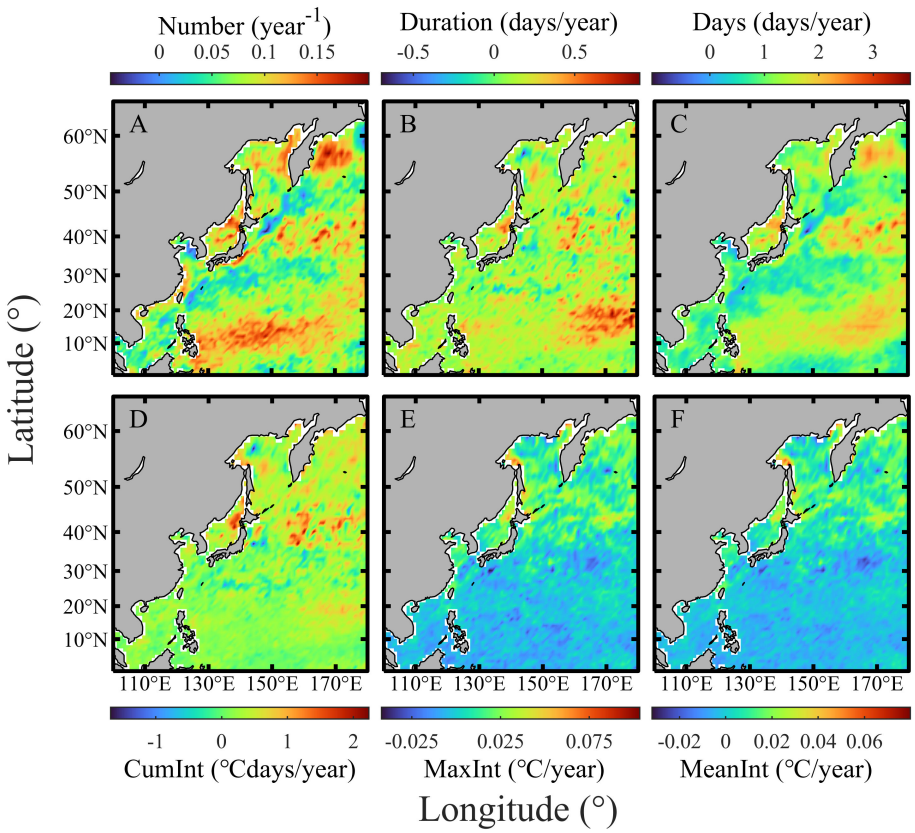


FIGURE 5
Spatial distribution of the MHWs characteristics trend during the historical period based on OISSTV2 data. Variation trend of MHWs **(A)** Number (units: year-1), **(B)** Duration (units: day), **(C)** Days (units: day), **(D)** CumInt (units: °C days), **(E)** MaxInt (units: °C), and **(F)** MeanInt (units: °C).

three different scenarios, please refer to Tables S4–S6 in the supporting information.

Figure 8A is consistent with the overall distribution pattern of Figure 7A, with an average of 2.34 ± 0.59 times/year, which less than that in SSP2-4.5. The maximum value is 5.22 times/year, located at (118.125°E, 24.125°N), and the minimum is 1.17 times/year. Regardless of the average and maximum or minimum values, the multi-year average MHWs number in SSP5-8.5 (Figure 8A) is less than that in SSP1-2.6 (Figures S1, S4) and SSP2-4.5 (Figure 7A). Comparing the historical period (Figure 4A) with the three future scenarios, the MHWs number and the regional difference increase. The MHWs occurrence is significantly more frequent in the south than in the north of the WNPCC region.

Figures 7B, 8B show the spatial distribution of the multi-year average MHWs duration under SSP2-4.5 and SSP5-8.5 scenarios, respectively. The spatial distributions are almost the same in the two scenarios, showing larger values in the north of the WNPCC area than in the south. The spatial average of MHWs duration is 1.21 ± 0.49 days/year, 86.83 ± 35.58 days/year, and 138.66 ± 43.03 days/year under SSP1-2.6 (Figure S1), SSP2-4.5 (Figure 7B) and SSP5-8.5 scenario (Figure 8B), respectively. That is, the average MHWs duration increases significantly with an increase in emissions.

The average difference of MHWs duration in the WNPCC area shows a 51.82 ± 14.32 days longer duration under SSP5-8.5 than SSP2-4.5 (Figure 9B) and 83.77 ± 24.31 days longer duration than SSP1-2.6 (Figure S4). The maximum difference is 143.69 days/year, which occurs at (124.125°E, 37.125°N) between the SSP5-8.5 and SSP2-4.5. Compared with the historical MHW events in Figure 4B, the multi-year average MHWs duration in the future scenario significantly increases, and the difference in their spatial distribution is also more apparent. The MHWs duration is longer in the high-latitude area of the WNPCC region.

The multi-year average MHWs days in Figures 7C, 8C show clear regional differences. The most noticeable feature is that the MHWs days in the Oyashio extension region are significantly shorter than in other areas. In the north of the Oyashio extension area (north of about 43°N) and south of 20°N, the MHWs days are relatively long. Under the SSP2-4.5, the longest MHWs cumulative days are 302.81 days, which occur at

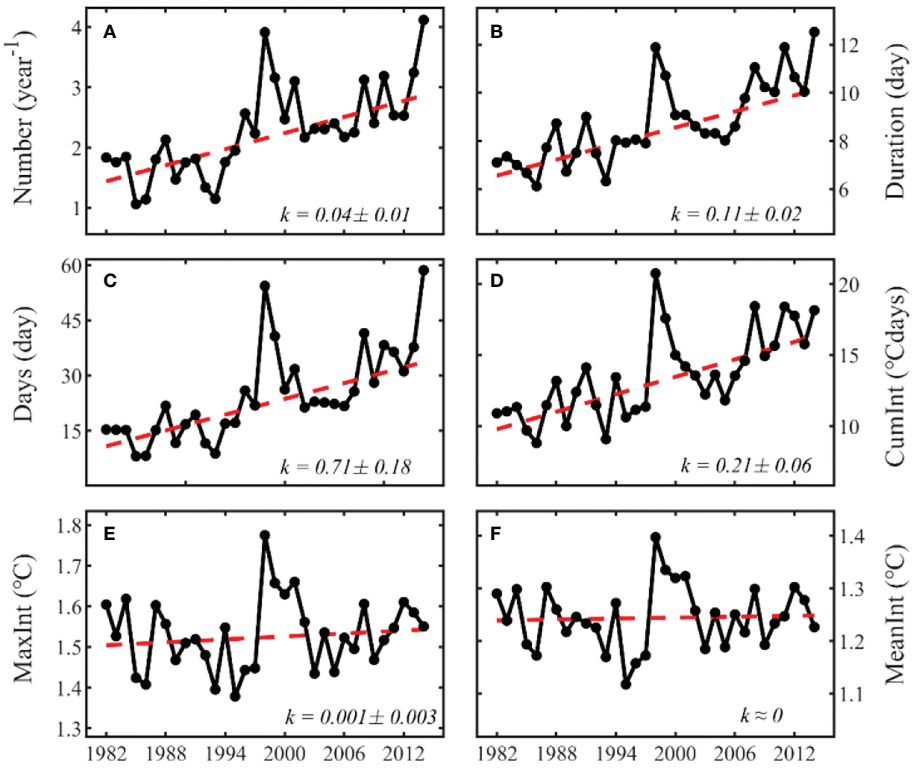


FIGURE 6
Annual trend of the spatially-averaged historical MHWs characteristics in the WNPCC area from OISSTV2 data. Annual trend of the MHWs **(A)** Number (units: year^{-1}), **(B)** Duration (units: day), **(C)** Days (units: day), **(D)** CumInt (units: °C days), **(E)** MaxInt (units: °C), and **(F)** MeanInt (units: °C).

(156.125°E, 50.125°N), and the shortest days are 117.16 days, occurring at (142.125°E, 50.125°N). Accordingly, under SSP5-8.5, the longest MHWs days are 310.10 days, which occur at (170.125°E, 60.125°N), and the shortest days are 154.06 days, which occur at (137.125°E, 54.125°N). For more detailed information about the extreme value of the MHWs characteristics under the SSP1-2.6, 2-4.5, and 5-8.5 scenarios, please refer to Tables S4–S6 in the supporting information.

Under the SSP1-2.6, 2-4.5 and 5-8.5 scenarios, the average MHWs days in the WNPCC area are 184.93 ± 32.73, 236.50 ± 29.28, and 271.59 ± 18.50 days, respectively. Almost contrary to the spatial distribution of the annual MHWs days, the difference between the SSP5-8.5 and SSP2-4.5 scenarios is manifested in the Oyashio extension, the Subtropical Countercurrent, the Japan Sea, and the South China Sea areas (Figure 9C; Table S9). The differences between SSP2-4.5 and SSP1-2.6 (Figure S5), and SSP5-8.5 and SSP1-2.6 (Figure S6) have similar spatial distributions (please refer to see Tables S7 and S8 for more detailed information). This indicates that the response of MHWs days in different regions is different under different warming scenarios.

Figures 7D–F, 8D–F show the spatial distribution of MHWs CumInt, MaxInt, and MeanInt under SSP2-4.5 and 5-8.5 scenarios, respectively. In both scenarios, the high MHWs CumInt areas are distributed north of the Oyashio extension region. MaxInt and MeanInt are larger in the Oyashio extension than in other regions. Compared with the historical period (Figure 4D), the high-value CumInt region changes from the Oyashio extension region in the historical period to the high-latitude areas. MaxInt and MeanInt in the future scenario are consistent with the spatial distribution of the historical period. They are significantly enhanced in the mid-latitude area from 20°N to 43°N between SSP5-8.5 and 2-4.5 scenarios (Figures 9E, F). However, there is no noticeable change in other areas. Please refer to the supporting information for specific values between SSP2-4.5 and SSP1-2.6 (Table S7), SSP5-8.5 and SSP1-2.6 (Table S8), and SSP5-8.5 and SSP2-4.5 (Table S9).

4.2 Spatial distribution of MHWs characteristics variation ratio

Figures 10–12 illustrate the spatial distribution of the multi-year average trend for SSP2-4.5 and 5-8.5 scenarios and their differences (SSP5-8.5 minus SSP2-4.5). Figures 10A–11A show that, overall, the annual variation trend of the MHWs number is

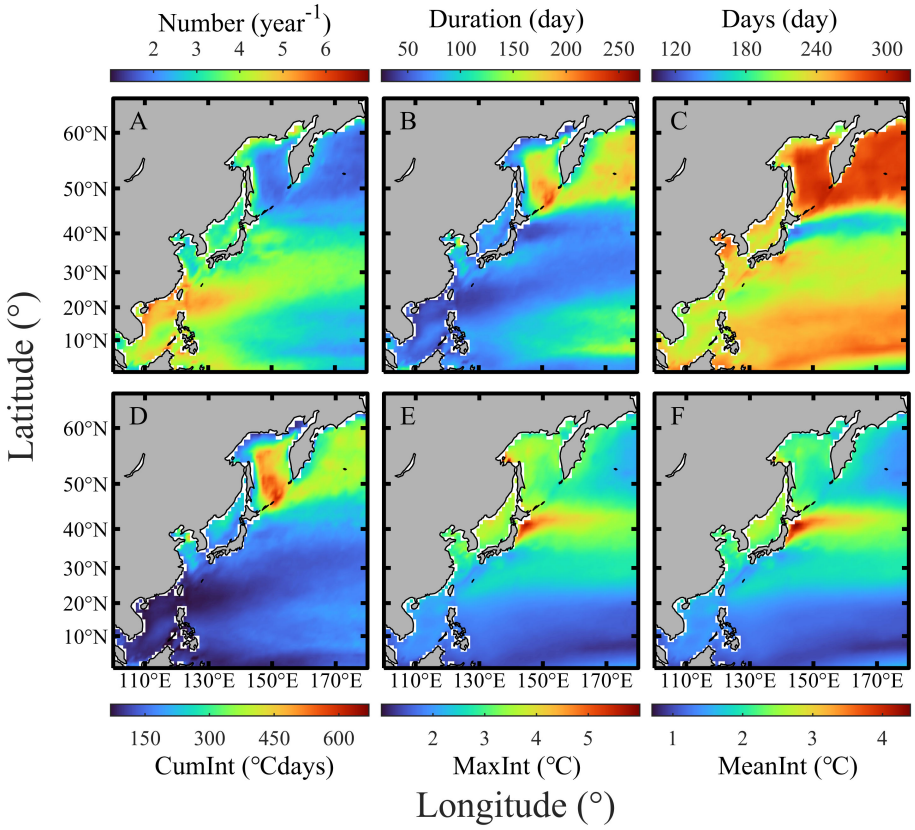


FIGURE 7
Spatial distribution of projected (2015 ~ 2100) MHWs characteristics in the WNPCC area under the SSP2-4.5 scenario. Multi-year average of MHWs **(A)** Number (units: year^{-1}), **(B)** Duration (units: day), **(C)** Days (units: day), **(D)** CumInt (units: °C days), **(E)** MaxInt (units: °C), and **(F)** MeanInt (units: °C).

reduced by an average of -0.03 ± 0.01 and -0.06 ± 0.01 times/year, respectively. The reduction of MHWs number is the smallest in the mid-latitudes region (about 20°N ~ 43°N), especially in the Oyashio extension region. The fastest decrease ratio is at (131.125°E, 0.125°N), reaching -0.09 times/year for the SSP2-4.5 scenario, and at (119.125°E, 1.125°N), reaching -0.11 times/year for the SSP5-8.5 scenario. For the SSP1-2.6 scenario, please refer to Figure S2 in the supporting information.

Figure 12A shows that the multi-year average trend for MHWs number is lower in SSP5-8.5 than in SSP2-4.5, and its average value is -0.03 ± 0.01 times/year. These two scenarios have significant spatial differences. The annual variation ratio for the MHWs frequency in the South China Sea, the East China Sea, and the east side of Taiwan island is more significant than in other regions. This result indicates the regional difference in MHWs characteristics response under different warming scenarios. For more detailed information about the extreme value of the MHWs characteristics trend under SSP1-2.6, 2-4.5 and 5-8.5 scenarios, please refer to Tables S10–S12, respectively, in the supporting information.

The average value of MHWs duration is 0.51 ± 0.34, 1.62 ± 0.44 and 2.56 ± 0.70 days/year for the SSP1-2.6 (Figure S2B), 2-4.5 (Figure 10B), and 5-8.5 scenario (Figure 11B), respectively. The maximum annual average duration variation ratio reaches 4.78 days/year at (119.125°E, 37.125°N) for SSP2-4.5. Correspondingly, for the SSP5-8.5 scenario, the maximum annual average duration variation ratio reaches 5.64 days/year, which occurs at (100.125°E, 5.125°N). From Figure 12B, the annual average duration variation ratio is more significant under SSP5-8.5 than under SSP2-4.5, and the regional average value is 0.94 ± 0.61 days/year. Please refer to Tables S13–S15 in the supporting information for the extreme value distribution of the spatial difference among these three scenarios.

Under the SSP2-4.5 scenario, the average variation ratio of MHWs days is 2.85 ± 0.28 days/year (Figure 10C). Accordingly, in the SSP5-8.5 scenario, it is 3.38 ± 0.24 days/year (Figure 11C). The variation ratio of MHWs days is larger under SSP5-8.5 than under the SSP2-4.5 scenario, with an average value of 0.53 ± 0.32 days/year (Figure 12C). The variation ratios under these two scenarios also have spatial

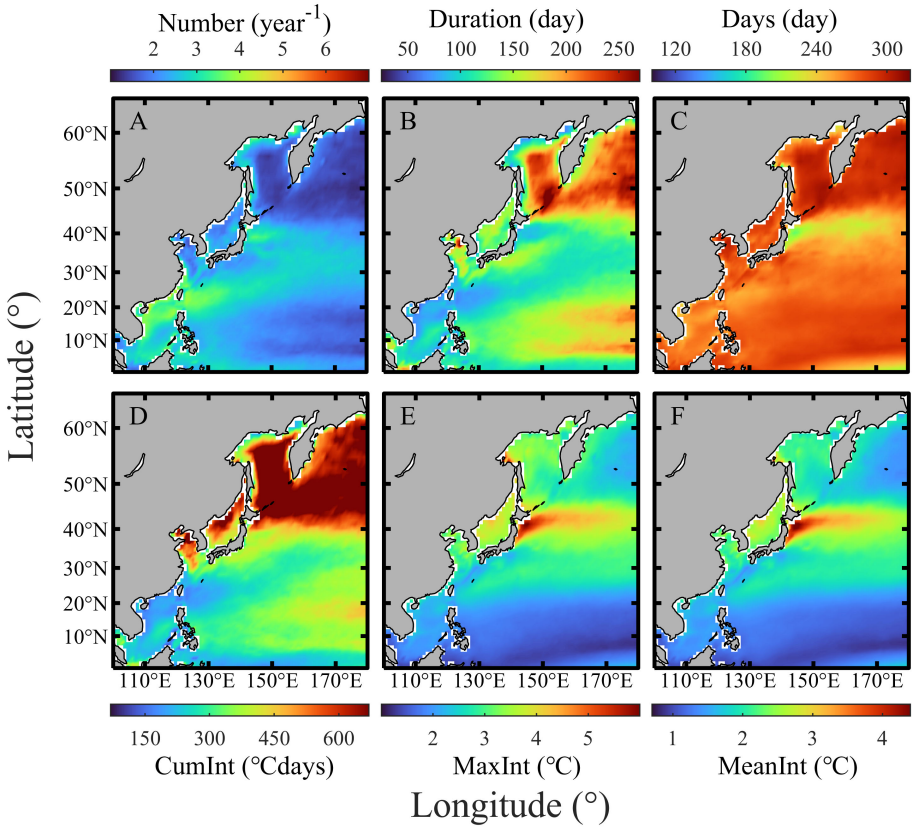


FIGURE 8
Spatial distribution of projected (2015 ~ 2100) MHWs characteristics in the WNPCC area under the SSP5-8.5 scenario. Multi-year average of **(A)** MHWs Number (units: year^{-1}), **(B)** Duration (units: day), **(C)** Days (units: day), **(D)** CumInt (units: °C days), **(E)** MaxInt (units: °C), and **(F)** MeanInt (units: °C).

differences, especially in the Oyashio extension and the South China Sea regions. For the differences among the SSP1-2.6, 2-4.5 and 5-8.5 scenarios, please refer to Figures S5, S6 in the supporting information.

Figures 10D–F, 11D–F show the spatial distribution of the annual variation ratio of MHWs cumulative intensity, maximum intensity, and mean intensity under the SSP2-4.5 and SSP5-8.5 scenarios, respectively. Under the SSP2-4.5 scenario, the spatial distribution of these three characteristics is relatively uniform, and their spatial average values in the WNPCC area are 3.83 ± 1.43°C days/year, 0.02 ± 0.01°C/year, and 0.01 ± 0.003°C/year, respectively. Correspondingly, under the SSP5-8.5 scenario, its spatial average value is 6.70 ± 2.61 °Cdays/year, 0.03 ± 0.01°C/year, and 0.01 ± 0.01 °C/year. Figures 12D–F show that the annual variation ratio for the MHWs cumulative intensity, maximum intensity, and mean intensity is more significant in the SSP5-8.5 than in the SSP2-4.5 scenario. In terms of spatial distribution, the Oyashio extension and the Subtropical Countercurrent regions are more intense than other areas. Please refer to Table S10 in the supporting information for the extreme value distribution of the variation ratio for MHWs cumulative intensity, maximum intensity, and mean intensity under the SSP1-2.6.

4.3 Future trend of the MHWs in the WNPCC region

Figure 13 illustrates the future trend of MHWs characteristics under the SSP1-2.6, 2-4.5 and 5-8.5 scenarios. The MHWs number has a two-segment distribution (Figure 13A). It has an increasing trend from 2015 to 2036, with a growth rate of 0.01 ± 0.01, 0.03 ± 0.01, and 0.03 ± 0.01 times/year for SSP1-2.6, 2-4.5 and 5-8.5 scenarios, respectively. From 2036 to 2100, it shows a decreasing trend, with an average decreasing rate of -0.002 ± 0.002, -0.03 ± 0.002, and -0.04 ± 0.003 times/year for SSP1-2.6, 2-4.5, and 5-8.5 scenarios, respectively. In short, the MHWs number gradually increases before 2036, and it decreases yearly due to the growth in the MHWs duration (Figure 13B).

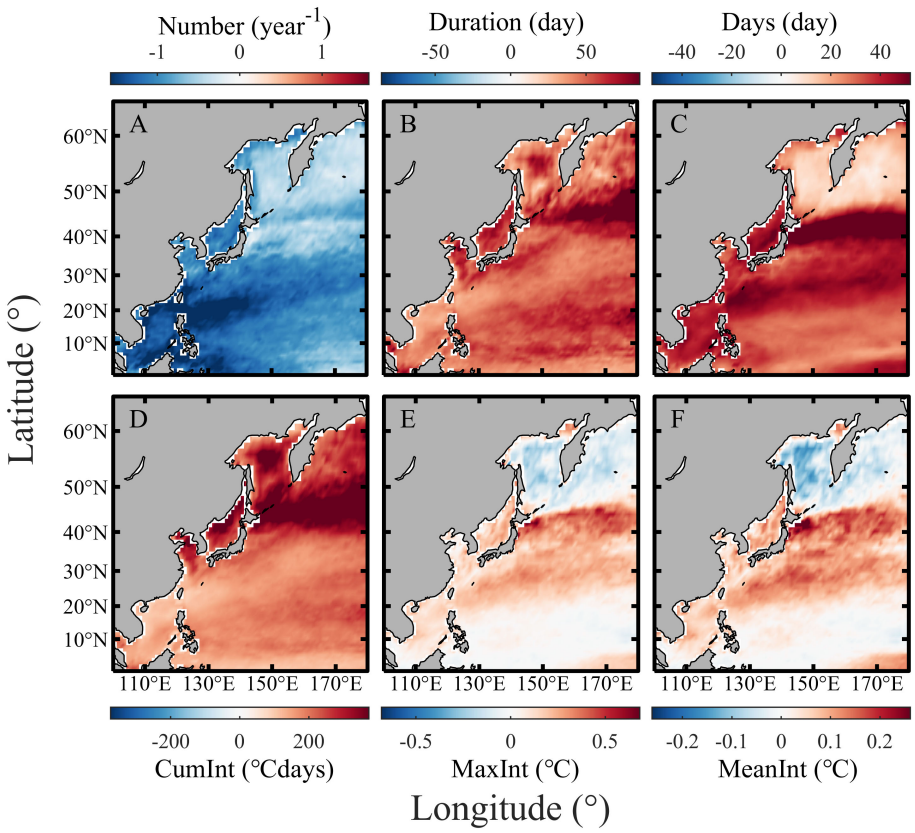


FIGURE 9
Spatial distribution of differences in projected MHWs characteristics under SSP2-4.5 and SSP5-8.5 scenarios (SSP5-8.5 minus SSP2-4.5). Multi-year average of **(A)** MHWs Number (units: year^{-1}), **(B)** Duration (units: day), **(C)** Days (units: day), **(D)** CumInt (units: °Cdays), **(E)** MaxInt (units: °C), and **(F)** MeanInt (units: °C).

Under the SSP1-2.6, 2-4.5 and 5-8.5 scenarios, the average MHWs duration increases by 0.49 ± 0.06, 1.34 ± 0.05, and 1.76 ± 0.10 days/year (Figure 13B). Before 2060, the duration for a single MHW increases rapidly (Figure 13C). The growth rates for the SSP1-2.6, 2-4.5 and 5-8.5 scenarios are 2.19 ± 0.21, 3.53 ± 0.12 and 4.64 ± 0.16 days/year, respectively. After 2060, the rate of increase slows down to -0.51 ± 0.15 (SSP1-2.6), 1.03 ± 0.14 (SSP2-4.5) and 0.77 ± 0.10 days/year (SSP5-8.5), respectively.

From the MHWs cumulative intensity (Figure 13D), maximum intensity (Figure 13E), and average intensity (Figure 13F), the projected MHW has a significant increasing trend, and the increase is more evident under the SSP5-8.5 than the other two scenarios. The growth rates are 0.96 ± 0.11 °C days/year, 0.005 ± 0.001°C/year and 0.002 ± 0.0002°C/year for the SSP1-2.6 scenario; 3.07 ± 0.12 °C days/year, 0.02 ± 0.001 °C/year, and 0.01 ± 0.0003 °C/year for the SSP2-4.5 scenario; and 5.41 ± 0.21 °C days/year, 0.03 ± 0.001 °C/year, and 0.02 ± 0.001 °C/year for the SSP5-8.5 scenario, respectively. For more detailed value information, please refer to Table S16 in the supporting information. Some previous studies divided the future simulation period into the near future (before 2060) and far future (from 2060 to 2100). However, it can be seen from Figure 13 that apart from the MHWs days, which have obvious differences around 2060, the other five variables have no particularly obvious differences. Therefore, this study does not separate the future period into near and far futures for discussion. This phenomenon may be because we use the fixed threshold method to detect MHWs.

5 Discussion

5.1 Seasonal variation of MHWs characteristics

The seasonal difference in MHWs is a fascinating scientific problem. We calculated the monthly change of the MHWs occurrence area percentage (Figure 14A) and the MHWs average intensity (Figure 14B) in the WNPCC area. The MHWs occurrence area percentage is defined as $\frac{S_1}{S_2} \times 100\,\%$,

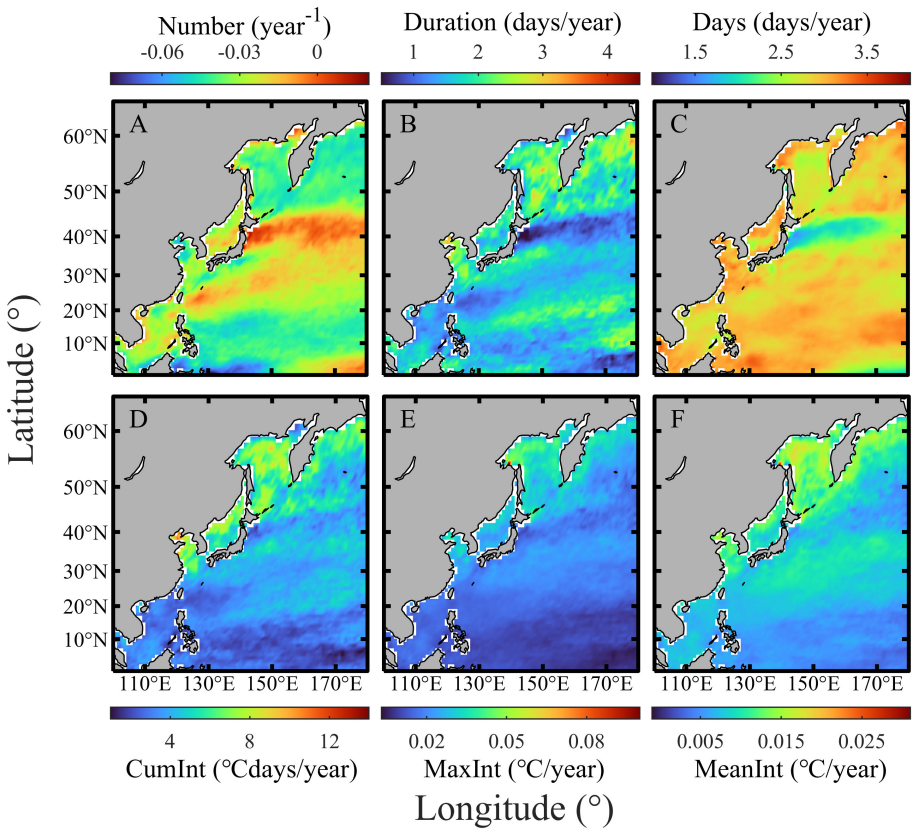


FIGURE 10
Spatial distribution of average annual variation ratio for MHWs characteristics under the SSP2-4.5 scenario. Average of annual variation ratio for MHWs **(A)** Number (units: year^{-1}), **(B)** Duration (units: day/year), **(C)** Days (units: day/year), **(D)** CumInt (units: °Cdays/year), **(E)** MaxInt (units: °C/year), and **(F)** MeanInt (units: °C/year).

where S_1 represents the size occupied by the MHWs, and S_2 represents the total size of the WNPCC area. From Figure 14A, the occurrence area proportion in the future scenario is significantly larger than that in the historical period. The MHWs occurrence area in summer is slightly smaller than in winter.

In terms of MHWs intensity, both historical and future scenarios show prominent characteristics of strong in summer and weak in winter (Figure 14B). Under the SSP1-2.6 (2-4.5, 5-8.5) scenario, the maximum intensity of the MHW reaches 1.66°C (1.82°C, 2.35°C) in August, and the minimum intensity in March (February, March), reaches 1.17°C (1.35°C, 1.79°C). Accordingly, in the historical period, the maximum MHW intensity occurs in August, reaching 1.44°C, and the minimum value occurs in February, reaching 1.17°C.

5.2 Impact of different climate thresholds

The MHW's definition is closely related to the selection of climate state threshold. Since the world's oceans have a long-term warming trend, using a fixed climate threshold causes a significant increase in MHWs (Chiswell, 2022). On the other hand, some marine species have quickly adapted to the temperature rise, so the MHW defined by the fixed threshold may not be harmful to them. With the rise in the climate temperature baseline under global warming, ecosystems may be reorganized (Smale et al., 2019). That is, the MHW deformation method with a fixed threshold is suitable for marine species with weak temperature adaptability. However, it is not applicable for species with strong temperature adaptability. This leads to results such as no obvious marine disasters, although an MHW has occurred, thus breaking away from the significance of MHW studies. This problem can be overcome to a certain extent by moving the average temperature of the climate state, for example, using the 20 or 30-year moving average threshold of the climate state.

Establishing a good relationship between the definition and intensity of MHW and its possible impact can provide a practical and effective reference for the prediction of MHW and policy formulation of ocean management departments. In addition, the

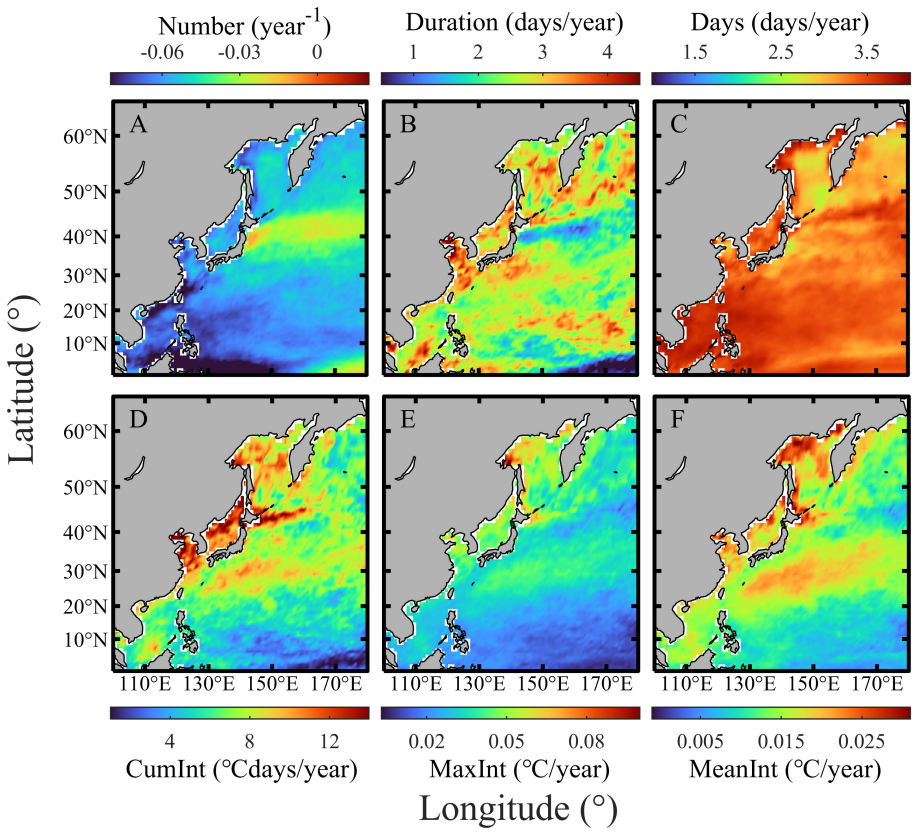


FIGURE 11
Spatial distribution of average annual variation ratio for MHWs characteristics under the SSP5-8.5 scenario. Average of annual variation ratio for MHWs **(A)** Number (units: year^{-1}), **(B)** Duration (units: day/year), **(C)** Days (units: day/year), **(D)** CumInt (units: °Cdays/year), **(E)** MaxInt (units: °C/year), and **(F)** MeanInt (units: °C/year).

definition of MHW should consider the impact of global warming and the characteristics of local marine ecological communities. There are also views that MHW can be measured by "thermal displacement", or the distance required to move to the same level of climate temperature habitat. However, this MHW definition applies to swimming marine species but is less applicable to immovable or benthic entities (including corals).

5.3 Subsurface MHWs

Current MHW discussions are usually based on SST data, i.e., MHW is a phenomenon occurring in the upper ocean layer. However, the warming phenomenon in the upper layer can contribute heat to the oceanic subsurface or even the interior through some physical processes (such as mesoscale eddy, Wang et al., 2022d). The surface warming caused by MHW in the northeast Pacific may penetrate the oceanic subsurface when the mixing is intense in winter (Scannell et al., 2020). In southeast Australia, Schaeffer and Roughan (2017) also found the enhancement of MHWs in the oceanic subsurface.

In addition to the influence of these surface MHWs on the oceanic subsurface layer, some studies have found that MHWs can occur directly in subsurface layers without the induction of surface warming. Hu et al. (2021) explored the subsurface MHW of the tropical western Pacific Ocean using high-resolution data collected by the Tropical Atmosphere Ocean/Triangle Trans-Ocean Buoy Network (TAO/TRITON) buoy. They pointed out that this particularly strong subsurface MHW seems unrelated to the warming of the ocean's surface.

6 Conclusions

The MHWs spatial distribution characteristics and variation trends in the WNPCC area are analyzed during the historical period (1982 ~ 2014) using OISSTV2 data. With the results from

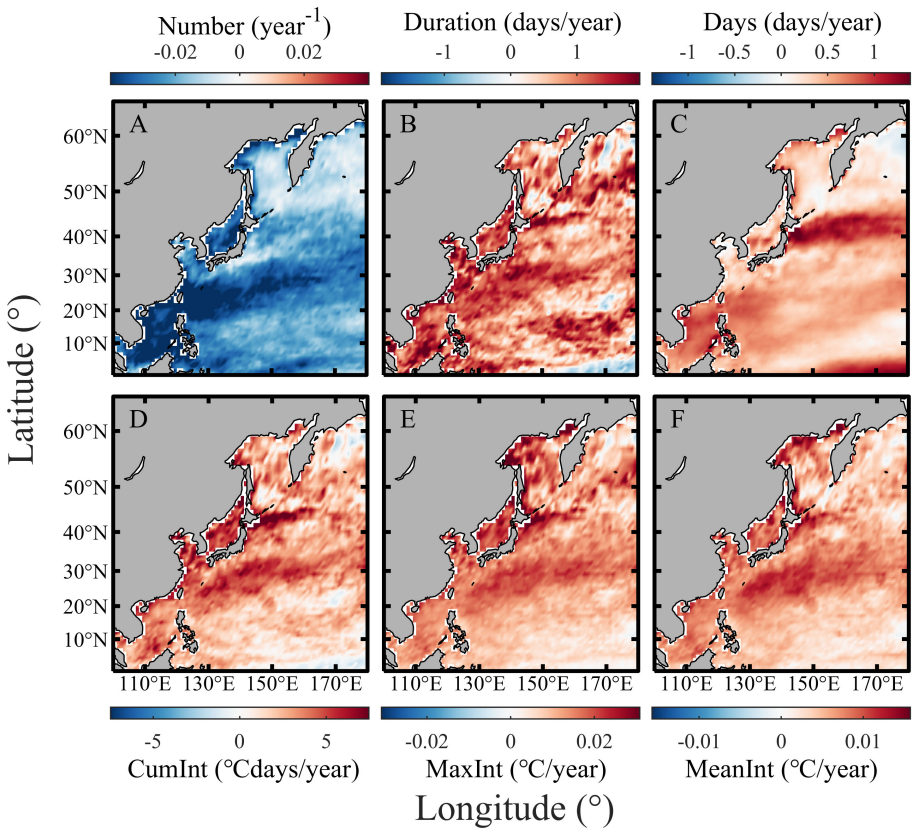


FIGURE 12
Spatial distribution of differences in projected annual variation ratio of MHWs characteristics for the SSP2-4.5 and 5-8.5 (SSP5-8.5 minus SSP2-4.5). Average annual variation ratio differences for MHWs **(A)** Number (units: year^{-1}), **(B)** Duration (units: day/year), **(C)** Days (units: day/year), **(D)** CumInt (units: °Cdays/year), **(E)** MaxInt (units: °C/year), and **(F)** MeanInt (units: °C/year).

OISSTV2 data as a comparison standard, five best-performing models are selected from 19 CMIP6 GCMs. Using the simulation results of these five models, the MHWs characteristics from 2015 to 2100 are studied under the SSP1-2.6, 2-4.5, and 5-8.5 scenarios. We also discuss the seasonal differences in the MHWs occurrence area and its intensity. The main conclusions are summarized as follows.

1. In the historical period, MHWs occur in most WNPCC areas, with an average number, duration, days, cumulative intensity, maximum intensity, and mean intensity of 1.95 ± 0.21 times/year, 11.38 ± 1.97 days, 22.06 ± 3.84 days, 18.06 ± 7.67 °Cdays, 1.84 ± 0.50°C, and 1.49 ± 0.42°C. The MHWs frequency is relatively low in the open ocean, especially in the southeast of the WNPCC area, while it is relatively high in the coastal region.
2. According to the optimization method proposed in this study, among the 19 CMIP6 GCMs, the five models that best reproduce MHWs in the WNPCC area relative to OISSTV2 are GFDL-CM4, GFDL-ESM4, AWI-CM-1-1-MR, EC-Earth3-Veg, and EC-Earth3.
3. In the future scenario (2015 ~ 2100), the projected MHWs characteristics under the SSP5-8.5 are more substantial than those under the SSP1-2.6 and SSP2-4.5, except for the MHWs frequency. The MHWs cumulative intensity is 96.36 ± 56.30, 175.44 ± 92.62, and 385.22 ± 168.00 °C days under the SSP1-2.6, 2-4.5 and 5-8.5, respectively. The maximum and average intensity of the MHWs in the Oyashio extension region are more robust than in other areas.
4. The annual variation ratio for the MHWs frequency is significant in the South China Sea, the East China Sea, and east side of Taiwan island. The annual average variation ratio of MHWs duration and cumulative days is more significant under the SSP5-8.5 than under SSP1-2.6 and 2-4.5.
5. The MHWs occurrence area in summer is slightly smaller than in winter, but the MHWs average intensity is stronger in summer than in winter.

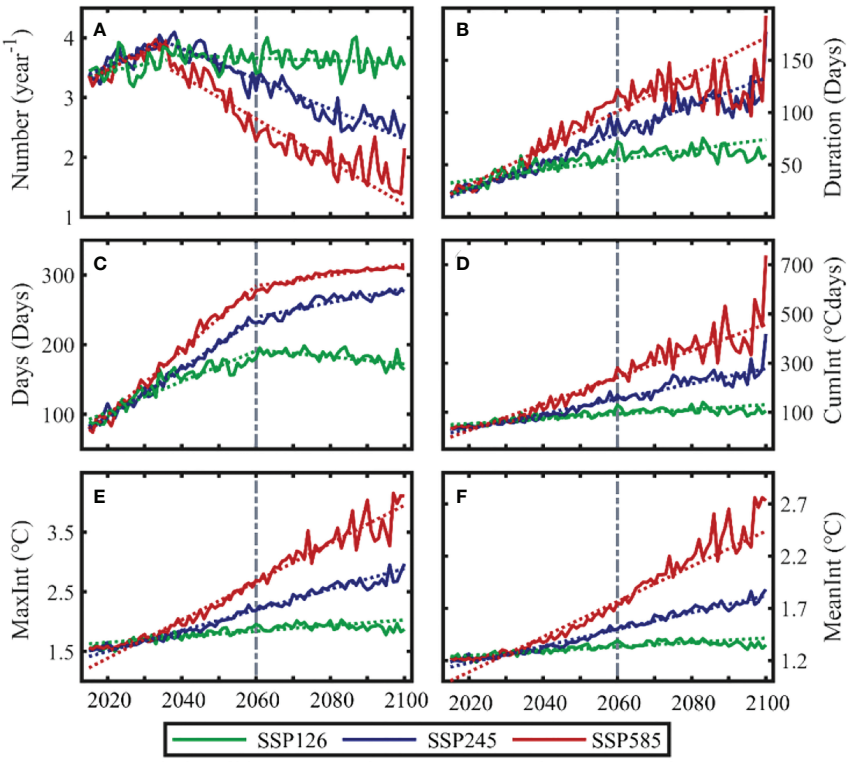


FIGURE 13
Projected interannual variability of MWHs parameters under the SSP1-2.6 (green line), SSP2-4.5 (blue line) and SSP5-8.5 (red line) scenarios from the ensemble mean of the four/five/five selected models. The solid line is the future change of the estimated parameters, and the dotted line is the linear regression result. The left side of the dotted line (2060) represents the near future scenario, and the right side of the dotted line represents the far future scenario. Interannual variability for MHWs **(A)** Number (unit: year^{-1}), **(B)** Duration (unit: day), **(C)** Days (unit: day), **(D)** CumInt (units: °C days), **(E)** MaxInt (units: °C), **(F)** MeanInt (units: °C).

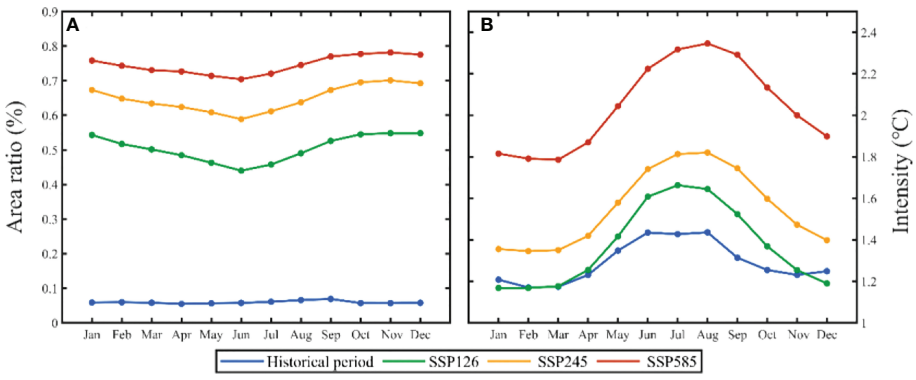


FIGURE 14
Monthly distribution of MHWs occurrence area percentage **(A)** and MHWs mean intensity **(B)** in the WNPCC area. The blue, green, yellow, and red curves represent the historical period, and the projection period under the SSP1-2.6, 2-4.5 and 5-8.5 scenarios, respectively.

Data availability statement

The original contributions presented in the study are included in the article/Supplementary Material. Further inquiries can be directed to the corresponding author.

Author contributions

YY, WS, JY, and CD conceived and designed the experiments. YY performed the experiments. WS, YY, JY, and JJ analyzed the data. WS and YY drafted the original manuscript. WS, YY, KL, JJ, and JY revised and edited the manuscript. All authors contributed to the article and approved the submitted version.

Funding

This study was supported by the National Natural Science Foundation of China under contract Nos. 42192562, 41906008, 51909100; the Open Fund of State Key Laboratory of Satellite Ocean Environment Dynamics, Second Institute of Oceanography, MNR under contract No. QNHX2231; the Innovation Group Project of Southern Marine Science and Engineering Guangdong Laboratory (Zhuhai) under contract No. 311020004; the National Natural Science Foundation of China under contract No. 42076162; and the Natural Science Foundation of Guangdong Province of China under contract No. 2020A1515010496.

Acknowledgments

We acknowledge the World Climate Research Programme's (WCRP) Working Group on Coupled Modelling, which is responsible for coordinating CMIP. We also thank the climate modeling groups for producing and making available their model output. We thank Zijie Zhao for providing the main function code to detect marine heatwaves (https://github.com/ZijieZhaoMMHW/m_mhw1.0).

Conflict of interest

The authors declare that the research was conducted in the absence of any commercial or financial relationships that could be construed as a potential conflict of interest.

Publisher's note

All claims expressed in this article are solely those of the authors and do not necessarily represent those of their affiliated organizations, or those of the publisher, the editors and the reviewers. Any product that may be evaluated in this article, or claim that may be made by its manufacturer, is not guaranteed or endorsed by the publisher.

Supplementary material

The Supplementary Material for this article can be found online at: https://www.frontiersin.org/articles/10.3389/fmars.2022.1048557/full#supplementary-material

References

Arias-Ortiz, A., Serrano, O., Masqué, P., Lavery, P. S., Mueller, U., Kendrick, G. A., et al. (2018). A marine heatwave drives massive losses from the world's largest seagrass carbon stocks. *Nat. Clim. Change.* 8 (4), 338–344. doi: 10.1038/s41558-018-0096-y

Benthuysen, J. A., Oliver, E. C. J., Feng, M., and Marshall, A. G. (2018). Extreme marine warming across tropical Australia during austral summer 2015–2016. *J. Geophys. Res.* 123 (2), 1301–1326. doi: 10.1002/2017JC013326

Black, E., Blackburn, M., Harrison, G., Hoskins, B., and Methven, J. (2004). Factors contributing to the summer 2003 European heatwave. *Weather.* 59 (8), 217–223. doi: 10.1256/wea.74.04

Bond, N. A., Cronin, M. F., Freeland, H., and Mantua, N. (2015). Causes and impacts of the 2014 warm anomaly in the NE pacific. *Geophys. Res. Lett.* 42 (9), 3414–3420. doi: 10.1002/2015GL063306

Capotondi, A., Newman, M., Xu, T., and Di Lorenzo, E. (2022). An optimal precursor of northeast pacific marine heatwaves and central pacific El niño events. *Geophys. Res. Lett.* 49 (5), e2021G–e97350. doi: 10.1029/2021GL097350

Caputi, N., Kangas, M., Chandrapavan, A., Hart, A., Feng, M., Marin, M., et al. (2019). Factors affecting the recovery of invertebrate stocks from the 2011 western australian extreme marine heatwave. *Front. Mar. Sci.* 6. doi: 10.3389/fmars.2019.00484

Caputi, N., Kangas, M., Denham, A., Feng, M., Pearce, A., Hetzel, Y., et al. (2016). Management adaptation of invertebrate fisheries to an extreme marine heat wave event at a global warming hot spot. *Ecol. Evol.* 6 (11), 3583–3593. doi: 10.1002/ece3.2137

Cavole, L., Demko, A., Diner, R., Giddings, A., Koester, I., Pagniello, C., et al. (2016). Biological impacts of the 2013–2015 warm-water anomaly in the northeast pacific: Winners, losers, and the future. *Oceanography* 29 (2), 273–285. doi: 10.5670/oceanog.2016.32

Chandrapavan, A., Caputi, N., and Kangas, M. I. (2019). The decline and recovery of a crab population from an extreme marine heatwave and a changing climate. *Front. Mar. Sci.* 6. doi: 10.3389/fmars.2019.00510

Chiswell, S. M. (2022). Global trends in marine heatwaves and cold spells: The impacts of fixed versus changing baselines. *J. Geophys. Res.* 127, e2022JC018757. doi: 10.1029/2022JC018757

Di Lorenzo, E., and Mantua, N. (2016). Multi-year persistence of the 2014/15 north pacific marine heatwave. *Nat. Clim. Change.* 6 (11), 1042–1047. doi: 10.1038/nclimate3082

Eyring, V., Bony, S., Meehl, G. A., Senior, C. A., Stevens, B., Stouffer, R. J., et al. (2016). Overview of the coupled model intercomparison project phase 6 (CMIP6) experimental design and organization. *Geosci. Model. Dev.* 9 (5), 1937–1958. doi: 10.5194/gmd-9-1937-2016

Feng, Y., Bethel, B. J., Dong, C., Zhao, H., Yao, Y., and Yu, Y. (2022). Marine heatwave events near weizhou island, beibu gulf in 2020 and their possible relations to coral bleaching. *Sci. Total Environ.* 823, 153414. doi: 10.1016/j.scitotenv.2022.153414

Frölicher, T. L., Fischer, E. M., and Gruber, N. (2018). Marine heatwaves under global warming. *Nature.* 560 (7718), 360–364. doi: 10.1038/s41586-018-0383-9

Gao, G., Marin, M., Feng, M., Yin, B., Yang, D., Feng, X., et al. (2020). Drivers of marine heatwaves in the East China Sea and the south yellow sea in three consecutive summers during 2016–2018. *J. Geophys. Res.* 125 (8), e2020J–e16518. doi: 10.1029/2020JC016518

Garrabou, J., Coma, R., Bensoussan, N., Bally, M., Chevaldonne, P., Cigliano, M., et al. (2009). Mass mortality in northwestern Mediterranean rocky benthic communities: Effects of the 2003 heat wave. *Global Change Biol.* 15 (5), 1090–1103. doi: 10.1111/j.1365-2486.2008.01823.x

Garrabou, J., Gómez Gras, D., Medrano, A., Cerrano, C., Ponti, M., Schlegel, R., et al. (2022). Marine heatwaves drive recurrent mass mortalities in the Mediterranean Sea. *Global Change Biol.* 28 (19), 5708–5725. doi: 10.1111/gcb.16301

Hamed, M. M., Nashwan, M. S., Shiru, M. S., and Shahid, S. (2022). Comparison between CMIP5 and CMIP6 models over MENA region using historical simulations and future projections. *Sustainability.* 14 (16), 10375. doi: 10.3390/su141610375

Han, W., Zhang, L., Meehl, G. A., Kido, S., Tozuka, T., Li, Y., et al. (2022). Sea Level extremes and compounding marine heatwaves in coastal Indonesia. *Nat. Commun.* 13 (1), 6410. doi: 10.1038/s41467-022-34003-3

Hobday, A. J., Alexander, L. V., Perkins, S. E., Smale, D. A., Straub, S. C., Oliver, E. C. J., et al. (2016). A hierarchical approach to defining marine heatwaves. *Prog. Oceanogr.* 141, 227–238. doi: 10.1016/j.pocean.2015.12.014

Holbrook, N. J., Hernaman, V., Koshiba, S., Lako, J., Kajtar, J. B., Amosa, P., et al. (2022). Impacts of marine heatwaves on tropical western and central pacific island nations and their communities. *Global Planet. Change.* 208, 103680. doi: 10.1016/j.gloplacha.2021.103680

Holbrook, N. J., Scannell, H. A., Sen Gupta, A., Benthuysen, J. A., Feng, M., Oliver, E. C. J., et al. (2019). A global assessment of marine heatwaves and their drivers. *Nat. Commun.* 10 (1), 2624. doi: 10.1038/s41467-019-10206-z

Holbrook, N. J., Sen Gupta, A., Oliver, E. C. J., Hobday, A. J., Benthuysen, J. A., Scannell, H. A., et al. (2020). Keeping pace with marine heatwaves. *Nat. Rev. Earth Environment.* 1 (9), 482–493. doi: 10.1038/s43017-020-0068-4

Huang, B., Wang, Z., Yin, X., Arguez, A., Graham, G., Liu, C., et al. (2021). Prolonged marine heatwaves in the Arctic: 1982–2020. *Geophys. Res. Lett.* 48 (24), e2021G–e95590. doi: 10.1029/2021GL095590

Hughes, T. P., Kerry, J. T., Álvarez-Noriega, M., Álvarez-Romero, J. G., Anderson, K. D., Baird, A. H., et al. (2017). Global warming and recurrent mass bleaching of corals. *Nature.* 543 (7645), 373–377. doi: 10.1038/nature21707

Hu, S., Li, S., Zhang, Y., Guan, C., Du, Y., Feng, M., et al. (2021). Observed strong subsurface marine heatwaves in the tropical western pacific ocean. *Environ. Res. Lett.* 16 (10), 104024. doi: 10.1088/1748-9326/ac26f2

Jacox, M. G., Alexander, M. A., Amaya, D., Becker, E., Bograd, S. J., Brodie, S., et al. (2022). Global seasonal forecasts of marine heatwaves. *Nature.* 604 (7906), 486–490. doi: 10.1038/s41586-022-04573-9

Jones, T., Parrish, J. K., Peterson, W. T., Bjorkstedt, E. P., Bond, N. A., Ballance, L. T., et al. (2018). Massive mortality of a planktivorous seabird in response to a marine heatwave. *Geophys. Res. Lett.* 45 (7), 3193–3202. doi: 10.1002/2017GL076164

Kajtar, J. B., Hernaman, V., Holbrook, N. J., and Petrelli, P. (2022). Tropical western and central pacific marine heatwave data calculated from gridded sea surface temperature observations and CMIP6. *Data Brief.* 40, 107694. doi: 10.1016/j.dib.2021.107694

Li, Y., Ren, G., Wang, Q., and You, Q. (2019). More extreme marine heatwaves in the China seas during the global warming hiatus. *Environ. Res. Lett.* 14 (10), 104010. doi: 10.1088/1748-9326/ab28bc

Liu, K., Xu, K., Zhu, C., and Liu, B. (2022). Diversity of marine heatwaves in the south china sea regulated by ENSO phase. *J. Climate.* 35 (2), 877–893. doi: 10.1175/JCLI-D-21-0309.1

Mawren, D., Hermes, J., and Reason, C. J. C. (2021). Marine heatwaves in the Mozambique channel. *Clim. Dynam.* 58 (1-2), 305–327. doi: 10.1007/s00382-021-05909-3

Mills, K., Pershing, A., Brown, C., Chen, Y., Chiang, F., Holland, D., et al. (2013). Fisheries management in a changing climate: Lessons from the 2012 ocean heat wave in the northwest Atlantic. *Oceanography.* 26 (2), 191–195. doi: 10.5670/oceanog.2013.27

Misra, R., Sérazin, G., Meissner, K. J., and Gupta, A. S. (2021). Projected changes to Australian marine heatwaves. *Geophys. Res. Lett.* 48 (7), e2020GL091323. doi: 10.1029/2020GL091323

Miyama, T., Minobe, S., and Goto, H. (2021). Marine heatwave of sea surface temperature of the oyashio region in summer in 2010–2016. *Front. Mar. Sci.* 7. doi: 10.3389/fmars.2020.576240

Morrison, T. H., Adger, N., Barnett, J., Brown, K., Possingham, H., and Hughes, T. (2020). Advancing coral reef governance into the anthropocene. *One Earth.* 2 (1), 64–74. doi: 10.1016/j.oneear.2019.12.014

Noh, K. M., Lim, H., and Kug, J. (2022). Global chlorophyll responses to marine heatwaves in satellite ocean color. *Environ. Res. Lett.* 17 (6), 64034. doi: 10.1088/1748-9326/ac70ec

O'Neill, B. C., Tebaldi, C., van Vuuren, D. P., Eyring, V., Friedlingstein, P., Hurtt, G., et al. (2016). The scenario model intercomparison project (ScenarioMIP) for CMIP6. *Geosci. Model. Dev.* 9 (9), 3461–3482. doi: 10.5194/gmd-9-3461-2016

Olita, A., Sorgente, R., Natale, S., Gaber˙sek, S., Ribotti, A., Bonanno, A., et al. (2007). Effects of the 2003 European heatwave on the central Mediterranean Sea: Surface fluxes and the dynamical response. *Ocean Sci.* 3 (2), 273–289. doi: 10.5194/os-3-273-2007

Oliver, E. C. J., Benthuysen, J. A., Bindoff, N. L., Hobday, A. J., Holbrook, N. J., Mundy, C. N., et al. (2017). The unprecedented 2015/16 Tasman Sea marine heatwave. *Nat. Commun.* 8 (1), 16101. doi: 10.1038/ncomms16101

Oliver, E. C. J., Burrows, M. T., Donat, M. G., Sen Gupta, A., Alexander, L. V., Perkins-Kirkpatrick, S. E., et al. (2019). Projected marine heatwaves in the 21st century and the potential for ecological impact. *Front. Mar. Sci.* 6. doi: 10.3389/fmars.2019.00734

Oliver, E. C. J., Donat, M. G., Burrows, M. T., Moore, P. J., Smale, D. A., Alexander, L. V., et al. (2018). Longer and more frequent marine heatwaves over the past century. *Nat. Commun.* 9 (1), 1324. doi: 10.1038/s41467-018-03732-9

Pearce, A. F., and Feng, M. (2013). The rise and fall of the "marine heat wave" off Western Australia during the summer of 2010/2011. *J. Mar. Syst.* 111-112, 139–156. doi: 10.1016/j.jmarsys.2012.10.009

Pörtner, H.-O., Roberts, D. C., Masson-Delmotte, V., Zhai, P., Tignor, M., and Poloczanska, E. (2019). *IPCC special report on the ocean and cryosphere in a changing climate* Vol. 755 (Cambridge, UK: Cambridge University Press). New York, NY, USA. doi: 10.1017/9781009157964

Reynolds, R. W., Smith, T. M., Liu, C., Chelton, D. B., Casey, K. S., and Schlax, M. G. (2007). Daily high-resolution-blended analyses for sea surface temperature. *J. Clim.* 20 (22), 5473–5496. doi: 10.1175/2007JCLI1824.1

Scafetta, N. (2022). CMIP6 GCM ensemble members versus global surface temperatures. *Clim. Dynam.* doi: 10.1007/s00382-022-06493-w

Scannell, H. A., Johnson, G. C., Thompson, L., Lyman, J. M., and Riser, S. C. (2020). Subsurface evolution and persistence of marine heatwaves in the northeast pacific. *Geophys. Res. Lett.* 47 (23), e2020GL090548. doi: 10.1029/2020GL090548

Scannell, H. A., Pershing, A. J., Alexander, M. A., Thomas, A. C., and Mills, K. E. (2016). Frequency of marine heatwaves in the north Atlantic and north pacific since 1950. *Geophys. Res. Lett.* 43 (5), 2069–2076. doi: 10.1002/2015GL067308

Schaeffer, A., and Roughan, M. (2017). Subsurface intensification of marine heatwaves off southeastern Australia: The role of stratification and local winds. *Geophys. Res. Lett.* 44 (10), 5025–5033. doi: 10.1002/2017GL073714

Smale, D. A., Wernberg, T., Oliver, E. C. J., Thomsen, M., Harvey, B. P., Straub, S. C, et al (2019). Marine heatwaves threaten global biodiversity and the provision of ecosystem services. *Nat. Clim. Change* 9 (4), 306–312. doi: 10.1038/s41558-019-0412-1

Straub, S. C., Wernberg, T., Thomsen, M. S., Moore, P. J., Burrows, M. T., Harvey, B. P., et al. (2019). Resistance, extinction, and everything in between – the diverse responses of seaweeds to marine heatwaves. *Front. Mar. Sci.* 6. doi: 10.3389/fmars.2019.00763

Taylor, K. E. (2001). Summarizing multiple aspects of model performance in a single diagram. *J. Geophys. Res.* 106 (D7), 7183–7192. doi: 10.1029/2000JD900719

Thomsen, M. S., Mondardini, L., Alestra, T., Gerrity, S., Tait, L., South, P. M., et al. (2019). Local extinction of bull kelp (Durvillaea spp.) due to a marine heatwave. *Front. Mar. Sci.* 6. doi: 10.3389/fmars.2019.00084

Wang, Q., Dong, C., Dong, J., Zhang, H., and Yang, J. (2022d). Submesoscale processes-induced vertical heat transport modulated by oceanic mesoscale eddies. *Deep Sea Res.* 202, 105138. doi: 10.1016/j.dsr2.2022.105138

Wang, D., Xu, T., Fang, G., Jiang, S., Wang, G., Wei, Z., et al. (2022c). Characteristics of marine heatwaves in the Japan/East Sea. *Remote Sens.* 14 (4), 936. doi: 10.3390/rs14040936

Wang, Y., Zeng, J., Wei, Z., Li, S., Tian, S., Yang, F., et al. (2022a). Classifications and characteristics of marine heatwaves in the northern south China Sea. *Front. Mar. Sci.* 9. doi: 10.3389/fmars.2022.826810

Wang, Q., Zhang, B., Zeng, L., He, Y., Wu, Z., and Chen, J. (2022b). Properties and drivers of marine heat waves in the northern south China Sea. *J. Phys. Oceanogr.* 52 (5), 917–927. doi: 10.1175/JPO-D-21-0236.1

Wei, M., Shu, Q., Song, Z., Song, Y., Yang, X., Guo, Y., et al. (2021). Could CMIP6 climate models reproduce the early-2000s global warming slowdown? *Sci. China Earth Sci.* 64 (6), 853–865. doi: 10.1007/s11430-020-9740-3

Wernberg, T., Smale, D. A., Tuya, F., Thomsen, M. S., Langlois, T. J., de Bettignies, T., et al. (2013). An extreme climatic event alters marine ecosystem structure in a global biodiversity hotspot. *Nat. Clim. Change.* 3 (1), 78–82. doi: 10.1038/nclimate1627

Xu, J., Lowe, R. J., Ivey, G. N., Jones, N. L., and Zhang, Z. (2018). Contrasting heat budget dynamics during two la niña marine heatwave events along northwestern Australia. *J. Geophys. Res.* 123 (2), 1563–1581. doi: 10.1002/2017JC013426

Yan, Y., Chai, F., Xue, H., and Wang, G. (2020). Record-breaking sea surface temperatures in the yellow and East China seas. *J. Geophys. Res.* 125, e2019JC015883. doi: 10.1029/2019JC015883

Yao, Y., and Wang, C. (2021). Variations in summer marine heatwaves in the south China Sea. *J. Geophys. Res.* 126 (10), e2021JC017792. doi: 10.1029/2021JC017792

Yao, Y., and Wang, C. (2022). Marine heatwaves and cold-spells in global coral reef zones. *Prog. Oceanogr.* 209, 102920. doi: 10.1016/j.pocean.2022.102920

Yao, Y., Wang, C., and Fu, Y. (2022). Global marine heatwaves and cold-spells in present climate to future projections. *Earth's Future* 10 (11), e2022EF002787. doi: 10.1029/2022EF002787

Yao, Y., Wang, J., Yin, J., and Zou, X. (2020). Marine heatwaves in china's marginal seas and adjacent offshore waters: Past, present, and future. *J. Geophys. Res.* 125 (3), e2019JC015801. doi: 10.1029/2019JC015801

Zhang, Y., Du, Y., Feng, M., and Hu, S. (2021). Longg, m-yng marine heatwaves instigated by ocean planetary waves in the tropical Indian ocean during 2015–2016 and 2019–2020. *Geophys. Res. Lett.* 48 (21), e2021GL095350. doi: 10.1029/2021GL095350

Zhang, N., Feng, M., Hendon, H. H., Hobday, A. J., and Zinke, J. (2017). Opposite polarities of ENSO drive distinct patterns of coral bleaching potentials in the southeast Indian ocean. *Sci. Rep.* 7 (1), 2443–2443. doi: 10.1038/s41598-017-02688-y

Zhang, X., Zheng, F., Zhu, J., and Chen, X. (2022). Observed frequent occurrences of marine heatwaves in most ocean regions during the last two decades. *Adv. Atmos. Sci* 39 (9), 1579–1587. doi: 10.11922/sciencedb.00872

frontiers | Frontiers in Marine Science

TYPE Original Research
PUBLISHED 04 January 2023
DOI 10.3389/fmars.2022.1028022

Check for updates

OPEN ACCESS

EDITED BY
Lei Ren,
Sun Yat-sen University, China

REVIEWED BY
Eugenio Fraile-Nuez,
Centro Oceanográfico de Canarias, Consejo Superior de Investigaciones Científicas (CSIC), Spain
Xiaogang Xing,
Ministry of Natural Resources, China

*CORRESPONDENCE
Andra Whiteside
andrawhiteside@gmail.com

SPECIALTY SECTION
This article was submitted to Ocean Observation, a section of the journal Frontiers in Marine Science

RECEIVED 25 August 2022
ACCEPTED 25 November 2022
PUBLISHED 04 January 2023

CITATION
Whiteside A, Dupouy C, Singh A, Bani P, Tan J and Frouin R (2023) Impact of ashes from the 2022 Tonga volcanic eruption on satellite ocean color signatures.
Front. Mar. Sci. 9:1028022.
doi: 10.3389/fmars.2022.1028022

COPYRIGHT
© 2023 Whiteside, Dupouy, Singh, Bani, Tan and Frouin. This is an open-access article distributed under the terms of the Creative Commons Attribution License (CC BY). The use, distribution or reproduction in other forums is permitted, provided the original author(s) and the copyright owner(s) are credited and that the original publication in this journal is cited, in accordance with accepted academic practice. No use, distribution or reproduction is permitted which does not comply with these terms.

Impact of ashes from the 2022 Tonga volcanic eruption on satellite ocean color signatures

Andra Whiteside[1,2]*, Cécile Dupouy[1,2,3], Awnesh Singh[2], Philipson Bani[3,4], Jing Tan[5] and Robert Frouin[5]

[1]Aix Marseille Université, Université de Toulon, Centre National de la Recherche Scientifique (CNRS)/ Línstitut national des sciences de lÚnivers (INSU), Institut de Recherche pour le Développement (IRD), Mediterranean Institute of Oceanography (MIO), Marseille, France, [2]Pacific Centre for Environment and Sustainable Development (PaCE-SD), University of the South Pacific, Suva, Fiji, [3]Institut de Recherche pour le Développement (IRD), Nouméa, New Caledonia, [4]Laboratoire Magmas Et Volcans, Université Clermont–Auvergne–CNRS–IRD, L'Observatoire de Physique du Globe de Clermont-Fd (OPGC), Aubière, France, [5]Scripps Institution of Oceanography, University of California, San Diego, CA, United States

A powerful eruption within the Hunga Tonga-Hunga Ha'apai (HTHH) volcano (20.64°S, 175.19°W) in the Kingdom of Tonga, occurred on 15 January 2022. The volcanic blast was enormous, leading many scientists to investigate the full impact and magnitude of this event *via* satellite observations. In this study, we describe a new ocean color signature from a discolored water patch created by the HTHH eruption using NASA and CMEMS products of satellite-derived biological and optical properties. Elevated surface chlorophyll-a concentration (Chl-a) between 0.15 to 2.7 mg.m^{-3} was not associated with phytoplankton growth, but to basalt-andesitic ash material expelled by the volcano and into the ocean, which resulted in erroneous Chl-a estimates. Distribution of the patch over time was aligned with CMEMS ocean currents for 19 days. The gradual decrease of light attenuation or diffuse attenuation coefficient for downward irradiance at 490 nm, K_d(490), was interpreted as due to the sinking of ash particles with time. It is suggested that due to high porosity of 30-40%, a density close to that of seawater, ash particles stay suspended in the water column for more than 10 days with sustained high values of satellite-derived Chl-a, K_d(490), and particulate backscattering coefficient at 443 nm. The high attenuation of light due to ash, reducing the penetration depth to less than 10 meters during the first period after the eruption may have had implications on ecological processes and biogeochemical cycles in Tongan waters.

KEYWORDS

chlorophyll-a (Chl-a), HTHH, light attenuation, particle backscattering, ocean currents, volcanic ash, remote sensing

1 Introduction

An extraordinary and powerful eruption within the mostly submerged Hunga Tonga-Hunga Ha'apai (HTHH) volcano (20.64° S, 175.19° W) in the Kingdom of Tonga, occurred on 15 January 2022 (Coordinated Universal Time). Situated in the Pacific Ocean, the HTHH volcano is approximately 60 km northwest from the largest Tongan island, Tongatapu.

The volcanic blast was enormous, sending shockwaves across the globe which were heard across the Pacific and as far as Alaska in the United States of America (Cappucci, 2022). Captured by Earth-orbiting satellites, the blast was strong enough to send a thick layer of volcanic ash into the lower stratosphere, subsequently covering islands across the Tongan group which comprises an archipelago of 169 islands, and is home to 105,000 people (NOAA, 2022). The volcano had been erupting at smaller scales between 20 December 2021 and 5 January 2022 prior to the main event (Cronin, 2022). According to literature, an eruption of this magnitude occurs once every thousand years and has never been seen in the modern scientific era (Witze, 2022). Within 30 minutes of the eruption, a giant umbrella-shaped ash plume covering 300 km in diameter was formed, propelling ash and volcanic gas over 30 km into the atmosphere (Cronin, 2022). The nearby Tongatapu and Eua island groups were blanketed with ash up to 5 to 50 mm thickness (The World Bank, 2022).

Prior to 2014, the HTHH consisted of two andesitic islands (Hunga Tonga in the northeast and Hunga Ha'apai in the west, and have had past major eruptions in 2014, 2009, 1988, 1937, and 1912 (Bryan et al., 1972; Mantas et al., 2011; Smithsonian Institute, 2019). Some information suggests that HTHH and the latter volcano described here has had catastrophic eruptions similar in scale to the 2022 eruption about 1000 and 2000 years ago, and the volcanic edifice was at times a huge volcano that periodically collapses during these catastrophic events (Cronin et al., 2017).

Ocean color observed *via* satellite sensors is a tool for detecting, monitoring, and mapping phytoplankton chlorophyll biomass and has already been used to investigate major features after submarine eruptions, typically resulting in a discoloration of seawater around the site and the emergence of consolidated or fragmented pumice rafts (Mantas et al., 2011; Eugenio et al., 2014). These discolored waters can last days or weeks, appearing milky in color or yellowish-brown compared to the surrounding ocean, depending on its composition. In 2019, discolored sea water was described from three different satellite sensors following an undersea volcanic eruption occurring off Fonualei, about 65 km north of Tongatapu (Whiteside et al., 2021). Ocean color (i.e., spectral reflectance) was utilized to discriminate between discolored waters, consolidated pumice, and fragmented pumice rafts (formed from magma that encounters water). In addition, sea surface temperature (SST) was examined and reflected changes in emissivity of pumice in the infra-red. A striking characteristic of the 2019 discolored waters, however, came from satellite estimates of chlorophyll-a concentration (Chl-a), which measured lower than the surrounding Chl-a. Their makeup is typically of hydrous oxides which are formed when aluminum and iron-rich acidic waters mix with seawater, or due to an outflow of neutral-pH waters (Urai and Machida, 2005; Sakuno, 2021). In contrast, after the 2022 January eruption, a giant Chl-a patch with unusually high concentration was found in the area of the discolored waters around the HTHH volcano. This patch was observed by satellite imagery for at least two weeks. A detail work on such discoloration were carried out following Tagoro eruption in October 2011 in the Canary Islands, Spain (Fraile-Nuez et al., 2012; Santana-Casiano et al., 2013; Ariza et al., 2014; Santana-González et al., 2017; González-Vega et al., 2022). The eruption has led to physical and chemical implications on the surrounding waters such as temperature changes, ocean acidification, nutrient enrichment, and deoxygenation (Fraile-Nuez et al., 2012; Santana-Casiano et al., 2013). As a result, the local marine ecosystem experienced high rates of mortality (González-Vega et al., 2022) including a reduction of epipelagic stocks and disruption of diel vertical migration of mesopelagic organisms (Ariza et al., 2014) and species richness decline during the eruptive phase (Ferrera et al., 2015).

The present work focuses on biological and optical properties extracted by Sea Data Analysis Software (SeaDAS) applied to a time series of National Aeronautics and Space Administration (NASA) satellite images acquired pre- and post-eruption (15 January - 2 February 2022). Importantly, the study aims at explaining the apparently high Chl-a values occurring post-eruption. We hypothesize that the origin of the material expelled by the volcano and the elevated Chl-a values are not related to phytoplankton growth but rather to the ash itself deposited in the upper ocean and, consequently, is the result of an erroneous calculation due to a specific optical signature confounded with the Chl-a signature. We further discuss the influence of ocean currents on dispersal patterns of the ash patch and of the gradual decrease of the attenuation signal, which is interpreted as due to the sinking of particles with time. The rest of the manuscript is organized as follows: Section 2 describes the data and methods used in the study, Sections 3 and 4 present and discuss results, and finally Section 5 provides concluding remarks.

2 Data and methods

2.1 Satellite data (MODIS, VIIRS and OLCI)

Ocean color products of NASA and Copernicus Marine Environment Monitoring Service (CMEMS) were used in this

study. A series of ocean color images from 14 January to 2 February 2022 were examined. Daily retrievals of satellite images from Moderate Resolution Imaging Spectroradiometer (MODIS) onboard the Aqua and Terra satellites at spatial resolution of 1 km and Visible Infrared Imaging Radiometer Suite (VIIRS) onboard Suomi-NPP at 750 m were selected and extracted from NASA's Ocean Color website (Table 1). Level 2 (L2) images were created using the NASA SeaDAS software package. For higher resolution viewing, a true color RGB Sentinel-2 mosaic image at a 60 m resolution acquired on 17 January 2022 was taken from the Copernicus Open Access Hub and visualized using the Sentinel Application Platform (SNAP) package (Figure 1A). The study area comprises the Tongan region at 18 to 23.5° S, 172 to 178°W (Figure 1B).

2.2 Satellite data analysis tools

Individual MODIS/VIIRS images were extracted and reprojected onto a Plate Carrée grid to allow comparisons for each date by applying the Cartopy geospatial data processing package into Python 3. As in Whiteside et al. (2021), we examined various daily products derived from the L2 product in SeaDAS using standard MODIS satellite processing. These included the Rrs suite and inherent optical properties in MODIS and VIIRS, i.e., Rrs (Rrs 443, Rrs 551 or 555, 671 or 678 nm in sr^{-1}), backscattering coefficient at 443 nm, b_{bp}(443) ("b_{bp_giop}" GIOP), Chl-a, K_d(490) and normalized fluorescence line height or nFLH. It should be noted that caution must be taken with K_d values presented in this paper, which were derived from Rrs ratios in the blue and green using the operational NASA algorithm based on (Austin and Petzold, 1981). In Case 2 waters, the situation after the eruption when ashes are present, the K_d retrievals may be inaccurate, although good performance was reported below 0.2 m^{-1} (Lee et al., 2005).

Gilerson et al. (2008) found from simulations that the relative contribution of the fluorescence component to the reflectance spectra peak in the near infrared (NIR) decreases rapidly with increasing concentration of non-algal particles mostly because of the increased contribution of the elastic component to the total reflectance, affecting the performance of the nFLH retrieval. Therefore, we examined the possibility to correct nFLH values in the case of the 2022 patch reflectance by applying an algal bloom index (ABI) to reduce the false-positive detection (Hu and Feng, 2016). For MODIS, ABI is defined as ABI = nFLH/[1 – (Rrs547 – 0.0015) a] where nFLH and Rrs547 are default MODIS products and a is an empirical factor.

The CMEMS "cloud free" daily interpolated K_d(490) product and the penetration depth ($1/K_d$) at 4 km resolution was specifically used (ref no. 2.6) over the MODIS and VIIRS K_d and $1/K_d$ products as it was already interpolated, making calculations for volume estimates of the discolored water patch possible. This product uses a combination of sensors including MODIS-Terra, VIIRS, OLCI S3A and S3B, and the algorithm used (Morel et al., 2007) and validation for interpolated "cloudless" K_d demonstrated good correlation (R^2 = 0.81) with global *in-situ* measurements according to the quality information document released for the K_d product. When extracting K_d values from CMEMS and MODIS on the 2022 patch, we found that values from CMEMS (which ranged from 0.05 to 0.12 m^{-1} at the center of the patch) were lower in comparison to MODIS (0.05 to 0.2 m^{-1}), and this discrepancy can result from both inversion algorithms and/or from the spatial averaging.

Using SeaDAS software, all MODIS-VIIRS optical parameters (Rrs, b_{bp}, Chl-a, K_d, nFLH) were extracted at

TABLE 1 List and acquisition period of L2 MODIS and VIIRS tiles used for this study.

Date (UTC)	Sensor	Tile ID	Acquisition time (UTC)
15 Jan 2022	MODIS Aqua	A2022015015000	01:50 - 01:54
16 Jan 2022	VIIRS S-NPP	V2022016014800	01:48 – 01:53
17 Jan 2022	MODIS Aqua	A2022017014000	01:40 – 01:45
18 Jan 2022	VIIRS S-NPP	V2022018011200	01:15 – 01:15
19 Jan 2022	MODIS Terra	T2022019214000	21:40 – 21:44
20 Jan 2022	MODIS Terra	T2022020222000	22:20 – 22:24
21 Jan 2022	VIIRS S-NPP	V2022021015400	01:54 – 01:59
22 Jan 2022	VIIRS S-NPP	V2022022013600	01:36 – 01:41
23 Jan 2022	MODIS Terra	T2022023211500	21:15 – 21:19
24 Jan 2022	MODIS Aqua	A2022024014500	01:47 – 01:47
25 Jan 2022	VIIRS S-NPP	V2022025004200	00:42 – 00:47
26 Jan 2022	MODIS Terra	T2022026214500	21:45 – 21:50
27 Jan 2022	VIIRS S-NPP	V2022027014200	01:42 – 01:47
02 Feb 2022	MODIS Terra	T2022033215000	21:50 – 21:54

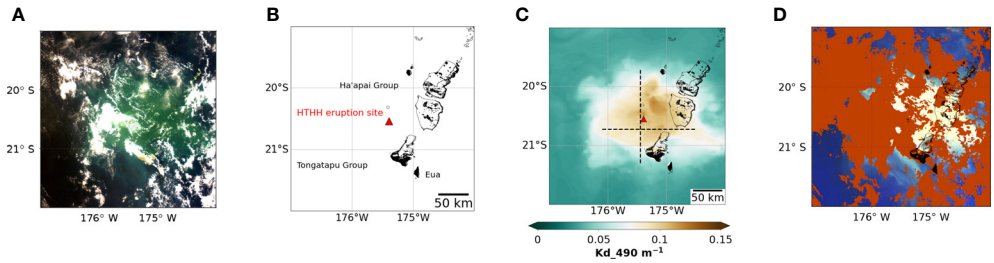


FIGURE 1
(A) True Color MODIS image showing the Tongan islands surrounded by discolored waters on 17 January 2022. **(B)** Map of Tongatapu island and other island groups in Tonga indicating the eruption site of HTHH (in red). **(C)** Interpolated CMEMS K_d concentration on 17 January 2022 with a coral reef shapefile overlay published by the Tongan Department of Environment (outlined in black around land masses). The dashed black lines across the patch depict the analyzed line transects along latitude of 20.73°S and longitude of 175.45°W. **(D)** RGB L2 composite image of Rrs at 443, 555 and 678 nm. Cloud cover is masked in red

source resolution and then averaged (on 9 x 9 pixels) from the center of each discolored water patch i.e., where the highest values were present (longitude [175.57° W, 174.1° W], latitude [20.79° S, 20.36° S]) at the eruption site. Extractions of these optical parameters were made at similar intervals before, during, and after the event (29 December 2021, 17 January 2022, 26 January 2022) to show the magnitude of the effect of the eruption.

From CMEMS K_d, Hovmöller diagrams were created using boundaries set along horizontal (longitude [176.1° W, 174.5° W], latitude [20.73° S]) and vertical (longitude [175.45° W], latitude [21.3° S, 19.7° S]) line transects (Figure 1C), to illustrate the distribution of the patch for each day in January from east to west and north to south. The diagrams were generated using the Matplotlib visualization library and Xarray package in Python 3. Time-evolution of the penetration depth ($1/K_d$) average values along the horizontal line transect was presented over time, and over longitude for the same period as the Hovmöller diagrams. It was checked that the same transect could be kept throughout the post-eruption study period as the patch moved sufficiently slowly. For comparison of the two eruption effects on ocean color, the same suite of parameters was extracted for the last 2019 eruption studied though the eruption site was farther north than the 2022 one (longitude [174.72°W, 174.6°W], latitude [18.48°S, 18.43°S]) (Whiteside et al., 2021).

To delineate the surface of the patch from the surrounding ocean, the b_{bp} threshold given in Whiteside et al. (2021) for the 2019 eruption (b_{bp_giop} 443 nm > 0.0032 m^{-1}) could not be used as it included too many "non-enriched" oceanic pixels. Therefore, to minimize non-enriched pixels in the calculation of the patch surface, a higher threshold for b_{bp_giop} 443 nm had to be chosen that was equivalent to a value of $K_d(490)$ > 0.052 m^{-1}, and similar to the value used for detecting high material-enriched waters in coastal areas (Zhang and Fell, 2007). Then, the penetration depth ($1/K_d(490)$) was used to give an estimate of the volume of water impacted by the total amount of material deposited using the formula:

$$Volume\ of\ patch = \sum \left(\frac{1}{K_d}\ x\ pixel\ width\ x\ pixel\ length \right)$$

where the discolored patch was present.

Daily mean surface current velocities were superimposed onto the b_{bp} L2 images on a Plate Carrée grid with the already available 'quiver' and 'quiverkey' functions within the Matplotlib library and generated in Python, displaying ocean current direction in meters per second ($m.s^{-1}$). This function allowed superimposing 9 km x 9 km current data over 4 km x 4 km pixels.

2.3 CMEMS nutrient and ocean surface current data

To further evaluate whether the high levels in the Chl-a band around the volcano (described in Section 3) were due to an unusual phytoplankton bloom (despite the time lag seeming inconsistent with growth) a modeled forecasted dataset from the CMEMS database for 4 types of nutrients were explored to identify whether available pre-eruption nutrients allowed phytoplankton growth. These nutrient parameters included dissolved iron (Fe(II)), nitrates(NO_{3-}), phosphate (PO_4), and dissolved silicate ($Si(OH)_4$). Daily mean levels of Fe(II), $Si(OH)_4$, PO_4 and NO_{3-} were extracted from CMEMS over a 4-month period from December 2021 to March 2022. The dataset is part of the output of a biogeochemical global ocean analysis and forecast system at 1/4-degree resolution that provides files of daily and monthly mean biogeochemical variables.

To analyze the influence of ocean currents on dispersal patterns of the enriched patch, daily mean surface horizontal velocities were used. The gridded CMEMS product consists of

daily global ocean forecasts and real-time data at a spatial horizontal gridded resolution of 0.083° (9.213 km).

2.4 Ash characterization

Ash samples were collected on 26 January 2022, eleven days after the eruption, at 3 different locations on Tongatapu island. These fine particles were black and powdered with different grain sizes. They were constituted by fine particles of mainly 200-700 μm with a large proportion of pumice. The samples were analyzed for major elements using the Inductively Coupled Plasma Atomic Emission Spectroscopy (ICP-AES) in two different laboratories, including LAMA (Laboratoire des Moyens Analytiques) at IRD (Institut de Recherche pour le Développement) in Nouméa, New Caledonia and Geo-Ocean in Brest, France. Samples were analyzed after dissolution of finely crushed samples by alkaline fusion.

3 Results

3.1 Satellite observations

Large water discoloration around the HTHH volcano was evidenced from L2 RGB true color MODIS images following the major eruption (Figure 1D) after the eruption's effect on the atmosphere on 15 January 2022. The masked L2 'MODGLINT' flag from MODIS and VIIRS products was applied to confirm that this was indeed water discoloration and not a result of sun glint (as glint can introduce similar features). This discoloration was directly associated with the new island formed during the 2015 eruption and then destroyed by the current eruption (oceanic patch elongated in a south-west direction). On 17 January 2022, the largest observed discolored water patch was captured by a Sentinel-3 image centered on the HTHH eruption reaching approximately the same size and center as the atmospheric ash plume which was 650 km in diameter. Chlorophyll-a concentration calculated in SeaDAS was within the range of 0.15 to 2.7 $mg.m^{-3}$. The optical signature of the MODIS discolored water patch was characterized by high attenuation coefficient $K_d(490)$ between 0.1 to 0.16 m^{-1} from its borders toward the center of the patch.

3.2 Optical characteristics of discolored waters

Figure 2 illustrates the main spectral patterns for three chosen dates: 18 days before the eruption (29 December 2021) (Figures 2A–E), 1 day after the eruption (Figures 2F–J), and 10 days after (Figures 2K–O) on 17 and 26 January 2022. There were no significant changes in the suite of products observed prior to the major eruption. High Chl-a (up to 1.93 $mg.m^{-3}$) for this region were observed immediately after the eruption using a standard OCI algorithm. Such concentrations are exceptional particularly in oligotrophic waters around Tonga (OUTPACE cruise, Dupouy et al., 2018) as even after 9 days, on 26 January 2022, Chl-a concentrations still experienced higher than expected values (> 0.3 $mg.m^{-3}$). On 17 January 2022, Rrs at 443 nm, Rrs443, was between 0.01-0.015 sr^{-1}. Such reflectance values were higher than observed in normal oligotrophic waters (~0.008-0.009 sr^{-1}). Nine days later, on 26 January 2022, Rrs443 values returned to normal with only restricted areas of higher absorption mainly related to coral reef areas within the Ha'apai group of islands east of the eruption in Tonga (~0.005 sr^{-1}). Similarly, high Rrs at 555 nm, Rrs555, in the green/yellow wavelength was observed in areas of water discoloration compared to the surrounding normal ocean values (0.0165 sr^{-1}). The Rrs555 reflectance in MODIS continued to measure 6 times higher than normal in the Tongan area. This influences the result of the calculation of Chl-a as the change is disproportionate in the green and blue channels (because this ratio is used in the polynomial equation of the algorithm).

Similar results of high reflectance values were seen in the Rrs at 678 nm, Rrs678. On 26 January 2022, values were still above the normal oceanic value (Rrs678 > 0.0003 sr^{-1}) within the zone of discolored waters. On 17 January 2022, values in the center of the patch (Rrs 678 > 0.0041 sr^{-1}) were approximately 12 times the normal predicted oceanic signal. Note the presence of high normalized fluorescence with values increasing by a factor of 3 from 0.11 to 0.347 from December to 17 January 2022, and then back to normal on 26 January (0.091 nFLH $mWcm^{-2}$ μm^{-1} sr^{-1}). Such high values are linked to elevated values of Rrs678.

The magnitude of simultaneous increases of reflectance in all channels just after the eruption is well illustrated at Figure 3, where Rrs spectra extracted on the 17 January 2022 (Jan_17) are compared with those selected in surrounding waters or outside of the patch and with pre- (Dec_29) and post-eruption (Jan_26) spectra (Figure 3). Note that there is no evidence of a fluorescence peak in the discolored water patch. One would expect a dip at 667 nm due to Chl-a absorption, but the Rrs values at 667 nm and 678 nm are similar in the brown curve, even slightly lower at 678 nm, suggesting that the baseline reflectance at 678 nm, estimated from Rrs values at 667 and 748 nm, was too low. This might be due to an underestimation of the Rrs at 748 nm in the iterative scheme designed to account for non-negligible Rrs in the near infrared (Bailey et al., 2010). In that scheme, the slope of the backscattering coefficient in the red and near infrared is estimated empirically using a dataset (Werdell and Bailey, 2005) that did not include the type of waters with volcanic ash considered in the present study.

Table 2 summarizes the optical properties of discolored waters pre- (29 December 2021), and post-eruption (2 days after, i.e., 17 January 2022, and 9 days after the eruption, i.e., 26 January 2022). Increases between 29 December 2021 and 17

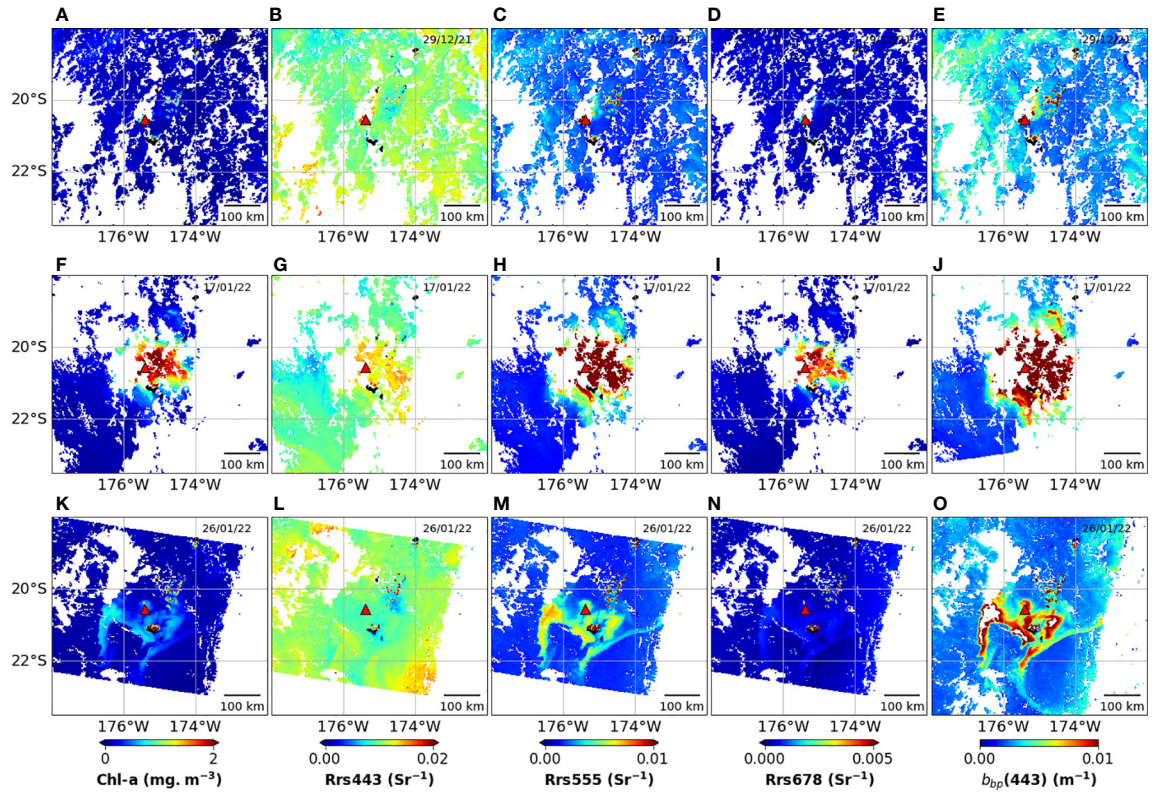


FIGURE 2
Comparison of MODIS and VIIRS extracted Chl-a, Rrs and Bbp products pre-eruption **(A–E)** on 29 December 2021, 2 days after the eruption **(F–J)** on 17 January 2022, and 9 days after the eruption **(K–O)** on 26 January 2022.

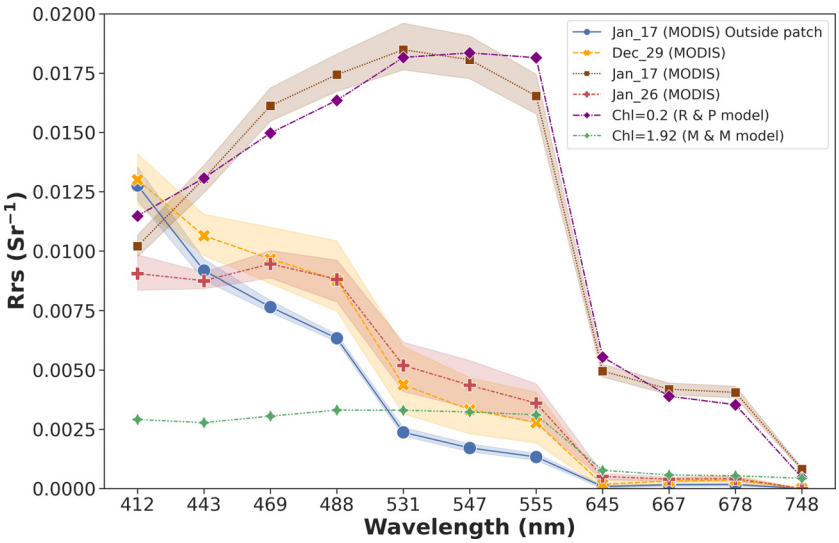


FIGURE 3
Rrs spectra of pixels inside the discolored water patch and outside the patch pre- and post-eruption (December 29, 2021; 2 days after the eruption on January 17, 2022; 9 days after the eruption on January 26, 2022) and another on 17 January if Chl=0.2 mg.m^{-3} using the Park and Ruddick (2005) model, and Chl=1.92 mg.m^{-3} using the Morel & Maritorena (2001) model. Pixels outside the patch were taken on 17 January 2022.

TABLE 2 Optical parameters for the 15 January 2022 eruption were extracted from MODIS/VIIRS products at the center of the patch and from CMEMS for K_d for comparison.

	BEFORE eruption (29 Dec 2021)	2 days AFTER eruption (17 Jan 2022)	9 days AFTER eruption (26 Jan 2022)	Ratio after (17 Jan 2022) to before (29 Dec 2021)
Chl-a ($mg.m^{-3}$)	0.17	1.93	0.34	11
Rrs 443 (sr^{-1})	0.0107	0.0131	0.0087	1
Rrs 555 (sr^{-1})	0.0030	0.0165	0.0035	6
Rrs 678 (sr^{-1})	0.0003	0.0041	0.0004	12
$K_d(490)$ (m^{-1})	0.040	0.158	0.055	43
CMEMS $K_d(490)$ (m^{-1})	0.034	0.105	0.045	
$b_{bp}(443)$ (m^{-1})	0.005	0.035	0.006	7
nFLH ($mWcm^{-2}$ μm^{-1} sr^{-1})	0.11	0.347	0.091	3

All spectral and IOP data in this table were obtained from MODIS products.

January 2022 by factors of slightly above 1, 6, and 12 for Rrs 443, Rrs 555 and Rrs 678, respectively, are not in favor of the time-lag of a phytoplankton bloom. Blooms of this magnitude would not occur immediately after an eruption. Table 2 also displays K_d (490) and $b_{bp}(443)$, calculated from SeaDAS. In the discolored patch, $K_d(490)$ and $b_{bp}(443)$ were respectively up to 0.16 and 0.035 m^{-1} at its center on 17 January 2022, which is 4 and 7 times greater than the pre-eruption December value. $K_d(490)$ for 17 January 2022 showed highest intensity at the center of the plume between 0.1 – 0.3 m^{-1}. Such $K_d(490)$ values in the patch center is 5 times the measured oceanic values for the Tonga region during the OUTPACE cruise in March 2015, i.e., 0.022 m^{-1} (Dupouy et al., 2018). Outer parts of the plume displayed < 0.1 m^{-1} attenuation coefficient. Nine days after the eruption, $K_d(490)$ and b_{bp} recovered to near normal values. Waters north of Tongatapu island, 57 km south of the volcano, and waters situated more than 100 kilometers off the center of the eruption, still experienced a $b_{bp}(443)$ value of 0.0011 m^{-1}, nine days after the eruption.

3.3 Spatial and temporal evolution of the patches

Time evolution of the CMEMS attenuation coefficient K_d (490) is shown in the Hovmöller diagrams along the longitudinal and latitudinal transects crossing the discolored patch (from 176°W to 174.5°W and from 19.75 to 21.25°S) (Figure 1C). At 20.73°S, Figure 4A shows high K_d (between 0.08-0.11 m^{-1}) the day after the eruption on 16 January 2022 between longitudes

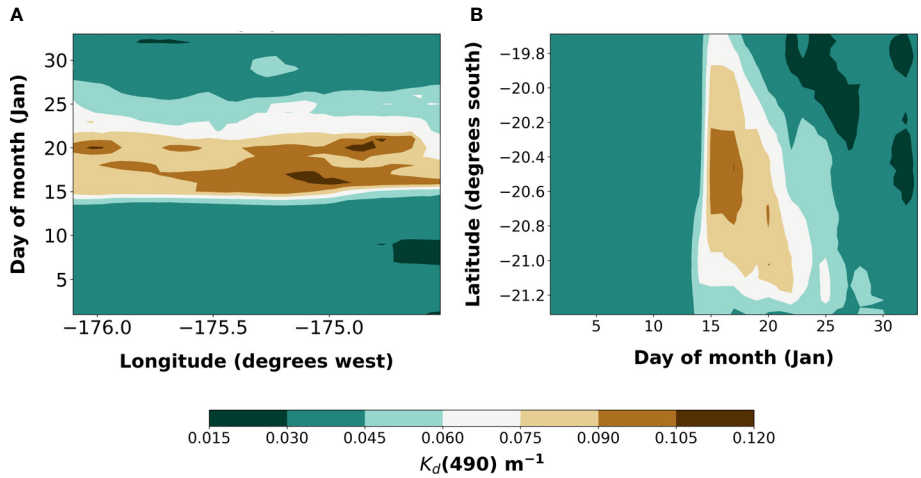


FIGURE 4
Hovmöller plots of CMEMS $K_d(490)$ (in m^{-1}) for the month of January 2022 representing the **(A)** latitudinal transect along 175.45°W, and **(B)** longitudinal transect along 20.73°S within the discolored water patch (location illustrated in Figure 1C). Values are represented from 0.015 to 0.120 m^{-1} for more contrast.

176.1°W and 174.5°W. These high K_d values were sustained for 5 days before gradually decreasing (< 0.075 m^{-1}) and eventually going back to normal (< 0.052 m^{-1}) by 28 January 2022. Along 175.45°W longitude, Figure 4B shows a sudden increase in K_d that had concentrated values (0.07-0.11 m^{-1}) between latitudes 20.2°S and 20.8°S from 16 to 18 January 2022. A shift in the patch southward over time resulted in higher-than-normal K_d values which were maintained until 30 January 2022 compared to the northern part of the transect which normalized to < 0.05 m^{-1} by 24 January.

3.4 Temporal evolution of K_d(490) and estimated volume of suspended material

The average and standard deviation of the penetration depth at 490 nm was extracted on all pixels along the 20.73°S horizontal transect of Figure 1C. The average penetration depth of pixels over the transect increased from 10 m on 17 January 2022 to 32 m by 2 February 2022 (Figure 5A). Water clarity became normal by 2 February 2022.

The penetration depth within the plume's center was approximately 8.8 to 10 m along the transect right after the eruption, and > 10 m in the outer parts of the plume on 17 January 2022 (Figure 5B) preventing most light from penetrating through the water deeper than 10 meters. The penetration depth increased to 17 m on 23 January 2022. Water clarity became normal between 27 January and 2 February 2022, like that of the surrounding open ocean waters (~ 35 meters), and comparable to normal ocean conditions. A measured penetration depth value during the OUTPACE oceanographic cruise off Tongan waters with a profiling spectroradiometer in the Chl-a bloom was 40 m (K_d(490) of < 0.03 m^{-1}) for a Chl-a concentration of 0.3 $mg.m^{-3}$ at the same location in March 2015 (Dupouy et al., 2018).

The associated estimation of the volume of water affected by backscattering material was estimated to be 482 km^3 on 17 January 2022, 257 km^3 on 22 January 2022, and 161 km^3 on 26 January 2022, which is 1 or 2 orders of magnitude higher than the expected volume of ash (0.5 to 10 km^3).

3.5 Ash mineral composition and characteristics

The ash compositions obtained by LAMA and Geo-Ocean are comparable (Table 3), indicating a silica content varying between 53 and 56 wt%, while TiO_2, Al_2O_3, Fe_2O_3, MnO, MgO and CaO fluctuate between 0.49-0.54 wt%, 13.8-15.2 wt%, 10.2-10.7 wt%, 0.164-0.171 wt%, 3.18-3.76 wt%, and 8.59-11.16 wt%, respectively. The total alkali (Na_2O+k_2O) fluctuates between 2.54 and 3.02 wt% whilst P_2O_5 ranges from 0.077 to 0.105 wt%.

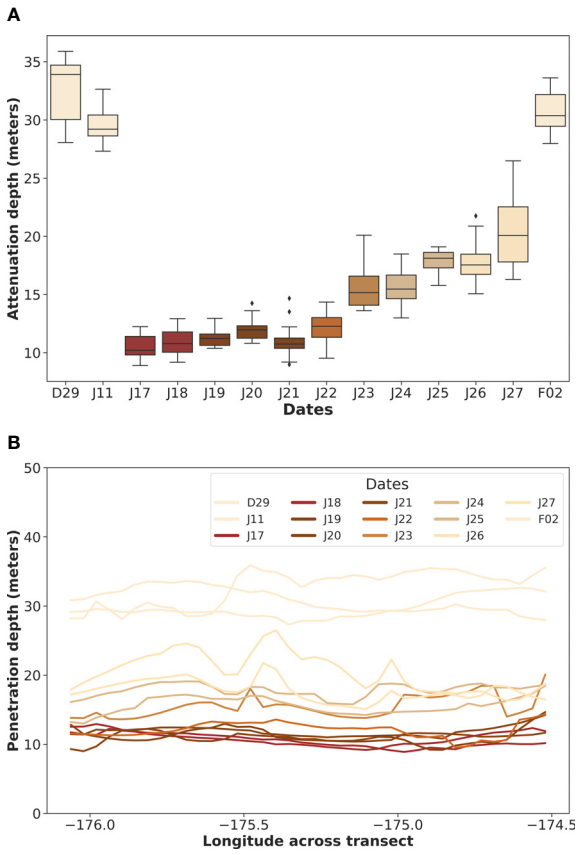


FIGURE 5
(A) Box and whisker plot showing light penetration depth (in meters) along the 20.73°Stransect (illustrated in Figure 1C within the patch) over time, from values of the CMEMS interpolated 1/K_d(490) data. **(B)** Time evolution of the penetration depth along 20.73°S from the earliest day of observations (17 January 2022) to the final day (2 February 2022).

When plotting the SiO_2 versus the total alkali, it appears that all the samples are of basaltic andesite origin (Figure 6).

4 Discussion

4.1 Confusion with an atmospheric patch

Confirmation that the observed plume was not a result of atmospheric release through the observation of sulfur dioxide (SO_2) was given by the TROPOspheric Monitoring Instrument (TROPOMI). The TROPOMI data showed that a SO_2 patch over Tonga was much greater than the oceanic patch and had drifted to the west in less than two days toward Fiji and Australia (https://so2.gsfc.nasa.gov/). Within four days of the eruption, no SO_2 signal could be recorded over the area of the discolored water patch.

TABLE 3 Chemistry of ash samples (in wt%) collected on Tongatapu island after the 15 January 2022 eruption.

	Geo-Ocean (Brest, France)			LAMA (IRD Noumea, New Caledonia)					
	Atele	Ngele'ia	Queen Salote college	Queen Salote college	Queen Salote college	Atele	Atele	Ngele'ia	Ngele'ia
SiO_2	55.3	54.1	53.2	55.1	55.1	55.2	54.6	53.6	56.8
TiO_2	0.54	0.52	0.52	0.53	0.52	0.52	0.49	0.52	0.50
Al_2O_3	15.0	14.6	14.5	14.3	14.8	14.0	15.0	13.8	15.2
Fe_2O_3	10.7	10.4	10.5	10.5	10.5	10.3	10.2	10.4	10.3
MnO	0.171	0.169	0.165	0.171	0.169	0.168	0.164	0.168	0.167
MgO	3.76	3.66	3.68	3.33	3.24	3.29	3.18	3.24	3.20
CaO	9.23	9.33	11.16	8.59	8.87	8.73	9.45	10.15	10.94
Na_2O	2.38	2.40	2.13	2.16	2.50	2.49	2.33	2.22	2.16
K_2O	0.42	0.41	0.42	0.52	0.50	0.52	0.48	0.51	0.49
P_2O_5	0.084	0.084	0.091	0.092	0.079	0.087	0.077	0.105	0.083
LOI	1.35	2.73	2.50						
Total	98.94	98.46	98.79	95.33	96.16	95.35	95.92	94.65	99.82

4.2 Comparison with the 2019 eruption

It is remarkable that discolored water signatures of the 2022 eruption are different from the ones in 2019. The 2019 eruption was accompanied by a spread of discolored waters which could be delineated and followed for 2 weeks (Whiteside et al., 2021) in addition to large consolidated and fragmented pumice rafts. The spectral signature of the discolored waters was described as "milky", as previously reported in Mantas et al. (2011). In 2019, Rrs in the 443-channel appeared higher than normal and calculated Chl-a was lower than the surrounding environment. Such discolored oceanic patches ("milky waters") were well visible from December 2021 on the NASA Worldview Earthdata website (https://worldview.earthdata.nasa.gov/), as first indications of eruptive events, following atmospheric effects above the HTHH volcano on 20 December, 22 December 2022. Such pre-eruption discolored waters were similar to the ones already observed in 2019 (Whiteside et al., 2021) or after the 2008 eruption (Mantas et al., 2011). Chlorophyll-a calculated in 2019 were low and waters considered to be more oligotrophic than the surrounding ocean. Moreover, change rates of OC and IOP products prior to and after the eruption were small (by a factor between 2 and 3, Table 4).

The discolored waters following the 2022 eruption thus differ immensely from previous ones already described in the literature for all parameters.

4.3 Evidence of non-biological origin of the patch

Conclusive evidence of rapid phytoplankton growth is lacking, as seen from the sudden large increase on 17 January 2022 in the Chl-a, K_d or b_{bp}, and nFLH series that occurred only a few days after little signal was observed just before the eruption, making it incompatible with a bloom formation. Chlorophyll-a was observed from 25 December 2021 to 26 January 2022. Conditions were normal up until 11 January, before clouds covered the area from 12 January to immediately post-eruption. A sudden rise in Chl-a (over 10 times greater) was evident at the location of the volcano directly afterwards, as similarly seen in a time series in Barone et al. (2022); see their Figure 2). The immediate positive effect of the eruption on Chl-a

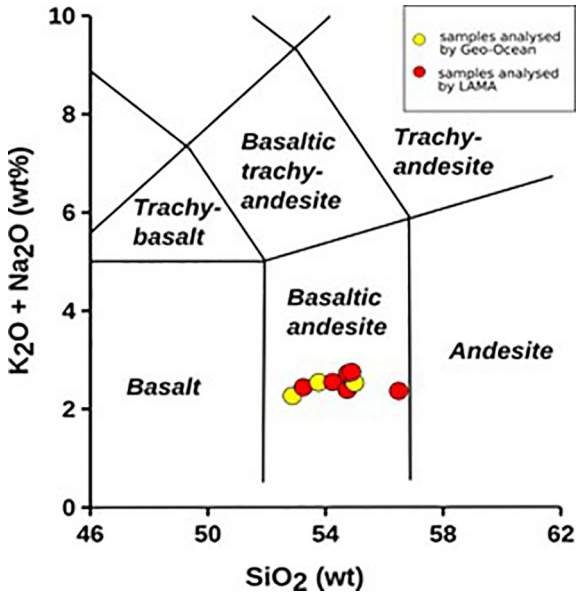


FIGURE 6
SiO_2 versus total alkali of ash samples analyzed by Geo-Ocean (in yellow) and LAMA (in red) indicating that the ash samples are of basaltic andesite composition.

TABLE 4 Optical parameters for the 9 August 2019 eruption were extracted from MODIS/VIIRS products at the center of the patch.

	BEFORE eruption (05 Aug 2019)	2 days AFTER eruption (09 Aug 2019)	9 days after eruption (16 Aug 2019)	Ratio after eruption (9 Aug 2019) to/before eruption (05 Aug 2019)
Chl-a ($mg.m^{-3}$)	0.07	0.10	0.08	2
Rrs 443 (sr^{-1})	0.0103	0.0175	0.0098	2
Rrs 555 (sr^{-1})	0.0019	0.0056	0.0019	3
Rrs 678 (sr^{-1})	0.0003	0.0005	0.0003	2
$K_d(490)$ (m^{-1})	0.029	0.044	0.033	2
$b_{bp}(443)$ (m^{-1})	0.002	0.005	0.002	2

All spectral and IOP data in this table were obtained from MODIS products.

has rarely been documented despite numerous analyses of the MODIS satellite imagery following eruptions. Mantas et al. (2011) did not find any Chl-a enrichment just after the 2008 eruption off Tonga and found no direct link spatially to the eruption. Some enrichment was observed about 2 months after the event, and without spatial relation to the eruption site. During the previous 2019 eruption, discolored waters were not accompanied by high Chl-a but rather characterized a lower-than-normal Chl-a in milky waters, and Whiteside et al. (2021) hypothesized that silica, phosphate, and iron from the eruption would not be available soon after as mineralization by bacteria is not rapid enough to invoke a phytoplankton bloom. Similarly, following the 2011 volcanic eruption in the Canary Islands, Eugenio et al. (2014) concluded that the accuracy in chlorophyll monitoring *via* remote sensing during the eruptive phase was flawed due to the alterations provoked in the composition of the water. They established that OC MODIS models completely fail in environments of moderate turbidity.

We consider that nFLH extracted from the default L2 MODIS products was overestimated due to the presence of ashes, and thus is not reliable, which is expected for Case 2 waters (Gilerson et al., 2008; Hu and Feng, 2016) Gilerson et al. (2008) found that for concentrations of non-algal particles >5 $g.m^{-3}$ the FLH algorithm was almost non-effective. Also, as indicated in Section 3, the retrieved water reflectance in the discolored patch does not exhibit a fluorescence signal, and the high nFLH values might be due to underestimating the baseline reflectance by using a very low water reflectance at 748 nm in the atmospheric correction scheme. Ahn and Park (2020) evaluated the Bailey et al. (2010) near-infrared reflectance model used to estimate Rrs at 748 nm in turbid waters against simulations and *in situ* data and concluded that it underestimated Rrs at 745 nm. Differences increased with increasing turbidity but were also large for retrieved Rrs values of <0.001 sr^{-1} at 745 nm, which corresponds to the Rrs values at 748 nm displayed in Figure 3. Furthermore, Ruddick et al. (2006)'s similarity spectrum, established from ship-based reflectance measurements in the red and near infrared and valid for a wide range of turbid waters, indicated that the Rrs values at 748 nm obtained in the discolored patch were much too low than those expected for the estimated Rrs values at 667 nm, providing additional indirect evidence of an underestimation of the baseline reflectance at 748 nm.

The ABI values within the patch center, obtained using an algorithm by Hu and Feng (2016), gave lower nFLH values than that of the MODIS operational algorithm, but higher than the surrounding waters. That coefficient, however, was determined for coastal waters of the Gulf of Mexico and may not be applicable to the discolored patch. According to our discussion above, there should not be significantly higher fluorescence in the patch after the eruption, and thus can calculate α which eliminates false-positive detection for the fluorescence signal. The α value used was three times higher than the one used for the phytoplanktonic blooms in Florida waters (i.e., 240 instead of 80). It corresponds to high turbidity, expected to characterize the patch, and correspond to extremely high values of MODIS $b_{bp}(443)$.

Such high Chl-a values were considered to be real in a recent study by Barone et al. (2022), who concluded that dramatic phytoplankton growth observed during the eruptive process was stimulated by nutrients released from volcanic ash. This is a strong counterhypothesis which unfortunately cannot be verified as no *in situ* data of Chl-a were available immediately after the eruption (*Ministry of Fisheries, Tonga via Pers. Comm.*). Based on the CMEMS modeled nutrient data, iron and nitrate levels were around 0 µM at the end of December 2021 preceding the first eruption, as expected for this ultra-oligotrophic region (e.g., Moutin et al., 2017). Modeled silica from the southwest of Tonga (1.09-1.17 µM) in December 2021 (1.12-1.88 µM) and modeled phosphate which is the main nutrient favoring diazotrophic blooms in the region (Moutin et al., 2012), i.e., 0.11-0.2 µM in December 2021 and January 2022, could not be a source for phytoplankton at the time of the eruption.

The discolored water patch's round shape and size in the true color imagery was proportional to the spread of the atmospheric ash cloud over the eruptive column. This suggests that such discoloration of the water could be the result of ash fallout. The ash cloud also covered Tonga's capital, Nuku'alofa, where ash samples were collected and analyzed in this work. The P_2O_5 content in the ash was relatively small (0.077-0.105 wt%)

and may not be the main nutrient source of phosphorus if blooming did occur. The iron content was not exceptional either in comparison to other volcanoes. The question of hydrothermal input of dissolved inorganic nutrients creating the fertilization of local phytoplanktonic communities has not yet been answered (González-Vega et al., 2020). However, the ash deposits were mainly of juvenile magma materials which thus suggest less input from hydrothermal manifestation if any.

Another aspect of the patch evolution is the lack of Photosynthetic Available Radiation (PAR) in the middle of the patch. A phytoplankton bloom is unexpected here, as the penetration depth was reduced right after the eruption to less than 6 meters, preventing light from permeating through waters deeper than 10 meters.

Thus, the explanation of high Chl-a associated with higher-than-normal reflectance in the blue and green channels must be found elsewhere than to a phytoplanktonic origin. As the MODIS Chl-a algorithm is based on a combination of blue/green reflectance ratios, and as this blue/green reflectance ratio is influenced by the high Rrs555 value, the resulting Chl-a concentration is likely erroneous. In such highly turbid waters, Rrs sensitivity to Chl-a becomes very small in that spectral range. Two algorithms designed for coastal turbid waters, those of (Tassan, 1994) and Gitelson et al. (2008), when applied to the average Rrs spectrum observed on January 17 (Figure 3, brown curve), also yielded high but very different Chl-a values, i.e., 1.4 and 9.8 $mg.m^{-3}$, respectively. Tassan's algorithm utilizes Rrs at 4 wavelengths in the blue and green (412, 443, 490, and 555 nm), while Gitelson et al. (2008) uses Rrs at three wavelengths in the red (665, 715, and 750 nm). Using wavelengths in the red is especially difficult, in view of the relatively low signal in this spectral range and the uncertainties in the SeaDAS atmospheric correction, especially in Rrs at 748 nm, as discussed above. All the proposed Chl-a algorithms, however, have not been established using data collected in waters contaminated by volcanic ash and are not expected to provide reliable results in such situations. It is therefore highly probable that those are incorrect Chl-a values, and that ashes themselves were controlling the ocean color signature.

To provide additional evidence about the non-biogenic nature of the highly reflective patch, we compared the b_{bp}(443)/Chl-a values retrieved by SeaDAS software from the various Rrs spectra of January 17 (Figure 3) to those of the (Morel and Maritorena, 2001) model developed for Case 1 waters, the type of waters encountered around Tonga. The average satellite-derived and model b_{bp}(443)/Chl-a values were 0.0187 ± 0.0002 $m^2.mg^{-1}$ and 0.0023 ± 0.0001 $m^2.mg^{-1}$, respectively, i.e., 8.1 times higher than the former, suggesting that non-algal particles dominated the backscattering coefficient. The 0.0187 $m^2.mg^{-1}$ value is probably underestimated because, as indicated above, Chl-a is likely overestimated. We also used the Park and Ruddick (2005) reflectance model in inverse mode to retrieve, from the spectral Rrs data, the 3 model parameters, Chl-a, fa, and fb. In this model, the last 2 parameters characterize variability in absorption by CDOM (Colored Dissolved Organic Matter) and non-algal particles and backscattering by phytoplankton and non-algal particles, respectively. The spectral matching applied to the January 17 Rrs spectra gave an average Chl-a of 6.3 $mg.m^{-3}$, which is large. The reflectance model, however, is constrained by bio-optical relations that do not consider ash-contaminated waters, and the retrieval only provides the best combination of the 3 parameters. However, if we fix Chl-a to 0.2 $mg.m^3$, a typical value for waters not contaminated by ash in the region, we obtain a very good match of the average Rrs spectrum of January 17 for $\log_{10}$fb = 1.76 and $\log_{10}$fa = -0.25 (Figure 3, purple curve). This translates, according to the model parameterizations, into a backscattering coefficient at 550 nm and an absorption coefficient at 443 nm for non-algal particles about 56 and 29 times higher than the respective coefficients for phytoplankton, which is not unrealistic in the presence of large amounts of absorbing ash. This much higher backscattering coefficient is consistent with the retrieved average b_{bp}(443) value from the Rrs spectra of January 17, i.e., 0.0359 m^{-1} instead of 0.00097 m^{-1} for phytoplankton (i.e., 37 times higher). In other words, the average Rrs spectrum observed on January 17 is not incompatible with a low Chl-a value of 0.2 $mg.m^{-3}$.

Furthermore, if the reflective patch were of biogenic origin with large Chl-a, i.e., 1.92 $mg.m^{-3}$on January 17 according to Table 2, the Rrs spectrum obtained using the Morel and Maritorena (2001) model would resemble that of Figure 3 (green curve), which is completely different from the observed spectrum (Figure 3, brown curve), with much lower values in the blue than those of non-contaminated waters.

4.4 Evidence of ash origin for the observed spectral signatures

A remarkable impact of the 2022 eruption was the increase of reflectance in all channels, consistent with large amounts of ash, a discolored material in contrast to phytoplankton which is green due to Chl-a absorption in the blue, deposited in the upper ocean layer. The high reflectance spectrum obtained inside the patch on January 17 is compatible with the gray color of the ashes which were collected on land in Tonga.

Considering the very specific optical signature of the patch during the period observed (17-26 January 2022, Table 2, Table 4) the abnormal Chl-a (K_d, or b_{bp}) concentration was much higher than expected for the Tonga region, we conclude that the optical signature described above cannot be attributed to phytoplankton itself but rather to other particles with a high scattering coefficient (i.e., mineral ones). Indeed, the specific backscattering coefficient of minerals is higher than those of living cells and this has already been proven in the post 2019 eruption discolored waters (Whiteside et al., 2021). This also

explains why the backscattering coefficient (much higher than that of phytoplankton cells) also remained at high levels for more than 2 weeks.

Magma released from the volcano erupted explosively, expelling large amounts of ash and pumice. Based on previous compositions, the magma released was not particularly rich in volatiles including sulfur or fluorine. According to their size and color, the ashes made good candidates for explaining the optical signature for the discolored waters. Powdered ash particles in the water column were likely to be the dominant substance and reason for the high Chl-a values and uncorrected fluorescence, extreme values of K_d, or b_{bp}, and Rrs at all channels. *Via* personal communication (Ngaluafe, 2022), ash and pumice were spotted in the Tonga region long after the eruption. Preliminary results from an ecological survey conducted around the HTHH volcano by the NIWA and NIPPON Foundation indicated that ash was still suspended in the water column, months later. Chlorophyll measurements immediately post-eruption around the volcano are unfortunately lacking.

4.5 Implications of the ash patch for the area

4.5.1 Comparison with CMEMS currents

The ash patch on 17 January decreased in size and intensity over time (Figure 7). Dispersal patterns and shape of the ash water patch seem to be influenced by ocean currents for 19 days (15 January to 2 February). Anticyclonic eddies dispersed the southern end of the plume southward and then eastward (see red boxes in Figure 6) eventually causing the plume to follow the currents in the eddy. The southward-oriented currents to the west of the plume (see green boxes in Figure 6) further dispersed the plume southward eventuating in an inverted crown-like shape for the southern end of it. The eastern part of the plume was affected by another anticyclonic eddy (see blue boxes in Figure 6) causing northwestward dispersion. The ash plume centroid moved southwards due to southward currents both to the west and east of the plume.

4.5.2 Permanence of the patch

Laboratory analysis of the ash samples indicated that the ejected material is basaltic and andesitic in composition, resulting in a corresponding rock density of 2600 kg/m^3. However, this is more than twice the density of seawater (1030 kg/m^3) and with such a difference, one would not expect to see suspended and floating material. By way of observation, the particles were small (70-200 μm), however, they had a porosity of 30-40%, which reduced their density to 780-1040 kg/m^3. Thus, we have a density much closer to the density of seawater, which would explain the long-term suspension of the particles. Attenuation decrease may also be linked to the gradual sinking of ashes in the water column as currents were weak in this area. The high porosity of the ashes might explain that the ashes stay in the water column with an almost constant value of K_d, b_{bp} and Chl-a, greater than 10 days in the water column (still visible and disappear only on 2 February).

There is a possibility that the ash optical signature changed over time due to their gradual sinking and filling of microscopic pumice ashes with sea water. Indeed, the reflectance in all

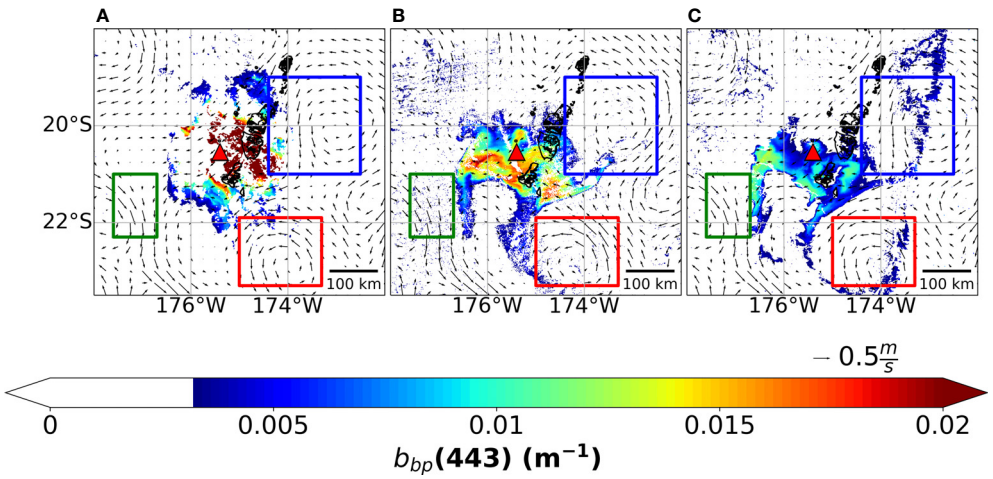


FIGURE 7
Backscattering of particles b_{bp}(443) with superimposed CMEMS ocean surface current velocity on **(A)** 17 January 2022, **(B)** 22 January 2022, and **(C)** 26 January 2022. Current scale is in meters per second (the reference length of the arrow represents 0.5 m/s). The backscattering coefficient threshold of Whiteside et al., 2021 (>0.0032 m^{-1}) was applied to delineate the patch from clouds and from oceanic water with no value.

channels decreases progressively within 10 days post-eruption (Figure 2 and Table 2), with K_d and b_{bp} and Chl-a reaching minimum values by 2 February (Figures 4A, B).

4.6 Implications for coral reefs of Tonga archipelago

Severe deoxygenation may have had serious implications within the surrounding area which was a main cause of mortality in marine life in the early weeks following the 2011 Tagoro eruption (González-Vega et al., 2022). Similarly, the reduction of light from the ashes raised immediate concerns over the health of the coral reef ecosystems after the eruption, notably the smothering of ash particles in waters over corals (Franklin and Storel, 2022). Though impossible to give exact penetration values of $K_d(490)$ above locations where corals are present due to the high bottom reflectance effect of reefs, utilizing $K_d(490)$ gave us an indication of the lack of light provided to corals from ash increase in surrounding waters. Localized decrease of the blue reflectance (linked to a phytoplankton or high CDOM concentration) near the northern reefs of the Ha'apai group of islands, disconnected to the patch, may result from a biological response occurring after several days (from a phytoplankton growth or absorbing CDOM released from reefs). It is likely that coral benthic organisms suffered from lower light penetration in the water during the first three weeks as a function of flushing times over reefs. *In-situ* observations to determine the current state of Tonga's corals that may have been exposed to high turbidity would be necessary. In addition, coral monitoring post-eruption is important to better understand past submarine eruptions in terms of their timing, duration, and intensity (Álvarez-Valero et al., 2018). Further studies are required to assist and aid in forecasting eruptive events.

5 Conclusion

The optical signature of discolored waters observed after the powerful 15 January 2022 eruption (high Chl-a, high reflectance in the blue-green channels) is most likely caused by ash material issued from the eruption that was ejected and deposited into the ocean. The high Chl-a values derived from satellite are likely to be incorrect as nutrients would not be sufficiently available for growth to occur immediately. The presence of ash influenced the ocean color signature, biasing the Chl-a estimates. Although phytoplankton can grow after such an event and even bloom, conclusive evidence for this to have occurred has been lacking and they typically do not develop as quickly as in a day. In addition, particle backscattering in the blue-green channels showed the discolored water patch shape being inconsistent with a Chl-a normal optical signature, further contradicting the observed 'high chlorophyll' using the NASA standard algorithm and therefore highlighting here the direct impact of ashes on ocean color.

To conclude, this study shows how ocean color products tracked the expanse of floating and suspended material (basalt andesitic powdered ashes, and potentially combined with some phytoplankton signature) post 2022 eruption. Surface pumice appeared in a few fragments after this eruption, contrary to the 2019 one which initially saw larger consolidated floating material travel west toward Fiji. The high attenuation of light due to ash, reducing the penetration depth to less than 10 meters during the first period after the eruption may have had strong implications on ecological processes and biogeochemical cycles in the Tongan waters. The study also showed the difficulty of interpreting ocean color signals in this area.

Data availability statement

The original contributions presented in the study are included in the article/Supplementary Material. Further inquiries can be directed to the corresponding author.

Author contributions

AW and CD designed the research. AW, RF, JT, PB, CD and AS analyzed and interpreted the data. AW wrote the original draft CD, RF, PB and AS reviewed and edited the manuscript. CD and AS supervised the study. All authors contributed to the article and approved the submitted version.

Funding

The University of Bergen and the University of the South Pacific supported publication costs through their support of the Norway-Pacific Chair in Ocean and Climate Change. AW's PhD is funded by the « Allocations de recherche pour une thése au Sud (ARTS-IRD) » program and receives support from the Ecole Doctorale Sciences de l'environnement—ED 251-Aix Marseille Université, 2019–2023 and UM 110 Mediterranean Institute of Oceanography.

Acknowledgments

The authors thank NASA for making available the MODIS/VIIRS Aqua data and the SeaDAS data processing software. We acknowledge CMEMS Copernicus data (modeled currents, modeled nutrients, interpolated data of Kd and bbp). We deeply thank Geo-ocean (GO) – UMR 6538 Institut Universitaire Europeen de la Mer (IUEM) and LAMA (Laboratoire des Moyens Analytiques of UAR IMAGO) at the Center IRD of Noumea (New Caledonia) for ash analyses. We also acknowledge

Mr. Poasi Ngaluafe of the Tongan Ministry of Fisheries for providing us with on the ground observations. This work would not have been possible without the ash collection in Tonga done by Etienne Hus of France Volontaires International. RF's and JT's work was supported by NASA under various grants. We acknowledge the University of Bergen and the University of the South Pacific who supported publication costs through their support of the Norway-Pacific Chair in Ocean and Climate Change.

Conflict of interest

The authors declare that the research was conducted in the absence of any commercial or financial relationships that could be construed as a potential conflict of interest.

Publisher's note

All claims expressed in this article are solely those of the authors and do not necessarily represent those of their affiliated organizations, or those of the publisher, the editors and the reviewers. Any product that may be evaluated in this article, or claim that may be made by its manufacturer, is not guaranteed or endorsed by the publisher.

Supplementary material

The Supplementary Material for this article can be found online at: https://www.frontiersin.org/articles/10.3389/fmars.2022.1028022/full#supplementary-material

References

Ahn, J.-H., and Park, Y.-J. (2020). Estimating water reflectance at near-infrared wavelengths for turbid water atmospheric correction: A preliminary study for GOCI-II. *Remote Sens.* 12, 3791. doi: 10.3390/rs12223791

Álvarez-Valero, A. M., Burgess, R., Recio, C., de Matos, V., Sánchez-Guillamón, O., Gómez-Ballesteros, M., et al. (2018). Noble gas signals in corals predict submarine volcanic eruptions. *Chem. Geol. noble gases as geochem. tracers – celebration Pete Burnard* 480, 28–34. doi: 10.1016/j.chemgeo.2017.05.013

Ariza, A., Kaartvedt, S., Røstad, A., Garijo, J. C., Arístegui, J., Fraile-Nuez, E., et al. (2014). The submarine volcano eruption off El hierro island: Effects on the scattering migrant biota and the evolution of the pelagic communities. *PloS One* 9, e102354. doi: 10.1371/journal.pone.0102354

Austin, R. W., and Petzold, T. J. (1981). *The determination of the diffuse attenuation coefficient of Sea water using the coastal zone color scanner* (New York, USA: SpringerLink).

Bailey, S. W., Franz, B. A., and Werdell, P. J. (2010). Estimation of near-infrared water-leaving reflectance for satellite ocean color data processing. *Opt. Express OE* 18, 7521–7527. doi: 10.1364/OE.18.007521

Barone, B., Letelier, R. M., Rubin, K. H., and Karl, D. M. (2022). Satellite detection of a massive phytoplankton bloom following the 2022 submarine eruption of the hunga Tonga-hunga ha'apai volcano. *Geophysical Res. Lett.* 49, e2022GL099293. doi: 10.1029/2022GL099293

Bryan, W. B., Stice, G. D., and Ewart, A. (1972). Geology, petrography, and geochemistry of the volcanic islands of Tonga. *J. Geophysical Res.* 1896-1977) 77, 1566–1585. doi: 10.1029/JB077i008p01566

Cappucci, M. (2022). *How the Tonga volcano generated a shock wave around the world* (Washington D.C., USA: Washington Post).

Cronin, S. (2022)A once in a 1000-year eruption [WWW document]. In: *A once on a 1000-year eruption*. Available at: https://www.spc.int/updates/blog/partners/2022/01/a-once-in-a-1000-year-eruption (Accessed 2.13.22).

Cronin, S., Brenna, M., Smith, I., Barker, S., Tost, M., Ford, M., et al. (2017). New volcanic island unveils explosive past. *Eos* 98, 1–6. doi: 10.1029/2017EO076589

Dupouy, C., Frouin, R., Tedetti, M., Maillard, M., Rodier, M., Lombard, F., et al. (2018). Diazotrophic trichodesmium impact on UV–vis radiance and pigment composition in the western tropical south pacific. *Biogeosciences* 15, 5249–5269. doi: 10.5194/bg-15-5249-2018

Eugenio, F., Martin, J., Marcello, J., and Fraile-Nuez, E. (2014). Environmental monitoring of El hierro island submarine volcano, by combining low and high resolution satellite imagery. *Int. J. Appl. Earth Observation Geoinformation* 29, 53–66. doi: 10.1016/j.jag.2013.12.009

Ferrera, I., Aristegui, J., Gonzalez, J., Montero, M., Fraile-Nuez, E., and Gasol, J. (2015). Transient changes in bacterioplankton communities induced by the submarine volcanic eruption of El hierro (Canary islands). *PloS One* 10, e0118136. doi: 10.1371/journal.pone.0118136

Fraile-Nuez, E., González-Dávila, M., Santana-Casiano, J. M., Arístegui, J., Alonso-González, I. J., Hernández-León, S., et al. (2012). The submarine volcano eruption at the island of El hierro: physical-chemical perturbation and biological response. *Sci. Rep.* 2, 486. doi: 10.1038/srep00486

Franklin, J., and Storel, M. (2022). *Satellite images show the aftermath of Tonga volcano's eruption* (Washington D.C., USA: NPR).

Gilerson, A., Zhou, J., Hlaing, S., Ioannou, I., Gross, B., Moshary, F., et al. (2008). Fluorescence component in the reflectance spectra from coastal waters. *II. Perform. retrieval algorithms. Optics express* 16, 2446–2460. doi: 10.1364/OE.16.002446

Gitelson, A. A., Dall'Olmo, G., Moses, W., Rundquist, D. C., Barrow, T., Fisher, T. R., et al. (2008). A simple semi-analytical model for remote estimation of chlorophyll-a in turbid waters: Validation. *Remote Sens. Environ.* 112, 3582–3593. doi: 10.1016/j.rse.2008.04.015

González-Vega, A., Callery, I., Arrieta, J. M., Santana-Casiano, J. M., Domínguez-Yanes, J. F., and Fraile-Nuez, E. (2022). Severe deoxygenation event caused by the 2011 eruption of the submarine volcano tagoro (El hierro, canary islands). *Front. Mar. Sci.* 9. doi: 10.3389/fmars.2022.834691

González-Vega, A., Fraile-Nuez, E., Santana-Casiano, J. M., González-Dávila, M., Escánez-Pérez, J., Gómez-Ballesteros, M., et al. (2020). Significant release of dissolved inorganic nutrients from the shallow submarine volcano tagoro (Canary islands) based on seven-year monitoring. *Front. Mar. Sci.* 6. doi: 10.3389/fmars.2019.00829

Hu, C., and Feng, L. (2016). Modified MODIS fluorescence line height data product to improve image interpretation for red tide monitoring in the eastern gulf of Mexico. *J. Appl. Remote Sens.* 11, 12003. doi: 10.1117/1.JRS.11.012003

Lee, Z.-P., Darecki, M., Carder, K., Davis, C., Stramski, D., and Rhea, W. (2005). Diffuse attenuation coefficient of downwelling irradiance: An evaluation of remote sensing methods. *J. Geophys. Res.* 110, 1–9. doi: 10.1029/2004JC002573

Mantas, V. M., Pereira, A. J. S. C., and Morais, P. V. (2011). Plumes of discolored water of volcanic origin and possible implications for algal communities. the case of the home reef eruption of 2006 (Tonga, southwest pacific ocean). *Remote Sens. Environ.* 115, 1341–1352. doi: 10.1016/j.rse.2011.01.014

Morel, A., Gentili, B., Claustre, H., Babin, M., Bricaud, A., Ras, J., et al. (2007). Optical properties of the "clearest" natural waters. *Limnol. Oceanogr. - LIMNOL OCEANOGR.* 52, 217–229. doi: 10.4319/lo.2007.52.1.0217

Morel, A., and Maritorena, S. (2001). Bio-optical properties of oceanic waters. *J. Geophys. Res.* doi: 10.1029/2000JC000319

Moutin, T., Doglioli, A., Verneil, A., and Bonnet, S. (2017). Preface: The oligotrophy to the UlTra-oligotrophy PACific experiment (OUTPACE cruise, 18 February to 3 April 2015). *Biogeosciences* 14, 3207–3220. doi: 10.5194/bg-14-3207-2017

Moutin, T., Wambeke, F., and Prieur, L. (2012). Introduction to the biogeochemistry from the oligotrophic to the ultraoligotrophic Mediterranean (BOUM) experiment. *Biogeosciences* 9, 3817–3825. doi: 10.5194/bg-9-3817-2012

Ngaluafe, P. (2022). *Volcanic eruption in Tonga*.

NOAA (2022). "The hunga Tonga-hunga ha'apai eruption, a multi-hazard event | nesdis [WWW document]," in *The hunga Tonga-hunga ha'apai eruption, a multi-*

hazard event. Maryland, USA: National Environmental Satellite Data and Information Service. Available at: https://www.nesdis.noaa.gov/news/the-hunga-tonga-hunga-haapai-eruption-multi-hazard-event.

Park, Y.-J., and Ruddick, K. (2005). Model of remote-sensing reflectance including bidirectional effects for case 1 and case 2 waters. *Appl. optics* 44, 1236–1249. doi: 10.1364/AO.44.001236

Ruddick, K. G., De Cauwer, V., Park, Y.-J., and Moore, G. (2006). Seaborne measurements of near infrared water-leaving reflectance: The similarity spectrum for turbid waters. *Limnol. Oceanogr.* 51, 1167–1179. doi: 10.4319/lo.2006.51.2.1167

Sakuno, Y. (2021). Trial of chemical composition estimation related to submarine volcano activity using discolored seawater color data obtained from GCOM-c SGLI. *A Case Study Nishinoshima Island Japan 2020. Water* 13, 1100. doi: 10.3390/w13081100

Santana-Casiano, J. M., González-Dávila, M., Fraile-Nuez, E., de Armas, D., González, A. G., Domínguez-Yanes, J. F., et al. (2013). The natural ocean acidification and fertilization event caused by the submarine eruption of El hierro. *Sci. Rep.* 3, 1140. doi: 10.1038/srep01140

Santana-González, C., Santana-Casiano, J. M., González-Dávila, M., and Fraile-Nuez, E. (2017). Emissions of Fe(II) and its kinetic of oxidation at tagoro submarine volcano, El hierro. *Mar. Chem. SI: Honoring Frank Millero* 195, 129–137. doi: 10.1016/j.marchem.2017.02.001

Smithsonian Institute (2019) *Most recent weekly report: 14 august to 20 august 2019 [WWW document]* (National Museum of Natural History: Global Volcanism Program). Available at: https://volcano.si.edu/volcano.cfm?vn=243091 (Accessed 11.30.20)

Tassan, S. (1994) *Local algorithms using SeaWiFS data for the retrieval of phytoplankton, pigments, suspended sediment, and yellow substance in coastal waters [WWW document]*. Available at: https://opg.optica.org/ao/abstract.cfm?uri=ao-33-12-2369 (Accessed 11.15.22).

The World Bank (2022). *THE JANUARY 15, 2022 HUNGA TONGA-HUNGA HA'APAI ERUPTION AND TSUNAMI, TONGA. GLOBAL RAPID POST DISASTER DAMAGE ESTIMATION (GRADE) REPORT*. Washington D.C., USA: International Bank for Reconstruction and Development

Urai, M., and Machida, S. (2005). Discolored seawater detection using ASTER reflectance products: A case study of Satsuma-iwojima, Japan. *Remote Sens. Environ. - Remote SENS Environ.* 99, 95–104. doi: 10.1016/j.rse.2005.04.028

Werdell, P. J., and Bailey, S. W. (2005). An improved in-situ bio-optical data set for ocean color algorithm development and satellite data product validation. *Remote Sens. Environ.* 98, 122–140. doi: 10.1016/j.rse.2005.07.001

Whiteside, A., Dupouy, C., Singh, A., Frouin, R., Menkes, C., and Lefèvre, J. (2021). Automatic detection of optical signatures within and around floating Tonga-Fiji pumice rafts using MODIS, VIIRS, and OLCI satellite sensors. *Remote Sens.* 13, 501. doi: 10.3390/rs13030501

Witze, A. (2022)Why the Tongan eruption will go down in the history of volcanology [WWW document]. In: *Why the Tongan eruption will down in the history of volcanology*. Available at: https://www.nature.com/articles/d41586-022-00394-y (Accessed 2.13.22).

Zhang, T., and Fell, F. (2007). An empirical algorithm for determining the diffuse attenuation coefficient kd in clear and turbid waters from spectral remote sensing reflectance. *Limnol. oceanogr. Methods* 5, 457–462. doi: 10.4319/lom.2007.5.457

frontiers | Frontiers in Marine Science

TYPE Original Research
PUBLISHED 13 January 2023
DOI 10.3389/fmars.2022.1103215

Check for updates

OPEN ACCESS

EDITED BY
Xiaoteng Shen,
Hohai University, China

REVIEWED BY
Miaohua Mao,
Yantai Institute of Coastal Zone Research (CAS), China
Changlin Chen,
Fudan University, China

*CORRESPONDENCE
Xiao-Hua Zhu
xhzhu@sio.org.cn

SPECIALTY SECTION
This article was submitted to Ocean Observation, a section of the journal Frontiers in Marine Science

RECEIVED 20 November 2022
ACCEPTED 27 December 2022
PUBLISHED 13 January 2023

CITATION
Li Z, Long Y, Zhu X-H and Papa F (2023) Intensification of "river in the sea" along the western Bay of Bengal Coast during two consecutive La Niña events of 2020 and 2021 based on SMAP satellite observations. *Front. Mar. Sci.* 9:1103215. doi: 10.3389/fmars.2022.1103215

COPYRIGHT
© 2023 Li, Long, Zhu and Papa. This is an open-access article distributed under the terms of the Creative Commons Attribution License (CC BY). The use, distribution or reproduction in other forums is permitted, provided the original author(s) and the copyright owner(s) are credited and that the original publication in this journal is cited, in accordance with accepted academic practice. No use, distribution or reproduction is permitted which does not comply with these terms.

Intensification of "river in the sea" along the western Bay of Bengal Coast during two consecutive La Niña events of 2020 and 2021 based on SMAP satellite observations

Zhiyuan Li[1,2], Yu Long[3], Xiao-Hua Zhu[2,3,4]* and Fabrice Papa[5,6]

[1]School of Water Conservancy & Environment Engineering, Zhejiang University of Water Resources and Electric Power, Hangzhou, China, [2]Southern Marine Science and Engineering Guangdong Laboratory (Zhuhai), Zhuhai, China, [3]State Key Laboratory of Satellite Ocean Environment Dynamics, Second Institute of Oceanography, Ministry of Natural Resources, Hangzhou, China, [4]School of Oceanography, Shanghai Jiao Tong University, Shanghai, China, [5]LEGOS, Université de Toulouse, IRD/CNRS/CNES/UT3, Toulouse, France, [6]Indo-French Cell for Water Sciences, IRD-IISc Joint Laboratory, Indian Institute of Science, Bangalore, India

A narrow strip of low salinity water that hugs the western Bay of Bengal (BoB) is known as a "river in the sea" (RIS). During the autumns of 2020 and 2021, Soil Moisture Active Passive (SMAP) identified an intensification of the RIS that was characterized by a continuous, uniform strip of low salinity water (<31 psu) that was 100 km wide extending along the western BoB coast to south of Sri Lanka. The analysis shows that the La Niña events in 2020–2021 were responsible for this intensification. During the La Niña events of 2020 and 2021, cyclonic circulation anomalies were generated along the BoB coast, causing a stronger Eastern Indian Coastal Current (EICC). Meanwhile, the northern BoB received increased river discharge during the summer monsoons of the two years. The stronger EICC and increased river discharge together led to anomalous freshwater transport that contributed to the intensification of the RIS. Notably, the RIS extended far southward during La Niña events of 2016 and 2017. However, the spatial structure of the RIS differed sharply between 2016–2017 and 2020–2021. The results indicate that pairs of eddies in the western BoB steered the freshwater offshore by several hundred kilometers. As a result, offshore extending tongue-shaped freshwater plumes were formed that inhibited the formation of an organized RIS structure along the western BoB coast during 2016–2017. This study highlights that the year-to-year variability of the RIS was significantly influenced by the La Niña events and modulated by mesoscale processes.

KEYWORDS

Bay of Bengal, river in the sea, SMAP, La Niña, Eastern Indian Coastal Current, mesoscale process

1 Introduction

The Bay of Bengal (BoB) is a semienclosed basin in the Northern Indian Ocean (NIO), with reversing winds that blow from the southwest during the summer monsoon and from the northeast during the winter monsoon. During the summer monsoon, the BoB receives substantial amounts of freshwater from precipitation and river runoff (Papa et al., 2010; Papa et al., 2012; Chaitanya et al., 2014; Li et al., 2021b). These freshwater influxes lead to a lower sea surface salinity (SSS) in the BoB than its western counterpart, the Arabian Sea (Figure 1). The low SSS in the BoB causes strong stratification in the upper layer, favoring the formation of a barrier layer between the bottom of the mixed layer and the top of the thermocline (Sprintall and Tomczak, 1992; Vinayachandran et al., 2002; Thadathil et al., 2007). Moreover, the freshwater in the BoB is transported to the Arabian Sea and equatorial Indian Ocean (EIO), playing an important role in the water and salt balances in the NIO (Sengupta et al., 2006; Trott et al., 2019).

Based on *in situ* and satellite data, many studies have observed freshwater plumes along the western BoB coast (Murty et al., 1992; Shetye et al., 1993; Shetye et al., 1996; Fournier et al., 2017; Sree Lekha et al., 2018; Li et al., 2021a). It was reported that the Eastern Indian Coastal Current (EICC) transports the river freshwater southward to form freshwater plumes along the coast (Han and McCreary, 2001; Jensen, 2001; Durand et al., 2009; Akhil et al., 2014; Akhil et al., 2016). Recently, based on salinity data collected by fishermen, Chaitanya et al. (2014) identified a narrow (~100 km wide) strip of low salinity water along the western BoB coast as a "river in the sea" (RIS). As a striking hydrographic feature in the BoB, the RIS has attracted attention from several investigators (Akhil et al., 2014; Fournier et al., 2017; Suneel et al., 2020). These studies confirmed the existence of the RIS from the evolution of the SSS averaged over a coastal strip box along the western BoB coast. However, the spatial and temporal variability of the RIS has not been well studied and the formation processes of the RIS remain unclear.

Influenced by the El Niño-Southern Oscillation (ENSO) and Indian Ocean Dipole (IOD), the BoB exhibits strong year-to-year variability (Saji et al., 1999; Webster et al., 1999; Thompson et al., 2006; Grunseich et al., 2011; Subrahmanyam et al., 2011; Du and Zhang, 2015; Pant et al., 2015; Sherin et al., 2018; Subrahmanyam et al., 2018). When an ENSO or IOD event occurs, remote equatorial waves propagate into the BoB to cause sea surface height anomalies (SSHAs) along the boundary. For

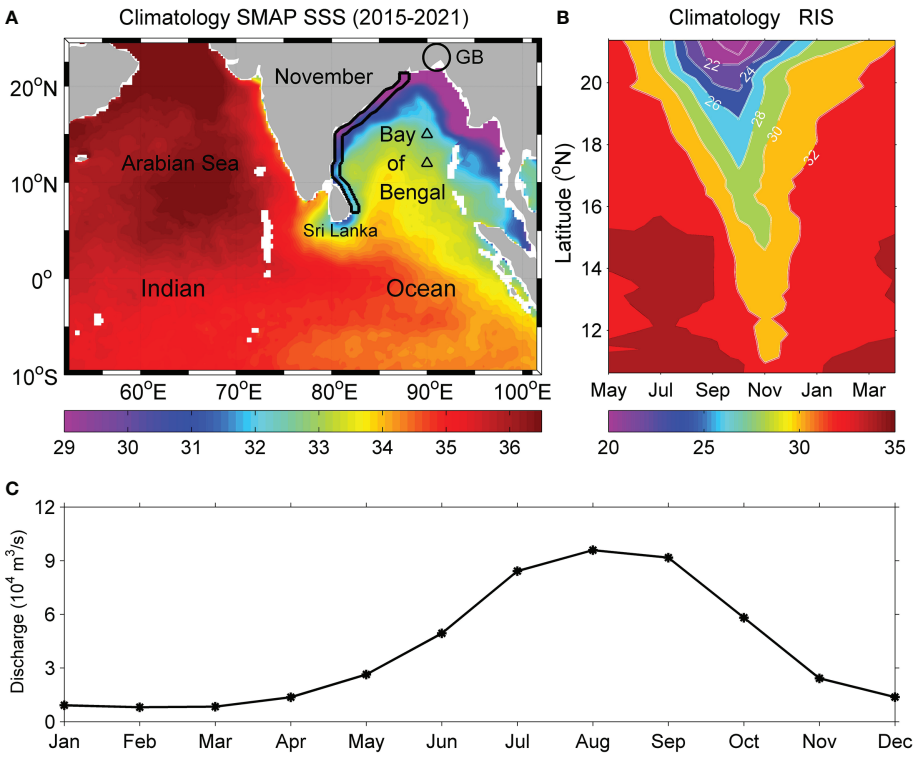


FIGURE 1
(A) November climatology of SMAP SSS in the northern Indian Ocean during 2015–2021. The black line denotes the coastal strip extending 1° away from the western BoB boundary to characterize the RIS. The black circle indicates the Ganges-Brahmaputra (GB) and the triangles represent the RAMA buoy at station B15 (15°N, 90°E) and B12 (12°N, 90°E). **(B)** Latitude–time plot of the climatological SMAP SSS in the strip shown in **(A)**. **(C)** Climatological monthly discharge of the GB river.

example, during La Niña or negative IOD (nIOD) events, positive SSHAs were observed off the western BoB coast (Grunseich et al., 2011; Aparna et al., 2012). The positive SSHAs (cyclonic circulation anomalies) contribute to a stronger EICC during October–December (OND), causing the RIS to extend farther southward along the coast (Akhil et al., 2016; Fournier et al., 2017; Suneel et al., 2020; Li et al., 2021b). For example, the RIS extended far southward along the western BoB coast in 2016, which was attributed to the influence of the nIOD in 2016 (Fournier et al., 2017; Suneel et al., 2020). However, the 2016 was a combination event of a nIOD and a La Niña, and the influences of the La Niña on the southward extension of the RIS still remain unclear in the studies of Fournier et al. (2017) and Suneel et al. (2020).

Launched in 2015, NASA's Soil Moisture Active Passive (SMAP) satellite provides a better SSS retrieval compared with that of other satellite data, especially in coastal regions (Tang et al., 2017; Bao et al., 2019; Fore et al., 2020). The SMAP data have been successfully used to study the freshwater extension in the BoB (Fournier et al., 2017; Akhil et al., 2020; Roman-Stork et al., 2020; Sree Lekha et al., 2020; Suneel et al., 2020; Li et al., 2021a; Paul et al., 2021). During the autumns of 2020 and 2021, a continuous, narrow strip of low salinity water extended southward along the western BoB coast to south of Sri Lanka, indicating the intensification of the RIS during these two years. However, the processes responsible for the intensification of the RIS during 2020–2021 remain unclear. In this study, we investigate the intensification of the RIS during 2020–2021 based on the SMAP satellite observations. We show that the two consecutive La Niña events of 2020 and 2021 were responsible for the intensification of the RIS.

The rest of this paper is organized as follows. In Section 2, the data used in this study are described. In Section 3, we use the SMAP SSS to quantify the spatial and temporal variability of RIS and the influences of the La Niña and mesoscale eddies on the year-to-year variability of the RIS are investigated. In Section 4, a discussion is provided. A summary and conclusion are given in Section 5.

2 Materials

We use the monthly and daily SMAP L3 V5.0 SSS produced by NASA's Jet Propulsion Laboratory (Fore et al., 2020). Although the goal of the SMAP mission is to measure soil moisture, its radiometer-radar instrument enables SMAP to provide estimates of SSS (Entekhabi et al., 2010). The SMAP data have a spatial resolution of 0.25° x 0.25° and are available from April 2015 to present. The data can be downloaded from the Asia-Pacific Data-Research Center of the International Pacific Research Center (IPRC). We use the daily SSS measured by the Research Moored Array for African-Asian-Australian Monsoon Analysis and Prediction (RAMA) moored buoys (McPhaden et al., 2009) at 15°N, 90°E (B15) and 12°N, 90°E (B12) in the northern BoB. The RAMA data are provided by the Global Tropical Moored Buoy Array Project Office of the National Oceanic and Atmosphere Administration and the Pacific Marine Environmental Laboratory (https://www.pmel.noaa.gov/). The RAMA data are smoothed with a 10-day running mean for analysis. Then, the RAMA SSS is used to validate the accuracy of the SMAP data. At both stations, the SMAP SSS shows reasonably good agreement with the RAMA SSS (Figure 2). At station B15 (15°N, 90°E), the correlation coefficient between the SSS of the two datasets is 0.76, and the root mean square error (rmse) is 0.45 psu. At station B12 (12°N, 90°E), the correlation coefficient between the SSS of the two

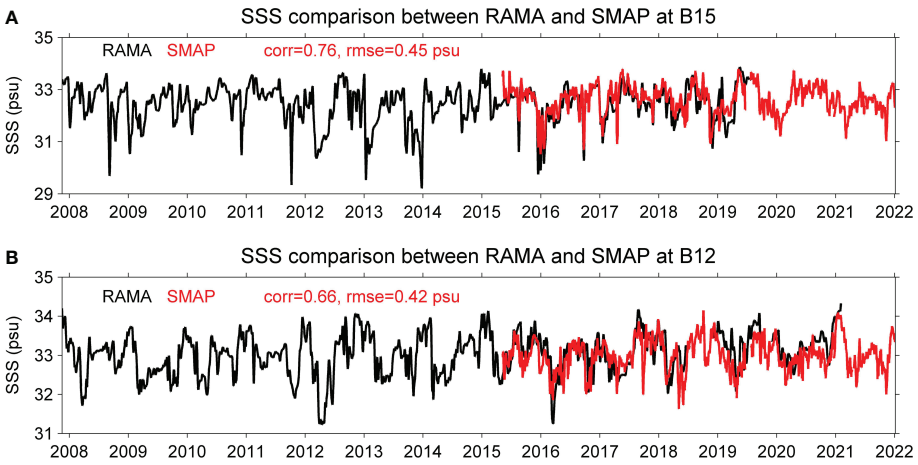


FIGURE 2
Comparison of SSS between RAMA and SMAP at station B15 **(A)** and **(B)** B12. The correlation coefficient and root mean square error is estimated for the period both data are available.

datasets is 0.66, and the rmse is 0.42 psu. This demonstrates the good ability of the SMAP SSS in studying the SSS variability in the BoB.

We use the monthly and daily maps of sea surface height (SSH) and geostrophic current obtained from the Copernicus Marine and Environment Monitoring Service (CMEMS). The SSH indicates the residual of the mean dynamic topography from the absolute dynamic topography. The IOD is indicated by the dipole mode index (DMI), which is defined as the difference of area-averaged sea surface temperature anomaly (SSTA) between the western (50°E-70°E, 10°S-10°N) and eastern (90°E-110°E, 10°S-0°) tropical Indian Ocean (Saji et al., 1999). The ENSO is characterized by the Oceanic Niño Index (ONI), which is defined as the area-averaged SSTA in the Niño 3.4 region. The monthly ONI and DMI indices can be accessed from the Ocean Observations Panel for Climate (https://stateoftheocean.osmc.noaa.gov/). Papa et al. (2010; 2012) used the altimetry-derived river discharge, based on the empirical regression curves of the altimetry-measured river water height and observed river discharge, to retrieve the variations in the Ganges-Brahmaputra (GB) River freshwater flux into the BoB. We use the updated satellite-derived monthly GB river discharge products, now available for 1993–2021 (Papa et al., 2012).

3 Results

3.1 Year-to-year variability of the RIS along the western BoB coast

To characterize the year-to-year variability of the RIS along the western BoB coast, a time–latitude plot of the 7-year (2015–2021) monthly SMAP SSS averaged over a coastal strip box is shown (Figure 3A). A common feature of the 7-year SMAP SSS is that very low salinity water (<25 psu) was present in the northern BoB during the summer monsoon, reflecting the freshwater input from rivers and precipitation. During the following autumn and winter, this low salinity water extended southward and formed an RIS structure along the western BoB coast. Meanwhile, the RIS exhibited a clear year-to-year variability in terms of the southward extension, indicated by the position of 32 psu SSS contour. Specifically, the 32 psu SSS contour extended southward to approximately 13.5°N, 13°N, and 12.5°N in 2015, 2018, and 2019, respectively, reflecting that the southward extension of the RIS was weakened during these years. In 2016, 2017, 2020, and 2021, the southward extension of the RIS along the western BoB coast was substantially intensified.

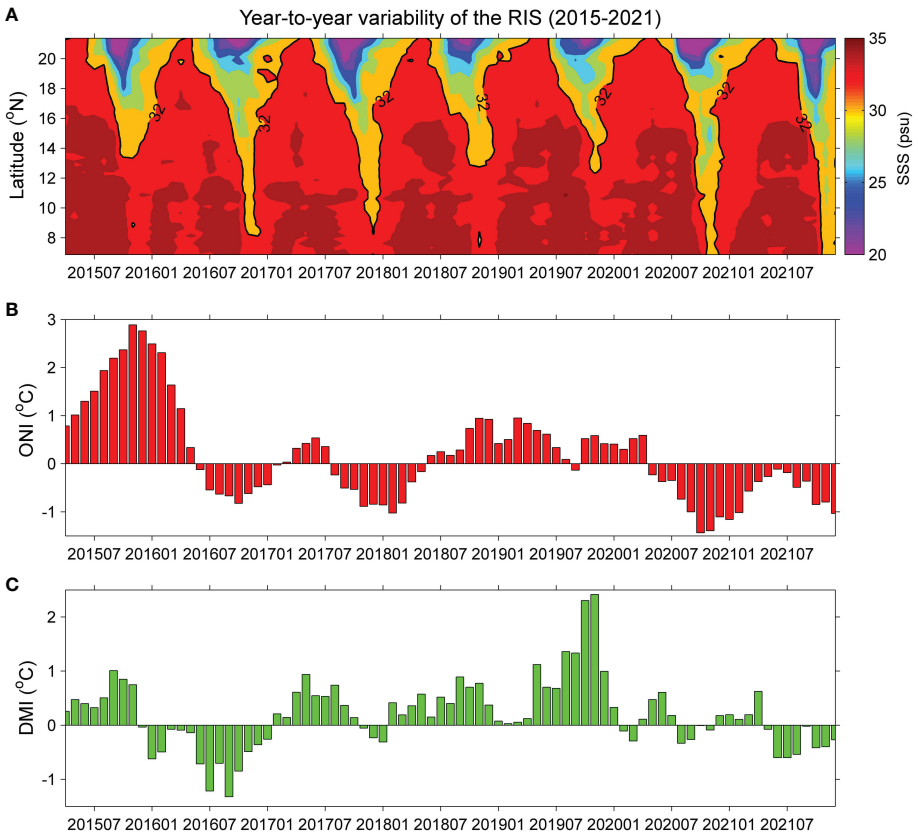


FIGURE 3
(A) Time–latitude plot of SMAP SSS averaged over the coastal strip Box 1, and **(B)** monthly Oceanic Niño Index (ONI) and **(C)** Dipole Mode Index (DMI) during April 2015 to December 2021.

The 32 psu SSS contour extended southward to approximately 8° N in 2016 and 2017. In particular, the southward extension of the RIS was the strongest in 2020 and 2021, which was characterized by the 32 psu SSS contour extending to south of Sri Lanka (Figure 3A).

The ENSO and IOD are two modes that influence the interannual variability in the BoB (Saji et al., 1999; Webster et al., 1999; Thompson et al., 2006; Pant et al., 2015; Sherin et al., 2018; Subrahmanyam et al., 2018; Li et al., 2021b). ENSO and IOD events can co-occur with each other: a positive IOD (pIOD) co-occurs with an El Niño event and a nIOD co-occurs with a La Niña event (Hong et al., 2008; Gnanaseelan et al., 2012; Stuecker et al., 2017). Li et al. (2021b) demonstrated that ENSO/IOD events can cause anomalous freshwater transport during the autumn and winter, contributing to the interannual variability of the SSS in the BoB. This motivates us to examine the relationships between the ENSO/IOD events and the year-to-year variability of the RIS during 2015–2021.

Considering that both the ENSO and IOD develop to a mature phase during the boreal autumn, an ENSO or IOD event is identified only when the ONI or DMI is larger than 0.5°C during September–November. Namely, an El Niño (La Niña) event corresponds to the ONI >0.5°C (<–0.5°C) and a pIOD (nIOD) event corresponds to the DMI >0.5°C (<–0.5°C). According to this criterion, El Niño/pIOD events were identified in 2015, 2018, and 2019, and La Niña/nIOD events were identified in 2016, 2017, 2020, and 2021 (Figures 3B, C). In detail, co-occurrences of El Niño and pIOD were identified in 2015 and 2018, and a pure pIOD event was identified in 2019. A co-occurrence of La Niña and nIOD was identified in 2016, and pure La Niña events were identified in 2017, 2020, and 2021. Therefore, these results indicate that the southward extension of the RIS along the western BoB coast was weakened during the El Niño/pIOD events of 2015, 2018, and 2019, and intensified during the La Niña/nIOD events of 2016, 2017, 2020, and 2021.

3.2 Composite analysis

It has been reported that the EICC played an important role in influencing the southward extension of the RIS (Akhil et al., 2014; Chaitanya et al., 2014; Akhil et al., 2016; Fournier et al., 2017; Li et al., 2021a). The EICC flows southward along the western BoB coast with a maximum speed in November (Jensen, 2001; Durand et al., 2009; Das et al., 2019). Thus, composite November SSHA for 2015, 2018, and 2019 (Figure 4A) and 2016, 2017, 2020, and 2021 (Figure 4B) are shown to investigate the influences of the El Niño/pIOD and La Niña/nIOD events on the EICC during these years. During the composite El Niño/pIOD events of 2015, 2018 and 2019, a negative SSHA was observed in the eastern EIO and the boundary of the BoB, forming anticyclonic circulation anomalies along the western BoB coast (Figure 4A) that led to a weaker EICC during these years. An organized southward EICC cannot be identified along the western BoB coast in 2019. Instead, the current in the western BoB was characterized by various cyclonic eddies (CEs) and anticyclonic eddies (ACEs) (Figure 4D). During the composite La Niña/nIOD events of 2016, 2017, 2020, and 2021, the SSHA indicated cyclonic circulation anomalies along the western BoB coast (Figure 4B) that led to a stronger EICC during these years (Figures 4E–H).

3.3 Local freshwater flux

During the summer monsoon (June–October), the GB River inputs a large amount of local freshwater into the BoB that influences the extension of the RIS (Han et al., 2001; Papa et al., 2010; Papa et al., 2012; Pant et al., 2015). Therefore, it is necessary to examine the contribution of the local freshwater flux to the year-to-year variability of the RIS during 2015–2021. The monthly evolution of the GB River discharge exhibits evident seasonal cycles, with large values occurring during the summer monsoon (Figure 5A). Meanwhile, a year-to-year variability of the river discharge was also observed during the 7 years. To better quantify the year-to-year variability, we use the accumulated river discharge during the summer monsoon for analysis (Figure 5B).

During the 7 years, the accumulated GB River discharge exhibited relatively smaller values in 2015 and 2018 and larger values in 2016, 2017, 2019, 2020, and 2021. This means that the BoB received less freshwater from the GB River during the summer monsoons of 2015 and 2018. Therefore, the reduced river discharge and weaker EICC together contributed the RIS to extending less southward along the western BoB coast during the two years. In contrast, the BoB received more freshwater from the GB River during the summer monsoons of 2016, 2017, 2020, and 2021. The increased river discharge and stronger EICC together led the RIS to extending farther southward along the western BoB coast during these four years (Figure 3A). In addition, the BoB received a substantial amount of freshwater during the summer monsoon of 2019. However, the RIS did not extend southward significantly along the western BoB coast in 2019 (Figure 3A). This is due to the absence of an organized southward EICC during that year (Figure 4D).

3.4 Spatial variability of RIS during 2015–2021

In the following, the November SSS distributions in the BoB are shown to characterize the spatial structure of the RIS during 2016, 2017, 2020, and 2021. During 2020–2021, the SMAP SSS exhibited low salinity water along the entire western BoB coast, with the 31 psu SSS contour reaching south of Sri Lanka. Moreover, the low salinity water comprised a uniform strip

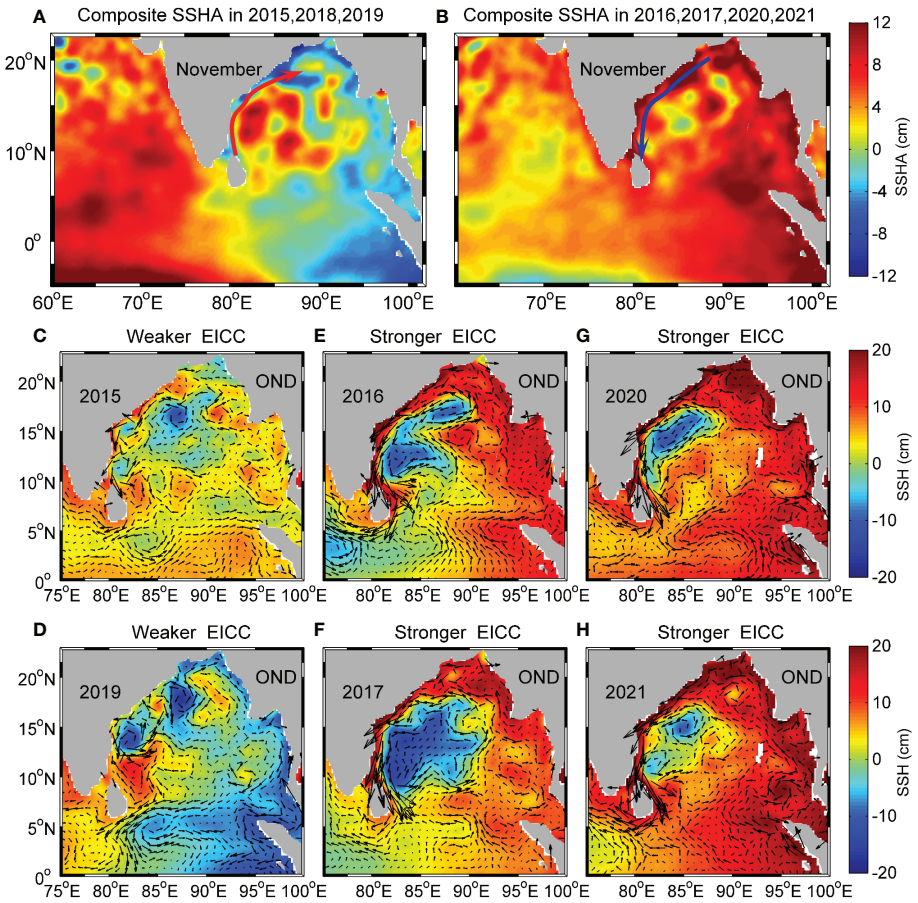


FIGURE 4
Composite November SSHA for 2015, 2018, and 2019 **(A, B)** 2016, 2017, 2020, and 2021. The red (blue) arrow indicates the cyclonic (anticyclonic) circulation anomalies along the western BoB coast. Weaker EICC in 2015 **(C, D)** 2019, stronger EICC in 2016 **(E)**, 2017 **(F)**, 2020 **(G, H)** 2021. The EICC is represented by the surface geostrophic current associated with the SSH during October–December (OND).

that was approximately 100 km wide (Figures 6A, B). These features indicate an organized RIS structure along the western BoB coast during these two years. During 2016–2017 (Figures 6C, D), however, the low salinity water along the western BoB coast showed distinct features from those during 2020–2021. During 2016–2017, the low salinity water was discontinuous along the western BoB coast, and its width was non-uniform. For example, the SSS distribution indicated two separate freshwater plumes in the western BoB in 2016; one plume was located approximately between 8°N–17°N and another one was located in the BoB north of 17°N (Figure 6C).

3.5 Formation processes of RIS during 2020–2021

It has been reported that the EICC plays an important role in the formation of the RIS (Akhil et al., 2014; Chaitanya et al., 2014). The magnitudes of the EICC during 2016–2017 and 2020–2021 were comparable (Figures 4E–H). Thus, the differences in the spatial structure of the RIS between 2016–2017 and 2020–2021 cannot be fully attributed to the EICC. This suggests that other processes influenced the formation of the RIS in the BoB, as shown below.

Figure 7 shows the consecutive snapshots of the weekly SMAP SSS in the BoB in 2020 and 2021, respectively. In both two years, the SMAP SSS provided good insights into how the freshwater in the northern bay extended southward to form an organized RIS structure along the western BoB coast. For 2020, the formation process of the RIS can be divided into three stages. During the first stage, substantial freshwater was distributed in the northern bay (Figure 7A). However, no evident southward extension of the freshwater could be recognized during this stage (Figures 7B, C). During the second stage, the freshwater extended southward quickly to form a narrow strip of low salinity water along the entire western BoB coast, namely the RIS (Figures 7D–G). During the third stage, the organized RIS gradually dissipated (Figure 7H).

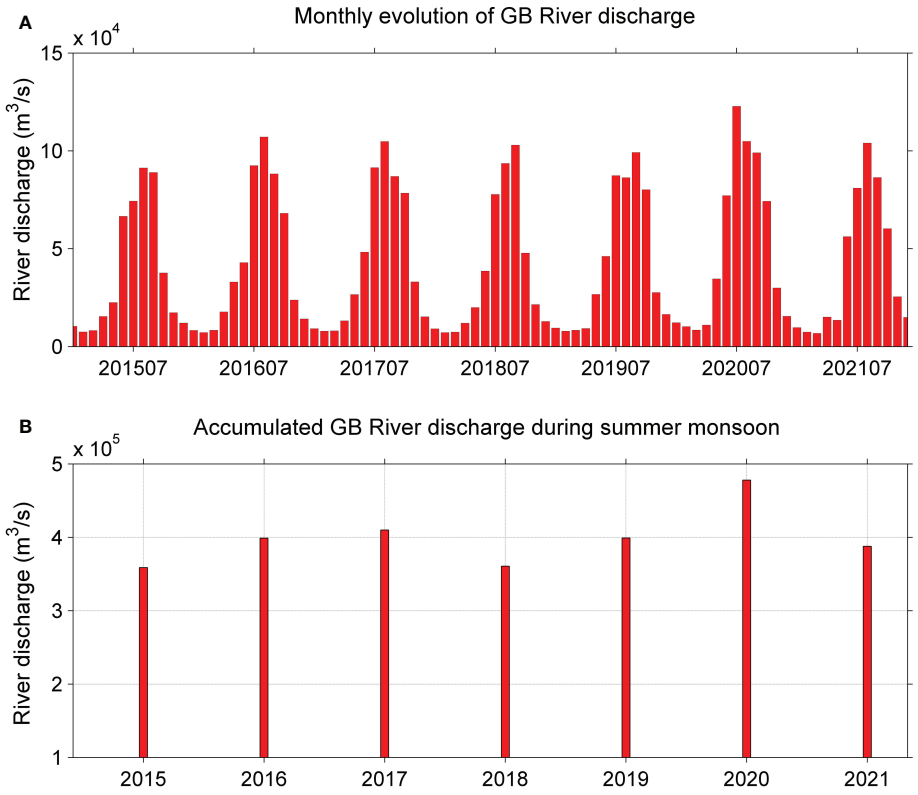


FIGURE 5
(A) Monthly and **(B)** accumulated GB River discharge during the summer monsoon from 2015 to 2021.

In contrast, the formation process of the RIS in 2021 can be roughly divided into four stages. During the first stage, the freshwater in the northern bay extended southward quickly and formed a narrow strip of low salinity water along the northwestern BoB coast (Figures 7I, J). During the second stage, the southward extension of the freshwater ceased, and substantial freshwater accumulated off the BoB coast. Interestingly, a bulge structure of freshwater was formed off the BoB coast (Figures 7K–M). During the third stage, the bulge structure disappeared, and the accumulated freshwater extended southward, forming an organized RIS along the entire western BoB coast (Figures 7N, O). During the fourth stage, the organized RIS gradually weakened (Figure 7P).

Figure 8 shows the representative snapshots of the weekly SSH and associated geostrophic currents in the BoB during the formation processes of the RIS, similar to that in Figure 7. During early September 2020, several eddies (one ACE and two CEs) in the western BoB and a high level of SSH in the northern BoB were prominent. However, an organized southward current along the western BoB coast is not visible (Figure 8A). The absence of a southward coastal current can explain why the freshwater in the northern bay did not extend southward along the coast (Figures 7A–C). In the following October, the high level of SSH in the northern BoB propagated southward to favor a southward EICC along the coast (Figure 8B). As a result, the EICC transported the freshwater in the northern BoB southward to form a narrow strip of freshwater (namely the RIS) along the BoB coast (Figures 7D, 8B). By November, an organized RIS along the entire western BoB coast could be clearly recognized (Figures 7G), corresponding to the strong EICC during this period (Figure 8C).

Similar features were found in 2021. For example, when a southward EICC was present (Figures 8D, F), it transported the freshwater to form an organized RIS along the western BoB coast (Figures 7J, N–P). The freshwater stopped extending further southward along the coast and formed a bulge structure off the BoB coast during late September to October (Figures 7K–M) because of the following reasons. First, a large ACE (centered at 14°N, 83.5°E) induced a strong anticyclonic current in the southwestern BoB (Figure 8D); Second, the high level of SSH in the central northern bay propagated westward to the BoB coast, causing the organized EICC in the northwestern BoB to be destroyed. Both aspects inhibited the southward extension of freshwater along the western BoB coast (Figure 7K). Notably, several CEs in the central BoB combined with the ACE (off the southwestern BoB coast) to induce an offshore current (white arrow in Figure 8E). This current steered the accumulated freshwater offshore, forming a bulge structure off the BoB

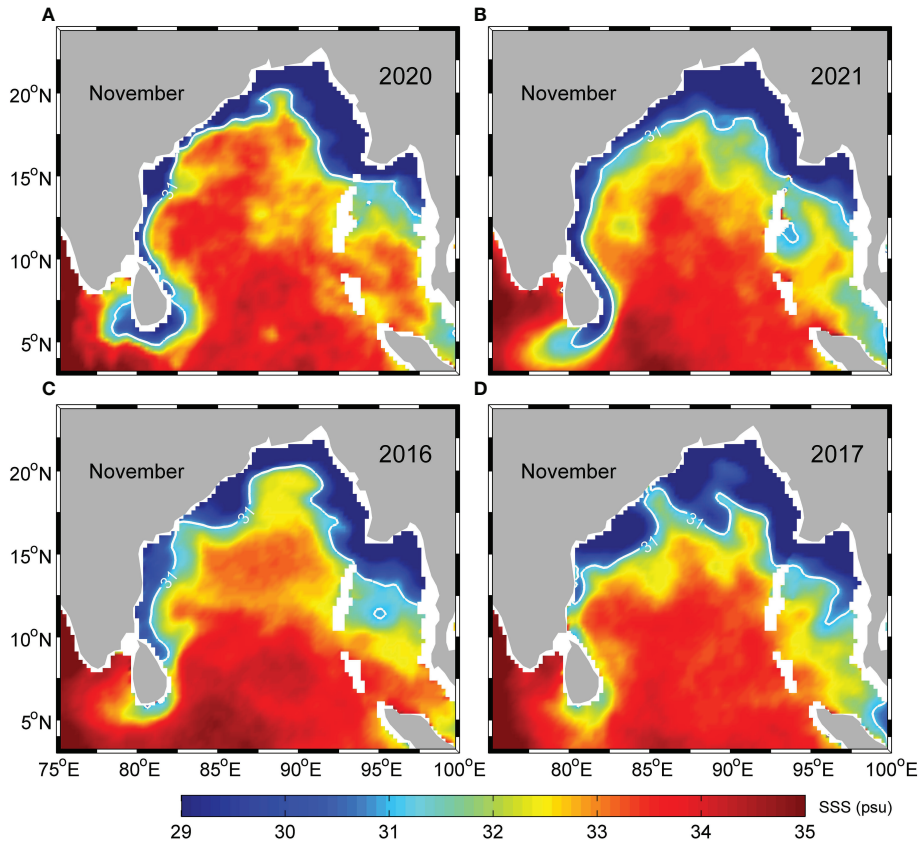


FIGURE 6
November SMAP SSS in the BoB for 2020 **(A)**, 2021 **(B)**, 2016 **(C)**, and **(D)** 2017. The white line indicates the SSS contour of 31 psu.

coast (Figures 7L, M). As indicated in Figures 7, 8, the EICC was a key factor forming the RIS structure along the western BoB coast. Meanwhile, the freshwater extension was also modulated by pairs of eddies off the western BoB coast.

3.6 Offshore extending tongue-shaped freshwater plumes during 2016 and 2017

Figure 9 shows the representative snapshots of the weekly SMAP SSS in the BoB from September to November of 2016 and 2017. In both years, tongue-shaped freshwater plumes extending from the coast to the central bay were particularly noticeable. For example, an offshore extending tongue-shaped freshwater plume with a double-branch structure could be clearly observed for September 2016 (Figure 9A). The length of this plume (distance from the front of the plume to the coastline) was approximately 700 km. Several weeks later, the double-branch structure of the plume could still be found, although its shape was slightly varied (Figure 9B). By November 2016, the two branches of the freshwater plume evolved into two separated freshwater plumes (Figure 9C). Similar offshore extending tongue-shaped freshwater plumes could also be found in 2017 (Figures 9D–F). The formation and evolution of the offshore extending tongue-shaped freshwater plumes during the two years are explained below.

During September of both years (2016 and 2017), several eddies formed a cyclonic circulation pattern in the northern BoB (white arrows in Figures 10A, D). The offshore/onshore currents associated with the cyclonic circulation steered the freshwater to the central northern BoB, leading to the formation of the tongue-shaped freshwater plumes that extended offshore (Figure 9A). Differently, an ACE (centered at 17.5°N, 89°E) divided the cyclonic circulation into two parts (green arrows in Figure 10A), leading the tongue-shaped freshwater plume exhibiting a double-branch structure in 2016 (Figure 9A). In the following October of each year, the position and shape of these eddies varied (Figures 10B, E), and the offshore extending freshwater plumes also evolved, while the spatial shape basically remained unchanged (Figures 9B, E). By November, the western BoB was characterized by a southward EICC in the southern part (white arrows in Figures 10C, F) and an anticyclonic current in the northern region (green arrows in Figures 10C, F). As a result, the offshore extending freshwater plume evolved into two

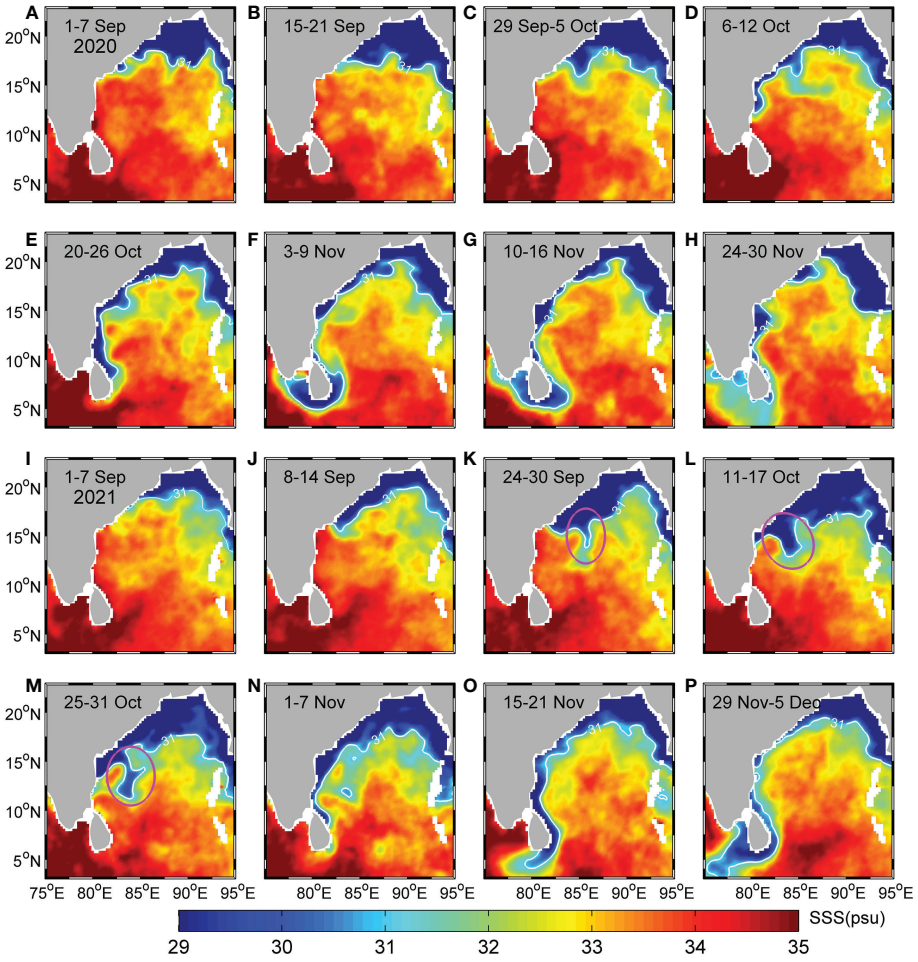


FIGURE 7
Consecutive snapshots of weekly SMAP SSS in the BoB for 2020 **(A–H)** and 2021 **(I–P)**, respectively. The white line indicates the SSS contour of 31 psu, and the purple ellipses represent the bulge structure of freshwater off the BoB coast.

separate freshwater plumes along the western BoB (Figures 9C, F).

4 Discussion

4.1 Important role of La Niña in the intensification of the RIS

The southward extension of the RIS along the western BoB coast exhibited clear year-to-year variability during 2015–2021. Especially, the RIS extended far southward in 2016, 2017, 2020, and 2021, reflecting the intensification of the RIS during these years (Figure 3). Fournier et al. (2017) and Suneel et al. (2020) attributed the intensification of the RIS in 2016 to the occurrence of a nIOD event during that year, while the La Niña's role was neglected. In this study, an intensification of RIS was observed in 2017, 2020, and 2021, which were three pure La Niña years without the co-occurrence of nIOD events (Figure 3). In particular, the RIS extended southernmost during 2020–2021, reaching south of Sri Lanka (Figures 6A, B). This strongly suggests that the La Niña events of 2017, 2020, and 2021 were responsible for the intensification of the RIS during these years. For the combination event of 2016, although the nIOD's role cannot be excluded, we argue that the La Niña's role in the intensification of the RIS must be considered. Our analysis demonstrates that during the autumns of 2016, 2017, 2020, and 2021, westerly anomalies favored positive SSHAs that cyclonically propagated from the eastern EIO into the BoB as coastal waves (Figure 4B). This agrees with the findings of Aparna et al. (2012) that positive SSHAs occurred off the western BoB coast during a La Niña event. The positive SSHAs associated with the coastal waves formed a stronger EICC along the western BoB coast (Figure 4), which was demonstrated in several previous studies (Grunseich et al., 2011; Akhil et al., 2016; Fournier et al., 2017).

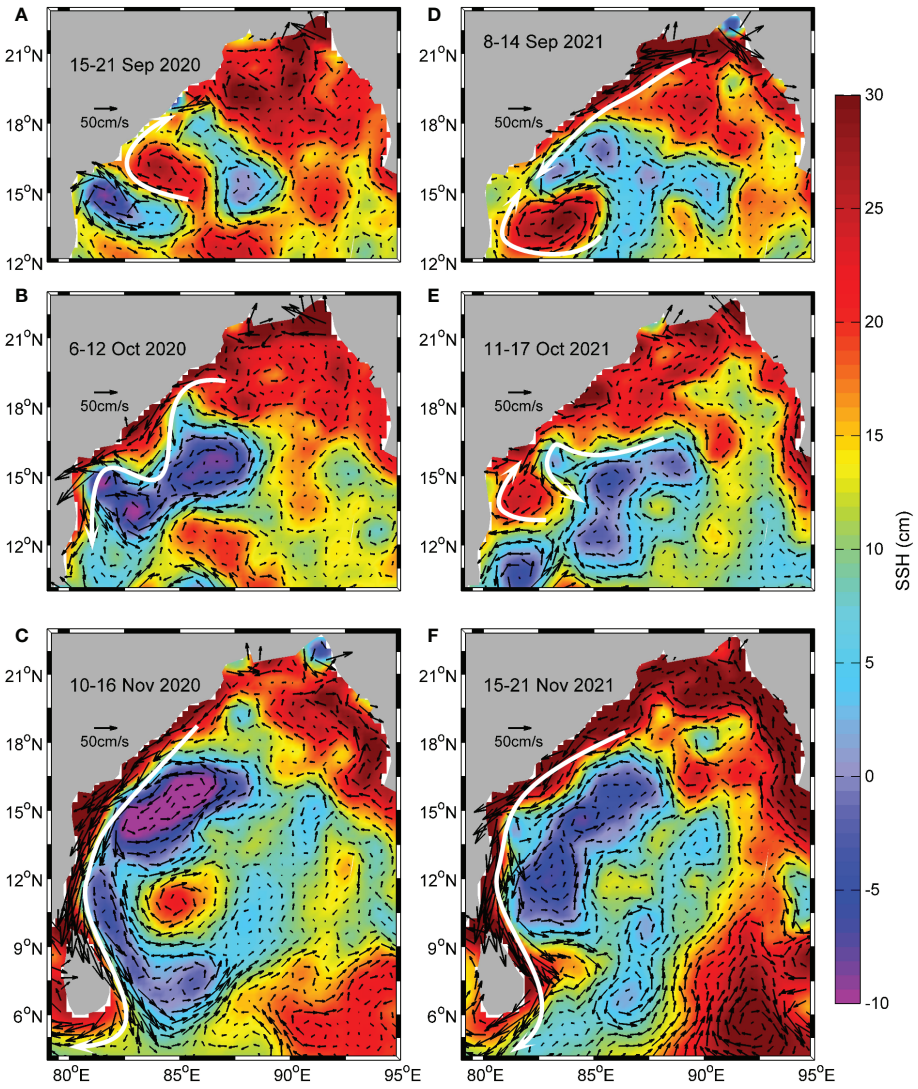


FIGURE 8
Snapshots of weekly SSH and associated geostrophic currents in the BoB during September to November of 2020 **(A–C)** and **(D–F)** 2021. The white arrow represents the eddy-induced current and the EICC in the western BoB.

To clarify the anomalies during the La Nina years, the GB River discharge for the years 1993–2021 is presented in Figure 11. It shows that the river discharge anomaly was positive during nine of the ten La Nina years (except 2005) (Figure 11C). This indicates that a positive GB River discharge anomaly occurred during the summer monsoons of La Niña years (Figures 11D). This is consistent with the findings of Webster et al. (1998) that the Indian Summer Monsoon Rainfall strengthens during La Niña years. This may explain why anomalous increased river discharges occurred in 2016, 2017, 2020, and 2021 (Figure 5). The influences of precipitation minus evaporation (P−E) anomalies on the RIS are not considered in this study, although the P−E also shows a prominent year-to-year variability (Behera et al., 1999; Pant et al., 2015). This is because the influences of P−E (integrated over the ocean only) on the RIS is much smaller than that of the GB River discharge because the horizontal scale of the RIS is only approximately 100 km wide. Consequently, we argue that the intensification of the RIS during 2016, 2017, 2020, and 2021 were the result of anomalous freshwater transport along the western BoB coast. The stronger EICC and increased river discharge both played important roles.

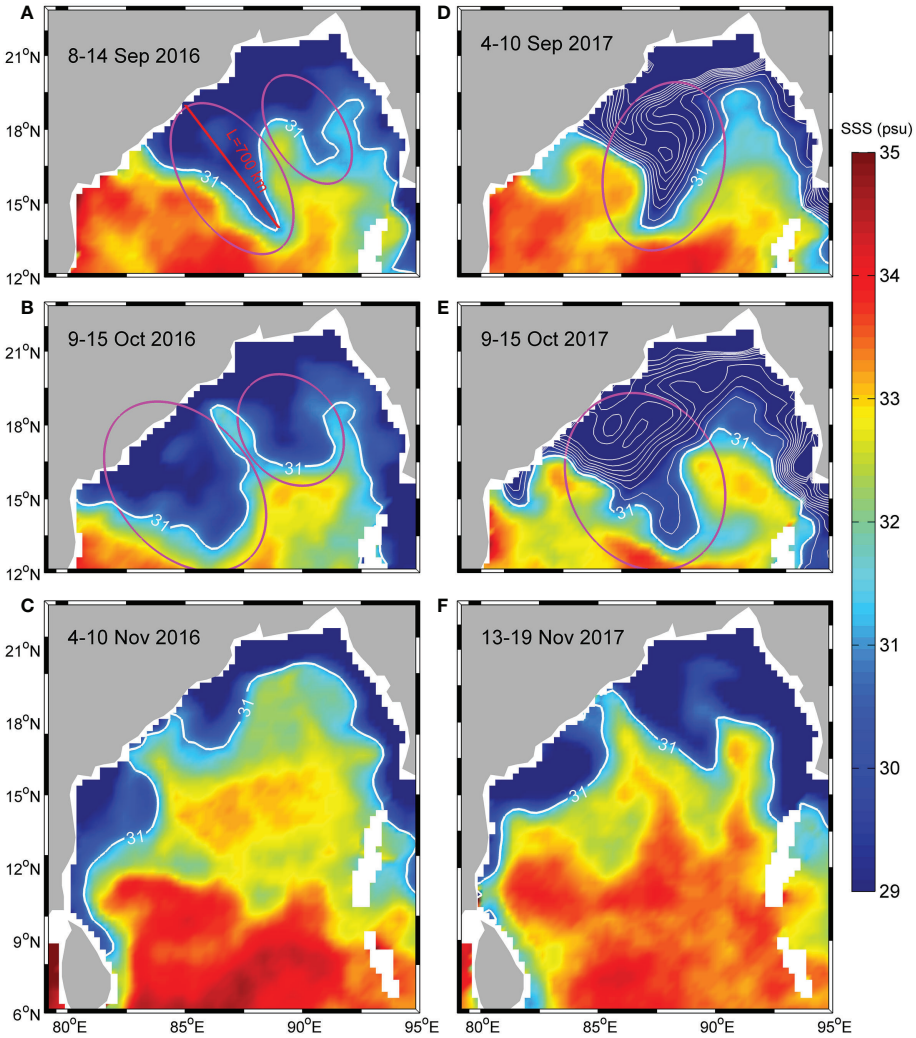


FIGURE 9
Snapshots of weekly SMAP SSS in the BoB during September to November of 2016 **(A–C)** and **(D–F)** 2017. The white lines indicate the SSS contours with an interval of 1 psu, and the SSS contour of 31 psu is bold. The purple ellipses highlight the offshore extending tongue-shaped freshwater plumes, with the red line indicating their lengths.

4.2 Year-to-year variability of the RIS modulated by mesoscale processes

It is interesting that the RIS also extended far southward during the La Niña events of 2016–2017 (Figure 3A). However, the spatial structure of the RIS differed sharply between 2016–2017 and 2020–2021 (Figure 6). During 2020–2021, the November SSS distribution showed a continuous, uniformly narrow (~100 km wide) strip of freshwater along the western BoB coast, which corresponds well with the representative features of the RIS proposed by Chaitanya et al. (2014). However, the November SSS distribution during 2016–2017 in the BoB indicated that such an organized RIS almost "did not exist". Combining the SMAP SSS and satellite altimeter data, we find that during the autumns of 2016 and 2017, pairs of eddies in the western BoB steered the freshwater offshore, extending several hundred kilometers, forming tongue-shaped plumes to the central bay (Figures 9, 10). The offshore extending freshwater plumes significantly affected the RIS through two aspects. First, the offshore extending freshwater plumes inhibited the formation of an RIS structure (narrow strip of freshwater) along the western BoB coast. This can explain why the spatial structures of the RIS were different between 2016–2017 and 2020–2021. Second, because the freshwater was transported offshore to the central bay, less freshwater remained to be transported southward along the coast. This can explain why the RIS did not extend as far southward during 2017 than during 2021, although the EICC and river discharge were comparable during the two years. Notably, such substantial offshore extending freshwater plumes were not formed during 2020–

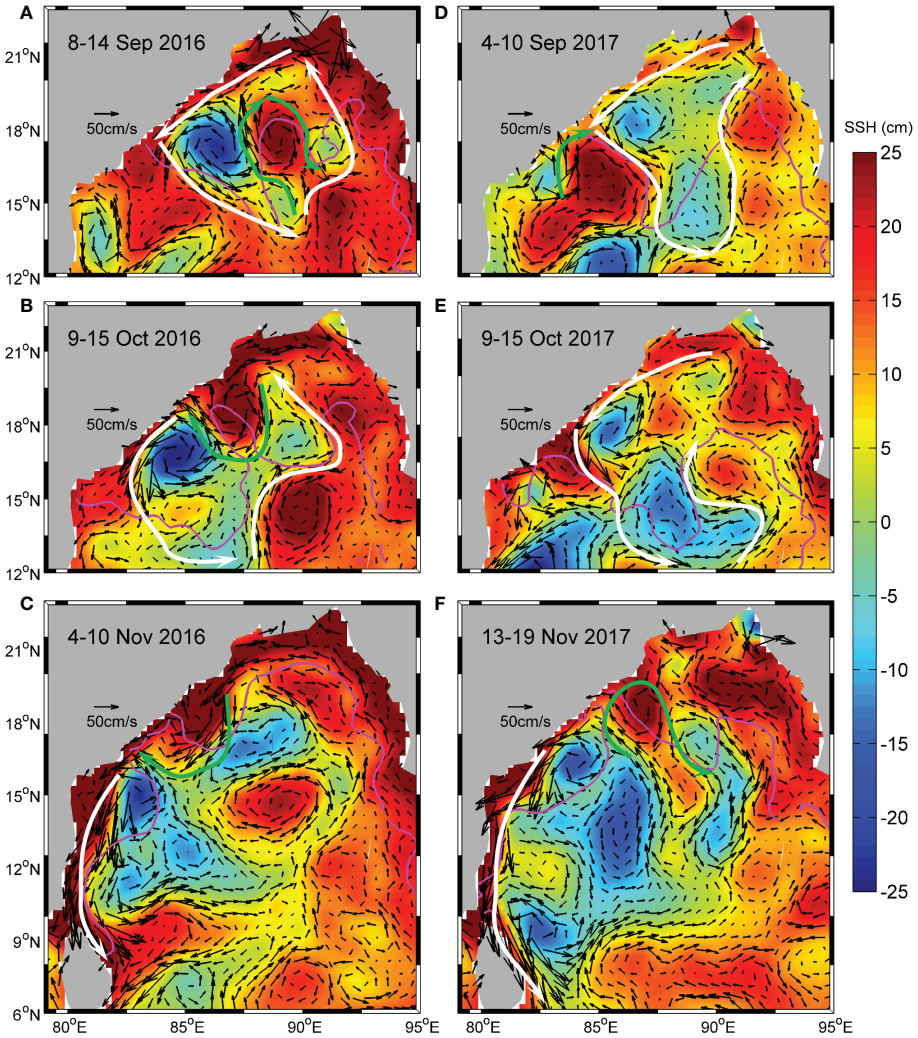


FIGURE 10
Snapshots of weekly SSH and associated geostrophic currents in the BoB during September to November of 2016 **(A–C)** and **(D–F)** 2017. The white arrows represent the cyclonic currents, and the green arrows indicate the ACE induced anticyclonic currents. The purple line indicates the SSS contour of 31 psu to represent the boundary of the freshwater plumes.

2021. Therefore, an organized RIS structure along the western BoB coast was observed during 2020–2021 (Figure 7).

By examining the 7-year SMAP SSS (2015–2021), offshore extending tongue-shaped freshwater plumes in the northern BoB were also found in 2015 (Figure 12). We attribute the formation of these plumes to the GB River freshwater modulated by pairs of eddies, which is consistent with the results of Li et al. (2021a). The western BoB is characterized by various ACEs and CEs (Chen et al., 2012; Cheng et al., 2013; Chen et al., 2018; Cheng et al., 2018; Lasitha Perera et al., 2019), and the influences of the pairs of eddies on the freshwater extension in the BoB need more consideration. We find that these tongue-shaped freshwater plumes can extend to the central northern BoB, which influence the stratification in the central bay. Moreover, the tongue-shaped freshwater plumes exhibit a strong SSS gradient (Figures 10D, E, 12A, B), which can further contribute to a large density gradient. The thermal–wind relationship indicates that a strong density gradient causes a vertical shear of velocity. Thus, the tongue-shaped freshwater plumes can influence the vertical structure of circulation in the BoB. In the future, eddy-resolving numerical models are necessary to simulate the formation of offshore extending tongue-shaped freshwater plumes in the BoB.

4.3 Advantages of SMAP SSS in quantifying the RIS

A narrow strip (~100 km) of freshwater hugs the western BoB coast, referred to as a "RIS" (Chaitanya et al., 2014). Limited by the

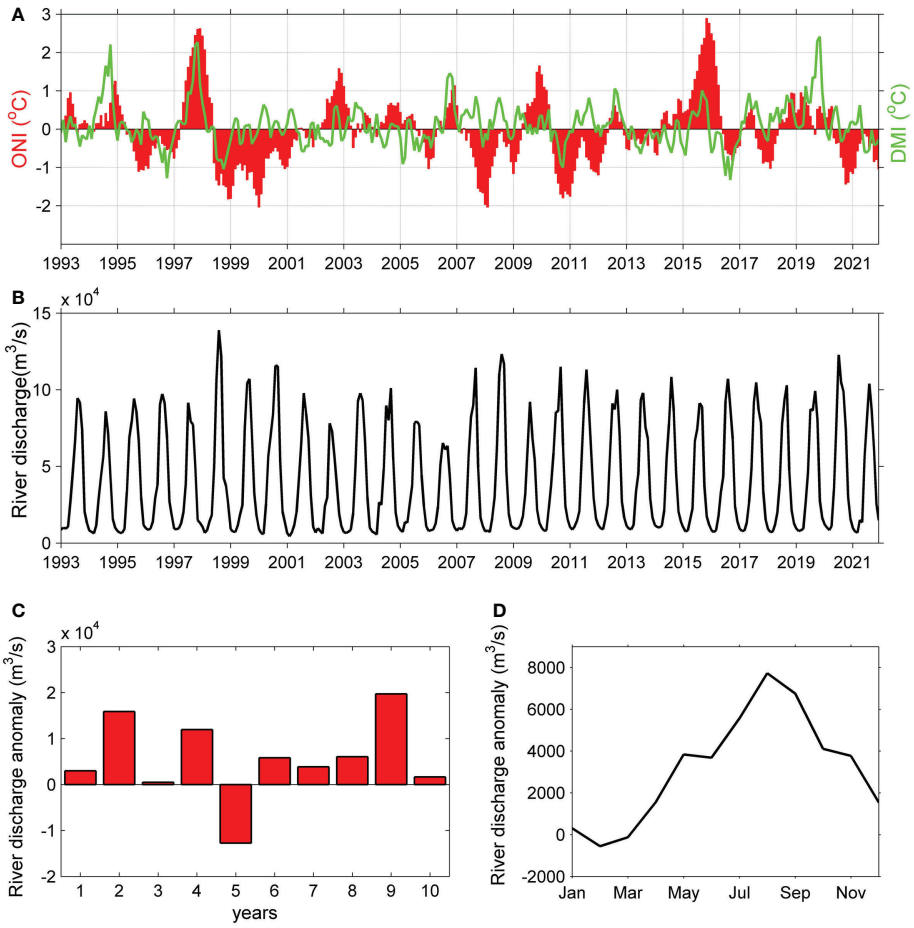


FIGURE 11
Monthly Oceanic Niño Index (ONI) and Dipole Mode Index (DMI) **(A)** and **(B)** GB River discharge during 1993–2021. **(C)** GB River discharge anomaly averaged over the summer monsoon during 10 La Niña years. **(D)** Composite GB River discharge anomaly averaged over the 10 La Niña years. In the composite analysis, the La Niña years are 1995, 1998, 1999, 2000, 2005, 2010, 2016, 2017, 2020, and 2021.

spatial sampling, *in-situ* salinity measurements are unable to capture the RIS in the BoB (Fournier et al., 2017). The SMAP provides a better SSS retrieval than other satellite observations, such as the Soil Moisture and Ocena Salinity (SMOS) (data quality in the northern BoB) and Aquarius missions (data are unavailable in coastal regions) (Akhil et al., 2016; Fournier et al., 2017), even if Akhil et al. (2020) recently show significant improvements in using SMOS to capture salinity variations close to the eastern coast of India. This motivates us to use the SMAP data to quantify the RIS in this study. Our results indicate that the SMAP data have significant advantages in quantifying the spatial and temporal variability of the RIS. First, the SMAP SSS shows a continuous, uniform strip of low salinity water that was 100 km wide hugging the entire western BoB coast (Figures 6A, B), confirming the findings of Chaitanya et al. (2014). To our knowledge, this is the first time that an organized RIS structure has been identified using the SSS distribution in the BoB. Second, the SMAP SSS can properly characterize the year-to-year variability of the RIS in terms of the southward extension. In the future, the long-term SMAP SSS opens new possibilities to study the interannual variability of the RIS in the BoB. Third, the SMAP SSS provides unprecedented views into the formation process of the RIS on short time scales of several weeks, which demonstrates that the mesoscale eddies profoundly modulate the spatial structure of the RIS (Figures 9, 10).

5 Summary and conclusion

In this study, we investigate the RIS along the western BoB coast using the SMAP satellite observations for 2015–2021. The SMAP data exhibit significant advantages in quantifying the

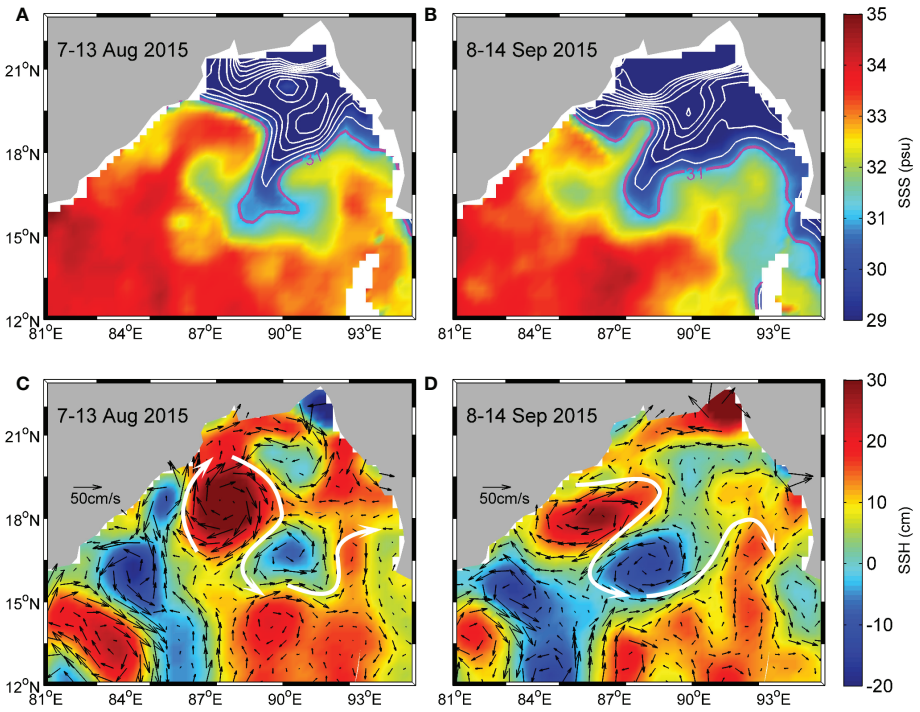


FIGURE 12
Distributions of SSS **(A, B)** and SSH and associated geostrophic currents **(C, D)** in the BoB for 7 August 2015 to 13 August 2015 (left) and (right) 8 September 2016 to 14 September 2015. The white lines indicate the contours of SSS with an interval of 1 psu. The purple line represents the SSS contour of 31 psu to highlight the boundary of the tongue-shaped freshwater plumes. The white arrows indicate the eddy-induced currents.

spatial and temporal variability of the RIS in the BoB. During the autumns of 2020 and 2021, SMAP SSS clearly identified a continuous, uniform strip of low salinity water (<31 psu) that was 100 km wide extending along the western BoB coast to south of Sri Lanka, reflecting the intensification of the RIS during these two years. Combining the SMAP SSS and satellite altimeter data, the processes responsible for the intensification of the RIS during 2020–2021 were explored.

The analysis indicates that the La Niña events of 2020–2021 were responsible for the intensification of the RIS. During these La Niña events, cyclonic circulation anomalies were generated along the boundary of the BoB to cause a stronger EICC. Meanwhile, the northern BoB received anomalous increased river discharge during the summer monsoons of the two years. The combination of the stronger EICC and increased river discharge led to anomalous freshwater transport along the western BoB coast that contributed to the intensification of the RIS. The SMAP SSS shows that the RIS extended far southward along the BoB coast during the La Niña events of 2016–2017. However, the spatial structures of the RIS differed sharply between 2016–2017 and 2020–2021. During 2016–2017, pairs of eddies in the western BoB steered the river freshwater offshore, extending several hundred kilometers, forming tongue-shaped freshwater plumes to the central bay. These offshore extending freshwater plumes inhibited the formation of an organized RIS structure along the western BoB coast during these two years. This study shows that the year-to-year variability of the RIS was significantly influenced by the La Niña events and modulated by mesoscale processes. In the future, eddy-resolving numerical models with high resolution are necessary to simulate the RIS in the BoB.

Data availability statement

The datasets presented in this study can be found in online repositories. The names of the repository/repositories and accession number(s) can be found in the article/supplementary material.

Author contributions

ZL carried out the analysis and wrote the manuscript with the supervision of X-HZ. YL and FP made contributions to the data collection and data processing. All authors discussed the results and commented on the manuscript. All authors contributed to the article and approved the submitted version.

Funding

This study was sponsored by the National Natural Science Foundation of China (41920104006, 42106035), the Scientific Research Fund of Second Institute of Oceanography, MNR (JZ2001), the Project of State Key Laboratory of Satellite Ocean Environment Dynamics, Second Institute of Oceanography (SOEDZZ2106 and SOEDZZ2207), the Oceanic Interdisciplinary Program of Shanghai Jiao Tong University (project number SL2021MS021), the Innovation Group Project of Southern Marine Science and Engineering Guangdong Laboratory (Zhuhai) (No. 311020004).

Conflict of interest

The authors declare that the research was conducted in the absence of any commercial or financial relationships that could be construed as a potential conflict of interest.

Publisher's note

All claims expressed in this article are solely those of the authors and do not necessarily represent those of their affiliated organizations, or those of the publisher, the editors and the reviewers. Any product that may be evaluated in this article, or claim that may be made by its manufacturer, is not guaranteed or endorsed by the publisher.

References

Akhil, V., Durand, F., Lengaigne, M., Vialard, J., Keerthi, M., Gopalakrishna, V., et al. (2014). A modeling study of the processes of surface salinity seasonal cycle in the bay of Bengal. *J. Geophysical Res.: Oceans* 119, 3926–3947. doi: 10.1002/2013JC009632

Akhil, V., Lengaigne, M., Vialard, J., Durand, F., Keerthi, M., Chaitanya, A., et al. (2016). A modeling study of processes controlling the bay of Bengal sea surface salinity interannual variability. *J. Geophysical Res.: Oceans* 121 (12), 8471–8495. doi: 10.1002/2016JC011662

Akhil, V., Vialard, J., Lengaigne, M., Keerthi, M., Boutin, J., Vergely, J., et al. (2020). Bay of Bengal sea surface salinity variability using a decade of improved SMOS re-processing. *Remote Sens. Environ.* 248, 111964. doi: 10.1016/j.rse.2020.111964

Aparna, S., Mccreary, J., Shankar, D., and Vinayachandran, P. (2012). Signatures of indian ocean dipole and El niño–southern oscillation events in sea level variations in the bay of bengal. *J. Geophysical Res.: Oceans* 117, 8055. doi: 10.1029/2012JC008055

Bao, S., Wang, H., Zhang, R., Yan, H., and Chen, J. (2019). Comparison of satellite-derived sea surface salinity products from SMOS, aquarius, and SMAP. *J. Geophysical Res.: Oceans* 124, 1932–1944. doi: 10.1029/2019JC014937

Behera, S., Krishnan, R., and Yamagata, T. (1999). Unusual ocean-atmospheric conditions in the tropical Indian ocean during 1994. *Geophysical Res. Letter* 26, 3001–3004. doi: 10.1029/1999GL010434

Chaitanya, A., Lengaigne, M., Vialard, J., Gopalakrishna, V., Durand, F., KranthiKumar, C., et al. (2014). Salinity measurements collected by fishermen reveal a "river in the sea" flowing along the Eastern coast of India. *Bull. Am. Meteorological Soc.* 95, 1897–1908. doi: 10.1175/BAMS-D-12-00243.1

Chen, G., Li, Y., Xie, Q., and Wang, D. (2018). Origins of eddy kinetic energy in the bay of Bengal. *J. Geophysical Res.: Oceans* 123, 2097–2115. doi: 10.1002/2017JC013455

Chen, G., Wang, D., and Hou, Y. (2012). The features and interannual variability mechanism of mesoscale eddies in the bay of Bengal. *Continental Shelf Res.* 47, 178–185. doi: 10.1016/j.csr.2012.07.011

Cheng, X., McCreary, J. P., Qiu, B., Qi, Y., Du, Y., and Chen, X. (2018). Dynamics of eddy generation in the central bay of bengal. *J. Geophysical Res.: Oceans* 123, 6861–6875. doi: 10.1029/2018JC014100

Cheng, X., Xie, S., McCreary, J. P., Qi, Y., and Du, Y. (2013). Intraseasonal variability of sea surface height in the bay of Bengal, *J. Geophysical Res.: Oceans* 118, 816–830, doi: 10.1002/jgrc.20075.

Das, B., Anandh, T., Kuttippurath, J., and Chakraborty, A. (2019). Characteristics of the discontinuity of western boundary current in the bay of Bengal. *J. Geophysical Res.: Oceans* 124, 4464–4479. doi: 10.1029/2019JC015235

Du, Y., and Zhang, Y. (2015). Satellite and Argo observed surface salinity variations in the tropical Indian Ocean and their association with the Indian Ocean Dipole mode. *J. Clim* 28 (2), 695–713. doi: 10.1175/JCLI-D-14-00435.1

Durand, F., Shankar, D., Birol, F., and Shenoi, S. (2009). Spatiotemporal structure of the East India coastal current from satellite altimetry. *J. Geophysical Res.* 114, C02013. doi: 10.1029/2008JC004807

Entekhabi, D., Njoku, E., O'Neill, P., Kellogg, K., Crow, W., Edelstein, W., et al. (2010). The soil moisture active passive (SMAP) mission. *Proc. IEEE* 98 (5), 704–716. doi: 10.1109/JPROC.2010.2043918

Fore, A., Yueh, S., Tanh, W., and Hayashi, A. (2020). *JPL SMAP ocean surface salinity products [Level 2B, level 3 running 8-day, level 3 monthly]* (Pasadena, CA, USA: Jet Propulsion Laboratory).

Fournier, S., Vialard, J., Lengaigne, M., Lee, T., Gierach, M., and Chaitanya, A. (2017). Modulation of the GangesBrahmaputra river plume by the Indian ocean dipole and eddies inferred from satellite observations. *J. Geophysical Res.: Oceans* 122, 9591–9604. doi: 10.1002/2017JC013333

Gnanaseelan, C., Deshpande, A., and McPhaden, M. (2012). Impact of Indian ocean dipole and El Niño/Southern oscillation wind-forcing on the wyrtki jets. *J. Geophysical Res.* 117, C08005. doi: 10.1029/2012JC007918

Grunseich, G., Subrahmanyam, B., Murty, V., and Giese, B. (2011). Sea Surface salinity variability during the Indian ocean dipole and ENSO events in the tropical Indian ocean. *J. Geophysical Res.* 116, C11013. doi: 10.1029/2011JC007456

Han, W., and McCreary, J. (2001). Modeling salinity distributions in the Indian ocean. *J. Geophysical Res.* 106 (C1), 859–877. doi: 10.1029/2000JC000316

Han, W., McCreary, J. P., and Kohler, K. E. (2001). Influence of precipitation minus evaporation and bay of Bengal rivers on dynamics, thermodynamics, and mixed layer physics in the upper Indian ocean. *J. Geophysical Res.* 106, 6895–6916. doi: 10.1029/2000JC000403

Hong, C., Lu, M., and Kanamitsu, M. (2008). Temporal and spatial characteristics of positive and negative Indian ocean dipole with and without ENSO. *J. Geophysical Res.* 113, D08107. doi: 10.1029/2007JD009151

Jensen, T. (2001). Arabian Sea And bay of Bengal exchange of salt and tracers in an ocean model. *Geophysical Res. Lett.* 28, 3967–3970. doi: 10.1029/2001GL013422

Lasitha Perera, G., Chen, G., McPhaden, M., Priyadarshana, T., Huang, K., and Wang, D. (2019). Meridional and zonal eddy-induced heat and salt transport in the bay of Bengal and their seasonal modulation. *J. Geophysical Res.: Oceans* 124, 8079–8101. doi: 10.1029/2019JC015124

Li, Z., Huang, S., Zhu, X., Sun, Z., Long, Y., and Xie, H. (2021a). Short-term offshore extension of Brahmaputra-Ganges and irrawaddy freshwater plumes to

the central northern bay of Bengal based on in situ and satellite observations. *Acta Oceanologica Sin.* 40 (5), 80–93. doi: 10.1007/s13131-021-1729-y

Li, Z., Lian, T., Ying, J., Zhu, X.-H., Papa, F., Xie, H., et al. (2021b). The cause of an extremely low salinity anomaly in the bay of Bengal during 2012 spring. *J. Geophysical Res.: Oceans* 126, e2021JC017361. doi: 10.1029/2021JC017361

McPhaden, M., Meyers, G., Ando, K., Masumoto, Y., Murty, V., Ravichandran, M., et al (2009). RAMA: The research moored array for African-Asian-Australian monsoon analysis and prediction. *Bull. Am. Meteorological Soc* 90, 459–480.

Murty, V. S. N., Sarma, Y. V. B., Rao, D. P., and Murty, C. S. (1992). Water characteristics, mixing and circulation in the bay of Bengal during southwest monsoon. *J. Mar. Res.* 50 (2), 207–228. doi: 10.1357/002224092784797700

Pant, V., Girishkumar, M., Udaya Bhaskar, T., Ravichandran, M., Papa, F., and Thangaprakash, V. (2015). Observed interannual variability of near-surface salinity in the bay of Bengal. *J. Geophysical Res.: Oceans* 120, 3315–3329. doi: 10.1002/2014JC010340

Papa, F., Bala, S., Pandey, R., Durand, F., Gopalakrishna, V., Rahman, A., et al. (2012). Ganga-Brahmaputra river discharge from Jason-2 radar altimetry: An update to the long-term satellite-derived estimates of continental freshwater forcing flux into the bay of Bengal. *J. Geophysical Res.* 117, C11021. doi: 10.1029/2012JC008158

Papa, F., Durand, F., Rossow, W., Rahman, A., and Bala, S. (2010). Satellite altimeter derived monthly discharge of the ganga-Brahmaputra river and its seasonal to interannual variations from 1993 to 2008. *J. Geophysical Res.* 115, C12013. doi: 10.1029/2009JC006075

Paul, N., Sukhatme, J., Sengupta, D., and Gayen, B. (2021). Eddy induced trapping and homogenization of freshwater in the Bay of Bengal. *J. Geophysical Res: Oceans* 126, e2021JC017180.

Roman-Stork, H., Subrahmanyam, B., and Murty, V. (2020). The role of salinity in the southeastern Arabian Sea in determining monsoon onset and strength. *J. Geophysical Res.: Oceans* 125, e2019JC015592. doi: 10.1029/2019JC015592

Saji, N., Goswami, B., Vinayachandran, P., and Yamagata, T. (1999). Nature 401, (6751), 360–363. doi: 10.1038/43855

Sengupta, D., Bharath, R., and Shenoi, S. (2006). Surface freshwater from bay of Bengal runoff and Indonesian throughflow in the tropical Indian ocean. *Geophysical Res. Lett.* 33, L22609. doi: 10.1029/2006GL027573

Sherin, R., Durand, F., Gopalakrishna, V., Anuvinda, S., Chaitanya, A., Bourdallé-Badied, R., et al. (2018). Signature of Indian ocean dipole on the western boundary current of the bay of Bengal revealed from 27 years of repeated *in situ* observations. *Deep-Sea Res. Part I* 136, 91–106. doi: 10.1016/j.dsr.2018.04.002

Shetye, S., Gouveia, A., Shankar, D., Shenoi, S., Vinayachandran, P., Sundar, D., et al. (1996). Hydrography and circulation in the western bay of Bengal during the northeast monsoon. *J. Geophysical Res.* 101 (C6), 14011–14025. doi: 10.1029/95JC03307

Shetye, S., Gouveia, A., Shenoi, S., Sundar, D., Michael, G., and Nampoothiri, G. (1993). The western boundary current of the seasonal subtropical gyre in the bay of Bengal. *J. Geophysical Res.* 98 (C1), 945–954. doi: 10.1029/92JC02070

Sprintall, J., and Tomczak, M. (1992). Evidence of the barrier layer in the surface layer of the tropics. *J. Geophysical Res.* 97 (C5), 7305. doi: 10.1029/92JC00407

Sree Lekha, J., Buckley, J. M., Tandon, A., and Sengupta, D. (2018). Subseasonal dispersal of freshwater in the northern bay of Bengal in the 2013 summer monsoon season. *J. Geophysical Res.: Oceans* 123, 6330–6348. doi: 10.1029/2018JC014181

Sree Lekha, J., Lucas, A., Sukhatme, J., Joseph, J., Ravichandran, M., Suresh Kumar, N., et al (2020). Quasi-biweekly mode of the Asiansummer monsoon revealed in Bay ofBengal surface observations. *J. Geophysical Res: Oceans* 125, e2020JC016271. doi: 10.1029/2020JC016271

Stuecker, M., Timmermann, A., Jin, F., Chikamoto, Y., Zhang, W., Wittenberg, A., et al. (2017). Revisiting ENSO/Indian ocean dipole phase relationships. *Geophysical Res. Lett.* 44, 2481–2492. doi: 10.1002/2016GL072308

Subrahmanyam, B., Murty, V., and Heffner, D. (2011). Sea Surface salinity variability in the tropical Indian ocean. *Remote Sense Environ.* 115, 944–956. doi: 10.1016/j.rse.2010.12.004

Subrahmanyam, B., Trott, C., and Murty, V. (2018). Detection of intraseasonal oscillations in SMAP salinity in the bay of Bengal. *Geophysical Res. Lett.* 45, 7057–7065. doi: 10.1029/2018GL078662

Suneel, V., Alex, M., Thomas, P., Gurumoorthi, K., Rao, V., Harikrishnan, S., et al. (2020). Impact of remote equatorial winds and local mesoscale eddies on the existence of "River in the sea" along the East coast of India inferred from satellite SMAP. *J. Geophysical Res.: Oceans* 125, e2020JC016866. doi: 10.1029/2020JC016866

Tang, W., Fore, A., Yueh, S., Lee, T., Hayashi, A., Sanchez-Franks, A., et al. (2017). Validating SMAP SSS with *in situ* measurements. *Remote Sens. Environ.* 200, 2561–2564. doi: 10.1109/IGARSS.2017.8127518

Thadathil, P., Muraleedharan, P. M., Rao, R. R., Somayajulu, Y. K., Reddy, G. V., and Revichandran, C. (2007). Observed seasonal variability of barrier layer in the bay of Bengal. *J. Geophysical Res.* 112, C02009. doi: 10.1029/2006JC003651

Thompson, B., Gnanaseelan, C., and Salvekar, P. (2006). Variability in the Indian ocean circulation and salinity and its impact on SST anomalies during dipole events. *J. Mar. Res.* 64, 853–880. doi: 10.1357/002224006779698350

Trott, C., Subrahmanyam, B., Murty, V., and Shriver, J. (2019). Large-Scale fresh and salt water exchanges in the Indian ocean. *J. Geophysical Res.: Oceans* 124, 6252–6269. doi: 10.1029/2019JC015361

Vinayachandran, P., Murty, V., and Ramesh Babu, V. (2002). Observations of barrier layer formation in the bay of Bengal during summer monsoon. *J. Geophysical Res.* 107 (C12), 8018. doi: 10.1029/2001JC000831

Webster, P., Magana, A., Palmer, T., Shukla, J., Tomas, R., Yanai, M., et al. (1998). Monsoons: processes, predictability, and the prospects for prediction. *J. Geophysical Res.: Oceans* 103 (C7), 14451–14510.

Webster, P., Moore, A., Loschnigg, J., and Leben, R. (1999). Coupled oscean-atmosphere dynamics in the Indian ocean during 1997-98. *Nature* 401 (6751), 356–360. doi: 10.1038/43848

frontiers | Frontiers in Marine Science

TYPE Original Research
PUBLISHED 18 January 2023
DOI 10.3389/fmars.2022.1100772

Check for updates

OPEN ACCESS

EDITED BY
Xiaoteng Shen,
Hohai University, China

REVIEWED BY
Wenjin Sun,
Nanjing University of Information Science and Technology, China
Qiyan Ji,
Zhejiang Ocean University, China
Yu Liu,
Zhejiang Ocean University, China

*CORRESPONDENCE
Zifeng Hu
huzifeng@mail.sysu.edu.cn

SPECIALTY SECTION
This article was submitted to Ocean Observation, a section of the journal Frontiers in Marine Science

RECEIVED 17 November 2022
ACCEPTED 27 December 2022
PUBLISHED 18 January 2023

CITATION
Chen J and Hu Z (2023) Seasonal variability in spatial patterns of sea surface cold- and warm fronts over the continental shelf of the northern South China Sea.
Front. Mar. Sci. 9:1100772.
doi: 10.3389/fmars.2022.1100772

COPYRIGHT
© 2023 Chen and Hu. This is an open-access article distributed under the terms of the Creative Commons Attribution License (CC BY). The use, distribution or reproduction in other forums is permitted, provided the original author(s) and the copyright owner(s) are credited and that the original publication in this journal is cited, in accordance with accepted academic practice. No use, distribution or reproduction is permitted which does not comply with these terms.

Seasonal variability in spatial patterns of sea surface cold- and warm fronts over the continental shelf of the northern South China Sea

Jiayuan Chen[1,2] and Zifeng Hu[2,3,4]*

[1]School of Cyber Science and Technology, Sun Yat-sen University & Southern Marine Science and Engineering Guangdong Laboratory (Zhuhai), Zhuhai, China, [2]School of Marine Sciences, Sun Yat-sen University, Zhuhai, China, [3]Pearl River Estuary Marine Ecosystem Research Station, Ministry of Education, Zhuhai, China, [4]Guangdong Provincial Key Laboratory of Marine Resources and Coastal Engineering, Zhuhai, China

Ubiquitous fronts are a key part of energy transfer from large scales to small scales and exert a great impact on material exchange and biogeochemical processes. The spatial pattern and seasonal variability of cold- and warm fronts over the wide shelf of the northern South China Sea (SCS) are investigated using a 20-year time series (2002–2021) of 1-km spatial resolution Group for High Resolution Sea Surface Temperature (GHRSST) images. Our analysis shows distinct spatial and temporal variability in the occurrence of the cold- and warm fronts. Over the inner shelf (depth <50 m), the band-shaped cold fronts are predominately observed during spring through autumn from east of Hainan Island to Taiwan Shoal, with the presence of the maximum intensity and probability in winter. The frontal formations are possibly associated with the joint effect of the Guangdong Coastal Current (GCC) and the South China Sea Warm Current. During summer, the inshore fronts have relatively low probability and gradient magnitude. The warm fronts mainly occur off the western Guangdong coast possibly due to the southwestward-flowing GCC, whereas the cold fronts dominate off the eastern Guangdong coast and the eastern Hainan Island largely because of the coastal upwelling. Over the outer shelf (depth >50 m), the finer-scale cold- and warm fronts are discretely observed, with relatively weaker intensity and lower probability. The frontal activities are very vigorous in winter but slightly quiescent in summer, apparently resulting from the influence of the rich submesoscale processes in the SCS. This study could help improve our understanding of the SCS oceanic multiscale dynamics.

KEYWORDS

cold fronts, warm fronts, spatial patterns, seasonal variability, the northern South China Sea

Introduction

Fronts in the ocean are the junction of different water masses and the narrow transition zones with relatively obvious changes in physical, biological, and/or chemical properties (Legeckis, 1978). Oceanic fronts are ubiquitous, with spatial scales ranging from O(1) to O(1000) km (Fedorov, 1986). The front dynamics are very active, where the energy transfers strongly from large scale to small scale, accompanied by the generation of internal waves, intense turbulence and upwelling, etc. (Chu and Wang, 2003). Strong material exchange induced by fronts could bring deep nutritive water to the upper layer, thereby enhancing local biological productivity (Fournier, 1978). Understanding the oceanic fronts and their variability is therefore essential for studying multiscale ocean dynamics, marine ecosystems and fishery productivity (Wang et al., 2020).

The South China Sea (SCS) is the largest marginal sea in the Western Pacific. It connects to the East China Sea and the Pacific Ocean by the Taiwan and Luzon Channels (Ren et al., 2015; Hu et al., 2016). Under the impact of seasonally varying monsoon, Kuroshio intrusion, and complex bathymetry (Liu et al., 2002; Qu et al., 2007), various fronts exist in the SCS and show pronounced spatiotemporal variability. Using hourly infrared satellite cloud maps, Chen (1983) explored the distribution of fronts in the northern South China Sea (NSCS) in winter. Using multi-year monthly sea surface temperature (SST) satellite data in the NSCS, Wang et al. (2001) analyzed the location and seasonal variability of several major fronts by calculating the frequency of frontal occurrences. Yao et al. (2012) used a visual graphical method to describe the monthly fronts in the entire SCS (Chen et al., 2012; Wang et al., 2012; Guo et al., 2017). Using 4-km spatial resolution SST satellite observations, Wang et al. (2020) identified wind-related fronts near the coast of northern Luzon and Vietnam.

Oceanic cold- and warm fronts were originally introduced by Ullman and Cornillon (1999). They presented the spatial pattern and temporal variability of cold- and warm fronts off the northeast U.S. coast. Based on local bathymetry and temperature gradients, Ullman and Cornillon (2001) further developed more detailed algorithms for distinguishing warm and cold fronts. Lately, Chang et al. (2008) explored the relationship between cold- and warm fronts in the East China Sea and chlorophyll-a concentration. However, the identification of cold- and warm fronts and the corresponding variations in the SCS have not yet been investigated for the present.

The main objectives of this study are to present a basic overview of the cold- and warm fronts in the NSCS, and to describe the seasonal cycle in the occurrence and strength of these fronts, based on the 1-km spatial resolution GHRSST (Group for High Resolution Sea Surface Temperature) SST data over a span of 20-year period (2002-2021). The paper is organized as follows: Section 2 describes the data and methods; Section 3 shows the mean seasonal cycle of the cold- and warm fronts over the NSCS shelf. Discussion and conclusions are given in section 4.

Data and methods

Study area

The area of interest for this study is a portion of the NSCS (108°-121°E, 17°-24°N), extending from the east coast of Hainan Island to the Taiwan Shoal. To subsequently present the front occurrence statistics, the study region has been subdivided into three sub-areas shown in Figure 1. The chosen boundaries are partly based on bathymetric and geographic features, e.g., the shelfbreaks, the Pearl River Estuary (PRE), and the Kuroshio-influenced Taiwan Shoal (Ren et al., 2015; Yu et al., 2020).

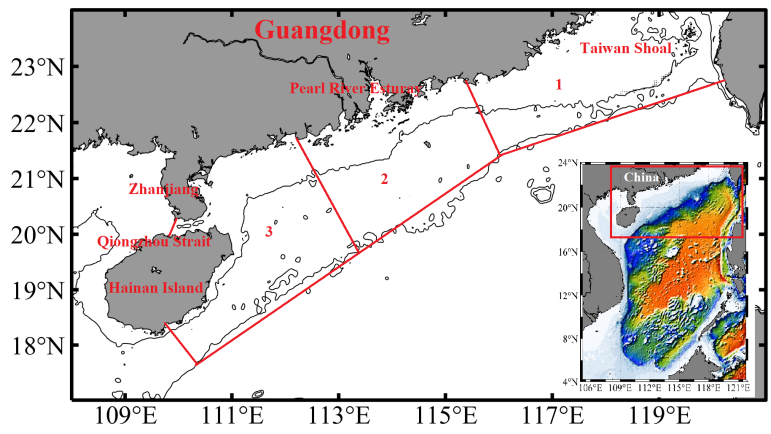


FIGURE 1
Bathymetry of the northern South China Sea (NSCS). Black contours indicate 50-m and 200-m isobaths. The study region is subdivided into three shelf zones (red lines) for subsequent analysis.

Data

The daily SST data from June 2002 to December 2021 are derived from the Group for High-Resolution Sea Surface Temperature (GHRSST) project based on several instruments, e.g., the NASA Advanced Microwave Scanning Radiometer-EOS (AMSR-E), the JAXA Advanced Microwave Scanning Radiometer 2 on GCOM-W1, the Moderate Resolution Imaging Spectroradiometers (MODIS) on the NASA Aqua and Terra platforms, the US Navy microwave WindSat radiometer, the Advanced Very High-Resolution Radiometer (AVHRR) on several NOAA satellites, and *in situ* SST observations from the NOAA iQuam project. The GHRSST data have a 1-km spatial resolution and are obtained from NASA's Physical Oceanography Distributed Active Archive Center (PO.DAAC) (https://podaac.jpl.nasa.gov/dataset).

SST front detection

An objective edge detection technique based on Jensen-Shannon divergence (JSD), called entropy-based algorithm, was proposed by Shimada et al. (2005) and used to identify surface thermal fronts. The method has independence from spatiotemporal varying geophysical parameters and shows better performance compared with other conventional methods [e.g., gradient magnitude and histogram edge detection algorithm) (Shimada et al., 2005; Chang and Cornillon, 2015; Hu et al., 2021). Specifically, four different JSD matrices are firstly calculated in each of two 5×5 pixel SST subwindows with four different directions (horizontal, vertical, and two diagonals, see Shimada et al. (2005)]. The final JSD value at each pixel is assigned with the maximum of the four JSD matrices. It ranges from zero to one and represents the spatial inhomogeneity of two neighboring SST subwindows across a front. Stronger fronts have higher JSD values. To detect more and finer-scale fronts, JSD≥0.4 in this study is used as a frontal pixel.

At subinertial time scales, it is anticipated that the flow associated with a density front is roughly be in geostrophic balance, with the flow primarily in the along-front direction. The orientation of the SST front reveals the direction of the along-front subinertial flow if SST fronts are supposed to have a density signature. The temperature gradient vector's direction, averaged along the length of the front, is assumed to be the direction of the mean frontal orientation (Ullman and Cornillon, 2001). Following Ullman and Cornillon (2001), the orientation of a front relative to the local bathymetry is measured by the normalized scalar product of the SST gradient and bathymetry gradient vectors. The normalized scalar product P is calculated with the formula:

$$\boldsymbol{P} = \frac{\nabla T \nabla H}{|\nabla T||\nabla H|} (1)$$

where T is the SST and H is the water depth. The P-value ranges from −1 to 1. When the front is parallel to the local isobath, P-value reaches the minimum (maximum) which corresponds to cold (warm) water on the shallow side. When P-value is zero, the front is perpendicular to the local isobath. The P domain is then classified into three ranges (Figure 2): cold fronts ($-1 \le P \le -0.6$), warm fronts ($0.6 \le P \le 1$), and cross-isobath fronts ($-0.6 < P < 0.6$).

Frontal probability (FP) at each pixel (Ullman and Cornillon, 1999; Shimada et al., 2005) is defined as follows:

$$FP = \frac{N_{front}}{N_{valid}} (2)$$

where N_{front} is the number of valid frontal pixels with JSD≥0.4, N_{valid} is the number of total valid pixels over 20 years. FP represents the mean probability of a front passing through a pixel.

The SST frontal gradient magnitude (GM), a measure of frontal strength, is defined as:

$$GM = \sqrt{(\partial T/\partial x)^2 + (\partial T/\partial y)^2} \ (^\circ C/km) (3)$$

where $\partial T/\partial x$ and $\partial T/\partial y$ correspond to the gradient magnitudes in x and y directions. Frontal gradient direction is the angle between

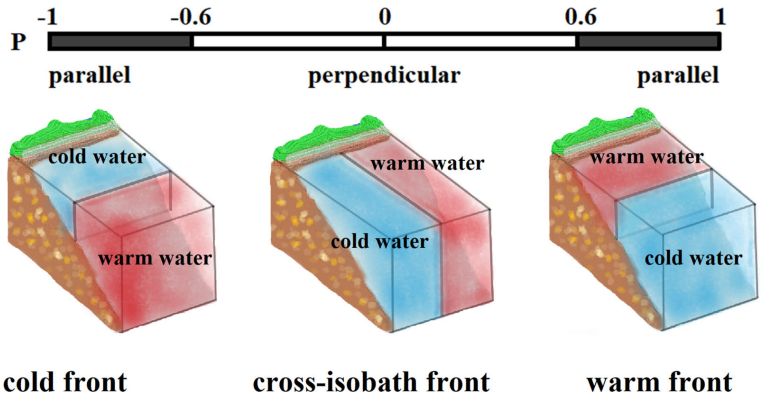


FIGURE 2
A schematic diagram illustrates the relationship between the P value and the classification of warm and cold fronts.

frontal gradient vector and due north direction. The cross-front length L, another measure of frontal strength, is calculated by the following formula (Ullman and Cornillon, 2001):

$$L = \frac{\Delta T}{\nabla T} \quad (4)$$

where ΔT is the mean cross-front temperature step and ∇T is the mean cross-front temperature gradient.

Results

Seasonal SST variability

Seasonal SST variability is briefly described for setting the stage for the discussion of the seasonal cycle in front occurrence. Figure 3 shows the seasonal SST averaged over 2002-2021, illustrating the differences between winter, spring, summer, and autumn SST patterns. In winter, the isotherms over the shelf are roughly parallel to the coast, and a band of cold water (< 21°C) is present nearshore, with large temperature gradients across the 25-m isobath. The SST warms up throughout the spring, with moderately warm water (27–29°C) off the coast of Hainan and cold water (24–26°C) off the coast of Guangdong. The peak temperature (>28°C) is recorded in summer, while two cold water cores are present near Hainan and Guangdong's northeastern coasts. As the SST cools throughout fall, a belt of cold water reoccurs along the Guangdong coast.

Seasonal variations of cold and warm fronts

Spatial variability

In order to determine the distribution of cold and warm fronts over the period of 20 years, we first calculate the P-value at frontal pixels for each image, and then composite all the images from each season. The seasonal variations in the occurrence of cold and warm fronts are shown in Figure 4. A strong distinctive cold (warm) front is one whose P-value is close to −1(1). Also, the seasonal FP (Figure 5), frontal gradient magnitude (Figure 6) and direction (Figure 7) are presented separately. In the following description, the frontal probabilities are categorized into three regimes: low (5%–10%), moderate (10%–20%), and high (> 20%).

Winter

In subregion 1, large-scale and pronounced cold fronts are observed in a broad band off the Guangdong coast, whereas warm fronts mainly appear around the Taiwan Shoal (Figure 4A). The crescent-shape highest probability zone (20–30%) is located on the onshore side of 50-m depth (Figure 5A). Over the continental shelf, the frontal gradient magnitudes on average range from 0.06 to 0.1°C/km (Figure 6A). The frontal gradient direction suggests the existence of a nearshore cold water (Figure 7A), consistent with the intrusion of cold water flowing southward along the Guangdong coast.

In subregion 2, there is a broad band of cold fronts within the 50-m isobath, with dispersed warm fronts near the PRE. These fronts have a moderate to high probability (Figure 5A), with offshore gradients (Figure 7A), closely associated with the mixing of the cool river discharge with the warm nearshore water. Finer-scale cold and warm fronts are sporadically scattered throughout the wide continental shelf between 50- and 200-m isobaths (Figure 4A), with a low probability (5–10%) and gradient magnitude (0.03–0.05°C/km).

In subregion 3, most of the nearshore areas are occupied by a right-angle-shaped cold front band, while a small area of warm

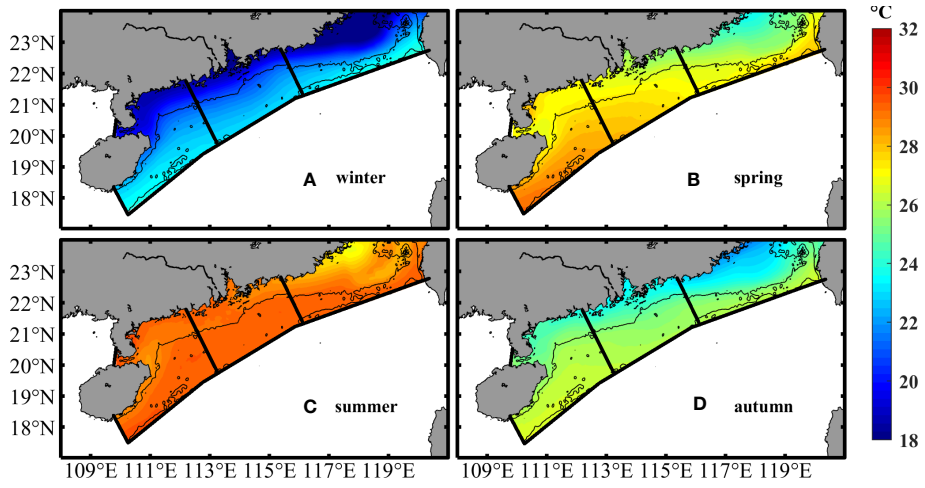


FIGURE 3
Seasonal SST averaged over 2002-2021 for **(A)** winter (January-March), **(B)** spring (April-June), **(C)** summer (July-September), and **(D)** autumn (October-December).The black lines are the 50-m and 200-m isobaths.

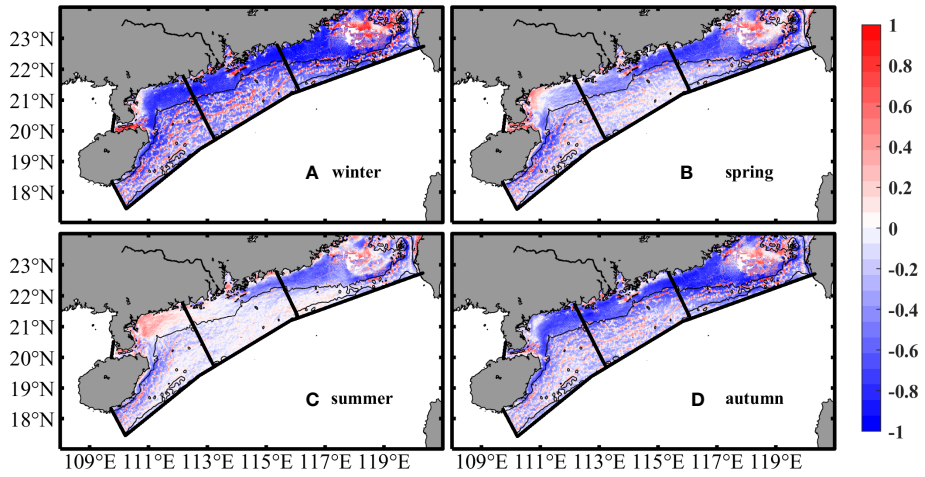


FIGURE 4
Seasonal distribution of cold and warm fronts averaged over 2002-2021 for **(A)** winter(January-March), **(B)** spring(April-June), **(C)** summer (July-September), and **(D)** autumn (October-December). Blue (red) represent cold(warm) fronts.The black lines are the 50-m and 200-m isobaths.

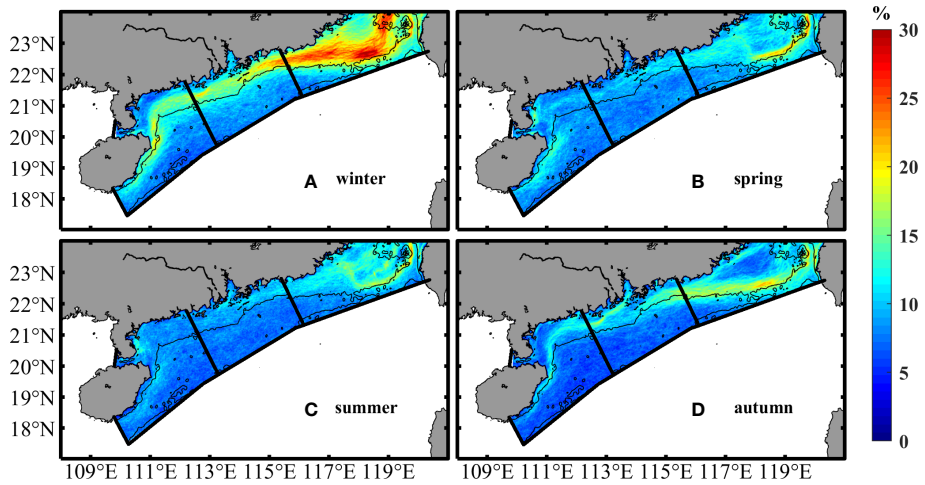


FIGURE 5
Seasonal frontal probability averaged over 2002-2021 for **(A)** winter (January-March), **(B)** spring (April-June), **(C)** summer (July-September), and **(D)** autumn (October-December).The black lines are the 50-m and 200-m isobaths.

fronts can be found off the Zhanjiang coast (Figure 4A). These fronts have a moderate probability, with their peak approximately along the 50m isobath (Figure 5A). The frontal gradient directions are 180°–225° off the coast of Zhanjiang, but 90°–135° to the east of Hainan (Figure 7A).

Spring

In subregion 1, while there are no noticeable spatial changes in the warm- and cold fronts pattern, the frontal probability has significantly decreased (Figure 5B). Around the Taiwan Shoal, a small band on the onshore side of the 50-m isobath has the highest frontal probabilities (about 20%). The gradient directions reveal that the fronts in the center of the shoal are roughly oriented northwest, while the surrounding cold fronts are directed northeast (Figure 7B).

In subregion 2, cold fronts continue to diminish on the shallow side of 50-m isobath around the PRE (Figure 4B). However, the fronts on the east side of the PRE are much larger than those on the west side in the terms of P-value, frontal probability, and gradient (Figures 5B, 6B). In the area between 50- and 200-m isobaths, the finer-scale warm- and cold fronts weaken, accompanied by a decrease in frontal probability (Figure 4B). These fronts steer northeast, probably an early signal of the SCS Warm Current (Figure 7B).

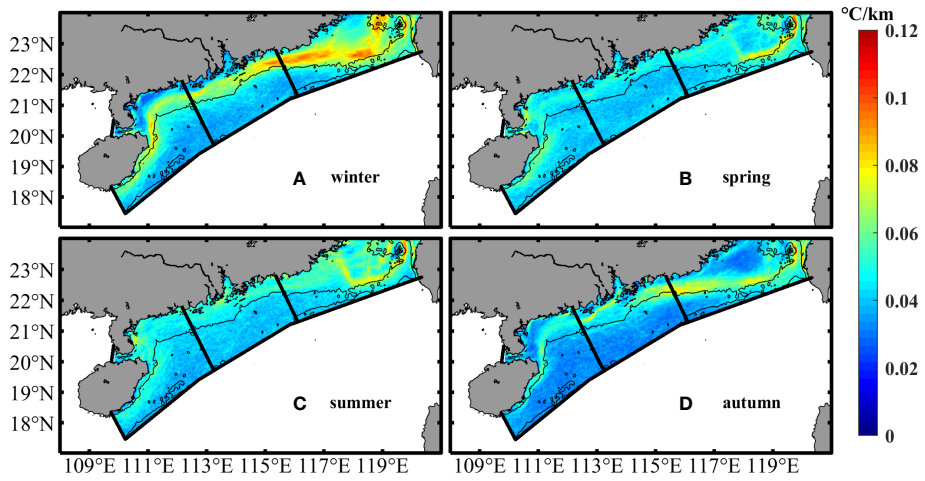


FIGURE 6
Mean SST gradient magnitude at frontal pixels averaged over 2002–2021 for **(A)** winter (January–March), **(B)** spring (April–June), **(C)** summer (July–September), and **(D)** autumn (October–December).The black lines are the 50-m and 200-m isobaths.

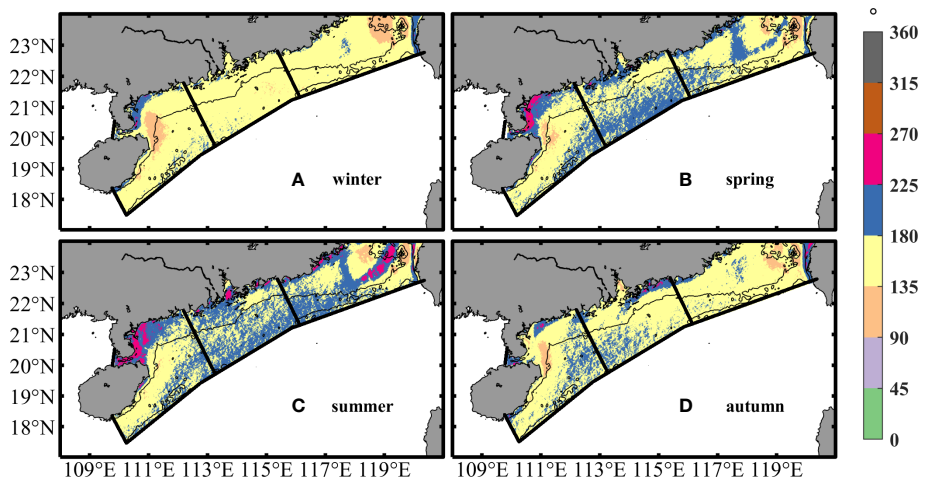


FIGURE 7
Mean SST gradient direction at frontal pixels averaged over 2002–2021 for **(A)** winter(January–March), **(B)** spring(April–June), **(C)** summer (July–September), and **(D)** autumn(October–December).The black lines are the 50-m and 200-m isobaths.

In subregion 3, cold fronts are primarily located off the western Guangdong and the coast of Hainan, while warm fronts appear around the Zhanjiang coast and the Qiongzhou Strait (Figure 4B). Each of these fronts has a low to moderate probability (Figure 5B). The gradient directions indicate that these fronts are created by southward warm water and cool nearshore water (Figure 7B).

Summer

In subregion 1, the spatial pattern of warm- and cold fronts is relatively stable, but the P-value and frontal probability are further decreased (Figures 4C, 5C). In contrast to spring, the frontal gradient does somewhat rise (Figure 6C). The gradient directions indicate that there is cold water close to the eastern Guangdong and Taiwan coasts (Figure 7C), due to the upwelling occurrence induced by the summer monsoon. The upwelling could create stronger fronts in summer than in spring, while surface heating may play a secondary role.

In subregion 2, warm fronts appear in the western portion of PRE within 50 m isobath, whereas cold fronts appear in the eastern portion (Figure 4C). The probability of both fronts is low probabilities (Figure 5C), smaller than in the spring. On the west side of PRE, the fronts have even more pronounced decline. The frontal gradients are largest near the PRE, and exhibit little variation, revealing a complex system of both river and offshore currents (Figure 6C).

In subregion 3, over the continental shelf, cold fronts mainly exist on the continental shelf to the east of Hainan. Weak warm fronts dominate in the nearshore area off the western Guangdong coast (Figure 4C), where the probability is further decreased (Figure 5C) with no insignificant variation in the frontal gradients (Figure 6C). The gradient directions suggest that the cold fronts are closely related to the local coastal upwelling (Figure 7C).

Autumn

In subregion 1, warm fronts appear around the Taiwan Shoal, and a vast range of strong cold front band reappears off the coast of eastern Guangdong (Figure 4D). These fronts have the highest probability observed in a relatively limited zone along the 50-m isobath (Figure 5D). The pattern of the frontal gradients is well consistent with the probability (Figure 6D). The frontal gradient directions indicate that the shoal is dominated by southward-flowing cool water (Figure 7D).

In subregion 2, the band of strong cold front reappears within the 50 m depth (Figure 4D). A zone of moderate probability surrounds the PRE and extends to the west side (Figure 5D). The formation of the cold fronts is closely associated with the relatively cool river discharge. Also, the activity of finer-scale warm- and cold fronts between 50- and 200- m isobaths gradually become stronger (Figure 4D).

In subregion 3, the cold fronts occupy a large portion of the coastal zone from the western Guangdong to Hainan Island, while warm fronts are essentially absent (Figure 4D). A narrow moderate probability band which originates from the PRE is generally located well inside the 50-m isobath. The frontal gradient directions are generally oriented to southward, indicating that the cold fronts may be the result of southwestward-flowing cold water from the Pearl River (Figure 7D).

Temporal variability

To quantitatively represent the temporal variability of the frontal properties, we first calculate, at each frontal pixel, the frontal temperature, SST gradient, cross-frontal temperature step, frontal proportion (i.e., the ratio of the number of warm or cold fronts to the number of total fronts), frontal probability, and water depth. These time series are subsequently averaged over all frontal pixels in the each subregion to obtain the corresponding mean time series for the entire 20 years (2002–2021).

Figure 8 shows the time evolution of the mean temperature (T), mean cross-frontal temperature step (ΔT), mean gradient (∇T), and

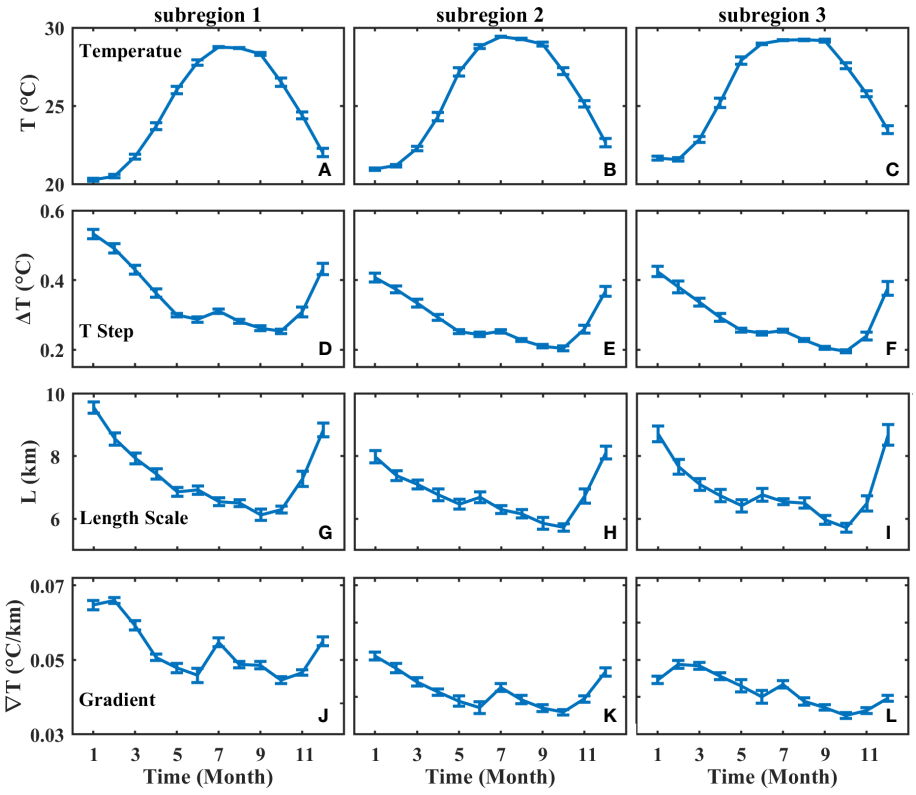


FIGURE 8
Mean monthly time series of frontal temperature **(A–C)**, cross-frontal temperature step **(D–F)**, cross-frontal length scale **(G–I)**, cross-frontal temperature gradient **(J–L)** for the three subregions averaged over 2002-2021. The error bars denote the 95% confidence intervals.

cross-frontal length scale (L) for each of the three subregions. Generally, each frontal property has similar significant seasonal variability for all the subregions. The mean SST has a maximum in summer and a minimum in winter (Figures 8A–C). The mean cross-front temperature step and cross-frontal length scale tend to reach their peaks in January-February before gradually decreasing from spring to summer (Figures 8D–I). The mean temperature step varies from 0.2 to 0.4°C (Figures 8D–F), and the cross-frontal length scale ranges from 6 to 9 km (Figures 8G–I), with large values occurring in January-December. The frontal gradient ranges from 0.02 to 0.07°C/km. It peaks in January and then declines through September, with a slow increase in July (Figures 8J–L).

Figure 9 shows the time evolution of the mean frontal proportion, mean frontal probability, mean frontal gradient and mean frontal water depth of the cold- and warm fronts for each of the three subregions. In the three subregions, the cold and warm frontal proportion varies in the opposite directions (Figures 9A–C). The mean proportion of the cold fronts is much higher compared with the warm fronts. Up to 70% of the cold fronts occur in winter, and then steadily drop to the lowest level in summer. In contrast, the proportion of the warm fronts reaches a maximum in summer and a minimum in winter. The mean FP of the cold fronts fluctuates roughly with its proportion, while the mean FP of the warm fronts shows less significant variability (Figures 9D–F). The mean frontal probability ranges from 2 to 3% for the warm fronts, and from 3 to 9% for the cold fronts, indicating that the cold fronts are primarily responsible for changes in the ratio of warm to cold fronts. The mean frontal gradient generally has similar variability for the cold and warm fronts. It ranges from 0.03 to 0.07°C/km (Figures 9G–I). For the mean frontal water depth, large differences between the cold and warm fronts are very apparent in the three subregions (Figures 9J–L). The cold fronts in the subregions 2 and 3 obviously move offshore in summer and onshore in winter, in opposite to the warm fronts, whereas there is little variation in the warm and cold front positions in the subregion 1.

To further understand the spatiotemporal variability of SST fronts, the empirical orthogonal function (EOF) analysis is performed for 20 years of monthly FP data including both cold and warm fronts. In this study, we only show the first EOF mode which could account for 11.27% of the total variance, since the second mode accounts for less than 4% of the variance. The first EOF mode and its time series amplitude are shown in Figure 10. Around the Taiwan Shoal, off the Guangdong coast, and to the east of Hainan, a significant EOF magnitudes are very

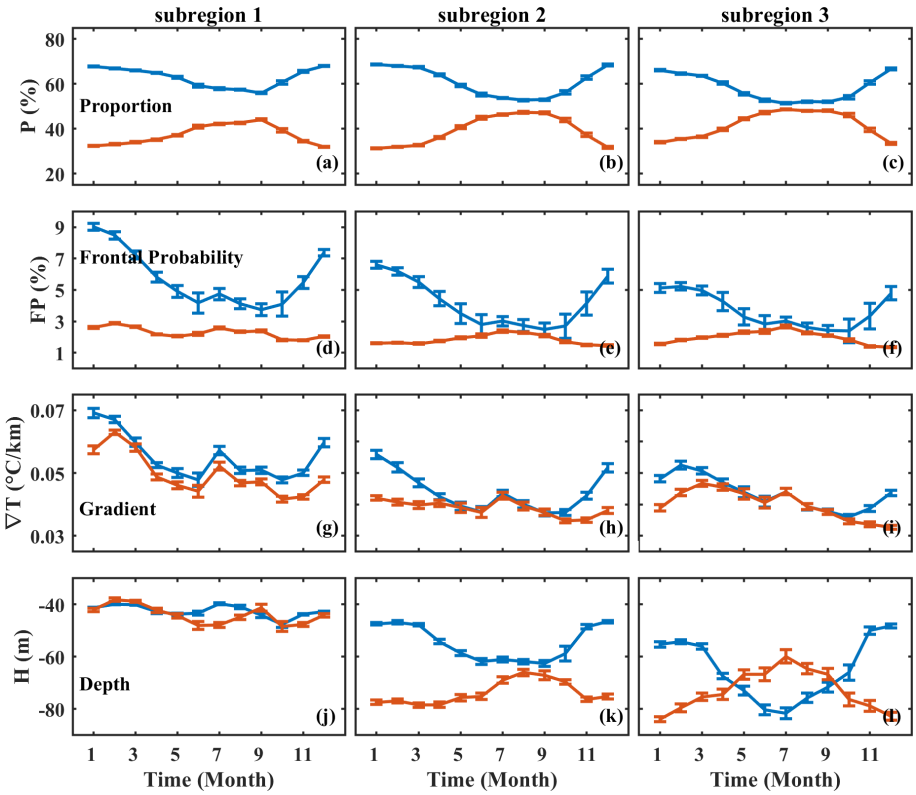


FIGURE 9
Mean monthly time series of cold and warm fronts in proportion **(A–C)**, frontal probability **(D–F)**, cross-frontal gradient **(G–I)**, and depth **(J–L)** at fronts for the three subregions averaged over 2002–2021. Blue (red) lines correspond to the cold (warm) fronts. The error bars denote the 95% confidence intervals.

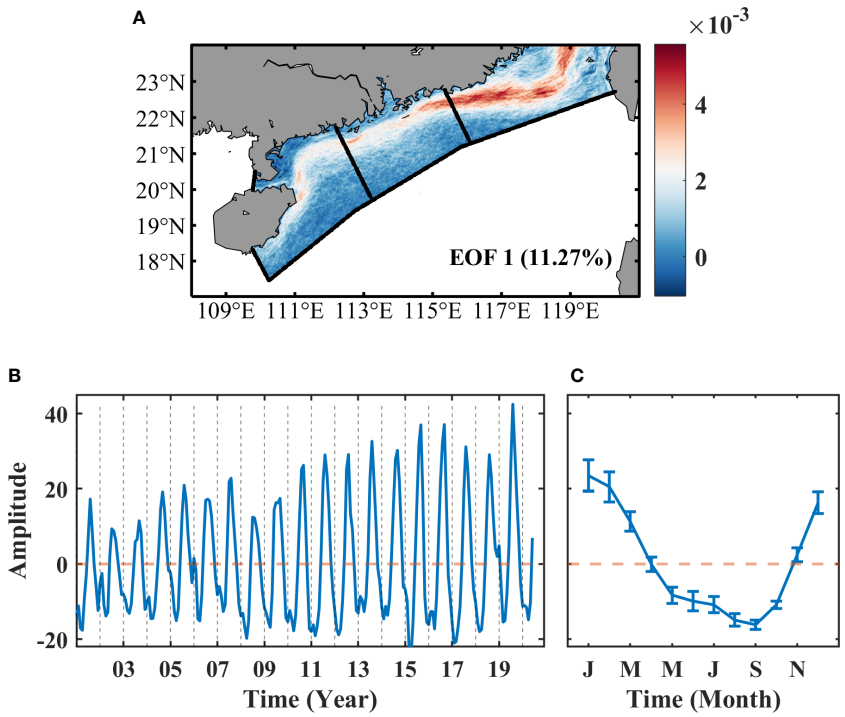


FIGURE 10
The first EOF mode **(A)**, its corresponding time series for FP **(B)**, and the mean monthly amplitudes averaged over the 20-yr period **(C)**.

apparent. The corresponding monthly mean time series also confirm the significant seasonal variability (Figure 10B), with peaks in January and troughs in September.

Discussion and conclusions

In this study, the cold- and warm-thermal fronts, and their seasonal variability over the NSCS shelf are investigated based on 20 years of high-resolution GHRSST images. Over the shallow continental shelf (< 50 m), a long and wide band of strong cold fronts is most frequently observed in winter, with weaker, less frontal activity present during other seasons. The persistence of the cold fronts may result from the advection of relatively cool water from the high latitudes by southwestward coastal cold current (i.e., Guangdong Coastal Current, GCC). The GCC offshore of the eastern Guangdong coast flows southwestward in winter and northeastward in summer (Guan and Chen, 1964; Fang et al., 1998), while offshore of the western Guangdong coast the GCC flows westward during both winter and summer (Ying, 1999; Bao et al., 2005; Xie et al., 2012). Also, a warm current exists south of the GCC. This current (i.e., South China Sea Warm Current) originates from east of Hainan Island and flows northeastward along the NSCS shelf against the northeasterly winds in winter (Guan, 1978; Fang et al., 1995; Guan and Fang, 2006), thus increasing the temperature contrast between coastal water and outer shelf water and leading to strengthen the cold fronts.

The summer fronts have showed that the warm fronts occur predominantly off the western Guangdong coast and the cold fronts are mainly observed off the eastern Guangdong coast and the eastern Hainan Island, despite relatively low probability and gradient magnitude. These fronts are possibly a response to the summer wind stress and the GCC. For the prevailing southwest summer monsoon, an alongshore component can induce offshore Ekman transport, thereby triggering coastal upwelling along the coast of the eastern Guangdong and the eastern Hainan Island (Jing et al., 2016; Shu et al., 2018). The upwelling would bring relatively cold bottom water to the surface, separating cool vertically mixed water in shallow areas from warm stratified offshore water in deep areas to form cold fronts. On the other hand, over the western inner shelf off the Guangdong coast, direct measurements suggested that the western inner shelf of Guangdong is mainly occupied by the warm GCC which primarily flows westward along the coast for summer monsoon (Yang et al., 2003; Chen et al., 2006). A relatively cold tongue appears south of the GCC and stretches northeastward from northeast of Hainan Island approximately along the 50-m isobath (Figure 2C). The combined effect of the GCC and the relatively cool northeastward-flowing water is presumably responsible for the formation of the warm fronts.

There is a very distinct separation between the nearshore fronts on the inner shelf and the offshore fronts in the vicinity of

the 50-m isobath, suggesting that a different mechanism induces the formation of the latter. Due to the most rapid changes of the bottom slope, the 50-m isobath seems to be the preferred location for frontogenesis. Garwood et al. (1981) suggested that the SST front formation could result from surface cooling over the midshelf where the shelf depth is shallower than the depth of wind-induced mixing. A similar effect could occur over the NSCS shelf. During both winter and autumn, the inner shelf of the NSCS is vertically well mixed because of the surface cooling and severe northeast monsoon, the depths of mixed layer are about 40-60 m (Wu and Chen, 2013). The uniform surface cooling can lead to a stronger offshore temperature gradient roughly along the 50-m isobath. Simultaneously, the winds can also induce a vigorous shoreward transport of warm surface water from the outer shelf (Jing et al., 2016). The joint effect of onshore surface Ekman transport of warm water and surface cooling of cold air is responsible for the midshelf frontogenesis, which is consistent with the findings of Oey (1986) in the South Atlantic Bight.

A striking aspect of the fronts to observe for the first time is that the finer-scale warm- and cold fronts discretely occur over the outer shelf (>50 m), with the aid of the high spatial resolution satellite images. These frontal activities are most observed in winter and then gradually decrease to become minimum in summer, despite relatively weak intensity and low probability of frontal activities. The fronts are possibly due to the ubiquitous submesoscale processes in the SCS (Lin et al., 2020; Ni et al., 2021; Qiu et al., 2022). Lin et al. (2020) characterized the SCS mesoscale and submesoscale features based on a submesoscale-permitting numerical simulation (MITgcm llc4320). They found that the submesoscale features in the NSCS is very rich and undergo significant seasonal variations. The submesoscale activities over the outer NSCS shelf are vigorous in winter but slightly quiescent in summer. Their findings are well consistent with our satellite observations.

Satellite remote sensing could only provide the surface signature of cold- and warm fronts. To fully understand their formation mechanisms, multiple vertical profile hydrographic data with high-enough spatiotemporal resolution, is still needed for analysis in a future study. In addition, previous studies have emphasized the important role of the cold- and warm fronts in the biogeochemical processes (e.g., Chang et al., 2008). The ecological effect of the cold- and warm fronts and the corresponding spatial and temporal variability in the SCS will be quantitatively analyzed in our following paper.

Data availability statement

Publicly available datasets were analyzed in this study. This data can be found here: https://podaac.jpl.nasa.gov/dataset.

Author contributions

ZH: Conceptualization, Methodology, Writing– review and editing, Funding acquisition. JC: Formal analysis, Data curation, Writing – original draft and Writing – review and editing. All authors contributed to the article and approved the submitted version.

Funding

This work is jointly funded by the National Natural Science Foundation of China (No. 41706205; 42176029), and the Innovation Group Project of Southern Marine Science and Engineering Guangdong Laboratory (Zhuhai) (No. 311020004).

Acknowledgments

The authors would like to thank the Physical Oceanography Distributed Active Archive Center (PO.DAAC) of the National Aeronautics and Space Administration (NASA) for sharing the satellite dataset (https://podaac.jpl.nasa.gov/dataset). We would like to acknowledge Shimada for algorithm support and an three reviewers whose comments have helped to improve the presentation of this paper.

Conflict of interest

The authors declare that the research was conducted in the absence of any commercial or financial relationships that could be construed as a potential conflict of interest.

The reviewer XZ declared a shared affiliation with the author ZH to the handling editor at the time of review.

Publisher's note

All claims expressed in this article are solely those of the authors and do not necessarily represent those of their affiliated organizations, or those of the publisher, the editors and the reviewers. Any product that may be evaluated in this article, or claim that may be made by its manufacturer, is not guaranteed or endorsed by the publisher.

References

Bao, X., Hou, Y., Chen, C., Chen, F., and Shi, M. (2005). Analysis of characteristics and mechanism of current system on the west coast of guangdong of China in summer. *Acta Oceanologica Sin.* 24, 1–9.

Chang, Y., and Cornillon, P. (2015). A comparison of satellite-derived sea surface temperature fronts using two edge detection algorithms. *Deep-Sea Res. Part Ii-Topical Stud. Oceanogr.* 119, 40–47. doi: 10.1016/j.dsr2.2013.12.001

Chang, Y., Lee, M. A., Shimada, T., Sakaida, F., Kawamura, H., Chan, J. W., et al. (2008). Wintertime high-resolution features of sea surface temperature and chlorophyll-a fields associated with oceanic fronts in the southern East China Sea. *International Journal of Remote Sensing* 29(21), 6249–6261.

Chen, J. (1983). Some explanation of sea surface temperature distribution in northern south China Sea in winter. *Acta Oceanologica Sin.* 5 (3), 391–395+397-398.

Chen, D., Chen, B., Jinhui, Y. A. N., and Huifen, X. U. (2006). The seasonal variation characteristics of residual currents in the qiongzhou strait. *Trans. Oceanol. Limnol.* 2), 12–17. doi: 10.3969/j.issn.1003-6482.2006.02.003

Chen, G. X., Gan, J. P., Xie, Q., Chu, X. Q., Wang, D. X., and Hou, Y. J. (2012). Eddy heat and salt transports in the south China Sea and their seasonal modulations. *J. Geophysical Research-Oceans* 117, C05021. doi: 10.1029/2011jc007724

Chu, P. C., and Wang, G. H. (2003). Seasonal variability of thermohaline front in the central south China Sea. *J. Oceanogr.* 59 (1), 65–78. doi: 10.1023/A:1022868407012

Fang, G., Fang, W., Fang, Y., and Wang, K. (1998). A survey of studies on the south China Sea upper ocean circulation. *Acta Oceanographica Taiwanica* 37, 1–16.

Fang, G. H., Zhao, J. P., Bole, J., Mathisen, J. P., Schjolberg, P., and Pan, H. (1995). Circulation, internal tides and solitons at the shelf break of the northern south China Sea–An analysis of measured currents. p. 50–51. In *Marine Science Conference in Taiwan Adjacent Seas—Program and Abstracts, Taipei, Taiwan*.

Fedorov, K. N. (1986). *The physical nature and structure of oceanic fronts* (New York, NY: Springer-Verlag), 10010. Medium: X; Size: Pages: 333 2008-2002-2007. doi: 10.1029/LN019

Fournier, R. O. (1978). Biological aspects of the Nova scotian shelfbreak fronts. *Oceanic Fronts Coast. Processes* M. J. Bowman and W. E. Esaias, (New York: Springer-Verlag) 69–77.

Garwood, R. W.Jr., Fett, R. W., Rabe, K. M., and Brandli, H. W. (1981). Ocean frontal formation due to shallow water cooling effects as observed by satellite and simulated by a numerical method. *J. Geophysical Res.* 86 (C11), 11000–11012. doi: 10.1029/JC086iC11p11000

Guan, B. (1978). The warm current in the south China Sea–a current flowing against the wind in winter in the open sea off guangdong province. *Oceanol. Limnol. Sin.* 9, 117–127.

Guan, B., and Chen, S. (1964). The current systems in the near-Sea area of China seas (in Chinese). *Tech. Rep.* pp. 1–85.

Guan, B., and Fang, G. (2006). Winter counter-wind currents off the southeastern China coast: A review. *J. Oceanogr.* 62 (1), 1–24. doi: 10.1007/s10872-006-0028-8

Guo, L., Xiu, P., Chai, F., Xue, H. J., Wang, D. X., and Sun, J. (2017). Enhanced chlorophyll concentrations induced by kuroshio intrusion fronts in the northern south China Sea. *Geophysical Res. Lett.* 44 (22), 11565–11572. doi: 10.1002/2017gl075336

Hu, Z., Pan, D., He, X., and Bai, Y. (2016). Diurnal variability of turbidity fronts observed by geostationary satellite ocean color remote sensing. *Remote Sens.* 8 (2), 147. doi: 10.3390/rs8020147

Hu, Z., Xie, G., Zhao, J., Lei, Y., Xie, J., and Pang, W. (2021). Mapping diurnal variability of the wintertime pearl river plume front from himawari-8 geostationary satellite observations. *Water* 14 (1), 43. doi: 10.3390/w14010043

Jing, Z., Qi, Y., Fox-Kemper, B., Du, Y., and Lian, S. (2016). Seasonal thermal fronts on the northern south China Sea shelf: Satellite measurements and three repeated field surveys. *J. Geophysical Research: Oceans* 121 (3), 1914–1930. doi: 10.1002/2015jc011222

Legeckis, R. (1978). A survey of worldwide sea surface temperature fronts detected by environmental satellites. *J. Geophysical Research: Oceans* 83 (C9), 4501–4522. doi: 10.1029/JC083iC09p04501

Lin, H., Liu, Z., Hu, J., Menemenlis, D., and Huang, Y. (2020). Characterizing meso- to submesoscale features in the south China Sea. *Prog. Oceanogr.* 188, 102420. doi: 10.1016/j.pocean.2020.102420

Liu, K. K., Chao, S. Y., Shaw, P. T., Gong, G. C., Chen, C. C., and Tang, T. Y. (2002). Monsoon-forced chlorophyll distribution and primary production in the south China Sea: Observations and a numerical study. *Deep-Sea Res. Part I-Oceanographic Res. Papers* 49 (8), 1387–1412. doi: 10.1016/S0967-0637(02)00035-3

Ni, Q., Zhai, X., Wilson, C., Chen, C., and Chen, D. (2021). Submesoscale eddies in the south China Sea. *Geophysical Res. Lett.* 48 (6), e2020GL091555. doi: 10.1029/2020gl091555

Oey, L.-Y. (1986). The formation and maintenance of density fronts on the U.S. southeastern continental shelf during winter. *J. Phys. Oceanogr.* 16 (6), 1121–1135. doi: 10.1175/1520-0485(1986)016<1121:Tfamod>2.0.Co;2

Qiu, C., Yang, Z., Wang, D., Feng, M., and Su, J. (2022). The enhancement of submesoscale ageostrophic motion on the mesoscale eddies in the south China Sea. *J. Geophysical Research-Oceans* 127 (9), e2022JC018736. doi: 10.1029/2022jc018736

Qu, T. D., Du, Y., Gan, J. P., and Wang, D. X. (2007). Mean seasonal cycle of isothermal depth in the south China Sea. *J. Geophysical Research-Oceans* 112 (C2), C02020. doi: 10.1029/2006jc003583

Ren, S., Wang, H., and Liu, N. (2015). Review of ocean front in Chinese marginal seas and frontal forecasting. *Advance Earth Sci.* 30 (5), 552–563. doi: 10.11867/j.issn.1001-8166.2015.05.0552

Shimada, T., Sakaida, F., Kawamura, H., and Okumura, T. (2005). Application of an edge detection method to satellite images for distinguishing sea surface temperature fronts near the Japanese coast. *Remote Sens. Environ.* 98 (1), 21–34. doi: 10.1016/j.rse.2005.05.018

Shu, Y., Wang, Q., and Zu, T. (2018). Progress on shelf and slope circulation in the northern south China Sea. *Sci. China-Earth Sci.* 61 (5), 560–571. doi: 10.1007/s11430-017-9152-y

Ullman, D. S., and Cornillon, P. C. (1999). Satellite-derived sea surface temperature fronts on the continental shelf off the northeast US coast. *J. Geophysical Research-Oceans* 104 (C10), 23459–23478. doi: 10.1029/1999jc900133

Ullman, D. S., and Cornillon, P. C. (2001). Continental shelf surface thermal fronts in winter off the northeast US coast. *Continental Shelf Res.* 21 (11-12), 1139–1156. doi: 10.1016/S0278-4343(00)00107-2

Wang, D., Liu, Y., Qi, Y., and Shi, P. (2001). Seasonal variability of thermal fronts in the northern south China Sea from satellite data. *Geophysical Res. Lett.* 28 (20), 3963–3966. doi: 10.1029/2001gl013306

Wang, G. H., Li, J. X., Wang, C. Z., and Yan, Y. W. (2012). Interactions among the winter monsoon, ocean eddy and ocean thermal front in the south China Sea. *J. Geophysical Research-Oceans* 117, C08002. doi: 10.1029/2012jc008007

Wang, Y., Yu, Y., Zhang, Y., Zhang, H. R., and Chai, F. (2020). Distribution and variability of sea surface temperature fronts in the south China sea. *Estuarine Coast. Shelf Sci.* 240, 106793. doi: 10.1016/j.ecss.2020.106793

Wu, Y., and Chen, G. (2013). Seasonal and inter-annual variations of the mixed layer depth in the south China Sea. *Mar. Forecasts*. 30, 9–17. doi: 10.11737/j.issn.1003-0239.2013.03.002

Xie, L., Cao, R., and Shang, Q. (2012). Progress of study on coastal circulation near the shore of Western guangdong. *Guangdong Ocean Univ* 32, 94–98. doi: 10.3969/j.issn.1673-9159.2012.04.019

Yang, S., Bao, X., Chen, C., and Chen, F. (2003). Analysis on characteristics and mechanism of current system in west coast of guangdong province in the summer. *Acta Oceanologica Sin.* 25 (6), 1–8. doi: 10.3321/j.issn:0253-4193.2003.06.001

Yao, J. L., Belkin, I., Chen, J., and Wang, D. X. (2012). Thermal fronts of the southern south China Sea from satellite and *in situ* data. *Int. J. Remote Sens.* 33 (23), 7458–7468. doi: 10.1080/01431161.2012.685985

Ying, B. (1999). On the coast current and its deposit along Western coast in guangdong. *Acta Scientiarum Naturalium Universitis Sunyatseni* 38, 85–89.

Yu, J., Chen, G., Tang, Z., and Zeng, L. (2020). Characteristics of the sea surface temperature strong front in the northern south China Sea. *Mar. Environ. Sci.* 39 (3), 367–373. doi: 10.13634/j.cnki.mes.2020.03.007

frontiers | Frontiers in Marine Science

TYPE Original Research
PUBLISHED 08 May 2023
DOI 10.3389/fmars.2023.1168486

Check for updates

OPEN ACCESS

EDITED BY
Salvatore Marullo,
Italian National Agency for New Technologies, Energy and Sustainable Economic Development (ENEA), Italy

REVIEWED BY
Michela Sammartino,
National Research Council (CNR), Italy
Giuseppe Manzella,
OceanHis, Italy

*CORRESPONDENCE
Qing Xu
xuqing@ouc.edu.cn

RECEIVED 17 February 2023
ACCEPTED 26 April 2023
PUBLISHED 08 May 2023

CITATION
Xie H, Xu Q, Cheng Y, Yin X and Fan K (2023) Reconstructing three-dimensional salinity field of the South China Sea from satellite observations.
Front. Mar. Sci. 10:1168486.
doi: 10.3389/fmars.2023.1168486

COPYRIGHT
© 2023 Xie, Xu, Cheng, Yin and Fan. This is an open-access article distributed under the terms of the Creative Commons Attribution License (CC BY). The use, distribution or reproduction in other forums is permitted, provided the original author(s) and the copyright owner(s) are credited and that the original publication in this journal is cited, in accordance with accepted academic practice. No use, distribution or reproduction is permitted which does not comply with these terms.

Reconstructing three-dimensional salinity field of the South China Sea from satellite observations

Huarong Xie[1,2], Qing Xu[3]*, Yongcun Cheng[4], Xiaobin Yin[3] and Kaiguo Fan[5]

[1]Key Laboratory of Marine Hazards Forecasting, Ministry of Natural Resources, Hohai University, Nanjing, China, [2]College of Oceanography, Hohai University, Nanjing, China, [3]College of Marine Technology, Faculty of Information Science and Engineering, Ocean University of China, Qingdao, China, [4]PIESAT Information Technology Co., Ltd., Beijing, China, [5]Troop 32021, PLA, Beijing, China

High-resolution salinity information is of great significance for understanding the marine environment. We here propose a deep learning model denoted the "Attention U-net network" to reconstruct the daily salinity fields on a 1/4° grid in the interior of the South China Sea (SCS) from satellite observations of surface variables including sea surface salinity, sea surface temperature, sea level anomaly, and sea surface wind field. The vertical salinity profiles from the GLORYS2V4 reanalysis product provided by Copernicus Marine Environment Monitoring Service were used for training and evaluating the network. Results suggest that the Attention U-net model performs quite well in reconstructing the three-dimensional (3D) salinity field in the upper 1000 m of the SCS, with an average root mean square error (RMSE) of 0.051 psu and an overall correlation coefficient of 0.998. The topography mask of the SCS in the loss function can significantly improve the performance of the model. Compared with the results derived from the model using Huber loss function, there is a significant reduction of RMSE in all vertical layers. Using sea surface salinity as model inputs also helps to yield more accurate subsurface salinity, with an average RMSE near the sea surface being reduced by 16.4%. The good performance of the Attention U-net model is also validated by *in situ* mooring measurements, and case studies show that the reconstructed high-resolution 3D salinity field can effectively capture the evolution of underwater signals of mesoscale eddies in the SCS. The resolution and accuracy of sea surface variables observed by satellites will continue to improve in the future, and with these improvements, more precise 3D salinity field reconstructions will be possible, which will bring new insights about the multi-scale dynamics research in the SCS.

KEYWORDS

ocean salinity, satellite observation, U-net, attention mechanism, South China Sea

1 Introduction

Ocean salinity is essential for the study of global hydrological cycle and ocean circulation, and its variation plays an important role in the ocean stratification, climate change and ecosystem (Lagerloef, 2002; Held and Soden, 2006; Schmitt, 2008; Ren and Riser, 2010; Schmidtko et al., 2017). However, changes in salinity within the ocean, especially within the marginal seas, have not been well captured and understood yet due to the lack of sufficient high-resolution three-dimensional (3D) data. *In situ* measurements from underwater moorings or profiling floats such as the global array for real-time geostrophic oceanography (Argo) are traditionally used for studying the salinity characteristics of the interior ocean. However, field observations are still sparse, discontinuous, and limited in coverage, which obscure the details of mesoscale and smaller-scale processes. Satellite remote sensing has provided long-term and high-resolution data of various sea surface variables worldwide. However, the sensors cannot directly see the deep ocean where the thermohaline structure shows significant variations due to complex dynamic processes such as mesoscale eddies and internal waves (Henning and Vallis, 2004; Huang et al., 2016; Keppler et al., 2018). By retrieving the 3D salinity field from a large set of satellite data (Klemas and Yan, 2014), it is possible to improve the skill of surface observations to deeper layers and thus better understand marine phenomena at different spatiotemporal scales.

Several methods have been applied to estimate salinity profiles from satellite observations. Before the operational application of salinity satellites such as Aquarius, Soil Moisture and Ocean Salinity (SMOS) and Soil Moisture Active and Passive (SMAP) missions, sea surface salinity (SSS) data were very sparse and very rarely used as model inputs (Carnes et al., 1994; Agarwal et al., 2007; Guinehut et al., 2012). For example, Guinehut et al. (2012) tried to estimate the 3D salinity anomaly field of the global ocean by establishing a linear relationship between monthly Argo salinity profiles on a 1° grid and 7-d sea level anomaly (SLA) with spatial resolution of 1/3°. They concluded that altimeter observed SLA could only reconstruct approximately 20% to 30% of the salinity signal, implying that it is necessary to consider more surface variables for accurate estimation of the vertical structure of salinity. Some studies used field observations of SSS to estimate underwater salinity and found that SSS was an essential parameter for 3D salinity reconstruction (Agarwal et al., 2007; Ballabrera-Poy et al., 2009). Yang et al. (2015) used linear regression and neural network models to retrieve vertical salinity profiles from SSS observed by SMOS. The nonlinear neural network provided more accurate estimation than the linear model in the upper 2000 m of the global ocean, and the root mean square error (RMSE) varies from 0.077 psu to 0.138 psu in different regions. This highlights the potential of artificial intelligence (AI) approach in underwater salinity reconstruction. However, due to the relatively short period of SMOS data at that time, the accuracy was not high enough.

The amount of satellite data has explosively increased in recent years, and as a result, oceanographic research has entered the "big data era" (Li et al., 2020). The combination of ocean big data and AI provides a new way of reconstructing 3D salinity fields from surface variables observed by satellites. Recently, Su et al. (2019) introduced a machine learning method called extreme gradient boosting to estimate global ocean subsurface salinity structure from the anomaly of several surface variables including SSS, sea surface temperature (SST), sea surface height and sea surface wind (SSW). The model uses monthly Argo salinity profiles on a 1° grid as label data, with resultant average normalized RMSE and correlation coefficient of 0.042 and 0.735, respectively. Other machine learning and deep learning methods have also been proposed to obtain the salinity or salinity anomaly profiles in the open ocean from satellite observations, such as the generalized regression neural network (Bao et al., 2019), long- and short-term memory (LSTM) (Buongiorno Nardelli, 2020), convolutional neural network (CNN) (Meng et al., 2022) and convolutional LSTM (Song et al., 2022). Generally, the surface variables used as model inputs include SSS/SSS anomaly, SST/SST anomaly, SLA, SSW/SSW anomaly, or absolute dynamic topography (ADT). However, less attention is given to the reconstruction of interior salinity structure in marginal seas, where it is more difficult to obtain accurate results due to complex topography and multi-scale dynamics. The South China Sea (SCS, Figure 1A) is one of the largest marginal seas adjacent to the West Pacific Ocean, where mesoscale and sub-mesoscale processes are very active (Wang et al., 2003; Zheng et al., 2007; He et al., 2018; Xie et al., 2022a). High-resolution 3D ocean observations are urgently needed to capture the fine structure and evolution of these dynamic processes. Therefore, the reconstruction of 3D salinity fields at high temporal and spatial resolution is necessary for the SCS. To achieve this goal, a U-net deep learning model combined with an attention mechanism (hereafter called "Attention U-net") is here presented to reconstruct the 3D salinity field in the upper 1000 m of the SCS from satellite observations of SSS, SST, SLA and SSW. The daily vertical salinity profiles on a 1/4° grid from the GLORYS2V4 reanalysis product were used for training and evaluating the network. The paper is organized as follows. Section 2 presents the satellite-observed sea surface variables and reanalysis data of ocean salinity profiles used here. The detailed configuration of the Attention U-net model is also described. The model performance in reconstructing 3D salinity field of the SCS is evaluated in Section 3. In Section 4, the estimation errors are analyzed, and the influence of SSS on the upper-layer salinity reconstruction is discussed. An applicative example of the reconstruction model in revealing the underwater salinity signals related to the mesoscale cold eddy is also shown. Finally, conclusions are given in Section 5.

2 Materials and methods

2.1 Satellite observations and reanalysis product

The surface variables used as inputs to the Attention U-net model are SSS, SST, SLA, and zonal and meridional components of SSW. The SSS data are provided by the European Space Agency (ESA) Sea Surface Salinity Climate Change Initiative (CCI) consortium (https://

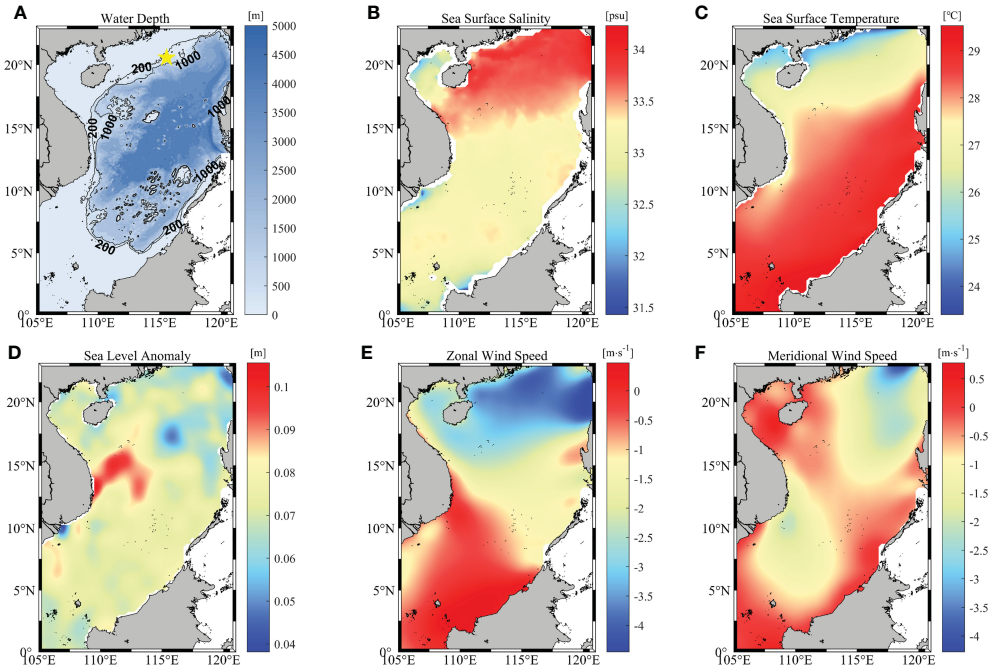


FIGURE 1
(A) Distribution of water depth in the SCS. Contours of 200 m and 1000 m depth are overlaid with black lines, and the location of a mooring station is marked as a yellow pentagram. **(B–F)** Climatology of sea surface variables in the SCS from 2010 to 2018. **(B)** Sea surface salinity, **(C)** sea surface temperature, **(D)** sea level anomaly, **(E)** zonal and **(F)** meridional wind speed.

data.ceda.ac.uk/neodc/esacci/sea_surface_salinity) which produces global multi-sensor SSS maps by merging SMOS, Aquarius and SMAP measurements with an optimal interpolation in the time domain, covering 2010 to 2020. The SMOS SSS dataset is based on the ESA Level 2 version 622 algorithm and is corrected for seasonal latitudinal biases and dielectric constants (Zine et al., 2008; CATDS, 2017). The SMAP and Aquarius products are obtained from SMAP version 4 and Aquarius version 5 retrieval algorithms, respectively, and they are all projected on the global cylindrical 25 km Equal Area Scalable Earth (EASE) grid to have the same spatial grid with the SMOS data (Meissner et al., 2018; Meissner et al., 2019). The CCI SSS products of version 03.21 are spatially sampled on a 25 km EASE grid at 1 day time sampling (Boutin et al., 2021). The daily optimally interpolated SST product (version 2.1) with a spatial resolution of 1/4° is from the National Oceanic Atmospheric Administration (https://www.ncei.noaa.gov/products/optimum-interpolation-sst). It incorporates observations from different platforms, such as satellites, ships, buoys, and Argo floats, and has a global coverage from 1981 to present (Reynolds et al., 2007; Huang et al., 2021). The multi-mission altimeter SLA product is available on the website of Copernicus Marine Environment Monitoring Service (CMEMS, https://resources.marine.copernicus.eu). Its delayed-time version (id: SEALEVEL_GLO_PHY_L4_REP_OBSERVATIONS_008_047) has a spatial and temporal resolution of 1/4° and 1 day, respectively and contains data from 1993 to 2020. The SSW data are derived from the version 2 of Cross-Calibrated Multi-Platform (CCMP) wind product, which consists of four daily 1/4° gridded surface vector winds maps based on various microwave scatterometers and radiometers, such as QuikSCAT, ASCAT, SSM/I, AMSR, SSMIS, WindSat, etc. (Atlas et al., 2011; Mears et al., 2019). The data cover a wide time range from July 1987 to April 2019 and can be obtained from the Remote Sensing Systems (https://www.remss.com/measurements/ccmp/). Figure 1 shows the water depth and climatological distribution of satellite observed surface variables in the SCS from 2010 to 2018.

The daily vertical salinity profiles on a grid of 1/4° are from the GLORYS2V4 reanalysis product, which was built to be in agreement with the model physics at eddy-permitting resolution (Garric et al., 2017). The assimilated observations include satellite observed SST, SLA, sea ice concentration and *in situ* profiles of temperature and salinity. The product (id: GLOBAL_REANALYSIS_PHY_001_031) is now supplied by CMEMS consisting of 75 vertical levels and covering a period from 1993 to 2019 (https://data.marine.copernicus.eu/product/GLOBAL_REANALYSIS_PHY_001_031).

2.2 Attention U-net model

The Attention U-net model is the combination of U-net architecture and attention mechanism. U-net is a classic CNN, which consists of a contracting path to capture context and a symmetric expansive path. The contracting path includes the repeated application of convolutions and a max pooling operation, while the pooling operators are replaced by upsampling operators in the expansive path to increase the resolution of outputs. In order to help the network precisely localize, the upsampled features are combined with the same resolution features from the contracting path. Then, the feature channels are doubled, which allows the network to propagate

contextual information to higher resolution layers. The U-net shows superiority in solving the small sample learning problems by producing accurate results with very few training samples and performs well in the multi-scale feature extraction of images (Ronneberger et al., 2015; Han and Ye, 2018; Li et al., 2020; Zhang et al., 2022). However, it might repeatedly extract similar lower-level features, which would lead to the redundant use of computational resources and poor model performance. The attention mechanism focuses selectively on important features and suppresses unnecessary ones. It can improve the calculation efficiency of the model by introducing a small number of parameters (Xu et al., 2015; Chaudhari et al., 2021). The addition of the attention module to U-net can effectively avoid paying the excessive attention to simple features of targets, and thus can be helpful to improve the model accuracy on the classification and regression tasks (Oktay et al., 2018; Li et al., 2022; Xie et al., 2022b).

The structure of the Attention U-net model is shown in Figure 2A. The maps of five surface variables are used as inputs and double convoluted to produce the feature maps, and then a 2×2 max pooling operation and convolutional block attention module (CBAM) are applied. As shown in Figure 2B, the CBAM consists of the channel attention module (CAM) and spatial attention module (SAM), which tells the model "what" and "where" to attend in the channel and space, respectively (Woo et al., 2018). The CAM first uses the average pooling and max pooling operations to obtain different features. The resulting features are merged by element-wise summation after the application of the shared network. Then, a sigmoid activation function is applied to yield the channel attention map. The element-wise multiplication between the channel attention map and original features is used as the input of SAM. Two feature maps are obtained through average pooling and max pooling operations along channels. The average-pooled and max-pooled features are concatenated and then convolved by a convolutional layer with the filter size of 7×7 followed by a sigmoid activation function to get the spatial attention map. It is multiplied with the input of SAM to produce the final output of

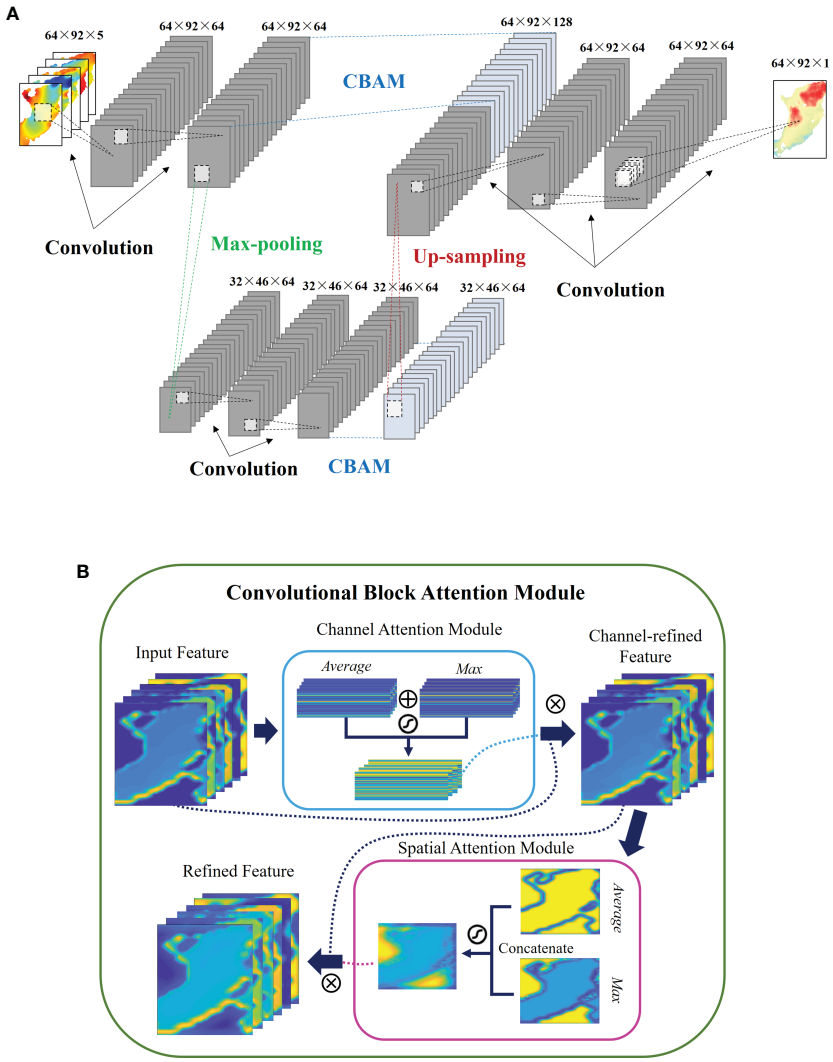


FIGURE 2
(A) Schematic diagram of Attention U-net model. The subtitles "Convolution", "Maxpooling", "Up-sampling" and "CBAM" represent the specific operations between two layers. **(B)** Schematic diagram of CBAM structure and sub-modules.

CBAM. Hence, the important feature maps of the original sized object are obtained after the first CBAM. The down-sampled features are also processed with a double convolution and put into the CBAM, which can capture significant object features on the coarse scale. Next, the output is up-sampled with a 2×2 filter to yield the original sized features, concatenated with the features derived from the first CBAM, and then convoluted twice. After the last convolution operation, a single feature map is produced as the model output, which is the interior salinity field for the study of 3D salinity reconstruction. Except for the output layer, all convolutional layers have a filter size of 3×3, followed by the rectified linear unit (ReLU) activation function. The filter size of the output layer is 1×1 and the activation function is linear. The adaptive moment estimation (Adam) optimizer is selected to help the network to rapidly converge to the optimal solution. In addition, the training epochs are set at 1000, and a varied learning rate, which is reduced by half if the loss value of validation data remains unchanged during 50 training rounds, is adopted to avoid the over-fitting problem.

The loss function is one of the key parameters for model evaluation and optimization in the training process. Our previous study (Xie et al., 2022b) proved that the Huber loss function is superior to the commonly used mean square error (MSE) function in the reconstruction of subsurface temperature in the SCS, as it helps the model to converge quickly and pays less attention to the invalid value brought by the topography, which is usually specified as a number far away from the actual water temperature in the model. The Huber loss function can be expressed as

$$L_{i,d,\delta} = \begin{cases} \frac{1}{2}(y_{d,i} - f(x_{d,i}))^2 & |y_{d,i} - f(x_{d,i})| \le \delta \\ \delta|y_{d,i} - f(x_{d,i})| - \frac{1}{2}\delta^2 & |y_{d,i} - f(x_{d,i})| > \delta \end{cases} \quad (1)$$

where $L_{i,d,\delta}$ is the value of the Huber loss function; $y_{d,i}$ and $f(x_{d,i})$ represent the real salinity and model estimation, respectively; d is the water depth, i is the number of the data point, and δ is the hyper parameter which determines the expression form of Huber loss function. In addition, a new loss function, denoted "mask based root mean square error" (Mrmse), was defined. It considers the topography mask $M_{d,i}$ of the marginal sea and is expressed as

$$L_d = \sqrt{\frac{1}{m}\sum_{i=1}^{m}[(y_{d,i} - f(x_{d,i}))^2 \cdot M_{d,i}]} \quad (2)$$

where L_d is the value of the Mrmse loss function; m is the total amount of the data points; $M_{d,i}$ is the topography mask, and if the ith point at the depth of d is on the land, its value is set to 0, otherwise it is set to 1. In this way, the model performance is only evaluated on the valid salinity data in the training process and would be less affected by the outliers from topography. The attention of the model to salinity features would also not be shared, which could help yield more accurate salinity fields. To investigate the effect of loss functions on the accuracy of 3D salinity reconstruction in the SCS, we first carry out comparative experiments using different loss functions in the Attention U-net model.

The reconstruction model was established by month for each vertical layer considering the seasonal variation of the ocean salinity field. Data from January 2010 to December 2018 were used to build and test the model, 3278 samples in total. All surface data were standardized to the same resolution as the vertical salinity profile data and normalized by clustering them with a zero mean and variance of one to eliminate the variable differences. 80% of the processed samples were randomly selected to train the model and divided into two groups at 9:1: training set (72%) and validation set (8%). The remaining samples were used as testing data.

3 Results

3.1 Influence of loss function on the performance of Attention U-net model

The performance of the Attention U-net model was evaluated by calculating the RMSE and correlation coefficient between the reconstructed salinity and GLORYS2V4 reanalysis product on the testing dataset. We take the 3D salinity reconstruction model in January as an example, with estimation results shown in Table 1 and Figure 3A. Here, the hyper parameter δ of the Huber loss function is set to be 1. The model with Huber loss function performs better than the one with MSE. This might be due to the lower penalty degree on the outliers of the Huber function, and as a result, the model focuses less on the invalid values caused by topography. However, larger RMSEs are present in the upper layers and the correlation coefficient decreases rapidly from 0.972 at the top layer to less than 0.6 in waters deeper than 700 m.

In contrast, the Mrmse loss function only calculates the errors between the estimation and ground truth at valid data points without consideration of outliers. When the Mrmse loss function is used, the model yields the most accurate construction results, especially in deeper waters. The RMSE at different vertical layers between the labelled and estimated salinity is half or even less than 85% of the error obtained by using the Huber loss function. The error decreases significantly as the water depth increases and the minimum value is 0.002 psu at 947 m depth. Meanwhile, the correlation coefficient is significantly increased from 23.0% to 108.9% in waters deeper than 200 m and its value remains above 0.975. It is marginally larger in the upper waters and changes slightly with the water depth. Similar results were obtained for the model in July (Table 1 and Figure 3B), where the RMSE has a large reduction between 44.0% and 86.7% and the correlation coefficient has a significant increase of 2.8% to 172.8% at different depths. This shows that the Mrmse loss function works better than the MSE or Huber loss function for 3D salinity reconstruction in the SCS. The Huber loss function greatly reduces the attention on the anomaly values, however, it is still not effective for the establishment of 3D salinity reconstruction model in the SCS, because invalid data always exist due to uneven distribution of topography. These invalid data regarded as outliers would induce noise in the training dataset and thus provide false data features, which may lead to unsatisfactory performance of the reconstruction model. On the other hand, the salinity changes slightly within a month. In this case, different features learned by the network are relatively few, and hence false features

10.3389/fmars.2023.1168486

TABLE 1 RMSE and correlation coefficient (R) between Attention U-net estimated salinity and GLORYS2V4 reanalysis in the upper 1000 m of the SCS in January and July.

Depth/m	Month	RMSE/psu				R			
		MSE	Huber	Mrmse	Relative difference	MSE	Huber	Mrmse	Relative difference
5	Jan.	0.262	0.189	0.095	-49.7%	0.945	0.972	0.993	2.2%
	Jul.	0.277	0.209	0.117	-44.0%	0.928	0.959	0.988	3.0%
10	Jan.	0.286	0.191	0.089	-53.4%	0.926	0.968	0.993	2.6%
	Jul.	0.277	0.198	0.092	-53.5%	0.902	0.951	0.990	4.1%
19	Jan.	0.266	0.184	0.095	-48.4%	0.929	0.966	0.991	2.6%
	Jul.	0.209	0.186	0.074	-60.2%	0.935	0.949	0.992	4.5%
31	Jan.	0.249	0.202	0.103	-49.0%	0.929	0.953	0.988	3.7%
	Jul.	0.223	0.162	0.072	-55.6%	0.933	0.966	0.993	2.8%
41	Jan.	0.279	0.186	0.100	-46.2%	0.887	0.951	0.986	3.7%
	Jul.	0.186	0.183	0.070	-61.7%	0.949	0.951	0.993	4.4%
54	Jan.	0.223	0.185	0.078	-57.8%	0.913	0.941	0.990	5.2%
	Jul.	0.202	0.160	0.062	-61.3%	0.904	0.941	0.991	5.3%
61	Jan.	0.238	0.170	0.073	-57.1%	0.886	0.944	0.990	4.9%
	Jul.	0.178	0.150	0.061	-59.3%	0.900	0.930	0.989	6.3%
69	Jan.	0.217	0.155	0.064	-58.7%	0.872	0.937	0.989	5.5%
	Jul.	0.169	0.123	0.052	-57.7%	0.889	0.943	0.990	5.0%
78	Jan.	0.187	0.130	0.057	-56.2%	0.874	0.942	0.989	5.0%
	Jul.	0.155	0.111	0.041	-63.1%	0.879	0.940	0.992	5.5%
87	Jan.	0.174	0.117	0.055	-53.0%	0.851	0.935	0.986	5.5%
	Jul.	0.132	0.094	0.039	-58.5%	0.865	0.934	0.989	5.9%
97	Jan.	0.146	0.098	0.046	-53.1%	0.833	0.928	0.984	6.0%
	Jul.	0.114	0.079	0.033	-58.2%	0.866	0.937	0.990	5.7%
147	Jan.	0.055	0.037	0.016	-56.8%	0.812	0.918	0.985	7.3%
	Jul.	0.058	0.038	0.015	-60.5%	0.774	0.911	0.986	8.2%
200	Jan.	0.039	0.037	0.011	-70.3%	0.788	0.800	0.984	23.0%
	Jul.	0.044	0.029	0.010	-65.5%	0.557	0.813	0.981	20.7%
245	Jan.	0.035	0.033	0.009	-72.7%	0.745	0.767	0.984	28.3%
	Jul.	0.038	0.032	0.009	-71.9%	0.482	0.606	0.973	60.6%
301	Jan.	0.029	0.025	0.007	-72.0%	0.577	0.647	0.975	50.7%
	Jul.	0.033	0.023	0.005	-78.3%	0.447	0.618	0.983	59.1%
412	Jan.	0.030	0.019	0.004	-78.9%	0.425	0.650	0.987	51.8%
	Jul.	0.028	0.022	0.004	-81.8%	0.517	0.642	0.990	54.2%
509	Jan.	0.030	0.020	0.004	-80.0%	0.521	0.732	0.989	35.1%
	Jul.	0.031	0.022	0.005	-77.3%	0.535	0.646	0.984	52.3%
628	Jan.	0.022	0.018	0.003	-83.3%	0.642	0.702	0.990	41.0%
	Jul.	0.027	0.019	0.003	-84.2%	0.547	0.684	0.993	45.2%
697	Jan.	0.026	0.016	0.004	-75.0%	0.519	0.664	0.978	47.3%

(Continued)

TABLE 1 Continued

Depth/m	Month	RMSE/psu				R			
		MSE	Huber	Mrmse	Relative difference	MSE	Huber	Mrmse	Relative difference
	Jul.	0.027	0.017	0.003	-82.4%	0.447	0.623	0.991	59.1%
773	Jan.	0.027	0.017	0.003	-82.4%	0.338	0.571	0.989	73.2%
	Jul.	0.025	0.016	0.003	-81.3%	0.385	0.578	0.987	70.8%
857	Jan.	0.021	0.013	0.003	-76.9%	0.350	0.573	0.983	71.6%
	Jul.	0.021	0.013	0.002	-84.6%	0.344	0.489	0.989	102.2%
947	Jan.	0.031	0.013	0.002	-84.6%	0.206	0.473	0.988	108.9%
	Jul.	0.029	0.015	0.002	-86.7%	0.151	0.364	0.993	172.8%
Average	Jan.	0.185	0.133	0.064	-51.9%	0.970	0.985	0.997	1.2%
	Jul.	0.160	0.125	0.055	-56.0%	0.978	0.987	0.997	1.0%

The MSE, Huber and Mrmse loss functions were used in the model. Relative difference of RMSE is ($RMSE_{Mrmse}$-$RMSE_{Huber}$)/$RMSE_{Huber}$ and a negative value indicates an improvement in accuracy. Relative difference of R is (R_{Mrmse}-R_{Huber})/R_{Huber} and a positive value indicates an improvement in correlation.

would have a considerable negative impact on the model performance. The influence of outliers on the model is particularly great in the deeper layers because the number of real salinity data will decrease with depth. When evaluating model errors between estimation and labels over the study domain, the model will learn unnecessary features from the outliers and pay relatively less attention to the useful information of the valid data. Ignoring outliers in the loss function can help the model efficiently learn the characteristics of the real salinity field and yield an estimation close to the ground truth. The generalization ability of the model can be significantly improved as well. Thus, the introduction of



FIGURE 3
Variations of RMSE and correlation coefficient (R) between Attention U-net estimated salinity and GLORYS2V4 reanalysis as a function of water depth in the SCS in January **(A)** and July **(B)**. The subscripts "MSE", "Huber" and "Mrmse" of RMSE and R represent the estimation derived from the model based on MSE, Huber and Mrmse loss functions, respectively.

the Mrmse loss function in the Attention U-net model has effectively improved the accuracy of salinity reconstruction result at all layers, especially in deeper waters of the SCS.

3.2 Overall performance of Attention U-net model

Based on the comparative experiment results, we finally established the 3D salinity reconstruction model by month for each vertical layer, in which the Mrmse loss function was used. In this section, we evaluated the performance of these models by comparing the model results with GLORYS2V4 reanalysis and *in situ* mooring measurements, respectively.

3.2.1 Estimated salinity vs. GLORYS2V4 reanalysis

The overall RMSE and correlation coefficient between estimation and the reanalysis in each layer is shown in Table 2. As the water depth increases, the RMSE rapidly decreases from 0.106 psu near the surface to 0.009 psu at 200 m depth. After that, it continues to decline and reaches a minimum value of 0.002 psu in waters deeper than 773 m. The vertical variation of the correlation coefficient is notably different than the RMSE. It remains stable at high values between 0.983 and 0.994. The estimation of testing samples at all depths and over all month has an average RMSE of 0.051 psu and a correlation coefficient of 0.998, suggesting an impressive performance in reconstructing 3D salinity field in the SCS. The RMSE is less than 0.03 psu in areas deeper than 100 m all year round (Figure 4). Relatively larger values are distributed in the upper 100 m layers of the SCS, but are still less than 0.14 psu, and the RMSE in the upper layers shows a seasonal difference. The vertical spatial variation pattern of RMSE is consistent with the results of Meng et al. (2022) in the Pacific Ocean using CNN model. The correlation coefficient always remains high above 0.965, and rarely changes between seasons. However, the value is a little lower in the water layers between 200 m and 400 m. This might be related to the higher variability of salinity at these depths.

We further calculated the number of salinity points in the testing dataset at intervals of 0.001 psu, divided it by the total number of the testing data, and then normalized it to a range of 0 to 1 to obtain the density of data points in each interval. Figure 5 shows the density scatterplots between the salinity derived from satellite observed variables and GLORYS2V4 reanalysis at different depths. One can see that most of the statistics are distributed along the isoline where the estimated salinity is equal to the true value, demonstrating that the Attention U-net model performs quite well. The points are concentrated in a wider salinity range of 33.3 psu to 34.2 psu at the depth of 54 m, and at a smaller range for deeper layers. This might be related to the relatively large variation of salinity in the upper SCS. As shown in the left panel of Figure 6, the spatial variability of salinity field is indeed more significant in shallower waters. The maximum horizontal difference is about 2.1 psu at 54 m depth but is only 0.3 psu at depth more than 500 m. Figure 6 also shows that the salinity field estimated from the Attention U-net model has a spatial distribution pattern highly consistent with the GLORYS2V4 reanalysis. The fresher waters within the 100 m depth are widely distributed in the southern SCS, while those at the depth of 509 m are mainly located in the west of the Luzon Strait. The estimation error is close to 0 in almost the whole SCS, especially in the deeper layers. However, errors are slightly larger in a few areas.

3.2.2 Estimated salinity vs. *in situ* measurements

Field measurements can provide reliable ocean salinity profile data, although these data are sparse in space. We collected the salinity data observed by a mooring chain consisting of eight Conductivity-Temperature-Depth (CTD) instruments deployed at 20.54°N, 115.57°E in the northern SCS (Figure 1A). The mooring measures underwater salinity and temperature in depth from about 50 m to 380 m. The salinity profiles from July 11 to 25 2016 were used to further evaluate the accuracy of the reconstructed salinity results. The daily reconstructed salinity profile and its evolution are in good agreement with the mooring observations (Figure 7), further indicating the good performance and applicability of the Attention U-net model. The depth-averaged RMSE between the model estimation and *in situ* measurements varies from 0.032 psu to 0.066 psu, and the correlation coefficient is greater than 0.94.

4 Discussion

4.1 Error analysis of Attention U-net model

Overall, the Attention U-net model performs quite well in estimating underwater salinity in the SCS and the accuracy is very high in deep waters. The RMSE of the reconstructed salinity in the upper 100 m is slightly larger than that in deeper layers, which may be caused by the more complex salinity structure resulting from

TABLE 2 RMSE and correlation coefficient (R) between Attention U-net estimated salinity and GLORYS2V4 reanalysis for each layer in the upper 1000 m of the SCS.

Depth/m	5	10	19	31	41	54	61	69	78	87	97
RMSE/psu	0.106	0.079	0.070	0.071	0.067	0.058	0.054	0.049	0.042	0.038	0.031
R	0.991	0.994	0.994	0.994	0.994	0.994	0.993	0.992	0.992	0.991	0.991
Depth/m	147	200	245	301	412	509	628	697	773	857	947
RMSE/psu	0.014	0.009	0.008	0.006	0.005	0.004	0.003	0.003	0.002	0.002	0.002
R	0.987	0.985	0.983	0.984	0.983	0.990	0.990	0.989	0.991	0.990	0.988

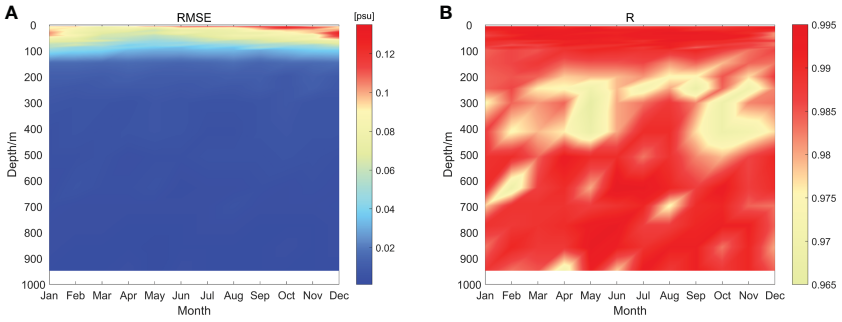


FIGURE 4
Variation of RMSE **(A)** and correlation coefficient (R) **(B)** between Attention U-net estimated salinity and GLORYS2V4 reanalysis with water depth and month.

active dynamic processes here. The horizontal distribution of the RMSE at three different surface depths is illustrated in Figures 8A–C. At a depth of 5 m, the relatively large error is mainly located in two coastal regions, but their values are still less than 0.3 psu. The regions correspond to the generation and extension of the Pearl River and Mekong River plumes that have a significant impact on the salinity field of the coastal and upper waters of the SCS (Chen et al., 2016; Zeng et al., 2022). The larger error near the Mekong River estuary is particularly notable in the upper 10 m, while the error near the Pearl River estuary is mainly distributed in the top

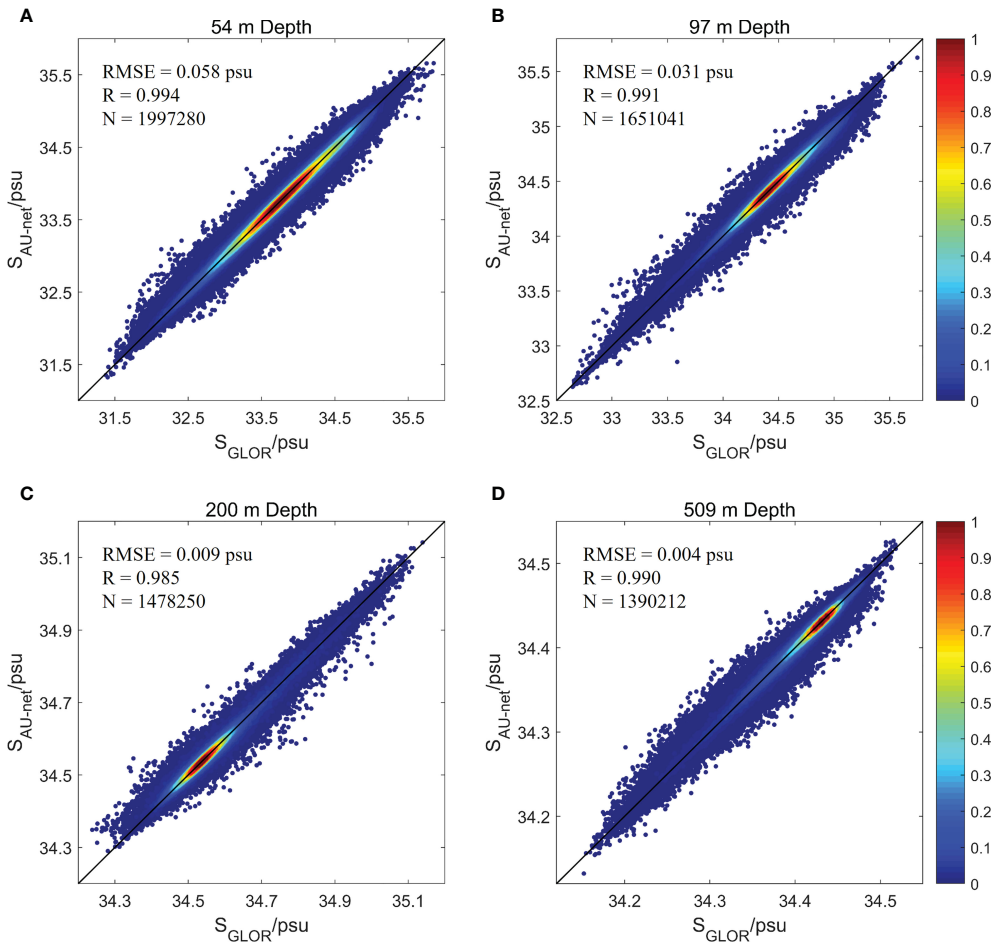


FIGURE 5
Density scatterplots between the Attention U-net model estimated salinity ($S_{AU\text{-}net}$) and GLORYS2V4 reanalysis (S_{GLOR}) at the depth of **(A)** 54 m, **(B)** 97 m, **(C)** 200 m and **(D)** 509 m in the SCS. The black line indicates the 1-to-1 line. N is the number of data points in all testing samples.

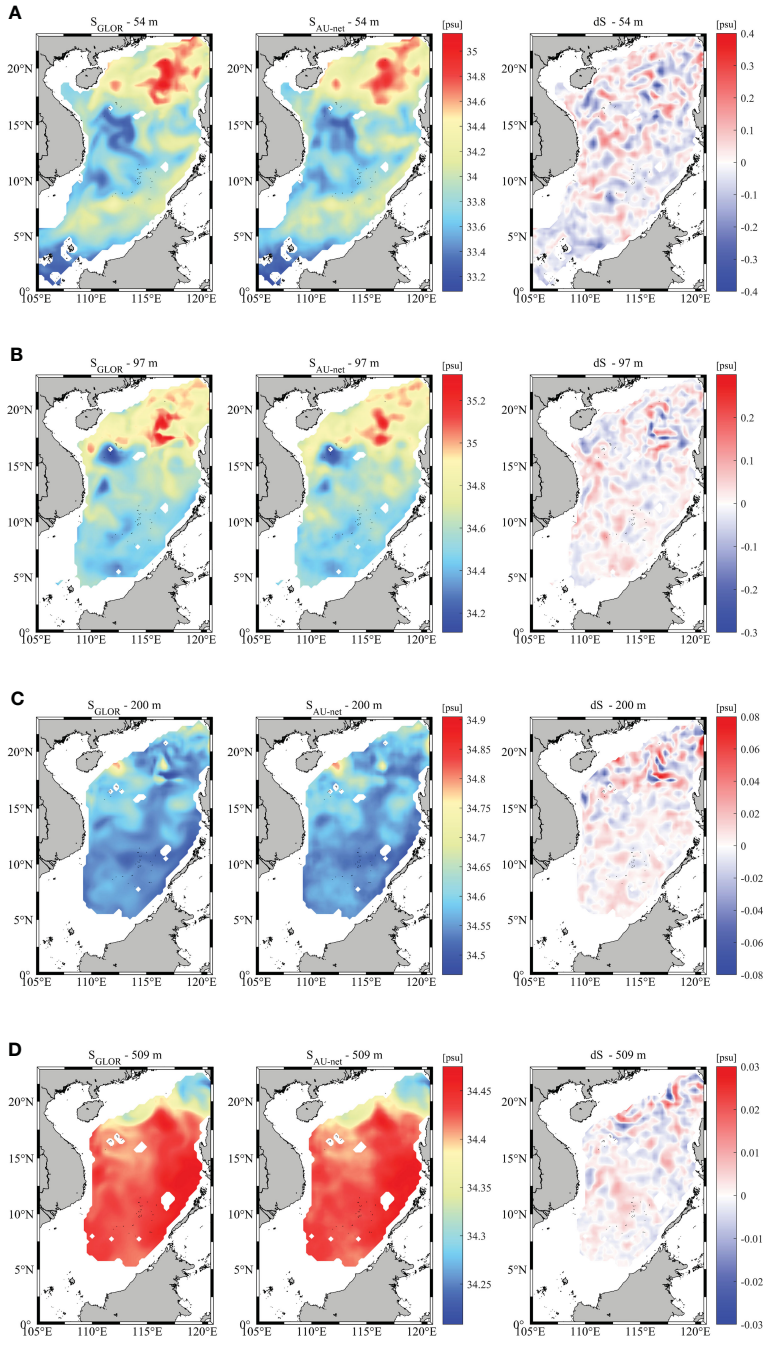


FIGURE 6
Distribution of salinity field estimated by the Attention U-net model compared to the GLORYS2V4 reanalysis and their difference (dS = $S_{AU\text{-}net}$ − S_{GLOR}) at the depth of **(A)** 54 m, **(B)** 97 m, **(C)** 200 m and **(D)** 509 m in the SCS on 1 May 2018.

layer. This might be associated with larger pulse of riverine flow into the SCS *via* the Mekong River, which results in a stronger halocline near the estuary (Gan et al., 2009; Zeng et al., 2022).

Figure 4A shows the upper-layer RMSE between the reconstructed salinity and reanalysis product for all samples in the testing dataset differing between seasons. It is smaller in spring (March-May) and summer (June-August) than in autumn (September-November) and winter (December-February). This seasonal variation is also evident in Figure 9. In summer, the RMSE within the top three layers is larger near the Pearl River and Mekong River estuaries than that in the other parts of the SCS. This might be related to the large amount of river discharge caused by the monsoon and wide extension of the river plumes to the SCS (Ou et al., 2007; Zeng et al., 2022). The southwest monsoon will bring a lot of precipitation over the ocean, thus increasing the river discharge. In winter, rainfall is less due to land breeze, and the

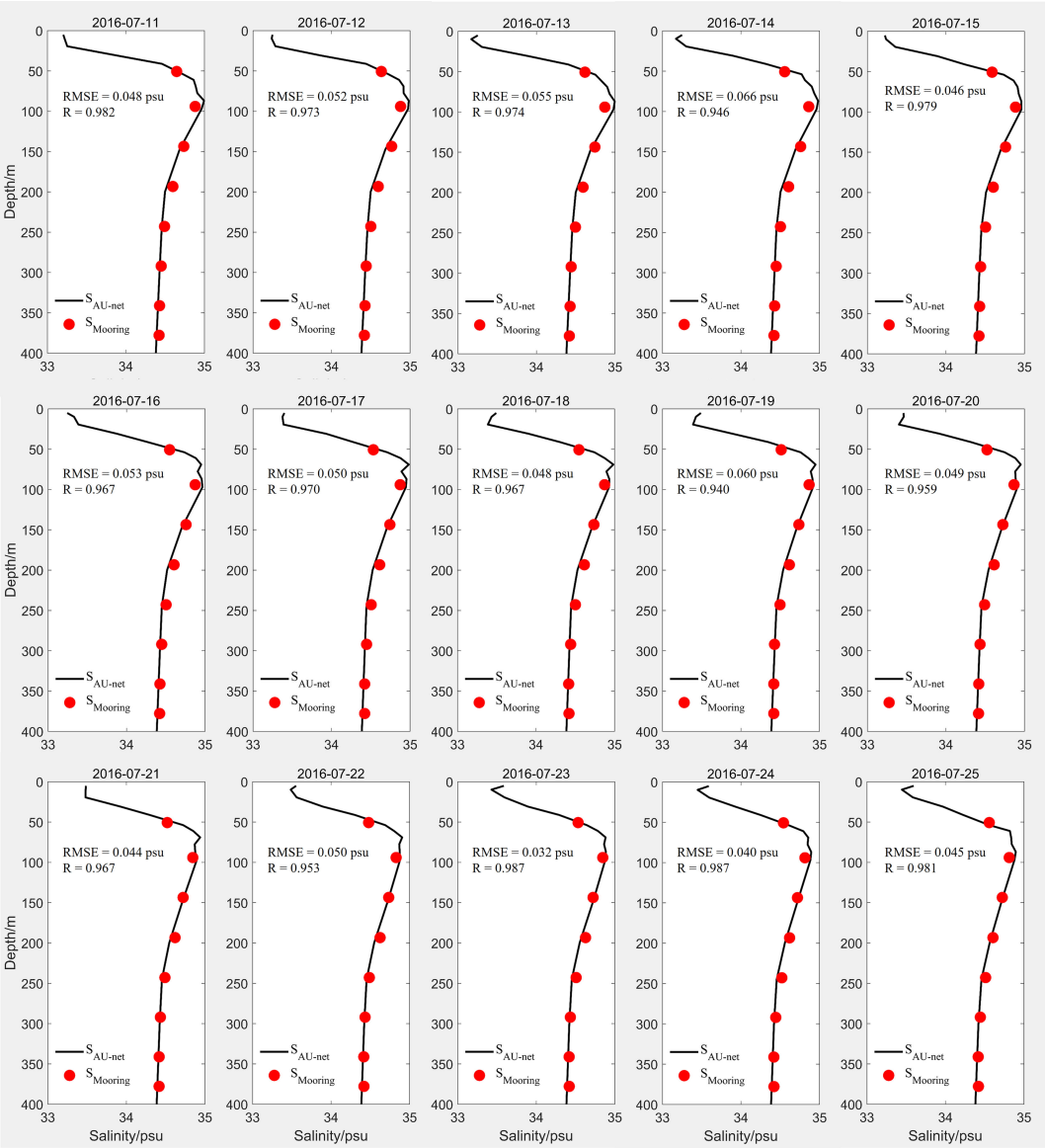


FIGURE 7
Attention U-net model estimated salinity profiles ($S_{AU\text{-}net}$) compared to mooring observations ($S_{Mooring}$) from July 11 to 25 2016.

corresponding river plume is weaker. As a result, the accuracy of upper-layer salinity reconstruction near the river plumes is much higher than that in summer.

4.2 Broader applications and limitations of salinity reconstruction model

The 0.25°×0.25° gridded satellite observations used as model inputs do not contain many smaller-scale signals which are usually smoothed from the filters in the data processing and might have a significant influence on the accuracy of reconstructed salinity field. To investigate whether the noisy features of sea surface variables would affect the estimation results, an additional group of experiments based on 3D salinity reconstruction model were conducted, in which Gaussian white noise was added to all input satellite data. The results for January are given in Figure 10. After adding noise to surface variables, the Attention U-net model still performs well in 3D salinity reconstruction. The RMSE ranges from 0.002 psu to 0.111 psu and the correlation coefficient is always higher than 0.973, which is close to the results obtained when using smooth data as model inputs. The RMSE in the upper 45 m is slightly larger, but compared to the noiseless case, the maximum increase is less than 0.011 psu. The correlation coefficient shows almost no change at all vertical layers. This indicates that our model is a robust model that can resist some possible noise interference from input data.

Thus, additional consideration of the river plume to the model input seems to be helpful to improve salinity estimation accuracy (see Section 4.1). However, the runoff discharge data that are usually used to describe the intensity of the river plume are dispersedly distributed on land where 3D salinity data are unavailable, which

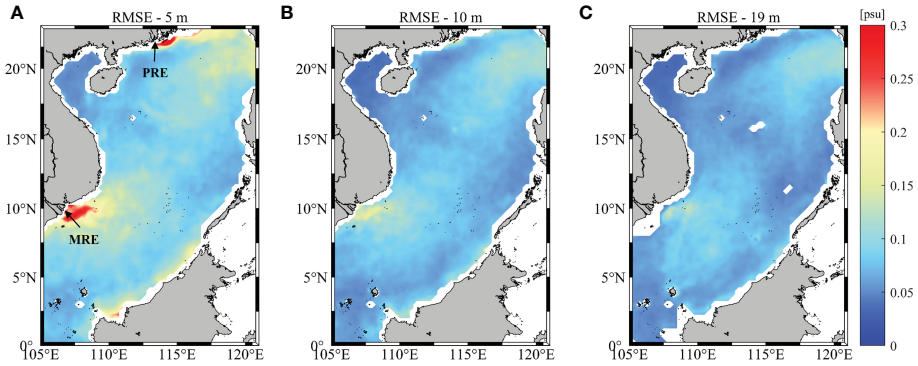


FIGURE 8
Distribution of RMSE between Attention U-net estimated salinity and GLORYS2V4 reanalysis at the depth of 5 m **(A)**, 10 m **(B)** and 19 m **(C)** in the SCS. Black arrows in **(A)** specify the location of Pearl River estuary (PRE) and Mekong River estuary (MRE), respectively.

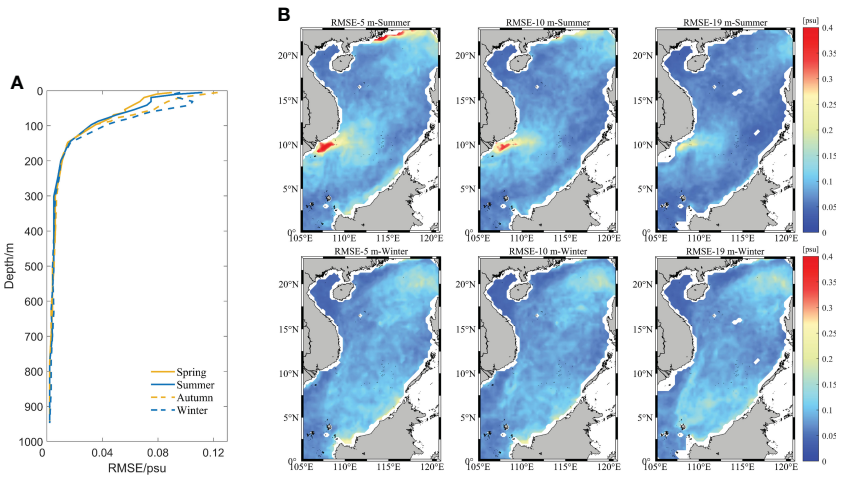


FIGURE 9
(A) Vertical variation of RMSE between Attention U-net estimated salinity and GLORYS2V4 reanalysis in four seasons. **(B)** RMSE maps at 5 m, 10 m and 19 m depth of the SCS in summer and winter.

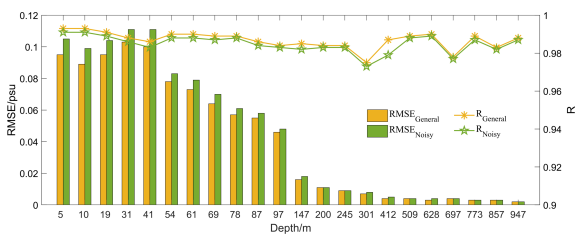


FIGURE 10
Variations of RMSE and correlation coefficient (R) between Attention U-net estimated salinity and GLORYS2V4 reanalysis as a function of water depth in the SCS in January. The subscripts "General" and "Noisy" of RMSE and R represent the estimation derived from sea surface variables without and with the Gaussian white noise, respectively. The Mrmse loss function is used in the model.

limits the input of runoff discharge in the model. It is also difficult to obtain these data because most of them are not public. Can we take the effect of river plumes into account indirectly when reconstructing the 3D salinity field in the SCS? This is possible, as SSS information provided by satellites already reflects the impact of river plumes on sea surface properties. To illustrate this, two comparative experiments were conducted to reconstruct 3D salinity fields in the upper 20 m of the SCS from surface variables with and without using SSS, respectively. The RMSE between the estimations and the GLORYS2V4 reanalysis at each vertical layer in summer and winter is given in Table 3. When SSS is added to the model inputs, the horizontally averaged RMSE decreases at each layer, and the maximum decline is 16.4% at a depth of 5 m. A more significant reduction of RMSE appears in summer than winter, while the estimation error near river estuaries is also much larger (see Figure 9B). The influence of SSS on the subsurface salinity reconstruction accuracy in the SCS, especially in the river plume

TABLE 3 RMSE between Attention U-net estimated salinity and GLORYS2V4 reanalysis in the upper 20 m of the SCS in summer and winter.

Depth/m	Summer			Winter		
	$RMSE_5$/psu	$RMSE_4$/psu	Relative difference	$RMSE_5$/psu	$RMSE_4$/psu	Relative difference
5	0.112	0.134	-16.4%	0.096	0.112	-14.3%
10	0.094	0.111	-15.3%	0.091	0.107	-15.0%
19	0.075	0.084	-10.7%	0.094	0.103	-8.7%
Average	0.095	0.112	-15.2%	0.094	0.108	-13.0%

Subscripts "5" and "4" of RMSE represent the estimation error derived from five surface variables (SSS/SST/SLA/SSW field) and four surface variables without SSS, respectively.The relative difference is ($RMSE_5$-$RMSE_4$)/$RMSE_4$ and a negative value indicates an improvement in accuracy when considering SSS as model input.

areas, is further investigated using a distribution map of the difference between RMSE derived from surface variables with and without SSS (Figure 11). When SSS is added to the model inputs, the RMSE near the Mekong estuary is significantly reduced in summer and the RMSE around the Pearl River plume also decreases. This indicates that SSS is crucial for 3D salinity reconstruction in the SCS, especially in river plume regions, as it can provide useful information about the impact of river discharge on the salinity. However, the accuracy of satellite-observed SSS is not high enough in coastal areas of the SCS, due to the contamination of land-based radio frequency interference (Zhang et al., 2023). The use of new technologies or satellite sensors to obtain more accurate SSS from satellites will further improve the accuracy of salinity reconstruction in the future.

4.3 Application of reconstructed salinity fields to a mesoscale eddy case study

The high-resolution 3D salinity field estimated from satellite observations using the Attention U-net model can be useful in the study of dynamic processes in the SCS, such as mesoscale eddies. We employ version 3.1 of the altimetric Mesoscale Eddy Trajectories Atlas, supplied by AVISO (https://aviso.altimetry.fr),

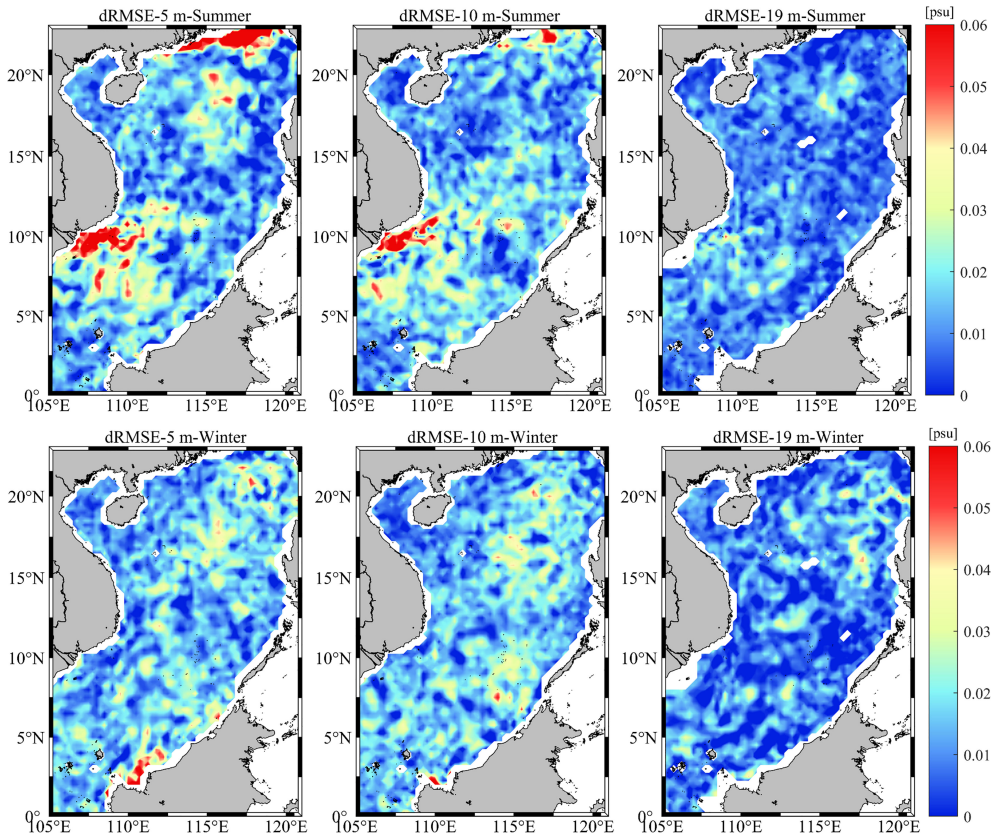


FIGURE 11
Distribution of differences between RMSE (dRMSE = $RMSE_4$ −$RMSE_5$) derived from sea surface variables with and without SSS at 5 m, 10 m and 19 m depth of the SCS in summer and winter.

which contains information of global mesoscale eddies (Mason et al., 2014; Pegliasco et al., 2022). Using this dataset, a mesoscale cyclonic eddy with the radius larger than 100 km was captured in the central SCS. The evolution of the eddy within 5 days from 13 to 17 November 2017 is presented in Figure 12A. The cyclonic eddy propagates northwestward as its shape and internal negative SLA signal slightly change, which means that the eddy may be stable at this stage. Meanwhile, the corresponding SSS anomaly field, obtained by subtracting the SSS from the climatology, is always positive within the eddy during the propagation (Figure 12B). This is associated with upwelling induced by the cyclonic eddy, which lifts the relatively saltier waters at the lower layers to the upper layers and hence increases the salinity at the sea surface. The positive SSS anomaly signal agrees well with the eddy signal detected from the SLA field, though it is slightly smaller. This indicates that the characteristics of the eddy can be at least partially described from the salinity field. Therefore, the reconstructed subsurface salinity anomaly is useful for tracking the evolution of eddy signal beneath the sea surface.

Figure 13 shows a contour map of subsurface salinity anomaly at different water depths (5 m, 10 m, 19 m and 31 m) in the same 5 days. Closed contours of positive subsurface salinity anomaly are present at the top three layers and disappear at a depth of 31 m, suggesting that the subsurface signal of the cyclonic eddy is strong in the upper 19 m. Compared with the surface signal, the underwater signal of eddy also moves towards northwest, but with much smaller radius and lower intensity. Additionally, the underwater center of the cyclonic eddy detected by the subsurface salinity anomaly field is located on the southeast side of that at sea surface captured from the SLA field, revealing the southeastward tilt of eddy axis in the vertical direction (Zhang et al., 2016). The subsurface salinity anomaly field provides a valuable view of the

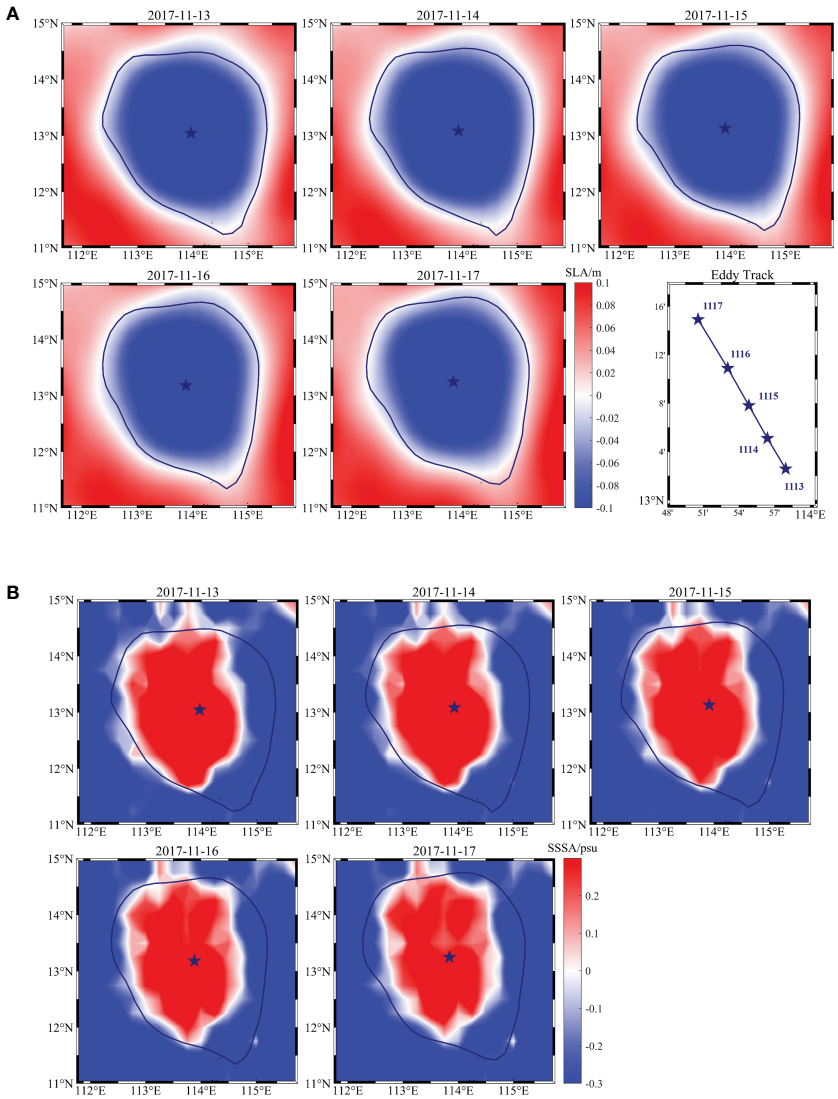


FIGURE 12
Daily **(A)** SLA and **(B)** SSS anomaly map from 13 to 17 November 2017 in the central SCS. The blue star and curve denote the center and contour of the cyclonic eddy, respectively. The movement of the eddy center within 5 days is presented as blue line in **(A)**.

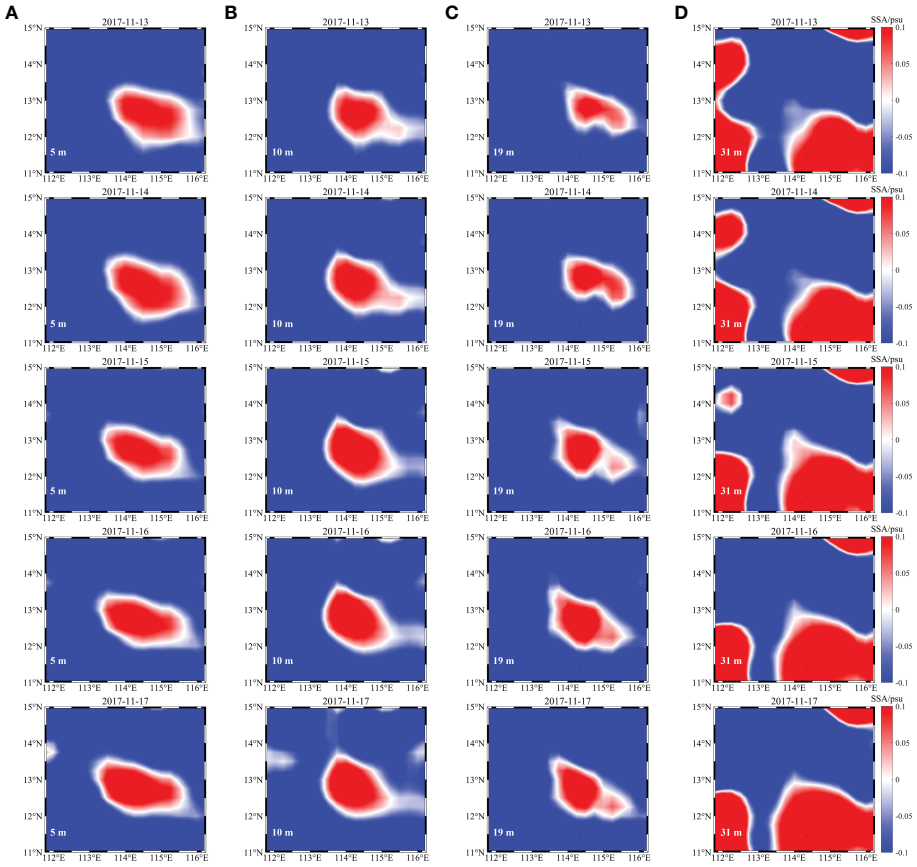


FIGURE 13
Daily subsurface salinity anomaly map at the depth of **(A)** 5 m, **(B)** 10 m, **(C)** 19 m and **(D)** 31 m from 13 to 17 November 2017 in the central SCS.

eddy-induced changes in the interior ocean, which will help us comprehensively understand the characteristics of mesoscale eddies in the SCS, especially their vertical structures.

5 Conclusions

The reconstruction of 3D ocean salinity fields is now much easier with the development of numerous remote sensing satellite missions and AI approaches. However, less attention has been paid to underwater salinity estimation in the SCS, where mesoscale and sub-mesoscale phenomena are active, and high-resolution observations are critically needed. We here adopted an Attention U-net model to reconstruct the 3D daily salinity field on a 1/4° grid in the upper 1000 m of the SCS from the satellite observed SSS, SST, SLA and SSW field. In general, the 3D salinity fields of the SCS, at high spatial and temporal resolution, can be well reconstructed. The average RMSE between the estimation results and salinity profiles from the GLORYS2V4 reanalysis product is 0.051 psu and the overall correlation coefficient is 0.998. The RMSE decreases with water depth and reaches a minimum value of 0.002 psu in waters deeper than 773 m, while the correlation coefficient is always higher than 0.983 at all layers. The comparison of salinity reconstruction results with mooring measurements also demonstrates the good performance of the Attention U-net model. In addition, the ability to resist noise interference indicates a strong robustness of the Attention U-net model.

The consideration of topography mask in the loss function is effective in reconstructing more accurate salinity fields in the SCS, especially in deeper waters. When only the estimation errors at valid data points are evaluated in the built model, the RMSE at different vertical layers is half of or even 85% less than the error obtained by using the Huber loss function. The corresponding correlation coefficient is increased by 23.0% to 108.9% in waters deeper than 200 m. Additionally, the use of SSS as model inputs can significantly improve the accuracy of salinity reconstruction in the upper layers of the SCS, especially in river plume regions. When SSS is added to the model inputs, the maximum decline of the RMSE is up to 16.4% at the depth of 5 m. The relatively larger estimation errors are mainly distributed in the coastal and upper waters of the SCS, which may be associated with the active dynamic processes here such as river plumes, as well as the poor quality of SSS satellite products in the coastal regions (González-Gambau et al., 2017; Zhang et al., 2023). The accuracy of coastal satellite SSS products will significantly improve in the near future, which will soon allow more precise reconstructions of 3D salinity fields.

Satellite observed sea surface variables, which determine the resolution of the model output, are of great importance for the 3D ocean salinity reconstruction. However, we can only construct the daily salinity field on a 1/4° grid due to the limitation of present

satellite data. Case studies show that the reconstructed salinity structure clearly reveals the underwater signals of mesoscale eddies in the SCS. Observations with higher spatial and temporal resolution can help us better understand the characteristics and evolution of ocean mesoscale or even sub-mesoscale processes. The Surface Water and Ocean Topography (SWOT) mission (Morrow et al., 2019) recently had a successful launch in December 2022. This mission will bring significant future improvement of salinity and wind sensors, and thus we will expect to observe sea surface variables from space with unprecedented resolution and precision. This advance will allow the resolution and accuracy of the 3D temperature and salinity fields to be further improved, which will in turn increase the knowledge of oceanic multi-scale dynamic processes.

Data availability statement

The original contributions presented in the study are included in the article/supplementary material. Further inquiries can be directed to the corresponding author.

Author contributions

Conceptualization: HX and QX. Methodology: HX and QX. Data curation: YC. Formal analysis: HX and KF. Investigation: HX and XY. Visualization: XY and KF. Writing-original draft preparation: HX. Writing-review and editing: QX. Supervision: QX. Funding acquisition: QX, YC and XY. All authors have read and agreed to the published version of the manuscript.

Funding

This work was supported by the National Natural Science Foundation of China under Grants 41976163 and T2261149752 and Guangdong Special Fund Program for Marine Economy Development under Grant GDNRC[2020]050. Hainan Key Research and Development Program under Grant ZDYF2023SHFZ089, Laoshan Laboratory Science and Technology Innovation Projects under Grants LSKJ202201202 and LSKJ202204301.

Conflict of interest

Author Yongcun Cheng was employed by PIESAT Information Technology Co., Ltd.

The remaining authors declare that the research was conducted in the absence of any commercial or financial relationships that could be construed as a potential conflict of interest.

Publisher's note

All claims expressed in this article are solely those of the authors and do not necessarily represent those of their affiliated organizations, or those of the publisher, the editors and the reviewers. Any product that may be evaluated in this article, or claim that may be made by its manufacturer, is not guaranteed or endorsed by the publisher.

References

Agarwal, N., Sharma, R., Basu, S., and Agarwal, V. K. (2007). Derivation of salinity profiles in the Indian ocean from satellite surface observations. *IEEE Geosci. Remote Sens. Lett.* 4 (2), 322–325. doi: 10.1109/lgrs.2007.894163

Atlas, R., Hoffman, R. N., Ardizzone, J., Leidner, S. M., Jusem, J. C., Smith, D. K., et al. (2011). A cross-calibrated, multiplatform ocean surface wind velocity product for meteorological and oceanographic applications. *B. Am. Meteorol. Soc* 92 (2), 157–174. doi: 10.1175/2010bams2946.1

Ballabrera-Poy, J., Mourre, B., Garcia-Ladona, E., Turiel, A., and Font, J. (2009). Linear and non-linear T-s models for the eastern north Atlantic from argo data: role of surface salinity observations. *Deep Sea Res. Pt. I: Oceanographic Res. Papers* 56 (10), 1605–1614. doi: 10.1016/j.dsr.2009.05.017

Bao, S., Zhang, R., Wang, H., Yan, H., Yu, Y., and Chen, J. (2019). Salinity profile estimation in the pacific ocean from satellite surface salinity observations. *J. Atmos. Ocean. Tech.* 36 (1), 53–68. doi: 10.1175/jtech-d-17-0226.1

Boutin, J., Reul, N., Koehler, J., Martin, A., Catany, R., Guimbard, S., et al. (2021). Satellite-based sea surface salinity designed for ocean and climate studies. *J. Geophys. Res.: Oceans* 126, 1–28. doi: 10.1029/2021jc017676

Buongiorno Nardelli, B. (2020). A deep learning network to retrieve ocean hydrographic profiles from combined satellite and *in situ* measurements. *Remote Sens.* 12 (3151), 1–14. doi: 10.3390/rs12193151

Carnes, M. R., Teague, W. J., and Mitchell, J. L. (1994). Inference of subsurface thermohaline structure from fields measurable by satellite. *J. Atmos. Ocean. Tech.* 11 (2), 551–566. doi: 10.1175/1520-0426(1994)011<0551:IOSTSF>2.0.CO;2

CATDS (2017). *Data from: CATDS-PDC L3OS 2P-daily valid ocean salinity values product from SMOS satellite*. Institut français de recherche pour l'exploitation de la mer (Paris, France: IFREMER). The location is Paris, France. doi: 10.12770/77edd308-4296-4774-b6f3-5b38301cee18

Chaudhari, S., Mithal, V., Polatkan, G., and Ramanath, R. (2021). An attentive survey of attention models. *ACM Trans. Intell. Syst. Technol.* 12 (5), 1–32. doi: 10.1145/3465055

Chen, Z., Pan, J., and Jiang, Y. (2016). Role of pulsed winds on detachment of low salinity water from the pearl river plume: upwelling and mixing processes. *J. Geophys. Res.: Oceans* 121 (4), 2769–2788. doi: 10.1002/2015jc011337

Gan, J., Li, L., Wang, D., and Guo, X. (2009). Interaction of a river plume with coastal upwelling in the northeastern south China Sea. *Cont. Shelf Res.* 29 (4), 728–740. doi: 10.1016/j.csr.2008.12.002

Garric, G., Parent, L., Greiner, E., Drévillon, M., Hamon, M., Lellouche, J.-M., et al. (2017). *Performance and quality assessment of the global ocean eddy-permitting physical reanalysis GLORYS2V4* (Vienna, Austria:EGU General Assembly Conference Abstracts). Vienna, Austria.

González-Gambau, V., Olmedo, E., Martinez, J., Turiel, A., and Duran, I. (2017). Improvements on calibration and image reconstruction of SMOS for salinity retrievals in coastal regions. *IEEE J. Sel. Top. Appl. Earth Obs. Remote Sens.* 10 (7), 3064–3078. doi: 10.1109/jstars.2017.2685690

Guinehut, S., Dhomps, A. L., Larnicol, G., and Le Traon, P. Y. (2012). High resolution 3-d temperature and salinity fields derived from *in situ* and satellite observations. *Ocean Sci.* 8 (5), 845–857. doi: 10.5194/os-8-845-2012

Han, Y., and Ye, J. C. (2018). Framing U-net *via* deep convolutional framelets: application to sparse-view CT. *IEEE trans. Med. Imaging* 37 (6), 1418–1429. doi: 10.1109/TMI.2018.2823768

He, Q., Zhan, H., Cai, S., He, Y., Huang, G., and Zhan, W. (2018). A new assessment of mesoscale eddies in the south China Sea: surface features, three-dimensional structures, and thermohaline transports. *J. Geophys. Res.: Oceans* 123 (7), 4906–4929. doi: 10.1029/2018jc014054

Held, I. M., and Soden, B. J. (2006). Robust responses of the hydrological cycle to global warming. *J. Clim.* 19 (21), 5686–5699. doi: 10.1175/JCLI3990.1

Henning, C. C., and Vallis, G. K. (2004). The effects of mesoscale eddies on the main subtropical thermocline. *J. Phys. Oceanogr.* 34 (11), 2428–2442. doi: 10.1175/JPO2639.1

Huang, X., Chen, Z., Zhao, W., Zhang, Z., Zhou, C., Yang, Q., et al. (2016). An extreme internal solitary wave event observed in the northern south China Sea. *Sci. Rep.* 6 (30041), 1–10. doi: 10.1038/srep30041

Huang, B., Liu, C., Banzon, V., Freeman, E., Graham, G., Hankins, B., et al. (2021). Improvements of the daily optimum interpolation sea surface temperature (DOISST) version 2.1. *J. Clim.* 34 (8), 2923–2939. doi: 10.1175/jcli-d-20-0166.1

Keppler, L., Cravatte, S., Chaigneau, A., Pegliasco, C., Gourdeau, L., and Singh, A. (2018). Observed characteristics and vertical structure of mesoscale eddies in the southwest tropical pacific. *J. Geophys. Res.: Oceans* 123 (4), 2731–2756. doi: 10.1002/2017jc013712

Klemas, V., and Yan, X.-H. (2014). Subsurface and deeper ocean remote sensing from satellites: an overview and new results. *Prog. Oceanogr.* 122, 1–9. doi: 10.1016/j.pocean.2013.11.010

Lagerloef, G. S. E. (2002). Introduction to the special section: the role of surface salinity on upper ocean dynamics, air-sea interaction and climate. *J. Geophys. Res.: Oceans* 107, 1–2. doi: 10.1029/2002jc001669

Li, X., Liu, B., Zheng, G., Ren, Y., Zhang, S., Liu, Y., et al. (2020). Deep-learning-based information mining from ocean remote-sensing imagery. *Natl. Sci. Rev.* 7 (10), 1584–1605. doi: 10.1093/nsr/nwaa047

Li, X., Zhou, Y., and Wang, F. (2022). Advanced information mining from ocean remote sensing imagery with deep learning. *J. Remote Sens.* 2022, 1–4. doi: 10.34133/2022/9849645

Mason, E., Pascual, A., and McWilliams, J. C. (2014). A new sea surface height-based code for oceanic mesoscale eddy tracking. *J. Atmos. Ocean. Tech.* 31 (5), 1181–1188. doi: 10.1175/jtech-d-14-00019.1

Mears, C. A., Scott, J., Wentz, F. J., Ricciardulli, L., Leidner, S. M., Hoffman, R., et al. (2019). A near-real-time version of the cross-calibrated multiplatform (CCMP) ocean surface wind velocity data set. *J. Geophys. Res.: Oceans* 124 (10), 6997–7010. doi: 10.1029/2019jc015367

Meissner, T., Wentz, F. J., Manaster, A., and Lindsley, R. (2019). Data from: remote sensing systems SMAP ocean surface salinities [level 2C], version 4.0 validated release s. r. doi: 10.5067/SMP40-2SOCS

Meissner, T., Wentz, F. J., and Vine, D. M. L. (2018). The salinity retrieval algorithms for the NASA aquarius version 5 and SMAP version 3 releases. *Remote Sens.* 10 (7), 1–25. doi: 10.3390/rs10071121

Meng, L., Yan, C., Zhuang, W., Zhang, W., Geng, X., and Yan, X.-H. (2022). Reconstructing high-resolution ocean subsurface and interior temperature and salinity anomalies from satellite observations. *IEEE Trans. Geosci. Remote Sens.* 60, 1–14. doi: 10.1109/tgrs.2021.3109979

Morrow, R., Fu, L.-L., Ardhuin, F., Benkiran, M., Chapron, B., Cosme, E., et al. (2019). Global observations of fine-scale ocean surface topography with the surface water and ocean topography (SWOT) mission. *Front. Mar. Sci.* 6 (232). doi: 10.3389/fmars.2019.00232

Oktay, O., Schlemper, J., Folgoc, L. L., Lee, M., Heinrich, M., Misawa, K., et al. (2018). "Attention U-net: learning where to look for the pancreas," in *Conference on Medical Imaging with Deep Learning*, Amsterdam, The Netherlands.

Ou, S., Zhang, H., Wang, D., and He, J. (2007). Horizontal characteristics of buoyant plume off the pearl river estuary during summer. *J. Coast. Res.* 50, 652–657.

Pegliasco, C., Delepoulle, A., Morrow, R., Faugère, Y., and Dibarboure, G. (2022). META3.1exp: a new global mesoscale eddy trajectories atlas derived from altimetry. *Earth Syst. Sci. Data* 14 (3), 1087–1107. doi: 10.5194/essd-2021-300

Ren, L., and Riser, S. C. (2010). Observations of decadal time scale salinity changes in the subtropical thermocline of the north pacific ocean. *Deep Sea Res. Pt. II: Topical Stud. Oceanography* 57 (13), 1161–1170. doi: 10.1016/j.dsr2.2009.12.005

Reynolds, R. W., Smith, T. M., Liu, C., Chelton, D. B., Casey, K. S., and Schlax, M. G. (2007). Daily high-resolution-blended analyses for sea surface semperature. *J. Clim.* 20 (22), 5473–5496. doi: 10.1175/2007jcli1824.1

Ronneberger, O., Fischer, P., and Brox, T. (2015). "U-Net: convolutional networks for biomedical image segmentation," in *Medical image computing and computer-assisted intervention-MICCAI* (Cham, Switzerland: Springer).

Schmidtko, S., Stramma, L., and Visbeck, M. (2017). Decline in global oceanic oxygen content during the past five decades. *Nat* 542 (7641), 335–339. doi: 10.1038/nature21399

Schmitt, R. W. (2008). Salinity and the global water cycle. *Oceanogr* 21 (1), 12–19. doi: 10.5670/oceanog.2015.03

Song, T., Wei, W., Meng, F., Wang, J., Han, R., and Xu, D. (2022). Inversion of ocean subsurface temperature and salinity fields based on spatio-temporal correlation. *Remote Sens.* 14 (11), 1–23. doi: 10.3390/rs14112587

Su, H., Yang, X., Lu, W., and Yan, X.-H. (2019). Estimating subsurface thermohaline structure of the global ocean using surface remote sensing observations. *Remote Sens.* 11 (1598), 1–22. doi: 10.3390/rs11131598

Wang, G., Su, J., and Chu, P. C. (2003). Mesoscale eddies in the south China Sea observed with altimeter data. *Geophys. Res. Lett.* 30 (21), 1–6. doi: 10.1029/2003gl018532

Woo, S., Park, J., Lee, J.-Y., and Kweon, I. S. (2018). "CBAM: convolutional block attention module," in *Europeon conference on computer vision* (Cham, Switzerland: Springer).

Xie, H., Xu, Q., Cheng, Y., Yin, X., and Jia, Y. (2022a). Reconstruction of subsurface temperature field in the south China Sea from satellite observations based on an attention U-net model. *IEEE Trans. Geosci. Remote Sens.* 60, 1–19. doi: 10.1109/tgrs.2022.3200545

Xie, H., Xu, Q., Zheng, Q.a., Xiong, X., Ye, X., and Cheng, Y. (2022b). Assessment of theoretical approaches to derivation of internal solitary wave parameters from multi-satellite images near the dongsha atoll of the south China Sea. *Acta Oceanol. Sin.* 41 (2), 1–9. doi: 10.1007/s13131-022-2015-3

Xu, K., Ba, J., Kiros, R., Cho, K., Courville, A., Salakhutdinov, R., et al. (2015). "Show, attend and tell: neural image caption generation with visual attention," in *Proceedings of the International Conference on Machine Learning*, Lille, France.

Yang, T., Chen, Z., and He, Y. (2015). A new method to retrieve salinity profiles from sea surface salinity observed by SMOS satellite. *Acta Oceanol. Sin.* 34 (9), 85–93. doi: 10.1007/s13131-015-0735-3

Zeng, X., Bracco, A., and Tagklis, F. (2022). Dynamical impact of the Mekong river plume in the south China Sea. *J. Geophys. Res.: Oceans* 127 (5), 1–15. doi: 10.1029/2021jc017572

Zhang, Z., Tian, J., Qiu, B., Zhao, W., Chang, P., Wu, D., et al. (2016). Observed 3D structure, generation, and dissipation of oceanic mesoscale eddies in the south China Sea. *Sci. Rep.* 6 (1), 24349. doi: 10.1038/srep24349

Zhang, S., Xu, Q., Wang, H., Kang, Y., and Li, X. (2022). Automatic waterline extraction and topographic mapping of tidal flats from SAR images based on deep learning. *Geophys. Res. Lett.* 49, 1–13. doi: 10.1029/2021gl096007

Zhang, L., Zhang, Y., and Yin, X. (2023). Aquarius sea surface salinity retrieval in coastal regions based on deep neural networks. *Remote Sens. Environ.* 284. (113357), 1–15. doi: 10.1016/j.rse.2022.113357

Zheng, Q. A., Susanto, R. D., Ho, C.-R., Song, Y. T., and Xu, Q. (2007). Statistical and dynamical analyses of generation mechanisms of solitary internal waves in the northern south China Sea. *J. Geophys. Res.* 112, 1–16. doi: 10.1029/2006jc003551

Zine, S., Boutin, J., Font, J., Reul, N., Waldteufel, P., Gabarro, C., et al. (2008). Overview of the SMOS sea surface salinity prototype processor. *IEEE Trans. Geosci. Remote Sens.* 46 (3), 621–645. doi: 10.1109/tgrs.2008.915543

frontiers | Frontiers in Marine Science

TYPE Original Research
PUBLISHED 25 May 2023
DOI 10.3389/fmars.2023.1197456

Check for updates

OPEN ACCESS

EDITED BY
Qing Xu,
Ocean University of China, China

REVIEWED BY
Yongcun Cheng,
PIESAT Ltd Inc, China
Qi Shu,
Ministry of Natural Resources, China

*CORRESPONDENCE
Meixiang Chen
chenmeixiang@hhu.edu.cn

RECEIVED 31 March 2023
ACCEPTED 08 May 2023
PUBLISHED 25 May 2023

CITATION
Jin Y, Chen M, Yan H, Wang T and Yang J (2023) Sea level variation in the Arctic Ocean since 1979 based on ORAS5 data. *Front. Mar. Sci.* 10:1197456. doi: 10.3389/fmars.2023.1197456

COPYRIGHT
© 2023 Jin, Chen, Yan, Wang and Yang. This is an open-access article distributed under the terms of the Creative Commons Attribution License (CC BY). The use, distribution or reproduction in other forums is permitted, provided the original author(s) and the copyright owner(s) are credited and that the original publication in this journal is cited, in accordance with accepted academic practice. No use, distribution or reproduction is permitted which does not comply with these terms.

Sea level variation in the Arctic Ocean since 1979 based on ORAS5 data

Ying Jin[1,2], Meixiang Chen[1,2]*, Han Yan[1,2], Tao Wang[1,2] and Jie Yang[3]

[1]Key Laboratory of Marine Hazards Forecasting, Ministry of Natural Resources, Hohai University, Nanjing, China, [2]College of Oceanography, Hohai University, Nanjing, China, [3]College of Harbor, Coastal and Offshore Engineering, Hohai University, Nanjing, China

The Arctic is currently experiencing unprecedented changes across all components of the climate system, primarily driven by global warming. As an important indicator of climate change in the Arctic, sea level reflects variations in both the atmosphere and ocean. This paper analyzes the sea level variation of the Arctic Ocean over the past four decades using ORAS5 data, which is the product of the latest reanalysis-analysis system produced by the European Centre for Medium-Range Weather Forecasts (ECMWF). ORAS5 accurately reproduces the main spatial features of the climatology and temporal evolution of sea surface height (SSH) in the Arctic Ocean, as observed by satellite altimeters, and reveals that seasonal variability is the most significant property of the sea level variation in this region. The seasonal cycle of SSH is closely linked to atmospheric circulation and sea ice formation. The first two dominant modes of the annual-mean SSH in the Arctic Ocean exhibit significant decadal variability. The first mode can be explained by the Ekman transport of wind related to the Arctic Oscillation (AO), which leads to antiphase changes in SSH on the continental shelves and in the deep basins. The second mode shows an antiphase oscillation of SSH between the Eurasian and Canadian Arctic Archipelago (CAA) sides and is driven by the wind anomaly associated with the Arctic dipole anomaly (DA). Due to the decadal variations associated with climate modes, particularly the AO, sea level in the Arctic Ocean has been continuously rising since the mid-1990s or early 2000s, with the most rapid sea level rise occurring in the Beaufort Sea.

KEYWORDS

Arctic Ocean, sea surface height, ORAS5, seasonal and low-frequency variability, decadal sea level trend

1 Introduction

The Arctic has undergone unprecedented climate change over the past few decades, with surface temperatures increasing at twice the global mean rate (a phenomenon known as Arctic amplification; Serreze et al., 2009; Serreze and Barry, 2011). This has been accompanied by a rapid decline in sea ice (Kwok et al., 2009), ice mass loss from the

Greenland ice sheet (Rignot et al., 2011), and changes in ocean temperature (Polyakov et al., 2005) and salinity (McPhee et al., 2009), which have altered both physical and biogeochemical conditions in the Arctic Ocean. The melting of the Greenland ice sheet is directly contributing to the overall sea level rise of the globe. The reduction in sea ice extent affects the reflection and absorption of heat at the ocean surface, altering the air-sea heat flux and potentially disrupting the regular pattern of atmospheric and thermohaline circulation, thereby influencing the global climate, including mid- and low-latitude regions, through large-scale circulation and climate variability such as the Arctic Oscillation (AO) and North Atlantic Oscillation (NAO, Thompson and Wallace, 1998; Vihma, 2014). Amplification in both the atmosphere and ocean highlights the vulnerability of the Arctic to climate change, making it crucial to closely monitor the region both presently and in the future (Shu et al., 2022).

Sea level variation is an important indicator of global and regional climate, as it integrates changes of almost all the components in the climate system, in response to both natural and anthropogenic forcing (Church et al., 2013; Stammer et al., 2013; Legeais et al., 2018). Regional sea level changes are associated with a variety of dynamical and thermodynamical processes in the ocean, such as sea surface heating and cooling, wind forcing, freshwater exchanges between the ocean and other components of the climate system, thermohaline circulation and interior mixing in the ocean (Wunsch et al., 2007; Stammer et al., 2013; Koldunov et al., 2014; Cazenave, 2020). These processes can alter the temperature, salinity, currents and mass of the ocean, and consequently contribute to sea level change through the change of seawater density or mass change. Given the dramatic changes occurring in the Arctic region due to global warming and its impact on global climate, it is critical to conduct research on sea level changes within the Arctic Ocean. Such research is essential for gaining a better understanding of how recent climate change is affecting this region.

The greatest limitation to the research of sea level changes in the Arctic Ocean lies in the scarcity of observational data. Most tide gauges with long sea level records are situated along the coast of Norway and Russia and only a small part of them are maintained after 1990 (Proshutinsky et al., 2001; Proshutinsky et al., 2004; Proshutinsky et al., 2007; Henry et al., 2012). Measurements of SSH by satellite altimeters since the 1990s cover most parts of the Arctic Ocean. However, due to the inclination of altimeters, there are still blank areas near the North Pole that have not been adequately measured (Prandi et al., 2012; Cheng et al., 2015). Furthermore, the conventional processing of satellite radar altimetry is not effective in the presence of sea ice. Consequently, sea level monitoring in a considerable portion of the Arctic Ocean is not sufficient due to the existence of seasonal or permanent sea ice (Cheng et al., 2015; Armitage et al., 2016). Observations of hydrographic profiles in the Arctic Ocean are also scarce, particularly in ice-covered areas, hindering our understanding of the steric change contributing to sea level variations (e.g., Dmitrenko et al., 2008; Rabe et al., 2014).

However, a significant amount of research has still been carried out and some useful results are obtained basing on the records of tide gauge, satellite altimetry-derived datasets and outputs from numerical models. Sea level in the Arctic has been found to have significant seasonal variability, partly due to the steric change of seawater and injection of river runoff from the land (e.g., Proshutinsky et al., 2004; Richter et al., 2012; Armitage et al., 2016). Interannual to decadal sea level variabilities in the Arctic Ocean have also been reported to be consistent with the pattern of atmospheric circulation around the Arctic, like AO, NAO and atmospheric dipole anomaly of the Arctic (DA, Proshutinsky and Johnson, 1997; Wu et al., 2006; Proshutinsky et al., 2009; Koldunov et al., 2014; Proshutinsky et al., 2015; Armitage et al., 2016; Armitage et al., 2018; Xiao et al., 2020; Wang et al., 2021). Additionally, trend of sea level in the Arctic Ocean has also been focused on in many studies (e.g., Proshutinsky et al., 2004; Henry et al., 2012; Prandi et al., 2012; Cheng et al., 2015; Xiao et al., 2020). According to recent research, positive trends have been observed across almost all areas of the Arctic Ocean, and a dramatic sea level rise has been found in the Beaufort Sea (Prandi et al., 2012; Cheng et al., 2015; Carret et al., 2017), which is thought to be a result of freshwater accumulation (Giles et al., 2012).

One issue with previous research is the limited availability of long time-series observational data on SSH that covers the entire Arctic Ocean. Numerical simulation results have been used instead, but the outputs of numerical models may have biases that do not reflect actual sea level changes. Furthermore, there are variety of discrepancies among the results of different models or even the same model with different resolutions (e.g., Koldunov et al., 2014; Wang et al., 2018b; Xiao et al., 2020; Lyu et al., 2022). From this point of view, reanalysis datasets that assimilate various observational data and cover the entire Arctic Ocean over a longer time span are a more reliable choice for studying sea level changes in this region. Among these, the ORAS5 dataset is currently the best option. This dataset is the product of ECMWF's latest operational system, OCEAN5. OCEAN5 includes a sea ice model and assimilates more observational data of the Arctic Ocean, resulting in significantly improved simulation accuracy in the Arctic region compared to previous versions with no sea ice model included.

In this paper, we will use the SSH data of ORAS5 to analyze the sea level variation in the Arctic Ocean. Compared with altimeter data, ORAS5 provides a longer time period of 40 years (1979-2018) with significantly increased spatial coverage (with no blanks near the North Pole), enabling more accurate estimation of sea level changes especially low-frequency variabilities of sea level in the Arctic Ocean. Due to assimilation of observed data as more as possible in the simulation, the sea level data provided by ORAS5 is more realistic than the numerical model results. Two sets of satellite sea level data are used to validate the SSH data in the Arctic Ocean of ORAS5. One dataset is from the Centre for Polar Observation and Modelling (CPOM) at University College London, and the other is from the Technical University of Denmark (DTU). Both datasets cover the area with sea-ice but have shorter time spans. The following parts of the paper are structured as follows: Section 2 gives detailed introduction to the data used in this study and method to calculate climate variability indices, Section 3 validates the SSH data of ORAS5, Section 4 presents the sea level variation described by ORAS5 data, and we give a summary of this study in Section 5.

2 Data and methods

This paper utilizes three sets of sea level data to analyze the characteristics of sea level variation in the Arctic Ocean. The first is the SSH data of ORAS5, which is the latest reanalysis product of the OCEAN5 system operated by the ECMWF. OCEAN5 is developed from the new generation of operation system ORAP5. The ORAP5 system assimilates *in-situ* profiles of temperature and salinity data from the quality-controlled EN3 dataset and along-track altimeter-derived sea level anomaly (SLA) data from AVISO. The new OCEAN5 system includes a prognostic thermodynamic-dynamic sea-ice model (LIM2) and assimilates sea-ice concentration data in the high-latitude region for the first time. Compared to its predecessor, OCEAN4, OCEAN5 provides a more accurate estimate of the historical ocean state in the Arctic Ocean and has a higher ocean model resolution of 0.25 degrees in the horizontal direction and 75 levels in the vertical. Additionally, the system introduces a novel generic ensemble generation scheme that accounts for both observation and forcing errors and provides an estimate of the historical global ocean state from 1979 to present with a few days delay. The OCEAN5 system is now an important tool for climate research in the Arctic Ocean, and it provides the ocean and sea-ice initial conditions for all ECMWF coupled forecasting systems. The monthly SSH data used in this paper is the mean values of outputs from five ensemble members that are opa0 to opa4.

Two additional sets of SSH data are utilized to validate the ORAS5 data. The first set is the monthly dynamic ocean topography (DOT) data based on satellite altimeter observations, provided by CPOM of University College London (Armitage et al., 2016). This dataset provides the DOT data south of 81.5° N on a longitude-latitude grid of 0.75° × 0.25° for the period spanning from 2003 to 2014. This satellite-derived monthly product combines observations from two altimeters, Envisat data for 2003-2011 and CryoSat-2 data for 2012-2014. It has been used for various Arctic Ocean studies (Armitage et al., 2016; Armitage et al., 2017; Armitage et al., 2018; Regan et al., 2019). The second set of data is the mean dynamic topography (MDT13) data provided by DTU, which covers the entire globe with a spatial resolution of 1 minute. MDT13 is derived from 20-year (1993-2012) satellite data, including altimetry data and Gravity Field and Steady-State Ocean Circulation Explorer (GOCE) data.

The monthly mean sea ice concentration data in the Arctic region (64.5° N to 90° N, 0-360° E) for the period of 1979-2018 is obtained from the National Snow and Ice Data Center (NSIDC). The dataset has a horizontal resolution of approximately 0.25°.

The monthly sea level pressure (SLP) data from ERA5 reanalysis dataset is used to calculate the AO and DA index. This dataset has a spatial resolution of 0.25 degrees and covers the time period from 1959 to present.

Conventionally, AO is the leading mode of wintertime (November–April) SLP variability for regions north of 20°N (Thompson and Wallace, 1998), and DA corresponds to the second-leading mode of SLP north of 70°N during the winter season (October–March) (Wu et al., 2006). In this paper, we used the SLP data with a spatial coverage of 64.5° N-90° N and 0°-360°E (Figure 1), and a temporal coverage of the entire year, as opposed to just wintertime, to calculate the AO and DA index. The index calculated by this unconventional approach better captures the sea level variability studied in this paper. Additionally, our findings show that the effects of both AO and DA on sea level variation in the Arctic Ocean can accumulate over time, consistent with previous studies by Xiao et al. (2020) and Wang et al. (2021). We used the cumulative AO and DA index when we discussed the relation between sea level variation in the Arctic Ocean with AO and DA. Specifically, we define the cumulative AO/DA index for a given year as the sum of the annual mean AO/DA index from 1959 to the current year, where the annual mean AO/DA index is the average value of the 12 monthly AO/DA index for that year.

3 Validation of ORAS5 SSH data

The CPOM DOT data is obtained by radar altimeters but processed using specialized method that differs from conventional techniques for the areas with sea-ice. As a result, it provides meaningful SSH values for both sea-ice free and sea-ice covered areas. In the study of Armitage et al. (2016), the CPOM data has been compared with the tide gauge data along the coast of the Arctic Ocean, revealing a strong agreement in regions with seasonal ice cover (R=0.65) and permanently ice-free areas (R=0.89).

For data validation, we compared the time-mean SSH of ORAS5 with CPOM (2003-2014) and DTU (1993-2013) during different time periods (Figure 2). It is revealed that ORAS5 closely agrees with the observational data. The highest SSH is located in the

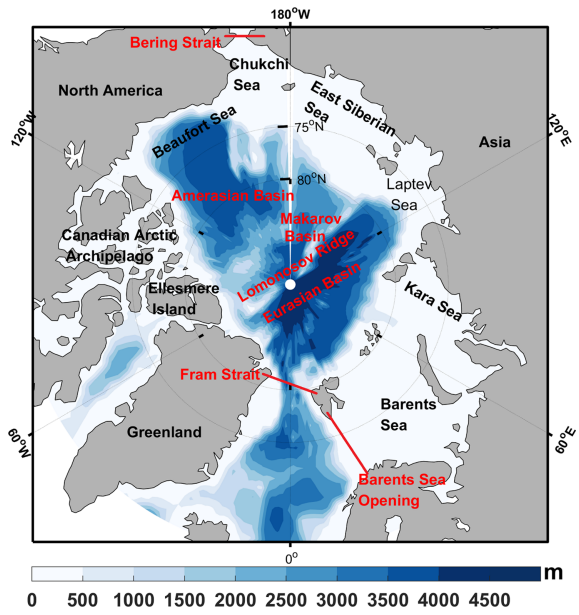


FIGURE 1
Ocean bathymetry of the Arctic Ocean (depth in meters), the studied domain in this paper is enclosed by the CAA, Fram Strait, Barents Sea Opening, and Bering Strait (red lines).

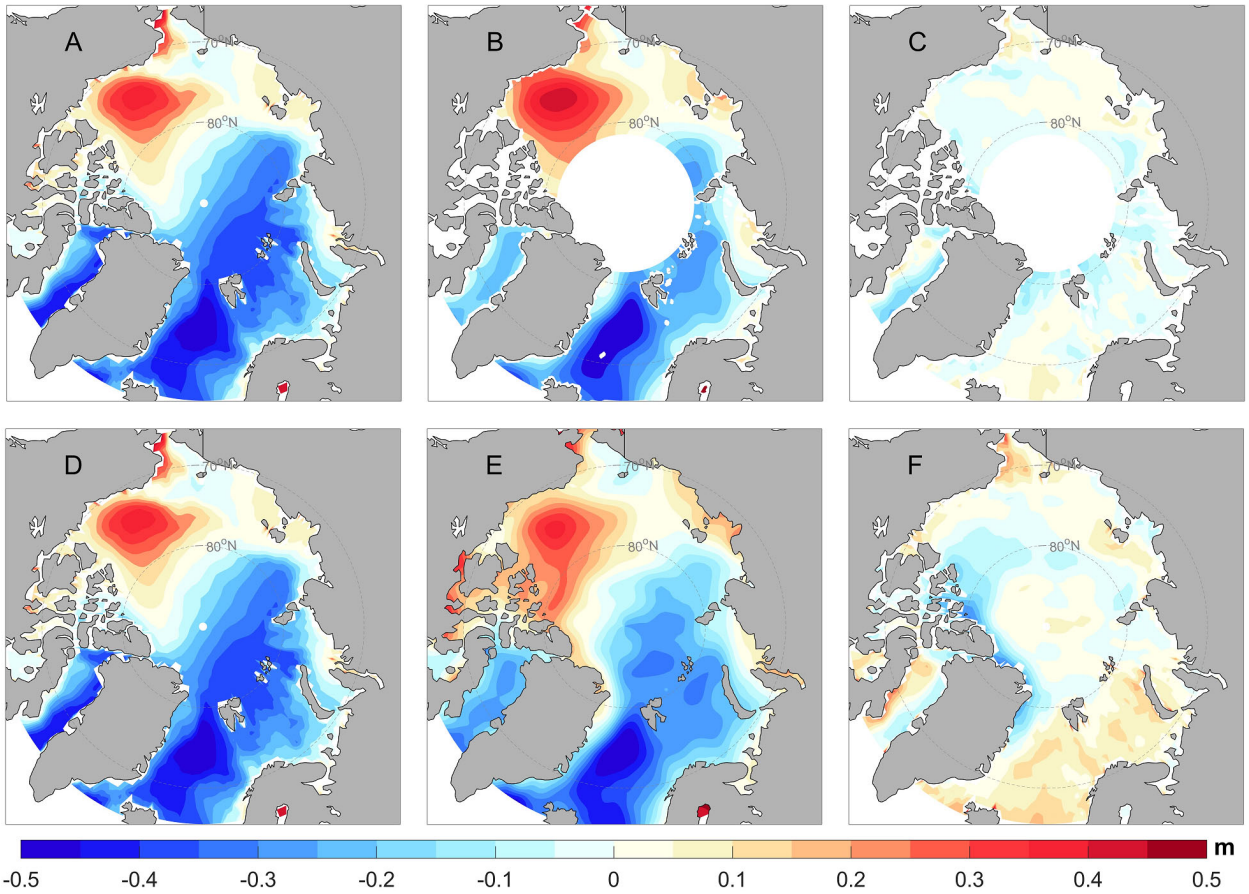


FIGURE 2
Time-mean SSH for the period 2003–2014 **(A, B)** and 1993–2013 **(D, E)**. From left to right are ORAS5 **(A, D)**, CPOM **(B)** and DTU **(E)**. **(C) (A, B)** and **(F) (D, E)** are the residuals between ORAS5 and observations.

Canadian Basin with a center in the Beaufort Sea, which is associated with the anticyclonic Beaufort Gyre. High sea levels are also present along the coast of marginal seas. Low sea levels occur in the Eurasian Basin and the Nordic seas, which is related to the cyclonic circulation of ocean. The significant SSH gradients between the two deep basins correspond to the transpolar drift. However, there are some biases in the ORAS5 data. The difference between ORAS5 and CPOM/DTU data is within ±0.1m, and ORAS5 overestimates the SSH in the Nordic Seas and East Siberian Sea while underestimating it in the Canadian Basin, the Canadian Arctic Archipelago, and north of Greenland (Figures 2C, F).

The time series of average SSH of the Arctic Ocean from ORAS5 data strongly correlates with CPOM altimeter data, with a correlation coefficient of 0.81 at a 0.01 significance level (Figure 3A). The standard deviation of the time series is 0.345cm for ORAS5 and 0.350cm for CPOM, respectively, which are very close. Meanwhile, we used the predictive skill S for point-to-point comparison of SSH time series (Figure 3B). Here, S is defined as $S=1-<(h_0-h_p)^2>/<h_0^2>$ (Qiu, 2002). In this paper, h_0 and h_p are the values of CPOM and ORAS5, respectively, and the angle brackets denote time averaging. A value of S closer to 1 indicates greater precision of the ORAS5 data. The values of S show that ORAS5 effectively reproduces the SSH evolution in most areas of the Arctic Ocean. Overall, ORAS5 accurately reproduces the temporal and spatial variation of sea level observed by satellites in the Arctic Ocean.

4 Sea level variation in the Arctic Ocean

In this paper, the domain of the Arctic Ocean refers to the regions studied by Armitage et al. (2016) and Xiao et al. (2020), which are separated by the CAA, Fram Strait, Barents Sea Opening, and Bering Strait from the Atlantic Ocean and the Pacific Ocean (Figure 1). The spatial pattern of climatological SSH in the Arctic Ocean from 1979-2018 (Figure 4A) is similar to that of 2003-2014 (Figure 2A), with the only notable difference being slightly weaker SSH gradients between the Canadian and Eurasian Basins. This suggests that both the anticyclonic gyre in the Beaufort Sea and the cyclonic circulation in the Nordic Seas during 1979-2018 were weaker compared to the recent two decades.

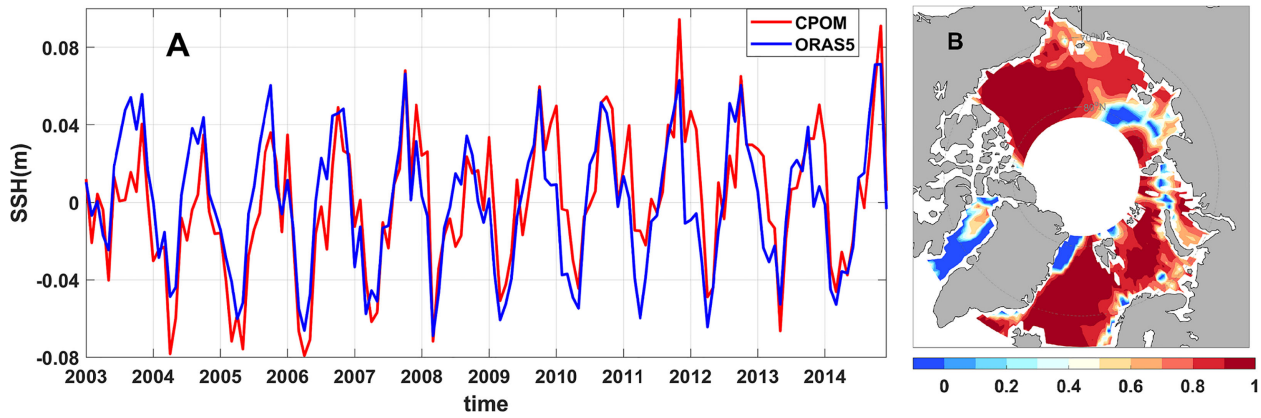


FIGURE 3
(A) Time series of the Arctic average SSH for the period 2003–2014 from ORAS5 (blue curve) and CPOM (red curve). **(B)** The predictive skills of SSH by ORAS5 to CPOM.

4.1 Seasonal SSH Variability in the Arctic Ocean

The standard deviation (STD) of SSH after 12 months high-pass filtering provides a good representation of the amplitude of seasonal variation in sea level (Figure 4B). In the Arctic Ocean, large seasonal amplitudes (exceeding 8 cm) can be found on the continental shelves, especially on the Eurasian side in the Chukchi Sea, East Siberian Sea, and Laptev Sea, while the deep basins have relatively weak seasonal variability of SSH (with amplitude less than 3 cm). The largest amplitude with values up to 13 cm occurs on the coast of East Siberian Sea and Laptev Sea, possibly related to the seasonal cycle of both sea-ice and river runoff (Armitage et al., 2016). Empirical Orthogonal Function (EOF) analysis of the monthly SSH indicates that the most significant mode (EOF1) of sea level variability in the Arctic Ocean is seasonal. EOF1 shows a consistent phase in SSH anomaly across the entire region, with a spatial pattern similar to Figure 4B and a significant period of 12 months in the time series (the figure is not given).

We found that the seasonal cycle of average SSH of the Arctic Ocean is closely related to the seasonal cycles of atmospheric circulation and sea-ice (Figure 5). Specifically, the average SSH of the Arctic Ocean reaches its lowest level in April, while SLP reaches its peak at the same time, one month after the maximum sea ice extent. This low sea level is attributed to salinization during sea ice formation and sea water divergence caused by SLP. The SSH then rises from April until it reaches its peak in September, which is accompanied by sea ice melting and SLP dropping until both of them reach their minimums in August. The rise in sea level during this period is attributed to desalination and convergence strengthening of sea water. There is a strong correlation between SSH and sea ice concentration, with the maximum correlation coefficient of -0.94 when SSH lags sea ice by one month, and a strong correlation between SSH and SLP, with the maximum correlation coefficient of -0.83 when SSH lags SLP by two months. The result reveals that seasonal changes in atmospheric circulation drive changes in ocean circulation and sea ice, which in turn contribute to changes in sea level in the Arctic Ocean.

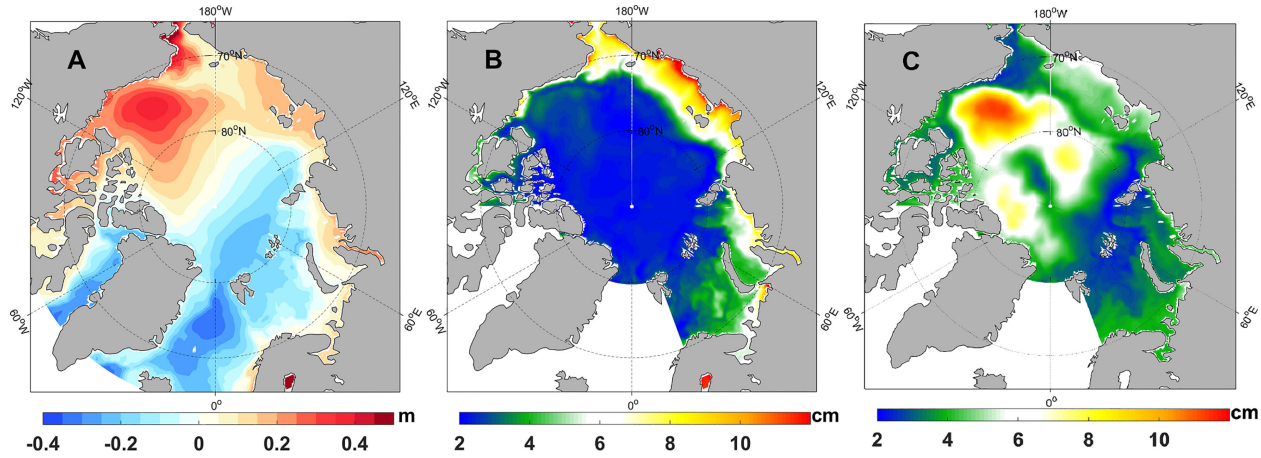


FIGURE 4
(A) Time-mean SSH of 1979-2018. STD of **(B)** monthly mean SSH (with 12 months high-pass filtering) and **(C)** annual mean SSH.

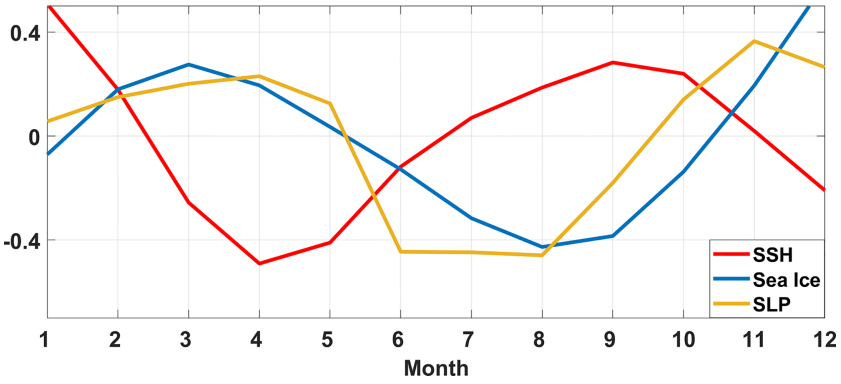


FIGURE 5
Seasonal cycles of average SSH (red curve), sea ice concentration (blue curve), and SLP (yellow curve) of the Arctic Ocean from 1979 to 2018. All data are normalized.

4.2 Interannual to decadal SSH Variability in the Arctic Ocean

Although the SSH in the Arctic Ocean is dominated by seasonal variability, low-frequency variability is more closely related to climate change. In this paper, we investigated the interannual-to-decadal SSH variabilities using ORAS5 data. The STD of annual mean SSH indicates the strength of low-frequency SSH variations in the Arctic Ocean (Figure 4C). The largest STD (about 11.4 cm) is observed in the Beaufort Sea of the Canadian Basin, while the Makarov Basin and area north of Ellesmere Island also show significant values (7-8 cm). The East Siberian Sea has moderately larger values (5-6 cm) in the coastal areas. The most significant inter-annual SSH variability mainly occurs in the deep basins, while the most significant seasonal variability of SSH happens mainly in the continental shelf seas. The largest amplitude of inter-annual SSH variability is almost of the same magnitude as seasonal variability (about 10 cm), as shown in Figures 4B, C.

We conducted an EOF decomposition on the annual mean SSH in the Arctic Ocean for the period 1979-2018, after removing the linear trend. The most principal mode (EOF1) is presented in Figure 6, which explains 39% of the annual mean SSH variance. This mode displays an antiphase sea level oscillation between deep basins and marginal seas. The timeseries of the annual mean SSH of the deep basins (depth > 500 m) and shallow waters (depth< 500 m) well support this antiphase pattern, particularly since the mid-1980s. Moreover, there is an obvious decadal oscillation in the antiphase change between the two areas, with two phase shifts occurring in the end of 1980s and in the mid-2000s (Figure 7). The time series of EOF1 (PC1, Figure 6B) also shows a decadal oscillation with two phase turning points at almost the same time as Figure 7. Additionally, there is a shift of the decadal trend of SSH in PC1 in 1995, which has also been noted by Xiao et al. (2020), based on a high-resolution numerical simulation of the Arctic Ocean. The low-frequency mode of SSH in the Arctic Ocean has only been found in the results of high-resolution numerical

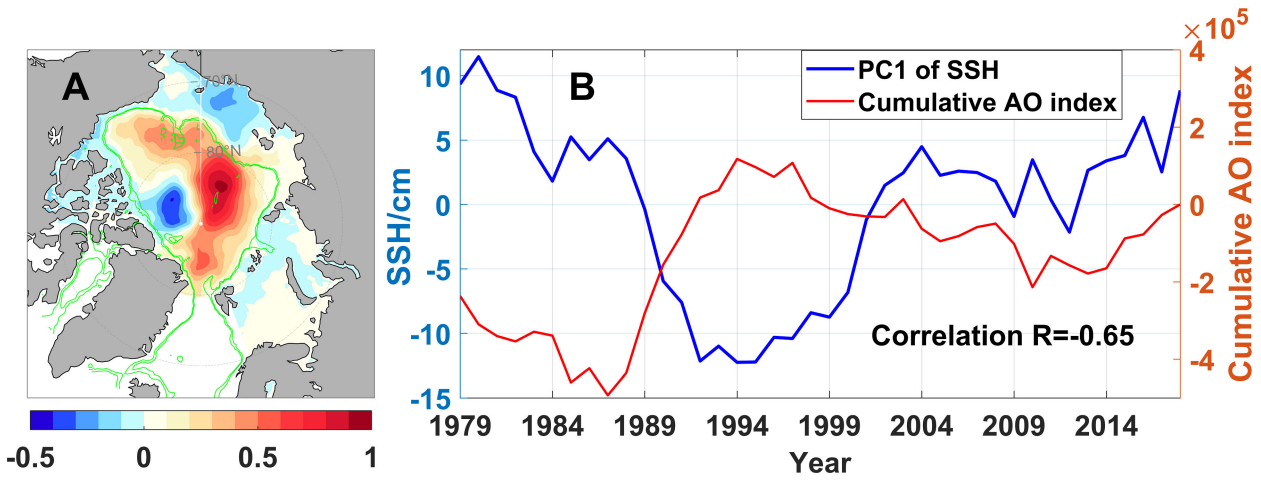


FIGURE 6
(A) EOF1 of the detrended annual-mean SSH. The green lines indicate the 500-m isobaths. **(B)** Time series of PC1 (blue curve) and cumulative AO index (red curve) for the period 1979–2018.

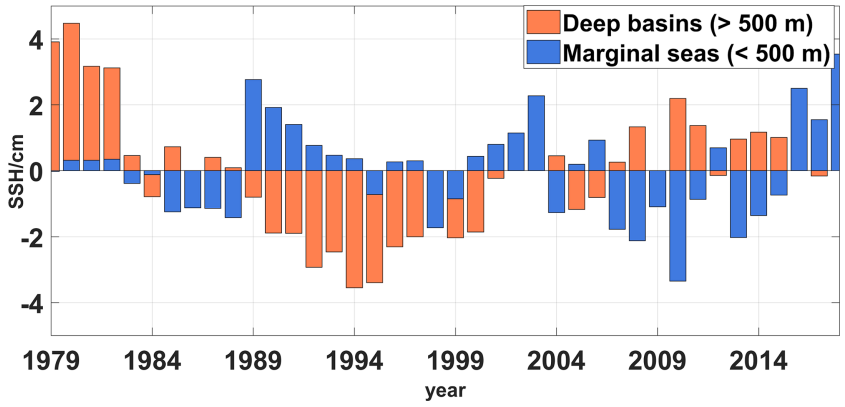


FIGURE 7
Annual-mean SSH of deep basins (> 500 m, orange bar) and marginal seas (< 500 m, blue bar) of the Arctic Ocean.

simulations (e.g., Proshutinsky and Kowalik, 2007; Koldunov et al., 2014; Xiao et al., 2020) due to the limited data length of observation, but the ORAS5 reanalysis data successfully captures this mode, even after assimilating the observed data.

We confirmed the dominant influence of AO, the primary mode of SLP variability in the extra-tropical Northern Hemisphere (Thompson and Wallace, 1998), on the first mode of annual mean SSH in the Arctic Ocean, which has been pointed out by Xiao et al. (2020). The AO-related wind anomaly changes the sea ice drift and cross-shelf Ekman transport, leading to the opposite sea level anomalies between the Arctic continental shelves and deep basins (Volkov and Landerer, 2013; Koldunov et al., 2014; Fukumori et al., 2015; Armitage et al., 2018; Xiao et al., 2020). In this paper, we calculated the correlations of PC1 of SSH with both the annual mean AO index and cumulative AO index and found that PC1 is better correlated with the cumulative AO index, with a correlation coefficient of -0.65 (significant at the 0.01 level, Figure 6B; the correlation of PC1 of SSH to annual mean AO index is -0.29). This proves that the ocean has a long memory in response to external forcing, leading to the effect of AO-related wind forcing on SSH accumulated over time (Xiao et al., 2020; Wang et al., 2021). The result is consistent with the high-resolution numerical simulation of Xiao et al. (2020), who explains the influence of AO on the EOF1 of annual SSH in the Arctic Ocean by wind-forced freshwater release/accumulation. However, the correlation obtained from ORAS5 is weaker than Xiao et al. (2020) (-0.65 Vs. -0.77), which may be due to the assimilation of observed data in ORAS5, leading to more processes included in the dataset compared with pure numerical models. Additionally, the coarser resolution of ORAS5 and spatial coverage of SLP used to calculate AO index may also affect the correlation coefficient.

The second-leading mode (EOF2) of annual mean SSH accounts for 22% of the variance, exhibiting a strong antiphase SSH anomaly between the Eurasian and CAA to Greenland sides of the ocean (Figure 8A). The corresponding PC2 displays significant decadal variability with a period shorter than that of PC1 (Figure 8B). The spatial pattern of EOF2 is similar to DA in the Arctic Ocean (Figure 8C), the second-leading mode of SLP in the region with two antiphase anomalous centers located on the Eurasia continent and CAA to Greenland, respectively (Figure 8C; Wu et al., 2006; Wang et al., 2009). The PC2 of annual mean SSH is well-correlated with the cumulative DA index, with a correlation coefficient of 0.67 at the 0.01 significance level. When DA is in positive phase, the pressure gradient between Eurasia and CAA drives wind anomaly towards the Fram Strait, causing a water mass transport from the Eurasian side to the Canadian side, resulting in SSH rising in the Canadian Basin and north of CAA and Greenland, and SSH descending in the Eurasian Basin and adjacent continental shelf seas. After removing the signals of EOF1 in Figure 6, the time series of residual SSH strongly correlates with the cumulative DA index (Figure 8D), with a pattern quite similar to EOF2 in Figure 8A. Compared with the results based on a high-resolution numerical simulation of Xiao et al. (2020), the dipole pattern of SSH obtained from ORAS5 is much closer to the SLP pattern of DA (Figure 8C) and the correlation between PC2 of SSH and cumulative DA index is higher, as Xiao et al. (2020) obtained a dipole pattern of SSH more focusing on the antiphase between the Canadian Basin and Eurasian Basin with a lower correlation to the cumulative DA index as well (0.56 at the 0.01 significance level). Instead of using cumulative values, we computed the correlation between PC2 of SSH with annual mean DA index. Our findings indicate a much weaker correlation coefficient (0.21 for annual mean DA index), providing further evidence for the long-lasting memory of the ocean to wind forcing.

The leading modes of annual mean SSH in the Arctic Ocean are generally strongly correlated with SLP modes, suggesting that atmospheric forcing is the primary driver of low-frequency sea level variability in this region. Previous studies have shown that anomalous atmospheric circulation associated with AO or DA can lead to changes in Ekman transport by sea surface winds, which can redistribute surface freshwater within the Arctic Ocean and alter water exchange between the Arctic Ocean and the Pacific and Atlantic Oceans (Wang et al., 2018a; Xiao et al., 2020). These changes ultimately cause fluctuations in SSH in the Arctic Ocean.

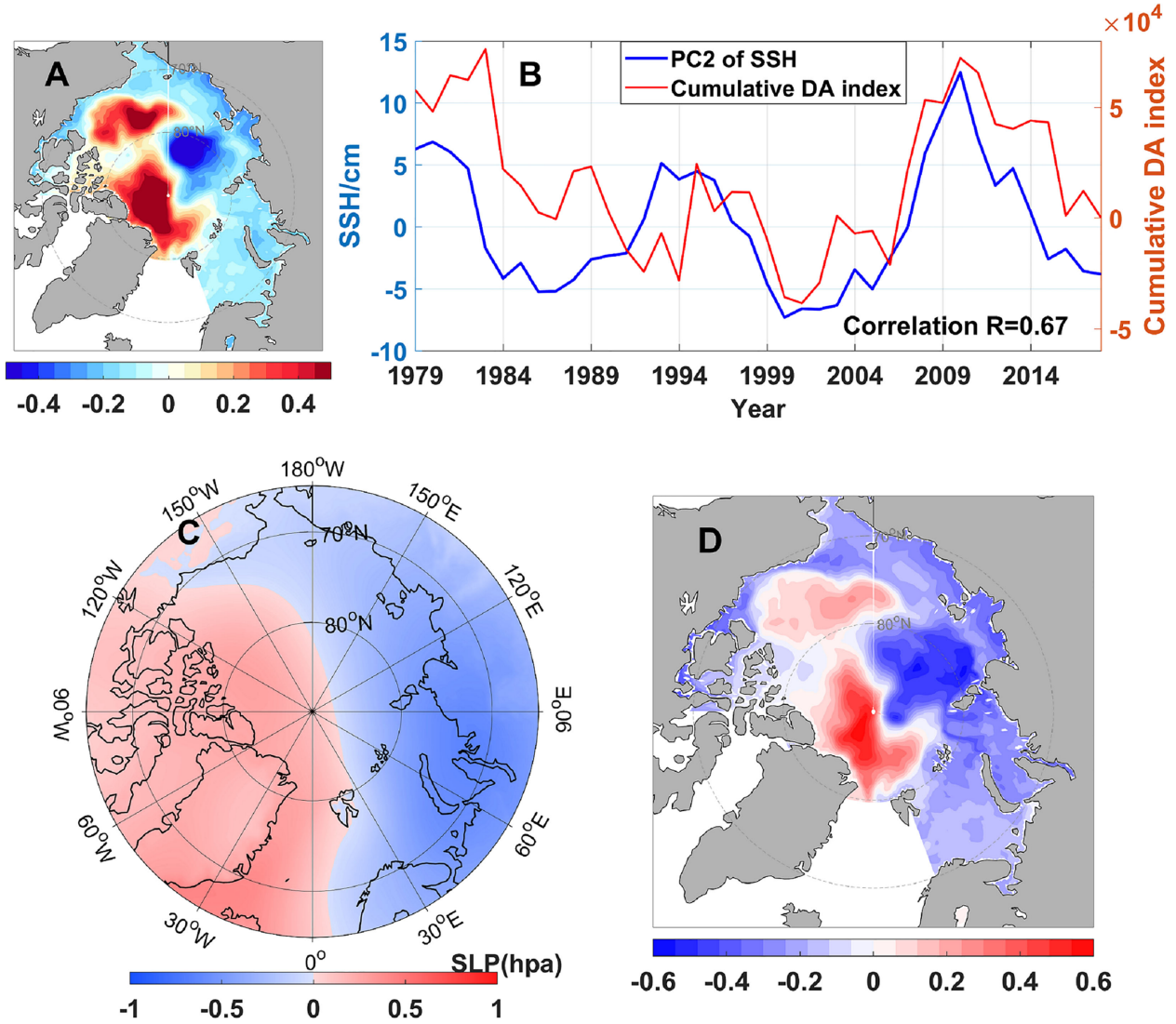


FIGURE 8
(A) EOF2 of the detrended annual-mean SSH in the Arctic Ocean. **(B)** Time series of PC2 (blue curve) and the cumulative DA index (red curve). **(C)** EOF2 of SLP in the Arctic Ocean. **(D)** The correlation between the cumulative DA index and SSH with EOF1 removed for the period 1979-2018.

4.3 Decadal sea level trend in the Arctic Ocean

The radar altimeter observations suggest a significant sea level rise in the Canadian Basin of the Arctic Ocean since 1993, with the highest rate of up to 10-15 mm/yr occurring in the Beaufort Sea (Cheng et al., 2015; Carret et al., 2017). This sea level rise is attributed to liquid freshwater accumulation resulting from wind forcing, particularly when the AO shifts to negative phase in the early 2000s, as reported in previous studies (Giles et al., 2012; Wang et al., 2018a; Wang et al., 2019). Numerical simulations reveal that sea ice decline in the last two decades has significantly contributed to the liquid freshwater accumulation in the Beaufort Sea (Wang et al., 2018a; Xiao et al., 2020).

According to ORAS5 data, positive sea level trends occurred in almost all parts of the Arctic Ocean from 1979 to 2018 (Figure 9A). The Canadian Basin, extending to north of the CAA, experienced the fastest sea level rise, with the center of rise located in the Beaufort Sea, where the SSH rate can reach 9 mm/yr. In contrast, the Eurasian Basin had a weak sea level drop, with the largest drop occurring north of the Laptev Sea, where the rate of SSH is about -1.4 mm/yr. These sea level changes throughout the Arctic Ocean are consistent with AO-related atmospheric forcing. In most time of the 1979-2018 period, the cumulative AO index is negative, indicating that negative AO phase dominates in this period (Figure 6B). Previous studies have found that when AO is in negative phase, anomalous anticyclonic wind over the Arctic lead to more water flowing into the Arctic Ocean from the Pacific and

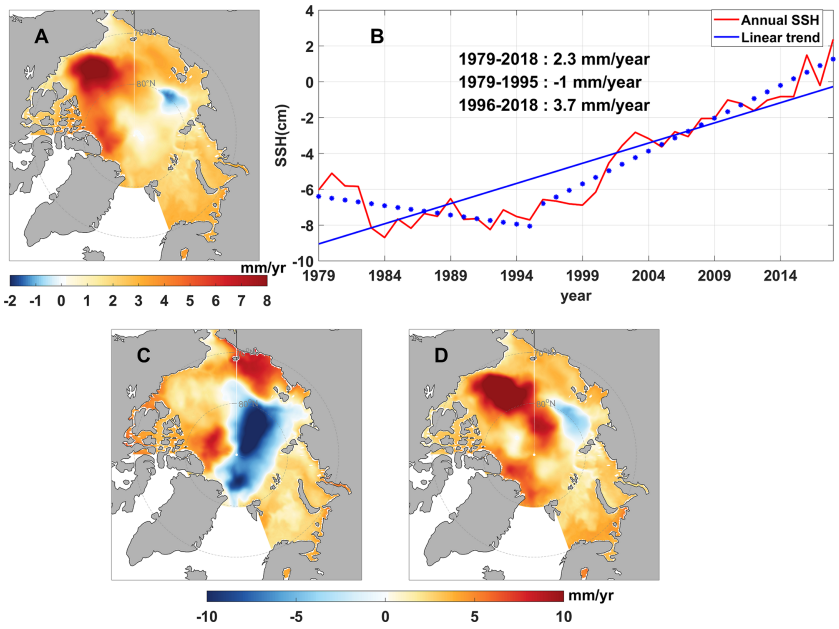


FIGURE 9
(A) Rate of SSH for 1979-2018 (mm/yr.). **(B)** Time series of annual mean (red curve) and linear trend (dashed and solid blue lines) of SSH averaged across the Arctic Ocean for 1979-2018. Rate of SSH for different periods **(C)** 1979-1995 and **(D)** 1996-2018.

Atlantic Oceans (Arthun et al., 2012; Woodgate et al., 2012; Asbjørnsen et al., 2020; Xiao et al., 2020), and this increasing of inflow will make the sea level of the Arctic Ocean rise. The rate of average SSH of the Arctic Ocean during this period is approximately 2.3 mm/yr, about 0.5 mm/yr larger than the rate of global mean sea level in the same period. This means that recent sea level trend in the Arctic Ocean also shows an effect of amplification. Due to the shallow water effect, it is expected that the Arctic sea level will continue to rise at a faster rate than the global mean sea level in the future (Griffies et al., 2014; Chen et al., 2021).

The time series of average SSH of the Arctic Ocean indicates that the sea level began to rise in 1995 after reaching its lowest level with a rate of -1mm/yr since 1979. The rate of sea level rise since 1995 was 3.7 mm/yr, and 1995 is the turning point in the time series of PC1 (Figure 6B). The sea level trends in the Arctic Ocean display different spatial patterns before and after 1995. From 1979 to 1995, there was a significant sea level drop in the Eurasian Basin and Makarov Basin with the maximum rate approaching -12.2 mm/yr, while almost all other areas of the ocean experienced sea level rise, with the largest rise occurring in the East Siberian Sea and north of Ellesmere Island (Figure 9C). From 1996 to 2018, the spatial pattern of sea level trends was similar to that of 1979-2018, but with higher rate in sea level rise. The fastest sea level rise occurred in the Beaufort Gyre, with a rate of 15.9 mm/yr, providing significant evidence of rapid climate changes in the Arctic over the past three decades (Figure 9D). Figure 9B also shows that decadal variability dominated in the Arctic sea level change before the 2000s, whereas the trend of sea level rise became the most important feature afterwards. Similar characteristics have been found in the air temperature, sea ice extent and volume, liquid freshwater content, and other thermodynamic factors in the Arctic in previous studies (Kwok et al., 2009; Rabe et al., 2011; Giles et al., 2012; Stroeve et al., 2012; Laxon et al., 2013; Polyakov et al., 2013; Rabe et al., 2014; Haine et al., 2015; Proshutinsky et al., 2015; Armitage et al., 2016; Wang et al., 2019). These findings highlight the importance of sea level as an indicator of ocean climate in the Arctic region.

5 Conclusions

This study investigates the sea level variations of the Arctic Ocean from 1979 to 2018 using the latest ORAS5 reanalysis data with a spatial resolution of 0.25° on monthly intervals. The results demonstrate that the ORAS5 data effectively reproduces the spatial pattern and temporal evolution of SSH in the Arctic Ocean during the period of 2003-2014 when compared with validated satellite altimeter data.

The Arctic Ocean's most striking feature in sea level variations is its seasonality, with large amplitude occurring along the coast of the Eurasian continent and the largest amplitude of 13 cm located on the coast of East Siberian Sea. EOF analysis reveals that the seasonal SSH variation has no phase difference across the entire Arctic Ocean, with the lowest SSH occurring in April and the highest SSH occurring in September. The seasonal cycle of SSH is consistent with changes in SLP and sea ice, with lags of one or two months due to the slow response of the ocean to external forcings.

Significant inter-annual variability of sea level is observed in the deep basins and some marginal seas of the Arctic Ocean, with the largest amplitude exceeding 10 cm located in the Beaufort Sea,

comparable to the largest amplitude of seasonal variability along the coast of East Siberian Sea. The leading mode of low-frequency SSH variability shows a clear decadal antiphase oscillation of SSH between the deep basins and marginal seas, with a trend turning point in 1995. This mode is linked to the anomalous atmospheric forcing of AO, which alters the sea surface wind and drives anomalous cross-shelf Ekman transport, leading to opposing sea level anomalies between the Arctic shelf seas and deeper basins. Previous studies indicate that the Ekman transport anomaly leads to redistribution of liquid freshwater in the Arctic Ocean, causing regional SSH variations through halosteric changes. The second leading mode of low-frequency SSH variability exhibits antiphase SSH changes between the areas on the Eurasian side and CAA side of the Arctic Ocean on decadal timescales, which can be explained by the trans-basin mass transport caused by DA related surface wind forcing. The antiphase SSH pattern of this mode is not limited to the deep basins but displays opposite signals between the two parts of the Arctic Ocean under the forcing of anomalous atmospheric circulation of DA, which differs slightly from the conclusion of Xiao et al. (2020) based on the results of a high-resolution ocean-sea ice model.

Over the past four decades, sea levels have risen in almost every part of the Arctic Ocean, with a mean rise rate of 2.3 mm/yr between 1979 and 2018, slightly higher than the global average. The fastest sea level rise occurred in the Beaufort Sea, where satellite altimeters observed the most dramatic increase since the 1990s. The spatial pattern of sea level trends changed around 1995, a turning point found in the time series of the leading mode of low-frequency SSH variability. This suggests that decadal variability plays a crucial role in sea level trends for a limited time length. Prior to 1995, the Eurasian Basin experienced a dramatic drop in sea levels, with the largest rate reaching -12.2 mm/yr. However, other areas of the Arctic Ocean experienced sea level rise at varying rates. The spatial pattern of SSH trends since 1995 resembles the whole period of 1979-2018, except that the rates of sea level rise since 1995 are higher. This implies that sea level rise of the recent two decades dominates the sea level trend in the past four decades.

Using ORAS5 data of 1° resolution, we obtained slightly different EOF modes of annual mean SSH and significantly different correlations between the sea level PCs and climate variability indices. Meanwhile, we found differences between our results and those of Xiao et al. (2020), who studied low-frequency SSH changes using a high-resolution sea ice-ocean model in the Arctic Ocean. This suggests that the spatial resolution of data impacts the results. Additionally, the calculated AO and DA index may vary depending on whether winter, summer, or the whole year's data is used, as well as the spatial domain. In this paper, we used SLP data for the whole year and selected the domain north of 64.5° N to calculate the AO and DA index, resulting in the best correlation between the changes of sea level and climate variability indices.

Data availability statement

The original contributions presented in the study are included in the article/supplementary material, further inquiries can be directed to the corresponding author.

Author contributions

YJ conducted the analysis of characteristics of the sea level variation in the Arctic Ocean, while MC performed the associated mechanism analyses. HY and TW assisted with data downloading, preprocessing and figure drawing. JY provided revision suggestions to the manuscript. MC and YJ co-wrote the manuscript. All authors contributed to the article and approved the final version.

Funding

The study is financially supported by the National Natural Science Foundation of China (Nos. 42076233 and 52271273).

Acknowledgments

We are very thankful to the European Centre for Medium-Range Weather Forecasts (ECMWF) for providing the ORAS5 reanalysis data and sea level pressure data of ERA5. The absolute dynamic topography data is provided by the Centre for Polar Observation and Modelling, University College London and the mean dynamic topography data is provided by Technical University of Denmark. Sea ice concentration data are from the National Snow and Ice Data Center. We thank the editor and two reviewers for their useful suggestions.

Conflict of interest

The authors declare that the research was conducted in the absence of any commercial or financial relationships that could be construed as a potential conflict of interest.

Publisher's note

All claims expressed in this article are solely those of the authors and do not necessarily represent those of their affiliated organizations, or those of the publisher, the editors and the reviewers. Any product that may be evaluated in this article, or claim that may be made by its manufacturer, is not guaranteed or endorsed by the publisher.

References

Armitage, T. W. K., Bacon, S., and Kwok, R. (2018). Arctic Sea Level and surface circulation response to the Arctic oscillation. *Geophys. Res. Lett.* 45 (13), 6576–6584. doi: 10.1029/2018gl078386

Armitage, T. W. K., Bacon, S., Ridout, A. L., Petty, A. A., Wolbach, S., and Tsamados, M. (2017). Arctic Ocean surface geostrophic circulation 2003–2014. *Cryosphere* 11 (4), 1767–1780. doi: 10.5194/tc-11-1767-2017

Armitage, T. W. K., Bacon, S., Ridout, A. L., Thomas, S. F., Aksenov, Y., and Wingham, D. J. (2016). Arctic Sea surface height variability and change from satellite radar altimetry and GRACE 2003-2014. *J. Geophys. Res.: Oceans* 121 (6), 4303–4322. doi: 10.1002/2015jc011579

Arthun, M., Eldevik, T., Smedsrud, L. H., Skagseth, O., and Ingvaldsen, R. B. (2012). Quantifying the influence of Atlantic heat on barents Sea ice variability and retreat. *J. Climate* 25 (13), 4736–4743. doi: 10.1175/JCLI-D-11-00466.1

Asbjørnsen, H., Årthun, M., Skagseth, Ø., and Eldevik, T. (2020). Mechanisms underlying recent Arctic atlantification. *Geophys. Res. Lett.* 47 (15), e2020GL088036. doi: 10.1029/2020gl088036

Carret, A., Johannessen, J. A., Andersen, O. B., Ablain, M., Prandi, P., Blazquez, A., et al. (2017). Arctic Sea Level during the satellite altimetry era. *Surveys Geophys.* 38 (1), 251–275. doi: 10.1007/s10712-016-9390-2

Cazenave, A. (2020). Sea Level rise, from global to local. *J. Geol. Soc. India* 96 (1), 3–8. doi: 10.1007/s12594-020-1500-6

Chen, C., Wang, G., Yan, Y., and Luo, F. (2021). Projected sea level rise on the continental shelves of the China seas and the dominance of mass contribution. *Environ. Res. Lett.* 16 (6), 064040. doi: 10.1088/1748-9326/abfdea

Cheng, Y., Andersen, O., and Knudsen, P. (2015). An improved 20-year Arctic ocean altimetric Sea level data record. *Mar. Geodesy* 38 (2), 146–162. doi: 10.1080/01490419.2014.954087

Church, J., Clark, P., Cazenave, A., Gregory, J., and Unnikrishnan, A. J. C. G. (2013). "Climate change 2013: the physical science basis," in *Contribution of working group I to the fifth assessment report of the intergovernmental panel on climate change*. (New York: Cambridge University Press).

Dmitrenko, I. A., Kirillov, S. A., and Tremblay, L. B. (2008). The long-term and interannual variability of summer fresh water storage over the eastern Siberian shelf: implication for climatic change. *J. Geophys. Res.* 113 (C3), C03007. doi: 10.1029/2007jc004304

Fukumori, I., Wang, O., Llovel, W., Fenty, I., and Forget, G. (2015). A near-uniform fluctuation of ocean bottom pressure and sea level across the deep ocean basins of the Arctic ocean and the Nordic seas. *Prog. Oceanogr.* 134, 152–172. doi: 10.1016/j.pocean.2015.01.013

Giles, K. A., Laxon, S. W., Ridout, A. L., Wingham, D. J., and Bacon, S. (2012). Western Arctic Ocean freshwater storage increased by wind-driven spin-up of the Beaufort gyre. *Nat. Geosci.* 5 (3), 194–197. doi: 10.1038/NGEO1379

Griffies, S. M., Yin, J., Durack, P. J., Goddard, P., Bates, S. C., Behrens, E., et al. (2014). An assessment of global and regional sea level for years 1993-2007 in a suite of interannual CORE-II simulations. *Ocean Model.* 78, 35–89. doi: 10.1016/j.ocemod.2014.03.004

Haine, T. W. N., Curry, B., Gerdes, R., Hansen, E., Karcher, M., Lee, C., et al. (2015). Arctic Freshwater export: status, mechanisms, and prospects. *Global Planetary Change* 125, 13–35. doi: 10.1016/j.gloplacha.2014.11.013

Henry, O., Prandi, P., Llovel, W., Cazenave, A., Jevrejeva, S., Stammer, D., et al. (2012). Tide gauge-based sea level variations since 1950 along the Norwegian and Russian coasts of the Arctic ocean: contribution of the steric and mass components. *J. Geophys. Res.: Oceans* 117 (C6), n/a–n/a. doi: 10.1029/2011jc007706

Koldunov, N. V., Serra, N., Koehl, A., Stammer, D., Henry, O., Cazenave, A., et al. (2014). Multimodel simulations of Arctic ocean sea surface height variability in the period 1970-2009. *J. Geophys. Research-Oceans* 119 (12), 8936–8954. doi: 10.1002/2014JC010170

Kwok, R., Cunningham, G. F., Wensnahan, M., Rigor, I., Zwally, H. J., and Yi, D. (2009). Thinning and volume loss of the Arctic ocean sea ice cover: 2003-2008. *J. Geophys. Research-Oceans* 114, C07005. doi: 10.1029/2009JC005312

Laxon, S. W., Giles, K. A., Ridout, A. L., Wingham, D. J., Willatt, R., Cullen, R., et al. (2013). CryoSat-2 estimates of Arctic sea ice thickness and volume. *Geophys. Res. Lett.* 40 (4), 732–737. doi: 10.1002/grl.50193

Legeais, J.-F., Ablain, M., Zawadzki, L., Zuo, H., Johannessen, J. A., Scharffenberg, M. G., et al. (2018). An improved and homogeneous altimeter sea level record from the ESA climate change initiative. *Earth System Sci. Data* 10 (1), 281–301. doi: 10.5194/essd-10-281-2018

Lyu, G. K., Serra, N., Zhou, M., and Stammer, D. (2022). Arctic Sea level variability from high-resolution model simulations and implications for the Arctic observing system. *Ocean Sci.* 18 (1), 51–66. doi: 10.5194/os-18-51-2022

McPhee, M. G., Proshutinsky, A., Morison, J. H., Steele, M., and Alkire, M. B. (2009). Rapid change in freshwater content of the Arctic ocean. *Geophys. Res. Lett.* 36, L10602. doi: 10.1029/2009GL037525

Polyakov, I. V., Beszczynska, A., Carmack, E. C., Dmitrenko, I. A., Fahrbach, E., Frolov, I. E., et al. (2005). One more step toward a warmer Arctic. *Geophys. Res. Lett.* 32 (17), L17605. doi: 10.1029/2005GL023740

Polyakov, I. V., Bhatt, U. S., Walsh, J. E., Abrahamsen, E. P., Pnyushkov, A. V., and Wassmann, P. F. (2013). Recent oceanic changes in the Arctic in the context of long-term observations. *Ecol. Appl.* 23 (8), 1745–1764. doi: 10.1890/11-0902.1

Prandi, P., Ablain, M., Cazenave, A., and Picot, N. (2012). Sea Level variability in the Arctic ocean observed by satellite altimetry. *Ocean Sci. Discuss.* 9, 2375–2401. doi: 10.5194/osd-9-2375-2012

Proshutinsky, A., Ashik, I. M., Dvorkin, E. N., Hakkinen, S., Krishfield, R. A., and Peltier, W. R. (2004). Secular sea level change in the Russian sector of the Arctic ocean. *J. Geophys. Research-Oceans* 109 (C3), C03042. doi: 10.1029/2003JC002007

Proshutinsky, A., Ashik, I., Haekkinen, S., Hunke, E., Krishfield, R., Maltrud, M., et al. (2007). Sea Level variability in the Arctic ocean from AOMIP models. *J. Geophys. Research-Oceans* 112 (C4), C04S08. doi: 10.1029/2006JC003916

Proshutinsky, A., Dukhovskoy, D., Timmermans, M.-L., Krishfield, R., and Bamber, J. L. (2015). Arctic Circulation regimes. *Philos. Trans. R. Soc. A-Mathemat. Phys. Eng. Sci.* 373 (2052), 20140160. doi: 10.1098/rsta.2014.0160

Proshutinsky, A. Y., and Johnson, M. A. (1997). Two circulation regimes of the wind driven Arctic ocean. *J. Geophys. Research-Oceans* 102 (C6), 12493–12514. doi: 10.1029/97JC00738

Proshutinsky, A., and Kowalik, Z. (2007). Preface to special section on Arctic ocean model intercomparison project (AOMIP) studies and results. *J. Geophys. Research-Oceans* 112 (C4), C04S01. doi: 10.1029/2006JC004017

Proshutinsky, A., Krishfield, R., Timmermans, M.-L., Toole, J., Carmack, E., McLaughlin, F., et al. (2009). Beaufort Gyre freshwater reservoir: state and variability from observations. *J. Geophys. Research-Oceans* 114, C00A10. doi: 10.1029/2008JC005104

Proshutinsky, A., Pavlov, V., and Bourke, R. H. (2001). Sea Level rise in the Arctic ocean. *Geophys. Res. Lett.* 28 (11), 2237–2240. doi: 10.1029/2000gl012760

Qiu, B. (2002). Large-Scale variability in the midlatitude subtropical and subpolar north pacific ocean: observations and causes. *J. Phys. Oceanogr.* 32 (1), 353–375. doi: 10.1175/1520-0485(2002)032<0353:LSVITM>2.0.CO;2

Rabe, B., Karcher, M., Schauer, U., Toole, J.M., Krishfield, R.A., Pisarev, S., et al. (2011). An assessment of Arctic Ocean freshwater content changes from the 1990s to the 2006-2008 period. *Deep-sea Research Part I: Oceanographic Research Papers* 58(2), 173–185. doi: 10.1016/j.dsr.2010.12.002

Rabe, B., Karcher, M., Kauker, F., Schauer, U., Toole, J. M., Krishfield, R. A., et al. (2014). Arctic Ocean basin liquid freshwater storage trend 1992-2012. *Geophys. Res. Lett.* 41 (3), 961–968. doi: 10.1002/2013gl058121

Regan, H. C., Lique, C., and Armitage, T. W. K. (2019). The Beaufort gyre extent, shape, and location between 2003 and 2014 from satellite observations. *J. Geophys. Research-Oceans* 124 (2), 844–862. doi: 10.1029/2018JC014379

Richter, K., Nilsen, J. E. O., and Drange, H. (2012). Contributions to sea level variability along the Norwegian coast for 1960-2010. *J. Geophys. Research-Oceans* 117, C05038. doi: 10.1029/2011JC007826

Rignot, E., Velicogna, I., van den Broeke, M. R., Monaghan, A., and Lenaerts, J. (2011). Acceleration of the contribution of the Greenland and Antarctic ice sheets to sea level rise. *Geophys. Res. Lett.* 38, L05503. doi: 10.1029/2011GL046583

Serreze, M. C., Barrett, A. P., Stroeve, J. C., Kindig, D. N., and Holland, M. M. (2009). The emergence of surface-based Arctic amplification. *Cryosphere* 3 (1), 11–19. doi: 10.5194/tc-3-11-2009

Serreze, M. C., and Barry, R. G. (2011). Processes and impacts of Arctic amplification: a research synthesis. *Global Planetary Change* 77 (1-2), 85–96. doi: 10.1016/j.gloplacha.2011.03.004

Shu, Q., Wang, Q., Arthun, M., Wang, S., Song, Z., Zhang, M., et al. (2022). Arctic Ocean amplification in a warming climate in CMIP6 models. *Sci. Adv.* 8 (30), eabn9755. doi: 10.1126/sciadv.abn9755

Stammer, D., Cazenave, A., Ponte, R. M., and Tamisiea, M. E. (2013). Causes for contemporary regional Sea level changes. *Ann. Rev. Mar. Sci.* 5 (1), 21–46. doi: 10.1146/annurev-marine-121211-172406

Stroeve, J. C., Kattsov, V., Barrett, A., Serreze, M., Pavlova, T., Holland, M., et al. (2012). Trends in Arctic sea ice extent from CMIP5, CMIP3 and observations. *Geophys. Res. Lett.* 39, L16502. doi: 10.1029/2012GL052676

Thompson, D. W. J., and Wallace, J. M. (1998). The Arctic oscillation signature in the wintertime geopotential height and temperature fields. *Geophys. Res. Lett.* 25 (9), 1297–1300. doi: 10.1029/98GL00950

Vihma, T. (2014). Effects of Arctic Sea ice decline on weather and climate: a review. *Surveys Geophys.* 35 (5), 1175–1214. doi: 10.1007/s10712-014-9284-0

Volkov, D. L., and Landerer, F. W. (2013). Nonseasonal fluctuations of the Arctic ocean mass observed by the GRACE satellites. *J. Geophys. Research-Oceans* 118 (12), 6451–6460. doi: 10.1002/2013JC009341

Wang, Q., Danilov, S., Mu, L., Sidorenko, D., and Wekerle, C. (2021). Lasting impact of winds on Arctic sea ice through the ocean's memory. *Cryosphere* 15 (10), 4703–4725. doi: 10.5194/tc-15-4703-2021

Wang, Q., Wekerle, C., Danilov, S., Koldunov, N., Sidorenko, D., Sein, D., et al. (2018a). Arctic Sea Ice decline significantly contributed to the unprecedented liquid freshwater accumulation in the Beaufort gyre of the Arctic ocean. *Geophys. Res. Lett.* 45 (10), 4956–4964. doi: 10.1029/2018gl077901

Wang, Q., Wekerle, C., Danilov, S., Sidorenko, D., Koldunov, N., Sein, D., et al. (2019). Recent Sea ice decline did not significantly increase the total liquid freshwater content of the Arctic ocean. *J. Climate* 32 (1), 15–32. doi: 10.1175/jcli-d-18-0237.1

Wang, Q., Wekerle, C., Danilov, S., Wang, X., and Jung, T. (2018b). A 4.5 km resolution Arctic ocean simulation with the global multi-resolution model FESOM 1.4. *Geoscientific Model. Dev.* 11 (4), 1229–1255. doi: 10.5194/gmd-11-1229-2018

Wang, J., Zhang, J., Watanabe, E., Ikeda, M., Mizobata, K., Walsh, J. E., et al. (2009). Is the dipole anomaly a major driver to record lows in Arctic summer sea ice extent? *Geophys. Res. Lett.* 36 (5). doi: 10.1029/2008gl036706

Woodgate, R. A., Weingartner, T. J., and Lindsay, R. (2012). Observed increases in Bering strait oceanic fluxes from the pacific to the Arctic from 2001 to 2011 and their impacts on the Arctic ocean water column. *Geophys. Res. Lett.* 39. doi: 10.1029/2012GL054092

Wu, B. Y., Wang, J., and Walsh, J. E. (2006). Dipole anomaly in the winter Arctic atmosphere and its association with sea ice motion. *J. Climate* 19 (2), 210–225. doi: 10.1175/JCLI3619.1

Wunsch, C., Ponte, R. M., and Heimbach, P. (2007). Decadal trends in Sea level patterns: 1993–2004. *J. Climate* 20 (24), 5889–5911. doi: 10.1175/2007jcli1840.1

Xiao, K., Chen, M., Wang, Q., Wang, X., and Zhang, W. (2020). Low-frequency sea level variability and impact of recent sea ice decline on the sea level trend in the Arctic ocean from a high-resolution simulation. *Ocean Dynam.* 70 (6), 787–802. doi: 10.1007/s10236-020-01373-5

frontiers | Frontiers in Marine Science

TYPE Original Research
PUBLISHED 29 February 2024
DOI 10.3389/fmars.2024.1250815

Check for updates

OPEN ACCESS

EDITED BY
Michael Hartnett,
University of Galway, Ireland

REVIEWED BY
Lucy Rhiannon Wyatt,
The University of Sheffield, United Kingdom
Lei Ren,
Sun Yat-Sen University, China

*CORRESPONDENCE
Lohitzune Solabarrieta
lsolabarrieta@azti.es

RECEIVED 30 June 2023
ACCEPTED 23 January 2024
PUBLISHED 29 February 2024

CITATION
Solabarrieta L, Fernandes M, Ruiz I, Ferrer M, Liria P, de Santiago I, Sánchez J, Aranda JA and Rubio A (2024) Waves from compact SeaSonde® High Frequency radars in the southeastern Bay of Biscay: measurement performance under different noise and wind conditions.
Front. Mar. Sci. 11:1250815.
doi: 10.3389/fmars.2024.1250815

COPYRIGHT
© 2024 Solabarrieta, Fernandes, Ruiz, Ferrer, Liria, de Santiago, Sánchez, Aranda and Rubio. This is an open-access article distributed under the terms of the Creative Commons Attribution License (CC BY). The use, distribution or reproduction in other forums is permitted, provided the original author(s) and the copyright owner(s) are credited and that the original publication in this journal is cited, in accordance with accepted academic practice. No use, distribution or reproduction is permitted which does not comply with these terms.

Waves from compact SeaSonde® High Frequency radars in the southeastern Bay of Biscay: measurement performance under different noise and wind conditions

Lohitzune Solabarrieta[1]*, Maria Fernandes[2], Irene Ruiz[1], Macu Ferrer[2], Pedro Liria[1], Iñaki de Santiago[1], Jorge Sánchez[2], Jose Antonio Aranda[3] and Anna Rubio[1]

[1]AZTI, Marine Research, Basque Research and Technology Alliance (BRTA), Pasaia, Gipuzkoa, Spain, [2]Department of Oceanography, Qualitas Instruments S.A., Madrid, Spain, [3]Dirección de Atención de Emergencias y Meteorología, Eusko Jaurlaritza, Basque Government, Vitoria-Gasteiz, Spain

Global concern on extreme events is increasing the need for real time monitoring of the wave fields in coastal areas. High Frequency (HF) radars, a remote sensing technology widely applied to measure near real time surface coastal currents with demonstrated accuracy, can also play a major role in the operational monitoring of waves height, period and direction. However, the ability of HF radar to measure waves can be jeopardized by specific ocean-meteorological and environmental conditions. Thus, a case-to-case analysis and parameterization is necessary to ensure the best data in each study area. In the southeastern (SE) Bay of Biscay, the EuskOOS HF radar network, composed by two compact HF radar stations provides hourly surface waves data in near real time. In this work, we analyze the effects of wind and noise levels on the radar skills for wave measurement, compared with existing *in-situ* data obtained by an offshore buoy. Then, the HF radar wave measurements for 2022 are analyzed with special focus on the most energetic observed wave events. The analysis performed versus *in-situ* data shows that both stations present reliable and accurate data for waves over 1.5 m, in agreement to what can be expected for a 4.46 MHz radar. The highest correlations are observed for waves > 4 m significant wave height, which demonstrates the capabilities for monitoring highly energetic events. Interference and noise detected on very precise time slots significantly reduced the availability and reliability of the measurements. Also, local winds blowing from land direction were found to affect the agreement between radar and *in-situ* measurements. Recommendations extracted from the analysis are provided, with the aim that they can be extended to other HF networks for more accurate wave monitoring.

KEYWORDS

waves, High Frequency radars, noise, environmental factors, Bay of Biscay, validation, coastal processes

1 Introduction

Global concern on extreme natural events is increasing, particularly for coastal areas that are more susceptible to these phenomena. Extreme natural events include, but are not limited to: heatwaves, heavy precipitation, intense storms and winds and extreme oceanic waves. As they become more frequent, severe, and long-lasting, coastal communities are likely to be more vulnerable. Extreme events interact with the diverse coastal ocean processes at different temporal and spatial scales threating morphological dynamics and ultimately affecting human socio-economics activities in coastal areas. In the context of the Blue Economy development, an adequate wave monitoring for real time assessment of coastal risk and historical data for analysis of extreme event regime has become crucial.

Traditionally, wave measurements have primarily relied on visual observations conducted by personnel onboard vessels and *in-situ* mooring instruments, with the associate scarceness of spatial measurements, and elevated installation and maintenance costs. In recent decades, the coverage of operational (automated and in real time) wave measurements has increased along the coasts, thanks to the growing number of coastal *in-situ* observatories and, at open sea, thanks to consolidated wave satellite data products (e.g. Copernicus Marine Services Global Ocean L 3 Significant Wave Height along-track product: https://doi.org/10.48670/moi-00179). Satellite data products exhibit decreased effectiveness as they approach near the coastline areas, where High Frequency (HF) radars can complete the gaps of satellite products. Wave data from global and local models have also increased in the past decades (e.g. the Copernicus Marine Services Global Ocean Waves Analysis and Forecast, based on the operational global ocean analysis and forecast system of Météo-France, https://doi.org/10.48670/moi-00017) and they have been improved with the assimilation of the existing *in-situ* and remote data.

Considerable efforts have been directed towards establishing an operational wave monitoring system in the southeastern Bay of Biscay (SE BoB) combining *in-situ* measurements and model data. Since 2007, within the framework of EuskOOS operational oceanography system (doi.org/10.57762/T4WH-DQ48), several buoys have been deployed across the SE BoB, seeking a better understanding of the wave dynamics from a more sustained and cost-effective perspective (Solabarrieta et al., 2022). *In-situ* measurements by buoys underpin operational early warning systems from wave impact in the area (Gaztelumendi et al., 2018) and enable to assess the performance of coastal wave models (Ferrer et al., 2010). Nonetheless, the spatial resolution achievable through *in-situ* systems is constrained by technical and economic limitations. In 2009, a coastal-based HF radar was installed to complete the *in-situ* observations and provides since then near-real-time surface currents fields. HF radars can be separated mainly in two types, based on the method they use to retrieve and interpret the echoes from the sea: beam forming (BF) and Direction Finding (DF). BF is used by phased array radars while DF is mainly used by compact antennas. The EuskOOS SeaSonde® compact HF radar (EuskOOS HF radar from now on) network has already been used to study surface coastal transport processes in the area in combination with multisource data (Rubio et al., 2011; Rubio et al., 2013; Solabarrieta et al., 2014; Solabarrieta et al., 2015; Solabarrieta et al., 2016; Manso-Narvarte et al., 2018; Rubio et al., 2018; Rubio et al., 2020; Manso-Narvarte et al., 2021). Besides measuring sea surface water velocity [Crombie (1955), Barrick et al., 1977, Paduan and Rosenfeld (1996) and Paduan and Graber (1997)], the HF radar can also monitor waves (Lipa, 1978; Lipa and Barrick, 1982; Lipa and Nyden, 2005; Gurgel et al., 2006; Wyatt, 2011; Wyatt, 2021). Although wave retrieval application is less common than currents retrieval, especially in real time, and this topic it is still being developed (Lopez et al., 2016), several studies have analyzed and validated waves information from compact (Lorente et al., 2018; Orasi et al., 2018; Lorente et al., 2019; Saviano et al., 2019; Basañez et al., 2020) and phased array (Wyatt and Green, 2009; Lopez and Conley, 2019; Mundaca-Moraga et al., 2021) HF radars in the last few years.

Wave information can be retrieved from the inversion of the second order component of the Doppler spectrum as defined in the literature (Barrick 1986; Gurgel et al., 1999; Lipa and Nyden, 2005). The relation between the ocean wave directional spectrum and the received HF radar Doppler spectrum, must be inverted to obtain wave parameters (Barrick, 1977; Green and Wyatt, 2006; Gurgel et al., 2006). Two main methods are currently used for waves data extraction: full integral inversion (used by phased array HF radars, which use Beam Forming) and ocean wave spectrum model fitting (mainly used by compact HF radars). Both phased array and compact HF radar systems can provide wave information based on the inversion of the second order component of the Doppler spectrum. However, the compact station HF radar systems (the ones analyzed in this study) also require assumptions about spatial homogeneity of the wave field and no depth effects along the rings centered in the stations during the ocean wave spectrum model fitting (Lipa and Barrick, 1986; Lipa and Nyden, 2005; Lipa and Nyden, 2005; Wyatt, 2021). Wave information from compact HF radars incorporates therefore the area of the analyzed ring around the station.

Environmental factors can affect currents data quality and acquisition from HF radars (Kohut and Glenn, 2003; Yang et al., 2018; Horstmann et al., 2019; Mantovani et al., 2020). HF radar wave measurements use a much lower signal level retrieved from the second order component of the Doppler spectrum than currents (retrieved from the first order component) and they are also affected by environmental conditions (Wyatt et al., 2010; Wyatt and Green, 2023). Indeed, wave retrieval methodology is susceptible to electromagnetic noise of environmental or human origin and to ocean-meteorological conditions to a greater extent than the measurement of currents. The ability of HF radar technology in capturing wave parameters with sufficient quality is highly dependent on ocean-meteorological and environmental conditions (e.g. bathymetry, coastline, radio interference, ionospheric noise, direction and intensity of winds and currents, direction, period and height of waves, simultaneous presence of bimodal waves and wind, etc…) present always in the measurement area of the HF radar. While the ability to measure bimodal seas using phased array radars has been demonstrated (e.g. Wyatt and Green, 2022), the dependency of ocean-meteorological conditions is even higher for compact HF

radar stations, due to the assumption of the spatial homogeneity of the wave characteristics along each range ring centred on the HF radar stations. Consequently, much more comprehensive analysis, configuration adjustments, parameterization, and validation procedures remain imperative to enhance understanding and optimization of the compact HF radar capabilities in providing operational wave measurements. To assess the ability of a specific compact HF radar to measure waves, it is therefore necessary to characterize the study area based on these conditions.

Although the global examples of the use of HF radar to collect operational information on ocean waves are more and more numerous, the limitations exposed in the previous paragraphs explain that compared to surface currents, wave information from HF radars is usually much less common. In fact, the European HFR Node is processing and sharing currents data from 280 HF radar stations (both compact and phased array HF radars) all around the world (https://www.hfrnode.eu/map/) but there is no operational wave dataflow from these stations.

The EuskOOS HF radar network, featuring 2 compact HF radar stations located in the SE BoB, stands as a testament to the underutilization of wave information owing to these challenges. The work presented in this paper is the first attempt to study the EuskOOS HF radar historical wave measurements compared with existing *in-situ* data in the SE BoB. The capabilities of compact HF radar networks to exploit operational wave data have been analyzed, taking advantage of the large existing worldwide HF radar network (https://www.hfrnode.eu/map/) that could be used for real-time wave data retrieval.

The objectives of this study for compact HF radars encompass the following aims: (i) conducting a comprehensive analysis and evaluation of wave measurements obtained from the EuskOOS HF radar network under different ocean-meteorological conditions. (ii) identifying the pertinent variables that should be taken into account to assess periods of optimal functionality within any compact HF radar network. (iii) identifying the potential ocean-meteorological conditions during which the wave data derived from the EuskOOS HF radar can offer valuable insights for operational and historical analysis. (iv) assessing the capabilities of the EuskOOS HF radar for monitoring intense (extreme) events.

2 Study area

The Bay of Biscay is located in the Northeast of the Atlantic Ocean, between Brest (France) and Cape Finisterre (Spain) (Lavín et al., 2006) (Figure 1). The wave climate of the Bay of Biscay is tied to its geographic position on the Northeast Atlantic, and it is modulated by its topographic and bathymetric characteristics (Gonzalez et al., 2004; Borja et al., 2019). Throughout the year, the primary swell direction is from the NW, driven by the low-pressure systems of the North Atlantic (typical winter wave field distribution is represented by the WAM model on March 23, 2023, in Figure 1). Seasonal variability characterizes the wave climate, with relatively mild conditions during summer owing to the extension of the Azorean anticyclone which buffers the intensity of storms and extremely energetic conditions during winter (Gonzalez et al., 2004). In fact, recent studies highlight the significant increase of the winter-mean wave height and variability over the last seven decades (Castelle et al., 2018). This is demonstrated by the concatenation of extreme events during the past years such as the Klaus storm (January 2009), which produced significant wave height (hereinafter Hs) of 13 m and peak period (hereinafter Tp) of 15 s at Bilbao-Vizcaya buoy (Lavaud et al., 2020), and the Xynthia storm (2010), which generated storm surges up to 1.5 m or the highly energetic 2013/2014 winter, which recorded the highest winter average wave height since 1948 (Masselink et al., 2016). In the last few years, events with these characteristics have generated wave overtopping of coastal structures in the study area with damages and risk to structures and humans. Traditional *in-situ* wave measurements are often damaged or they failure connectivity during such important moments. High Frequency radars located in the study area can help on the real time characterization of the waves without data disruption especially during extreme events. The historical measurements can also help on the characterization and prediction of the increasing frequency and severity of these extreme events.

3 Data and methods

3.1 Waves from the EuskOOS compact HF radar

The EuskOOS HF radar network is a Seasonde® compact CODAR system of high frequency radars, composed of two radio stations (Matxitxako and Higer) which operate at a central frequency of 4.46MHz, with an operational bandwidth of 30 kHz. In this study, we use wave and wind data from each of the stations independently (Table 1; Figure 1) in the period 2020-2022. HF radar radial data cover a spatial range of up to approximately 180 km from the coastline and provides information on surface currents, Hs, Tp and wave direction (hereinafter Wdir). The network is equipped with CODAR's Radial Suite Release 8 update 5 software for radial and wave data processing. As a component of JERICO-RI (https://www.jerico-ri.eu/) the EuskOOS HF radar operates in accordance with the best practices, standards, and recommendations outlined in the JERICO-S3 project (see Solabarrieta et al., 2016; Mantovani et al., 2020 and Rubio et al., 2018, for details). They are shared as part of Copernicus Global Ocean- *in-situ* Near real- and delayed-time surface ocean currents products (https://doi.org/10.48670/moi-00041 & https://doi.org/10.17882/86236). The network has provided surface current hourly data (with 3 hours rolling average) since 2009, with some interruptions mostly due to maintenance stops or malfunctioning related to severe atmospheric conditions. The performance of this network for ocean currents measurements and its potential for the study of ocean processes and transport patterns have already been demonstrated by previous works (e.g., Rubio et al., 2011; Solabarrieta et al., 2014; Solabarrieta et al., 2015; Solabarrieta et al., 2016; Manso-Narvarte et al., 2018; Rubio et al., 2018; Rubio et al., 2019; Manso-Narvarte et al., 2020; Rubio et al., 2020; Manso-Narvarte et al., 2021; Ruiz et al., 2022). However, wave information has so far remained unexploited.

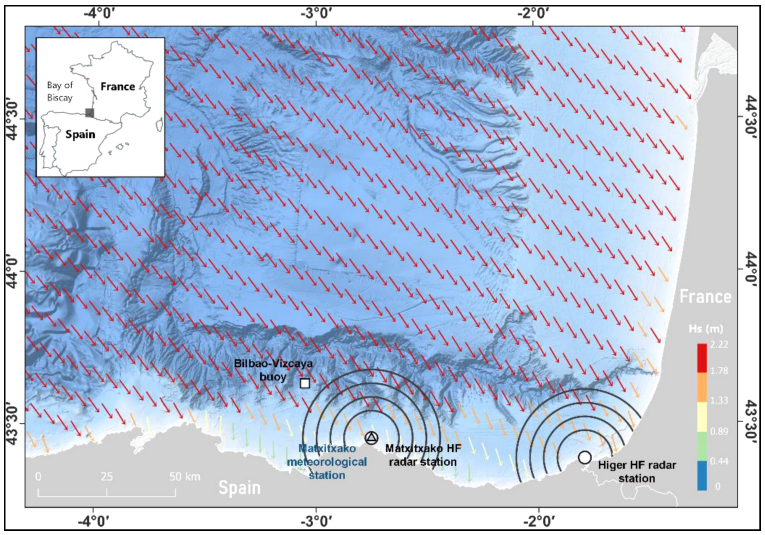


FIGURE 1
Location of Matxitxako and Higer HF radar stations (white filled dots), Bilbao-Vizcaya buoy (white filled square, and Euskalmet wind station (blue triangle). Black inner circles represent the center of range cells (rings) RC2-RC5 for wave measurements by HF radar stations. Colored arrows over the water area represent the significant wave height (Hs) from WAM wave model on March 23, 2023 (representative of typical winter wave field in the study area).

The EuskOOS compact HF radar stations, produce short time CrossSpectra files (CSS) every 10 minutes. CSS measurements are site-centred and include the information from ~5 km spaced circular range cells (RC). These files are processed using the Seasonde® Radial Suite R8u5 proprietary software, applying Pierson-Moskowitz model (Lipa and Nyden, 2005) to the second order spectrum of the spatially averaged wave parameters for a given range of RCs. RCs used in this study were located between 10 and 25 km (RC2-RC5) as indicated in Figure 1. SeaSonde HF radar wave data are typically stored in monthly WVLM text files from each radial station. WVLM files are filtered using all RCs and then averaged over time and range, producing hourly wave parameters directly from the proprietary software. Those files also include quality controlled hourly wave parameters and relevant QC metrics, such as Spectra Counts, Doppler Bins and Vector Flags, specifically used to discard or include data in the output quality-controlled wave files. Only values that passed all the imposed QC metric values by the software are available in the final WVLM text files from each radial station. These values have been considered as hourly wave parameters for this study. For further information on the waves retrieval files, the reader is referred to the CODAR support documentation manual in www.support.codar.com, in Radial Suite 8 wave file format section (http://support.codar.com/Technicians_Information_Page_for_SeaSondes/Manuals_Documentation_Release_8/File_Formats/File_Wave.pdf) (accessed November 21, 2023).

At operational frequencies ranging from 3 to 10 MHz, HF radars can measure longer waves with periods typically ranging from 5 to 20 seconds and wavelengths from 50 to 300 meters. These lower operating frequencies enable extended range coverage but are not able to measure low Hs waves. Due to this intrinsic limitation, for HF radar operating at 4.46 MHz, when the Hs is below 1.5 m, the second-order spectrum, which has lower energy than the first-order one, approaches the noise floor, and consequently, it is easily contaminated (Lipa and Nyden, 2005). As a result, sea states with Hs below 1.5 m from EuskOOS HF radar cannot efficiently reflect the radar transmitted electromagnetic signal and cannot properly be retrieved from the backscattered echo (Wyatt and Green, 2009; Wyatt, 2011; Lopez et al., 2016). Maximum Hs retrievable with 4.46MHz radars is 20m, which is out of the range of expected Hs in the study area.

TABLE 1 Measuring system locations, network and data periods used in this study.

Measuring system	Location	Network	Data availability for this work
Matxitxako HF radar station	02°45.2'W, 43° 27.3'N	EuskOOS	2020-2022
Higer HF radar station	01° 47.7'W, 43° 23.5'N	EuskOOS	2020-2022
Bilbao-Vizcaya buoy	03° 2.81'W, 43° 38.70'N	Puertos del Estado	2021-2022
Euskalmet weather station	02° 45.816' W, 43 26.25'N	EuskOOS	2021-2022

3.2 Waves from Bilbao-Vizcaya offshore buoy

Bilbao-Vizcaya offshore buoy, integrated into the measuring network of Puertos del Estado (http://portus.puertos.es), was deployed in 1990 in the coastal waters of the SE BoB (Table 1; Figure 1). It is a Seawatch directional buoy, with a diameter of 2.8 m and anchored at a 600 m depth. It conducts measurements for 20 minutes each hour and provides hourly near real time wave parameters (Hs, mean and peak wave period and direction), extracted from directional spectrum [E(f, θ)], as follows:

- Directional spectrum $E(f,\theta) = S(f)D(\theta,f)$
  Where, $D(\theta,f) = \frac{1}{2\pi} + \frac{1}{\pi}\sum_{n=1}^{M} a_n\ (f)\cos n\theta\ + b_n\ (f)\sin n\theta$, and $M=2$ in case of a Pitch Roll buoy
- Significant Wave height: $Hs = 4m_0^{\frac{1}{2}}$, $m_k = \int_{f=0}^{\infty} f^k S(F)df$
- Mean wave period: $Tm = m_0/m_1$
- Peak period: $T_p = 1/f_p$, $S(f_p) = max_f S(f)$
- Mean wave direction: $\theta_1(f) = \text{atan2}(b_1(f), a_1(f))$

This buoy was selected for validation considering the location of the HF radar stations (northwest from the two HF radar stations) and its alignment with the prevailing wave direction within the study area.

3.3 Wind from Matxitxako coastal meteorological station

Wind-fields were collected from Matxitxako meteorological station (Table 1; Figure 1). This station is located at 433 m high, and it is part of the hydro-meteorological network of the Basque Country, which consists of more than 120 stations connected in real-time. This station was selected after checking that direction from observed wind-fields showed the best correlation to HF radar wind direction measurements (extracted following Lipa and Nyden, 2005), when compared to simulated winds provided by available meteorological models (e.g. the model from the Meteorological Agency of Galicia close to Bilbao-Vizcaya buoy location).

3.4 Data analysis

Ocean-meteorological and environmental data collected during 2020, 2021 and 2022 underwent analysis and classification to characterize the waves in the study area. 2022 was used as target year for statistical analysis since it presented the highest data availability from the HF radar and the offshore buoy. The following data and parameters were used as foundational background information to assess and optimize the HF radar data processing configuration:

On one hand, the information on the coastline and bathymetry in the measurements from HF radar: (i) Spatial coordinates of HF radar measurements, (ii) HF radar operating frequency and (iii) Antenna pattern used.

On the other hand, environmental and ocean-meteorological data from *in-situ* sources (buoy and weather stations) within or near the HF radar coverage area: (i) Spatial coordinates of the *in-situ* measurements; (ii) Existing bathymetry and coastline in the proximity of these *in-situ* measurements; (iii) Measurements of significant height/peak swell, swell period, swell direction; (iv) Measurements of wind direction and intensity; (v) Ocean-meteorological data of waves (height, period, direction) and wind (direction and intensity) provided by numerical models (e.g. CMEMS).

To validate and assess the wave retrieval capabilities of the EuskOOS HF radar network, Hs, Tp and Wdir from the two HF radar stations and from the Bilbao-Vizcaya buoy were compared on a monthly basis. Monthly mean values of Hs were calculated for Higer and Matxitxako HF radar stations and for Bilbao-Vizcaya buoy. However, in calculating monthly means, only waves with Hs>1,5m were included due to the limitations of the 4,46 MHz radars for the retrieval of smaller waves. The statistics to analyze and compare data were the following:

Considering two series of data, $\{X(t_i);\ i= 1,\ldots, N\}$, $\{Y(t_i);\ i=1, \ldots, N\}$,

- Mean Value of X time series: $\bar{X} = \frac{\sum_{i=1}^{N} X(t_i)}{N}$
- Bias: $bias = \bar{Y} - \bar{X}$
- Root Mean Square: $RMSE = \sqrt{\frac{\sum_{i=1}^{N}(X_i - Y_i)^2}{N}}$
- Correlation Coefficient: $r = \frac{\sum_{i=1}^{N}((X_i-\bar{X})\ (Y_i-\bar{Y}))}{\sqrt{\sum_{i=1}^{N}(X_i-\bar{X})^2}\ \sqrt{\sum_{i=1}^{N}(Y_i-\bar{Y})^2}}$

Monthly winds from Matxitxako meteorological station were plotted together with the wind direction from HF radar stations to determine the local wind conditions throughout the year. HF radar skills for waves retrieval in periods with different wind conditions were also analyzed. Statistical comparisons were conducted to check HF radar skills during specific wind directions, considering wind sectors of 45 degrees.

Extreme wave events within the study area were defined as instances where Hs measured by the buoy exceeded 4m for time periods over 12h (Gorman, 2018). This threshold was applied to showcase HF radar data available exclusively for periods when Bilbao-Vizcaya buoy Hs > 4m.

Noise interferes widely in the quality and availability of the wave data derived from HF radar technology. Since Matxitxako and Higer HF radar stations experienced periodic high noise periods, with an associated data availability decrease, a qualitative and quantitative inspection of the wave data and spectra provided by both stations were performed to assess the noise impact over the wave dataset quality and availability.

4 Results

Wave data from EuskOOS HF radar network underwent statistical analysis and later comparison with data from an *in-situ* buoy. An analysis on a monthly basis was conducted, followed by the analysis of extreme events. Moreover, the effect of different wind and noise conditions on the data availability and accuracy was undertaken.

4.1 Analysis of measured wave data

Monthly mean values of Hs were calculated for Higer and Matxitxako HF radar stations and for the Bilbao-Vizcaya buoy in 2022 (Table 2). Results unveiled a clear seasonal cycle that peaks during winter, especially in February and November. Bilbao-Vizcaya buoy wave data represent the seasonal variations, showing mild conditions during summer and extreme energetic conditions during winter, as previously described by Gonzalez et al., (2004). The absolute minimum Hs for both HF radar stations

TABLE 2 Mean values of Hs>1.5m for Bilbao-Vizcaya buoy (referred as "Buoy") and HF radar stations (referred as Higer and Matx, for Higer and Matxitxako HF radar stations, respectively) during 2022.

Month	$\overline{H_S}$ Buoy	$\overline{H_S}$ Matx	$\overline{H_S}$ Higer
Jan-22	3.15	1.70	3.44
Feb-22	3.40	3.15	3.73
Mar-22	2.78	2.64	3.33
Apr-22	2.31	2.11	2.50
May-22	1.84	1.97	1.94
Jun-22	2.00	2.10	2.39
Jul-22	1.69	1.80	1.95
Aug-22	1.83	1.43	1.75
Sep-22	2.50	1.60	1.94
Oct-22	2.08	2.33	2.50
Nov-22	3.43	3.54	4.37
Dec-22	2.21	2.17	3.05
2022	**2.50**	**2.18**	**2.80**

Bold values are for the whole 2022.

andBilbao-Vizcaya buoy occurred in July. Hs monthly mean values measured by Higer HF radar station ($\overline{H_S}$ Higer = 2.8m) were higher than those provided by HF radar Matxitxako station ($\overline{H_S}$ Matx = 2.18m) and Bilbao-Vizcaya buoy ($\overline{H_S}$ Buoy = 2.5m). Higher values near Higer HF radar station can be related to the local conditions of the data retrieval coverage area of the station (Figure 1).

Hs, Tp and Wdir measured by Matxitxako and Higer HF radar stations and Bilbao-Vizcaya buoy have been plotted for each month of 2022. An illustrative example of February 2022, depicting data from Matxitxako and Higer HF radar stations is presented in Figure 2.

Tables 3, 4 delineate the monthly statistical comparison between Bilbao-Vizcaya buoy and both Matxitxako and Higer HF radar stations during 2022, for Hs>1.5m. Overall, the buoy data availability (86.4%) was higher than HF radar Matxitxako (60.31%) and Higer (52.3%) stations, respectively. Concerning the Hs, comparisons between Matxitxako HF radar station and Bilbao-Vizcaya buoy (Table 3), show monthly r values up to 0.83 (and typically over 0.6), except for January when there is a significant lack of HF radar data (only 25.68% Matxitxako HF radar station data availability).

In the comparison of Tp, r values vary between 0.34-0.90. Conversely, Wdir comparisons show lower r values (0.07-0.4) than these found for Hs and Tp, with very low minimum values in some months (e.g. February, June, August and November).

Similarly, Higer HF radar station and Bilbao-Vizcaya buoy comparison (Table 4) also shows r values up to 0.78 for Hs and up to 0.85 for Tp. However, certain months present lower Hs r values, as November, when very low buoy data availability existed, or July when there was low HF radar data availability. Wdir comparison shows again low minimum values, as observed in Matxitxako HF station.

4.2 Performance of wave measurements under variable noise conditions

Noise significantly affects both data availability and quality. For 2020-2022, monthly data availability values were plotted for all-day,

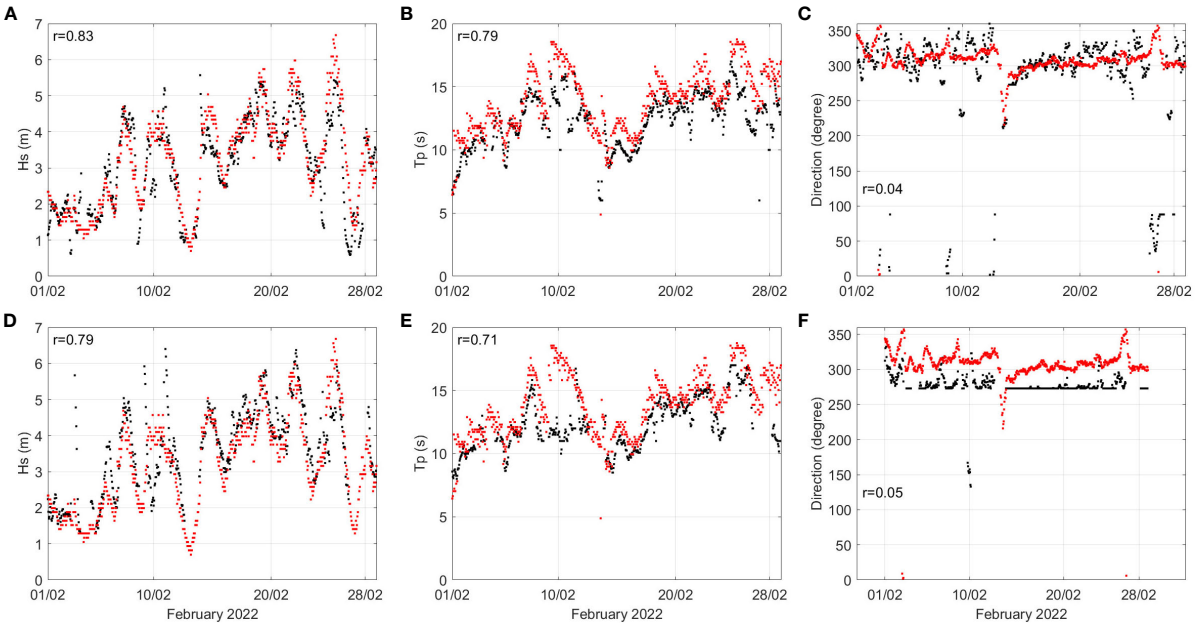


FIGURE 2
(A, D) Hs, **(B, E)** Tp and **(C, F)** Wdir comparison for February 2022, between Bilbao-Vizcaya buoy and **(A–C)** Matxitxako HF radar station and **(D–F)** Higer HF radar station. Black dots correspond to HF radars and red dots correspond to the Bilbao-Vizcaya buoy. Units are provided in the axis labels.

TABLE 3 Data availability and statistical comparison of Hs>1.5m values for Bilbao-Vizcaya buoy and Matxitxako HF radar station, during 2022.

Month	HF radar Matxitxako Availability (%)	Buoy Availability (%)	Hs			Tp			Wdir		
			Bias	RMSE (m)	r	Bias	RMSE (s)	r	Bias	RMSE (°)	r
Jan-22	25.68	100.00	-0.12	1.37	0.27	-0.37	1.78	0.85	46.06	63.31	0.41
Feb-22	88.38	96.41	-0.20	0.75	0.83	-1.61	2.22	0.79	24.97	37.37	0.04
Mar-22	61.98	100.00	-0.23	1.16	0.49	-2.71	3.71	0.34	34.99	50.02	0.20
Apr-22	63.99	99.71	-0.26	0.73	0.74	-0.56	2.34	0.55	27.80	38.50	0.51
May-22	54.95	99.43	0.10	0.71	0.58	-0.05	1.54	0.74	30.56	41.52	0.11
Jun-22	64.42	99.71	0.14	0.58	0.68	-0.51	2.14	0.45	21.92	32.96	0.04
Jul-22	56.53	99.71	0.01	0.63	0.50	1.03	2.28	0.48	37.41	49.73	0.16
Aug-22	70.01	59.83	0.05	0.53	0.81	0.26	1.58	0.72	35.43	45.88	0.05
Sep-22	46.48	86.08	-0.31	0.69	0.75	-0.70	2.21	0.54	33.20	51.41	0.20
Oct-22	60.55	72.45	0.37	0.83	0.55	-0.50	1.50	0.66	20.26	27.29	0.18
Nov-22	81.21	10.33	-0.22	0.84	0.67	-1.63	1.79	0.90	11.57	15.35	-0.07
Dec-22	49.50	85.08	0.19	0.90	0.64	-0.35	2.83	0.46	36.86	54.75	0.45
2022	**60.31**	**84.06**	**-0.04**	**0.81**	**0.63**	**-0.64**	**2.16**	**0.62**	**30.09**	**42.34**	**0.19**

Bold values are for the whole 2022.

night-time (6 p.m. to 6 a.m.), and day-time (6 a.m. to 6 p.m.) periods (Figure 3). Clear differences are observed between day-time and night-time (Figure 3) for the two HF radar stations. Data availability ranged between 20% and 60%, reaching up to 80% by the end of 2021. Day-time data availability ranges around 30-40% while night-time data availability oscillates between 10% and 20%. Please note that lower data availability observed in 2020 and 2021, compared to 2022, is partially related to system failures.

SNR from the 3 loops reported by each antenna were plotted (not shown) to understand the relation of the data availability and noise. Daily noise level fluctuations were observed in the two HF radar antennas, ranging from 0 to 70, with higher SNR during day-

TABLE 4 Data availability and statistical comparison of Hs>1.5m values for Bilbao-Vizcaya buoy and Higer HF radar station, during 2022.

Month	HF radar Higer Availability (%)	Buoy Availability (%)	Hs			Tp			Dir		
			bias	RMSE (m)	r	Bias	RMSE (m)	r	bias	RMSE (m)	r
Jan-22	42.32	100.00	0.08	1.25	0.78	-1.69	2.64	0.81	48.50	57.25	-0.23
Feb-22	78.62	96.41	0.22	0.80	0.79	-1.65	2.41	0.71	34.26	39.94	0.05
Mar-22	51.65	100.00	0.49	1.12	0.64	-2.22	2.97	0.46	29.78	40.21	0.01
Apr-22	50.36	99.71	0.33	1.00	0.76	-1.06	2.11	0.60	28.68	36.79	0.15
May-22	49.35	99.43	0.22	0.69	0.49	-0.39	1.30	0.84	36.87	43.00	0.54
Jun-22	57.10	99.71	0.32	0.87	0.50	-1.04	1.85	0.62	31.12	32.98	0.52
July-22	41.89	99.71	0.38	1.22	0.17	0.25	1.72	0.55	38.30	44.51	0.06
Aug-22	47.63	59.83	0.32	1.19	0.15	-0.50	1.21	0.85	43.22	49.29	-0.14
Sep-22	38.31	86.08	0.29	1.43	0.24	-0.79	2.45	0.19	25.75	28.83	-0.09
Oct-22	61.12	72.45	0.42	0.82	0.52	-0.99	1.49	0.78	29.60	32.88	0.28
Nov-22	76.04	10.33	1.17	2.28	-0.08	-1.55	1.81	0.85	-21.92	22.17	0.14
Dec-22	33.57	85.08	0.70	1.59	0.40	-1.41	2.10	0.58	24.24	36.81	0.46
2022	**52.33**	**84.06**	**0.41**	**1.19**	**0.45**	**-1.09**	**2.01**	**0.65**	**32.69**	**38.72**	**0.15**

Bold values are for the whole 2022.

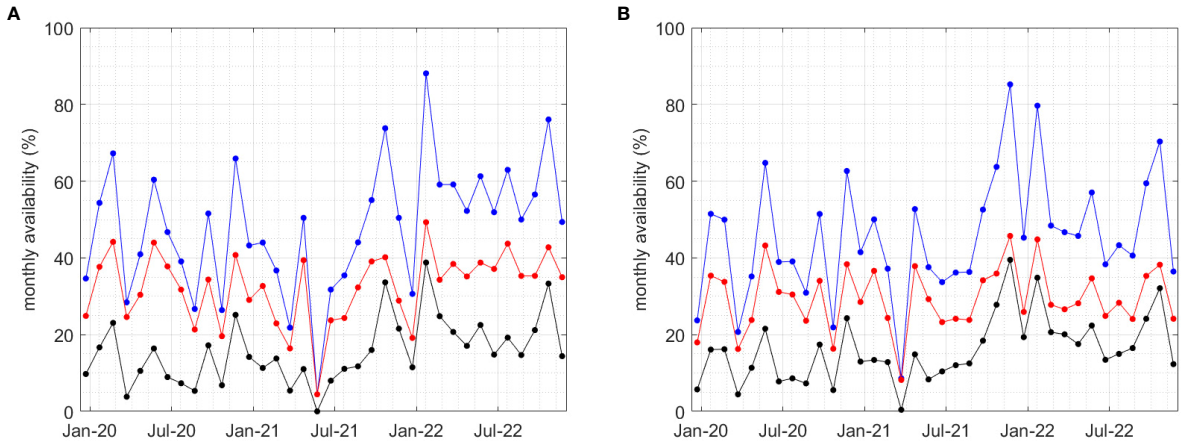


FIGURE 3
Day-time (6 a.m. to 6 p.m., red line) and night-time (6 p.m. to 6 a.m., black line) monthly data availability % from **(A)** Matxitxako HF radar station and **(B)** Higer HF radar station, for 2020-2022. Blue line represents the whole data availability %.

time and lower SNR during night-time. The 3 loops mean SNR for day-time was 47 (41) and night-time 37 (35) for Matxitxako and Higer HF radar stations respectively, showing 11-21% lower SNR during night-time periods than day-time periods. Moreover, results show that there is no wave data availability for SNR values below 30 for Matxitxako and Higer radar stations. Approximately 20% of the night-time periods, SNR is below 30 in both HF radar stations, explaining the data availability decrease observed in Figure 3. Only 5% of the time SNR are below this threshold during day-time periods.

Hs correlations between the HF radar stations depending on SNR intervals were computed for the whole 2022 year (Table 5). No correlation decrease is observed for SNR over 40 values in Matxitxako and Higer HF radar stations (r values around 0.62 to 0.92). Low correlation values are observed for data with SNR between 30-40 in Matxitxako and Higer HF radar stations. Although wave data with SNR below the previous threshold only represent around 10% of the whole extracted wave data, those results suggest not only wave data availability decrease during noisy periods but also a small reduction in data quality related to the lowest SNR values.

For intense noise periods, when data retrieval becomes not possible (occurring 20% of the night-time periods), the interferences in the received signal are easily visible in the spectra from the HF radar stations and the patterns generated by the reflection of the emitted signal become difficult to identify. Spectra from CODAR HF radar contain three individual spectra, from two antennas and a monopole used for the detection of the incoming angle of the received signal (Kohut and Glenn, 2003) (see examples in Figures 4, 5). Each spectrum contains two main peak pairs (first and second order) in both left and right side of the spectra, used for surface currents and wave information retrieval, respectively (see Barrick, 1977). Visual inspection of the spectra during systematically noisy and low noise periods, identified by Figures 4, 5, showcase how high noise levels prevent the correct detection of the second order peaks, which contain the wave information. Figures 4, 5 show examples of the day-time (clean) spectra on February 11, 2022, and nighttime (noisy) spectra on February 10, 2022, respectively. The right side second order peaks are clearly identified in Figure 4 (short light-blue peaks at the right side of the right first order green peak) while the second order peaks are shadowed by the interference noise in Figure 5 (just first order peaks are identified, both in the left and right sides of the spectra). In both cases, the first order peaks are clearly identified showing that the current measurement, inferred from a much stronger signal in the spectra, is not affected by the interference noise.

4.3 Differences between *in-situ* and HF radar wave measurements under variable wind conditions

Bias, RMSE and *r* values have been calculated for Hs, Tp and Wdir, for 8 wind sectors of 45°, to investigate possible differences

TABLE 5 Correlation values between Bilbao Vizcaya Buoy and Matxitxako and Higer HF radar stations, for different SNR levels in 2022.

	Matxitxako station			Higer station		
	r	Mean Hs	Buoy mean Hs	r	Mean Hs	Buoy mean Hs
30-40	0.183	3.19	2.075	0.280	3.404	2.320
40-50	0.773	2.31	2.337	0.815	2.530	2.283
50-60	0.844	1.818	2.028	0.928	2.245	2.307

Mean Hs values from HF radar stations and Bilbao Vizcaya Buoy are also included.

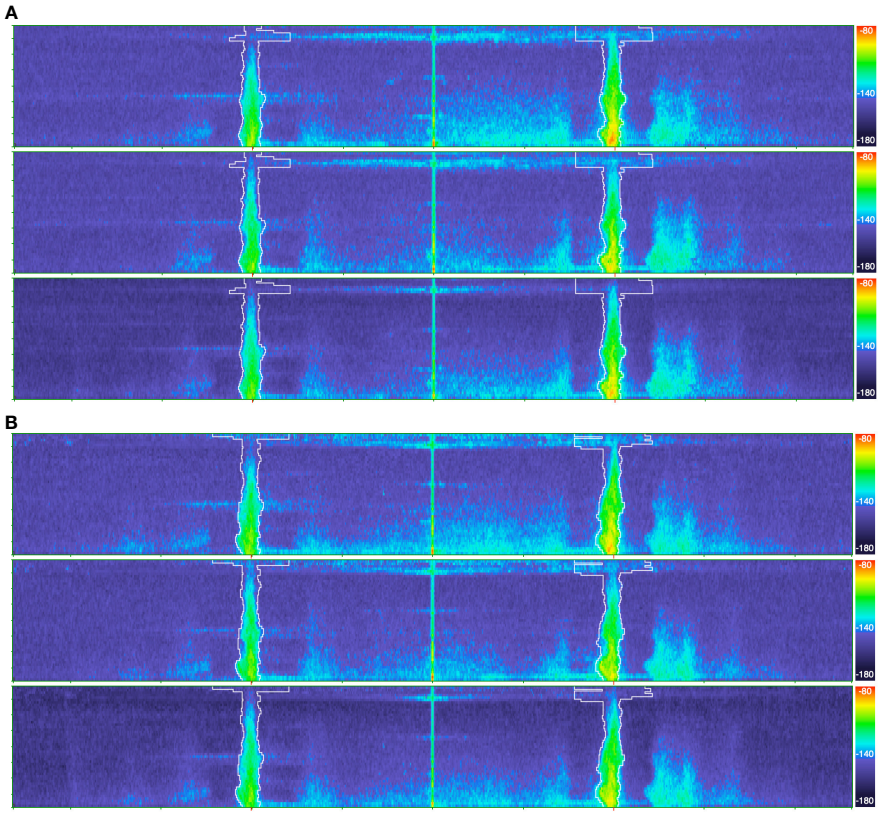


FIGURE 4
Day-time (6 a.m. to 6 p.m.) spectra maps from Matxitxako HF radar station at 12:00 **(A)** and 15:30 **(B)**, in February 11, 2022. Lower spectra on each **(A, B)** subplot, is from Loop 1, the middle spectra from Loop 2 and to upper spectra is from the Monopole antenna. Y axes show the range from 0-250 km.

for different wind directions (Table 6). Results for 2022 show Hs correlation values around 0.80 for Matxitxako HF radar station and around 0.7 for Higer HF radar station and similar results are obtained for Tp. Overall, small but not significant differences are observed for the different wind sections.

It is known that HF radar and *in-situ* wave data measurements often reveal significant discrepancies under specific wind conditions, although no significant differences have been identified in Table 6 for specific angles. To delve deeper into this investigation, monthly plots of wave height from Matxitxako HF radar station and Bilbao-Vizcaya buoy, together with wind direction from Matxitxako HF radar station vs. Matxitxako meteorological station have been plotted to analyze the differences observed under specific different wind conditions. Examples from March 2021 in Figure 6 (northward winds and waves in same direction) and from February 2021 in Figure 7 (southward winds and waves in opposite directions), were examined to elucidate these differences.

Figure 6 shows Hs and wind direction recorded during March 2021. Wave events with Hs>=5m occurred on March 14 and 27 (indicated with dashed blue vertical lines in Figure 6). These occurrences coincided with predominant northern winds measured by the Matxitxako meteorological station and by the Matxitxako HF radar station. Figure 6A shows similar Hs measurements from HF radar Matxitxako station and Bilbao-Vizcaya buoy on those two days, when both wave and wind direction had the same main direction.

Figure 7 shows Hs and wind direction during February 2021. Hs discrepancies are observed for example in Figure 7A on February 2nd and 22nd (blue dashed vertical lines), between Matxitxako HF radar and the Bilbao Vizcaya buoy. Similar situations have been observed in other (not shown) months and they are related systematically to periods when different wind conditions are measured by the HF radar and the coastal Matxitxako meteorological station. In these situations, wind conditions are spatially not uniform along the HF radar measuring area and results suggest this has a direct effect on the estimation of Hs.

4.4 Extreme events

The analysis of the HF radar capability in identifying extreme events was made by comparing Hs, Tp, and Wdir for both Matxitxako and Higer HF radar stations and Bilbao-Vizcaya buoy through 2021 and 2022 (see examples for February 2022 in Figures 8, 9). Monthly graphics indicate that as expected, the extreme events occur predominantly from November to March (figures not shown).

Throughout 2021 and 2022, the Matxitxako HF radar station identified a total of 21 extreme events. The Hs exceeded 8 m for one

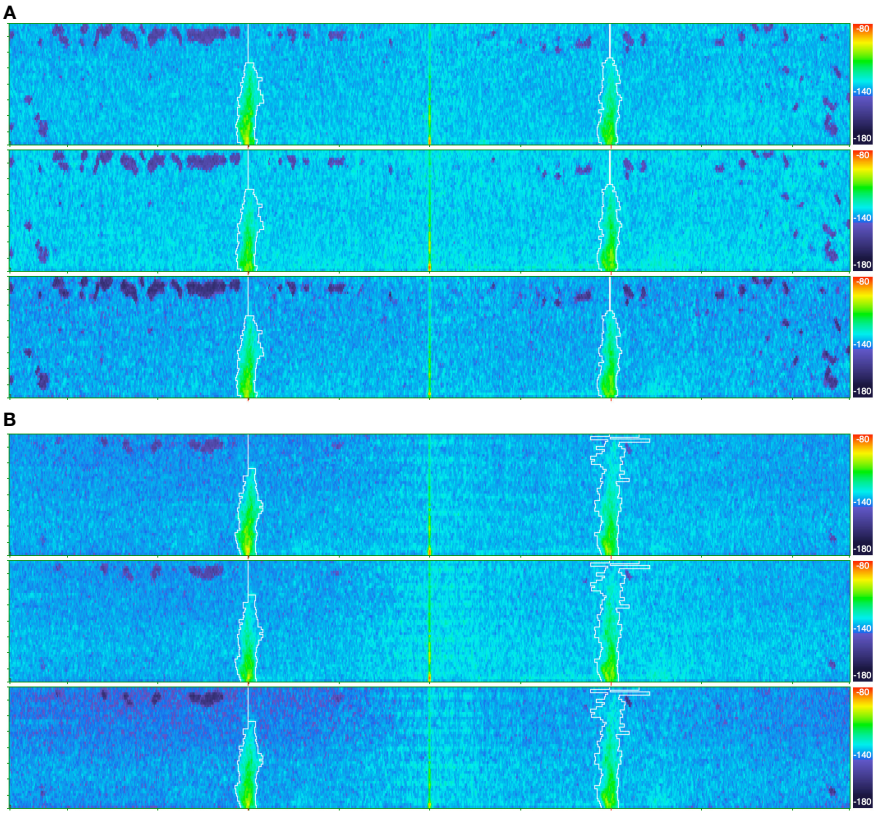


FIGURE 5
Night-time (6 p.m. to 6 a.m.) spectra maps from Matxitxako HF radar station **(A)** at 23:00 on February 10, 2022, and **(B)** at 02:00 on February 11, 2022. Lower spectra on each **(A, B)** subplot, is from Loop 1, the middle spectra from Loop 2 and to upper spectra is from the Monopole antenna. Y axes show the range from 0-250 km.

of these events (February 2021), 6 m during seven events and the remaining events exceed 4m. The Wdir ranged between 270° and 350° being the most frequent around 300°. The Tp ranged between 10 and 18 seconds, which is consistent with the extreme events that reach the Basque coast from the North Atlantic Ocean. Higer HF radar station identified the same extreme events as in Matxitxako HF radar station, showing lower Wdir variability in Higer HF radar station than in Matxitxako HF radar station and Bilbao-Vizcaya buoy.

5 Discussion

HF radars play a crucial role in the coastal ocean by offering synoptic current and wave measurements across extensive areas in near real-time. Integration of these measurements into numerical models has the potential to greatly improve the accuracy of coastal forecasts. Currently, HF radars are integral components of numerous European Coastal Observatories, opening the possibility of widespread distribution of wave data (alongside coastal surface currents) through various channels in Europe, including Copernicus Marine Services. Furthermore, they have the potential to serve as a reliable complement to traditional wave monitoring systems such as buoys and satellites, enhancing the overall wave monitoring capabilities. Despite the utilization of HF radar wave data spanning several decades, its operational availability for complementing traditional wave datasets remains restricted due to a range of limitations for the operational retrieval of accurate measurement, especially for compact HF radar systems. It is imperative to acquire a deeper comprehension of these limitations, which are closely linked to geographical, physical, and environmental conditions specific to each compact HF radar installation. The analysis conducted here has contributed to this direction by shedding light on the impact of wind and noise levels on the reliability of wave measurements over a span of several years.

Comparisons conducted in 2022 between Matxitxako and Higer HF radar stations and the Bilbao-Vizcaya buoy reveal monthly mean values of r, up to 0.83 and RMSE mean values below 1m for Hs comparison. However, this performance decreases significantly in periods when the HF radar data availability is lower (e.g. January 2022) and in periods of unfavorable wind and noise conditions. Those values align with previous studies using HF radar for wave retrieval (e.g. Lipa et al., 2014; Atan et al., 2015; Bué et al., 2020). Differences observed between HF radars and the Bilbao-Vizcaya buoy are mainly related to different issues. On the one hand challenges associated to the retrieval of wave data from the spectra of the backscattered signal (limitations for waves with Hs<1.5m related to the operating frequency and lower performance under unfavorable noise conditions). On the other hand, differences associated with the nature of the measurement

TABLE 6 Bias, RMSE and correlation (r) values of Hs, Tp and Wdir for Matxitxako and Higer HF radar stations and Bilbao Vizcaya Buoy, for 2022.

Matxitxako vs. Bilbao buoy										
		Hs			Tp			Wdir		
2022	N	Bias	RMSE	r	Bias	RMSE	r	Bias	RMSE	r
0°-45°	186	0.04	0.74	0.79	-0.06	1.94	0.78	38.57	51.77	0.07
45°-90°	418	-0.01	0.55	0.79	-0.08	2.28	0.62	31.38	45.61	0.24
90°-135°	461	-0.03	0.98	0.78	-0.69	2.21	0.64	29.68	44.43	0.24
135°-180°	412	0.02	0.85	0.80	-1.05	2.45	0.70	27.44	42.54	0.15
180°-225°	800	-0.19	0.85	0.79	-1.10	2.65	0.69	27.87	40.73	0.27
225°-270°	931	-0.03	0.89	0.69	-0.55	2.53	0.62	30.04	42.93	0.25
270°-315°	531	-0.07	0.57	0.78	-0.46	1.90	0.68	33.31	45.75	0.42
315°-360°	169	-0.08	0.58	0.85	-0.39	1.88	0.74	34.08	49.72	0.32
Higer vs. Bilbao buoy										
		Hs			Tp			Wdir		
2022	N	Bias	RMSE	r	Bias	RMSE	r	Bias	RMSE	r
0°-45°	155	0.35	0.86	0.74	-0.80	1.70	0.86	37.41	43.09	0.19
45°-90°	339	0.34	1.03	0.68	-0.85	1.79	0.77	33.01	38.82	0.03
90°-135°	424	0.23	0.77	0.77	-0.97	1.87	0.75	32.89	39.82	0.03
135°-180°	341	0.38	1.07	0.73	-1.31	2.31	0.75	34.33	43.19	-0.32
180°-225°	673	0.34	1.06	0.75	-1.64	2.60	0.72	31.51	37.24	-0.06
225°-270°	802	0.37	1.15	0.63	-0.73	2.01	0.76	30.36	37.58	-0.05
270°-315°	453	0.40	1.23	0.48	-0.66	1.49	0.80	31.59	38.07	0.39
315°-360°	135	0.49	1.20	0.58	-0.68	1.46	0.85	31.84	37.11	0.52

N is the number of hours from each HF radar station used for comparison, during each month. 315°-360° and 0°-45° sectors represent winds from sea and 135°-180° and 180°-225° sectors represent winds from land.

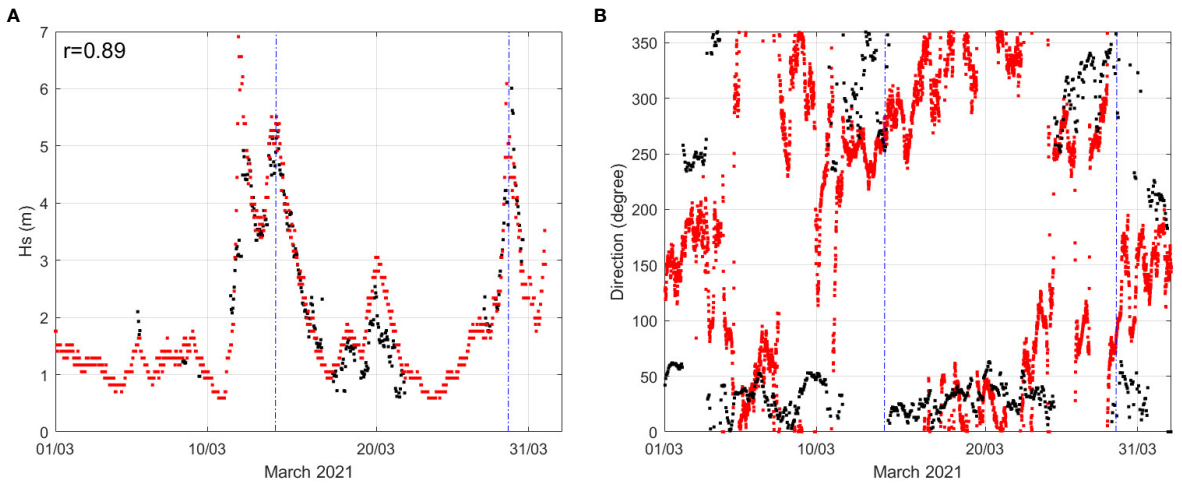


FIGURE 6
(A) Wave height from Matxitxako HF radar station (black dots) and Bilbao-Vizcaya buoy (red dots) and **(B)** wind direction from Matxitxako HF radar station (black dots) and Matxitxako meteorological station (red dots) in March 2021. Blue dashed lines mark March 14 and March 28 events.

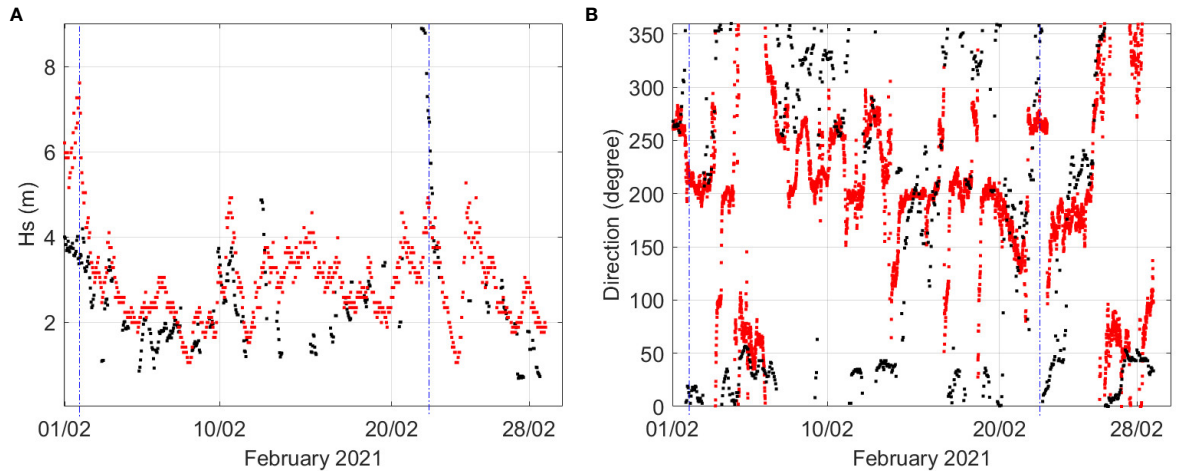


FIGURE 7
(A) Wave height from Matxitxako HF radar station (black dots) and Bilbao-Vizcaya buoy (red dots) and **(B)** wind direction from Matxitxako HF radar station (black dots) and Matxitxako meteorological station (red dots) in February 2021. Blue dashed lines mark February 2nd and 22nd events.

itself (spatial integration of wave HF radar data and pointwise measurements of the offshore buoy) and the existing spatial variability of the wave field along the RC, where we assume wave spectra homogeneity for compact SeaSonde® HF radars.

The fact that the minimum Hs that can be measured by a radar operating at 4.46 MHz is 1.5m (Lipa and Nyden, 2005) can explain Hs differences measured by the HF radar when compared to the buoy if all Hs ranges are considered (including Hs< 1.5 m, not shown). During low energetic sea states the strength of the second-order spectra can be very weak, and any spurious contributions to the spectrum would have a significant impact on the ability of the processing scheme to retrieve the correct Hs values.

Noise is a critical factor that interferes widely in the availability of data and on its quality. In the case of Matxitxako and Higer both stations suffer high periods of night-time noise. Noisy periods have been identified based on the SNR from the HF radar station, from approximately 6 p.m. to 6 a.m. (night-time) with high noise levels (Figure 5) and low noise levels from 6 a.m. to 6 p.m. (day-time) (Figure 4). This will affect data availability and quality during night-time as seen in section 4.2. Noise is affecting data availability and measuring values but also when interference is very significant, it may directly not retrieve wave information. The origin of this intense interference is still unknown. However, it seems to be local as it does not affect to Galician HF radars (not shown) located in northwestern Spain. We recommend doing further inspection of the data during noisy periods before the data usage for both operational and post-processing purpose of EuskOOS HF radar network.

Tp, and Wdir *r* values span between 0.34-0.85 and 0.04-0.54, respectively. The lower *r* values observed for Tp and Wdir can be related to the contribution of the errors associated with the definition of the dominant characteristics of the waves during bimodal sea states. In these situations, big errors are common when comparing different datasets (Cahill and Lewis, 2014) and the differences in the methodology used in this study between the two measuring systems can increase the discrepancies. Consequently, the values of direction measured by the buoy and the HF radar should be seen as a whole, ensuring that both, compact HF radar stations and Bilbao-Vizcaya buoy measure on the same range of Wdir values. This is the case for this study, where HF radar stations and buoy present values between 250° - 360° (Figures 8C, 9C).

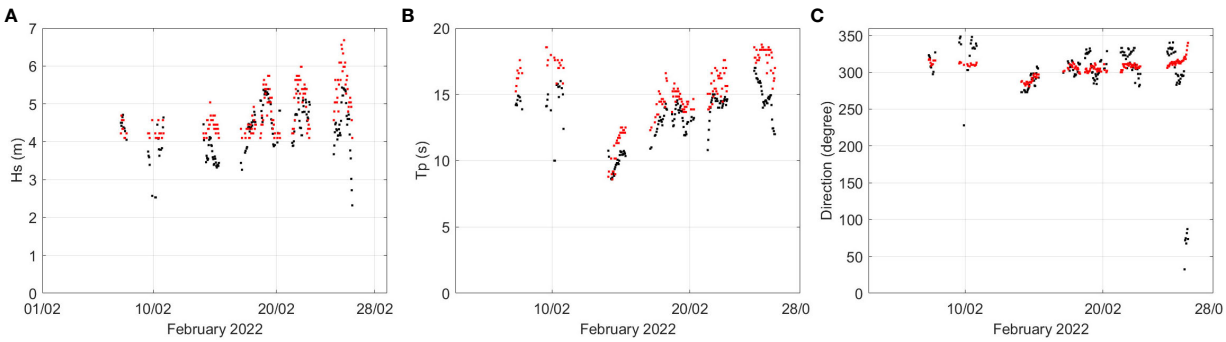


FIGURE 8
(A) Hs, **(B)** Tp and **(C)** Wdir during extreme events (Hs> 4m) from Bilbao-Vizcaya buoy (red dots) and Matxitxako HF radar station (black dots) for February 2022.

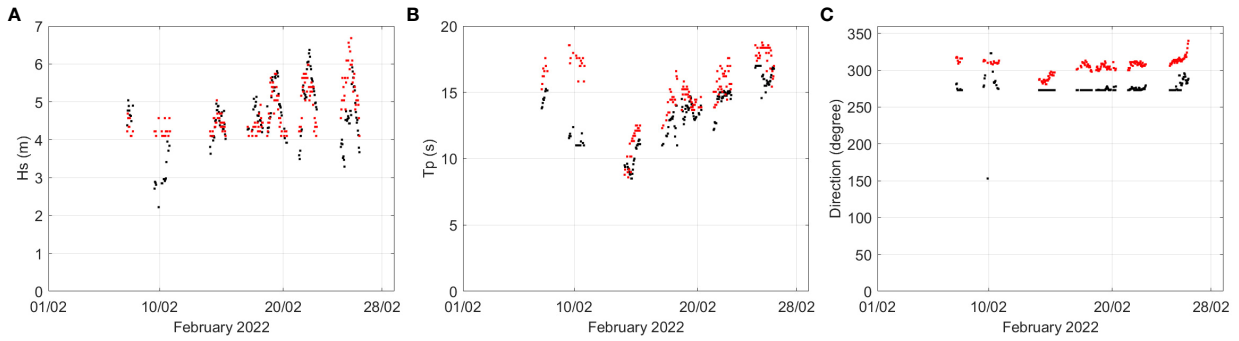


FIGURE 9
(A) Hs, **(B)** Tp and **(C)** Wdir during extreme events (Hs> 4m) from Bilbao-Vizcaya buoy (red dots) and Higer HF radar station (black dots) for February 2022.

Hs, Tp and Wdir values present also differences between both HF radar stations (Matxitxako and Higer). These differences are related to: (i) the measuring location of Bilbao Vizcaya buoy and the covering area of the RCs from Matxitxako (closer) and Higer (no overlapping area) stations; (ii) both HF radar stations are measuring slightly different wave conditions, as they are set up in different coastal locations. In fact, there is a larger (smaller) bathymetry steepness in Matxitxako (Higer) which may explain the lower (higher) measured wave heights (to be further investigated); and (iii) they are under environmental (noise and wind) conditions that can present spatial variability.

Spatial heterogeneity in wind conditions can also generate differences between HF radar and *in-situ* measurements. Results in section 4.3 show that there are no significant differences for different wind direction sections when spatially homogeneous winds affect the study area. It has also been shown how wind can affect the HF radar measurements and originate significant differences in the Hs estimation, when comparing the two measuring systems in presence of local non-homogeneous wind conditions. The area monitored by Matxitxako and Higer HF radar stations can reach ~50 km in length and ~25 km wide. Results suggest that Matxitxako HF radar station is highly influenced by local winds from land due to its geographical position. We have noted that swell and wind-waves with opposite directions (influence of local wind), can interfere in data quality. This should be taken into consideration in other SeaSonde® HF radar networks too, when local winds (not covering the whole HF radar footprint) are present. Depending on the direction and intensity, wave local conditions could spatially vary, and this variability can be as high as the variability of the wind direction and intensity. Since compact SeaSonde® HF radar stations will always measure the most energetic signal, either from swell or wind-waves, in bi-modal seas, swell conditions can be missed by the radar in case of an intense wind-wave field. The buoy will measure the full wave movement, whether it is swell or wind-waves or both mixed. If the buoy is quite far from the HF radar station, this difference can be more noticeable. The discrepancies found in this work between HF radar and buoy measurements do not demonstrate unavailability or malfunctioning of any of these instruments, but the consequence of the different nature of the measurements made by them. This highlights the importance of understanding the physical processes behind the measured variability. We recommend analyzing the performance of the HF radar system under different wind conditions. Further analysis is required to understand the mechanism under the underestimation or overestimation of Hs from the analyzed HF radar observed in spatially non-uniform wind conditions. The influence of the fetch and wind duration have not been analyzed in this work because due to the geographical location and configuration of the study area, waves may only be limited by fetch or wind duration during marginal time periods. But those factors should be considered and analyzed in other areas with different geographical configurations.

Monthly analysis of the extreme events for 2021-2022 (section 4.4) shows that the extreme events from HF radar occur during winter months, mainly February, March, and April, also observed by the Bilbao-Vizcaya buoy and as previously described in the study area (Gonzalez et al., 2004). The fact that both Matxitxako and Higer HF radar stations identify previously known extreme events features, together with the good agreement with the Bilbao-Vizcaya buoy suggest that EuskOOS HF radar network is capable of measuring sea states during extreme events. This is especially interesting as extreme event periods are when *in-situ* instruments usually suffer technical problems, being at the same time less accessible, which leads to longer periods with no data. Further work should include the analysis of the whole available wave time series from the EuskOOS HF radar data for the characterization of changes in the extreme wave regime and its variability. In the EuskOOS HF radar network, sea states with Hs<1.5m occur commonly in the study area (according to the Bilbao-Vizcaya buoy), this in turn limits the use of the HF radar for the characterization of less energetic sea states.

The analysis of the EuskOOS HF radar network capabilities for wave data retrieval under different conditions conducted in this paper allowed us to extract some key points to be taken into consideration for more accurate wave retrieval from HF radars:

- HF radar measurements performance for low/high Hs waves depend on their operating frequency and should be taken with caution during the QC process. For this reason, we recommend checking the limitations of the HF radar configuration to find the min/max Hs limits of the operating frequency and comparing these values with the Hs range values expected in the study area.

- An interference and noise analysis in the frequency range of operation of the HF radar in the study area should be done if wave data from the HF radar want to be exploited. The best scenario will be to analyze the noise levels prior to the installation of any new system, to avoid interferences that could make wave data retrieval impossible. Note that the origin of the interferences can be environmental or human source, and as shown in this contribution it can be strongly variable with time. For the installed HF radar scenarios, SNR should be analyzed to quantify and understand the existence of noise in each HF radar station and its affection to data quality and availability.
- Wind affects waves, and local wind spatial variability can create differences in the data retrieval from different measuring systems, such as buoys and HF radars. A deep analysis of local wind effects on the wave field is recommended prior to the analysis of HF radar wave data against *in-situ* measurements.

The combination of all the previous conditions should enhance the reliability and performance for the wave's retrieval from SeaSonde® HF radars and optimize the installation and maintenance of new HF radars for wave retrieval during specific wave/wind/noise conditions.

6 Conclusions

An assessment of the wave measurement capabilities of the EuskOOS HF radar network has been conducted, identifying the key variables that need to be considered when determining reliable operational periods. Statistical validation and comparison analysis of the HF radar performance for wave measurement versus *in-situ* data (from the Bilbao-Vizcaya buoy) have demonstrated the performances of the HF Radars for the characterization of seasonal variability of the Hs and Tp (with much lower performances for Wdir) in the SE Bay of Biscay; with values in agreement to independent *in-situ* data and those that can be found in the literature about compact HF radar systems. The best correlations are obtained for homogeneous wind and favorable noise conditions. Matxitxako and Higer HF radar stations showed as well good performance for the identification of extreme events, also identified (with similar Hs and frequency) by the *in-situ* buoy, which reveals the advantage of this technology comparing to the problems and data availability decrease of *in-situ* instruments during such extreme events. The measurements in Matxitxako and Higer HF radar stations also accounted for the spatial variability of the wave field in the area. Noise influence on the quality of waves retrieval of the EuskOOS HF radar network was also analyzed. High interference and noise detected during night-time were observed to significantly reduce the availability and (to a lesser extent) the reliability of the wave data. The importance of wind on the HF radar measurements was also highlighted, as the wind directly affects the waves and their characteristics and can explain differences observed between *in-situ* and radar measurements for SeaSonde® HF radars. Gaining a comprehensive understanding of the limitations associated with accurate retrieval of wave data from HF radars, including factors related to geographical, physical, and environmental conditions, is crucial for enhancing their reliability. This understanding enables informed decisions regarding the optimal location and configuration of new and existing radar installations, ultimately boosting their operational availability for effectively complementing standard wave data measurements.

Finally, this analysis and the obtained conclusions will be useful for the historical wave data analysis (2009-nowadays) in the study area. The analysis of the evolution of extreme events will specially be interesting to see the increase of the extreme events, both in magnitude and frequency, that is happening not only in the Bay of Biscay but also worldwide.

Data availability statement

The original contributions presented in the study are included in the article/supplementary materials, further inquiries can be directed to the corresponding author/s.

Author contributions

LS worked on the setup of the methodology, data and results analysis, paper writing and final submission. MarF worked on the setup of the methodology, data analysis and paper writing. IR worked on the results analysis, figures creation and paper writing. MacF worked on the setup of the methodology, data analysis and paper writing. PL worked on the results analysis and paper writing. IS worked on the results analysis and paper writing. JS worked on the setup of the methodology and data analysis. JA worked on the results analysis. AR worked on the setup of the methodology, data and results analysis and paper writing. All authors contributed to the article and approved the submitted version.

Funding

The author(s) declare financial support was received for the research, authorship, and/or publication of this article. This research has been partially funded by the PI-BREAK project, through the Grant PLEC2021-007810 funded by MCIN(AEI)10.13039/501100011033 and, by European Union NextGenerationEU/PRTR. This research has also been partially funded through the EU's H2020 Program JERICO-S3 project (grant agreement no. 871153) and the project LAMARCA (PID2021-123352OB-C33) funded by MICIN/AEI /10.13039/501100011033/ and by FEDER (UE).

Acknowledgments

We thank the Emergencies and Meteorology Directorate (Security department) of the Basque Government for public data provision from the Basque operational Oceanography System EuskOOS. This research was partially carried out under the framework of KOSTARISK, Cross-Border Laboratory for Coastal

Risk Research. The joint laboratory KOSTARISK is supported by E2S UPPA, the AZTI Foundation and the center Rivages Pro Tech of SUEZ. This paper is contribution nº 1163 from AZTI, Marine Research, Basque Research and Technology Alliance (BRTA).

Conflict of interest

Authors MarF, MacF, and JS are employed by the company Qualitas Instruments S.A.

The remaining authors declare that the research was conducted in the absence of any commercial or financial relationships that could be construed as a potential conflict of interest.

The author AR declared that they were an editorial board member of Frontiers, at the time of submission. This had no impact on the peer review process and the final decision.

Publisher's note

All claims expressed in this article are solely those of the authors and do not necessarily represent those of their affiliated organizations, or those of the publisher, the editors and the reviewers. Any product that may be evaluated in this article, or claim that may be made by its manufacturer, is not guaranteed or endorsed by the publisher.

References

Atan, R., Goggins, J., Harnett, M., Nash, S., and Agostinho, P. (2015). "Assessment of extreme wave height evens in Galway Bay using High Frequency radar (CODAR) data," in *Renewable Energies Offshore* (Boca Raton, FL, USA: CRC Press), 49–56.

Barrick, D. E. (1977). Extraction of wave parameters from measured HF radar sea-echo Doppler spectra. *Radio Sci.* 12, 415–424. doi: 10.1029/RS012i003p00415

Barrick, D. E., Evans, M. W., and Weber, B. L. (1977). Ocean surface currents mapped by radar. *Science* 198, 138–144. doi: 10.1126/science.198.4313.138

Basañez, A., Lorente, P., Montero, P., Álvarez-Fanjul, E., and Pérez-Muñuzuri, V. (2020). Quality assessment and practical interpretation of the wave parameters estimated by HF radars in NW Spain. *Remote Sens.* 12, 598. doi: 10.3390/rs12040598

Borja, A., Amouroux, D., Anschutz, P., Gómez-Gesteira, M., Uyarra, M. C., and Valdés, L. (2019). *Chapter 5 - The Bay of Biscay, World Seas: an Environmental Evaluation. 2nd ed.* (Academic Press), 113–152, . doi: 10.1016/B978-0-12-805068-2.00006-1

Bué, I., Semedo, Á., and Catalão, J. (2020). Evaluation of HF radar wave measurements in Iberian Peninsula by comparison with satellite altimetry and *in situ* wave buoy observations. *Remote Sens.* 12 (21), 3623. doi: 10.3390/rs12213623

Cahill, B., and Lewis, T. (2014). "Wave period ratios and the calculation of wave power," in *Proceedings of the 2nd Marine Energy Technology Symposium, METS 2014*, Seattle, WA, USA, 15–18 April.

Castelle, B., Dodet, G., Masselink, G., and Scott, T. (2018). Increased winter-mean wave height, variability, and periodicity in the Northeast Atlantic over 1949–2017. *Geophysical Res. Lett.* 45, 3586–3596. doi: 10.1002/2017GL076884

Ferrer, L., Liria, P., Bolaños, R., Balseiro, C., Carracedo, P., González-Marco, D., et al. (2010). Reliability of coupled meteorological and wave models to estimate wave energy resource in the Bay of Biscay. In *Proc. 3rd Int. Conf. Ocean Energy (ICOE)*, 6 october, *Bilbao*.

Gaztelumendi, S., Egaña, J., Liria, P., and Aranda, J. A. (2018). Description of a coastal impact event in Basque Country: the 9 February 2016 case. *Adv. Sci. Res.* 15, 137–143. doi: 10.5194/asr-15-137-2018

Gonzalez, M., Uriarte, A., Fontan, A., Mader, J., and Gyssels, P. (2004). "Chapter 6: marine dynamics," in *Oceanography and Marine Environment of the Basque Country*, vol. 70 . Eds. A. Borja and M. Collins (Amsterdam: Elsevier Oceanography Series), 133–158.

Gorman, R. (2018). "Extreme wave indices for New Zealand coastal and oceanic waters updated to 2017," in *Prepared for the Ministry for the Environment. NIWA Client Report No: 2018325HN*.

Green, J. J., and Wyatt, L. (2006). Row-action inversion of the Barrick–Weber equations. *J. Atmos Oceanic Technol.* 23, 501–510. doi: 10.1175/JTECH1854.1

Gurgel, K.-W., Antonischki, G., Essen, H.-H., and Schlick, T. (1999). Wellen radar (WERA), a new ground-wave based HF radar for ocean remote sensing. *Coast. Eng.* 37, 219–234. doi: 10.1016/S0378-3839(99)00027-7

Gurgel, K.-W., Essen, H.-H., and Schlick, T. (2006). An empirical methodto derive ocean waves from second-order Bragg scattering:prospects and limitations. *IEEE J. Ocean. Eng.* 31, 804–811. doi: 10.1109/JOE.2006.886225

Horstmann, J., Corgnati, L., Mantovani, C., Quentin, C., Reyes, E., Rubio, A., et al. (2019). Report on Best Practice in the implementation and use of new systems in JERICO-RI.. In *Part 1: HF-radar systems and Part 2: Cabled coastal observatories*. WP2, Deliverable 2.4. Version 1.0. Brest, France, Ifremer for JERICO-NEXT, 141pp. (JERICO-NEXT-W2-D2.4.-07052019-V1.0). doi: 10.25607/OBP-1005

Kohut, J. T., and Glenn, S. M. (2003). Improving HF radar surface current measurements with measured antenna beam patterns. *J. Atmospheric Oceanic Technol.* 20 (9), 1303–1316. doi: 10.1175/1520-0426(2003)020<1303:IHRSCM>2.0.CO;2

Lavaud, L., Bertin, X., Martins, K., Arnaud, G., and Bouin, M. N. (2020). The contribution of short-wave breaking to storm surges: The case Klaus in the Southern Bay of Biscay. *Ocean Model.* 156 (January), 101710. doi: 10.1016/j.ocemod.2020.101710

Lavín, A., Valdés, L., Sánchez, F., Abaunza, P., Forest, A., Bouucher, J., et al. (2006). "Chapter 24. The Bay of Biscay: The encountering of the Ocean and the shelf," in *The Sea, Volume 14. Part B. The Global Coastal Ocean: Interdisciplinary Regional Studies and Synthesis. First Edition. Chapter, 24*. Eds. A. R. Robinson and K. H. Brink Harvard University Press, 933–1001.

Lipa, B. (1978). Inversion of second—order radar echoes from the sea. *J. Geophys. Res.* 83-C2, 959–962. doi: 10.1029/JC083iC02p00959

Lipa, B., and Barrick, D. (1982). "Wave propagation laboratory. Analysis methods for narrow-beam high-frequency Radar Sea Echo," in *Wave propagation laboratory. U.S. Department of Commerce, National Oceanic and Atmospheric Administration, Environmental Research Laboratories*. Available at: https://books.google.es/books?id=Lw9UAAAAMAAJ.

Lipa, B. J., and Barrick, D. E. (1986). Extraction of sea state from HF radar sea echo: mathematical theory and modelling. *Radio Science* 21, 81–100. doi: 10.1029/RS021i001p00081

Lipa, B., Barrick, D., Alonso-Martirena, A., Fernandes, M., Ferrer, M., and Nyden, B. (2014). Brahan project high frequency radar ocean measurements: currents, winds, waves and their interactions. *Remote Sens* 6, 12094–12117. doi: 10.3390/rs61212094

Lipa, B., and Nyden, B. (2005). Directional wave information from the SeaSonde. *IEEE Journal of Oceannographic Engineering* 30, 221–231. doi: 10.1109/JOE.2004.839929

Lopez, G., and Conley, D. C. (2019). Comparison of HF radar fields of directional wave spectra against *in situ* measurements at multiple locations. *J. Mar. Sci. Eng.* 7, 271. doi: 10.3390/jmse7080271

Lopez, G., Conley, D. C., and Greaves, D. (2016). Calibration, validation, and analysis of an empirical algorithm for the retrieval of wave spectra from HF radar sea echo. *J. Atmos OceanicTechnol* 33 (2), 245–261. doi: 10.1175/JTECH-D-15-0159.1

Lorente, P., Basañez Mercader, A., Piedracoba, S., Pérez-Muñuzuri, V., Montero, P., Sotillo, M. G., et al. (2019). Long-term skill assessment of SeaSonde radar-derived wave parameters in the Galician coast (NW Spain). *Int. J. Remote Sens.* 40 (24), 9208–9236. doi: 10.1080/01431161.2019.1629714

Lorente, P., Sotillo, M. G., Aouf, L., Amo-Baladrón, A., Barrera, E., Dalphinet, A., et al. (2018). Extreme wave height events in NW Spain: A combined multi-sensor and model approach. *Remote Sens.* 10, 1. doi: 10.3390/rs10010001

Manso-Narvarte, I., Caballero, A., Rubio, A., Dufau, C., and Birol, F. (2018). Joint analysis of coastal altimetry and high-frequency (HF) radar data: Observability of seasonal and mesoscale ocean dynamics in the Bay of Biscay. *Ocean Sci.* 14, 1265–1281. doi: 10.5194/os-14-1265-2018

Manso-Narvarte, I., Fredj, E., Jordà, G., Berta, M., Griffa, A., Caballero, A., et al. (2020). 3D reconstruction of ocean velocity from high-frequency radar and acoustic Doppler current profiler: A model-based assessment study. *Ocean Sci.* 16, 575–591. doi: 10.5194/os-16-575-2020

Manso-Narvarte, I., Rubio, A., Jordà, G., Carpenter, J., Merckelbach, L., and Caballero, A. (2021). Three-dimensional characterization of a coastal mode-water eddy from multiplatform observations and a data reconstruction method. *Remote Sens.* 13, 674. doi: 10.3390/rs13040674

Mantovani, C., Corgnati, L., Horstmann, J., Rubio, A., Reyes, E., Quentin, C., et al. (2020). BestPractices on high frequency radarDeployment and operation for oceanCurrent measurement. *Front. Mar. Sci.* 7. doi: 10.3389/fmars.2020.00210

Masselink, G., Castelle, B., Scott, T., Dodet, G., Suanez, S., Jackson, D., et al. (2016). Extreme wave activity during 2013/2014 winter and morphological impacts along the Atlantic coast of Europe. *Geophysical Res. Lett.* 43 (5), 2135–2143. doi: 10.1002/2015GL067492

Mundaca-Moraga, V., Abarca-del-Rio, R., Figueroa, D., and Morales, J. (2021). A preliminary study of wave energy resource using an HF marine radar, application to an eastern Southern Pacific location: advantages and opportunities. *Remote Sens.* 13, 203. doi: 10.3390/rs13020203

Orasi, A., Picone, M., Drago, A., Capodici, F., Gauci, A., Nardone, G., et al. (2018). HF radar for wind waves measurements in the Malta-Sicily Channel. *Measurement* 128, 446–454. doi: 10.1016/j.measurement.2018.06.060

Rubio, A., Fontán, A., Lazure, P., González, M., Valencia, V., Ferrer, L., et al. (2013). Seasonal to tidal variability of currents and temperature in waters of the continental slope, southeastern Bay of Biscay. *J. Mar. Syst.* 109–110, S121–S133. doi: 10.1016/j.jmarsys.2012.01.004

Rubio, A., Caballero, A., Orfila, A., Hernández-Carrasco, I., Ferrer, L., González, M., et al. (2018). Eddy-induced cross-shelf export of high Chl-a coastal waters in the SE Bay of Biscay. *Remote Sens. Environ.* 205, 290–304. doi: 10.1016/j.rse.2017.10.037

Rubio, A., Hernández-Carrasco, I., Orfila, A., González, M., Reyes, E., Corgnati, L., et al. (2020). A Lagrangian approach to monitor local particle retention conditions in coastal areas, in: Copernicus Marine Service Ocean State Report. *J. Operational Oceanography* 13:sup1 (4), S1–S172. doi: 10.1080/1755876X.2020.1785097

Rubio, A., Manso-Narvarte, I., Caballero, A., Corgnati, L., Mantovani, C., Reyes, E., et al. (2019). The seasonal intensification of the slope Iberian Poleward Current, in: Copernicus Marine Service Ocean State Report. *J. Oper. Oceanogr.* 12 (3), 13–18. doi: 10.1080/1755876X.2019.1633075

Rubio, A., Reverdin, G., Fontán, A., González, M., and Mader, J. (2011). Mapping near-inertial variability in the SE Bay of Biscay from HF radar data and two offshore moored buoys. *Geophys. Res. Lett.* 38, 19. doi: 10.1029/2011GL048783

Ruiz, I., Rubio, A., Abascal, A. J., and Basurko, O. C. (2022). Modelling floating riverine litter in the south-eastern Bay of Biscay: a regional distribution from a seasonal perspective. *Ocean Sci.* 18, 1703–1724. doi: 10.5194/os-18-1703-2022

Saviano, S., Kalampokis, A., Zambianchi, E., and Uttieri, M. (2019). A year-long assessment of wave measurements retrieved from an HF radar network in the Gulf of Naples (Tyrrhenian Sea, Western Mediterranean Sea). *J. Oper. Oceanogr.* 12, 1–15. doi: 10.1080/1755876X.2019.1565853

Solabarrieta, L., del Campo, A., Alvarez, D., Abalia, A., Nieto, A., Epelde, I., et al. (2022). "Revamping data system and portal in the Basque Operational Oceanography," in *2022 IEEE International Workshop on Metrology for the Sea; Learning to Measure Sea Health Parameters (MetroSea)*, Milazzo, Italy. 193–197. doi: 10.1109/MetroSea55331.2022.9950947

Solabarrieta, L., Frolov, S., Cook, M., Paduan, J., Rubio, A., González, M., et al. (2016). Skill assessment of hf radar–derived products for lagrangian simulations in the bay of biscay. *J. Atmos. Ocean. Tech.* 33, 2585–2597. doi: 10.1175/JTECH-D-16-0045.1

Solabarrieta, L., Rubio, A., Cárdenas, M., Castanedo, S., Esnaola, G., Méndez, F. J., et al. (2015). Probabilistic relationships between wind and surface water circulation patterns in the SE Bay of Biscay. *Ocean Dynam.* 65, 1289–1303. doi: 10.1007/s10236-015-0871-5

Solabarrieta, L., Rubio, A., Castanedo, S., Medina, R., Charria, G., and Hernández, C. (2014). Surface water circulation patterns in the southeastern Bay of Biscay: New evidences from HF radar data. *Cont. Shelf Res.* 74, 60–76. doi: 10.1016/j.csr.2013.11.022

Wyatt, L. R. (2011). "Wave mapping with HF radar," in *IEEE/OES 10th current, waves and turbulence measure-ments (CWTM)*, Monterey, CA, USA. 25–30, IEEE. doi: 10.1109/CWTM.2011.5759519

Wyatt, (2021). "Chapter 6: ocean wave measurements," in eds. W. Huang and E.W. Gil *Ocean Remote Sensing Technologies: High frequency, marine and GNSS-based radar*. IET Digital Library. 2021. doi: 10.1049/SBRA537E_ch6

Wyatt, L. R., and Green, J. J. (2009). "Measuring high and low waves with HF radar," in *OCEANS 2009-EUROPE. Oceans 09: Balancing technology with future needs*, Bremen, Germany, 11-14 May 2009. 1–5. doi: 10.1109/OCEANSE.2009.5278328

Wyatt, L. R., and Green, J. J. (2022). Swell and wind-sea partitioning of HF radar directional spectra. *J. Operational Oceanography* 17, 28–39. doi: 10.1080/1755876X.2022.2127232

Wyatt, L. R., and Green, J. J. (2023). Developments in scope and availability of HF radar wave measurements and robust evaluation of their accuracy. *Remote Sens.* 15 (23), 5536. doi: 10.3390/rs15235536

Wyatt, L. R., Green, J. J., and Middleditch, A. (2010). HF radar data quality requirements for wave measurement. *Coast. Eng.* 58 (4), 327–336. doi: 10.1016/j.coastaleng.2010.11.005

Yang, L., Dang, R., Li, M., Zhao, K., Song, C., and Xu, Z. (2018). A fast calibration method for phased arrays by using the graph coloring theory. *Sensors* 18 (12), 4315. doi: 10.3390/s18124315

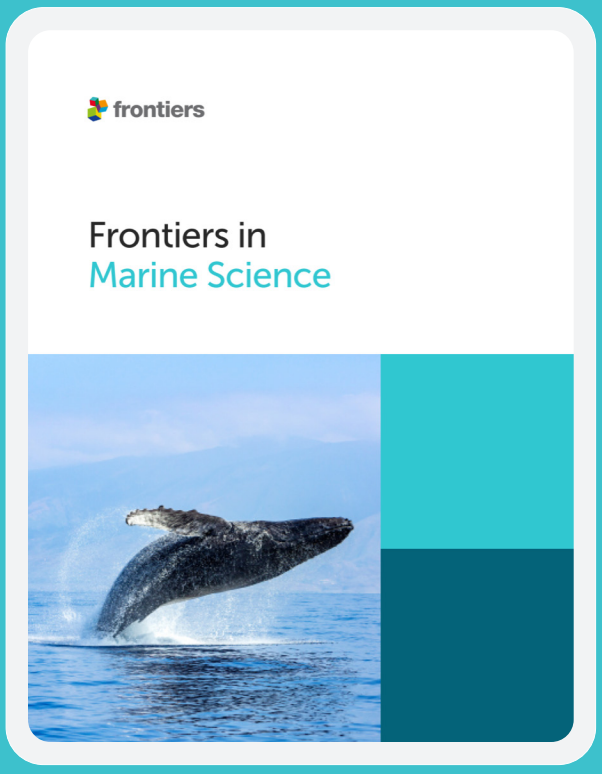
Frontiers in Marine Science

Explores ocean-based solutions for emerging global challenges

The third most-cited marine and freshwater biology journal, advancing our understanding of marine systems and addressing global challenges including overfishing, pollution, and climate change.

Discover the latest Research Topics

See more →



Frontiers

Avenue du Tribunal-Fédéral 34
1005 Lausanne, Switzerland
frontiersin.org

Contact us

+41 (0)21 510 17 00
frontiersin.org/about/contact